

Dissertation zur Erlangung des Doktorgrades  
der Fakultät für Chemie und Pharmazie  
der Ludwig-Maximilians-Universität München

**Azobenzene photoswitches for near-infrared modulation of  
bioactivity and high-performance imaging applications**

Benedikt Baumgartner (geborener Winkler)

aus

Regensburg, Deutschland

2024





### Erklärung

Diese Dissertation wurde im Sinne von §7 der Promotionsordnung vom 28. November 2011 von Herrn Dr. Oliver Thorn-Seshold betreut.

### Eidesstattliche Versicherung

Diese Dissertation wurde eigenständig und ohne unerlaubte Hilfe erarbeitet.

München, 16.09.2024

---

(Benedikt Baumgartner)

Dissertation eingereicht am 27.06.2024

1. Gutachter: Dr. Oliver Thorn-Seshold

2. Gutachter: Prof. Dr. Don C. Lamb

Mündliche Prüfung am 13.09.2024



**Parts of this work have been deposited on a preprint server:**

(1) Benedikt Baumgartner, Viktorija Glembockyte, Alberto J. Gonzalez-Hernandez, Abha Valavalkar, Robert Mayer, Lucy L. Fillbrook, Adrian Müller-Deku, Jinhua Zhang, Florian Steiner, Christoph Gross, Martin Reynders, Hermany Munguba, Anisul Arefin, Armin Ofial, Jonathon E. Beves, Theobald Lohmueller, Benjamin Dietzek-Ivanšić, Johannes Broichhagen, Philip Tinnefeld, Joshua Levitz, Oliver Thorn-Seshold

A general method for near-infrared photoswitching in biology, demonstrated by the >700 nm photocontrol of GPCR activity in brain slices

*ChemRxiv*, **2024**; DOI: 10.26434/chemrxiv-2024-vm4n3

(2) Benedikt Baumgartner, Viktorija Glembockyte, Robert J. Mayer, Alberto J. Gonzalez-Hernandez, Robert O. Kindler, Abha Valavalkar, Alexander J. Wiegand, Adrian Müller-Deku, Lutz Grubert, Florian Steiner, Christoph Gross, Martin Reynders, Vincent Grenier, Johannes Broichhagen, Stefan Hecht, Philip Tinnefeld, Armin R. Ofial, Benjamin Dietzek-Ivanšić, Joshua Levitz, Oliver Thorn-Seshold

Azobenzenes can achieve near-infrared photocontrol in biological systems, with quantitative Z→E photoisomerization, via singlet manifold photoredox

*ChemRxiv*, **2023**; DOI: 10.26434/chemrxiv-2023-37sv4



## Abstract

Visualization and control of cellular pathways in freely-moving, wildtype animals at subcellular and millisecond resolution holds great promise for basic biomedical research in health and disease. Chemical photoswitches, small molecules that can undergo light-induced, reversible isomerizations, are powerful building blocks in material science, data storage, and photopharmacology. In photopharmacology, a photoswitch is integrated in or extended from a bioactive pharmaceutical. Photoswitching between the two isomers triggers a structural change, ideally between more and less active isomers, enabling photocontrol of biological activity with the same high spatial and temporal precision as that with which light can be applied. Azobenzenes are the gold standard for applications in chemical biology, due to their high photostability, large changes of dipole moment, structure, and absorption spectra difference between the isomers, and their efficient photoswitching properties. Within the last decades, huge efforts were performed to optimize azobenzene photoswitches in regards to more complete bidirectional photoswitching, and tuning the isomers' absorption profiles, and  $Z \rightarrow E$  spontaneous relaxation rates. All these approaches required chemical tuning of the azobenzene structure, at huge synthetic cost. Nevertheless, azobenzenes still have not overcome three disadvantages, of: (1) non-quantitative bidirectional switching, due to spectral overlap of  $E$  and  $Z$  isomers, typically causing high background activity in biological experiments; (2) efficient photoswitching only being possible in the UV/blue-cyan spectral region, causing limited applicability for deep tissue and live animal applications; and (3) azobenzenes are non-fluorescent, so their location of action cannot be imaged by fluorescence microscopy, which makes applications in basic and clinical research more tricky.

In this work, I present two generally applicable methods for (near-) quantitative, NIR-induced  $Z \rightarrow E$  isomerization that do not require redesign of the azobenzene.

(1) We show that intramolecular energy transfer from organic fluorophores to azobenzenes induces near-quantitative (up to 98% complete)  $Z \rightarrow E$  isomerization, and can be triggered by NIR illumination (even  $>1000$  nm). We show a general scope, that includes widely-used xanthene-, polymethine- and oxazine-based fluorophores, with a variety of azobenzenes. Furthermore, we prove that this approach is fully biocompatible, by applying it in cell culture and acute mouse brain slices showing the first ever single photon NIR triggered modulation of cellular activity.

(2) We show that intramolecular singlet-manifold photoredox catalysis enables quantitative (100%)  $Z \rightarrow E$  isomerization at up to 740 nm illumination. We provide an oxidation and reduction potential database for  $\sim 30$  azobenzene types and  $\sim 10$  organic fluorophores enabling the prediction of photoredox applicability. We identified the phenoxazine fluorophore Nile Blue as an ideal candidate, as it combines low intersystem crossing quantum yield, high excited state reduction potential and an absorption maximum around 640 nm. Ultrafast transient absorption spectroscopy supports singlet-manifold photoredox catalysis as the major mechanism. We show full biocompatibility of photoredox switching by applying it on the modulation of mGluR2 ion channels in live cells.

The methods advance of *super-resolution microscopy* has increased the resolution of optical microscopy by  $> 20$ -fold. However, fluorophore chemical development has not had a similar breakthrough, meaning that the current state of the art fluorophores have been developed decades ago, for performance in essentially low-demanding applications; and they limit the potential of super-resolution and single molecule localization microscopy techniques.

(3) In an ongoing study, we show an innovative approach based on the energy transfer results from part (1), which utilizes azobenzenes as intramolecular triplet state quenchers enabling extraordinarily photostable fluorophores with drastically increased photon budget, brightness and survival time. For example, AlexaFluor647 is one of the most used fluorophores in single molecule localization microscopy; but our first synthesised conjugate of AlexaFluor647 to an azobenzene photoswitch already delivered 10 times higher photon budget, 3 times higher brightness and 3 times longer survival time compared to parent AlexaFluor647. We prepared a library of 9 additional fluorophore azobenzene conjugates whose evaluation for super-resolution is ongoing. Based on this, we show that in a modular approach, azobenzenes can drastically increase the performance of fluorophores, chemically enabling so-far unimaginable temporal and spatial resolution for fluorescence microscopy.

In summary, the research performed within this PhD thesis shows how azobenzene photoswitches and small molecule organic fluorophores can interplay, to foster each other's beneficial properties, whether as bioactivity actuators enabling precise deep tissue modulation of biological processes, or as superior imaging tools to uncover the mysteries of life.

## Kurzzusammenfassung

Die Visualisierung und Kontrolle zellulärer Vorgänge in sich frei bewegenden Tieren mit subzellulärer und millisekundengenauer Auflösung ist ein vielversprechender Ansatz für die biomedizinische Grundlagenforschung zu Gesundheit und Krankheit. Chemische Photoschalter - kleine Moleküle, die durch Licht reversibel isomerisiert werden können - sind leistungsstarke Bausteine in der Materialwissenschaft, Datenspeicherung und Photopharmakologie. In der Photopharmakologie wird ein Photoschalter in ein bioaktives Arzneimittel integriert oder von diesem abgeleitet. Durch das Umschalten zwischen den beiden Isomeren wird eine strukturelle Veränderung ausgelöst, idealerweise zwischen mehr und weniger aktiven Isomeren, wodurch die biologische Aktivität mit der gleichen hohen räumlichen und zeitlichen Präzision gesteuert werden kann, mit der Licht eingesetzt werden kann. Azobenzole sind der Goldstandard für Anwendungen in der chemischen Biologie, und zwar aufgrund ihrer hohen Photostabilität, der großen Änderungen des Dipolmoments, der Struktur und der Unterschiede in den Absorptionsspektren zwischen den Isomeren sowie ihrer effizienten Photoschalt-Eigenschaften. In den letzten Jahrzehnten wurden enorme Anstrengungen unternommen, um die Azobenzol-Photoschalter im Hinblick auf eine vollständigere bidirektionale Photoschaltung und die Abstimmung der Absorptionsprofile der Isomere und der spontanen  $Z \rightarrow E$ -Relaxationsraten zu optimieren. All diese Ansätze erforderten eine chemische Optimierung der Azobenzolstruktur, welche mit enormem synthetischem Aufwand verbunden war. Dennoch haben die Azobenzole drei Nachteile noch nicht überwunden: (1) nicht-quantitatives bidirektionales Schalten aufgrund der spektralen Überlappung von  $E$ - und  $Z$ -Isomeren, was typischerweise zu einer hohen Hintergrundaktivität in biologischen Experimenten führt; (2) effizientes Photoschalten ist nur im UV/blau-cyan Spektralbereich möglich, was die Anwendbarkeit in tief gelegenem Gewebe und bei lebenden Tieren einschränkt; und (3) Azobenzole sind nicht-fluoreszierend, so dass ihr Wirkungsort nicht durch Fluoreszenzmikroskopie abgebildet werden kann, was Anwendungen in der Grundlagen- und klinischen Forschung erschwert.

In dieser Arbeit stelle ich zwei allgemein anwendbare Methoden für die (nahezu) quantitative, NIR-induzierte  $Z \rightarrow E$ -Isomerisierung vor, die kein Neudesign des Azobenzols erfordern.

(1) Wir zeigen, dass der intramolekulare Energietransfer von organischen Fluorophoren auf Azobenzole eine nahezu quantitative (bis zu 98 % vollständige)  $Z \rightarrow E$ -Isomerisierung induziert und durch NIR-Beleuchtung (sogar  $>1000$  nm) ausgelöst werden kann. Wir zeigen einen allgemeinen Anwendungsbereich, der weit verbreitete Xanthen-, Polymethin- und Oxazin-basierte Fluorophore mit einer Vielzahl von Azobenzolen umfasst. Darüber hinaus beweisen wir, dass dieser Ansatz vollständig biokompatibel ist, indem wir ihn in Zellkulturen und akuten Gehirnschnitten von Mäusen anwenden und die erste durch Einzelphotonen ausgelöste NIR-Modulation der Zellaktivität zeigen.

(2) Wir zeigen, dass durch intramolekulare Singulett-Photoredox-Katalyse eine quantitative (100 %)  $Z \rightarrow E$ -Isomerisierung bei einer Beleuchtung von bis zu 740 nm ermöglicht wird. Wir stellen eine Datenbank mit Oxidations- und Reduktionspotenzialen für  $\sim 30$  Azobenzole und  $\sim 10$  organische Fluorophore zur Verfügung, die eine Vorhersage der Photoredox-Anwendbarkeit ermöglicht. Wir haben das Phenoxazin-Fluorophor Nilblau als idealen Kandidaten identifiziert, da es eine niedrige Quantenausbeute beim Übergang in den Triplet Zustand hat, ein hohes Reduktionspotenzial im angeregten Zustand und ein

Absorptionsmaximum bei 640 nm aufweist. Die ultraschnelle, transiente Absorptionsspektroskopie unterstützt die Singulett-Mannigfaltigkeit der Photoredox-Katalyse als Hauptmechanismus. Wir zeigen die vollständige Biokompatibilität der Photoredox-Schaltung, indem wir sie auf die Modulation von mGluR2-Ionenkanälen in lebenden Zellen anwenden.

Der methodische Fortschritt in der superhoch aufgelösten Mikroskopie hat die Auflösung der optischen Mikroskopie um mehr als das 20-fache erhöht. Die chemische Entwicklung von Fluorophoren hat jedoch keinen vergleichbaren Durchbruch erzielt, was bedeutet, dass die derzeitigen modernen Fluorophore vor Jahrzehnten für Anwendungen mit geringen Anforderungen entwickelt wurden und das Potenzial der Superauflösungs- und Einzelmolekül-Lokalisierungsmikroskopietechniken einschränken.

(3) In einer laufenden Studie zeigen wir einen innovativen Ansatz, der auf den Ergebnissen aus Teil (1) basiert und Azobenzole als intramolekulare Triplett-Zustandslöscher einsetzt, die außerordentlich photostabile Fluorophore mit drastisch erhöhtem Photonenbudget, Helligkeit und Überlebensdauer ermöglichen. AlexaFluor647 beispielsweise ist eines der am häufigsten verwendeten Fluorophore in der Einzelmolekül-Lokalisierungsmikroskopie. Unser erstes synthetisiertes Konjugat von AlexaFluor647 mit einem Azobenzol-Photoschalter lieferte jedoch bereits ein 10-mal höheres Photonenbudget, eine 3-mal höhere Helligkeit und eine 3-mal längere Überlebenszeit im Vergleich zum ursprünglichen AlexaFluor647. Wir haben eine Bibliothek mit 9 weiteren Fluorophor-Azobenzol-Konjugaten erstellt, deren Bewertung für die Superauflösung derzeit läuft. Auf dieser Grundlage zeigen wir, dass Azobenzole in einem modularen Ansatz die Leistung von Fluorophoren drastisch erhöhen können und auf chemischem Wege eine bisher unvorstellbare zeitliche und räumliche Auflösung für die Fluoreszenzmikroskopie ermöglichen.

Zusammenfassend zeigt die im Rahmen dieser Doktorarbeit durchgeführte Forschung, wie Azobenzol-Photoschalter und organische Fluorophore zusammenwirken können, um die vorteilhaften Eigenschaften des jeweils anderen zu fördern, sei es als bioaktive Aktoren, die eine präzise Modulation biologischer Prozesse im tief gelegenen Gewebe ermöglichen, oder als überlegene Bildgebungsinstrumente, um die Geheimnisse des Lebens zu ergründen.



## Table of contents

<b>1</b>	<b>Introduction</b>	<b>3</b>
1.1	Small-molecule photoswitches	3
1.1.1	N=N double bond-based photoswitches	4
1.1.2	Approaches for red-shifting absorption wavelengths of azobenzenes	6
1.1.3	Assisted $Z \rightarrow E$ isomerization of azobenzene	8
1.2	Artificial control of biological phenomena by light	14
1.2.1	Optogenetics	14
1.2.2	Photocages	15
1.2.3	Photopharmacology with photoswitches	17
1.3	Fluorophores for single molecule localization- and super resolution microscopy	25
1.3.1	Imaging beyond the classical resolution limit	25
1.3.2	Photoinstability problems of organic fluorophores	26
1.3.3	Increasing the photostability and performance of organic fluorophores	28
1.3.4	Azobenzenes having ultra-short lived low lying triplet states	30
<b>2</b>	<b>Aims of the thesis</b>	<b>33</b>
<b>3</b>	<b>PhD Research</b>	<b>35</b>
3.1	A general method for near-infrared photoswitching in biology, demonstrated by the >700 nm photocontrol of GPCR activity in brain slices	35
3.2	Azobenzenes can achieve near-infrared photocontrol in biological systems, with quantitative $Z \rightarrow E$ photoisomerization, via singlet manifold photoredox	50
<b>4</b>	<b>Ongoing projects</b>	<b>62</b>
4.1	Single-photon photoisomerization of azobenzenes above 1000 nm enabled by energy transfer from a polymethine dye	62
4.2	Azobenzene photoswitches as next generation photostabilizing agents for single molecule localization and super resolution microscopy	64
<b>5</b>	<b>Summary and Outlook</b>	<b>69</b>
5.1	Summary	69
5.2	Outlook I: NIR triggered energy transfer enables $E \rightarrow Z$ photoisomerization of stilbene photoswitches for <i>in vivo</i> photopharmacology	72
5.3	Outlook II: Dual-colour photouncaging for convenient red-light release of APIs	75
<b>6</b>	<b>References</b>	<b>77</b>
<b>7</b>	<b>Appendix</b>	<b>91</b>
7.1	Supporting Information to chapter 3.1	91
7.2	Supporting Information to chapter 3.2	205
7.3	Supporting Information to chapter 4.1	291
7.4	Supporting Information to chapter 4.2	293

7.5	Supporting Information to chapter 5.2	322
<b>8</b>	<b>Abbreviations</b>	<b>325</b>
<b>9</b>	<b>Acknowledgements</b>	<b>327</b>

## 1 Introduction

Light is a fundamental energy source for all domains of life. Especially in photosynthesis, plants, algae and cyanobacteria use light to convert carbon dioxide and water into chemical energy (carbohydrates) and oxygen. Huber, Deisenhofer and Michel pioneered our understanding of how nature harvests light energy by solving the crystal structures of the transmembrane proteins of photosynthesis, resulting in their 1988 Chemistry Nobel prize.<sup>1</sup>

Motion is also fundamental for biology. In the reverse reaction of photosynthesis, chemical energy, e.g. locked in the carbohydrates produced by photosynthesis, are metabolized to drive the production of adenosine triphosphate (ATP), an energy currency in all forms of life. ATP is produced by the "splendid molecular machine"<sup>2</sup> called ATP synthase, for whose discovery Boyer, Skou and Walker were awarded the 1997 Chemistry Nobel prize. ATP goes on to drive a multitude of biochemical processes, including the macro-scale motions resulting from muscle contractions and thus the physical locomotion of living organisms.<sup>2,3</sup> Inspired by nature and by supramolecular chemistry (1987 Chemistry Nobel prize for Lehn, Cram and Pederson for the discovery of cryptands), researchers began investigating artificial molecular machines. "A 'molecular machine' is a system in which a stimulus triggers the controlled motion of one molecular or submolecular component relative to another, potentially resulting in a net task being performed."<sup>4</sup> For example, a molecular motor converts chemical, thermal or light energy into kinetic energy and thereby make things move.<sup>5</sup> The first examples of artificial molecular machines started with the discovery of catenanes (two physically interlocked rings) by Jean-Pierre Sauvage, and rotaxanes by Sir Fraser Stoddart.<sup>6</sup> Further progress by Feringa developing the first light driven molecular rotor in 1999<sup>7</sup> and the a "nano car" in 2011<sup>8</sup> resulted in their shared 2016 Chemistry Nobel prize for molecular machines.

Stoddart had suggested already in 2000 that photons and electrons are the best energy sources for molecular machines.<sup>9</sup> These are the energy sources that power this PhD.

### 1.1 Small-molecule photoswitches

Small-molecule photoswitches are molecules that can undergo reversible structural changes under illuminations by light at different wavelengths. The most prominent classes of photoswitches (**Figure 1**) show light-induced structural changes either by  $E \leftrightarrow Z$  double bond isomerization, or by electrocyclization. Since the discovery of azobenzene in 1834 by Eilhard Mitscherlich<sup>10</sup> and its light-induced reversible photoswitching by Hartley in 1937,<sup>11</sup> a variety of photochromic molecules have been developed and applied in many fields including data storage<sup>12</sup>, material science<sup>13</sup> and photopharmacology<sup>14</sup>. Depending on the targeted performance or application there are several criteria for designing a molecular photoswitch:<sup>15</sup> (1) absorption band separation between the isomers; (2) reversibility and bidirectional switching; (3) rapid thermal relaxation to thermodynamically stable isomer (T-type), or bistable isomers (P-type); (4) excitation wavelength; (5) easy and reliable synthetic access.

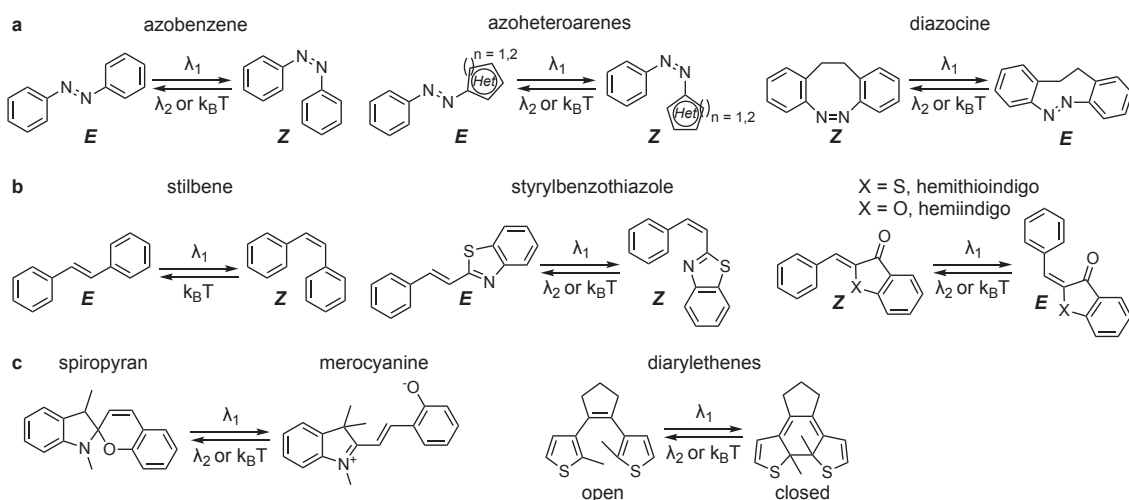


**Figure 1:** Examples for a) N=N double bond isomerization-based photoswitches; b) C=C double bond isomerization-based photoswitches; c) 6 $\pi$  electron cyclisation-based photoswitches.

N=N double bond-based photoswitches (**Figure 1a**) and especially azobenzenes are by far the most present class of molecular photoswitches and will be discussed in detail in the next chapter. Small-molecule photoswitches that rely on  $E \leftrightarrow Z$  isomerization of a C=C double bond include stilbenes, heterostilbenes (e.g. styrylbenzothiazoles) and hemi(thio)indigos (**Figure 1b**). Stilbenes can undergo isomerization from their stable *E* to the metastable *Z* isomer by illumination with UV light around 300 nm. The spontaneous  $Z \rightarrow E$  reaction is hindered by a high energetic barrier (~41–46 kcal/mol) but partial conversion can be achieved by light at 280 nm, though this can also cause irreversible side reactions such as 6 $\pi$ -electrocyclisation or photoinduced [2+2] cycloaddition.<sup>16–18</sup> Compared to these, heterostilbenes like styrylbenzothiazoles can have slightly red-shifted absorption spectra of the *E* isomer, allowing substantially complete  $E \rightarrow Z$  photoisomerization with light at 360 nm; and some back-isomerization to re-enrich the *E* isomer is also possible by illumination at 420 nm, without causing such photochemical degradation.<sup>19</sup> However, for near-complete bidirectional “C=C” switching, indigoids such as hemithioindigos are the photoswitches of choice. They can be robustly switched between their thermodynamically stable *Z* and metastable *E* isomers and backwards using blue light ( $Z \rightarrow E$ ; quantum yield ~12%) and green light ( $E \rightarrow Z$ ; ~5%).<sup>20</sup> Near quantitative bidirectional photoswitching can be achieved by substituent tuning.<sup>21</sup>

A second class of photoswitches relies on reversible 6 $\pi$  electrocyclisations. The important representatives include diarylethenes and spiropyran-merocyanines (SP-MCs). Diarylethene can be switched between its stable open, and the metastable closed, forms. In SP-MC type photoswitches, it is usually the spiropyran closed form that is thermodynamically more stable than the open merocyanine form. Both types have been used for a variety of applications in data storage and material science.<sup>22–26</sup> A recent application of SP-MCs has been shown by Hecht and coworkers.<sup>13</sup> In their study they introduce xolography, a volumetric 3D printing method where they use SP-MCs as photoswitchable photoinitiators for local polymerization. Xolography is dual wavelength induced, wherein one wavelength induces the opening of the SP-MC and the second wavelength initiates the polymerization reaction, which is only possible in the open merocyanine form.

### 1.1.1 N=N double bond-based photoswitches

Azobenzenes are the most used class of small molecule photoswitches. They can be switched from a thermodynamically stable *E* isomer towards the metastable *Z* isomer by UV/blue light,

and backwards by cyan/green light (**Figure 2a**).<sup>27</sup> The  $\pi \rightarrow \pi^*$  ( $S_0 \rightarrow S_2$ ) and  $n \rightarrow \pi^*$  ( $S_0 \rightarrow S_1$ ) bands are the two transitions per isomer that must be considered to understand the direct photoisomerisation of azobenzenes. The *E* isomer has an intense  $\pi \rightarrow \pi^*$  ( $S_0 \rightarrow S_2$ ) and a weak  $n \rightarrow \pi^*$  transition band ( $S_0 \rightarrow S_1$ ). The *Z* isomer has a more intense  $n \rightarrow \pi^*$  transition band than the *E* isomer but a less intense  $\pi \rightarrow \pi^*$  band; and crucially the ( $S_0 \rightarrow S_2$ ) band of the *Z* isomer is at shorter wavelength, and the ( $S_0 \rightarrow S_1$ ) at longer wavelength, than those of the *E* isomer, so that there is only partial spectral overlap of *E* and *Z* isomer absorptions (**Figure 2b**): this allows partially selective excitation of the *E* or the *Z* isomer at UV ( $\pi \rightarrow \pi^*$ ; mainly *E* isomer) or cyan ( $n \rightarrow \pi^*$ ; mainly *Z* isomer) spectral regions respectively, resulting in net photoswitching towards the opposite isomer. However, the residual spectral overlap prevents complete bidirectional switching: typically, populations of 80-95% *Z* isomer and 70-85% *E* isomer are yielded at the "optimal" UV and cyan wavelengths for photoswitching completeness, respectively (PSS<sub>365</sub> and PSS<sub>490</sub> in **Figure 2b**). The *E/Z* isomer ratio reached under illumination at a certain wavelength of light is called a photostationary state (PSS). The PSS is a real photoequilibrium under saturated illumination conditions and is dependent on the quantum yields for *E*→*Z* and *Z*→*E* isomerization and the molar extinction coefficient  $\epsilon$  at the wavelength of illumination.<sup>15</sup>

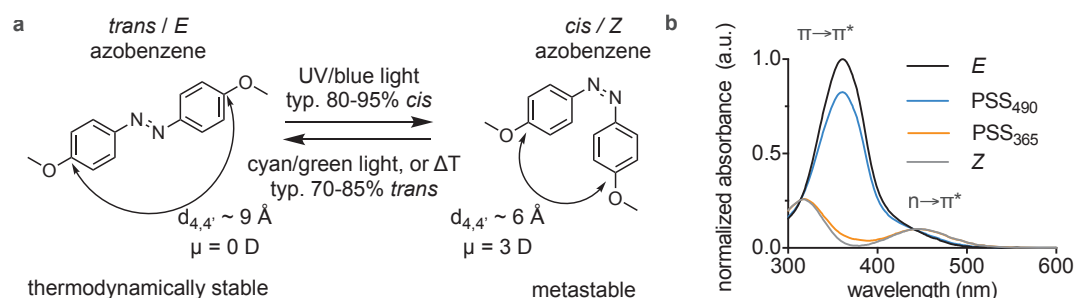


**Figure 2:** a) characteristics on *E* and *Z* isomer of azobenzene photoswitches; b) relative UV/Vis spectra of pure *E* and *Z* isomer of 4,4'-bismethoxy-azobenzene and the photostationary states at 365 nm (mainly *Z* isomer) and 490 nm (mainly *E* isomer).

The energy and strength of these four absorption bands can be substantially affected by structure. For example, bathochromic shifts of all bands result if the azobenzene is substituted with electron donating groups in *ortho* or *para* positions, or has a 4,4'-push-pull substitution pattern (more details below).<sup>15,28</sup> The rate of spontaneous ("thermal") *Z*→*E* relaxation can also be tuned by substitution pattern: half-times for *Z*→*E* relaxation at room temperature can range from years (for tetra-*ortho*-fluoro substitution<sup>29</sup>) to milliseconds (4,4'-push-pull substitution<sup>30</sup>) or below. Those properties are also environment-dependent (solvent, pH, polarity, H-bonding,  $\pi$ -stacking, *H*- or *J*-aggregate formation, etc).

Moving beyond tuning only the substitution pattern of azobenzenes to alter their photoresponse or relaxation rates, Fuchter, Ravoo, and coworkers instead pioneered the applications of heteroarylazobenzenes.<sup>31,32</sup> By substituting one phenyl ring of azobenzenes with e.g., a 3-methylpyrazole (**Figure 3a**) the  $\pi \rightarrow \pi^*$  transitions of the *E* and *Z* isomers become more separated (very hypsochromic *Z*- $\pi \rightarrow \pi^*$  shift, now allowing near-quantitative *E*→*Z* photoswitching: >98% *Z* isomer at PSS 355 nm;  $\Delta\lambda_{\max}(\pi \rightarrow \pi^*_{E-Z}) = -48$  nm); and although the *E* and *Z*  $n \rightarrow \pi^*$  transitions overlap, high-*E* PSSs are possible by illuminating in the long-wavelength tail of this band (97% *E* isomer at 532 nm) which is assigned to a difference in the oscillator strength (probability of absorption) of the  $n \rightarrow \pi^*$  transition that is higher in the T-shaped *Z*-isomer compared to the flat *E* isomer. Nevertheless, their population-level

photoswitching kinetics become slower, particularly at 532 nm for  $Z \rightarrow E$  switching due to low extinction coefficients (**Figure 3b** uses 40-fold more intense light at 532 nm than 355 nm).

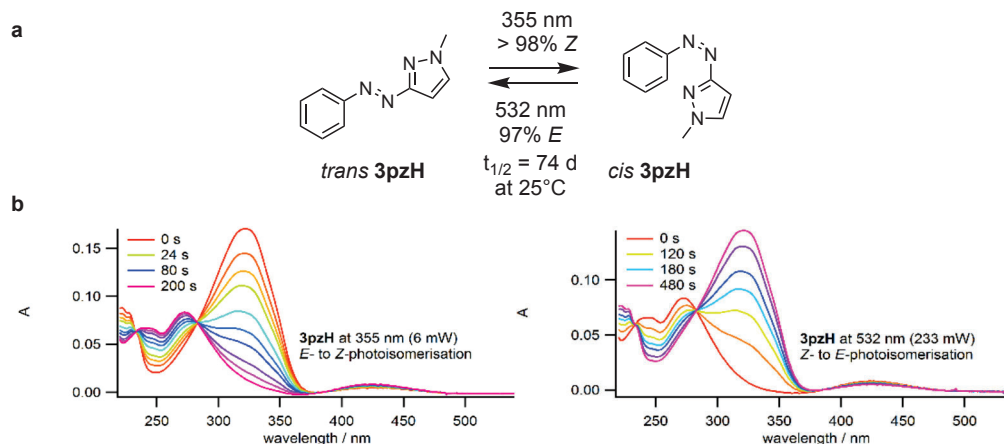


**Figure 3:** a) Photoisomerization properties of heteroarylazobenzene **3pzH**, including isomeric ratio at different PSS and thermal half-time; b) UV/Vis absorption spectra indicating change over time during illumination for  $E \rightarrow Z$  (left) and  $Z \rightarrow E$  (right) isomerization under 355 nm and 532 nm laser illumination, respectively. Panel b) was reprinted with permission from Fuchter, *JACS*, **2017**<sup>33</sup>, open access article, Copyright © 2016, American Chemical Society.

Heteroarylazobenzenes' dipole moment can easily be tuned towards long thermal relaxation half-times ( $\sim 74$  days for  $Z$ -**3pzH**, **Figure 3a**), improved solubility in aqueous buffer, reduced lipophilicity, and perhaps increased metabolic stability. These characteristics may increase their druglikeness and be beneficial for applications in e.g. photopharmacology.<sup>32,33</sup>

### 1.1.2 Approaches for red-shifting absorption wavelengths of azobenzenes

Azobenzenes and related photoswitches have gained much attention for their robust photoswitching and for several impressive applications in basic research (e.g., biological applications in ion channel modulation<sup>34</sup>, targeted protein degradation<sup>35</sup> and cytoskeleton research<sup>14</sup>). Nevertheless, they suffer some important limitations that largely prevent them from reaching applications beyond fundamental research. A major drawback is their limited photoswitch wavelength response. Azobenzenes typically switch from  $E \rightarrow Z$  in the UV/blue and  $Z \rightarrow E$  in the cyan/green. For example, applications in complex biological tissue or live animal settings would essentially require wavelengths within the biological transparency window (between 600–1100 nm)<sup>36</sup> to enable deep tissue penetration and avoid phototoxicity.<sup>28,37–40</sup> Over the last 10–15 years several attempts have been performed to shift the single-photon-photoresponse towards low-energy red light. The most important ones are discussed in the following section.

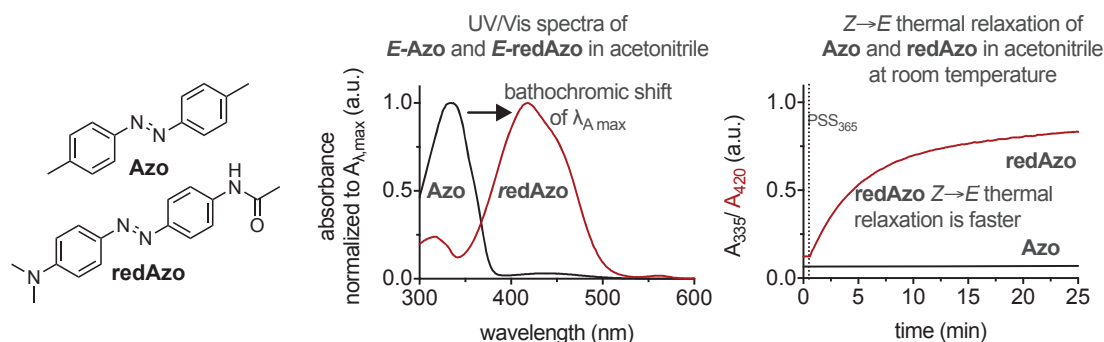


**Figure 4:** Chemical structures (left), difference in absorption spectra (middle) and thermal driven  $Z \rightarrow E$  isomerization (right) of azobenzenes **Azo** (R = alkyl) and electron-rich substituted **redAzo** (data measured for Chapter 3.1).



Azobenzenes with electron-donating substituents in both *para* positions of the N=N double bond have red-shifted absorption maxima (**redAzo**, **Figure 4**). Even further shifted maxima can be obtained by so-called “push-pull” azobenzenes with an electron-donating substituent on one side of the azobenzene and an electron-withdrawing one on the other,<sup>15,28</sup> which allow visible light  $E \rightarrow Z$  photoswitching (in the blue/green).

However, electron-rich and push-pull substitution patterns also shorten thermal half-times from minutes down to milliseconds (**Figure 4**, right), which can be beneficial or detrimental depending on the targeted application.<sup>30,41</sup> Alternative ways to red-shift the absorption wavelengths while maintaining good thermal stability of the *Z*-isomer (often abbreviated as “azobenzene bistability”) were pioneered and popularised by Hecht and Woolley (**Figure 5**),<sup>29,42</sup> with tetra-*ortho*-substitution patterns that allow near-quantitative, visible light photoswitching for both  $E \rightarrow Z$  (green) and  $Z \rightarrow E$  (violet/blue) photoisomerizations; tremendously slow  $Z \rightarrow E$  relaxation (often termed “*Z* isomer stability”) is also possible, with half-lives up to 2 years.<sup>29</sup> Hecht and coworkers introduced tetra-*ortho*-fluoro-substituted azobenzenes, that allow bidirectional isomerisation just by illuminations of the  $n \rightarrow \pi^*$  transition, since this is well separated between a very hypsochromically shifted *Z* isomer (fluorine substituents are responsible for lower n-orbital energies), and the relatively unaffected *E* isomer (separation up to 50 nm with electron withdrawing groups in both *para* positions). Tetra-*ortho*-methoxy substituted azobenzenes, introduced by Woolley and coworkers, show  $E \rightarrow Z$  isomerization up to 660 nm.<sup>42</sup> The  $n \rightarrow \pi^*$  transition in the *E* isomer is bathochromically shifted since the *E* isomer has a higher n-orbital energy, due to electron repulsion of the nitrogen and oxygen lone-pairs. Easier synthetic access was enabled by the works of Konrad and Trauner, and Müller-Deku and Thorn-Seshold, who introduced catalytic methods for late stage tetra-*ortho*-chloro and -alkoxy substitution of azobenzenes, respectively.<sup>43,44</sup> Mixed tetra-*ortho*-substitution patterns have been studied by Konrad and Thorn-Seshold (**Figure 5**).<sup>44,45</sup>

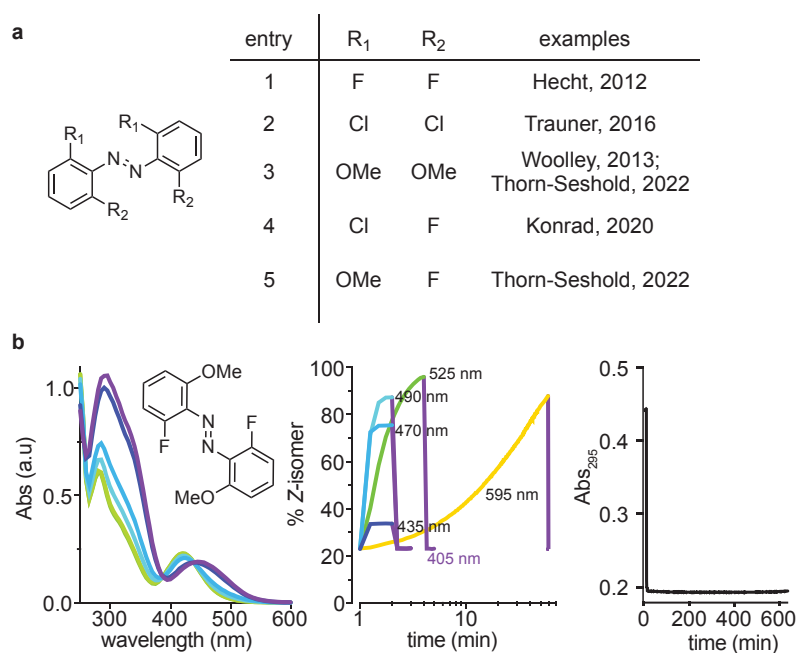


**Figure 5:** a) Examples for tetra-*ortho*-substituted azobenzenes: F<sub>4</sub><sup>29</sup>, Cl<sub>4</sub><sup>43</sup>, OMe<sub>4</sub><sup>42,44</sup>, Cl<sub>2</sub>F<sub>2</sub><sup>45</sup>, OMe<sub>2</sub>F<sub>2</sub><sup>44</sup>; b) UV/Vis absorption spectra of a OMe<sub>2</sub>F<sub>2</sub> tetra-*ortho*-substituted azobenzene at different photostationary states (left) photoswitch kinetics at different wavelength illumination (middle) and thermal stability of *Z* isomer (right, no change in absorbance, i.e. no thermally induced  $Z \rightarrow E$  isomerization). Panel b) was reprinted with permission from Thorn-Seshold, *JOC*, **2022**<sup>44</sup>, Copyright © 2022, American Chemical Society.

A third approach for red-shifting the absorption wavelengths of N=N double bond-based photoswitches was pioneered by Herges and augmented by Trauner, by introducing diazocines, i.e. *ortho*-bridged cyclic 8-membered azobenzenes (**Figure 6**).<sup>46–49</sup> Diazocines show inverse thermodynamic isomer preference compared to standard azobenzenes: the thermodynamically stable isomer is the *Z*, which can be switched to the metastable *E* isomer by blue light (~400 nm), with *E*→*Z* switching by green light (~520 nm). Both isomers are non-planar, causing a separation of the  $n\rightarrow\pi^*$  bands. Photoswitching in both directions is near-quantitative (*E*→*Z* > 95% and *Z*→*E* ~ 90%) for unsubstituted diazocine but is highly dependent on the substitution pattern (e.g. 3,3'-bismethoxydiazocine, compound 34 in Trauner's JACS 2019 paper, only reaches 45% *E* isomer<sup>48</sup>). Diazocines have higher quantum yields compared to azobenzenes (diazocine:  $\phi_{Z\rightarrow E} = 0.7$  at 385 nm and  $\phi_{E\rightarrow Z} = 0.9$  at 520 nm vs. azobenzene:  $\phi_{Z\rightarrow E} = 0.47$  at 436 nm and  $\phi_{E\rightarrow Z} = 0.16$  at 317 nm) but vastly lower molar extinction coefficients, which can compromise their utility in settings where overall light exposure needs should be minimised: such as in biology.<sup>50</sup>

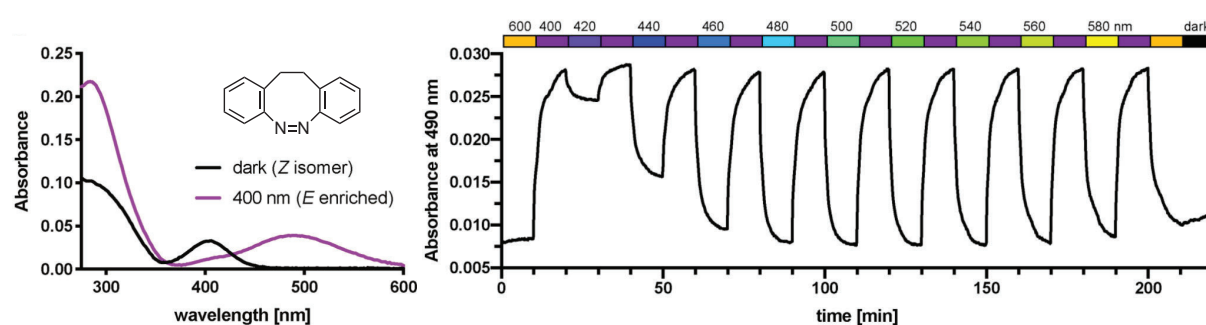


**Figure 6:** UV/Vis absorption spectrum of diazocine (compound 2) at *Z* enriched dark and *E* enriched (after illumination with 400 nm light) photostationary states; measured 50 μM in DMSO (left) and photoswitch response under illumination of different colors of light (right). Reprinted with permission from Trauner, *JACS*, 2019<sup>48</sup>, Copyright © 2019, American Chemical Society.

### 1.1.3 Assisted *Z*→*E* isomerization of azobenzene

Besides auxochrome- or structure-based tuning of azobenzenes' "direct" photoswitching properties (light is absorbed by the azoarene itself: chapter 1.1.2), methods for "assisted" or "indirect" isomerization have also been developed, where the energy required for isomerisation is initially harvested by another chromophore. These assisted methods enable photoswitching that is independent of the absorption spectra or quantum yields of the azobenzene itself. Two methods have gained most attention and will be discussed in detail in the following section: *Z*→*E* isomerization by triplet energy transfer (TET), and *Z*→*E* isomerization by photoinduced electron transfer (PET).



### 1.1.3.1 Triplet Energy Transfer (TET) triggered Z→E isomerization of azobenzene

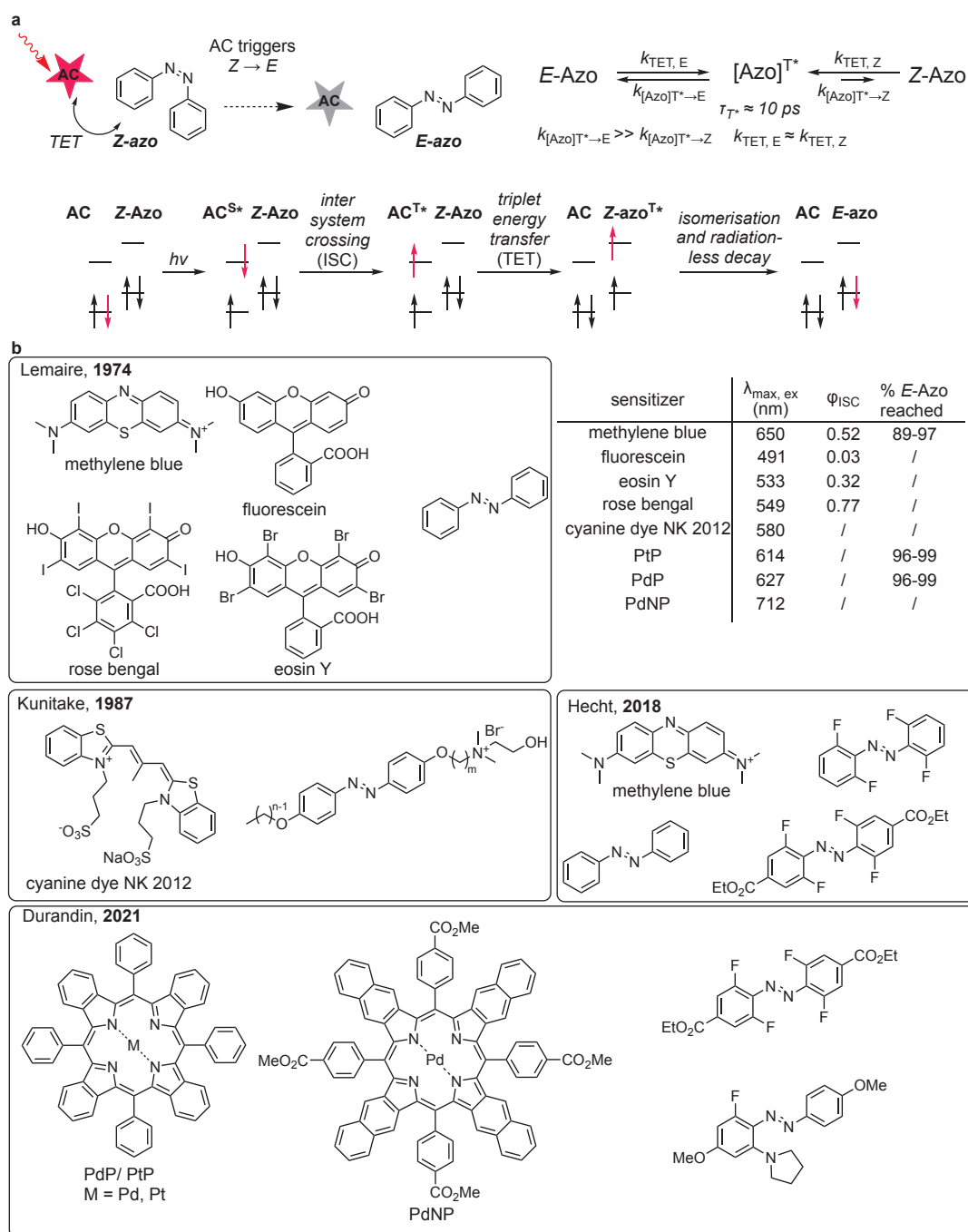


**Figure 7:** a) proposed mechanism for TET based Z→E isomerization of azobenzenes; b) literature examples of azobenzene and triplet sensitizers: Lemaire, 1974<sup>51,52</sup>; Kunitake, 1987<sup>53</sup>; Hecht, 2018<sup>54</sup>; Durandin, 2021<sup>55</sup>; table (right) summarizes  $\phi_{\text{ISC}}$  of triplet sensitizers and photostationary state in % E isomer reached after sensitization.

TET is a prominent energy transfer pathway in photophysics and photochemistry. The triplet sensitizer itself should reach  $T_1$  after excitation from  $S_0$  to  $S_1$  if intersystem crossing (ISC) is efficient (high ISC quantum yield,  $\phi_{\text{ISC}}$ ) (Figure 7a). Then, in TET, the  $T_1$  triplet sensitizer collides with and transfers its energy and spin to another molecule in its ground state (triplet acceptor), yielding the triplet sensitizer in its  $S_0$  ground state and the triplet acceptor in its triplet excited state  $T_1$ . The efficiency of TET is most dependent on thermodynamics and collision rate. TET is rapid if the triplet energy  $E_T$  of the triplet sensitizer is higher than that of the triplet acceptor (exergonic), but can also happen endergonically, if a subsequent reaction

of the triplet acceptor occurs rapidly. In a bimolecular sensitization reaction the collision rate is dependent on the diffusion speeds.<sup>56,57</sup>

Azobenzenes are known to have a low-lying triplet state (~120–160 kJ/mol) and a very short triplet lifetime  $\tau_{\text{triplet}} \sim 10$  ps.<sup>58–61</sup> These properties have been exploited in several studies to control the isomeric ratio of azobenzenes by TET from triplet sensitizers.<sup>51,53–55</sup> Once triplet energy has been transferred to a typical azobenzene, its  $T_1$  relaxes mainly to the *E* isomer ("TET-stationary-state" can contain e.g. ~98% *E* isomer). Orlandi and coworkers studied the mechanism of *Z*→*E* isomerization of azobenzenes and showed that the  $T_1$  minimum of the potential energy surface (PES) is located at a twisted geometry that is below the ground state transition energy barrier between *Z* and *E* azobenzene (**Figure 8**, orange line represents PES of  $T_1$ , blue line represents PES of  $S_0$ ). The lower energy crossing point of PES  $T_1$  with PES  $S_0$  (red circle) is located on the side of the *E* isomer's energy minimum, close to the minimum of the  $T_1$  PES, favouring the decay of the triplet into the *E* isomer. This confirms the plausibility of quantum yields for TET-based *Z*→*E* isomerization close to 1 and *E*→*Z* isomerization around 0.01.<sup>61</sup> TET-based isomerization of azobenzenes thus enables a powerful pathway for near-quantitative *Z*→*E* isomerization of azobenzenes, independent of the azobenzene's own spectral absorption or of the thermal stability of its *Z* isomer.

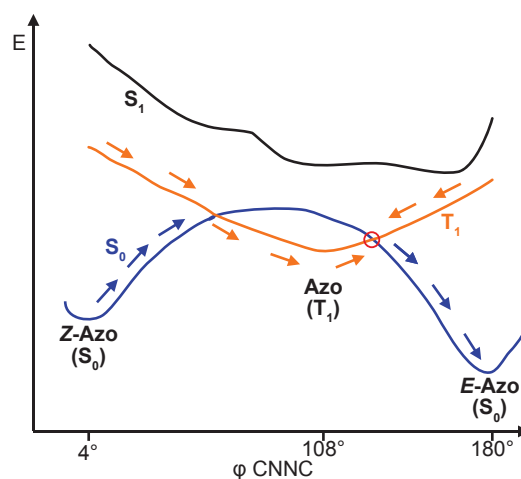


**Figure 8:** Potential energy surface of azobenzenes  $S_0$  ground state,  $S_1$  excited singlet state and  $T_1$  excited triplet state. Adapted from Orlandi, JACS, 2004<sup>61</sup>.

The first example of TET-based azobenzene isomerization was shown by Lemaire and colleagues already in 1974 (**Figure 7b**).<sup>51</sup> They show that unsubstituted azobenzene's *Z*→*E* photoisomerization can be sensitized by organic small molecules with low-lying triplet-state-energy: xanthene-based chromophores Rose Bengal, Eosin Y, and fluorescein, and the thiazine-based Methylene Blue (MB). For example, Rose Bengal sensitizes the photoisomerization under 546 nm to yield a TET-stationary state of 95% *E* isomer. In 1987, Shimomura and Kunitake investigated the photoswitching of azobenzene-lipid-containing bilayers in the presence of substoichiometric, membrane-bound cyanine dye NK 2012 (**Figure 7b**).<sup>53</sup> The cyanine dye was able to catalyze *Z*→*E* isomerization of the azobenzenes within the bilayer membrane, which was attributed to TET from the cyanine dye to the azobenzene. These reports were seminal, but seemingly forgotten for 30 years. In this time, hundreds of azobenzene-chromophore conjugates have been developed, particularly as enzymatically unquenchable FRET probes<sup>62–64</sup> although also as fluorescently tagged azobenzenes.<sup>65,66</sup> However, it seems that only one observation of single-photon TET-based

isomerisation was published in this time, although its basis had been unexplained by the authors.<sup>67</sup>

The topic was soundly resurrected with the 2018 work of Hecht and coworkers.<sup>54</sup> While studying photoinduced electron transfer-based isomerization of azobenzenes (see **chapter 1.1.3.2**) they found that azobenzenes which could not be photooxidized to a radical cation by the triplet-manifold photooxidant MB were still isomerized towards the *E* isomer under MB excitation at 660 nm (**Figure 7b**), reaching TET-SSs ranging from 89-97% *E* isomer, dependent on the electronic properties of the azobenzene. In 2021, Durandin and Priimagi shifted the wavelength used for TET-based *Z*→*E* isomerization even further towards the NIR.<sup>55</sup> Applying Pd/Pt porphyrins (**Figure 7b**) as triplet sensitizers, they could reach up to 99% *E* isomer of a tetra-*ortho*-fluorinated azobenzene at up to 770 nm. Interestingly, they also reported that TET is also possible at endothermic conditions ( $E_T$  of the sensitizers is substantially (>0.2 eV) lower than  $E_T$  of the azobenzenes, which was said to be compensated by entropy). Both Hecht and Durandin showed that the triplet sensitizers used in their studies suffer photoinduced degradation (photobleaching) when TET-based isomerization was performed under air, which drastically limits the application of the systems.

### 1.1.3.2 Photoredox- and electrocatalysis enables quantitative *Z*→*E* isomerization of azobenzenes

Hecht and coworkers showed in three pioneering publications in 2017 and 2018 that azobenzenes can be quantitatively switched from their majority *Z*-PSS to all-*E* isomer by electro and/or photoredox catalysis.<sup>54,68,69</sup> In the first "radical anion" publication,<sup>68</sup> it is shown that *Z* and *E* azobenzene isomers can be electrochemically reduced to their radical anions  $Z^{\cdot-}$  and  $E^{\cdot-}$ , respectively. The *bulk* absorption spectra of the reduced anion samples were however identical, which was interpreted as indicating a very fast transformation of  $Z^{\cdot-}$ → $E^{\cdot-}$  (this thermal relaxation being calculated as  $10^{13}$  times faster than for neutral *Z*→*E*: **Figure 9**, top right). They support that this isomerization mechanism is catalytic, as a substoichiometric number of electrons could achieve full conversion towards the *E* isomer: presenting the model that any reduced  $Z^{\cdot-}$  rapidly relaxes to  $E^{\cdot-}$ , which transfers an electron to another neutral *Z* isomer, propagating relaxation as a chain reaction. Thus, reduction can perform quantitative *Z*→*E* electroswitching, at least in principle. Furthermore, they showed that the reduction to the radical anion can also be induced by triplet manifold photoelectron transfer (PET) (mechanism, **Figure 9a** bottom). A known PET iridium complex, whose excited state oxidation potential matches the ground state reduction potential of the azobenzene, was added to a solution of azobenzene at a *Z*-enriched PSS; its photoexcitation catalyzed formation of an *E*-enriched stationary state (photocatalyst up to 10 mol-%; **Figure 9b**, top left). Critical defects of the PET-system were that (a) quantitative PET-driven isomerization to the *E* isomer was not achieved, due to strong absorption by the azobenzene at the wavelength needed for the photoredox catalyst (365 nm: direct isomerisation competes with PET-driven isomerisation), which resulted in only a 76% *E* PSS, that is less complete than direct azobenzene isomerisation at longer wavelengths; (b) inert-atmosphere conditions were needed for effective PET-isomerisation, since molecular oxygen acts as a competing quencher of the iridium-complex triplet state; (c) population switching relies on collision with the catalyst: so the population switching rate is strongly dependent on the overall concentration.

In a follow-up radical anion study,<sup>69</sup> an improved system was shown, with a tetra-*ortho*-fluoro azobenzene (good separation of  $n$ → $\pi^*$  bands) that can be directly switched from *E*→*Z* with green light (reaching 89% *Z* isomer at  $\lambda = 500$  nm), then isomerized from *Z*→*E* by triplet-

manifold photoredox catalysis ( $\lambda = 380$  nm) from a covalently coupled iridium complex (**Figure 9b**, top right). The wavelength used to drive the photoredox catalyst for the  $Z \rightarrow E$  step was intended to cause less direct excitation of the azobenzene, by positioning at an absorption minimum between the azobenzene's  $\pi \rightarrow \pi^*$  and  $n \rightarrow \pi^*$  bands, but still only 76%  $E$  was reached at 380 nm. Beneficially, covalent coupling of azobenzene and photoredox catalyst allowed efficient switching by PET, at concentrations below 10  $\mu\text{M}$  where intermolecular PET was inefficient. However, the presence or absence of oxygen still strongly affected performance: the PSS at 380 nm was 53%  $E$  when aerated.

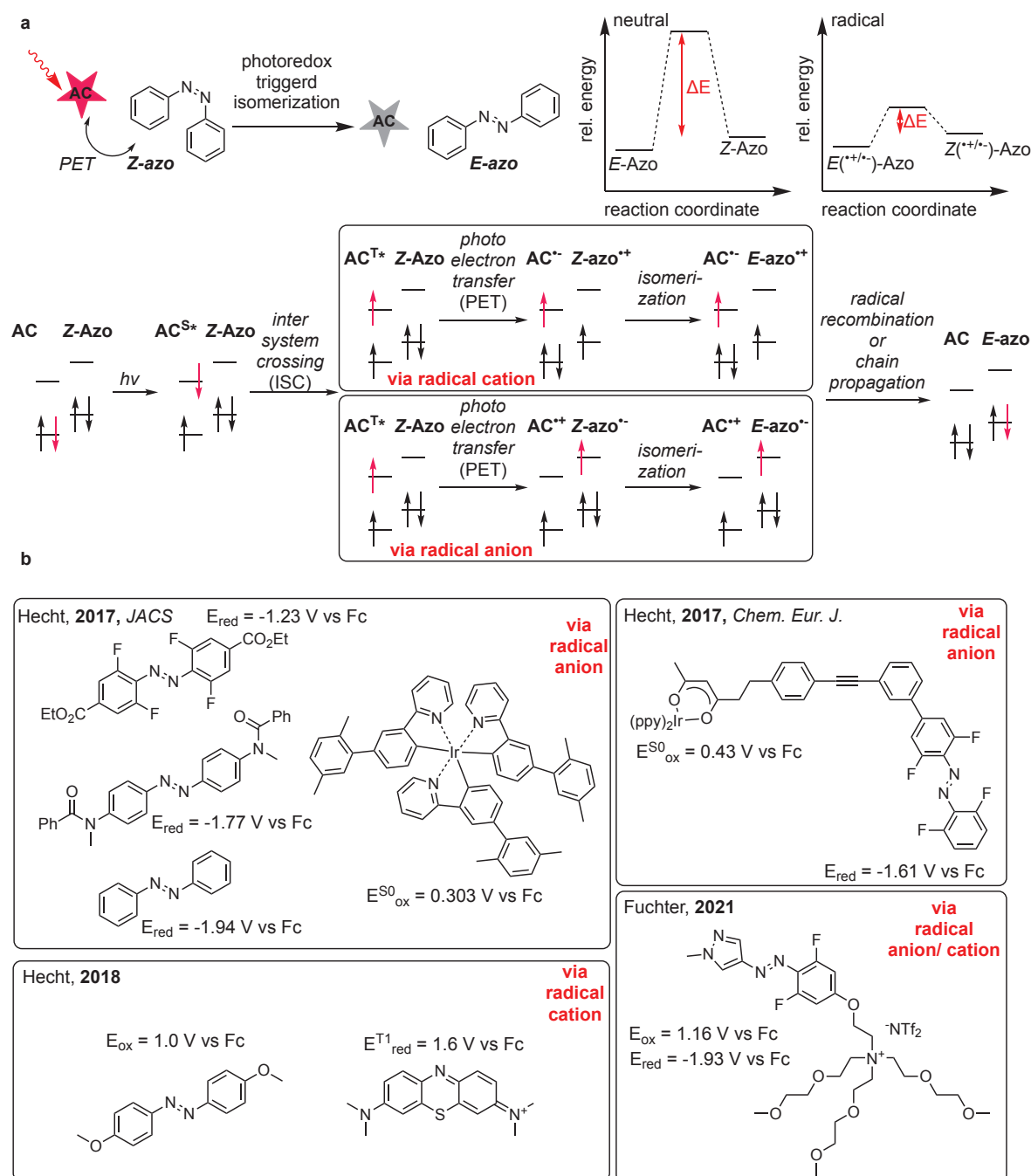


**Figure 9:** a) proposed mechanism for PET based  $Z \rightarrow E$  isomerization of azobenzenes via radical anion and radical cation. b) Literature examples of azobenzene and photoredox catalyst, indication oxidative or reductive pathway and redox potentials in V vs. Fc.: (top left) Hecht, JACS, 2017<sup>68</sup>; (top right) Hecht, Chem. Eur. J., 2017<sup>69</sup>; (bottom left) Hecht, 2018<sup>54</sup>; (bottom right) Fuchter, 2021<sup>70</sup>. Energy vs. reaction coordinate scheme was adapted from Hecht, JACS, 2017<sup>68</sup>.

A third "hole catalysis" study<sup>54</sup> focuses on an oxidative pathway of photoredox-/ electrocatalytic isomerization of azobenzenes, using electron-rich azobenzenes that are more easily oxidized than reduced (strong electron-donating groups in *ortho* or *para* to the N=N double bond leading to lower oxidation potential and higher reduction potential). Initially, they showed that azobenzenes in Z-enriched PSS can, upon addition of 0.3 mol % ceric ammonium nitrate (CAN) and subsequent formation of up to 0.3 mol % azobenzene radical cation, be rapidly and quantitatively switched to their all-*E* form supporting the catalytic nature of the effect. The mechanism was shown to be conceptually similar to that for the radical anion: as soon as the Z isomer is oxidized to its radical cation Z<sup>•+</sup> it relaxes very fast (orders of magnitude faster than the neutral Z isomer, **Figure 9a** top right) to the corresponding E<sup>•+</sup> that again oxidizes another neutral Z isomer and propagates the catalytic chain: hence, "hole catalysis". This poses an advantage as compared to the radical anion mechanism since one electron oxidizing agents (e.g., CAN) are bench stable salts allowing the reaction to be done under ambient conditions (oxygen tolerant). In a next step, they were interested in PET-based hole catalysis. They used up to 20 mol-% of the known triplet sensitizer methylene blue (MB;  $\lambda_{\text{max}} = 660 \text{ nm}$ ,  $\phi_{\text{ISC}} = 0.5$ ,  $E_{\text{red}}^{\text{T}} = 1.2 \text{ V vs Fc}$ ) to photoredox catalyze the Z→E isomerization of 4,4'-bismethoxy azobenzene (**Azo(OMe)<sub>2</sub>**,  $E_{\text{ox}} = 1.0 \text{ V vs. Fc}$ , **Figure 9b**, bottom left). MB was able to quantitatively catalyze the Z→E of **AzoOMe<sub>2</sub>** in a triplet-manifold PET with 660 nm excitation. MB could reach quantitative isomerization of **AzoOMe<sub>2</sub>** because **AzoOMe<sub>2</sub>** does not absorb at the excitation wavelength of MB. They could show the catalytic potential of the reaction by measuring an isomerization quantum yield  $\phi_{\text{isomerization}} > 1$  in the absence of oxygen. In the presence of oxygen  $\phi_{\text{isomerization}} < 1$ , due to quenching the MB triplet (associated with singlet oxygen production and photobleaching).

In summary, the work of Hecht and coworkers describes two novel mechanisms for azobenzene isomerization where the PSS is not anymore dependent on intrinsic quantum yields or absorption spectra of the azobenzenes' isomers.

Fuchter and colleagues showed in their 2021 study that azoheteroarenes (**Figure 9b**, bottom right) can undergo fast and quantitative electrocatalytic Z→E isomerization in solution and in condensed phase.<sup>70</sup> Interestingly, the efficiency of electrocatalytic switching is improved by one order of magnitude in the condensed phase compared to in solution measurements, and they suggest that the electrocatalytic isomerization of azoheteroarenes is thus a promising direction for the development of molecular solar-thermal materials.

## 1.2 Artificial control of biological phenomena by light

### 1.2.1 Optogenetics

Optogenetics, which was selected as Nature Method of the Year 2010<sup>71</sup>, is a powerful technique for artificial, light-induced protein control: with landmark results including on-and-off photoswitching of neuronal activity, with high spatiotemporal precision, in freely moving animals.<sup>72</sup> Optogenetics grew from the discovery that some microorganisms produce proteins that can light-dependently control cation flow through the cell membrane (**Figure 10a**, left).<sup>72</sup> Bacteriorhodopsin was the first example, discovered by Oesterhelt and Stoekenius in 1971.<sup>73</sup> Further research in this direction yielded the discovery of halorhodopsin by Mukohata and Matsuno-Yagi in 1977<sup>74</sup> and channelrhodopsin (**Figure 10a**, left) by Nagel, Bamberg and Hegemann in 2002.<sup>75</sup> All rhodopsins rely on the cofactor all-*E*-retinal, bound as a Schiff base, that absorbs a photon and subsequently undergoes isomerization (to 13- or 11-*Z*-isomers), which causes structural change following ion uptake (**Figure 10a**, c).<sup>76</sup>

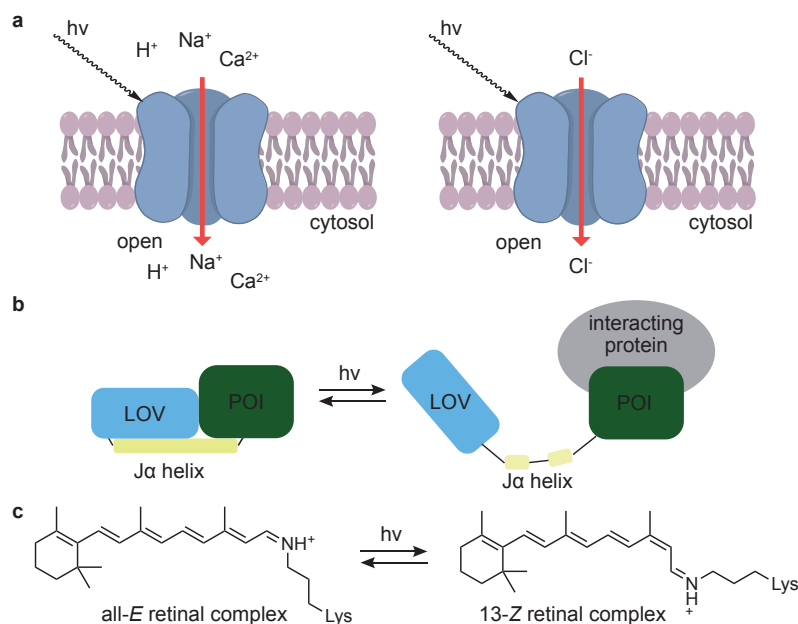


**Figure 10:** a) Principle of channelrhodopsins as light induced cation (left) and chloride (right) uptake channels; b) light-oxygen voltage (LOV) domains are fused to a protein of interest and can undergo a light mediated order-disorder transition, allowing e.g., protein interaction only after illumination; c) photoisomerization of the rhodopsin co-factor from an all-*E*-retinal complex, here giving a 13-*Z*-retinal.

In 2005 Bamberg and Nagel teamed up with Deisseroth and showed that channelrhodopsins can be used to control neural activity with high temporal precision.<sup>77</sup> Also in 2005, the group around Alexander Gottschalk and Georg Nagel described the first application of channelrhodopsin-2 to control neuronal activity in intact, freely-moving *C. elegans*, just by illumination.<sup>78</sup> In 2014, Hegemann and Oertner mutated channelrhodopsin's active center to make it anion selective, giving a light-driven chloride ion channel, called chloride-conducting channelrhodopsin (**Figure 10a**, right).<sup>79</sup>

Besides light-induced regulation of ion passage by microbial rhodopsins, light regulated protein actuators are the second major class in the optogenetics toolbox. These actuators rely on different mechanisms. Light-oxygen voltage sensor (LOV) domains undergo a blue light-modulated, order-disorder transition. In contrast to rhodopsins, LOV domains allow for intracellular applications of optogenetics and have been successfully utilized in the field of gene expression, cytoskeleton research and signal transduction (**Figure 10b**).<sup>80–82</sup>



## 1.2.2 Photocages

Photocages are chemical protecting groups that can be cleaved by light. They have been applied in several fields of research to modulate or study biological function with spatiotemporal precision: including (1) caged drugs (non-active before illumination, releases the active drug after illumination), (2) caged small-molecule fluorophores (non-fluorescent before photocage cleavage) (3) caged enzyme active sites, (4) caged mRNA (e.g. light-induced protein synthesis) (**Figure 11a-d**). Activation wavelengths for photouncaging range from UV to short wave infrared (SWIR).<sup>83</sup> Common photocage groups are *ortho*-nitrobenzyls (ONBs, activation: UV to blue)<sup>84</sup>, coumarins (activation: blue)<sup>85</sup>, boron-dipyrromethenes (BODIPYs, activation: green to NIR)<sup>86</sup>, xanthenes (activation: green to NIR)<sup>87</sup> and polymethines (activation: green to SWIR)<sup>83,88–92</sup>.

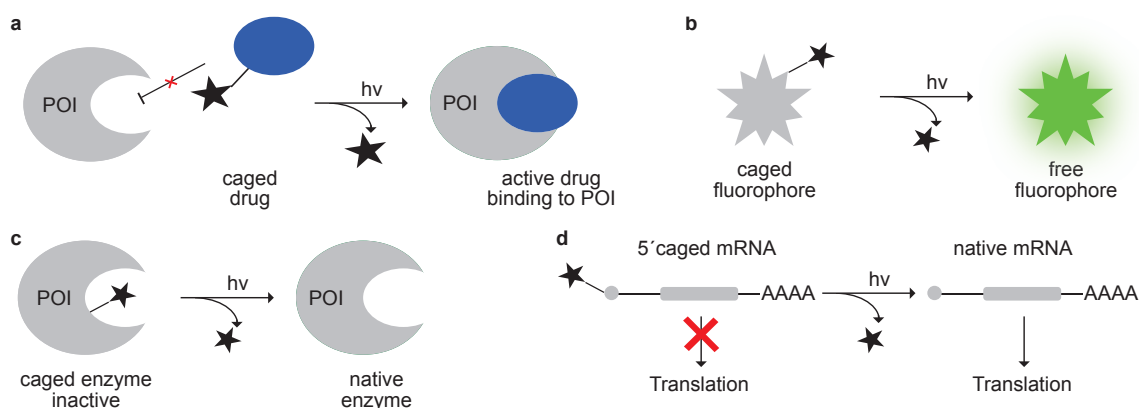


**Figure 11:** Working principals of photocages applied for light mediated biological modulation a) photocaged drugs; b) photocaged fluorophores; c) photocaged enzymes; d) photocaged mRNA.

Brief examples of recent applications in each class are now given. (1) In 2011, Deiters and coworkers showed light-mediated protein interaction in living cells by a photocaged analogue of rapamycin (**Figure 12e**).<sup>93</sup> Following a similar approach, Feringa and coworkers developed a strategy to photocage antibiotics (benzylpenicillin and fluoroquinolone) controlling bacterial growth by light (**Figure 12b**).<sup>94</sup> Schnermann and colleagues developed a method for NIR mediated uncaging of small molecules, based on a Cy 7 polymethine derivative (**Figure 12f**).<sup>88</sup> (2) Light-triggered fluorescence (photocaged fluorophores) has been investigated by several groups. Johnsson and coworkers showed a photocaged rhodamine 110 derivative (**Figure 12a**) that enables high contrast and fluorescence quantum yield after deprotection making it ideal for superresolution photoactivatable localization microscopy (PALM).<sup>95</sup> Broichhagen and coworkers developed a photocaged version of the DNA stain Hoechst33342 (**Figure 12d**) that enables subnuclear selective staining of DNA in living cells. Furthermore, they showed uncaging and cell tracking in live zebrafish.<sup>96</sup> (3) Photocages have also been key for light activation of enzyme activity as shown by Chin and coworkers (**Figure 12g**). They investigated a photocaging strategy for the active site of MEK1 kinase. An unnatural, photocaged lysine amino acid was introduced by genetic code expansion that was deprotected after light illumination and allowed fast and specific activation of a signaling pathways.<sup>97</sup> (4) The synthesis of proteins within cells is regulated by the translation of mRNA and associated to multiple diseases. Rentmeister and coworkers introduced FlashCaps, a method to 5' photocage mRNA that allows translation and subsequent protein synthesis after illumination with the spatiotemporal precision of light (**Figure 12c**).<sup>98</sup>

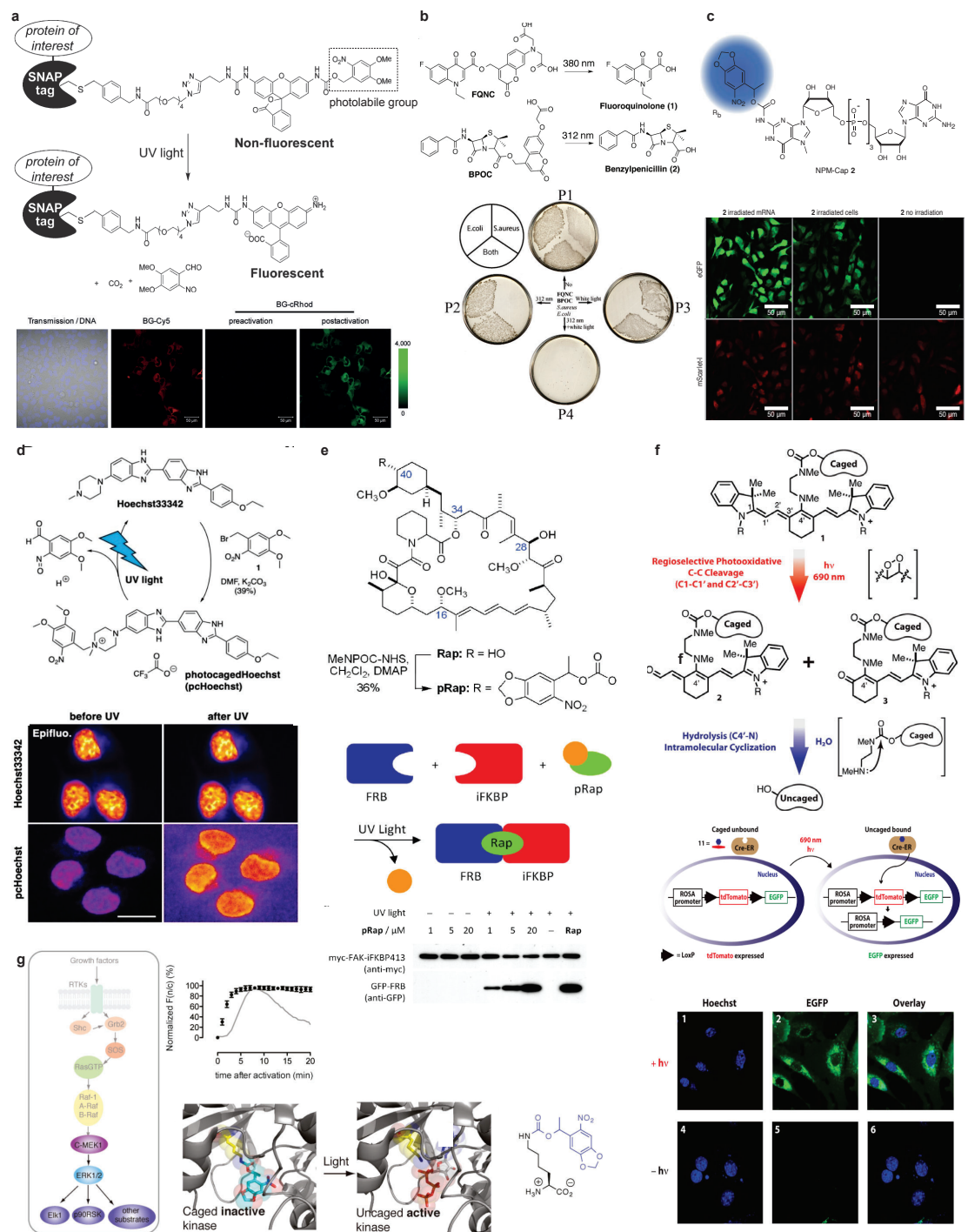


**Figure 12:** a) photocaged rhodamine 110 fluorophore for superresolution microscopy, reprinted with permission from Johnsson, *ACS Chem Biol* 2012<sup>95</sup> Copyright © 2012, American Chemical Society; b) photocaged antibiotics for light induced growth inhibition of bacteria, reprinted with permission from Feringa, *ACS Chem Biol*, 2014<sup>94</sup>, Copyright © 2014, American Chemical Society; c) photocaged 5' mRNA enable light induced mRNA translation, reprinted with permission from Rentmeister, *Nat. Chem.* 2022<sup>98</sup>, Copyright © 2022, The Authors; d) photocaged DNA stain Hoechst33342 enabling subnuclear selective stain of DNA, reprinted with permission from Broichhagen, *ChemBioChem* 2020<sup>96</sup> Copyright © 2020, The Authors. *ChemBioChem* published by Wiley-VCH GmbH; e) photocaged rapamycin enables light induced protein interaction, reprinted with permission from Deiters, *JACS*, 2011<sup>93</sup> Copyright © 2011, American Chemical Society; f) NIR mediated photouncaging is enabled by polymethine fluorophore, reprinted with permission from Schnermann, *JACS*, 2014<sup>88</sup>, open access article, Copyright © This article not subject to U.S. Copyright. Published 2014 by the American Chemical Society; g) light mediated activation (uncaging) of MEK1 kinase allows spatiotemporal precise activation of signaling pathways, reprinted with permission from Chin, *JACS*, 2011<sup>97</sup>, open access article, Copyright © 2011, American Chemical Society.



### 1.2.3 Photopharmacology with photoswitches

Photopharmacology aims to achieve light-dependent pharmacological activity by using light-responsive drugs. For this PhD, I focus on photopharmacology using small-molecule photoswitches (**Figure 13**). Various classes of photoswitches have been applied for a wide spectrum of biological targets from *in vitro* and *in cellulo* to *in vivo* in freely-moving animals. Azobenzene photoswitches are by far the most used photoswitches in photopharmacology and will be discussed first; other photoswitch classes which play an emerging role in photopharmacology are shown afterwards.<sup>28,39,40,99</sup>

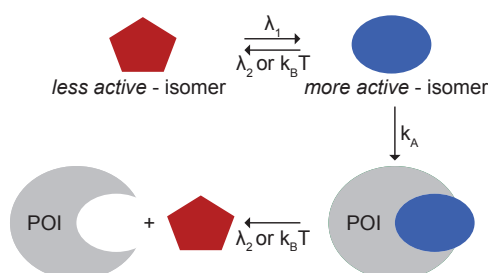


**Figure 13:** Photopharmaceuticals can be switched from their less active to the more active one and backwards by light of different wavelength. Only the more active isomer can bind the protein of interest (POI).

#### 1.2.3.1 Azobenzene-based photopharmaceuticals, 1: "PCLs" for the cytoskeleton

Azobenzenes are by far the most used photoswitches for applications in photopharmacology. Within the last 20 years many examples have been published that show the power of photopharmaceuticals as tool compounds to help solving important biomedical questions.

The cytoskeleton is a recent target for azobenzene photopharmacology, which showcases two classic reagent design strategies within the area of "photochromic ligands" or PCLs, i.e. freely-diffusing photoswitches with different bioactivity between their *E* and *Z* photoisomers. The first example of reversibly photochromic cytoskeleton modulation was shown by Trauner and Thorn-Seshold in 2015. The natural product combretastatin A-4 is a destabilizer of microtubules that contains a central *Z* stilbene moiety, which was exchanged to a fast and robustly-photoisomerizable N=N double bond in the azobenzene photopharmaceutical PST-1. This approach of exchanging a part of an active pharmacophore with an azobenzene is called **azologisation** (**Figure 14a**). PST-1 is 76-fold more cytotoxic in its *Z* isomer compared to the less active *E* isomer, and can be switched from *E*→*Z* and from *Z*→*E* by UV/violet and green light, respectively. PST-1 has been successfully applied for acute reversible microtubule inhibition in the early mouse embryo.<sup>14,100</sup> Another approach to make drug activity photoswitchable is to extend an azobenzene photoswitch (**azoextension**). In 2020, Trauner and Thorn-Seshold showed on the natural product paclitaxel (**Figure 14b**) that extension with an azobenzene (AzTax3MP) allows to control its potency by illumination: AzTax3MP is 6-fold more potent in its metastable *Z*-isomer.<sup>101</sup> Azoextension has also been applied for the natural product jasplakinolide, a stabilizer of F-actin, by Arndt and Trauner in 2022 (**Figure 14c**). By attaching an electron-rich azobenzene, a fast-relaxing ( $t_{1/2} \sim 2$  s) visible-light-activated (410 nm) photopharmaceutical was obtained (*Z* isomer half as potent as the parent compound, and 13-fold more potent than the *E*); this can be used with unidirectional photoisomerisation since the *Z* relaxes back to the less-potent *E* soon after illumination is stopped.<sup>102,103</sup> PCLs act on native receptors allowing them to be easiest transferred between applications in different species. Nevertheless, they are freely diffusing, limiting their spatial precision and the subtype specificity. PTLs and PORTLs, discussed in the following, overcome

these limitations by covalently tethering the photopharmaceutical onto the protein of interest allowing very high special precision and protein subtype specificity even if the pharmacophore is not subtype selective.

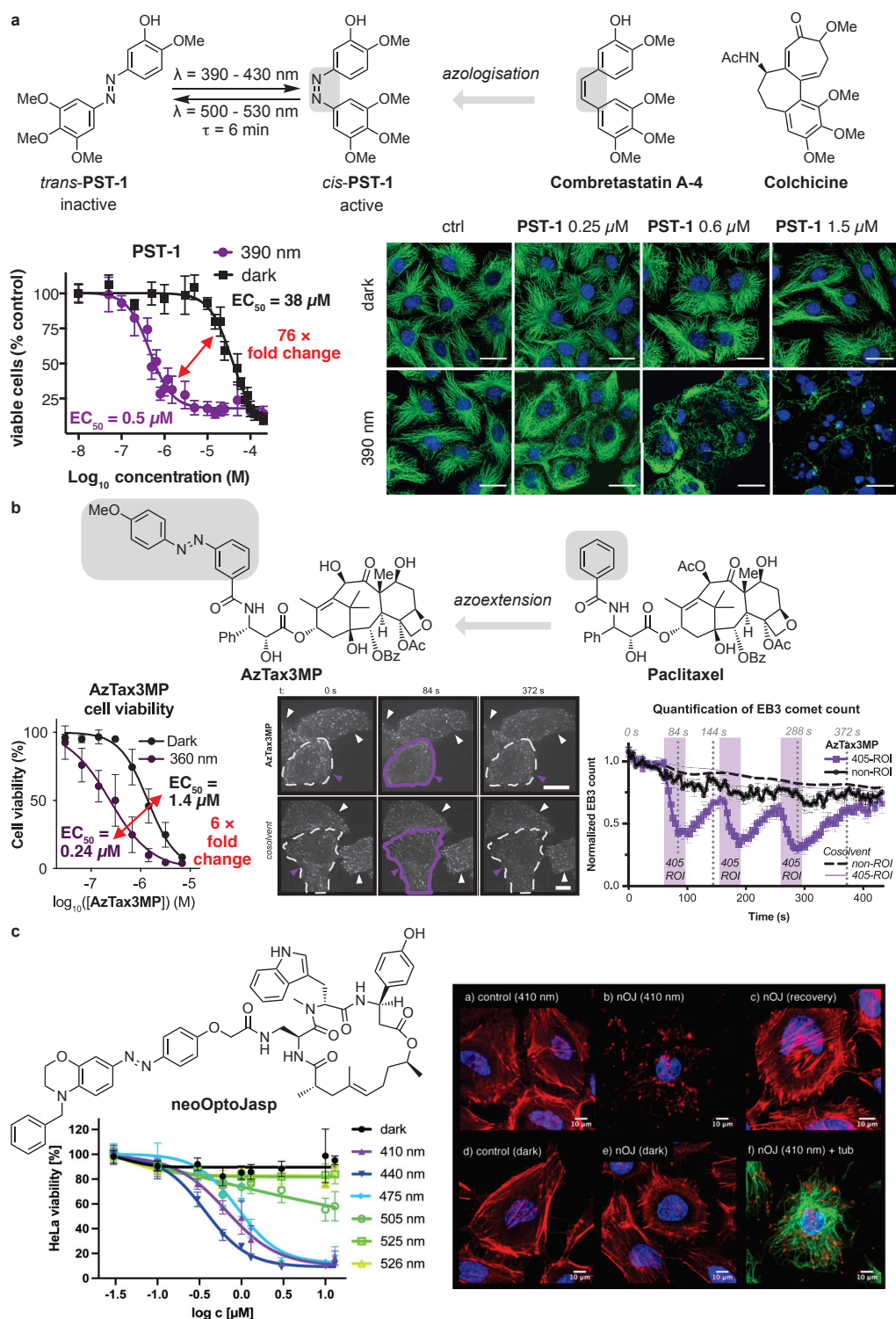


**Figure 14:** a) photoswitchable microtubule destabilizer PST-1, developed by azologisation of natural product combretastatin A-4, reprinted with permission from Trauner and Thorn-Seshold, *Cell*, **2015**<sup>14</sup>, Copyright © 2015, Elsevier Inc, All rights reserved; b) azoextended photoswitchable microtubule destabilizer AzTax3MP, derived from natural product paclitaxel, adapted from Trauner and Thorn-Seshold, *Nat Commun.*, **2020**<sup>101</sup>, Copyright © 2020, The Authors; c) fast relaxing photoswitchable F-actin stabilizer neoOptoJasp, reprinted with permission from Arndt and Trauner, *ACIE*, **2022**<sup>103</sup>, Copyright © 2022 Wiley-VCH GmbH.

### 1.2.3.2 Azobenzene-based photopharmaceuticals, 2: Examples of "PTLs"

Photoswitchable tethered ligands (PTLs) in contrast are tethered, in most cases closely next to the active site, on the protein of interest, so could offer higher spatial precision and subtype selectivity. The photoswitch part in PTLs controls in most cases, but not always, the relative position of the pharmacophore but not the bioactivity (binding affinity) as in PCLs.<sup>104</sup> PTLs can in principle be tethered (covalently attached) to a target protein via naturally occurring (usually nucleophilic), engineered (e.g. cysteines via cysteine maleimide ligation) or unnatural amino acid residues (via bioorthogonal ligation strategies).

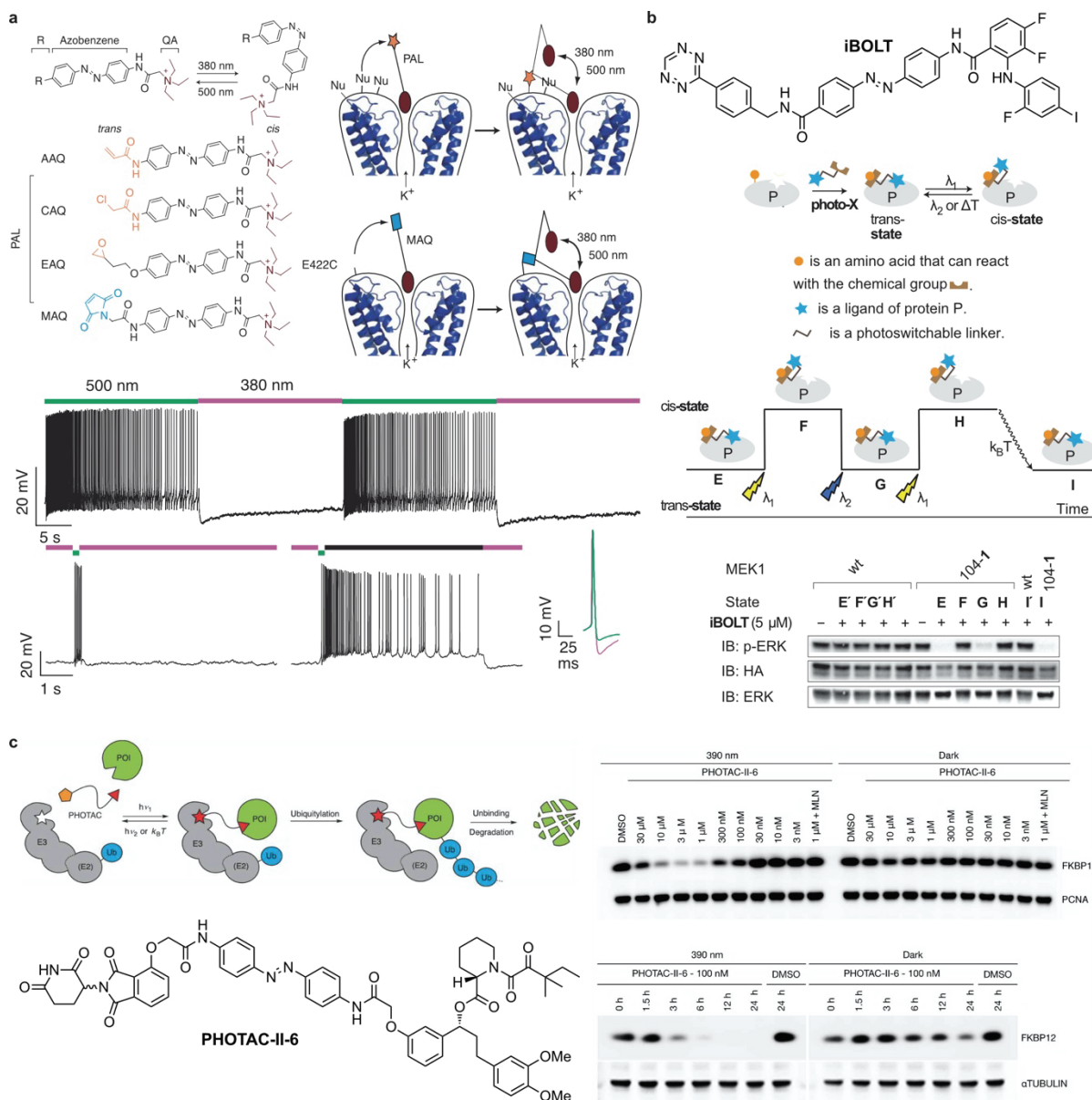


**Figure 15:** a) PTLs (photoswitchable tethered ligands; here abbreviated with PAL) for tethered potassium ion channel modulation, reprinted with permission from Trauner and Kramer, *Nat Methods*, 2008<sup>34</sup>, Copyright © 2008, Nature Publishing Group; b) photoswitchable tethered MEK1 kinase inhibitor iBOLT, adapted from Chin, *Nat Chem.*, 2015<sup>105</sup>, Copyright © 2015, Nature Publishing Group; c) photoswitchable induced protein degradation enabled by PHOTACs, reprinted with permission from Trauner, *Science Advances*, 2020<sup>35</sup>, Copyright © 2020, The Authors.

Ion channels are the most prominent target classes addressed with PTLs. Key steps were taken by Trauner and Kramer, showing methods to target either engineered<sup>106</sup> or endogenous<sup>34</sup> potassium ion channels with PTLs. The PTLs used for these channels

consisted of the covalent attachment handle, an azobenzene linker, and a quaternary ammonium that can mimic a potassium ion; the azobenzene linker in its extended *E* configuration allows the quaternary ammonium to block the channel pore, whereas the “shorter” *Z* isomer does not (**Figure 15a**). Light sensitivity of either engineered or endogenous  $K^+$  channels was shown by electrophysiology in rat neurons.<sup>34</sup> PTLs require tethering by a small reactive group that typically is genetically mutated in, near a binding site. Often this should be a rarely-exposed, reactive, natural amino acid, so cysteine is a prime choice, e.g. for maleimide chemistry, see MAQ (**Figure 15a**) the example used in their landmark publications by Trauner and Kramer.

Selective targeting of proteins that have many similar family members is difficult, especially in kinase research. Chin and colleagues introduced in 2015 the first selective inhibition of MEK1 kinase by a genetic code expansion / bioorthogonal ligation strategy. An unnatural tetrazine reactive amino acid was introduced to the protein of interest (MEK1 kinase), that selectively reacts with a photoswitchable but nonselective kinase inhibitor (iBOLT), covalently tethering it close to the active site of MEK1 (via tetrazine cyclopropene/cyclooctyne ligation, i.e. inverse electron demand Diels Alder reaction). iBOLT is active in its dark *E*-isomer but can be switched to a less-potent *Z* isomer by light (**Figure 15b**).<sup>105</sup>

However, these PTL ligation methods suffer some disadvantages, as maleimides have e.g. low selectivity (cross reactions with native cysteines), hydrolyse under physiological conditions (retro-Michael addition), and are incompatible with use on intracellular targets due to their reactivity against glutathione.<sup>34</sup> The introduction of unnatural amino acids for bioorthogonal ligation strategies requires an engineered tRNA/ tRNA-synthetase pair and a cell-permeable unnatural amino acid, which is technically challenging, especially in eukaryotic cells. This makes the iBOLT approach not suitable for easy transfer across species.<sup>107</sup>

Photoswitchable orthogonal remotely tethered ligands (PORTLs), a third photopharmaceutical tethering approach that aims to overcome these limitations and that is applied within this thesis is discussed in **chapter 1.2.3.4**.

### **1.2.3.3 Azobenzene-based photopharmaceuticals, 3: "Mesoscale" Bifunctionals**

Many other target systems have been addressed with PCL and PTL photopharmacology, such as TRP channels<sup>43,108–110</sup>, GPCRs<sup>104,111–113</sup> circuits involved in vision restoration<sup>99,114,115</sup>, as has been extensively reviewed<sup>28,37,39,40,116,117</sup>. However, from the design viewpoint, an interesting intermediate situation has been highlighted recently, with heterobifunctional photoswitches.

Regulating protein levels within cells is crucial for modern biomedical research and drug discovery. Small molecule approaches to regulate proteins levels have been pioneered by Crews and colleagues within the last decades by developing proteolyzing targeting chimeras (PROTACs). PROTACs are bifunctional molecules that consist of ligands for an E3 ubiquitin ligase and a protein of interest (POI) connected by a covalent linker. PROTACs bring the E3 ubiquitin ligase and the POI in physical proximity, followed by POI polyubiquitination and subsequent proteasomal degradation of the POI.<sup>118</sup> Reynders and Trauner<sup>35</sup>, simultaneously with Carreira and Crews<sup>119</sup>, and You and Jiang<sup>120</sup>, developed photoresponsive PROTACs.<sup>121</sup> For example, Reynders and Trauner applied this concept by introducing PHOTACs (Photochemically Targeting Chimeras) whereby the E3 ubiquitin ligase ligand is extended by



an azobenzene to make the recruitment of the E3 ligase controllable by light (**Figure 15c**). They showed light induced and reversible degradation of BET family proteins and FKBP12.<sup>35</sup>

PHOTACs and other approaches to photoresponsive small-molecule protein degraders combine aspects of both, PCLs and PTLs. They can act via covalent interactions to one of the proteins they bring in physical proximity but are also based on two individual functional interactions, whereby one can be photo-controlled. I think this method is only in its initial phase and can be applied for several other targets in the future, where protein-protein-interactions should be controlled by light.

#### 1.2.3.4 Azobenzene "PORTLs" and tethered photocontrol of GPCRs

Besides freely diffusing (PCL) or chemically tethered (PTL) photopharmaceuticals, a third class of photopharmaceuticals, the PORTLs ("photoswitchable orthogonal remotely tethered ligands") were developed by Trauner and Broichhagen, to address the practical shortcomings of both approaches (**Figure 16a**)<sup>104</sup>, i.e. low spatial precision and low subtype differentiation in PCLs and inconvenient biorthogonal ligation in PTLs, enabling super-selective photopharmaceuticals (PORTLs) with any possible selectivity profile and probable increasing potency that can be easily transferred between any model organism.

Self-labeling proteins (SLPs), such as the SNAP-tag<sup>122</sup> CLIP-tag<sup>123</sup> and HALO-tag,<sup>124</sup> are protein domains composed entirely of natural amino acids, that are rapidly, irreversibly, and highly selectively alkylated by specific, and otherwise unreactive, small molecule substrates. For example, SNAP-reactive benzylguanines (BGs) are, in contrast to maleimides, inert to water and other intra- and extracellular nucleophiles, making them ideal for the use in physiological settings. SLPs have gained huge attention in molecular biology since they can be easily fused onto any protein of interest as an attachment site for any chemical of interest that is appended to the appropriate small molecule substrate.

Broichhagen *et al.* introduced the "PORTL" approach by using BG-appended photopharmaceuticals to label SNAP-tag-fused receptors of interest. The BG was connected to the photoswitchable pharmacophore by a long flexible linker (e.g. polyethyleneglycol); thus, changes in bioactivity are dictated by e.g. changes in binding affinity of the different isomers, just as for PCLs.<sup>104,107,125,126</sup> The proteins of interest for these PORTLs were G-protein coupled receptors (GPCRs).<sup>104</sup> GPCRs are the largest class of drug targets; and Lefkowitz and Kobilka were awarded the 2012 Chemistry Nobel Prize for the elucidation of their function.<sup>127</sup> GPCRs have many subtypes, where it is difficult to make subtype specific ligands: thus they are an especially well suited target for the specificity of PORTLs. Levitz, Broichhagen and others showed in several studies how metabotropic glutamate receptors (e.g., mGluR2), which are neuromodulative GPCRs, can be photocontrolled by BGAG-PORTLs (BGAG  $\equiv$  benzylguanine – azobenzene – glutamate) in cell culture electrophysiology, mouse brain slices and in *in vivo* behavioral studies in freely-moving mice (**Figure 16b-c**).<sup>104,111–113,128–130</sup> mGluR2 signaling could be effectively turned on and off with subsecond precision. Furthermore, they developed branched PORTLs that also have a small-molecule fluorophore (e.g. Cy5, see **Figure 16b, c**) as well as the photoswitchable pharmacophore, allowing simultaneous imaging and manipulation of mGluR2.<sup>111,129</sup>

*Chapters 3.1 - 3.2 will work within this PORTL design, but re-engineering the photoswitching.*

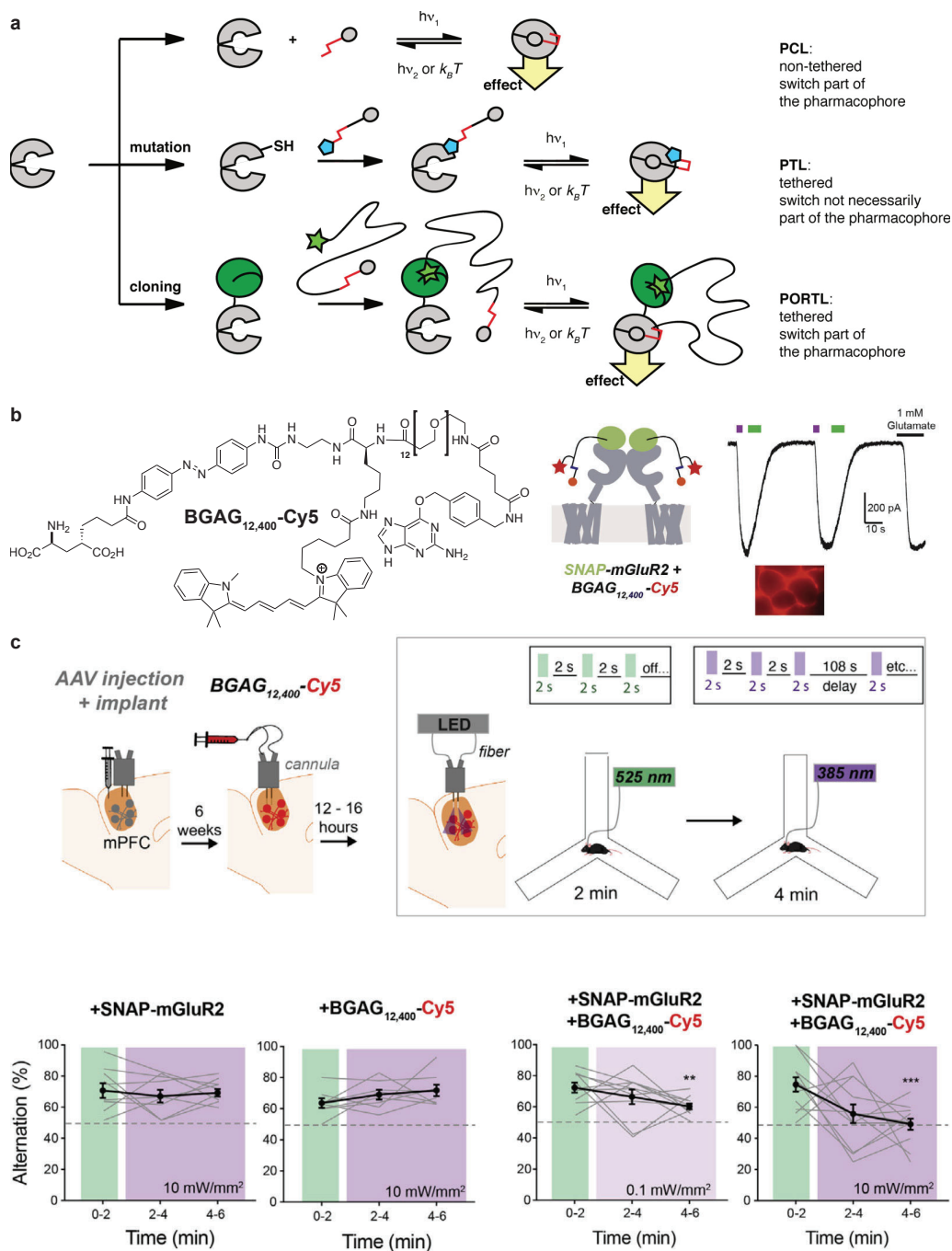


**Figure 16:** a) Principles for different classes of photopharmaceuticals, reprinted with permission from Trauner, ACS Central Science, 2015<sup>104</sup>, open access article, Copyright © 2015, American Chemical Society; b) mGluR2 PORTL BGAG<sub>12,400</sub>-Cy5 and its performance in cell culture light mediated control of SNAP-mGluR2, c) Experimental setup and results of behavioral studies in freely moving mice with PORTL BGAG<sub>12,400</sub>-Cy5; b-c) reprinted with permission from Levitz and Broichhagen, *Cell Chem Biol*, 2021<sup>111</sup>, Copyright © 2021 Elsevier, Ltd.

### 1.2.3.5 Non-azobenzene-based photopharmaceuticals

Non-azobenzene-based photopharmaceuticals are recently emerging for photochromic modulation of biological activity. Much of the non-azobenzene photopharmacology that has succeeded in live cell and *in vivo* biological assays has been driven by the Thorn-Seshold group, especially in the field of microtubule modulation. One example are the styrylbenzothiazole photoswitches, initially used to create "SBTub" photopharmaceutical mimics of the microtubule depolymerizer natural product combretastatin A-4. SBTub-A4P and

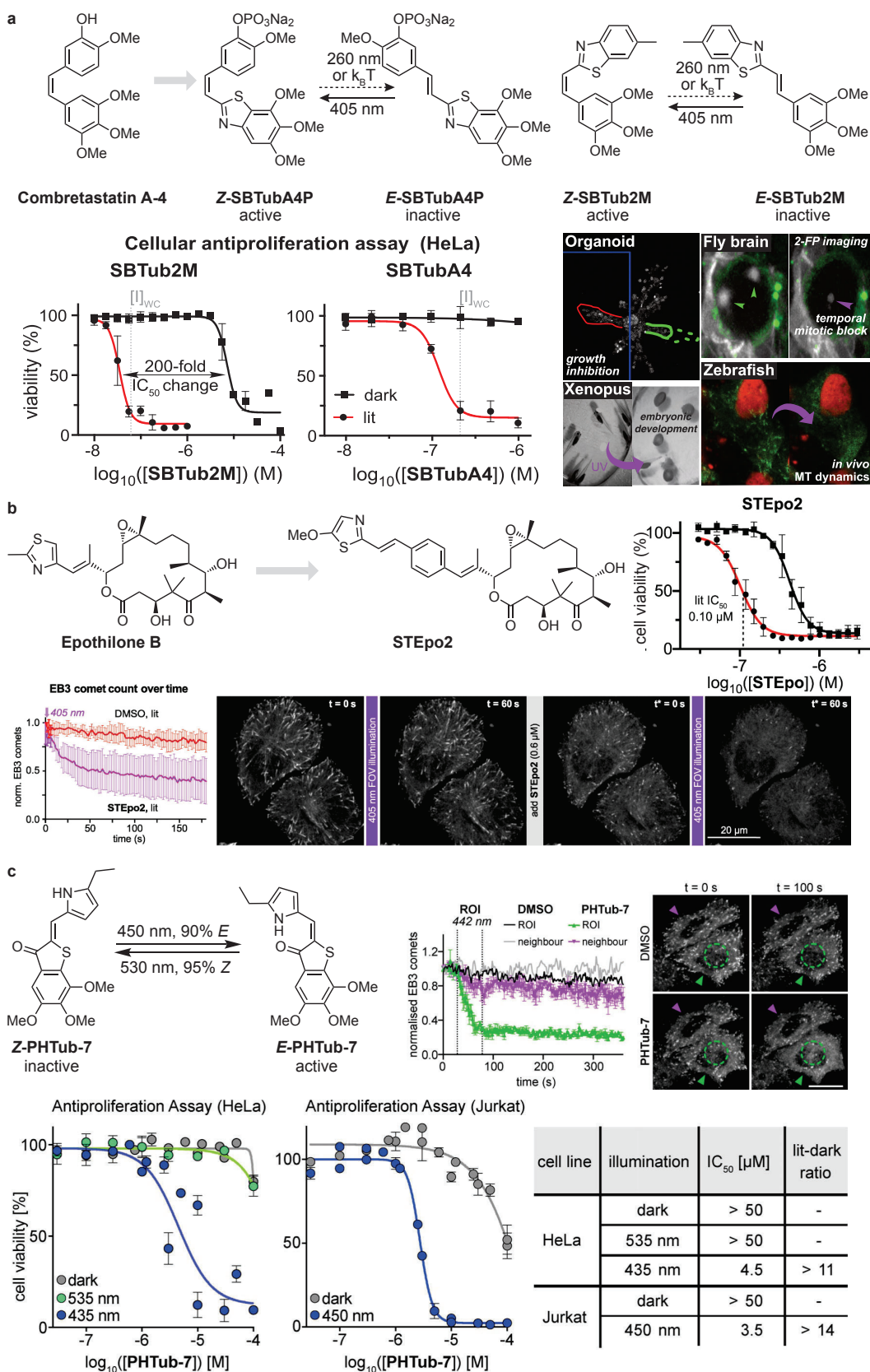


**Figure 17:** a) Styrylbenzothiazole based microtubule destabilizers SBTubA4P and SBTub2M, reprinted with permission from Thorn-Seshold, *JACS*, **2022**<sup>131</sup>, open access article, Copyright © 2022, The Authors. Published by American Chemical Society.; b) Styrylbenzothiazole based microtubule stabilizer STEpo2, reprinted with permission from Thorn-Seshold, *ACIE*, **2022**<sup>132</sup>, Copyright © 2021, The Authors. *Angewandte Chemie International Edition* published by Wiley-VCH GmbH; Hemithioindigo based microtubule destabilizers PHTub-7, reprinted with permission from Thorn-Seshold, *ACIE*, **2021**<sup>21</sup>, Copyright © 2021, The Authors. *Angewandte Chemie International Edition* published by Wiley-VCH GmbH.

SBTub2M showed 31- and 200-fold bioactivity increase, respectively, after  $E \rightarrow Z$  photoswitching with 405 nm light, to mid-nanomolar antimitotic  $Z$ -isomers (**Figure 17a**). Due to their sharp absorption cutoff around 450 nm they are unaffected by (i.e. compatible with) standard imaging techniques based on green-, yellow-, or red fluorescent proteins. Furthermore, C=C double bond-based photopharmaceuticals have been proven to show increased metabolic stability compared to N=N double bond-based photoswitches, which is likely to be important for any photopharmaceutical with systemic exposure rather than local release or tethering. SBTubA4P was also notable as it was designed as a fully water-soluble prodrug, for easier biological applications, that succeeded in live zebrafish, xenopus and fly brains.<sup>131</sup> The group also investigated an approach to control the activity of the microtubule stabilizer natural product epothilone B by photoswitch extension, yielding a star photopharmaceutical STEpo2 (**Figure 17b**). STEpo2 gave a ~4-fold increase in activity after photoisomerization to the more potent  $Z$  isomer.<sup>132</sup> Another emerging class of photopharmaceuticals was pioneered, tuned, and optimised by Sailer *et al.*<sup>21,133,134</sup>, working on the hemithioindigo photoswitch scaffold, again as an analogue of combretastatin A-4 (**Figure 17c**). In their final iteration, PHTub-7 was delivered, as the strongest-performing photopharmaceutical based on an indigoid pharmacophore yet known: a microtubule destabilizer that can be switched near-quantitatively between its less-active  $Z$  isomer and the more potent  $E$  isomer with visible light, with an 11-14-fold change in potency upon photoisomerization and acute photoswitching in live cells.<sup>21</sup>

PCLs, based on SBTs or HTIs, cannot offer currently what azobenzenes do in regards of straightforward reversible photoswitching and high difference in isomer activity. However, readers should notice that the druglikeness of SBTs and other stilbene based photoswitches is superior to azobenzenes, if only their photoresponse can be fixed, to be bidirectional, at wavelengths that are as tuneable as azobenzenes. I will return to this aspect in the outlook of this thesis.



### 1.3 Fluorophores for single molecule localization- and super resolution microscopy

After having introduced small-molecule photoswitches, their properties and applications, the focus in the next chapter is on synthetic organic fluorophores and their application in single molecule localization- and super resolution microscopy. Fluorescence microscopy is a very powerful technique<sup>135</sup> that helps to answer fundamental questions in many subjects ranging from cell biology to neurobiology and molecular biology. Chemists have developed thousands of fluorescent probes to label vast numbers of biological targets. Furthermore, the development of fluorescent proteins like the green fluorescent protein GFP - which led to the 2008 chemistry Nobel Prize for Tsien, Shimomura and Chalfie - allows biologists to genetically label nearly any protein in biological systems.<sup>136</sup> Recently, the limits in multiplexed biological imaging have been pushed beyond 1000 nm by Schnermann and Bruns resulting in advanced whole-body live-animal fluorescence imaging techniques.<sup>91</sup>

#### 1.3.1 Imaging beyond the classical resolution limit

The resolution of classical optical imaging techniques is however limited by the diffraction of light, with length uncertainties that are often far greater than researchers would wish. The theory of diffraction limitation was described by Ernst Karl Abbe in 1873 (Abbe diffraction limit; **Figure 18a**). Abbe found that the distance  $d$  of two individual spots that can be resolved is proportional to the wavelength  $\lambda$  that is used for the observation, divided by the objective's numerical aperture  $NA$  ( $NA = n \times \sin \alpha$ ).

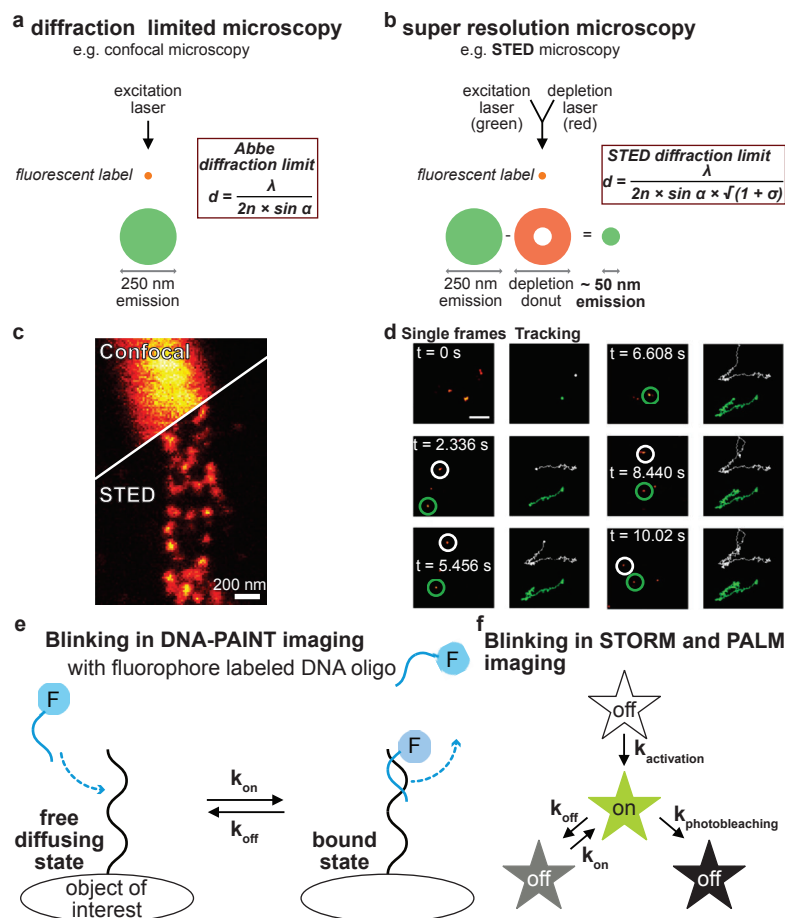


**Figure 18:** Diffraction limits in conventional (a) and STED microscopy (b); c) different in spatial resolution comparing diffraction limited confocal microscopy with super resolution techniques STED and MINSTED, reprinted with permission from Hell, *Nat Photonics*, 2021<sup>137</sup>, Copyright © 2021 The Authors; d) Example for high temporal resolution in STED super resolution microscopy,

reprinted with permission from Hell, *Nat Methods*, **2015**<sup>138</sup>, Copyright © 2015 Nature Publishing Group, a division of Macmillan Publishers Limited. All Rights Reserved; e) Schematic of how blinking is generated in DNA-PAINT imaging based on transient hybridization of DNA labeled fluorophore and object of interest; f) Schematic of how blinking is generated in STORM (reversible switching between an “ON” and “OFF” state of the fluorophore, left part) and PALM (irreversible bleaching of the fluorophore after a certain number of photons is emitted, right part); panel f is adapted from Xiao, *PLOS ONE*, **2012**.<sup>139</sup>

In a best case example where  $NA = 1$  the resolution limit  $d$  for green light ( $\lambda = 500$  nm) is 250 nm.<sup>140</sup> The resolution is good enough for imaging of cells ( $\sim 5 - 80$   $\mu\text{m}$ ) but for most cellular compartments ( $\sim 100 - 700$  nm), viruses ( $\sim 90$  nm) and proteins ( $\sim 10$  nm) it is not sufficient.<sup>141</sup> In the last 30 years, technological improvements have led to super resolution microscopy techniques. In 1994, Stefan Hell discovered stimulated emission depletion (STED) microscopy showing the first experimental evidence that it is possible to overcome Abbe's diffraction limit in microscopy.<sup>142</sup> In a STED microscopy setup there is a second donut shaped beam (the so called STED beam) at a wavelength that “silences” (de-excites fluorophores by stimulated emission) within the beam, so only the fluorophores within the center of the donut where the STED beam intensity is zero are actively fluorescing.<sup>143</sup> STED was able to reduce the resolution limit of optical microscopy from  $\sim 250$  nm to  $\sim 10$  nm (**Figure 18b-d**).

Other, independently-developed approaches also give sub-diffraction-limited resolution. These are based on single-molecule localization microscopy (SMLM). In contrast to high-intensity laser-induced stimulated depletion in STED, SMLM relies on conventional wide-field excitations, and super resolution is achieved by computational reconstruction of thousands of frames, ultimately enabling tracking of single labelled biological molecules, or studying the interactions between them (e.g. by single-molecule FRET).<sup>144</sup> Recently, SMLM techniques have been shown to enable resolutions  $< 5$  nm.<sup>145</sup> All SMLM methods have in common that they rely on fluorophore blinking (i.e. fluorophores switching between fluorescent “ON” and dark “OFF” states, so that in each frame only a subset of fluorophores is in their “ON” state). In photoactivated localization microscopy (PALM, **Figure 18f**), blinking is achieved by laser-induced photobleaching of fluorescent proteins (i.e. activated fluorescent proteins get excited and emit a certain number of photons before undergoing irreversible photobleaching; for the next activation cycle, another subset of fluorescent proteins is photoactivated and imaged).<sup>146</sup> Stochastic optical reconstruction microscopy (STORM) relies on “ON”-and-“OFF” blinking of reversibly fluorescent photoswitchable small organic fluorophores (**Figure 18f**).<sup>147</sup> In DNA-PAINT, the most common application of point accumulation in nanoscale topography (PAINT), fluorophore blinking is generated by transient hybridization of DNA strands (**Figure 18e**)<sup>148</sup>. Thereby, the object of interest is labelled with a single DNA strand and the fluorophore with a short (usually 8-10 nucleotide) complementary single DNA strand allowing the fluorophore switching between a bound (signal-accumulating) and free-diffusing (diffuse background) state.<sup>144,145</sup> Super resolution microscopy and SMLM techniques led to the Nobel Prize for Hell, Betzig and Moerner in 2014.<sup>149</sup>

### 1.3.2 Photoinstability problems of organic fluorophores

All super resolution microscopy and SMLM techniques rely on small-molecule organic fluorophores; but most of them come from classes that have been developed 100 years ago, and have not been optimized for high-intensity excitation settings as e.g. in STED. From a microscopist's viewpoint, these cause drawbacks as (1) state-of-the-art organic fluorophores spend relatively little time in their active fluorescent state, due to long-lived “dark” (triplet and radical) states that do not fluoresce (note: these can also be chemically reactive with other components of assays); and that low photon output limits the potential spatiotemporal

resolution of microscopy; (2) Particularly, these long-lived dark states can be chemically and photochemically reactive; and overall, there is only a relatively low photon "budget" (number of emitted photons before photo-mediated destruction) allowed by the current fluorophores, which in turn restricts imaging to relatively low total imaging times or emitted photon counts.

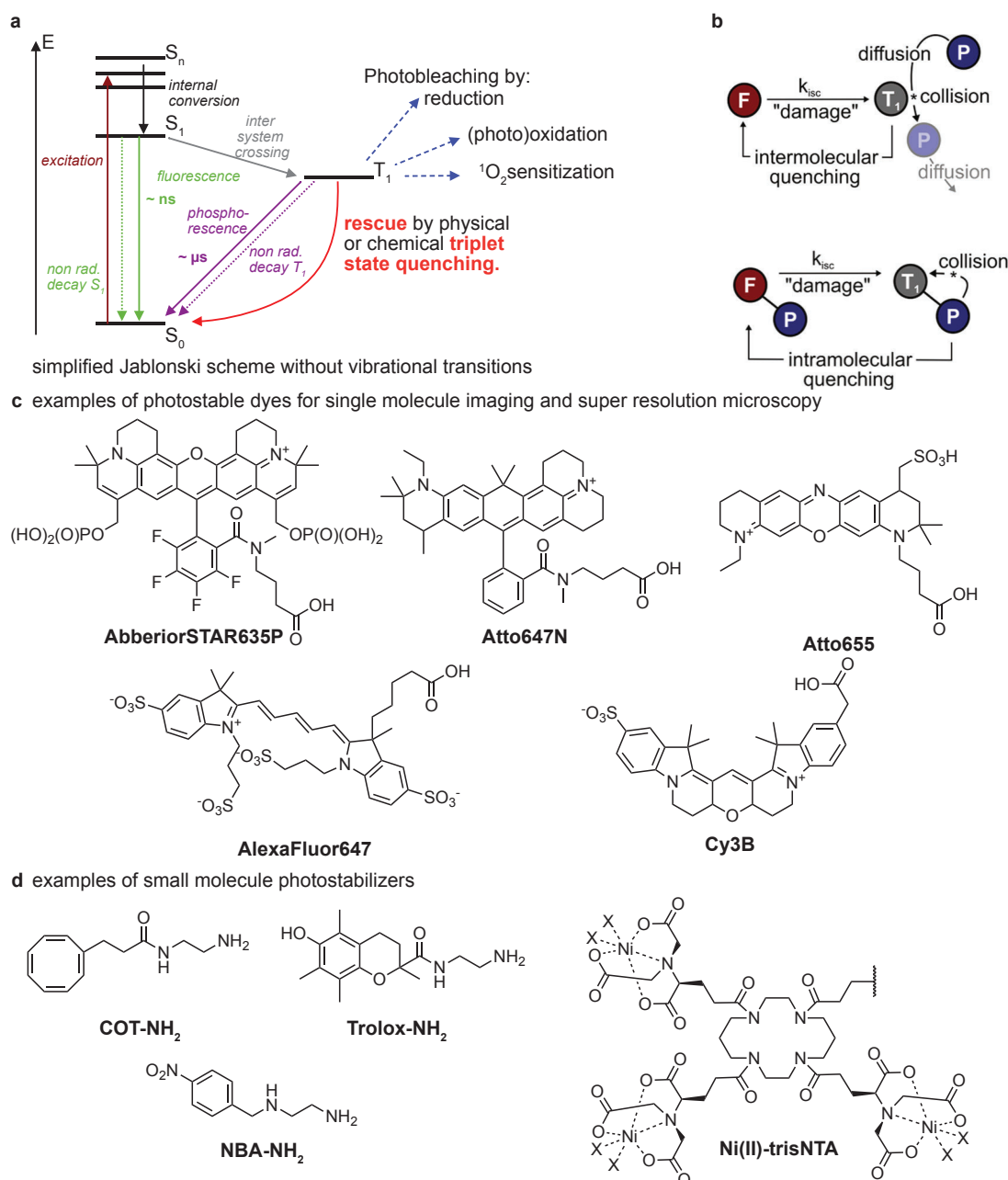


**Figure 19:** a) Simplified Jablonski scheme indicating pathways for fluorophore photobleaching and rescuing techniques; b) Scheme of inter- and intramolecular triplet state quenching, reprinted with permission from Cordes, *J. Phys. Chem. Lett.*, **2020**<sup>150</sup>, open access article, Copyright © 2020, American Chemical Society; c) Examples of state-of-the-art small molecule fluorophores for single molecule imaging and super resolution microscopy; d) examples of small-molecule triplet state quencher that have been applied in self-healing dyes.

From a chemical viewpoint, one major problem is that they tend to suffer photoinduced degradation (photobleaching) after a limited number of excitations.<sup>151</sup> A main pathway for fluorophore degradation arises from molecular oxygen that can react with excited states, especially with long lived ( $\tau_T \sim 100 \mu s$  typically) triplet states (**Figure 19a**). Oxygen can either directly oxidise the fluorophore, or else evolve to generate a variety of reactive species. The

typical example of this is the generation of reactive singlet oxygen by collisional quenching of fluorophore triplet states. While this returns the fluorophore to its bright singlet manifold, singlet oxygen can later react with the fluorophore, or the binding site it needs to complex with, or can perturb biological systems. Therefore, oxygen scavenger systems are widely used to enzymatically remove oxygen within the samples, preserving fluorophores from oxygen-related bleaching.<sup>152</sup> Nevertheless, if oxygen is removed, triplet (inter system crossing) and radical (photooxidation) states cannot be quenched by oxygen therefore resulting in long-lived triplet and/or radical states of the fluorophore: triplet-lifetime  $\tau_T$  is approximately 3 orders of magnitude longer than fluorescence-lifetime  $\tau_F$  and radicals can have even longer half-times (ms-range is not uncommon), so in this time, the fluorophore remains dark and does not emit photons. These processes result in triplet and redox "blinking".

More photostable and brighter fluorophores are necessary to overcome these limitations of state-of-the-art fluorophores and therefore increasing the theoretically possible resolution in fluorescence microscopy.

### 1.3.3 Increasing the photostability and performance of organic fluorophores

The area of research towards more photostable fluorophores and methods to stabilize established fluorophores is very active.

#### 1.3.3.1 Reducing excited state reactivity

Chemical **strategies** include reduction of twisted internal charge transfer (TICT) states by azetidine substituted xanthene dyes from Lavis<sup>153,154</sup>, conformationally restricted cyanine dyes (enabling reduction of cis $\leftrightarrow$ trans photoisomerization) from Schnermann,<sup>155</sup> and suppressing secondary isotope effects by *N*-alkyl deuteration of rhodamines from Broichhagen<sup>156</sup> and Lavis<sup>157</sup>. These tend to focus on increasing the survival time and fluorescence quantum yield of the fluorophore, without considering the survival of other molecules around it.

#### 1.3.3.2 Shortening dark state lifetimes: towards self-healing dyes

Shortening problematic triplet and radical ion lifetimes would lead to signal increase and therefore higher practically achievable resolution,<sup>151</sup> and contribute more photostable fluorophores for imaging and microscopy.<sup>150</sup> Also, if these reactive dark states lifetimes can be reduced to a minimum, so that even in presence of molecular oxygen no side reactions (like singlet oxygen production) happen, it would give less damage to surrounding molecules (e.g., neighbouring biomolecules) allowing to raise fluorescence microscopy in ambient live cell settings to a new level of temporal and spatial resolution.

In contrast to chemical strategies that rely on chemical modifications to result in more photostable fluorophores, so-called "physical" strategies focus on reducing the triplet and radical ion lifetime by small-molecule triplet state- or redox quenchers (**Figure 19d**). Approaches can be divided in intermolecular, solution-based methods vs. intramolecular stabilisation, where a "[triplet] quencher" and the fluorophore are covalently linked (**Figure 19b**); or can be considered according to their mechanism for how they depopulate the triplet state (i.e., triplet-triplet energy transfer, or photoelectron transfer that is rescued by a complimentary redox partner).

**Intermolecular photostabilization** uses triplet and/or radical state quenchers as solution additives within the samples. One of the first reported examples was  $\beta$ -mercaptoethanol, that was found to suppress photobleaching of rhodamine fluorophores in fluorescence microscopy. Since then it has been widely used as it functions as a triplet state quencher and radical

scavenger.<sup>158</sup> More recently, other solution additives to rescue fluorophores from triplet and radical states have been developed, including Trolox and *para*-nitrobenzyl-compounds (both quenching by photoelectron transfer)<sup>159</sup> and cyclooctatetraene (COT, quenching by Dexter-type triplet-triplet-energy transfer).<sup>160</sup> Another solution based approach, a reducing and oxidizing system (ROXS, quenching by photo electron transfer), was introduced by Tinnefeld and coworkers.<sup>161</sup> In ROXS a reducing and an oxidizing agent are added simultaneously to the fluorophore solution. The reducing agent of choice is ascorbic acid and oxidizing agent methyl viologen. The method requires oxygen free conditions. As soon as the fluorophore enters a long lived, reactive triplet state it is either reduced or oxidized, yielding the fluorophore's radical anion ( $F^{\cdot-}$ ) or cation ( $F^{\cdot+}$ ) respectively.  $F^{\cdot-}$  or  $F^{\cdot+}$  is afterwards oxidized or reduced by the corresponding agent yielding the ground state of the fluorophore. ROXS is a broadly applicable system for a large range of fluorophores (like Atto647N, Cy3B, Alexa647 and Atto565) and showed significant decreases of the triplet state lifetime and increase in photostability. However, intermolecular photostabilization approaches often require high concentrations (typically around 2 mM) of photostabilizers to achieve efficient quenching, which are incompatible with e.g., live cell imaging (some compounds are toxic at high concentrations or affect biological processes). Furthermore, all quenching processes require collision between the quencher and the fluorophore, which is limited by diffusion, especially at high dilutions in biological systems.<sup>150</sup>

**Intramolecular photostabilisation with self-healing dyes:** To overcome these limitations, so called self-healing dyes have gained much attention. In self-healing dyes, the fluorophore and the quencher are covalently linked, enabling higher local concentration (collisions are not diffusion limited) without needing high concentrations of triplet or radical state quenchers in solution. Conceptually, the first self-healing dyes have been studied in the 1980s<sup>162</sup>, but most promising results towards application in biological imaging have only been made in the last 10-15 years. Some examples are described in the following. Blanchard and colleagues published a strategy where they covalently couple the small-molecule triplet state quenchers (TSQs) COT, Trolox and 4-nitrobenzylamine (NBA) on the polymethine fluorophore Cy5 and investigated the influence on the photostability and photon output of Cy5 (**Figure 20**).<sup>163</sup> All Cy5-TSQ conjugates showed a significant increase in photostability (2-7-fold) and furthermore Cy5-COT showed increase in fluorescence intensity of 60% compared to its parent dye. In another study Blanchard investigated the triplet state energies ( $E_T$ ) of different COT derivatives and compared them to common fluorophores  $E_T$ .<sup>164</sup> They found that  $E_T$  can be increased by 20 kJ/mol for diacetyl-COT (DCA) compared to methyl-COT which leads to a better fit with  $E_T$  of Cy5 and Atto647N (**Figure 21a**). In 2013, Cordes and colleagues showed that attaching the vitamin E analog Trolox to Cy5 increases the photobleaching decay time constant by a factor of 16.<sup>165</sup> In 2018, Glembockyte and Cosa demonstrated that the photon output of Ni(II)trisNTA---Alexa647 (**Figure 19c-d**) was 25 times higher than Alexa647.<sup>166</sup> However, note that these figures all relate to performance in deoxygenated conditions.



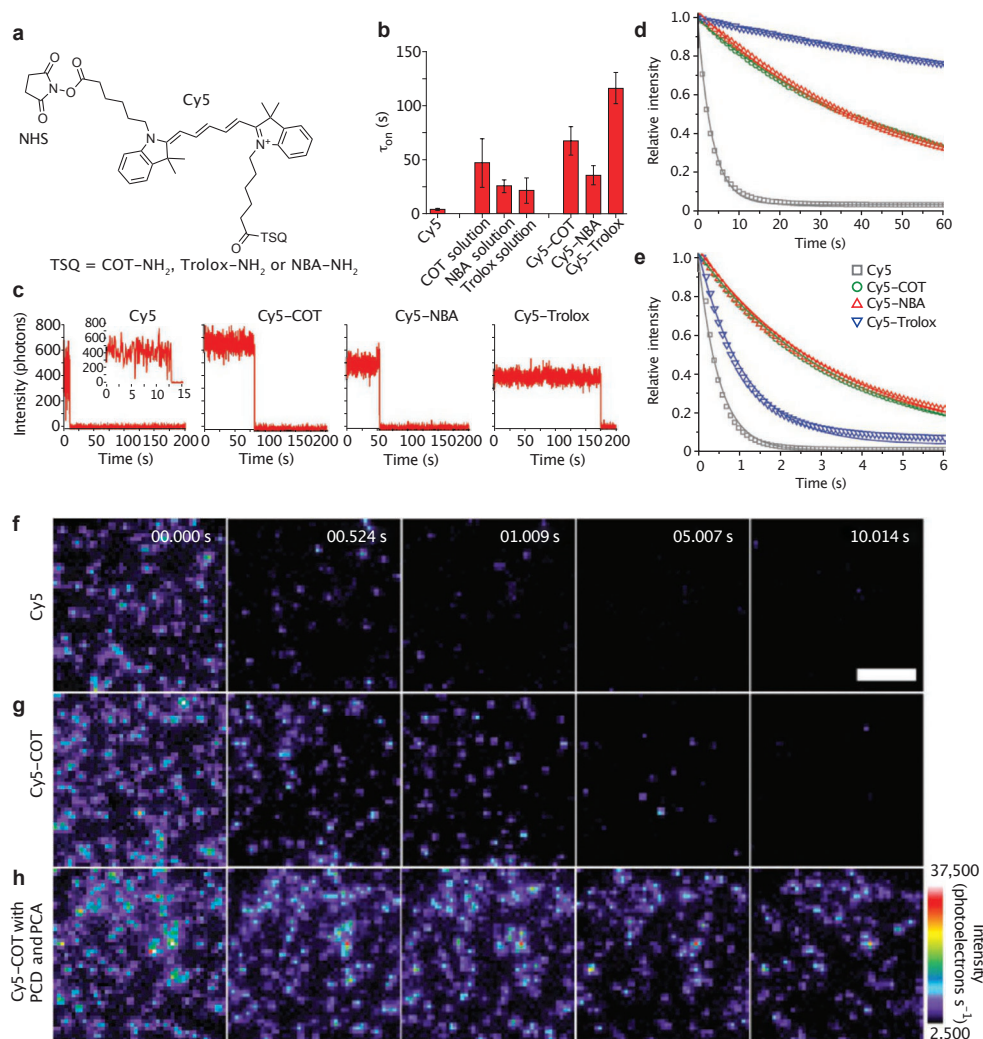


**Figure 20:** a) structure of Cy5 attached to small molecule triplet state quenchers; b) average dwell times (on time of the fluorophore) comparing Cy5 with Cy5 + TSQ solution and Cy5-TSQ conjugate; c) fluorescence traces under direct excitation comparing Cy5 in presence and absence of TSQs; d-e) photostability of Cy5 and Cy5-TSQ conjugates in absence (d) and presence (e) of oxygen; f-h) single molecule total internal reflection fluorescence images in live CHO cells labeled with Cy5 (f), Cy5-COT (g) and Cy5-COT under oxygen free conditions; a-h) reprinted with permission from Blanchard, *Nat Methods*, **2012**<sup>163</sup>, Copyright © 2011 Nature Publishing Group, a division of Macmillan Publishers Limited. All Rights Reserved.

However, so far, self-healing dyes did not, or only slightly, outperform solution-based methods. Especially in the presence of molecular oxygen, which is the ultimate goal for the application of self-healing dyes in ambient biological environment, they could not increase photostability significantly. To do so, they would need to outperform diffusion of molecular oxygen, by showing triplet state quenching rates above  $10^{-6} \text{ s}^{-1}$  (COT only shows quenching rates of  $10^{-4} - 10^{-6} \text{ s}^{-1}$ ).<sup>150</sup> Linker geometry and compositions are highly important to improve quenching rates, but optimization did so far not lead to success in out-competing molecular oxygen.<sup>166</sup> Furthermore, despite approaches to tune COT's triplet energy, so far there are no COT methods to efficiently stabilize blue and green fluorophores such as fluoresceins, due to the large difference of triplet energies that makes TET inefficient.<sup>167</sup>

### 1.3.4 Azobenzenes having ultra-short lived low lying triplet states

Azobenzenes have medium-lying triplet state energies ( $E_T \sim 120-160 \text{ kJ/mol}$ , slightly higher than COTs, **Figure 20a**) and a very short triplet lifetimes  $\tau_T \sim 10 \text{ ps}$  (7 orders of magnitude shorter than COTs).<sup>59-61</sup> Since the 1970s it is known that azobenzenes can accept the triplet

energy of small-molecule organic fluorophores, which can drive isomerisation towards a nearly all-*E* TET-stationary state (see chapter 1.1.3.1).<sup>51–55</sup>

Despite the common knowledge that azobenzenes are applied very successfully as FRET quenchers (commercially available BHQs, DABCYL)<sup>62</sup> Shimomura and Kunitake showed already in 1987 that fluorescence does not necessarily have to be quenched in the presence of azobenzenes.<sup>53</sup> (They even showed that azobenzenes within a lipid bilayer can efficiently transfer their excitation energy from the UV, where the cyanine dye does not absorb strongly, to the cyanine dye, which can fluoresce). **Figure 21** shows triplet energies of common fluorophores used for imaging, and those of state-of-the-art triplet state quenchers used for self-healing dyes, and of some azobenzenes.

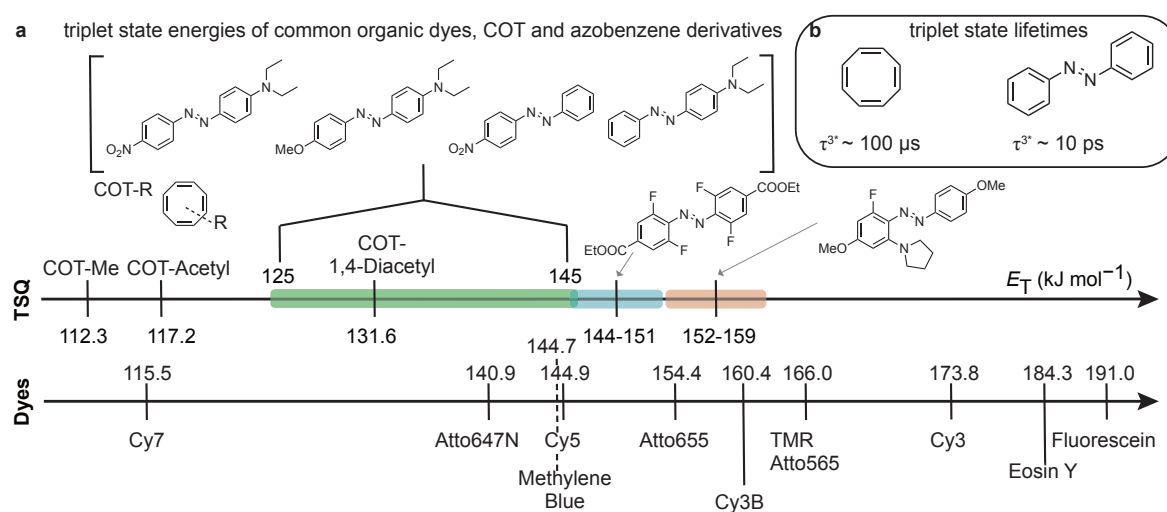


**Figure 21:** a) Triplet state energies  $E_T$  of common organic fluorophores, known triplet state quenchers and azobenzenes, data from Blanchard, 2020<sup>164</sup>; Blanchard, 2016<sup>167</sup>; Bortulus, 1983<sup>60</sup>; Nicewitz, 2016<sup>168</sup> and Durandin, 2021<sup>55</sup>; b) Triplet state lifetime of COT and azobenzene, data from Orlandi, 2004<sup>61</sup> and Scherf, 2009<sup>169</sup>.

Azobenzenes have never been used on purpose to quench the triplet states of small-molecule organic fluorophores in order to increase their performance in high precision imaging techniques. However, they are measured to have 3 orders of magnitude higher triplet state quenching rates than COT, suggesting they should be able to outcompete the diffusion based quenching of molecular oxygen.<sup>59</sup> Cordes and coworkers showed in 2021 that azobenzenes can photostabilize GFP and increase the total detected photon number by 5-fold under the absence of oxygen (**Figure 22c**, bottom left), outperforming other types of small molecular TSQ such as COT and Trolox (**Figure 22b**).<sup>170</sup> The effect was highly dependent on illumination conditions and the presence/absence of oxygen (**Figure 22c**). In the presence of oxygen, the total number of photons emitted only increases by 2-fold which limited the utility of the stabilizing system in biological imaging of GFP. The authors did not propose a mechanism for this kind of stabilization; but a collision-based mechanism such as TET seems unlikely because the attachment site for the stabilizer is outside the GFP barrel, whereas the chromophore part is inside (**Figure 22a**).

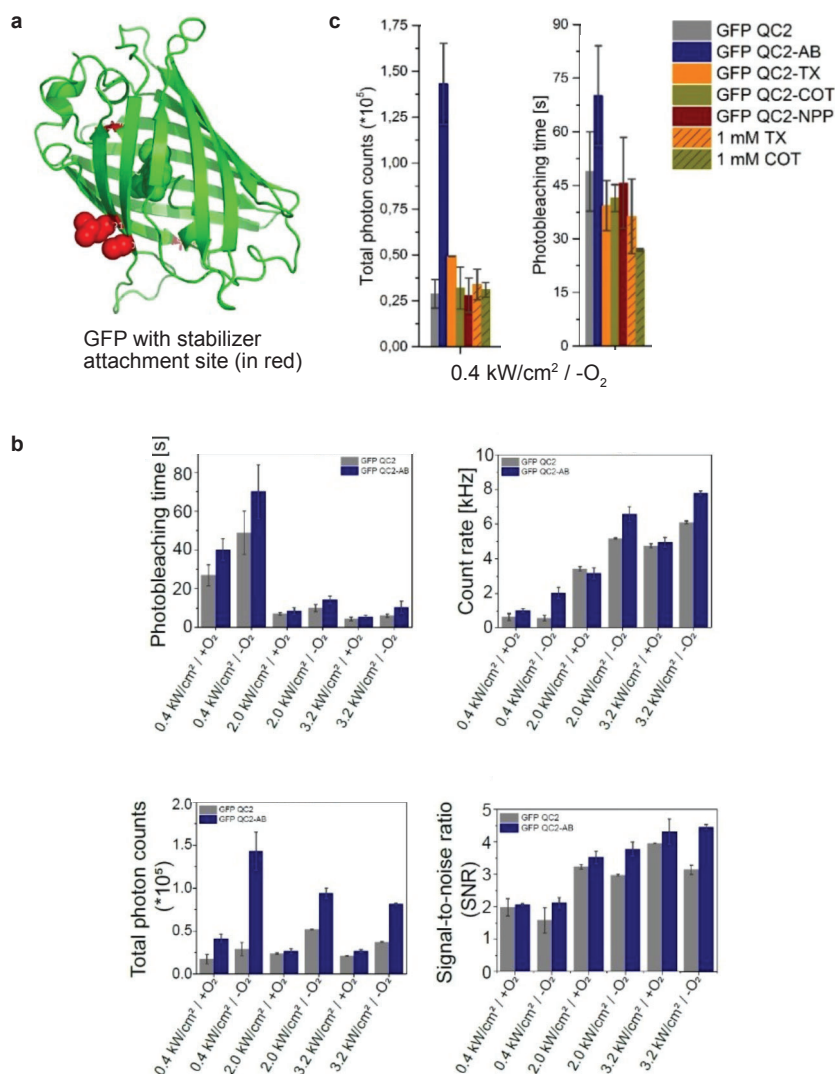


**Figure 22:** a) crystal structure of GFP-QC2, cysteine modification in red, which allows stabilizer attachment by cysteine maleimide chemistry; b) Total photon counts (left) and photobleaching time (right) of GFP fluorescence in absence and presence of stabilizers in the absence of oxygen under special illumination conditions; c) photobleaching time, count rate, total photon count and signal-to-noise ratio of GFP-azobenzene conjugate in absence and presence of oxygen under different illumination conditions; a-c) reprinted with permission from Cordes, *ChemBioChem*, 2021<sup>170</sup> Copyright © 2021 The Authors. *ChemBioChem* published by Wiley-VCH GmbH.

Taken together, there seem to be two opportunities to use azobenzenes: either (1) to perform near-complete isomerisations by harvesting energy of biologically-compatible long-wavelength light that is absorbed by other chromophores, either via triplet state energy transfer or photoredox (part 1.2), or else (2) to harvest triplet energy from fluorophores without quenching their singlet excited states, as a way of increasing the survivability and reducing the dark state lifetime of fluorophores that need to perform in high-intensity imaging (part 1.3).



## 2 Aims of the thesis

**State of the Art 1:** Azobenzenes are by far the most used small-molecule photoswitches in applications ranging from material science and data storage to photopharmacology. In the latter they have shown to be powerful tools to reversibly modulate the bioactivity of small molecular drugs with the spatiotemporal precision that light offers. They have been successfully applied to photocontrol biological activity of important cellular targets such as the cytoskeleton<sup>14,21,101–103,131</sup>, ion channels<sup>30,34,171–173</sup>, TRP channels<sup>43,108–110</sup>, GPCRs<sup>104,111–113</sup>, kinases<sup>105,174</sup>, protein degraders,<sup>35,119</sup> circuits involved in vision restoration<sup>99,114,115</sup>.

Nevertheless, azobenzenes suffer some important limitations: (1) high background-activity in biological experiments, due to non-quantitative bidirectional switching (*E/Z* spectral overlap); (2) only limited tissue penetration, due to photoswitching wavelengths in the UV/blue-cyan spectral region; (3) not suitable for fluorescence imaging (azobenzenes are non-fluorescent).

Approaches have been developed to overcome some of these limitations, but there is still a need for innovative chemistries to solve *all* these problems simultaneously, and usher in the next generation of photopharmacology tools: more powerful, more applicable, better usable.

**Aim 1:** We aimed to identify and exploit pathways for azobenzene isomerization that are independent of its intrinsic photoresponse, to allow fast, (near-) quantitative isomerization within the tissue-penetrating biological window (600–1100 nm) without changing the azobenzenes' substitution pattern. We aim at systems which can be retrofitted onto any existing azobenzene-based photopharmaceutical, and that allow for spectral tuning, i.e., photoisomerization wavelength can be freely chosen in a way that it is suitable for the experimental setup (available laser, LED wavelengths; imaging compatibility; etc.). Two suitable pathways were identified: triplet energy transfer, and photoredox, that had been shown to trigger up to quantitative *Z*→*E* isomerization based on small molecular fluorophores/catalysts as light harvesting antennas, usually in intermolecular settings. We now aimed to study the scope and potential of using these methods flexibly, on a range of chromophores and azobenzene types, to give rational design rules for how assisted switching might be successful in e.g., single photon NIR-induced photomodulation of bioactivity in cell culture and in biological tissues.

**State of the Art 2:** Super resolution microscopy techniques drastically expanded the scope of what can be studied by fluorescence microscopy. While these techniques have had massive technical improvements enabling better resolution there is a lack of innovative fluorophores. Currently used fluorophores lead to drawbacks such as (1) limited imaging time due to relatively low photostability (2) limited temporal resolution due to relatively low photon output and intensity fluctuations (3) limited experimental setups due to induced phototoxicity (oxygen free environment is often required).

**Aim 2:** We aim to develop a chemically novel approach to photostable fluorophores that overcome these limitations, using azobenzenes as small-molecule photostabilizing agents. This goes somewhat against common practice that uses azobenzenes as non-fluorescent species that quench the fluorescence of nearby fluorophores; but based on triplet energy accepting properties and ultra-short triplet state lifetimes azobenzenes seemed likely to act as good photostabilizers for super resolution and single molecule localization microscopy. We aimed to study the power and generality of this effect, with the hope to push still further the current limits of photon output and photostability, towards better resolution.

**Extrinsic vs. Intrinsic properties:** With the exception of one example (triplet photoredox via radical anion<sup>69</sup>) all other published systems for small-molecule-assisted azobenzene isomerization were based on intermolecular reactions: so providing extrinsic performance properties that are highly dependent on concentration and diffusion (and thus are not suitable for highly diluted applications as in live cell applications). Self-healing-dyes have been developed for a similar reason: overcoming the limitations of bimolecular "solution-based photostabilization" systems, to enable fluorophore photostabilization as an intrinsic property. Yet, coupling systems that work in isolated intermolecular setups, and applying them in intramolecular approaches, is not a trivial task. Even though the effective local concentration of a stabiliser around a fluorophore in solution-based stabilization (2 mM photostabilizer solution) is similar or even lower than in self-healing dyes (1:1 ratio in covalently-linked conjugates), state-of-the-art self-healing-dyes did not yet outperform solution-based approaches. A similar situation was the case for assisted isomerization approaches. After several ground-breaking works, it was still not possible to translate them to fully biocompatible intrinsically acting systems. There are several properties (linker geometry and length, triplet energies, collision rates...) that must be considered when aiming to evolve intermolecular to intramolecular systems, which will be a guiding question studied within this PhD.

### 3 PhD Research

#### 3.1 A general method for near-infrared photoswitching in biology, demonstrated by the >700 nm photocontrol of GPCR activity in brain slices

##### **Summary:**

Azobenzenes are by far the most used molecular photoswitches in photopharmacology and have been applied to photomodulate various high demand biological targets in *in vitro*, cell culture and *in vivo* settings. Nevertheless, azobenzenes suffer substantial limitations, e.g. (1) their limited photoresponse (low  $\epsilon$  above 530 nm), which limits their application in deep tissue and animal models; (2) their incomplete bidirectional photoswitching, which can result in high background activity and side effects in biological experiments; (3) their non-fluorescent nature, which makes it impossible to image their biodistribution by fluorescence microscopy.

In this chapter we show how intramolecular energy transfer from a small-molecule organic fluorophore to an azobenzene photoswitch, can yield near-quantitative (up to 98% *E* isomer) *Z*→*E* photoisomerization of azobenzene with up to 770 nm single photon response, while keeping the fluorescence properties of the fluorophore active (**Figure 2**). I synthesised a library of 15 azobenzene fluorophore conjugates and analyzed their photoswitching behaviour at long wavelengths (**Figure 3**). We could show that this is a general mechanism and based on intrinsic properties of the molecules. Our aim in the beginning was to make new tools for photopharmacology that can be operated in the NIR and allow for near-quantitative bidirectional switching and self-reporting by fluorescence. Therefore, we reevaluated the known PORTL BGAG<sub>12,400</sub>-Cy5 that our collaborators Josh Levitz and Johannes Broichhagen developed in a previous study (they showed that it can reversibly modulate neurons with 385 nm and 525 nm light in the prefrontal cortex of mice and can be applied in behavioral studies in freely-moving mice). We now show a proof-of-concept of 770 nm triggered energy transfer-based *Z*→*E* photoisomerization of BGAG<sub>12,400</sub>-Cy5 in cell culture (**Figure 5**) and acute mouse brain slices (**Figure 6**). NIR light switches the channels “off” to the same degree as if the azobenzene switch is directly excited at 525 nm. While the mechanism is not completely conclusive, we provide a proposal based on spectroscopic studies. These data support the first ever NIR single photon triggered modulation of bioactivity where the degree of switching is not depending on the absorption spectrum of the azobenzene isomers.

**Personal Challenge:** For a long time, the mechanism of long-wavelength-induced *Z*→*E* photoisomerization of azobenzenes triggered by organic fluorophores was completely unclear to us. Literature only showed triplet energy transfer for *Z*→*E* photoisomerization of azobenzenes in intermolecular systems, and almost only using known photosensitizers with high intersystem crossing quantum yields. In contrast, most of the fluorophores we investigated have very low intersystem crossing quantum yields, so in the beginning we had excluded triplet mediated pathways. Furthermore, we had excluded photoredox as a pathway since oxidation and reduction potentials, determined by electrochemical measurements, did not match, and the isomerization did not show to be quantitative, which it would need to be for photoredox (see **chapter 3.2**). However, when our collaborators performed ultrafast transient absorption spectroscopy and fluorescence quantum yield measurements, these showed that the singlet excited state was not affected, orienting us away from singlet-manifold mechanisms. Fluorescence correlation spectroscopy comparing Eosin Y ( $\phi_{ISC} \sim 0.3$ ) and an Eosin Y-azobenzene conjugate proved that indeed the triplet state of the attached fluorophore is totally depopulated by the azobenzene but fluorophores with low  $\phi_{ISC} < 0.01$  having similar

assisted photoswitching rates resulting in our current exciplex-based understanding (Figure 4).

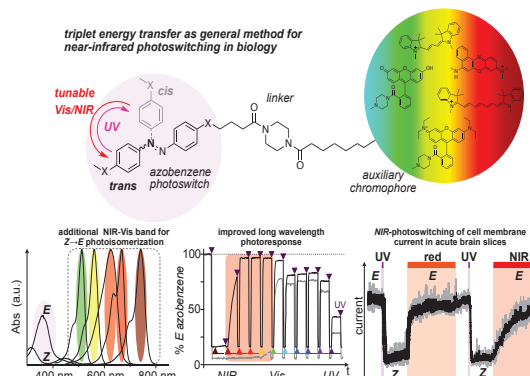
**Own contribution:** I designed and synthesised all compounds (besides BGAGs), in particular, the library of 15 azobenzene-fluorophore conjugates: featuring three azobenzene scaffolds that are most often used in photopharmacology, and 8 common fluorophores (oxazine, xanthene and cyanine). I established the experimental setup for action spectra, photoswitch kinetics, and photostationary state quantification, which was key for the success of this project. The setup includes two illumination light sources (low intensity monochromatic and high intensity broad band LED) for sample illumination during UV/Vis measurements. The broad band LED illumination source (pE4000 from CoolLED) was controlled by a custom script written in the open-source software  $\mu$ Manager and allows for automated action spectra (from 770 to 365 nm, with precise light intensity settings) and kinetic measurements. Furthermore, I designed a cuvette adapter that tightly closes the cuvette and allows constant sample concentrations even over long experiment durations (> 120 min) with precise, repeatable localization of the liquid light guide at reproducible distance and angle of illumination. I performed all photostationary state quantifications by high performance liquid chromatography and correlated them to absorbance values determined by UV/Vis spectroscopy allowing for calibration curves for absorbance to %-E isomer determinations; as well as all other UV/Vis, low-intensity fluorescence spectroscopy, and HPLC experiments. I analyzed experimental data, coordinated results, assembled data in figures and contributed to manuscript preparation.

*This paper is being refined for submission to Nature Methods.*

# A general method for near-infrared photoswitching in biology, demonstrated by the >700 nm photocontrol of GPCR activity in brain slices

Benedikt Baumgartner<sup>1</sup>, Viktorija GlembocYTE<sup>2,3</sup>, Alberto J. Gonzalez-Hernandez<sup>4</sup>, Abha Valavalkar<sup>5</sup>, Robert Mayer<sup>2</sup>, Lucy L. Fillbrook<sup>6</sup>, Adrian Müller-Deku<sup>1</sup>, Jinhua Zhang<sup>7</sup>, Florian Steiner<sup>2,3</sup>, Christoph Gross<sup>2</sup>, Martin Reynders<sup>1</sup>, Hermany Munguba<sup>4</sup>, Anisul Arefin<sup>4</sup>, Armin Ofial<sup>2</sup>, Jonathon E. Beves<sup>6</sup>, Theobald Lohmueller<sup>7</sup>, Benjamin Dietzek-Ivanšič<sup>5,8</sup>, Johannes Broichhagen<sup>9</sup>, Philip Tinnefeld<sup>2,3</sup>, Joshua Levitz<sup>4</sup>, Oliver Thorn-Seshold<sup>1\*</sup>

Azobenzene molecular switches are widely used to photocontrol material properties, and biological activity in cell culture, via photoisomerisation between *E* and *Z* isomers. However, because population photoswitching is incomplete, their dynamic range of property control is often small; and because they cannot be operated with red/NIR light, they are usually not applicable in deep tissue. Here, we demonstrate a general method for efficient single-photon photocontrol of azobenzenes, and of glutamate receptor activity, at >700 nm in live tissue. We use red/NIR chromophore auxiliaries to perform intramolecular energy transfer to bioactive azobenzenes, which drives fast bulk *Z*→*E* isomerisation up to even >97% completeness. The auxiliary/azobenzene dyads allow >700 nm photoswitching with photon-efficiency that can be even higher than for direct azobenzene *E*→*Z* isomerisation in the UV region; and they are biocompatible and photostable. Crucially, their performance properties are *intrinsic*, i.e. auxiliary-based intramolecular switching will perform identically at any dilution and will not be affected by biodistribution. We show that these dyads can be created straightforwardly from most azobenzene systems, with most auxiliary chromophores, without tricky molecular redesign or re-optimisation. After outlining some rules of auxiliary-based photoswitching, which can guide its broader adoption, we conclude by using dyads to make the first demonstration of single-photon NIR chemical photoswitching control over biological activity, in cell culture and intact brain tissue.



## 1. INTRODUCTION

Azobenzenes are the major synthetic molecular photoswitches.<sup>1</sup> They allow chemical effectors to be actuated with high spatial and/or temporal precision, in a range of applications from photo-patterned materials<sup>2,3</sup> to photocontrolled biology in cell culture<sup>4-7</sup>, in model animals<sup>8,9</sup>, and recently in a human clinical trial<sup>10</sup>. In each use, an azobenzene scaffold is decorated with substituents so that its *E* and *Z* isomers affect the system differently; and samples are locally photoswitched between majority-*E* and majority-*Z* populations to locally pattern compound activity (Figure 1a).

Two major factors limit the utility of azobenzene photoswitches. In brief, (1) on the population level, *E*→100%*Z* or *Z*→100%*E* photoswitching is not possible, due to overlap of *E*/*Z* absorptions. *Z*→*E* switching is the more incomplete direction. Since *Z*-active reagents are usually targeted,<sup>11</sup> this results in high background activity during bidirectional photoswitching: giving *more-on/less-on* activity switching, not ideal on/off control. Even 'good' azobenzenes typically allow just ~5-fold functional dynamic range of photoswitching ("FDR": the ratio of the fraction of active isomer  $\Phi$  at best "forward" isomerisation ( $\Phi_F$ , e.g. *E*→*Z*) to that at best "backward" isomerisation ( $\Phi_B$ , e.g. *Z*→*E*), i.e.  $FDR = \Phi_F/\Phi_B$ ).<sup>12</sup> Most materials or biosystems need many-fold higher FDR, i.e., *Z*→*E* completeness (smaller  $\Phi_B$ ). The *Z*→*E* problem is worsened in practice, since *Z*→*E* switching also has much lower photon-efficiency (a metric for how much bulk isomerisation is generated per mole of photons applied; like fluorescence brightness, it is proportional to both  $\epsilon(\lambda)$  and  $\Phi_{\text{isom}}(\lambda)$ ).<sup>13</sup> (2) No broadly-usable biocompatible strategy to operate azobenzenes with well-penetrating red/NIR light is known. Typical azobenzenes only respond well to light <530 nm, which is strongly scattered and absorbed in biological tissues or complex samples. Thus, most azobenzenes are limited to use in superficial, simplified, optically transparent systems (e.g. 2D cell culture or material surfaces). Together, these two limits have blocked photoswitches from many valuable applications that require high activity fold-changes deep in materials, or in tissues *in vivo*<sup>13-16</sup> (see Supporting Note 1).

Strategies to improve the completeness and photon-efficiency of *Z*→*E* photoswitching with red/NIR light, that can work in complex as well as simple systems, are highly sought after. Direct substituent tuning can rarely even achieve yellow-light photoresponse; and no generally useful, synthetically accessible, biocompatible red/NIR designs are known that do not compromise features such as *Z*-isomer stability, or bioactivity, or chemical stability. The closest approaches are green/yellow-responsive tetra-*ortho*-substitutions of Woolley, Hecht, and others,<sup>17-21</sup> and the strained cyclic azobenzenes of Herges<sup>22,23</sup>. Their switching can be more complete than with classical azobenzenes; but their visible extinction coefficients are low (ca. < 1000 M<sup>-1</sup>cm<sup>-1</sup>); far-red/NIR photoswitching is still inaccessible; and by forcing multiple substitutions around the diazene, these designs restrict the chemical and applications space available: a particular problem for photopharmacology, where these positions are often needed for target binding.

We aimed at a simple method for high-completeness as well as high-photon-efficiency *Z*→*E* photoresponse in the NIR, that can be applied practically and in complex settings. Many promising classes of photopharmaceuticals have been developed up to cell culture uses over the last two decades. We aimed to develop a general chemical approach that can retrofit them, allowing them to now be broadly applied *in vivo* in biology (thanks to an *intrinsic* method to photocontrol them in the red/NIR), without putting their target binding at risk through large molecular changes around the azobenzene. We now present methods using biocompatible *auxiliary chromophores* that absorb strongly in the green/red/NIR, then efficiently trigger selective *Z*→*E* isomerisation, to achieve this. This paper will focus on auxiliaries that inject energy for photoswitch isomerisation only by first entering a *proximity-induced triplet* state that then collapses to excite the azobenzene. This concept differs importantly in its performance from what can be achieved with a *typical* triplet sensitizer auxiliary such as methylene blue or palladium porphyrin, that efficiently undergo intersystem crossing (ISC) in their isolated excited state. A parallel paper<sup>24</sup> is reporting on auxiliary chromophores that act via photoredox, with similar benefits.



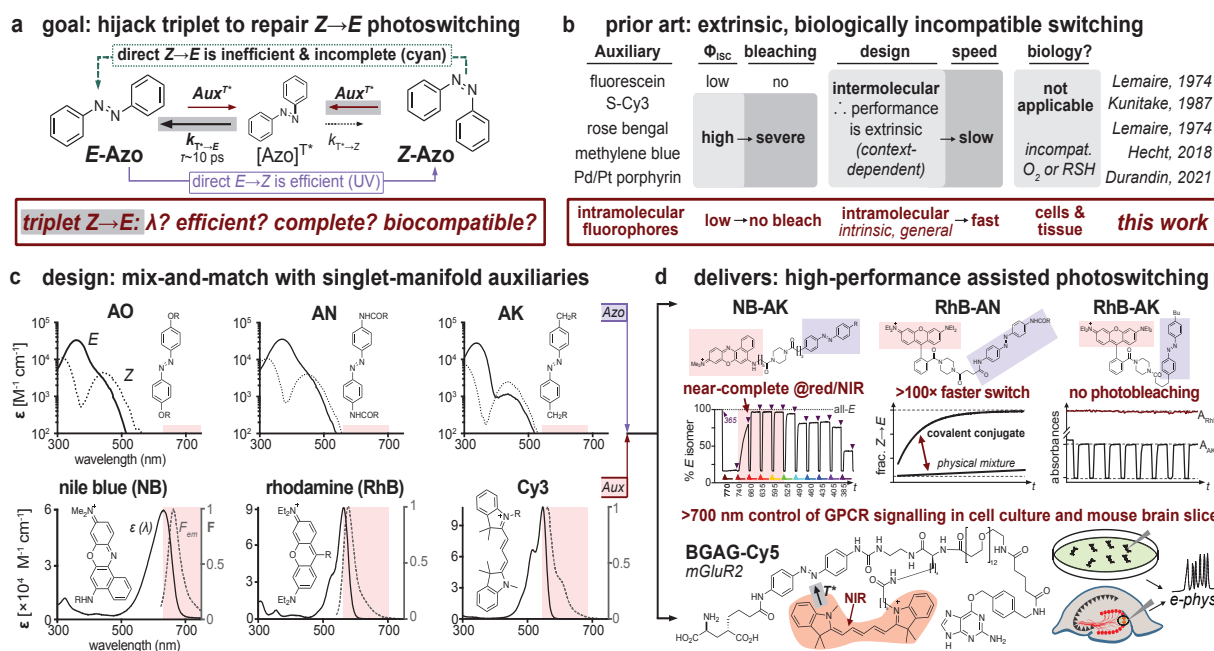


**Figure 1:** (a) Scheme of how TET-based switching may complement direct UV switching. (b) Intermolecular TET is known and inapplicable for biology. *This work* presents intramolecular, proximity-induced, conditional TET to solve the challenges of efficiency, photostability, and biocompatibility. (c) Spectra for typical dyad components. (d) Key properties of high performance conditional-TET-based photoswitching (this work).

Auxiliary chromophores that isomerise azobenzenes by single-photon processes are sparsely reported; none have been used in biology. The main known auxiliaries are triplet sensitisers (Figure 1b). Triplet sensitisers can perform triplet energy transfer (TET) to suitably lower-energy triplet acceptors (azobenzene: ca. 150 kJ/mol<sup>25,26</sup>). Azobenzene T1 states collapse to S0 after an unusually short triplet lifetime (ca. 10 ps; large spin-orbit coupling<sup>27</sup>), mostly giving the E-isomer: TET-equilibria can reach E:Z ratios ca. 0.985 : 0.015<sup>26,28</sup>, i.e. near-complete Z→E isomerization (Figure 1a). There are only ten significant experimental reports in this area (Figure 1b; Supporting Note 2).<sup>26,28–34</sup> Though the desirability of TET-based Z→mostly-E isomerisation at wavelengths decoupled from azobenzene's own absorption is clear,<sup>32</sup> these systems could not be generally applied (Supporting Note 3). In brief, this is because they were intermolecular schemes, requiring collisional TET to the azobenzene without TET to competitive quenchers e.g. O<sub>2</sub> or thiols: so (i) they are unlikely to work at the high dilutions expected in biology, and (ii) they lose isomerisation efficiency by 500-fold and undergo continual photobleaching unless O<sub>2</sub> is excluded.<sup>31</sup> We thus aimed at auxiliary-azobenzene dyads for intramolecular TET to give concentration- and environment-independent *intrinsic* performance (Figure 1c-d; note that it has been unknown whether dyads could ever reach fully intramolecular TET, and so allow O<sub>2</sub>-tolerance without photo-damage to auxiliary, switch, biological target, or environment).

The choice of triplet sensitisers was also unclear. Prior TET schemes chose to maximise intersystem crossing yields  $\Phi_{ISC}$ , so used bio-incompatible photocatalysts (redox cycling organics,<sup>29,31</sup> cell-impermeable heavy metal complexes<sup>32</sup> and dyes<sup>30</sup>); and by absorbing UV-blue light they reduce direct E→Z azobenzene isomerisation yields<sup>31</sup>.

However, we had seen very photon-efficient, near-complete Z→E azobenzene isomerization upon exciting a covalently-attached Rhodamine B auxiliary.<sup>35</sup> The mechanism of this isomerisation was unknown, but resonant energy transfer seemed unlikely due to near-zero overlap of Z-azo absorbance (<530 nm) and rhodamine emission (>570 nm; Figure S13, Table S2). Since this highly photostable and biocompatible auxiliary has a vanishingly low  $\Phi_{ISC}$ , we wondered if proximity to the azobenzene with its large spin-orbit

coupling coefficients was driving the energy of the singlet excited auxiliary ultimately into an azobenzene triplet, that then collapsed to the observed mostly-E photostationary state (PSS; discussion in Supporting Note 4). If this were true, low- $\Phi_{ISC}$  auxiliaries might have unique power for biocompatible TET switching: (a) when the azobenzene motif contacts it, even a low- $\Phi_{ISC}$  chromophore might pump isomerisation via the triplet state with high efficiency; but (b) when the azobenzene motif is not in molecular contact (e.g. linker-extended conformation), the chromophore should stay in a biocompatible singlet manifold photocycle. (We later found a 1987 report by Targowski and coworkers, potentially showing conditional TET from rhodamine to cyclooctatetraene<sup>36</sup>, that may support the plausibility of this idea.) This *conditional TET* might avoid the O<sub>2</sub>-incompatibility of previous TET approaches. It would also allow using validated fluorophores, optimised for high absorption, long excited state lifetimes, and excellent biological tractability, that have known biodistribution, cell entry and localisation.

Thus, despite their small  $\Phi_{ISC}$  values, we explored fluorophores such as rhodamines and cyanines as photoswitching auxiliaries. We can now report that their dyads are a generally applicable strategy for intrinsically high-performing, biocompatible, O<sub>2</sub>-tolerant, high-photon-efficiency and near-complete Z→E-isomerisable photopharmacology tools, with red/NIR response and deep-tissue potential.

## 2. RESULTS

### 2.1 Design of conditional TET dyads

To test for conditional TET, we first excluded dyads that can perform intramolecular singlet state photoredox. For highly absorbing chromophores with low  $\Phi_{ISC}$ , such dyads can be predicted from their excited state reduction potential  $E_{red}^{S1}$  (Tables S8-S9) and the azobenzene ground state oxidation potential (Tables S10-S11, Figure S14), allowing us to exclude such dyads from the present study. (In a parallel study, these values were measured, and dyads that would be predicted to undergo photoredox from these values were confirmed to undergo characteristically 100%-complete, Z→E photoredox isomerisation; see Supporting Note 5).<sup>24</sup>

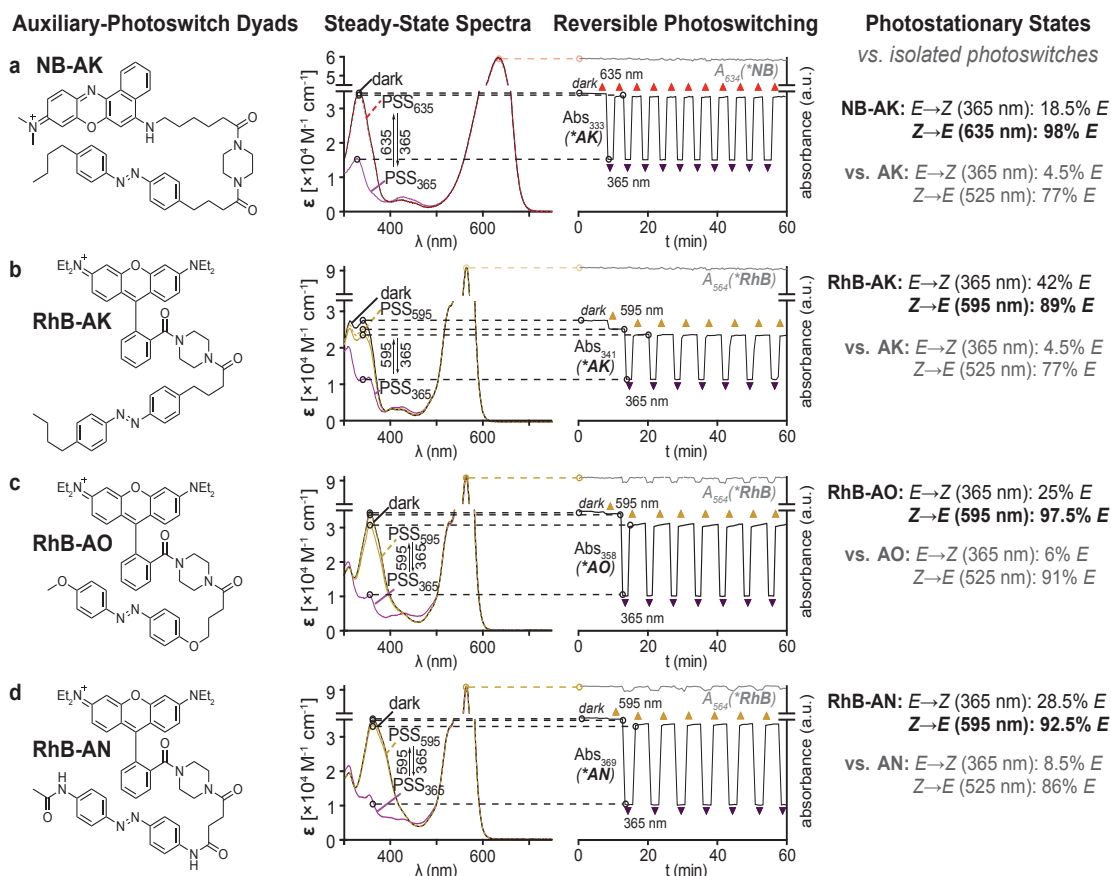


**Figure 2:** Azobenzene-chromophore dyads can access photostable, triplet-sensitisation-based, long-wavelength  $Z \rightarrow E$  photoswitching that is nearly complete. This allows highly photostable, fast, reversible, bidirectional photoswitching with the major classes of bistable azobenzenes.

We focused on finding chromophores for "bistable" azobenzene types, i.e. those whose metastable  $Z$ -isomer spontaneously isomerises to the thermodynamic  $E$  isomer more slowly than typical experimental timescales (e.g. half-life > 12 hours; **Supporting Note 6**). These bidirectionally-photoisomerisable switch types are the ones that have been the most useful in materials and photopharmacology, and which would benefit most from better  $Z \rightarrow E$  completion. This includes switches with alkyl substituents (**AK**; e.g. "photolipids"<sup>13,37,38</sup>), alkoxy groups at both *para* positions (**AO**; e.g. actin and tubulin cytoskeleton modulators<sup>6,35,39-41</sup>), and anilides at both *para* positions (**AN**; e.g. ion channel modulators<sup>4,8,42-44</sup>).

Electron-neutral **AK**-type azobenzenes are difficult to oxidize ( $E_{1/2}(Az^{*+}/Az) = E_{ox}^{S0} \sim 1.7 \text{ V vs Fc}$ )<sup>24</sup>, so **AK**s could be paired with nearly all chromophores we measured ( $E_{red}^{S1} \sim 0.5 - 1.2 \text{ V}$ )<sup>24</sup> without complications from photoredox-based processes. Electron-rich **AO** and **AN** ( $E_{ox}^{S0} \sim 1 \text{ V}$ ) are compatible with e.g. xanthene and cyanine chromophore sensitisation, but were excluded from pairing with stronger photooxidants like the naphthoxazine Nile Blue (**NB**,  $E_{red}^{S1} = 1.1 \text{ V}$ )<sup>24</sup> (**Supporting Note 4**). The spectral and photoelectrochemical properties of the chosen azobenzenes and chromophores are summarised in **Figure 1c** and **Tables S9-S11**.

## 2.2 Red/NIR photoswitching in sensitisation dyads

A range of dyads with bistable **AK**, **AO** and **AN** azobenzenes connected via flexible linkers to photostable chromophores (rhodamine **B RhB**, cyanine-3 **Cy3**, Nile Blue **NB**, etc) were synthesized by standard chemistries; the dyads are denoted e.g. **RhB-AO**, **Cy3-AN**, **NB-AK** according to constitution (**Figure 2-3**). The dyads' photoswitching was investigated by UV/VIS spectroscopy, in dilute aqueous conditions ( $\sim 10 \mu\text{M}$ ), at neutral pH, under normal aerated conditions that lead to photobleaching for the known intermolecular triplet sensitizer systems<sup>31,32</sup>. HPLC measurements of the  $E/Z$

ratios at fixed PSSs were used to calibrate those during bulk population switching in UV-Vis: a method that is faster, cheaper, more convenient, and photochemically more appropriate, than the costly and slow in-NMR-illumination methods that are typically used<sup>45,46</sup> (**Supporting Information section 5**). Considering  $E \rightarrow Z$  switching, the dyads were switched to a mostly- $Z$  state by UV light, reaching PSS % $Z$  values slightly lower than for the unconjugated azobenzenes (typically 70-85%  $Z$  in the dyad vs 85-95%  $Z$  without the chromophore), although with comparably rapid bulk photoswitching speed (**Supporting Table S3** and **Table S5**). The lower UV-PSS % $Z$  is likely due to competitive absorption by the chromophores, which then promote  $Z \rightarrow E$  switching (see below); but since  $FDR = \Phi_F/\Phi_B$ , these marginally smaller forward-switching fractions  $\Phi_F$  for the dyads only slightly affect their resultant FDRs.

To analyse practical bulk photoswitching performance, we define bulk switching "rates" in this work as being proportional to the progress of isomerisation towards PSS, per mole of photons. Considering  $Z \rightarrow E$  switching, typical unconjugated **AK**, **AN** and **AO** photoswitches are isomerised to 75-90%  $E$  by 490-525 nm light, with bulk photoswitching rates that are roughly 10-30 times smaller than for isomerisation with UV light: due to smaller extinction coefficients and more  $E/Z$ -absorbance overlap in the visible. When assays stringently use optical filters or true monochromatic light sources rather than broadband LEDs, they usually have no photoresponse above 550 nm except to high-intensity focused lasers (**Figure 3c**).

Uniquely, however, their dyads were rapidly  $Z \rightarrow E$  photoisomerised by yellow/red/NIR light, with high completeness (**Figures 2-3**). Rhodamine dyads were particularly effective, with 595 nm PSSs of  $\geq 97\% E$  (**Figure 3a**; FDRs up to 28), and bulk  $Z \rightarrow E$  yellow-light-photoswitching rates that were faster than the unconjugated azobenzenes' photoresponse to UV light (**Supporting Table S5**).



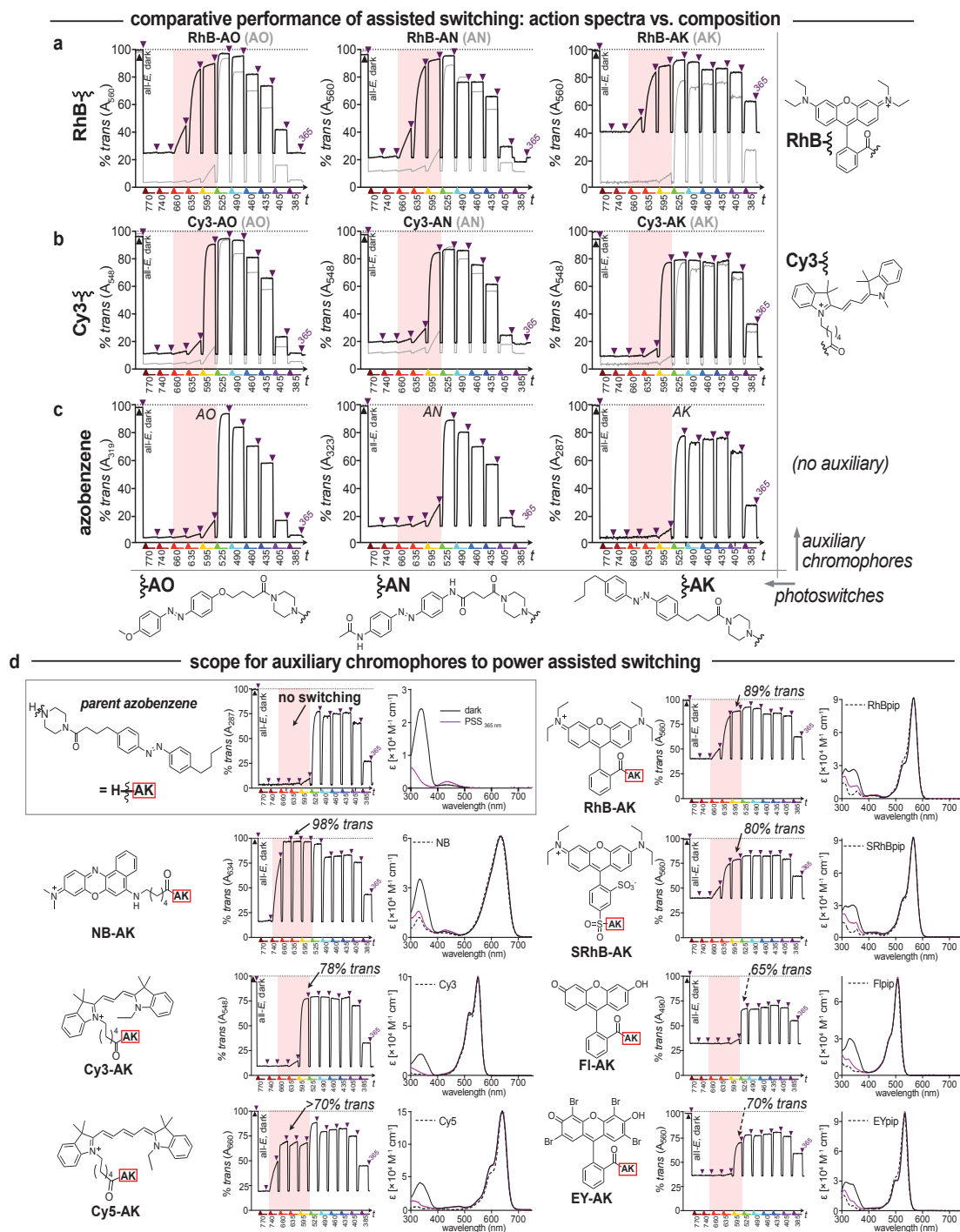


**Figure 3: The spectrally-extended photoresponses of azobenzene-chromophore dyads that undergo triplet energy transfer:** Action spectra (%*E* photoresponse), while phases of 365 nm (isomerises to mostly-*Z*) are alternated with phases at up to 770 nm (observation by UV-Vis, calibration to %*E* by HPLC). (a-c) Photoresponses of AO, AN and AK, and their RhB / Cy3 conjugates. The longer-wavelength photoresponses of the dyads, based on absorption by the chromophore motifs (red shading), are photon-efficient and approach *E*-enriched states. (d) Photoresponse of AK and a range of its conjugates. Sensitization is a common phenomenon over a wide range of chromophore classes and absorption wavelengths. NB-AK shows the most-complete sensitized isomerization (98% *E*), responding up to 740 nm.

Cy 5 dyads were particularly NIR-shifted, allowing rapid *Z*→*E* photoresponses even up to ca. 750 nm (Figure 3d; PSS: >70% *E* with half the rate of azobenzene UV-photoswitching). For alkylazobenzene AK this represents a ≥250 nm bathochromic shift of *Z*→*E* switch wavelength, plus 3-fold more complete *Z*→*E* photoswitching and 20-fold faster photoresponse in the NIR dyad than with typical wavelengths used for its *Z*→*E* photoswitching (460–500 nm). Alternatively, when combined with naphthoxazine (Figure 3d), the NB-AK dyad reached a PSS under 635 nm light of 98% *E* and with similar bulk photoswitching rate as unconjugated AK under UV light (Figure 2; bulk photoswitching rates are determined

from the "half-power"  $p_{1/2}$  for half-conversion towards PSS, calibrated over a range of source intensities, and thus reflect the photon efficiency of switching: see Figures S6-S7, Tables S3 and S5 and Supporting Note 7). Consistent with this sensitisation being an intrinsic, intramolecular process, 1:1 physical mixtures of the free chromophores with the azobenzenes under biologically plausible conditions (e.g. NB with AK, 10 μM each) showed no TET-assisted photoswitching: they did not respond to light >530 nm, and their response below 530 nm was almost identical to that of the free azobenzene (slightly slowed, consistent with optical shielding by the chromophores: Figure S8). The dyads could be reversibly

photoswitched between their PSSs by alternating phases of UV and yellow/red/NIR light over tens of cycles, with vast excesses of light applied in each phase, without or with less than 1% photodegradation observed (**Figure 2**). The photon-efficient, high-completeness, fully reversible long-wavelength photoresponse is the most important aspect of the dyads' behaviour. Further features are discussed in **Supporting Note 8**.

### 2.3 Spectral response profiling of sensitisation dyads

Beyond the two-colour photoswitch cycling (**Figure 2**), we also profiled the spectral photoresponses of key **RhB** and **Cy3** dyads across the NIR/Vis/nUV range (**Figure 3a-b**). All six dyads had reliable functional performance, giving more-complete and much faster  $Z \rightarrow E$  photoswitching by the longer-wavelength sensitised process than by direct azobenzene photoexcitation (**Figure 3c**; see also **Table S3**). For illumination wavelengths above 525 nm, where only the **RhB/Cy3** chromophores absorb efficiently, their photoresponses were dominated by the mostly-complete  $Z \rightarrow E$  sensitised switching process; <500 nm, their photoresponses (bulk switching speeds and PSSs reached) somewhat resemble those of the unconjugated azobenzenes, but with lower  $Z$ -percentages at equilibrium, consistent with residual TET-based  $Z \rightarrow E$  isomerisation.

### 2.4 A range of chromophores can be used for sensitizer dyads

Electron-neutral azobenzenes like **AK** have hundreds of reports from materials through to chemical biology. In biological applications they are excellent lipid mimics,<sup>47,48</sup> and are understood to be more resistant to biothiols than electron-rich bistable switches like **AO** and **AN**. However, compared to **AO** and **AN**, they have less-complete  $Z \rightarrow E$  photoswitching, and blue-shifted photoresponses, which restrict the power they could otherwise exert.<sup>49</sup> We had observed excellent photoswitching enhancement in **NB-AK** and **RhB-AK** dyads (**Figure 2**), so we now created a range of **AK** dyads to study how efficiently and completely different chromophores sensitise the isomerisation of these standard photoswitches (**Figure 3d**).

We found that sensitisation is a very general phenomenon (**Figure 3d**). Compared to the switch **AK**, its dyads with chromophores that absorb at longer wavelengths had longer-wavelength photoresponses; and even where chromophore absorption overlapped with **AK** (e.g. fluorescein), the sensitisation was clear from the different PSS % $E$  reached and the much smaller half-powers required to reach these PSSs (**Fl-AK** vs **AK**; **Figure 3d**; **Supporting Table S5**).

### 2.5 Mechanistic hypothesis for general assisted switched

So far, the mechanism driving dyad isomerisation was unknown. We excluded intermolecular processes, either between conjugates or involving short-lived intermediates, since the physical mixtures did not show sensitised switching (**Figure 3d** vs **Figure S8**). We had excluded photoredox, not only due to the mismatch of redox potentials, but also since their assisted isomerisation reaches <98% $E$  (whereas conjugates whose potentials match for photoredox, all isomerise to >99.7%  $E$ <sup>24</sup>). Energy transfer from the chromophore to promote an  $S_0 \rightarrow S_1$  transition of the azobenzene (e.g. FRET) was also excluded since light >700 nm was able to drive the sensitised process rapidly, but this is >250 nm beyond the azobenzene's own absorption i.e. spectral overlap is insufficient (**Supporting Note 4**).

However, azobenzenes' low-lying triplet state, reported at ca. 120-150 kJ/mol<sup>25,26</sup> (equivalent to ca. 800-1000 nm) is energetically accessible; and the observation that all PSSs with significant sensitisation are  $E$ -enriched, up to but not exceeding 98%, supports populating the azobenzene triplet as it mirrors the ten previously reported

intermolecular studies' PSS results (typ. 90-98%  $E$ )<sup>26,28-32</sup>. We noted that azobenzene has very high spin-orbit coupling coefficients<sup>27,50</sup>; and that it is a remarkably rapid intermolecular quencher of triplet states (~diffusion-limited),<sup>29,31,32</sup> which suggests that a triplet-mediated process might be energetically and kinetically reasonable.

Nevertheless, our observations are incompatible with a normal triplet sensitisation process where triplet energy is transferred to the azobenzene *only after* self-ISC ( $S_1 \rightarrow T_1$ ) occurs on the "isolated" chromophore moiety, for several reasons (**Supporting Note 4**). These include, that (i) for self-ISC, the rate of sensitised isomerisation should be proportional to the chromophore's  $\Phi_{ISC}$ : whereas dyads had nearly identical rates across  $\geq 2$  orders of magnitude of  $\Phi_{ISC}$  (eosin ~ 0.3 vs rhodamine <0.01); and (ii) for self-ISC, the long lifetime of a chromophore triplet ought always to allow it to collide with its azobenzene, such that for a given azobenzene, all chromophores should drive an identical sensitised PSS % $E$ : whereas in dyads, substantially different PSSs were seen (e.g. 98% $E$  for **NB-AK** but 70-80% $E$  with **Cy3/Cy5-AK**).

**We therefore propose that the mechanism for long wavelength sensitised photoresponse is:** (i) excitation of the auxiliary part within the conjugates gives its  $S_1$  state with its usual photochemistry (as in the isolated chromophore state); (ii) some fraction of the dyad molecules are *pre-associated*: their azobenzene and chromophore are in close enough molecular contact to form an exciplex; (iii) the exciplex brings the azobenzene's spin-orbit coupling coefficients to bear on the excited state, allowing much more efficient ISC to make an exciplex triplet, than the chromophore could usually perform when isolated; (iv) the exciplex triplet then separates to give the *azobenzene* triplet, which undergoes its usual ultrafast  $T_1 \rightarrow S_0$  relaxation that can be accompanied by isomerisation favouring an  $E$ -enriched state (**Figure 4a**). This predicts that the assisted switching efficiency can be much higher than the  $\Phi_{ISC}$  of the isolated chromophore. (In parallel, the fraction of  $S_1$  dyad that is *not pre-associated* undergoes its usual mix of radiative and non-radiative  $S_1 \rightarrow S_0$  decay, without azobenzene isomerisation.)

It seems reasonable that  $E$ - and  $Z$ -isomers of the azobenzene should have different likelihoods of being pre-associated to undergo the exciplex-ISC process, according to the dyad structure. This in turn predicts that the sensitised PSSs of the same azobenzene will differ, depending on the linker and on the chromophore in its dyad. (An extreme case of pre-association being used to tune PSSs was recently published by Klajn, Schapiro *et al.* as "DESC": exploiting  $E/Z$ -dependent triplet sensitisation based on  $E/Z$ -dependent steric fit to achieve up to 95% $Z$  long-wavelength sensitised PSS<sup>33</sup>, rather than the 98% $E$  that would be expected from solution-state sensitisation).

We will propose below that typical pre-associated fractions may be ca. 5-50%, and are up to four-fold larger for the  $Z$  than the  $E$  isomer of the same dyad. Since this fraction is relatively high, it will be seen to explain plausibly the two observations that (i) the sensitised process is so photon-efficient that the bulk sensitised photoisomerisation rates are comparable with those for direct azobenzene isomerisation, regardless of whether the chromophore in the dyad has a very low or very high  $\Phi_{ISC}$ ; and relatedly, (ii) at UV wavelengths where the azobenzenes' absorbance is often 2-5 times stronger than that of the chromophore, PSS% $E$  values are typically 20-30% higher for conjugates than for the free azobenzenes (see **section 2.6**).

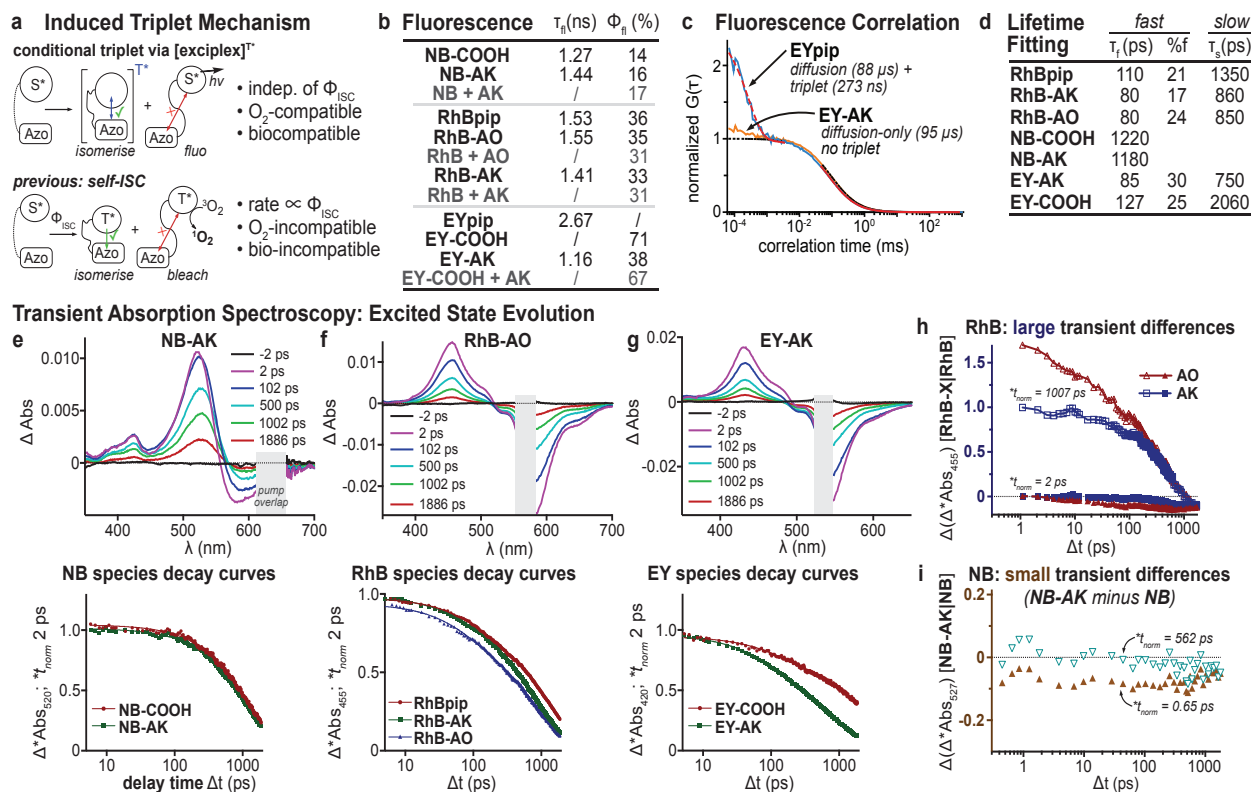


**Figure 4: Spectroscopic experiments to study the sensitization-based photoswitching mechanism.** (a) mechanistic proposal for dyad photoreponse. (b) Fluorescence lifetimes and quantum yields for parent chromophores, *E*-dyads, and physical mixtures (grey) ("/" indicates not measured). (c) Fluorescence correlation function normalized to the diffusion component (as 1) for eosin (EYpip, blue) and eosin-azobenzene dyad (EY-AK, orange). The FCS curve for EYpip fits a triplet model, but EY-AK fits a pure diffusion model (no triplet or other dark states are present). (d) Excited state decay kinetics extracted from mono- or biexponential fitted TAS traces. (e,f,g) Transient absorption spectra at selected delay times ( $\Delta\text{Abs}(\Delta t, \lambda)$ ) for (e) NB-, (f) RhB-, and (g) EY- dyads, and excited state decay kinetics of dyads and their parent fluorophores, with "early" (2 ps) normalization. (h)  $\Delta(\Delta^*\text{Abs}(\Delta t, \lambda))$  for (RhB-AO minus RhBpip) and for (RhB-AK minus RhBpip), at early (2 ps) and late (1007 ps) normalization. (i)  $\Delta(\Delta^*\text{Abs}(\Delta t, \lambda))$  for (NB-AO minus NB-COOH) and for (NB-AK minus NB-COOH), at early (0.65 ps) and late (562 ps) normalization.

It is a crucial feature of the exciplex proposal that the triplet sensitisation in azobenzene dyads does not require prior generation of long-lived triplet states on the chromophores (Figure 4a). The triplet can be created on the exciplex then collapse to the azobenzene, and these triplets are expected to have ultrashort lifetimes (e.g. azobenzene: picoseconds), quite unlike typical chromophore triplets (microseconds). Therefore, by using chromophores which have tiny  $\Phi_{ISC}$ , there will be no significant population of triplet states, *except in the exciplexes from pre-associated dyads* which decay rapidly. Thus triplet sensitisation can be achieved without the photochemical drawbacks of long-lived isolated chromophore triplets: making the exciplex triplet process efficient under normal air atmosphere, without singlet oxygen generation, photobleaching, and phototoxicity. Indeed, this is in line with all our experimental observations, where photoswitching was conducted exclusively under air, and without observing photobleaching. This performance is in strong contrast to all previous methods involving azobenzene triplet sensitisation, since in those methods it was assumed that efficient prior generation of a chromophore triplet would be required, but those methods did not allow to quench those triplets quantitatively by the azobenzene. For example, molecular oxygen greatly quenched the triplet-mediated azobenzene isomerisation in solution-state intermolecular triplet sensitisation (isomerisation slows, photobleaching rises); and even with DESC sensitisation, it would be expected that any photosensitiser that is not currently complexed to an azobenzene could be quenched instead by molecular oxygen. Such a predictable "escape" of triplet states with high- $\Phi_{ISC}$  dyes would be completely incompatible with biological applications: but in the dyad process with low- $\Phi_{ISC}$  dyes, we expected that triplet escape and singlet oxygen

generation would not occur since the triplets are only formed *in contact with the azobenzene that is ready to receive and dissipate them fast*.

In case a chromophore itself performs ISC and enters a triplet, this (potentially long-lived) triplet can still perform collisional triplet energy transfer to the azobenzene in its dyad. This "self-ISC" route should be most visible with chromophores that have high  $\Phi_{ISC}$ , such as eosin EY ( $\Phi_{ISC} \sim 0.3$ ): if efficiently quenched by the azobenzene, then its dyads should not have long-lived triplet states (confirmed: Figure 4c). However, the exciplex-ISC process does not imply, nor necessarily benefit from, self-ISC running in parallel (see below). Taken together, we simply propose that chromophores do not need a high  $\Phi_{ISC}$  to drive the exciplex triplet process in azobenzene dyads; but if their  $\Phi_{ISC}$  is high, then the self-ISC dyads *can* escape the negative photochemistries associated with triplet states, as long as the energy match is reasonable and the linker/attachment design allows the azobenzene to collide more efficiently with the chromophore than e.g. O<sub>2</sub> or other environmental triplet quenchers.

## 2.6 Mechanistic analysis

We now studied the dyads to test this proposed mechanism: using fluorescence lifetime ( $\tau_f$ ) and fluorescence quantum yield ( $\Phi_f$ ) of the *E*-dyads; fluorescence correlation spectroscopy (FCS) and transient absorption spectroscopy (TAS) of the mostly-*E* dyads (TET-sensitised stationary states, often ca. 6:1 *E:Z*); and relative fluorescence intensities of the *E* vs *Z* isomers from fluorimetry during bulk isomerisation. We do not consider these studies mechanistically conclusive, so we only highlight some of the coherent mechanistic aspects, with a full presentation of the data in the **Supporting Information** (Chapters 6-9, Tables S13-S14, Figures S18-S23).



(1) We proposed that typically 10% of the *E*-dyads are pre-associated and undergo the exciplex triplet mechanism (we bundle pre-association and exciplex ISC together in the quantum yield  $\Phi_{\text{exciplex},E}$ ). This is not easy to prove, since most measurements (TAS,  $\tau_{\text{a}}$ ,  $\Phi_{\text{a}}$ ) are at best accurate to  $\pm 15\%$ . However, for low- $\Phi_{\text{ISC}}$  chromophores **RhB** and **NB**,  $\tau_{\text{a}}$  and  $\Phi_{\text{a}}$  of the *E*-dyads are indeed within measurement error of their isolated chromophores (**Figure 4b**), coherent with  $\lesssim 15\%$  of their singlet excited states funneling to isomerisation. Dyad  $\Phi_{\text{a}}$  were strongly *E/Z*-dependent however, with ratios of  $\Phi_{\text{a},E}/\Phi_{\text{a},Z}$  up to 3.8 for **RhB-AO** (1.9 for **RhB-AK**, etc: **Figure S22-S23**), indicating much more depletion of chromophore S1 states in *Z*-dyads: thus we assume their  $\Phi_{\text{exciplex},Z}$  values are higher than their  $\Phi_{\text{exciplex},E}$  by this factor. With  $\Phi_{\text{exciplex},E}$  values ca. 0.1, this gives  $\Phi_{\text{exciplex},Z}(\text{RhB-AO}) = 0.2$ ,  $\Phi_{\text{exciplex},Z}(\text{RhB-AK}) = 0.4$ , which matches the trend in their bulk 595 nm *Z*→*E* isomerisation kinetics (**RhB-AO** ca. twice as photon-efficient as **RhB-AK**, **Table S3**). These *E/Z*-differences of fluorescence are also coherent with **RhB-AO** having a more *E*-rich sensitised PSS than **RhB-AK** (97% vs 89%, **Fig 1**).

(2) It is also coherent that as conjugates' TAS decays became more rapid than their parent fluorophore (increasing chance of harvesting the chromophore's energy to switch on the single-molecule level), their bulk sensitised photoswitching rates also increased. For example, **RhB** dyads bulk isomerise substantially faster than **NB** dyads (e.g. **Table S5**, half-power 0.23 vs 3.7 mJ/mm<sup>2</sup>), which suggests that harvesting energy from **RhB** for switching is more likely than from **NB**. Matching this, while no significant differences are seen in the evolution of **NB-AK** vs **NB-COOH** excited state populations by TAS (**Figure 4eh**), the differences between **RhB-AK/-AO** vs **RhBpip** are noticeable (**Figure 4fi**). For **EY-AK**, which had even faster bulk photoswitching, the difference of its TAS decay rate compared to **EY-COOH** was even larger (**Figure 4g**).

(3) **EY** is a chromophore that can perform self-ISC ( $\Phi_{\text{ISC}} \sim 0.3$ ). FCS shows a large triplet fraction for **EYpip**, but no triplet fraction in dyad *E*-**EY-AK** even under high-power illumination (**Figure 4cd**, **Figure S19**). We can interpret this as indicating that  $\sim 30\%$  of the excitations of **EY** in the *E*-**EY-AK** dyad are transferred as triplet energy onto **AK**, which reaches a plausible triplet-sensitised PSS (88%*E* at 535 nm). We now compare the switching rates of **EY-AK** to chemically similar dyads whose chromophores should undergo only exciplex-ISC (low  $\Phi_{\text{ISC}}$ ; **FI-AK** and **RhB-AK**). The bulk photoswitching rates of these species are within 20% of those of **EY-AK** under UV (*E*→*Z*) or green (*Z*→*E*) light; and the green light PSS with **RhB-AK** (89%*E* at 564 nm) is also similar to that for **EY-AK** (**Table S5**). This is plausible if  $\Phi_{\text{exciplex}}$  for **FI-AK** and **RhB-AK** are similar to the  $\Phi_{\text{ISC}}$  of **EY**: matching the proposed  $\Phi_{\text{exciplex}}$  range (ca. 0.05-0.5). The similar speeds confirm that self-ISC is not required for photon-efficient assisted switching, and that the exciplex-ISC route can be an efficient assisted switching mechanism regardless of  $\Phi_{\text{ISC}}$ .

(4) We understood these sensitised effects on photoswitching and triplet state depletion are caused by proximity of the switch and fluorophore. We next tested if these behaviours of high- $\Phi_{\text{ISC}}$  and low- $\Phi_{\text{ISC}}$  chromophores in dyads, are reproduced by *noncovalently* associating them to azobenzenes. For this we assembled 100% alkylazobenzene lipid vesicles, doped them with 1 mol% of lipidated high- $\Phi_{\text{ISC}}$  methylene blue (**MB**,  $\Phi_{\text{ISC}, 630 \text{ nm}} \sim 0.5$ ) or low- $\Phi_{\text{ISC}}$  **NB**, and studied the photoswitching of the azo-lipid as well as the chromophores' photostability. Mirroring the results for dyads **EY-AK** vs **RhB-AK**, (i) lipidated high- $\Phi_{\text{ISC}}$  **MB** drove effective photocatalytic 630 nm *Z*→*E* isomerisation of the azolipid vesicles (**Figure S12b**), but (ii) lipidated low- $\Phi_{\text{ISC}}$  **NB** was *similarly* photon-efficient in its 630 nm sensitisation of *Z*→*E* vesicle isomerisation as high- $\Phi_{\text{ISC}}$  **MB**

lipid (**Figure S12d**); (iii) lipidated **MB** was entirely photostabilised by the azolipid (quenching of self-ISC triplets which otherwise cause its photobleaching, **Figure S12a**; predictably, **NB** did not photobleach either with or without azolipid: **Figure S12c**). Taken together, this supports that low- $\Phi_{\text{ISC}}$  chromophores can drive highly photon-efficient assisted switching, without requiring direct triplet generation on the chromophore to initiate it (**Supporting Note 9**).

(5) We also attempted to use the dyads' higher %*E* fraction at UV PSSs, compared to their isolated azobenzenes, to roughly estimate  $\Phi_{\text{exciplex}}$ . Although this involves weak assumptions, it indicated that  $\Phi_{\text{exciplex}}$  values can be similar to azobenzene  $\Phi_{E \rightarrow Z}$  and  $\Phi_{Z \rightarrow E}$  values (e.g. for **RhB** conjugates, ca. 0.05 -0.5) which plausibly fits the proposed mechanism (**Supporting Information** section 8.4). We also tried using several modelling techniques to fit the isomerisation *kinetics* as well as the PSS values; but the number of degrees of freedom in these models seems to make data-constrained fitting impossible. We are confident however, that the observed fast isomerisation kinetics and strongly-shifted PSS values indicate that  $\Phi_{\text{exciplex}}$  can plausibly be on the order of >0.1, even for dyads containing low- $\Phi_{\text{ISC}}$  chromophores.

By combining this good quantum yield  $\Phi_{\text{exciplex}}$  with the high long-wavelength extinction coefficients of the chromophores chosen, it seemed that assisted photoswitching could be very photon-efficient. Also, the exciplex proposal does not need to generate damaging chromophore triplets (and the **EY-AK** results show that dyad systems can even *remove* high levels of chromophore triplets generated by self-ISC). Therefore, while the mechanism operating in these dyads remains unclear to us, it seemed that they possessed the right, and unique, combination of photon-efficient unimolecular isomerisation at long wavelengths plus biologically "innocent" photochemistry, that would be needed to apply them in living systems; and we moved forward to testing them in living cells and tissues.

## 2.7 Sensitiser dyads can harness near-infrared light for biological photocontrol in living cells and acute brain slices

So far, we established that sensitisation by a range of auxiliary chromophores can drive near-complete *Z*→*E* photoisomerization of azobenzenes at 550-770 nm, with high photon efficiency, in biocompatible media, under air, with high photostability: and without re-engineering azobenzene substituents. We next wished to leverage these advances to perform the first single-NIR-photon chemical photoswitching-based control of functions of live cells (**Figure 5**).

NIR-photocontrolling the activity of metabotropic glutamate receptors (mGluRs) is an ideal system that can test all these features while also making excellent use of this performance. mGluRs are G-protein coupled receptors (GPCRs) whose important roles in neuromodulation in the central and peripheral nervous systems make them major drug targets for a range of disorders.<sup>51,52</sup> Due to the importance of discriminating their tissue- and cell-type-specific roles, they have also been a target for photopharmacology for over a decade.<sup>53,54</sup> mGluR2 has seen the most advanced tool development, with photoswitchable glutamates termed "PORTLs" (photoswitchable orthogonal remotely-tethered ligands) that can be covalently tethered with 1:1 stoichiometry onto the receptor via SNAP-tag ligation (**Figure 5a**).<sup>53,55,56</sup> These were chemically refined for higher FDR (more complete photoswitching) as the *para,para'*-anilide/urea "BGAG<sub>12,400</sub>"-type azobenzenes (**Figure 5d**);<sup>49</sup> reworked as branched oligoglutamates that improved the potency of receptor activation,<sup>8</sup> and biological studies have shown how their efficacy translates from cell culture to tissue slice,<sup>53</sup> to acute *in vivo* experiments in freely moving mice, where photocontrol was used to show state-dependent influences of mGluR2 on working memory.<sup>8,49</sup>

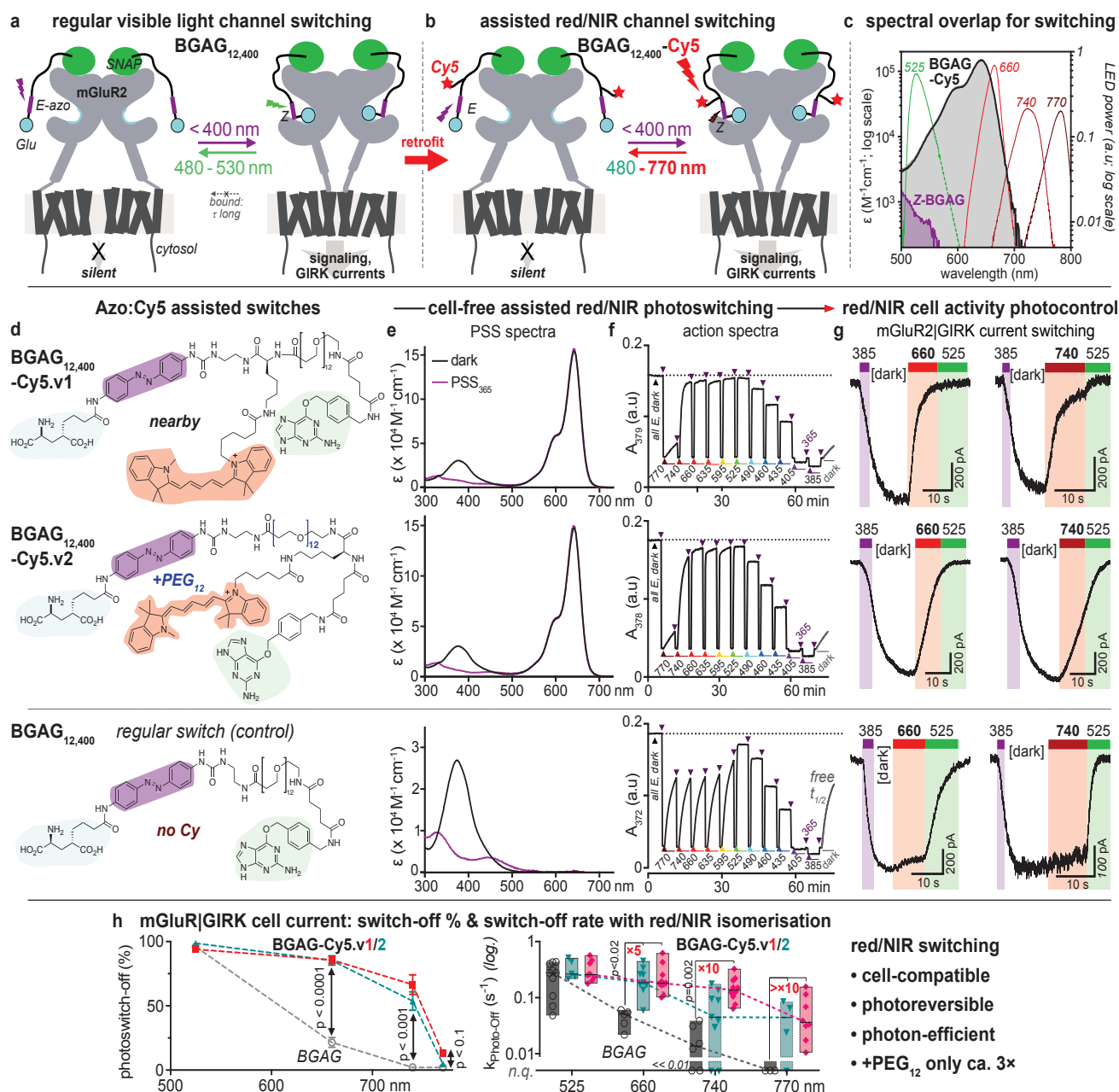


**Figure 5: Single-red/NIR-photon photocontrol of GPCR activity in live cells.** (a)  $\text{BGAG}_{12,400}$  is a tethered UV/green-photoswitchable agonist of the SNAP-mGluR2 fusion receptor. (b-d) Retrofitting  $\text{BGAG}_{12,400}$  with Cy5 gives  $\text{BGAG}_{12,400}\text{-Cy5s}$ , primed for operation by LEDs at 660-740 nm. (e-f) Cell-free spectra and photoswitching show the unique far-red/NIR photoresponse of  $\text{BGAG}\text{-Cy5s}$ ; the apparent response of  $\text{BGAG}_{12,400}$  in this region is due to its spontaneous relaxation when free (i.e. not receptor-bound); c.f. dark phase relaxation in panel f). (g) Near-complete Z $\rightarrow$ E red/NIR-sensitised "photoswitch-off" of  $\text{BGAG}_{12,400}\text{-Cy5}$  at 660 nm or 740 nm enables fast, bidirectionally photoreversible switching of mGluR2-evoked GIRK potassium currents in live cells (representative cell current electrophysiology traces in voltage clamp mode during photoswitching). (h) Completeness and photon-efficiency rate of mGluR2|GIRK current photoswitch-off (one cell per datapoint, as mean  $\pm$  SEM; switch-off % at 10 s after start of illumination, with 100% defined as current with all-E ligand; g-h: HEK293T cells expressing SNAP-mGluR2 and GIRK channels; details in **Figure S24**).

The PORTL tools for ligand:receptor-tethered mGluR2 photopharmacology have powerful performance, particularly as compared to more common photopharmaceutical types e.g. freely-diffusing affinity photoswitches that have usually struggled to reach *in vivo* utility (which we ascribe to the incompleteness and photon-inefficiency of their Z $\rightarrow$ E photoswitching, as complicated by biodistribution, *in vivo* inhomogeneity, and light dose limits: **Supporting Note 10**). Nevertheless, we reasoned that by *intrinsically* increasing both the photon efficiency and the completeness of Z $\rightarrow$ E photoswitching, while leaving the good performance of the UV E $\rightarrow$ Z step untouched, the sensitisation approach might usefully enhance even advanced mGluR2 photopharmaceutical toolsets. Since this ought to be possible without substantially redesigning the photoswitchable ligands, and the red/NIR-light response might even be useful for transcranial

photoswitching (fully noninvasive) due to the transparency of biological tissues in the red/NIR, we chose this system for a proof of concept test of whether *in vivo*-capable bidirectional switching could be reached by simple molecular retrofitting. We therefore aimed to test the bidirectionally reversible photoswitchability of mGluR2 currents driven by alternating violet (385 nm) and red/NIR (640-770 nm) illuminations of Cy5-conjugated SNAP-tethered glutamate ligands of type  $\text{BGAG}_{12,400}\text{-Cy5}$ , compared to their nearly identical congener lacking the cyanine auxiliary,  $\text{BGAG}_{12,400}$  (**Figure 5d**).

The conjugates had fast, near-complete red/NIR Z $\rightarrow$ E switching in cuvette in physiological media over the whole wavelength range from 595-740 nm (**Figure 5ef**); comparing strongly to the simple ligand  $\text{BGAG}_{12,400}$  that is only efficiently switchable  $\leq 525$  nm. The isomeric Cy-conjugate  $\text{BGAG}_{12,400}\text{-Cy5.v2}$ , where the Cy5 motif is

separated from the azobenzene by a PEG<sub>12</sub> spacer, also reached nearly identical PSSs in cuvette as the proximal **BGAG<sub>12,400</sub>-Cy5.v1**, with only 2.5-fold slower rate for red/NIR-sensitised switching (**Supporting Figure S11**). This was a less severe penalty than we expected for placing the chromophore far from the photoswitch.

We tested these conjugates in HEK293 cells expressing SNAP-mGluR2, which drives G protein-coupled inward rectifier potassium channel (GIRK) currents that allow electrophysiology readouts. Red/NIR-sensitised *Z*→*E* photoswitching at 660-740 nm controlled GPCR activity, with full photoreversibility when cycled with 385 nm *E*→*Z* illuminations. As expected from the absorption profile (**Figure 5c**), *Z*→*E* photoswitching with 660 nm reached near-completion for switch-off of mGluR2 currents more photon-efficiently than 740 nm (**Figure 5gh**): but neither wavelengths switched the simple **BGAG<sub>12,400</sub>**. This provides the first demonstration of nearly *biologically* complete chemical photoswitching-based control of live cell functions using red/NIR light.

Thus, remote functionalisation of a bioactive photoswitch allows it to be operated in sensitised mode, using red/NIR light, to reach excellent efficiency and completion for *in situ* *Z*→*E* switching

in cell culture. To push towards complex tissue applications, we next investigated whether sensitised switching can also be applied in acute mouse brain slices. For this, we followed a recent protocol<sup>49</sup> injecting Grm2-Cre mice with an adeno-associated virus (AAV) encoding SNAP-mGluR2 allowing the expression of SNAP-mGluR2 in the ventral hippocampus (vHipp). The mice were allowed to express the SNAP-mGluR2 for 2 weeks before locally injecting either **BGAG<sub>12,400</sub>** or **BGAG<sub>12,400</sub>-Cy5.v1** into the vHipp (**Figure 6ab**). After 2 h, acute horizontal slices were prepared, and patch-clamp recordings of granule cells of the dentate gyrus (DG) were performed. As expected, both compounds showed hyperpolarization of the cells following 385 nm induced *E*→*Z* switching, which was stable when UV light was switched off. Both compounds enabled repolarization of the cells after direct excitation of the azobenzene at 525 nm; but only **BGAG<sub>12,400</sub>-Cy5.v1** also shows repolarization with 660 nm or 740 nm illumination (Cy5-sensitised *Z*→*E* isomerization; **Figure 6c**), and this red/NIR-based repolarization reaches similar photoswitch-off response as direct 525 nm *Z*→*E* excitation of the azobenzene in the parent ligand **BGAG<sub>12,400</sub>** (**Figure 6de**). This shows the first ever single-photon far red-operated photoreversible chemical modulation of protein function in acute brain slices.

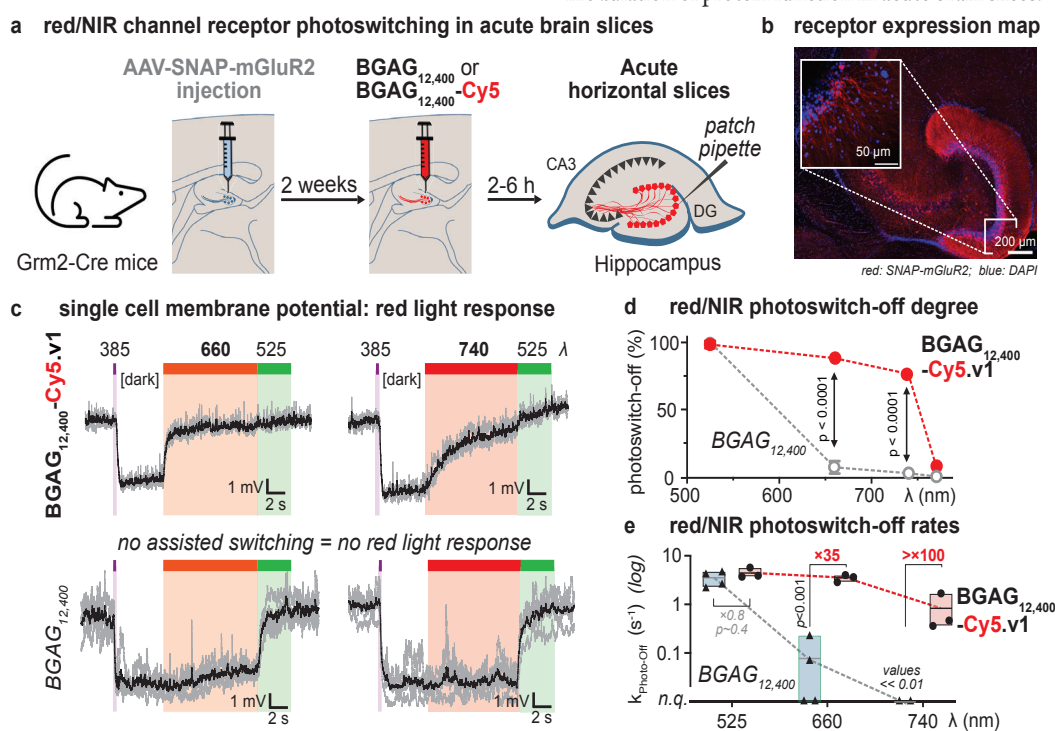


**Figure 6: Red/NIR OFF-photoswitching of mGluR2 in intact tissue.** (a) Schematic of experimental timeline and configuration of slice recordings. (b) SNAP-mGluR2 expression in granule cells of the dentate gyrus as detected by immunohistochemistry (blue: DAPI; red: SNAP-mGluR2). (c) Representative whole cell current clamp recordings showing reversible light-induced hyperpolarization/depolarization during five measurement cycles in the same cell (averaged traces in bold). For **BGAG<sub>12,400</sub>-Cy5.v1**, hyperpolarization (385 nm) is reversed by 660 nm or 740 nm illumination, as well as by 525 nm; while for **BGAG<sub>12,400</sub>**, only 525 nm is effective. (d) The completeness of "photoswitch-off" (degree of return to 525 nm-equilibrated state, after 10 s illumination with the given wavelength) (2-way ANOVA with multiple comparisons). (e) The rate of "photoswitch-off": **BGAG<sub>12,400</sub>-Cy5.v1** has significant switchoff rates up to 740 nm; **BGAG<sub>12,400</sub>** does not. Note the log scale vertical axis with break (n.q.: value <0.01 but not quantifiable).

### 3. DISCUSSION AND CONCLUSION

The chromophore-azobenzene dyads reported in this study show a broadly applicable, biocompatible strategy to enable longer-wavelength azobenzene photoisomerisation, and control over downstream biological functions that can be made dependent upon it, than has hitherto been possible. The strategy can be retrofitted onto existing functional photoswitches, with minimal structural changes in the vicinity of the photoswitch itself, and achieves very high-photon-efficiency compared to traditional photoswitch tuning methods. The *Z*→*E* isomerisation following this sensitisation

approach can reach 98% red/NIR-completeness with very high efficiency. Although the *Z*→*E* isomerisation of photoredox dyads, discussed in a parallel paper, is ~100% complete, we feel that the *Z*→*E* photoisomerisation of these sensitised dyads is not only *better* than any classical azobenzenes, but is also "complete and efficient enough" in an absolute sense: so that now at last, factors other than *Z*→*E* photoresponse efficiency, wavelengths, and completeness, will become the limiting factors for the performance of azobenzene photoswitches in their intended functional settings.

The two most visible potential drawbacks of this dyad approach are not serious limitations for their performance, in our opinion.



Firstly, the *E*→*Z* isomerisation of the dyads is less complete than the unconjugated azobenzenes, due to competing UV absorption (thus *Z*→*E* sensitisation) by the chromophore. We had chosen **Cy3**, **NB**, and **RhB** for initial dyad studies with the hope that their absorption minima in the near-UV region (**Figure 1c**) could be used as wavelengths for nearly-selective azobenzene excitation, so approaching the typical *E*→*Z* photoswitching completion that azobenzenes are known for. This was reasonably successful, with UV/violet *E*→*Z* ca. 80% complete for conjugates, vs ca. 85-95% complete for free switches; chromophores with lower photoresponses in this region should improve on this. However, since "lit-active" photopharmaceuticals are always preferred for biology,<sup>11</sup> such a small decrease in *E*→*Z* completion is unlikely to make a difference to experimental outcomes: for example, with ca. 1 μM of a *Z*-active **AK**-type lipid photopharmaceutical (as **AK** or as dyad **NB-AK**), 0.95 μM *Z* is not likely to give significantly different performance than 0.8 μM *Z* during an "on-switching" phase - it is rather the completion of the "off-switching" phase which will determine the assay power: in this case, 0.2 μM residual *Z* for **AK** at 500 nm, vs just 0.02 μM residual for **NB-AK** at 640 nm: equating to a 4.5-fold functional dynamic range for **AK** versus 40-fold functional dynamic range for **NB-AK**.

Secondly, the chromophore may bring complications, such as the potential for chemical or metabolic degradation in the target (biological) system, as well as difficulties in synthesis. However, we believe these can both be mitigated by (a) using the repertoire of (often commercial) chromophores that have been widely developed as highly stable, biocompatible fluorophores, and by (b) optimising the *biological E/Z-based photoswitchability of function* with the simplest possible, non-conjugated azobenzenes, then only *afterwards* attaching auxiliary chromophores that deliver satisfactory sensitised photoswitching performance. This is something of a paradigm shift: until now, photopharmaceutical research has tediously interleaved cycles improving the *E/Z* potency differential with cycles of *E*↔*Z*-photoswitchability improvement; in many cases, making severe trade-offs such as accepting fast-relaxing compounds even where bistable ligands are biologically more appropriate. Even so, it has often failed to cross the barrier of delivering *in situ bidirectionally photoswitchable* tools that conceptually out-perform unidirectionally photoactuated systems such as photocaged ligands. The decoupling of photochemistry and biology that the sensitisation approach provides should immediately ensure that almost any *Z*-active ligand can now be remotely modified to yield a highly-performing reversibly photoswitchable reagent, which can be used as bistable photopharmaceuticals were always intended: for off/on-photoswitching that is efficient and near-complete in both directions. This decoupling should seriously accelerate research in the current specialist groups, while greatly lowering the barriers for other groups to enter the field.

Alternatively, a poorly chosen chromophore may ruin the systemic or intracellular biodistribution of the dyad, as we suffered with undesired mitochondrial localisation;<sup>35</sup> or if a chromophore is linked in a way which blocks target binding, that will also ruin bioactivity<sup>39</sup>: in some systems, it may not be possible to overcome these. However, reagents whose biodistribution is genetically controlled by ligation to bioorthogonal protein tags, such as the SNAP-Tag ligated reagent used here (**Figure 5** and **6**), offer a very attractive method to avoid both risks. Indeed, many other SNAP- or Halo-ligatable photoswitchable reagents have been published,<sup>53</sup> several of them (particularly for HaloTag) with a fluorophore even incorporated in the system - although none had been examined for the sensitised switching, which we expect that they too will be capable of. Several groups already use fluorescently-labelled photoswitchable ligands, for

imaging then photocontrol; by making it known that the fluorescence imaging channel can probably be used to *actuate* these ligands, we hope that this work will promote an inventive variety of conjugates that can complement or out-perform and replace known photopharmaceuticals. Sensitised tethered ligands based around HaloTag may be particularly favoured, since the rates of cellular entry and ligation of HaloTag ligands are multiplied by up to 10<sup>4</sup> when rhodamine derivatives are present next to the chloroalkane warhead<sup>57</sup>: an ideal site for rhodamine-based auxiliaries, that are effective sensitisers.

The advantages of this photostable exciplex-ISC sensitised system also give hope for its wide adoption, in biology and beyond. By overcoming the problems of concepts such as the intermolecularity of classical self-ISC triplet sensitisation (inefficient and highly concentration- and environment-dependent), with its associated singlet oxygen mediated photobleaching and phototoxicity (also environment-dependent), this conjugation method usefully enhances the performance of the most important classes of photopharmaceutical scaffolds. Chiefly, the photon efficiency and completeness of the sensitised isomerisation repairs the key problems blocking *Z*→*E* photoisomerisation of any *Z*-active photopharmaceuticals in complex systems or *in vivo*. It is crucial to stress that the intramolecular sensitisation is an *intrinsic* property of the dyads: its operation is independent of concentration, intensity, and assay geometry, so it can be applied in a diversity of settings. These range from sparsely decorated cell-surface receptors in **Figure 5** and **6**, through to moderate concentrations as in the batch switching studies, and we anticipate also to high concentration settings as in films and materials. By avoiding the geometry-/concentration-dependency of two-component photochemistries,<sup>58</sup> the consistent and predictable behavior of such conjugates will be a great benefit for rational development and applications across many labs and uses.

Other advantages may be more relevant to specialised purposes. (1) Simply enabling NIR photocontrol in biology has often been considered a desirable<sup>14,15</sup> although as-yet unreach goal. Our approach now makes that performance available in easily-applicable single-photon mode, at least in the *Z*→*E* direction. We imagine that the challenge of sensitising also the single-photon *E*→*Z* switching process, so that it occurs at distinct but also well-penetrating wavelengths, to allow noninvasive bidirectional photoswitching very deep in tissue or complex media, will attract significant attention. We hope that these hitherto unsuspected opportunities for biocompatible, effective, sensitised photoswitching, which to a degree have been hiding in plain sight, will give that research a significant boost. (2) The self-reporting nature of the photoswitch conjugates can have additional benefits for assessing when sufficient ligand has penetrated to or remains in a target area. (3) Conceptually, this method will also expand possibilities for multi-state addressing of multiplexed photoswitches: e.g., a mixture of (**AK**, **AK-RhB**, **AK-Cy5**) may be set to (*ZZZ*) with 360 nm, (*ZZE*) with 360 then 740 nm, (*ZEE*) with 360 then 595 nm, reset to (*EEE*) with 525 nm, etc; and it should be possible to add further components with spectrally distinct chromophores. On that note, while we did not see any limits on the scope of chromophores that can be used for intramolecular triplet sensitisation, the success of the **Cy3** and **Cy5** scaffolds in our work directs attention to (i) long-wavelength congeners such as **Cy7/Cy7.5/ICG**, that have nearly identical bio-relevant properties such as logD, solubility, redox potentials, and biolocalisation, so should operate similarly on cell-surface-labelled receptors; (ii) analogues with different compartmentalisation (e.g. DiI / DiR lipophilic cyanines for lipid environment sensitisation or in-liposome



isomerisation); (iii) new polymethines such as Sletten's MeOFlav7 and JuloFlav7<sup>59,60</sup> which can be excited in the SWIR above 1000 nm; as well as to the increasing range of NIR / SWIR rhodamines<sup>61,62</sup>. It should be noted that the fluorescence brightness of these chromophores should not directly impact their performance as auxiliaries.

In conclusion, we have developed a broadly-applicable, photon-efficient method to perform near-complete  $Z \rightarrow E$  photoisomerization of a range of azobenzene photoswitches at wavelengths up to the well-penetrating near-infrared region. This method operates within triplet photochemical manifold but is biocompatible, O<sub>2</sub>-tolerant, and photostable. No specific re-engineering of azobenzene substituents is needed, so bioactivity or materials properties can be conserved. The auxiliary chromophore of choice can simply be covalently attached in the vicinity of the photoswitch; even when separated by a very long spacer, the sensitised photoresponse can be surprisingly fast, and distance does not compromise the completion it reaches. The quantum yield of the sensitised process can be comparable to that for direct azobenzene  $Z \leftrightarrow E$  isomerisations, but the far greater extinction coefficients possible for the sensitised  $Z \rightarrow E$  process allowed our dyads already to reach >50-fold higher photon-efficiency, and at long wavelengths, than optimal direct *blue*-light azobenzene  $Z \rightarrow E$  switching. We achieve the first ever instance of single-NIR-photon photoswitching of biological activity in acute (live) tissue slices, by actuating metabotropic glutamate receptors labelled with an auxiliary-bearing photoswitchable ligand, whose receptor-binding-photoswitch moiety is otherwise identical to ligands that have been known and painstakingly engineered to deliver multiple cycles of gains in photoresponse over the course of a decade. The straightforward route we now present to overcome the challenges of the  $Z \rightarrow E$  isomerisation direction, at drastically altered photoresponse wavelengths that can be rationally chosen independently of the photoswitch chemistry, should drive significant progress and innovation in using photoswitches across their full spectrum of applications, from single molecules and logic systems, to bulk materials, and to biology.

## ASSOCIATED CONTENT

### Supporting Information

PDF containing **Supporting Notes 1-10**, synthetic protocols, NMR spectra, photocharacterisation, analysis and discussion, and biology. **Datafile (XLSX)** with  $E/Z$  and PSS spectra of selected compounds.

**KEYWORDS:** Azobenzene, photoswitch, isomerization, triplet energy transfer, photopharmacology, photochemistry, NIR, photocontrol, molecular switch, exciplex.

## AUTHOR INFORMATION

### Corresponding Author

**Oliver Thorn-Seshold** – Department of Pharmacy, Ludwig-Maximilians University Munich, D-81377 Munich, Germany  
Email: [oliver.thorn-seshold@cup.lmu.de](mailto:oliver.thorn-seshold@cup.lmu.de)

### Author Contributions

BB designed targets, performed synthesis, assembled UV/Vis setup, performed UV/Vis and fluorescence spectroscopy, HPLC analysis, analyzed and coordinated data, assembled figures and contributed to manuscript preparation. VG and FS performed fluorescence lifetime experiments. VG performed fluorescence correlation spectroscopy. AJGH, HM and IA performed cell culture and brain slice experiments. AV performed transient absorption spectroscopy and fluorescence quantum

yield measurements. LF designed and wrote the python scripts for mechanism modeling. AMD and MR performed synthesis and photo-characterization. RM and CG performed electrochemical measurements. AO supervised electrochemical measurements. JEB supervised molecular modeling. BDI analyzed and supervised transient absorption spectroscopy and fluorescence quantum yield measurements. JB synthesized BGAG<sub>12,400</sub>-Cy5.v1/2. PT supervised fluorescence lifetime experiments and fluorescence correlation spectroscopy. JL analyzed and supervised cell culture and brain slice experiments. OTS conceived the study, performed synthesis, UV/Vis, data analysis, supervised all other experiments, and wrote the manuscript with input from all authors.

## Author Affiliations

(1) Department of Pharmacy, Ludwig-Maximilians University of Munich, D-81377 Munich, Germany; (2) Department of Chemistry, Ludwig-Maximilians University of Munich, D-81377 Munich, Germany; (3) Center for NanoScience, Ludwig-Maximilians University of Munich, D-81377 Munich, Germany; (4) Department of Biochemistry, Weill Cornell Medicine, New York, NY 10065, USA; (5) Leibniz Institute for Photonic Technology Jena e.V. (Leibniz-IPHT), Research Department Functional Interfaces, D-07745 Jena, Germany; (6) School of Chemistry, The University of New South Wales, NSW-2052 Sydney, Australia; (7) Chair for Photonics and Optoelectronics, Nano-Institute Munich, Department of Physics, Ludwig-Maximilians University of Munich, D-80539 Munich, Germany; (8) Institute for Physical Chemistry (IPC), Friedrich Schiller University Jena, D-07743 Jena, Germany; (9) Leibniz Institute for Molecular Pharmacology, D-13125 Berlin, Germany.

## Funding Sources

This research was supported by funds from the German Research Foundation (DFG: SPP 1926 project number 426018126 to OTS; SFB1032 Nanoagents for Spatiotemporal Control number 201269156 project B09 to OTS and project A13 to PT and project A08 to TL; Emmy Noether grant TH2231/1-1 number 400324123 to OTS; SFB TRR 152 project P24 number 239283807 to OTS); the National Institutes of Health (R01NS129904 to JL); a Rohr Family Research Scholar Award (to JL); a Monique Weill-Caulier Award (to JL); the Australian Research Council (DP220101847 to JEB); and the Munich Center for Nanoscience (CeNS: to OTS).

## ACKNOWLEDGMENTS

BB thanks the Boehringer Ingelheim Fonds for a PhD fellowship. We thank Andrea Stegner and Katja Fußer (LMU) for synthetic support, and Yves Carstensen (FSU) for quantum yield measurements. We are grateful for many insightful and constructive discussions during the ten years of preparation of this paper; in particular we wish to thank Stefan Hecht, as well as Achim Hartschuh, Dirk Trauner, Guglielmo Lanzani, Bert Nickel, Matthew Fuchter, Eberhard Riedle, Thomas Nauser, the attendees of the international Photopharmacology conferences from 2017-2021, and numerous other colleagues, for their insights, encouragement and support.

## ABBREVIATIONS

Cy5: cyanine 5; EY: Eosin Y; Fc: ferrocene; FDR: functional dynamic range; Fl: fluorescein; MB: methylene blue; NB: Nile blue; NIR: near-infrared; pip: piperazinamide; PORTL: photoswitchable orthogonal remotely tethered ligand; PSS: photostationary state; RhB: rhodamine B; SRhB Sulforhodamine B; TAS: transient absorption spectroscopy;  $\tau_f$ : fluorescence lifetime;  $\Phi_f$ : fluorescence quantum yield.

## REFERENCES

- (1) *Molecular Photoswitches: Chemistry, Properties, and Applications*; Pianowski, Z., Ed.; Wiley, 2022. <https://doi.org/10.1002/9783527827626>.
- (2) Merino, E. Synthesis of Azobenzenes: The Coloured Pieces of Molecular Materials. *Chem. Soc. Rev.* **2011**, *40* (7), 3835–3853.
- (3) Pernpeintner, C.; Frank, J. A.; Urban, P.; Roeske, C. R.; Pritzl, S. D.; Trauner, D.; Lohmüller, T. Light-Controlled Membrane Mechanics and Shape Transitions of Photoswitchable Lipid Vesicles. *Langmuir* **2017**, *33* (16), 4083–4089. <https://doi.org/10.1021/acs.langmuir.7b01020>.
- (4) Volgraf, M.; Gorostiza, P.; Szobota, S.; Helix, M. R.; Isacoff, E. Y.; Trauner, D. Reversibly Caged Glutamate: A Photochromic Agonist of Ionotropic Glutamate Receptors. *J. Am. Chem. Soc.* **2007**, *129* (2), 260–261. <https://doi.org/10.1021/ja067269o>.
- (5) Müller, M.; Niemyer, K.; Urban, N.; Ojha, N. K.; Zufall, F.; Leinders-Zufall, T.; Schaefer, M.; Thorn-Seshold, O. BTDAzo: A Photoswitchable TRPCS Channel Activator\*. *Angewandte Chemie International Edition* **2022**, *61* (36), e202201565. <https://doi.org/10.1002/anie.202201565>.
- (6) Borowiak, M.; Nahaboo, W.; Reynders, M.; Nekolla, K.; Jalinet, P.; Hasserodt, J.; Rehberg, M.; Delattre, M.; Zahler, S.; Vollmar, A.; Trauner, D.; Thorn-Seshold, O. Photoswitchable Inhibitors of Microtubule Dynamics Optically Control Mitosis and Cell Death. *Cell* **2015**, *162* (2), 403–411. <https://doi.org/10.1016/j.cell.2015.06.049>.
- (7) Tsai, Y.-H.; Essig, S.; James, J. R.; Lang, K.; Chin, J. W. Selective, Rapid and Optically Switchable Regulation of Protein Function in Live Mammalian Cells. *Nature Chemistry* **2015**, *7* (7), 554–561. <https://doi.org/10.1038/nchem.2253>.
- (8) Acosta-Ruiz, A.; Gutzeit, V. A.; Skelly, M. J.; Meadows, S.; Lee, J.; Parekh, P.; Orr, A. G.; Liston, C.; Pleil, K. E.; Broichhagen, J.; Levitz, J. Branched Photoswitchable Tethered Ligands Enable Ultra-Efficient Optical Control and Detection of G Protein-Coupled Receptors In Vivo. *Neuron* **2020**, *105* (3), 446–463.e13. <https://doi.org/10.1016/j.neuron.2019.10.036>.
- (9) Laprell, L.; Tochitsky, I.; Kaur, K.; Manookin, M. B.; Stein, M.; Barber, D. M.; Schön, C.; Michalakis, S.; Biel, M.; Kramer, R. H.; Sumser, M. P.; Trauner, D.; Van Gelder, R. N. Photopharmacological Control of Bipolar Cells Restores Visual Function in Blind Mice. *The Journal of Clinical Investigation* **2017**, *127* (7), 2598–2611. <https://doi.org/10.1172/JCI92156>.
- (10) ClinicalTrials.gov. *A Phase I/II Dose-escalating Study of the Safety, Tolerability and Efficacy of Small Molecule KIO-301 Administered Intravitreally to Patients With Retinitis Pigmentosa (ABACUS)*. <https://clinicaltrials.gov/study/NCT05282953> (accessed 2023-07-17).
- (11) Matsuo, K.; Tamaoki, N. Rational Design and Development of a Lit-Active Photoswitchable Inhibitor Targeting CENP-E. *Org. Biomol. Chem.* **2021**, *19* (32), 6979–6984. <https://doi.org/10.1039/D1OB01332G>.
- (12) Sailer, A.; Meiring, J. C. M.; Heise, C.; Pettersson, L. N.; Akhmanova, A.; Thorn-Seshold, J.; Thorn-Seshold, O. Pyrrole Hemithioindigo Antimitotics with Near-Quantitative Bidirectional Photoswitching Photocontrol Cellular Microtubule Dynamics with Single-Cell Precision. *Angewandte Chemie International Edition* **2021**, *60* (44), 23695–23704. <https://doi.org/10.1002/anie.202104794>.
- (13) Fuchter, M. J. On the Promise of Photopharmacology Using Photoswitches: A Medicinal Chemist's Perspective. *J. Med. Chem.* **2020**, *63* (20), 11436–11447. <https://doi.org/10.1021/acs.jmedchem.0c00629>.
- (14) Hüll, K.; Morstein, J.; Trauner, D. In Vivo Photopharmacology. *Chem. Rev.* **2018**, *118* (21), 10710–10747. <https://doi.org/10.1021/acs.chemrev.8b00037>.
- (15) Velema, W. A.; Szymanski, W.; Feringa, B. L. Photopharmacology: Beyond Proof of Principle. *J. Am. Chem. Soc.* **2014**, *136* (6), 2178–2191. <https://doi.org/10.1021/ja413063e>.
- (16) Beharry, A. A.; Woolley, G. A. Azobenzene Photoswitches for Biomolecules. *Chem. Soc. Rev.* **2011**, *40* (8), 4422–4437. <https://doi.org/10.1039/C1CS15023E>.
- (17) Konrad, D. B.; Frank, J. A.; Trauner, D. Synthesis of Redshifted Azobenzene Photoswitches by Late-Stage Functionalization. *Chemistry – A European Journal* **2016**, *22* (13), 4364–4368. <https://doi.org/10.1002/chem.201505061>.
- (18) Dong, M.; Babalhavaij, A.; Samanta, S.; Beharry, A. A.; Woolley, G. A. Red-Shifting Azobenzene Photoswitches for in Vivo Use. *Acc. Chem. Res.* **2015**, *48* (10), 2662–2670. <https://doi.org/10.1021/acs.accounts.5b00270>.
- (19) Hansen, M. J.; Lerch, M. M.; Szymanski, W.; Feringa, B. L. Direct and Versatile Synthesis of Red-Shifted Azobenzenes. *Angewandte Chemie International Edition* **2016**, *55* (43), 13514–13518. <https://doi.org/10.1002/anie.201607529>.
- (20) Bléger, D.; Schwarz, J.; Brouwer, A. M.; Hecht, S. O -Fluoroazobenzenes as Readily Synthesized Photoswitches Offering Nearly Quantitative Two-Way Isomerization with Visible Light. *J. Am. Chem. Soc.* **2012**, *134* (51), 20597–20600. <https://doi.org/10.1021/ja310323y>.
- (21) Müller-Deku, A.; Thorn-Seshold, O. Exhaustive Catalytic Ortho-Alkoxylation of Azobenzenes: Flexible Access to Functionally Diverse Yellow-Light-Responsive Photoswitches. *J. Org. Chem.* **2022**, *87* (24), 16526–16531. <https://doi.org/10.1021/acs.joc.2c02214>.
- (22) Maier, M. S.; Hüll, K.; Reynders, M.; Matsuur, B. S.; Leippe, P.; Ko, T.; Schäffer, L.; Trauner, D. Oxidative Approach Enables Efficient Access to Cyclic Azobenzenes. *J. Am. Chem. Soc.* **2019**, *141* (43), 17295–17304. <https://doi.org/10.1021/jacs.9b08794>.
- (23) Siewertsen, R.; Neumann, H.; Buchheim-Stehn, B.; Herges, R.; Näther, C.; Renth, F.; Temps, F. Highly Efficient Reversible Z–E Photoisomerization of a Bridged Azobenzene with Visible Light through Resolved S1( $\pi\pi^*$ ) Absorption Bands. *J. Am. Chem. Soc.* **2009**, *131* (43), 15594–15595. <https://doi.org/10.1021/ja906547d>.
- (24) Baumgartner, B.; Glembockyte, V.; Mayer, R.; Gonzalez-Hernandez, A.; Kindler, R.; Valavalkar, A.; Wiegand, A.; Müller-Deku, A.; Grubert, L.; Steiner, F.; Gross, C.; Reynders, M.; Grenier, V.; Broichhagen, J.; Hecht, S.; Tinnefeld, P.; Ofial, A.; Dietzek-Ivansic, B.; Levitz, J.; Thorn-Seshold, O. Azobenzenes Can Achieve Near-Infrared Photocontrol in Biological Systems, with Quantitative Z→E Photoisomerization, via Singlet Manifold Photoredox. *ChemRxiv* **2023**. <https://doi.org/10.26434/chemrxiv-2023-37sv4>.
- (25) Monti, S.; Dellonte, S.; Bortolus, P. The Lowest Triplet State of Substituted Azobenzenes: An Energy Transfer Investigation. *Journal of Photochemistry* **1983**, *23* (2), 249–256. [https://doi.org/10.1016/0047-2670\(83\)80065-3](https://doi.org/10.1016/0047-2670(83)80065-3).
- (26) Bortolus, Pietro.; Monti, Sandra. Cis-Trans Photoisomerization of Azobenzene. Solvent and Triplet Donors Effects. *J. Phys. Chem.* **1979**, *83* (6), 648–652. <https://doi.org/10.1021/j100469a002>.
- (27) Cembran, A.; Bernardi, F.; Garavelli, M.; Gagliardi, L.; Orlandi, G. On the Mechanism of the Cis–trans Isomerization in the Lowest Electronic States of Azobenzene: S0, S1, and T1. *J. Am. Chem. Soc.* **2004**, *126* (10), 3234–3243. <https://doi.org/10.1021/ja038327y>.
- (28) Jones, L. B.; Hammond, G. S. Mechanisms of Photochemical Reactions in Solution. XXX.1 Photosensitized Isomerization of Azobenzene. *J. Am. Chem. Soc.* **1965**, *87* (18), 4219–4220. <https://doi.org/10.1021/ja01096a059>.
- (29) Ronayette, J.; Arnaud, R.; Lemaire, J. Isomérisation photosensibilisée par des colorants et photoréduction de l'azobenzène en solution. II. *Can. J. Chem.* **1974**, *52* (10), 1858–1867. <https://doi.org/10.1139/v74-265>.
- (30) Shimomura, M.; Kunitake, T. Fluorescence and Photoisomerization of Azobenzene-Containing Bilayer Membranes. *J. Am. Chem. Soc.* **1987**, *109* (17), 5175–5183. <https://doi.org/10.1021/ja00251a022>.
- (31) Goulet-Hanssens, A.; Rietze, C.; Titov, E.; Abdullah, L.; Grubert, L.; Saalfrank, P.; Hecht, S. Hole Catalysis as a General Mechanism for Efficient and Wavelength-Independent Z → E Azobenzene Isomerization. *Chem* **2018**, *4* (7), 1740–1755. <https://doi.org/10.1016/j.chempr.2018.06.002>.
- (32) Isoquortti, J.; Kuntze, K.; Virkki, M.; Ahmed, Z.; Vuorimaa-Laukkanen, E.; Filatov, M. A.; Turshatov, A.; Laaksonen, T.; Priimagi, A.; Durandin, N. A. Expanding Excitation Wavelengths for Azobenzene Photoswitching into the Near-Infrared Range via Endothermic Triplet Energy Transfer. *Chem. Sci.* **2021**, *12* (21), 7504–7509. <https://doi.org/10.1039/D1SC01717A>.
- (33) Gemen, J.; Church, J. R.; Ruoko, T.-P.; Durandin, N.; Bialek, M. J.; Weißenfels, M.; Feller, M.; Kazes, M.; Odaybat, M.; Borin, V. A.; Kalepu, R.; Diskin-Posner, Y.; Oron, D.; Fuchter, M. J.; Priimagi, A.; Schapiro, I.; Klajn, R. Disequilibrating Azobenzenes by Visible-Light Sensitization under Confinement. *Science* **2023**, *381* (6664), 1357–1363. <https://doi.org/10.1126/science.adh9059>.
- (34) Isoquortti, J.; Griebenow, T.; Glasenapp, J.-S. von; Raeker, T.; Filatov, M. A.; Laaksonen, T.; Herges, R.; Durandin, N. A. Triplet Sensitization Enables Bidirectional Isomerization of Diazocine with 130 Nm Redshift in Excitation Wavelengths. *Chem. Sci.* **2023**, *14* (34), 9161–9166. <https://doi.org/10.1039/D3SC02681G>.
- (35) Thorn-Seshold, O.; Trauner, D.; Borowiak, M.; Hasserodt, J. EP3137554 - Azoaryls as Reversibly Modulatable Tubulin Inhibitors.
- (36) Targowski, P.; Ziętek, B.; Bączynski, A. Luminescence Quenching of Rhodamines by Cyclooctatetraene. *Zeitschrift für Naturforschung A* **1987**, *42* (9), 1009–1013. <https://doi.org/10.1515/zna-1987-0914>.
- (37) Urban, P.; Pritzl, S. D.; Konrad, D. B.; Frank, J. A.; Pernpeintner, C.; Roeske, C. R.; Trauner, D.; Lohmüller, T. Light-Controlled Lipid

- Interaction and Membrane Organization in Photolipid Bilayer Vesicles. *Langmuir* **2018**, *34* (44), 13368–13374. <https://doi.org/10.1021/acs.langmuir.8b03241>.
- (38) Pritzl, S. D.; Konrad, D. B.; Ober, M. F.; Richter, A. F.; Frank, J. A.; Nickel, B.; Trauner, D.; Lohmüller, T. Optical Membrane Control with Red Light Enabled by Red-Shifted Photolipids. *Langmuir* **2022**, *38* (1), 385–393. <https://doi.org/10.1021/acs.langmuir.1c02745>.
- (39) Reynders, M.; Oliver Thorn-Seshold. PST2. *in preparation*.
- (40) Engdahl, A. J.; Torres, E. A.; Lock, S. E.; Engdahl, T. B.; Mertz, P. S.; Streu, C. N. Synthesis, Characterization, and Bioactivity of the Photoisomerizable Tubulin Polymerization Inhibitor Azo-Combretastatin A4. *Org. Lett.* **2015**, *17* (18), 4546–4549. <https://doi.org/10.1021/acs.orglett.5b02262>.
- (41) Sheldon, J. E.; Dcona, M. M.; Lyons, C. E.; Hackett, J. C.; Hartman, M. C. T. Photoswitchable Anticancer Activity via Trans–Cis Isomerization of a Combretastatin A-4 Analog. *Org. Biomol. Chem.* **2015**, *14* (1), 40–49. <https://doi.org/10.1039/C5OB02005K>.
- (42) Banghart, M.; Mourot, A.; Fortin, D.; Yao, J.; Kramer, R.; Trauner, D. Photochromic Blockers of Voltage-Gated Potassium Channels. *Angew. Chem. Int. Ed.* **2009**, *48* (48), 9097–9101. <https://doi.org/10.1002/anie.200904504>.
- (43) Fortin, D. L.; Banghart, M. R.; Dunn, T. W.; Borges, K.; Wagenaar, D. A.; Gaudry, Q.; Karakossian, M. H.; Otis, T. S.; Kristan, W. B.; Trauner, D.; Kramer, R. H. Photochemical Control of Endogenous Ion Channels and Cellular Excitability. *Nature Methods* **2008**, *5* (4), 331–338. <https://doi.org/10.1038/nmeth.1187>.
- (44) Donthamsetti, P. C.; Broichhagen, J.; Vyklicky, V.; Stanley, C.; Fu, Z.; Visel, M.; Levitz, J. L.; Javitch, J. A.; Trauner, D.; Isacoff, E. Y. Genetically Targeted Optical Control of an Endogenous G Protein-Coupled Receptor. *J. Am. Chem. Soc.* **2019**, *141* (29), 11522–11530. <https://doi.org/10.1021/jacs.9b02895>.
- (45) Konrad, D. B.; Savasci, G.; Allmendinger, L.; Trauner, D.; Ochsenfeld, C.; Ali, A. M. Computational Design and Synthesis of a Deeply Red-Shifted and Bistable Azobenzene. *J. Am. Chem. Soc.* **2020**, *142* (14), 6538–6547. <https://doi.org/10.1021/jacs.9b10430>.
- (46) Stadler, E.; Tassoti, S.; Lentjes, P.; Herges, R.; Glasnov, T.; Zangger, K.; Gescheidt, G. In Situ Observation of Photoswitching by NMR Spectroscopy: A Photochemical Analogue to the Exchange Spectroscopy Experiment. *Anal. Chem.* **2019**, *91* (17), 11367–11373. <https://doi.org/10.1021/acs.analchem.9b02613>.
- (47) Frank, J. A.; Moroni, M.; Moshourab, R.; Sumser, M.; Lewin, G. R.; Trauner, D. Photoswitchable Fatty Acids Enable Optical Control of TRPV1. *Nat Commun* **2015**, *6* (1), 7118. <https://doi.org/10.1038/ncomms8118>.
- (48) Frank, J. A.; Yushchenko, D. A.; Hodson, D. J.; Lipstein, N.; Nagpal, J.; Rutter, G. A.; Rhee, J.-S.; Gottschalk, A.; Brose, N.; Schultz, C.; Trauner, D. Photoswitchable Diacylglycerols Enable Optical Control of Protein Kinase C. *Nat Chem Biol* **2016**, *12* (9), 755–762. <https://doi.org/10.1038/nchembio.2141>.
- (49) Gutzeit, V. A.; Acosta-Ruiz, A.; Munguba, H.; Häfner, S.; Landra-Willm, A.; Mathes, B.; Mony, J.; Yarotski, D.; Börjesson, K.; Liston, C.; Sandoz, G.; Levitz, J.; Broichhagen, J. A Fine-Tuned Azobenzene for Enhanced Photopharmacology in Vivo. *Cell Chemical Biology* **2021**. <https://doi.org/10.1016/j.chembiol.2021.02.020>.
- (50) Reimann, M.; Teichmann, E.; Hecht, S.; Kaupp, M. Solving the Azobenzene Entropy Puzzle: Direct Evidence for Multi-State Reactivity. *J. Phys. Chem. Lett.* **2022**, *13* (46), 10882–10888. <https://doi.org/10.1021/acs.jpcclett.2c02838>.
- (51) Reiner, A.; Levitz, J. Glutamatergic Signaling in the Central Nervous System: Ionotropic and Metabotropic Receptors in Concert. *Neuron* **2018**, *98* (6), 1080–1098. <https://doi.org/10.1016/j.neuron.2018.05.018>.
- (52) Nicoletti, F.; Bockaert, J.; Collingridge, G. L.; Conn, P. J.; Ferraguti, F.; Schoepp, D. D.; Wroblewski, J. T.; Pin, J. P. Metabotropic Glutamate Receptors: From the Workbench to the Bedside. *Neuropharmacology* **2011**, *60* (7), 1017–1041. <https://doi.org/10.1016/j.neuropharm.2010.10.022>.
- (53) Broichhagen, J.; Levitz, J. Advances in Tethered Photopharmacology for Precise Optical Control of Signaling Proteins. *Current Opinion in Pharmacology* **2022**, *63*, 102196. <https://doi.org/10.1016/j.coph.2022.102196>.
- (54) Gómez-Santacana, X.; Panarello, S.; Rovira, X.; Llebaria, A. Photoswitchable Allosteric Modulators for Metabotropic Glutamate Receptors. *Current Opinion in Pharmacology* **2022**, *66*, 102266. <https://doi.org/10.1016/j.coph.2022.102266>.
- (55) Broichhagen, J.; Damijonaitis, A.; Levitz, J.; Sokol, K. R.; Leippe, P.; Konrad, D.; Isacoff, E. Y.; Trauner, D. Orthogonal Optical Control of a G Protein-Coupled Receptor with a SNAP-Tethered Photochromic Ligand. *ACS Cent Sci* **2015**, *1* (7), 383–393. <https://doi.org/10.1021/acscentsci.5b00260>.
- (56) Levitz, J.; Broichhagen, J.; Leippe, P.; Konrad, D.; Trauner, D.; Isacoff, E. Y. Dual Optical Control and Mechanistic Insights into Photoswitchable Group II and III Metabotropic Glutamate Receptors. *Proc. Natl. Acad. Sci. U. S. A.* **2017**, *114* (17), E3546.
- (57) Wilhelm, J.; Kühn, S.; Tarnawski, M.; Gotthard, G.; Tünnermann, J.; Tänzer, T.; Karpenko, J.; Mertes, N.; Xue, L.; Uhrig, U.; Reinstein, J.; Hiblot, J.; Johnsson, K. Kinetic and Structural Characterization of the Self-Labeling Protein Tags HaloTag7, SNAP-Tag, and CLIP-Tag. *Biochemistry* **2021**, *60* (33), 2560–2575. <https://doi.org/10.1021/acs.biochem.1c00258>.
- (58) Walden, S. L.; Rodrigues, L. L.; Alves, J.; Blinco, J. P.; Truong, V. X.; Barner-Kowollik, C. Two-Colour Light Activated Covalent Bond Formation. *Nature Communications* **2022**, *13* (1), 2943. <https://doi.org/10.1038/s41467-022-30002-6>.
- (59) Cosco, E. D.; Arús, B. A.; Spearman, A. L.; Atallah, T. L.; Lim, I.; Leland, O. S.; Caram, J. R.; Bischof, T. S.; Bruns, O. T.; Sletten, E. M. Bright Chromenylium Polymethine Dyes Enable Fast, Four-Color In Vivo Imaging with Shortwave Infrared Detection. *J. Am. Chem. Soc.* **2021**, *143* (18), 6836–6846. <https://doi.org/10.1021/jacs.0c11599>.
- (60) Cosco, E. D.; Spearman, A. L.; Ramakrishnan, S.; Lingg, J. G. P.; Saccomano, M.; Pengshung, M.; Arús, B. A.; Wong, K. C. Y.; Glasl, S.; Ntziachristos, V.; Warmer, M.; McLaughlin, R. R.; Bruns, O. T.; Sletten, E. M. Shortwave Infrared Polymethine Fluorophores Matched to Excitation Lasers Enable Non-Invasive, Multicolour in Vivo Imaging in Real Time. *Nature Chemistry* **2020**, *12* (12), 1123–1130. <https://doi.org/10.1038/s41557-020-00554-5>.
- (61) Sauer, M.; Nasufovic, V.; Arndt, H.-D.; Vilotijevic, I. Robust Synthesis of NIR-Emissive P-Rhodamine Fluorophores. *Org. Biomol. Chem.* **2020**, *18* (8), 1567–1571. <https://doi.org/10.1039/D0OB00189A>.
- (62) Daly, H. C.; Matikonda, S. S.; Steffens, H. C.; Ruehle, B.; Resch-Genger, U.; Ivanic, J.; Schnermann, M. J. Ketone Incorporation Extends the Emission Properties of the Xanthene Scaffold Beyond 1000 Nm†. *Photochemistry and Photobiology* **2022**, *98* (2), 325–333. <https://doi.org/10.1111/php.13544>.



### 3.2 Azobenzenes can achieve near-infrared photocontrol in biological systems, with quantitative Z→E photoisomerization, via singlet manifold photoredox

#### Summary:

Azobenzene photoswitches are powerful tools in chemical biology, data storage and material science. Nevertheless, there is a need for innovative chemistries on how photoswitching can be conducted independent on intrinsic properties as isomer absorption spectra overlap and absorption wavelength. In chapter 3.1 we showed how azobenzene Z→E photoisomerization can be induced by NIR triggered energy transfer yielding in near-quantitative E isomer.

In this story we introduce an intramolecular singlet-manifold photoredox-based pathway that allows for NIR triggered, quantitative (100%) photoisomerization from Z to E isomer.

Based on the seminal work of Hecht and coworkers discovering an electrocatalytic and *intermolecular triplet-manifold photoredox* pathway for azobenzene Z→E photoswitching, we were keen whether *intramolecular, singlet photoredox* can be a red shifted, assisted approach to modulating bioactivity *in vivo*. We knew that *intermolecular* triplet-manifold approaches are limited, since triplet photoredox catalysts generate reactive oxygen species under oxygenated conditions (as in biological samples) which causes photobleaching and other side reactions with biological tissue. Furthermore, intermolecular reactions are limited by diffusional collision rate, which will not be sufficient at concentrations used in biology. We hoped however that a photoredox catalyst with low inter-system-crossing quantum yield will perform photoredox catalysis via a non-phototoxic singlet-manifold mechanism, and that covalent tethering of azobenzene and photoredox catalyst make the mechanism an intrinsic property of the conjugate therefore independent of concentration. I therefore started with chemically simpler intermolecular systems, to prepare for more costly syntheses of intramolecular ones.

**Intermolecular / Identification:** Through collaboration with the Ofial group, a library of ~30 azobenzenes (**Table 2**) and ~10 fluorophores (**Table 1**) was screened in electrochemical measurements to find their ground state reduction and oxidation potentials, excited state potentials were calculated by Rehm-Weller equation; and predict suitable azobenzene-fluorophore pairs for singlet-manifold photooxidation of the azobenzene by the fluorophore excited state. The most promising fluorophore found was the phenoxazine Nile Blue (**NB**) that had been suggested by Philip Tinnefeld, due to a high excited state reduction potential (1.2 V vs Fc), low  $\phi_{ISC}$  (< 0.03) and absorption maximum in the red ( $\lambda_{max} = 635$  nm). Its excited state reduction potential is suitable to oxidize common electron-rich azobenzene as 4,4'-bisalkoxy (**AO**) or bis anilide (**AN**) substituted ones that are used frequently in photopharmacology. We tested the most promising combination **NB** and **AO** in equimolar solution mixtures and found indeed quantitative Z→E isomerization at 635 nm illumination without any photobleaching of the fluorophore: but the intermolecular singlet-manifold photoredox showed awfully slow kinetics ( $t_{1/2} >$  minutes) attributed to short excited singlet state lifetime and low probability of collision with an azobenzene molecule (**Figure 1**).

**Intramolecular / Proof of Concept:** I synthesized the most promising conjugates **NB-AO** and **NB-AN** and evaluated their photoswitch properties (as in chapter 3.1). We showed for both molecules that intramolecular singlet-manifold photoredox enables quantitative Z→E isomerization at orders of magnitude faster kinetics (compared to intermolecular photoredox) at 635 nm illumination without any photobleaching (**Figure 1**). Based on these results we became interested in how flexible linker length influences the performance of intramolecular photoredox. We tested a library of carbopyronine azobenzene conjugates having linkers

ranging from PEG<sub>0</sub> to PEG<sub>24</sub> and showed that by increasing the distance by ~ 5-fold, the kinetics only decrease by ~ 6-fold, still allowing for efficient photoisomerization rates. This suggests that the photoredox catalyst can even be placed far from where a biologically active azobenzene would need to bind, so as not to interfere with ligand binding, but retain assisted switching efficacy (**Figure 3**).

**All-Visible Light:** So far, we had only shifted the  $Z \rightarrow E$  photoisomerization step into the red, so we investigated the combination of photoredox with methodologies to shift also the  $E \rightarrow Z$  wavelength into the visible spectrum. I synthesized a tetra-*ortho*-methoxy substituted azobenzene (that has a suitable redox potential) and coupled it to NB. By this we show the first all-visible-light-photoswitching azobenzene that has fast kinetics not only for the common  $E \rightarrow Z$  direction, here using green light (525 nm), but also for the never-before-shown quantitative  $Z \rightarrow E$  isomerization using red light (660 nm) (**Figure 3**).

**Mechanism:** We used mechanistic studies to prove that singlet-manifold photoredox triggers quantitative  $Z \rightarrow E$  isomerization by femtosecond transient absorption spectroscopy (TAS) and fluorescence quantum yield experiments. **NB-AO** shows an additional band appearing after excitation at 630 nm that was identified by spectroelectrochemical measurements as **NB**'s radical anion; and the fluorescence quantum yield of **NB-AO** is half of the parent **NB**, proving that the singlet excited state of **NB** is affected in the conjugate. The negative control **NB-AK** which should not do photoredox due to non-matching redox potentials, did not show any changes in femtosecond TAS or fluorescence quantum yield compared to **NB** (**Figure 2**). Taken together this supports singlet-manifold photoredox as major mechanism for red-light induced quantitative  $Z \rightarrow E$  isomerization in **NB-AO**.

**Biological Application:** Our goal had been to develop creative chemistries for novel photoswitching pathways in photopharmacology. Following our proof-of-concept application of triplet energy transfer-based modulation of neuronal activity (chapter 3.1), we were interested in making a PORTL system for NIR-based photomodulation of neuronal activity that is operated by photoredox. Therefore, we synthesized **BANG** (benzylguanine - azobenzene - nile blue - glutamate), a PORTL system whose azobenzene/chromophore pairing was predicted to allow photoredox. We showed quantitative  $Z \rightarrow E$  photoswitching in cuvette, as well as biological mGluR2 receptor off-photoswitching at 660 nm, which indicates the first ever photoredox-based azobenzene switching in a live biological system (**Figure 4**).

#### **Own contribution:**

I designed the compounds and performed synthesis of all compounds except for PST-PEGn-CPY-HALOs (Robert Kindler), and BAG and BANG (synthesis performed together with my intern Alexander Wiegand). I performed all action spectra and photoswitch kinetic measurements using the experimental setup I previously established (**chapter 3.1**). I performed all UV/Vis, fluorescence spectroscopy and HPLC experiments. I analyzed experimental data, coordinated results, assembled data in figures and wrote the manuscript together with Oliver Thorn-Seshold.

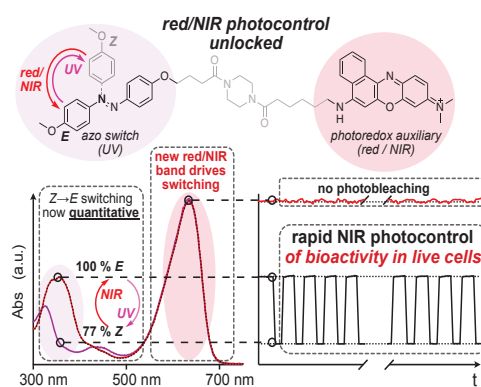
*This paper is being refined for submission to Nature Methods.*

# Azobenzenes can achieve near-infrared photocontrol in biological systems, with quantitative $Z \rightarrow E$ photoisomerization, via singlet manifold photoredox

Benedikt Baumgartner<sup>1</sup>, Viktorija Glembockyte<sup>2,3</sup>, Robert J. Mayer<sup>2</sup>, Alberto Jesus Gonzalez-Hernandez<sup>4</sup>, Robert O. Kindler<sup>5</sup>, Abha Valavalkar<sup>6</sup>, Alexander J. Wiegand<sup>1</sup>, Adrian Müller-Deku<sup>1</sup>, Lutz Grubert<sup>7</sup>, Florian Steiner<sup>2,3</sup>, Christoph Gross<sup>2</sup>, Martin Reynders<sup>1</sup>, Vincent Grenier<sup>5</sup>, Johannes Broichhagen<sup>10</sup>, Stefan Hecht<sup>7,8</sup>, Philip Tinnefeld<sup>2,3</sup>, Armin R. Ofial<sup>2</sup>, Benjamin Dietzek-Ivanšić<sup>6,9</sup>, Joshua Levitz<sup>4</sup>, Oliver Thorn-Seshold<sup>1\*</sup>

(1) Department of Pharmacy, LMU Munich, 81377 Munich, Germany; (2) Department of Chemistry, LMU Munich, 81377 Munich, Germany; (3) Center for Nano-Science, LMU Munich, 81377 Munich, Germany; (4) Department of Biochemistry and Department of Psychiatry, Weill Cornell Medicine, New York, NY 10065, USA; (5) Department of Chemical Biology, Max Planck Institute for Medical Research, 69120 Heidelberg, Germany; (6) Leibniz Institute for Photonic Technology Jena e.V. (Leibniz-IPHT), Research Department Functional Interfaces, 07745 Jena, Germany; (7) Department of Chemistry & Center for the Science of Materials Berlin, Humboldt-Universität zu Berlin, 12489 Berlin, Germany; (8) DWI – Leibniz Institute for Interactive Materials, 52074 Aachen, Germany; (9) Institute for Physical Chemistry (IPC), Friedrich Schiller University Jena, 07743 Jena, Germany; (10) Leibniz-Forschungsinstitut für Molekulare Pharmakologie, 13125 Berlin, Germany.

**ABSTRACT:** Here we develop a high-performance approach to photoswitching, by exploiting singlet manifold photoredox between azobenzenes and covalently attached auxiliary chromophores. This enables well-penetrating red/NIR light of 630-740 nm, to which azobenzenes usually do not respond, to perform  $Z \rightarrow E$  photoisomerisation that is also 100% complete and highly photon-efficient. Crucially, this process is biocompatible,  $O_2$ -tolerant, photostable, and it avoids the drawbacks of triplet photochemistry; and substituent patterns of azobenzenes do not need re-engineering to harness it. We provide a library of redox potentials to predict photoredox performance, show its tolerance to linker length, and show that  $E \rightarrow Z$ -promoting tetra-*ortho*-substitutions can be combined with photoredox to give fast and efficient bidirectional  $Z \rightleftharpoons E$  photoswitches for the visible/NIR. We then demonstrate the first use of single photon NIR light for reversible photopharmaceutical control in live cells under physiological conditions, by modulating G protein-coupled receptor activity. These stringent assays show singlet photoredox switching is a robust method for NIR photocontrol that should find high-performance applications in materials, in biophysics, and for "chemical optogenetics v2.0" in living systems.



## INTRODUCTION

The control of cellular pathways with subcellular and microsecond precision in complex biological tissue holds great promise for basic biomedical research and drug development.<sup>1</sup> Photopharmacology is a small molecule-based method to control biological processes with the precision offered by the application of light. Typically, a small molecule photoswitch is extended from or incorporated into a drug pharmacophore, such that light can spatiotemporally pattern its bioactivity by photoisomerising it.<sup>2</sup> Azobenzenes are the dominant photoswitch class, and besides their many uses in photoresponsive materials, they are driving the frontiers of photopharmacology from cellular applications in neuroscience, cytoskeleton, and signaling, to therapeutic clinical trials *in vivo*.<sup>3-7</sup> Nevertheless, two major limits on the performance of azobenzene tools remain: (1) population-level photoswitching is not binary (all- $E \rightleftharpoons$  all- $Z$ ) but is incomplete, especially in the  $Z \rightarrow E$  direction (that also is less photon-efficient); (2) no broadly applicable strategy to operate azobenzenes with well-penetrating red/NIR light is known (typically,  $\epsilon(\lambda)$  are significant only below 530 nm). The last decade has witnessed major efforts to overcome these limits, primarily through tetra-*ortho*-substitutions and cyclic azobenzenes.<sup>8-10</sup> However, both approaches suffer from low molar extinction coefficients in the better-tissue-penetrating red

spectral region, resulting in slow and inefficient photoswitching; true NIR response is lacking; and both methods require redesigning the photoswitch, which restricts their scope and can result in dramatic losses of potency (for further background, see **Supporting Note 1**). Two alternative routes to photocontrol azobenzene isomer ratios, with high switching completion and efficient red/NIR response, recently emerged in materials sciences: photoredox catalysis<sup>11-14</sup>, which we address in this work, and triplet energy transfer<sup>11,15-18</sup>, which we address in a parallel manuscript<sup>19</sup>. Hecht showed excellent azobenzene  $Z \rightarrow E$  isomerisation using triplet photoredox catalysts, via transient photooxidation to the radical cation<sup>11</sup> (electron-rich azobenzenes; e.g. **AO+MB**, **Fig 1a-b**) or photoreduction to the radical anion<sup>12,13</sup> (if electron-poor). This arises as the radicals isomerise to their thermodynamically preferred  $E$  isomer ca.  $10^{13}$  times faster than do the neutral forms, so a 100% $E$  population accumulates after back-electron transfer. However, these systems are not applicable to biology. Among the many challenges, (i) with one exception,<sup>13</sup> they are intermolecular concepts, so are unlikely to work at  $\leq \mu\text{M}$  levels needed for biocompatible reagents; (ii) as triplet systems, they require  $O_2$  exclusion to work efficiently, and with  $O_2$  they also produce reactive species that photobleach the catalyst and are too toxic for use in biology (discussed in **Supporting Note 1**).



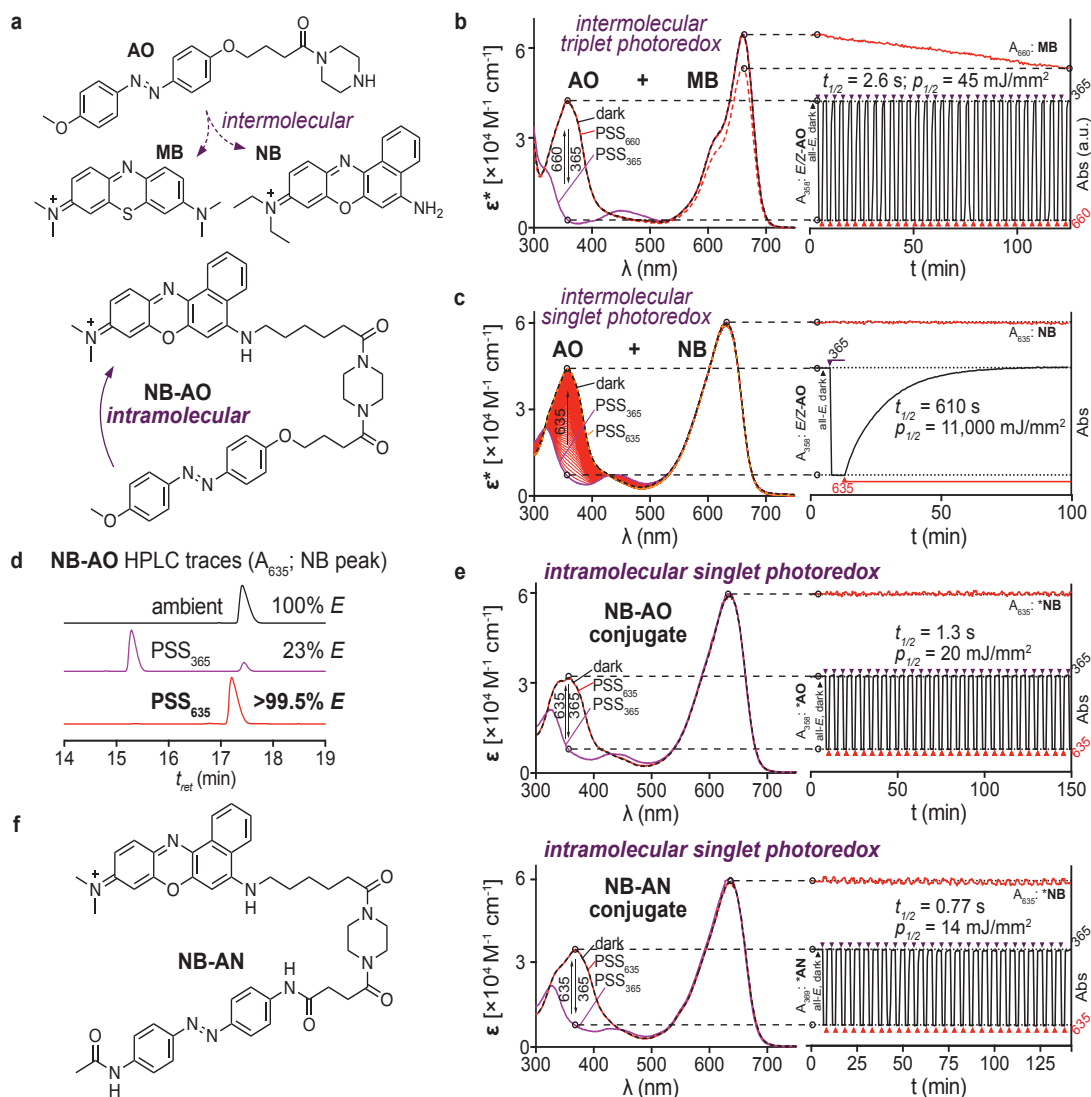


**Figure 1: Route to singlet-manifold intramolecular photoredox switching.** Dyads NB-AO and NB-AN use singlet photoredox for efficient and complete  $Z \rightarrow E$  isomerisation with red light. Their reversible bidirectional photoswitching has >100-fold greater dynamic range than the direct photoisomerisation of azobenzene. (a) MB, NB, and AO, for intermolecular ("physical mixture") experiments; vs covalent dyad NB-AO. (b,c,e,f) absorption spectra and  $E \rightleftharpoons Z$  isomerisations: (b-c) physical mixtures: triplet photoredox in MB + AO (red light: fast), singlet photoredox in NB + AO (red light: slow); (e-f) dyads: singlet photoredox in NB-AO and NB-AN (red light: fast). (d) HPLC: red light  $Z \rightarrow E$  isomerisation in NB-AO is complete.

We aimed to overcome these major sources of biological incompatibility in a way that enables existing photopharmaceuticals to be easily modified for high-efficiency and near-complete photoswitchability in the biological transparency window: thereby greatly improving their performance and practical applicability. We therefore aimed to build systems based on intramolecular (concentration-independent) photoredox, in the singlet manifold (compatible with oxygen and living systems), to perform quantitative red/NIR-light  $Z \rightarrow E$  isomerisation with fast kinetics, without the need to reengineer the azobenzene moiety. Red/NIR photoredox chromophores would offer an additional advantage: azobenzenes do not directly absorb in this spectral range, nor will they accept energy from the chromophore by FRET; thus red light should only trigger photoredox ( $Z \rightarrow \text{all-}E$ ), avoiding the incomplete isomerisation seen for prior, spectrally overlapping triplet systems.

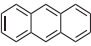
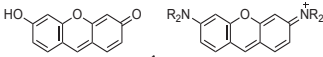
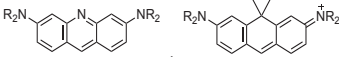
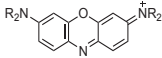
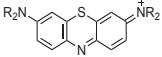
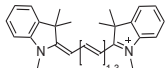
Here we outline the rational steps, from electrochemical screening to predict singlet photoredox pairs, to analysis of the isomerisation and studies of its chemical scope, to spectroscopic mechanistic studies, which culminated in a biological proof-of-concept application of singlet photoredox as a biocompatible method for high-performance NIR photocontrol over metabotropic glutamate receptors in living cells.

## RESULTS

### Singlet Photoredox: Pre-Screening

We wished to identify red/NIR-absorbing chromophores, with very low yields of intersystem crossing to the triplet state ( $\Phi_{ISC}$ ), with singlet excited state reduction potentials that are appropriately high enough to photooxidise the azobenzene scaffolds commonly used in photopharmacology; and we also required them to have good biological compatibility and synthetic access (more details in ref<sup>9</sup>). This oriented us towards biologically validated organic fluorophores (low  $\Phi_{ISC}$ ). Their singlet excited state redox potentials are poorly known. We thus performed cyclic and square wave voltammetry of 11 common, red/NIR organic fluorophores, and assembled **Table 1** to summarise their most relevant properties as potential singlet photooxidants (incl. excitation maxima  $\lambda_{\text{max, ex}}$  approximate  $\Phi_{ISC}$  if known; and singlet excited state oxidation potentials  $E_{\text{red}}^{\text{S1}}$ ; see **Table S4** for further data and experimental details).

**Table 1:** Spectral properties, ground and excited state redox properties, and  $\Phi_{ISC}$ , of common chromophores (see also **Table S4**).

Core Scaffolds & examples	$\lambda_{max, ex}$ [nm]	$\lambda_{max, em}$ [nm]	ex/em cross [nm]	$\rightarrow E_{00}$ [eV]	$\Phi_{ISC}$ [lit. values]	$E^{S0}_{red}$ [V vs. Fc]	$E^{S1}_{red} \{E^{T1}_{red}\}^{[c]}$ [V vs. Fc]	$E^{S0}_{ox}$ [V vs. Fc]	$E^{S1}_{ox} \{E^{T1}_{ox}\}^{[c]}$ [V vs. Fc]
<b>Anthracenes</b>									
9,10 dicyanoanthracene (DCA)	423	435	428	2.90	0.0085 <sup>20</sup>	-1.31 <sup>[f]20</sup>	1.59 <sup>[f]20</sup>	[g]	[g]
<b>Xanthenes</b>									
Fluorescein	516	531	521	2.38	0.03 <sup>20</sup>	-1.61 <sup>[d]</sup>	0.85 <sup>[f]20</sup>	0.98 <sup>[d]</sup>	-1.95 <sup>[f]20</sup>
Eosin Y	538	555	545	2.27	<b>0.32</b> <sup>20</sup>	-1.48 <sup>[f]20</sup>	0.83 <sup>[f]20</sup> { <b>0.43</b> } <sup>[f]20</sup>	0.76 <sup>[f]20</sup>	-1.98 <sup>[f]20</sup> { <b>-1.55</b> } <sup>[f]20</sup>
Rhodamine B	557	577	566	2.19	0.0024 <sup>20</sup>	-1.26 <sup>[d]</sup>	0.93	0.82 <sup>[d]</sup>	-1.37
Sulforhodamine B	553	571	561	2.21	[a]	-1.36	0.85	0.79	-1.42
<b>Acridines, Carbopyronines</b>									
Acridine Orange	425	525	509	2.44	[a]	-2.40	0.04	0.77	-1.67
Carbopyronine CPY	616	635	627	1.98	[a]	-1.09	0.89	0.66	-1.32
<b>Phenoxazines</b>									
Oxazine 170	620	638	631	1.96	[a]	-0.81	1.15	0.75	-1.21
Atto 655	663 <sup>21</sup>	680 <sup>21</sup>	672 <sup>21</sup>	1.86 <sup>22</sup>	[a]	-0.82 <sup>[f]22</sup>	1.04	0.91 <sup>[f]22</sup>	-0.55
Nile Blue <b>NB</b>	639	663	652	1.90	<<0.03 <sup>23</sup>	-0.80 <sup>[d]</sup>	1.10	0.81 <sup>[d]</sup>	-1.09
Nile Red	542	613	582	2.13	[a]	[b]	[b]	[b]	[b]
<b>Phenothiazines</b>									
Methylene Blue <b>MB</b>	658	669	664	1.87	<b>0.52</b> <sup>20</sup>	-0.72	1.15 <sup>[f]20</sup> { <b>1.20</b> } <sup>[f]20</sup>	0.85	-1.02 <sup>[f]20</sup> { <b>-1.08</b> } <sup>[f]20</sup>
<b>Cyanines</b>									
Cy 3	549	560	555	2.23	[a]	-1.37	0.86	0.63	-1.60
Cy 5	644	659	653	1.90	0.025 <sup>24</sup>	-1.28	0.62	0.48	-1.42
Cy 7	746	766	756	1.64	[a]	-1.14	0.50	[e]	[e]

[a] no appropriate literature  $\Phi_{ISC}$  found. [b]  $E^{S0}_{red/ox}$  values for Nile Red are not given since its solubility in MeCN was too poor for measurement under our standard conditions (MeCN with 0.1 M  $NBu_4ClO_4$ ); this also prevents giving  $E^{S1}_{red/ox}$  values. However, we assume them to be close to those of structurally similar Oxazine 170. [c]  $E^{T1}_{red}$  and  $E^{T1}_{ox}$  are only indicated for Eosin Y and Methylene Blue, since only they have high enough  $\Phi_{ISC}$  for plausible triplet photoredox. [d] CV data measured with  $NBu_4PF_6$  (0.1 M) instead of  $NBu_4ClO_4$ . [e] We did not resolve  $E^{S0}_{ox}$  during measurement, so no value is given, and  $E^{S1}_{ox}$  cannot be calculated. [f] reported in V vs. SCE, converted to (V vs. Fc) = (V vs. SCE) - 0.40 V<sup>25</sup>. [g] not measured, and no appropriate literature  $E^{S0}_{ox}$  found.

This evaluation of chromophores identified phenoxazines e.g. Nile Blue (**NB**; similar to Atto655 and Oxazine 170) as promising, with red/NIR excitation (**NB** ~635 nm) and high singlet excited state reduction potential (**NB** ~1.1 V; potentials vs. Fc). In these, they parallel methylene blue (**MB**) that Hecht used for red light triplet photoredox isomerisation (~655 nm, 1.2 V): the key difference is that the phenoxazines have a tiny  $\Phi_{ISC}$ , whereas that of **MB** is ~0.52. Structure/redox relationships are poorly known for azobenzenes. We measured a library of 33 azobenzenes, including scaffold types widely used in photopharmacology (**Table S5** and **Supporting**

**Note 2**; selected biologically relevant chemotypes in **Table 2**). This may be the first comprehensive study of how common bioactive substituent patterns tune redox properties, and it will allow others to predict photoredox partners for azobenzene photopharmacology.

Pleasingly, many of the azobenzene types commonly employed in photopharmacology use electron-donating +M substituents such as alkoxy and anilide (<1.1 V): so they should allow photoredox operation with **NB**-type phenoxazines. Other azobenzenes (e.g. alkyl-type **AK**, as found in photoswitchable lipids and membranes<sup>26</sup>) will be compatible with different photoredox partners.

**Table 2:** Ground state oxidation potentials and photopharmacology use examples, of common azobenzene types (full data in **Table S5**).

Structure (R = alkyl, not H/aryl)	$E_{1/2}(\text{Az}^+/\text{Az}) = E_{\text{ox}}^{\text{SO}}$ [V vs. Fc] [a]	Biological use example	Structure	$E_{\text{ox}}^{\text{SO}}$ [V vs Fc]	Biological use example
	1.71	PKC <sup>27</sup> , TRPV1 <sup>30</sup> , lipids <sup>26,29</sup> our example: <b>AK</b>		1.07	cell adhesion <sup>30</sup> our example: <b>AO</b>
	0.97	glutamate receptors <sup>31</sup> our example: <b>AN</b>		1.08	Nav and Kv <sup>32</sup>
	0.82	Kv, HCN <sup>33</sup>		0.73	none yet
	1.25	none yet		0.94	microtubules <sup>34-36</sup> , actin <sup>37</sup>
	1.64	TRPV1 <sup>38</sup> , lipids <sup>39,40</sup>		0.89	none yet

[a] All potentials determined in MeCN with 0.1 M NBu<sub>4</sub>ClO<sub>4</sub>. Both cyclic voltammetry (CV, scan rate: 0.5 V/s) and square wave voltammetry (SWV) were used, with ferrocene as an internal standard. Values given in V vs. Fc. R in structures represents general alkyl substituents (not aryl, H, or heteroatoms).

### Intermolecular Singlet Photoredox: Observation

We next tested whether the electrochemical screening would predict chromophore-azobenzene pairs capable of singlet manifold photoredox-based *Z*→*E* isomerisation (which has not been reported before). We began with an intermolecular study. As a reference, we took triplet photoredox catalyst **MB** ( $\Phi_{\text{ISC}} \sim 0.5$ ,  $\tau_{\text{T}} = 65 \mu\text{s}$ ,  $E_{\text{red}}^{\text{T1}} = 1.20 \text{ V}$ ) and *para, para*-bisalkoxy azobenzene **AO** ( $E_{\text{ox}} = 1.04 \text{ V}$ ) in a near-equimolar "physical mixture" (**MB** + **AO**), as previously studied<sup>11</sup>; and we compared its switching to a physical mixture of **AO** + **NB** ( $\tau_{\text{S1}} \sim 1.3 \text{ ns}$ ,  $E_{\text{red}}^{\text{S1}} = 1.10 \text{ V}$ ). In both cases, direct  $\pi \rightarrow \pi^*$  excitation of the **AO** with UV light efficiently reached mostly-*Z* photostationary states (PSSs) (**Fig 1a-c**, 365 nm response). As known, while direct *Z*→*E* photoswitching of pure **AO** at 525 nm would give a PSS of 91%*E* (**Fig S4**), red light excitation of **MB** in the physical mixture instead gives efficient and quantitative *Z*→all-*E* isomerisation (**Fig 1b**; power for half-complete switching:  $p_{1/2} \sim 45 \text{ mJ/mm}^2$ , see **Table S1**); although even under these favourable conditions,  $\geq 15\%$  photobleaching of **MB** occurred within a few cycles (red  $A_{660}$  trace in **Fig 1b**: <sup>1</sup>O<sub>2</sub> from intermolecular use of a triplet-manifold chromophore). Red light illumination of **NB** also drives quantitative *Z*→all-*E* isomerisation (**Fig 1c**), which proves a mechanism based on photoredox rather than triplet energy transfer. However, it is 250-fold less photon-efficient ( $p_{1/2} \sim 11,000 \text{ mJ/mm}^2$  at 635 nm), as expected for the shorter-lived **NB** singlet excited state (**NB**: ns, compared to **MB**:  $\mu\text{s}$ ; see too **Fig S4**). Encouragingly though, the expected photostability of a singlet manifold system was confirmed (red  $A_{635}$  trace in **Fig 1c**).

### Intramolecular Singlet Photoredox: Observation

We believe chromophore-assisted isomerisation can only be biologically useful if it is intramolecular, so that switching performance is intrinsic (identical at any concentration/dilution). For singlet photoredox, we also expected intramolecularity to fix the photon-inefficiency of its intermolecular case, by maximising the chromophore-photoswitch collision rate. We thus synthesised the covalent dyad **NB-AO** (**Fig 1a**; for syntheses, see **Supporting Information**). Its absorbance spectrum matches the sum of spectra of its electronically non-communicating motifs **NB** and **AO**, indicating no strong coupling in the ground state (**Fig 1c,e**). **NB-AO** switches efficiently to its *Z*-rich PSS at 365 nm ( $p_{1/2} \sim 3 \text{ mJ/mm}^2$ ; compare pure **AO**:  $p_{1/2} \sim 2 \text{ mJ/mm}^2$ ). Outstandingly, it offers red-light *Z*→*E* photoswitching that is 100% complete (**Fig 1d**, 635 nm), at photon-efficiency ( $p_{1/2} = 20 \text{ mJ/mm}^2$ ) that is even better than direct *Z*→*E* photoswitching of the pure azobenzene (**AO**  $p_{1/2} = 38 \text{ mJ/mm}^2$  at 525 nm); and its fast bidirectional UV/red photoswitching is repeatable over many cycles without photobleaching (**Fig 1e**).

We next tested **NB-AN** (**Fig 1f**; **AN/NB**  $\Delta E_{\text{redox}} = +0.13 \text{ V}$  so singlet photoredox expected) and **NB-AK** (**Fig S5**; **AN/NB**  $\Delta E_{\text{redox}} = -0.61 \text{ V}$ , photoredox not expected). **NB-AN** has similar red light *Z*→all-*E* photoswitching as **NB-AO** (**Fig 1f**, **Table S1**); whereas red light switching of **NB-AK** is distinctly incomplete (<98.2%*E*, **Fig S4-5**). The difference between <98.2% and >99.5% might seem small, but it is one of several signs of their different isomerisation mechanisms (others reported below; analysis of *Z*-**NB-AK** is reported in a parallel paper<sup>19</sup> indicating it accesses azo-induced intersystem crossing without redox, which brings several performance differences).

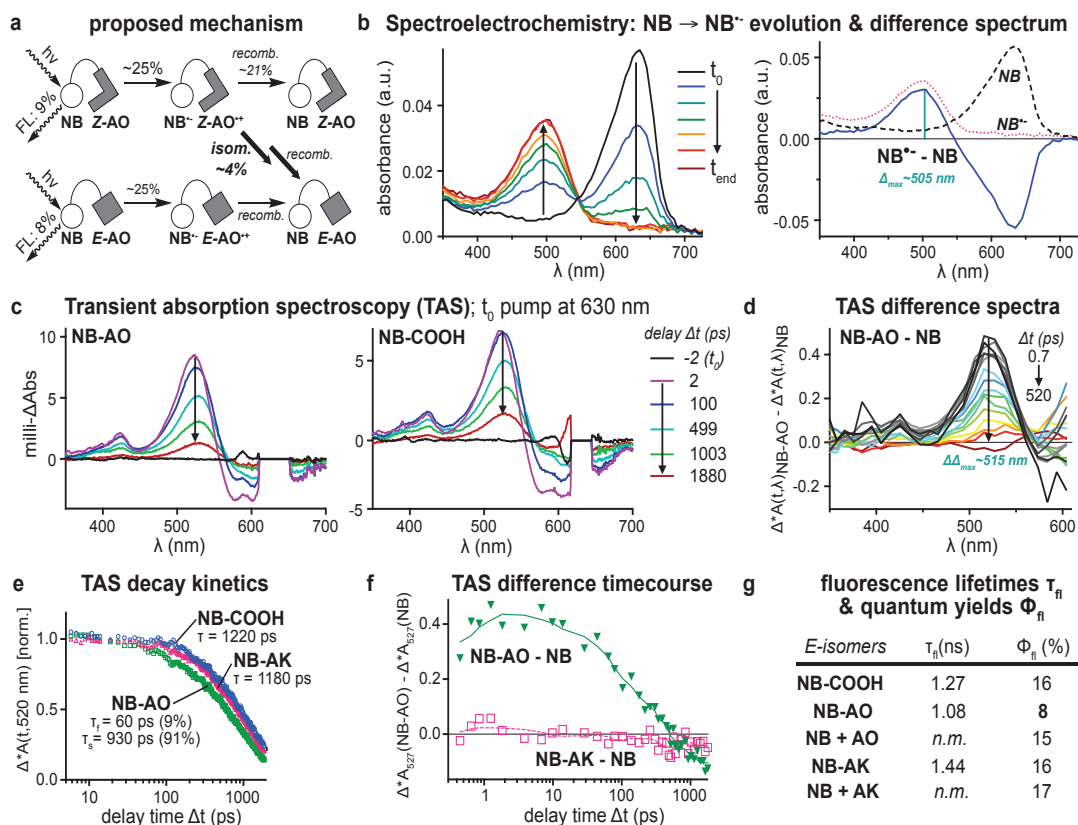


**Figure 2: Photoredox switching driven by NB.** (a) proposed NB<sup>\*</sup>-AO decay pathways (nonradiative decay not shown). (b) Spectroelectrochemistry of NB reduction: timecourse, and spectra assigned as NB, NB<sup>\*</sup>, and [NB<sup>\*</sup> - NB]. (c-f) Transient absorption spectroscopy (TAS): (c) NB-AO(Δt) and NB(Δt); (d) [NB-AO(Δt) - NB(Δt)]; note the similarity at 0.7 ps to panel (b) trace [NB<sup>\*</sup> - NB]; (e) excited state decay kinetics; (f) significantly different evolution is seen for NB<sup>\*</sup>-AO than NB<sup>\*</sup> during the first 1-100 ps after pump, but not for NB<sup>\*</sup>-AK. (g) Fluorescence lifetimes (τ<sub>fl</sub>) and quantum yields (Φ<sub>fl</sub>) (*n.m.* indicates not measured). (Data and details at Fig S12-16; full legend in Supporting Note 3, discussion in Supporting Note 4.)

### Intramolecular, Singlet Photoredox: Mechanism

We expected *Z*- and *E*-NB-AO to be capable of singlet photoredox under red light: i.e. some of the singlet excited state *E/Z*-NB<sup>\*</sup>-AO should evolve by photoredox to *E/Z*-NB<sup>-</sup>-AO<sup>+</sup>, that can optionally unidirectionally Z<sup>+</sup>→E<sup>+</sup> isomerise, then recombine to *E/Z*-NB-AO; while the remaining *E/Z*-NB<sup>\*</sup>-AO follows typical non-photoredox radiative and nonradiative NB<sup>\*</sup>→NB decays (Fig 2a; Supporting Note 2). We tested key aspects of this mechanism by spectroscopy, using unconjugated "NB" (as acid NB-COOH), non-photoredox dyad NB-AK, and NB+AO physical mixture, as controls.

Spectroelectrochemistry of both NB→NB<sup>-</sup> and AO→AO<sup>+</sup> redox reactions showed positive absorption differentials around 500 nm, with NB→NB<sup>-</sup> the stronger contributor (Fig 2b and Fig S13). We then used transient absorption spectroscopy (TAS) to study the evolution of NB-AO after excitation of its NB motif (Fig 2c). To subtract non-photoredox decays from the overall evolution, we analysed difference spectra (NB-AO - NB spectra; Fig 2d, Fig S14-S16). These suggest that a strong component (~25% of *Z*-NB<sup>\*</sup>-AO) evolves via photoredox: having a NB<sup>-</sup> moiety by 0.7 ps (close match to NB→NB<sup>-</sup> electrochemical spectrum, Fig 2b), then returning to NB with half-life ca. 70 ps. By comparison, NB<sup>\*</sup>-AK evolves just as NB<sup>\*</sup> does (Fig 2e-f, Fig S14e, Fig S16) supporting that photoredox is insignificant in NB-AK (mismatched redox potentials; see also Supporting Note 4). Consistent with these results, *E*-NB-AO has a lowered fluorescence lifetime τ<sub>fl</sub> and quantum yield Φ<sub>fl</sub>, i.e. additional quenching of the singlet excited state compared to NB, NB+E-AO, or *E*-NB-AK (Fig 2g, Fig S12, Table S7-8); and the Φ<sub>fl</sub> of NB-AO is isomer-dependent (Fig S17).

### Intramolecular, Singlet Photoredox: Scope and Performance

We confirmed 3 key aspects of singlet photoredox switching scope:

- (1) It operates in the spectral region that the chromophore absorbs, even if the azobenzene is (conveniently) transparent there. For NB dyads, *Z*→all-*E* photoswitching is efficient at 540 - 680 nm, and extends to 740 nm, even with azobenzenes that typically isomerise only below 530 nm (Fig 3a,b). This allows choosing chromophores for any desired wavelength response(s): so permits *Z*→*E*-switching that previously required cyan/blue, to now operate in the red/NIR.
- (2) The chromophore can be attached far from the switch, when the linker between them is flexible. For carbopyronine CPY dyads (λ<sub>max</sub> 600 nm, 0.92 V), growing the linker from PEG<sub>0</sub> to PEG<sub>24</sub> cost only a ~6-fold decrease of photoswitching efficiency, and did not sabotage performance (Fig 3c). This tolerance is only possible due to switching occurring in the singlet manifold (Supporting Note 4).
- (3) Photoredox can be rationally combined with *E*→*Z* redshifting strategies to redshift both *E*→*Z* and *Z*→*E* switching steps by ≥200 nm. Bidirectional photoswitching of bistable azobenzenes usually needs UV & blue light (*E*→*Z* 360; *Z*→*E* 440 nm). Tetra-*ortho*-alkoxylation<sup>6</sup> is a strategy to shift the *E*→*Z* response of *para*-substituted switches to the green (~550 nm) with little disturbance of function: but it leaves the *Z*→*E* response in the blue (Fig 3d, lower left). We saw that *per-ortho*-alkoxylation, which can be done catalytically and late-stage,<sup>41</sup> is excellently suited for *Z*→*E* photoredox since it lowers the oxidation potential of even previously inaccessible azobenzenes by ~0.8 V (Table S5): promising a solution to also redshift the tricky *Z*→*E* step. Indeed, NB-AO(OMe)<sub>4</sub> retained the efficient green *E*→*Z* switching, but photoredox now enabled *Z*→*E* in the red/NIR (Fig 3d). Thus, not only can singlet photoredox freely shift *Z*→*E* wavelengths, but it can be rationally combined with known spectral shifting methods to give higher-performance *bidirectional* photoswitching with both steps redshifted by ≥two microscopy excitation channels (≥200 nm).



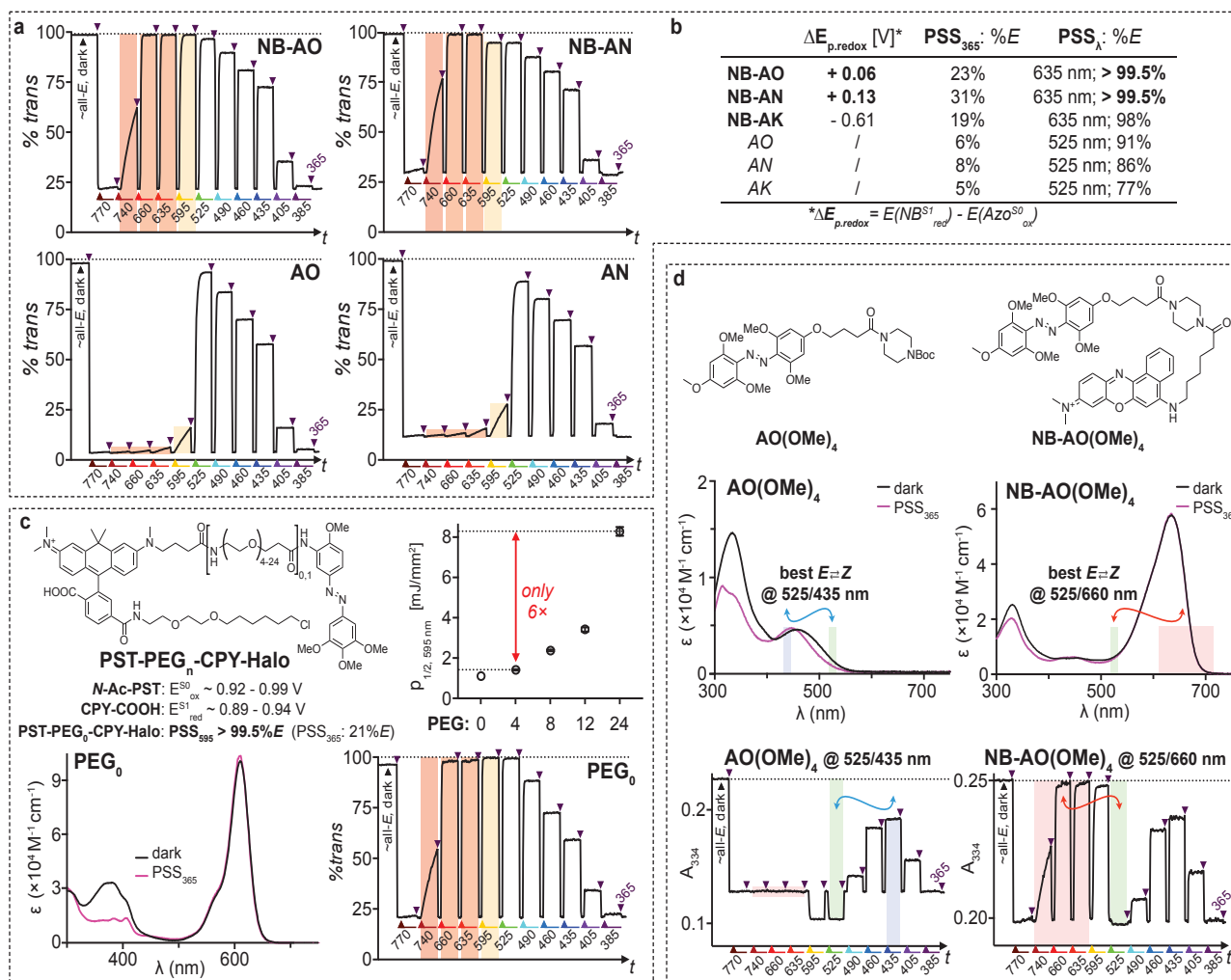


**Figure 3: Scope and performance of singlet photoredox switching.** (a) Action spectra show the extent of red/NIR response with NB photoredox conjugates (c.f. Table S1). (b) Photostationary states (PSSs) found by HPLC. (c) Linker-length dependency for photoredox switching response. (d) Tetra-ortho-substituted NB-AO(OMe)<sub>4</sub> allows direct E→Z switching at 525 nm, and Z→100%-E photoredox switching around 620-700 nm.

### Singlet Photoredox allows NIR photocontrol of live cell biology

By now we had outlined the rules and features of singlet photoredox switching in cell-free conditions, which are directly applicable for chemical and material sciences. We next aimed to test its biological utility, while stringently testing its biocompatibility. Thus we aimed to tether a bioactive NIR singlet photoredox-switchable ligand to a sparsely-expressed receptor: hoping for a functional readout of potential photodamage around the switch that should be much more sensitive than "overall cell toxicity" or "dyad photobleaching". We chose to target a metabotropic glutamate receptor (mGluR2), by using a photoredox analogue of the established photoswitchable "BGAG" ligands (benzylguanine-azobenzene-glutamates). After BGAGs ligate to a SNAP-fused-mGluR2, UV/green switching of the azobenzene controls mGluR2 in cells and *ex vivo* tissue (E→Z at 400 nm activates mGluR2; Z→E at 525 nm switches it off). With light delivered by brain-implanted fibre optics, BGAGs were even used in mobile adult mice *in vivo* to reveal the influence of cortical mGluR2 activation on working memory.<sup>2,42-45</sup>

NIR-responsive BGAG analogues could instead allow biological photocontrol by non-invasive, *through-skull illumination*, suiting larger animals that are better as models in neuroscience. The quantitative NIR activity switch-off (Z→E) brings four complex but significant additional biological advantages (Supporting Note 5).

Electron-rich BGAGs should be photooxidisable by NB (Table 2): so we synthesised NIR-photoredox dyad **BANG** (Benzylguanine-Azobenzene-Nile Blue-Glutamate) alongside its non-NIR control **BAG** (Fig 4a-d). In cuvette, **BANG** is efficiently Z→all-E switched by 590-720 nm light, to which **BAG** does not respond (Fig 4e,f). Next, HEK293T cells cotransfected to express SNAP-mGluR2 as well as the G protein-coupled inward rectifying potassium channel GIRK1 were labelled with **BANG**/**BAG** at just 1 μM for 60 min. Whole cell patch clamp recordings showed excellent translation from chemical photoswitching to biological photoactuation. Bidirectionally reversible UV/green switching of **BANG** and **BAG** drove similar GIRK photocurrents, indicating that the distally-attached photoredox catalyst is indeed tolerated without loss of bioactivity. Uniquely though, **BANG** could be operated with red/NIR (660-740 nm), with similar switch-off as **BAG** at 525 nm (Fig 4g-i). **BANG** was a reproducible tool, with results from typically 10 cycles per cell and 8 cells per test overlaying well (i.e. no photodamage over time). Thus, singlet manifold photoredox is a practical, biocompatible route to rationally empower bioactive photopharmaceuticals with quantitative NIR Z→E isomerisation.

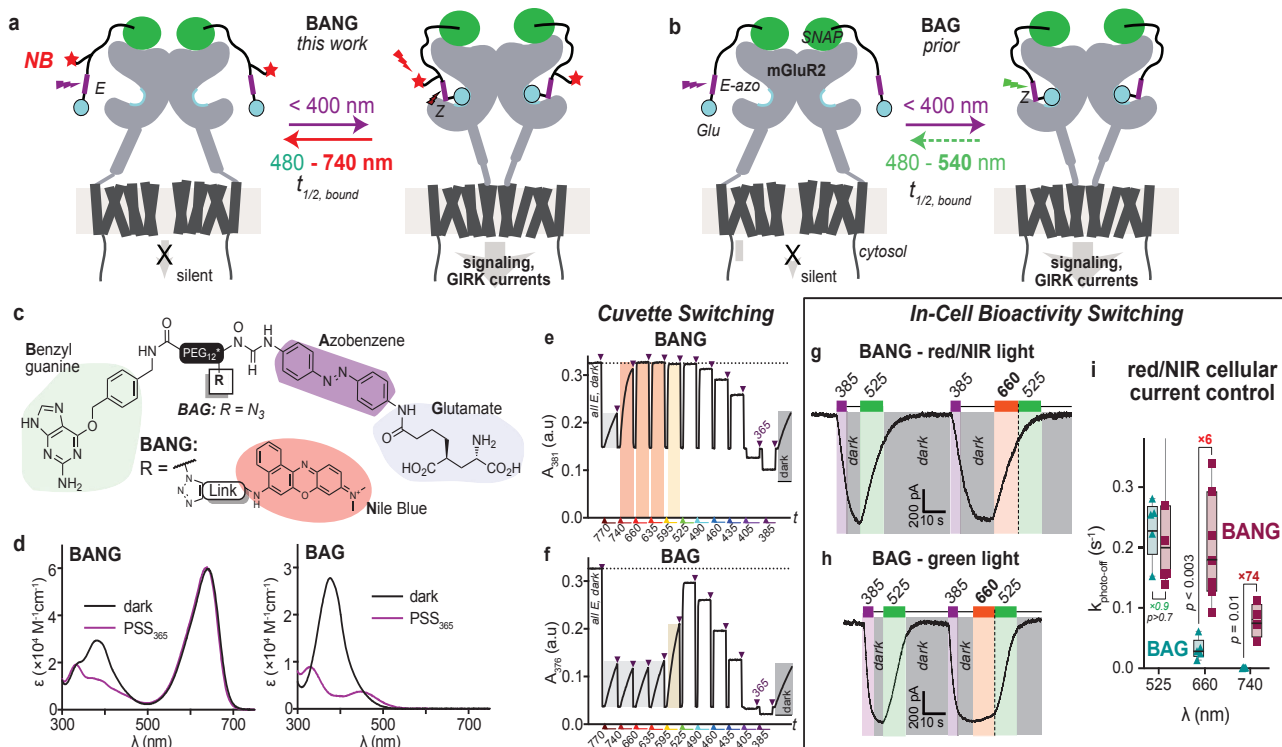


**Figure 4: Quantitative singlet photoredox switching achieves NIR photocontrol in biology.** (a-c) BANG and BAG are BGAG-based ligands for SNAP-mGluR2 photocontrol. (d-f) Absorption and action spectra in cuvette highlight BANG's red/NIR photoresponse (BAG only relaxes thermally during red light phases). (g-i) BANG allows red/NIR photocontrol over SNAP-mGluR activity in live cells (full legend in Supporting Note 3).

## DISCUSSION

Reversibly photoswitchable chemicals and proteins, i.e. photopharmaceuticals and optogenetic tools, deliver outstanding spatiotemporal precision when modulating biological activity in cell culture and thin tissue slices: and a plethora of toolsets for these model systems have been applied to great effect. However, single-photon operation in the NIR/SWIR has remained inaccessible to both methods, as they require energetically costly S<sub>0</sub>→S<sub>1</sub> excitation usually at 360-500 nm to surmount their activation barriers and initiate their photochemical cycles. This UV/blue/green light is poorly tissue-penetrating and highly scattered. Since implanted light delivery sources bring severe practical and conceptual problems, no broadly used methods for biological photocontrol deep in tissues *in vivo* have emerged. In addition, photopharmaceuticals are often hampered by their incomplete photoisomerisation, in that their background activity limits the power and scope of their applications. Here, we developed a general method to solve these outstanding challenges which have hindered *in vivo* photopharmacology. Known azobenzene photoswitches can be rationally retrofitted with biologically tolerated chromophores, with nearly no redesign requirements and without compromising their activity, to allow photoredox-powered switching. This switching paradigm reaches Z→E isomerisation that is quantitative, and highly photon-efficient, and can be driven by light even in the well-penetrating NIR region. We provide  $E_{redox}$  data for ~30 azobenzenes and ~10 chromophores to help others to retrofit their switches appropriately. We show that photoredox tolerates long linkers (up to PEG<sub>24</sub>) without much loss of photoswitching efficiency. We show that photoredox solutions to tune Z→E isomerisation can be combined with tetra-*ortho*-substitution methods for E→Z tuning, to bring each step of bidirectional switching  $\geq 200$  nm further into the visible/NIR than current standards. Finally, we show the first demonstration ever of rationally designed, NIR-photoswitching-based photocontrol over

biological function: a spectral challenge that optogenetics has still not solved despite two decades of effort.

We thus anticipate broad applications retrofitting azobenzene reagents for singlet manifold photoredox, that can usher in a new generation of photopharmacology tools. Bioorthogonal labelling to tether photoredox photopharmaceuticals near or onto genetically engineered fusion proteins, as we have demonstrated here, then promises to be a powerful route allowing red/NIR light to precisely actuate genetically-defined protein targets from a diverse range of classes: of which we see ion channels and ligand receptors as particularly relevant. The biocompatibility of singlet manifold photoredox switching may indeed allow photocontrol over the activity of excitable cells deep inside the CNS of freely-moving animals, by simple transcranial illumination (rather than the invasive, complex, study-limiting procedures for *in situ* light delivery that have been unavoidable over the last 20 years). We therefore look forward to a wave of chemical retrofitting to convert the many existing cell culture photopharmaceutical tools into *in vivo*-competent reagents suitable for deep tissue use, as well as a range of biological applications where their non-invasive photocontrol can make them irreplaceable tools, such as in behavioural studies and in larger animal models.

## ASSOCIATED CONTENT

### Supporting Information

PDF: Supporting Notes, chemical synthesis, photocharacterisation, electrochemistry, and cell biology (incl. Fig S1-S17 and Table S1-S8).

## AUTHOR INFORMATION

### Corresponding Author

Oliver Thorn-Seshold – Department of Pharmacy, LMU Munich, 81377 Munich, Germany  
Email: [oliver.thorn-seshold@cup.lmu.de](mailto:oliver.thorn-seshold@cup.lmu.de)



## Author Contributions

BB designed targets, performed synthesis, UV/Vis and fluorescence spectroscopy, HPLC analysis, analyzed and assembled data. AJW, AMD and MR performed synthesis and photocharacterisation. VGlembocyste and FS performed fluorescence lifetime experiments. AJGH performed mGluR2 electrophysiology. RK synthesised PST-PEG-CPY dyads, supervised by VGrenier. RJM, CG and LG performed electrochemistry. AV determined fluorescence quantum yields and performed transient absorption spectroscopy, supervised by BDI. JB performed synthesis and supplied building blocks. JL performed and supervised mGluR2 electrophysiology. SH and ARO supervised electrochemical measurements. PT supervised fluorescence lifetime experiments. OTS conceived the study, designed targets, analyzed data, and supervised all other experiments. BB and OTS wrote the manuscript with input from all authors.

## Funding Sources

This research was supported by funds from the German Research Foundation (DFG: SPP 1926 project number 426018126 to OTS; SFB1032 Nanoagents for Spatiotemporal Control number 201269156 project B09 to OTS and project A13 to PT; Emmy Noether grant TH2231/1-1 number 400324123 to OTS; SFB TRR 152 project P24 number 239283807 to OTS); the Munich Center for Nanoscience (CeNS, to OTS); the National Institutes of Health (R01NS129904 to JL); a Rohr Family Research Scholar Award (to JL); and a Monique Weill-Caulier Award (to JL).

## ACKNOWLEDGMENTS

BB thanks the Boehringer Ingelheim Fonds for a PhD fellowship. AJGH thanks the Ministry of Universities of Spain for a Margarita Salas Fellowship. We are grateful for many insightful and constructive discussions over the nine years of preparation of this work. In particular, we wish to thank Bert Nickel, Christian Schrader, Matthew Fuchter, Thomas Nausser, Guglielmo Lanzani, and the attendees of the international Photopharmacology conferences from 2017-2022. We thank Richard Wombacher (MPI Heidelberg) for technical support and Kai Johnsson (MPI Heidelberg) for generous support with reagents.

## ABBREVIATIONS

**BAG** (benzylguanine-azobenzene-glutamate); **BANG** (benzylguanine-azobenzene-nile blue-glutamate); CV (cyclic voltammetry); Fc (Ferrocene); FRET (fluorescence resonant energy transfer); **NB** (nile blue); **MB** (methylene blue); NIR (near-infrared); PEG (polyethylene glycol); PET (photoinduced electron transfer); PORTL (photoswitchable orthogonal remotely tethered ligands); PSS (photostationary state); SCE (standard calomel electrode); SWV (square wave voltammetry); TAS (transient absorption spectroscopy);  $\tau_f$  (fluorescence lifetime);  $\phi_f$  (quantum yield).

## KEYWORDS

Photoswitch, isomerisation, photoredox, photopharmacology, photochemistry.

## REFERENCES

- (1) Jia, S.; Sletten, E. M. Spatiotemporal Control of Biology: Synthetic Photochemistry Toolbox with Far-Red and Near-Infrared Light. *ACS Chem. Biol.* **2022**, *17* (12), 3255–3269. <https://doi.org/10.1021/acscchembio.1c00518>.
- (2) Broichhagen, J.; Levitz, J. Advances in Tethered Photopharmacology for Precise Optical Control of Signaling Proteins. *Current Opinion in Pharmacology* **2022**, *63*, 102196. <https://doi.org/10.1016/j.coph.2022.102196>.
- (3) Hüll, K.; Morstein, J.; Trauner, D. In Vivo Photopharmacology. *Chem. Rev.* **2018**, *118* (21), 10710–10747. <https://doi.org/10.1021/acs.chemrev.8b00037>.

- (4) Velema, W. A.; Szymanski, W.; Feringa, B. L. Photopharmacology: Beyond Proof of Principle. *J. Am. Chem. Soc.* **2014**, *136* (6), 2178–2191. <https://doi.org/10.1021/ja413063e>.
- (5) Fuchter, M. J. On the Promise of Photopharmacology Using Photoswitches: A Medicinal Chemist's Perspective. *J. Med. Chem.* **2020**, *63* (20), 11436–11447. <https://doi.org/10.1021/acs.jmedchem.0c00629>.
- (6) Dong, M.; Babalhavaeji, A.; Samanta, S.; Beharry, A. A.; Woolley, G. A. Red-Shifting Azobenzene Photoswitches for in Vivo Use. *Acc. Chem. Res.* **2015**, *48* (10), 2662–2670. <https://doi.org/10.1021/acs.accounts.5b00270>.
- (7) Daniels, E.; Barras, C.; Dwyer, A.; Strem, B.; Wykoff, C. C.; Van Gelder, R. N.; Casson, R. J. An Intravitreal “Photoswitch” Molecule (KIO-301) for Reanimation in Retinitis Pigmentosa: A First-in-Human Trial. *Investigative Ophthalmology & Visual Science* **2023**, *64* (8), 5444–5444.
- (8) Samanta, S.; Beharry, A. A.; Sadoski, O.; McCormick, T. M.; Babalhavaeji, A.; Tropepe, V.; Woolley, G. A. Photoswitching Azo Compounds in Vivo with Red Light. *J. Am. Chem. Soc.* **2013**, *135* (26), 9777–9784. <https://doi.org/10.1021/ja402220t>.
- (9) Bléger, D.; Schwarz, J.; Brouwer, A. M.; Hecht, S. O-Fluoroazobenzenes as Readily Synthesized Photoswitches Offering Nearly Quantitative Two-Way Isomerization with Visible Light. *J. Am. Chem. Soc.* **2012**, *134* (51), 20597–20600. <https://doi.org/10.1021/ja310323y>.
- (10) Siewertsen, R.; Neumann, H.; Buchheim-Stehn, B.; Herges, R.; Näther, C.; Renth, F.; Temps, F. Highly Efficient Reversible Z–E Photoisomerization of a Bridged Azobenzene with Visible Light through Resolved S1(N $\pi^*$ ) Absorption Bands. *J. Am. Chem. Soc.* **2009**, *131* (43), 15594–15595. <https://doi.org/10.1021/ja906547d>.
- (11) Goulet-Hanssens, A.; Rietze, C.; Titov, E.; Abdullah, L.; Grubert, L.; Saalfrank, P.; Hecht, S. Hole Catalysis as a General Mechanism for Efficient and Wavelength-Independent Z  $\rightarrow$  E Azobenzene Isomerization. *Chem* **2018**, *4* (7), 1740–1755. <https://doi.org/10.1016/j.chempr.2018.06.002>.
- (12) Goulet-Hanssens, A.; Utecht, M.; Mutruc, D.; Titov, E.; Schwarz, J.; Grubert, L.; Bléger, D.; Saalfrank, P.; Hecht, S. Electrocatalytic Z  $\rightarrow$  E Isomerization of Azobenzenes. *J. Am. Chem. Soc.* **2017**, *139* (1), 335–341. <https://doi.org/10.1021/jacs.6b10822>.
- (13) Moreno, J.; Grubert, L.; Schwarz, J.; Bléger, D.; Hecht, S. Efficient Sensitized Z $\rightarrow$ E Photoisomerization of an Iridium(III)-Azobenzene Complex over a Wide Concentration Range. *Chem. Eur. J.* **2017**, *23* (56), 14090–14095. <https://doi.org/10.1002/chem.201703376>.
- (14) Greenfield, J. L.; Gerkman, M. A.; Gibson, R. S. L.; Han, G. G. D.; Fuchter, M. J. Efficient Electrocatalytic Switching of Azoheteroarenes in the Condensed Phases. *J. Am. Chem. Soc.* **2021**, *143* (37), 15250–15257. <https://doi.org/10.1021/jacs.1c06359>.
- (15) Arnaud, R.; Lemaire, J. Isomérisation *cis* – *trans* de l'azobenzène catalysée par l'iode. III. *Can. J. Chem.* **1974**, *52* (10), 1868–1871. <https://doi.org/10.1139/v74-266>.
- (16) Ronayette, J.; Arnaud, R.; Lemaire, J. Isomérisation photosensibilisée par des colorants et photoréduction de l'azobenzène en solution. II. *Can. J. Chem.* **1974**, *52* (10), 1858–1867. <https://doi.org/10.1139/v74-265>.
- (17) Shimomura, M.; Kunitake, T. Fluorescence and Photoisomerization of Azobenzene-Containing Bilayer Membranes. *J. Am. Chem. Soc.* **1987**, *109* (17), 5175–5183. <https://doi.org/10.1021/ja00251a022>.
- (18) Isokuortti, J.; Kuntze, K.; Virkki, M.; Ahmed, Z.; Vuorimaa-Laukkanen, E.; Filatov, M. A.; Turshatov, A.; Laaksonen, T.; Priimagi, A.; Durandin, N. A. Expanding Excitation Wavelengths for Azobenzene Photoswitching into the Near-Infrared Range via Endothermic Triplet Energy Transfer. *Chem. Sci.* **2021**, *12* (21), 7504–7509. <https://doi.org/10.1039/D1SC01717A>.
- (19) Baumgartner, B.; Glembocyste, V.; Gonzalez-Hernandez, A. J.; Valavalkar, A.; Mayer, R.; Fillbrook, L.; Müller-Deku, A.; Steiner, F.; Gross, C.; Reynders, M.; Munguba, H.; Arefin, I.; Ofial, A.; Beves, J.; Dietzek-Ivanšić, B.; Broichhagen, J.; Tinnfeld, P.; Levitz, J.; Thorn-Seshold, O. A General Method for Near-Infrared Photoswitching in Biology, Demonstrated by the >700 Nm Photocontrol of Glutamate Receptors in Brain Slices. *in preparation* **2023**.
- (20) Romero, N. A.; Nicewicz, D. A. Organic Photoredox Catalysis. *Chem. Rev.* **2016**, *116* (17), 10075–10166. <https://doi.org/10.1021/acs.chemrev.6b00057>.

- (21) values taken from <https://www.atto-tec.com/ATTO-655.html> (measured in PBS), last visited 15.09.2022.
- (22) Vogelsang, J.; Cordes, T.; Forthmann, C.; Steinhauer, C.; Tinnefeld, P. Controlling the Fluorescence of Ordinary Oxazine Dyes for Single-Molecule Switching and Superresolution Microscopy. *Proc. Natl. Acad. Sci. U.S.A.* **2009**, *106* (20), 8107–8112. <https://doi.org/10.1073/pnas.0811875106>.
- (23) Becker, R. S.; Chakravorti, S.; Das, S. The Photosensitizers Benzophenoxazine and Thiazines: Comprehensive Investigation of Photophysical and Photochemical Properties. *Photochem Photobiol* **1990**, *51* (5), 533–538. <https://doi.org/10.1111/j.1751-1097.1990.tb01962.x>.
- (24) Zhao, X.; Yao, Q.; Long, S.; Chi, W.; Yang, Y.; Tan, D.; Liu, X.; Huang, H.; Sun, W.; Du, J.; Fan, J.; Peng, X. An Approach to Developing Cyanines with Simultaneous Intersystem Crossing Enhancement and Excited-State Lifetime Elongation for Photodynamic Antitumor Metastasis. *J. Am. Chem. Soc.* **2021**, *143* (31), 12345–12354. <https://doi.org/10.1021/jacs.1c06275>.
- (25) Connelly, N. G.; Geiger, W. E. Chemical Redox Agents for Organometallic Chemistry. *Chem. Rev.* **1996**, *96* (2), 877–910. <https://doi.org/10.1021/cr940053x>.
- (26) Pernpeintner, C.; Frank, J. A.; Urban, P.; Roeske, C. R.; Pritzl, S. D.; Trauner, D.; Lohmüller, T. Light-Controlled Membrane Mechanics and Shape Transitions of Photoswitchable Lipid Vesicles. *Langmuir* **2017**, *33* (16), 4083–4089. <https://doi.org/10.1021/acs.langmuir.7b01020>.
- (27) Frank, J. A.; Yushchenko, D. A.; Hodson, D. J.; Lipstein, N.; Nagpal, J.; Rutter, G. A.; Rhee, J.-S.; Gottschalk, A.; Brose, N.; Schultz, C.; Trauner, D. Photoswitchable Diacylglycerols Enable Optical Control of Protein Kinase C. *Nat Chem Biol* **2016**, *12* (9), 755–762. <https://doi.org/10.1038/nchembio.2141>.
- (28) Frank, J. A.; Moroni, M.; Moshourab, R.; Sumser, M.; Lewin, G. R.; Trauner, D. Photoswitchable Fatty Acids Enable Optical Control of TRPV1. *Nat Commun* **2015**, *6* (1), 7118. <https://doi.org/10.1038/ncomms8118>.
- (29) Urban, P.; Pritzl, S. D.; Konrad, D. B.; Frank, J. A.; Pernpeintner, C.; Roeske, C. R.; Trauner, D.; Lohmüller, T. Light-Controlled Lipid Interaction and Membrane Organization in Photolipid Bilayer Vesicles. *Langmuir* **2018**, *34* (44), 13368–13374. <https://doi.org/10.1021/acs.langmuir.8b03241>.
- (30) Weber, T.; Chandrasekaran, V.; Stamer, I.; Thygesen, M. B.; Terfort, A.; Lindhorst, T. K. Switching of Bacterial Adhesion to a Glycosylated Surface by Reversible Reorientation of the Carbohydrate Ligand. *Angew. Chem. Int. Ed.* **2014**, *53* (52), 14583–14586. <https://doi.org/10.1002/anie.201409808>.
- (31) Broichhagen, J.; Damijonaitis, A.; Levitz, J.; Sokol, K. R.; Leippe, P.; Konrad, D.; Isacoff, E. Y.; Trauner, D. Orthogonal Optical Control of a G Protein-Coupled Receptor with a SNAP-Tethered Photochromic Ligand. *ACS Cent Sci* **2015**, *1* (7), 383–393. <https://doi.org/10.1021/acscentsci.5b00260>.
- (32) Fehrentz, T.; Kuttruff, C. A.; Huber, F. M. E.; Kienzler, M. A.; Mayer, P.; Trauner, D. Exploring the Pharmacology and Action Spectra of Photochromic Open-Channel Blockers. *ChemBioChem* **2012**, *13* (12), 1746–1749. <https://doi.org/10.1002/cbic.201200216>.
- (33) Tochitsky, I.; Polosukhina, A.; Degtyar, V. E.; Gallerani, N.; Smith, C. M.; Friedman, A.; Van Gelder, R. N.; Trauner, D.; Kaufer, D.; Kramer, R. H. Restoring Visual Function to Blind Mice with a Photoswitch That Exploits Electrophysiological Remodeling of Retinal Ganglion Cells. *Neuron* **2014**, *81* (4), 800–813. <https://doi.org/10.1016/j.neuron.2014.01.003>.
- (34) Reynders, M.; Oliver Thorn-Seshold. PST2. *in preparation*.
- (35) Thorn-Seshold, O.; Trauner, D.; Borowiak, M.; Hasserodt, J. EP3137554 - Azoaryls as Reversibly Modulatable Tubulin Inhibitors.
- (36) Borowiak, M.; Nahaboo, W.; Reynders, M.; Nekolla, K.; Jalinot, P.; Hasserodt, J.; Rehberg, M.; Delattre, M.; Zahler, S.; Vollmar, A.; Trauner, D.; Thorn-Seshold, O. Photoswitchable Inhibitors of Microtubule Dynamics Optically Control Mitosis and Cell Death. *Cell* **2015**, *162* (2), 403–411. <https://doi.org/10.1016/j.cell.2015.06.049>.
- (37) Borowiak, M.; Küllmer, F.; Gegenfurtner, F.; Peil, S.; Nasufovic, V.; Zahler, S.; Thorn-Seshold, O.; Trauner, D.; Arndt, H.-D. Optical Manipulation of F-Actin with Photoswitchable Small Molecules. *J. Am. Chem. Soc.* **2020**, *142* (20), 9240–9249. <https://doi.org/10.1021/jacs.9b12898>.
- (38) Konrad, D. B.; Frank, J. A.; Trauner, D. Synthesis of Redshifted Azobenzene Photoswitches by Late-Stage Functionalization. *Chem. Eur. J.* **2016**, *22* (13), 4364–4368. <https://doi.org/10.1002/chem.201505061>.
- (39) Pritzl, S. D.; Konrad, D. B.; Ober, M. F.; Richter, A. F.; Frank, J. A.; Nickel, B.; Trauner, D.; Lohmüller, T. Optical Membrane Control with Red Light Enabled by Red-Shifted Photolipids. *Langmuir* **2022**, *38* (1), 385–393. <https://doi.org/10.1021/acs.langmuir.1c02745>.
- (40) Chander, N.; Morstein, J.; Bolten, J. S.; Shemet, A.; Cullis, P. R.; Trauner, D.; Witzigmann, D. Optimized Photoactivatable Lipid Nanoparticles Enable Red Light Triggered Drug Release. *Small* **2021**, *17* (21), 2008198. <https://doi.org/10.1002/smll.202008198>.
- (41) Müller-Deku, A.; Thorn-Seshold, O. Exhaustive Catalytic Ortho-Alkoxylation of Azobenzenes: Flexible Access to Functionally Diverse Yellow-Light-Responsive Photoswitches. *J. Org. Chem.* **2022**, *87* (24), 16526–16531. <https://doi.org/10.1021/acs.joc.2c02214>.
- (42) Broichhagen, J.; Damijonaitis, A.; Levitz, J.; Sokol, K. R.; Leippe, P.; Konrad, D.; Isacoff, E. Y.; Trauner, D. Orthogonal Optical Control of a G Protein-Coupled Receptor with a SNAP-Tethered Photochromic Ligand. *ACS Cent Sci* **2015**, *1* (7), 383–393. <https://doi.org/10.1021/acscentsci.5b00260>.
- (43) Acosta-Ruiz, A.; Gutzeit, V. A.; Skelly, M. J.; Meadows, S.; Lee, J.; Parekh, P.; Orr, A. G.; Liston, C.; Pleil, K. E.; Broichhagen, J.; Levitz, J. Branched Photoswitchable Tethered Ligands Enable Ultra-Efficient Optical Control and Detection of G Protein-Coupled Receptors In Vivo. *Neuron* **2020**, *105* (3), 446–463.e13. <https://doi.org/10.1016/j.neuron.2019.10.036>.
- (44) Gutzeit, V. A.; Acosta-Ruiz, A.; Munguba, H.; Häfner, S.; Landra-Willm, A.; Mathes, B.; Mony, J.; Yarotski, D.; Börjesson, K.; Liston, C.; Sandoz, G.; Levitz, J.; Broichhagen, J. A Fine-Tuned Azobenzene for Enhanced Photopharmacology in Vivo. *Cell Chem. Biol.* **2021**, *28* (11), 1648–1663. <https://doi.org/10.1016/j.chembiol.2021.02.020>.
- (45) Donthamsetti, P. C.; Broichhagen, J.; Vyklicky, V.; Stanley, C.; Fu, Z.; Visel, M.; Levitz, J. L.; Javitch, J. A.; Trauner, D.; Isacoff, E. Y. Genetically Targeted Optical Control of an Endogenous G Protein-Coupled Receptor. *J. Am. Chem. Soc.* **2019**, *141* (29), 11522–11530. <https://doi.org/10.1021/jacs.9b02895>.

## 4 Ongoing projects

### 4.1 Single-photon photoisomerization of azobenzenes above 1000 nm enabled by energy transfer from a polymethine dye

Benedikt Baumgartner<sup>1</sup>, Syed M. Usama<sup>2</sup>, Alexander J. Wiegand<sup>1</sup>, Martin J. Schnermann<sup>2</sup>, Oliver Thorn-Seshold<sup>1</sup>

1) Department of Pharmacy, Ludwig-Maximilians University of Munich, Butenandtstr. 7, 81377 Munich, Germany;  
2) Chemical Biology Laboratory, National Cancer Institute, 376 Boyles Street, Frederick, Maryland 21702, United States.

**Background:** In chapter 3.1 we showed that  $Z \rightarrow E$  isomerization of azobenzenes can be operated by intramolecular energy transfer from a synthetic fluorophore that enables near-quantitative isomerization (up to 98%  $E$  isomer) and rapid bulk photoswitching up to 770 nm. This phenomenon was shown to be general and independent of absorption maximum of the applied fluorophores tested; and Durandin and Priimagi even showed that azobenzene isomerization, via intermolecular energy transfer from a photosensitizer (by triplet energy transfer, TET), can also happen endothermically driven, if entropically compensated.<sup>55</sup>

**Aims and Design:** Recent developments of short wave infrared (SWIR) dyes by groups around Schnermann and Sletten allow for excitation above 1000 nm, presumably accessing only very low energy triplet states ( $ET < 120$  kJ/mol) which is somewhat below those reported for azobenzenes ( $ET$  ca. 125-160 kJ/mol)<sup>91,92</sup> - but if endothermic driving is possible, then, TET might also be possible with such dyes. We were keen to see how far an azobenzene's photoresponse can be shifted towards low energy, deep tissue penetrating light. Therefore, we synthesized a covalent conjugate **NorCy7-AO** consisting of the 4,4'-bisalkoxy azobenzene **AO** and the SWIR dye **NorCy7** (**Figure 23a**). **NorCy7** has an absorption maximum at 961 nm but the low energy tail shows absorption above 1000 nm. **NorCy7-AO** was switched to a  $Z$ -enriched PSS by illumination with 365 nm (pE 4000, CoolLed) directly exciting the  $\pi$ - $\pi^*$  band of the **AO** part.  $Z \rightarrow E$  isomerization was then achieved by illumination with a 1050 nm LED (M1050L4, ThorLabs; FWHM 37 nm, 160 mW max optical output of which est. 10 mW reaches the sample surface area of  $2 \times 10$  mm) (**Figure 23b**). The spectral overlap of the LED's emission spectrum and the absorption spectrum of **NorCy7-AO** is rather small. Optionally, to ensure that light only above 1000 nm drives the isomerization, the LED illumination was applied through a 1000 nm longpass filter (FELH1000, ThorLabs), minimising intensity loss from its large-angle emission by focusing the LED via a polycarbonate lens.

**Key Result:** **NorCy7-AO** is the first ever system that allows single photon  $Z \rightarrow E$  photoisomerization of an azobenzene above 1000 nm. Unsurprisingly, **AO** does not show any difference in its  $Z \rightarrow E$  isomerization kinetics with or without 1050 nm LED illumination (**Figure 23c**), indicating that the **NorCy7** conjugation is crucial.

Its bulk " $>1000$  nm" isomerisation seems less photon-efficient than the green/red/NIR-driven conjugates developed in our initial study (chapter 3.1), although the quantities cannot be strictly compared in these studies since the illuminations of the long-wavelength tails are not done with monochromatic light (**Figure 23b**) and better quantification will be performed in later work. If the "1000 nm" kinetics are indeed shown to be slower than those of the conjugates in chapter 3.1, that could perhaps be due to a relatively large endothermicity for triplet energy transfer, potentially slowed even more by restricted collisions between **AO** and **NorCy7** due to the shorter and more rigid linker used here (collision is necessary for TET).

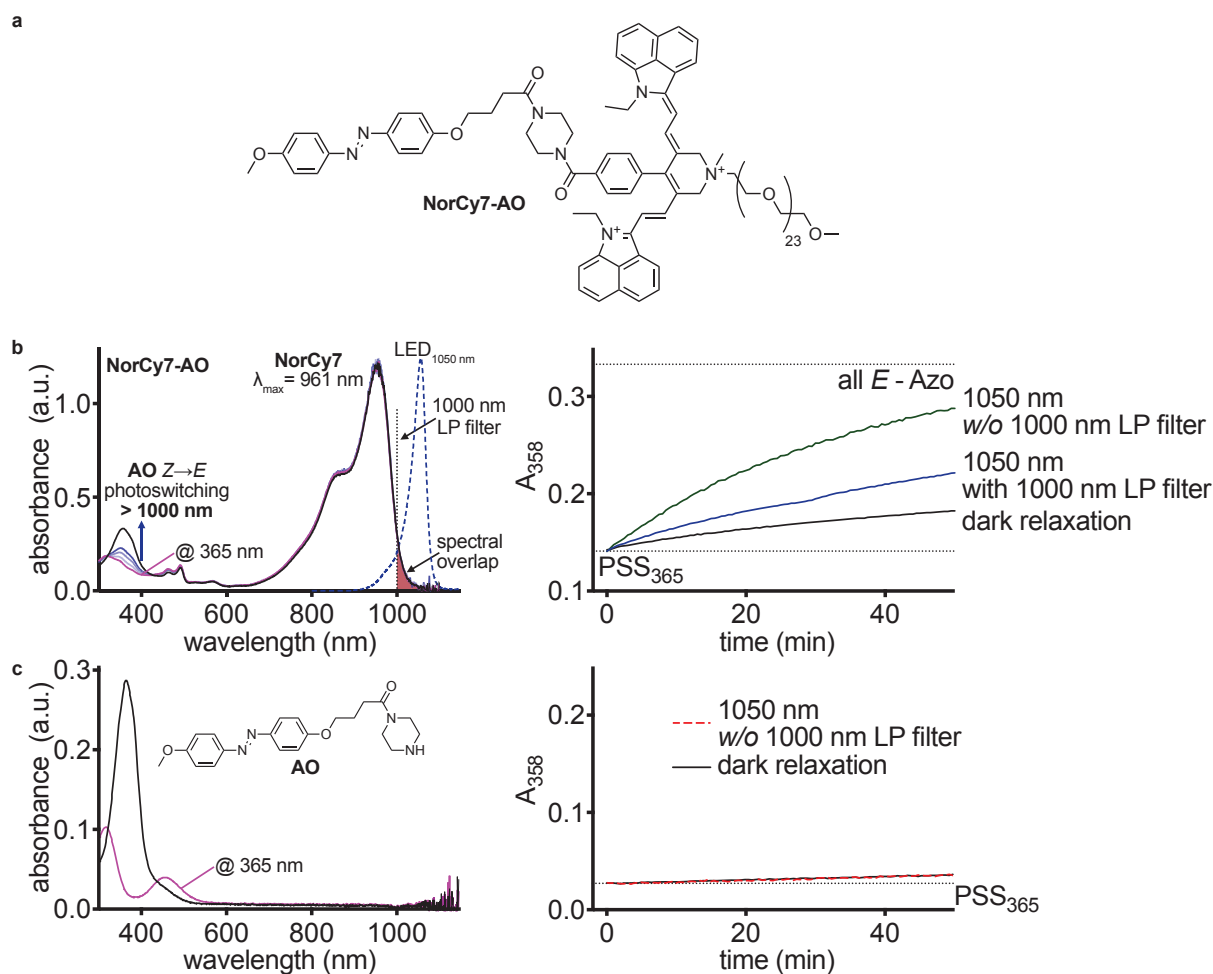


**Figure 23:** a) chemical structure of covalent conjugate **NorCy7-AO** consisting of the 4,4'-bisalkoxy azobenzene **AO** and the SWIR dye **NorCy7**; b) Absorption spectra and photoswitch kinetics of **NorCy7-AO** at 1050 nm LED illumination with and without a 1000 nm long pass filter. Removing the background of spontaneous relaxation gives photoisomerisation-only "effective time constants" of ca.  $\tau \sim 35$  min without filter and ca.  $\tau \sim 65$  min with filter. These could be only very roughly compared to the illuminations at ca.  $2 \text{ mW/mm}^2$  (roughly 3-fold higher intensity) into the long-wavelength absorption tails of conjugates in chapter 3.1, resulting in effective photoisomerisation time constants ca. 3 min (roughly 10-fold faster). c) Absorption spectra and photoswitch kinetics of **AO** with and without 1050 nm illumination.

In summary, **NorCy7-AO** provides proof-of-concept for single-photon SWIR triggered  $Z \rightarrow E$  isomerization of azobenzenes above 1000 nm. Further investigations will enable its application in photopharmacology allowing body-wide modulation of bioactivity in mice without invasive methods.

**Own contribution:** Design and synthesis of the fluorophore **NorCy7-COOH** has been performed by Syed M. Usama in the lab of Martin J. Schnermann. I designed the other compounds, performed and supervised the synthesis of the azobenzene photoswitch **AO** and the azobenzene-fluorophore conjugate **NorCy7-AO**. I performed UV/Vis spectroscopy. I analyzed experimental data, coordinated results and assembled data in figures.

*This work is being prepared as a Communication in e.g. JACS.*



## 4.2 Azobenzene photoswitches as next generation photostabilizing agents for single molecule localization and super resolution microscopy

Benedikt Baumgartner<sup>1#</sup>, Michael Scheckenbach<sup>2#</sup>, Niklas Kölbl<sup>2#</sup>, Alexander J. Wiegand<sup>1#</sup>, Philip Tinnefeld<sup>2</sup>, Viktorija Glembockyte<sup>2\*</sup>, Oliver Thorn-Seshold<sup>1\*</sup>

1) Department of Pharmacy, Ludwig-Maximilians University of Munich, 81377 Munich, Germany; 2) Department of Chemistry and Center for Nanoscience, Ludwig-Maximilians University of Munich, 81377 Munich, Germany.

#authors contributed equally; \*corresponding authors

**Background:** Fluorescence microscopy is a powerful technique that enabled scientists to discover much of what we know about biological structures. In the last decades fluorescence microscopy techniques drastically improved by increasing the resolution from ~250 nm to below 10 nm, enabled by the development of super resolution microscopy techniques as STED<sup>138</sup>, PALM<sup>146</sup>, STORM<sup>147</sup>, MINSTED<sup>137</sup> and DNA-PAINT<sup>145</sup>. Nevertheless, these techniques still rely on fluorophore classes that have been developed 100 years ago. To show the full potential of these super resolution methods, there is a need for innovative strategies to develop novel super photostable fluorophores.

**Aims and Approach:** In our work on triplet energy transfer-triggered  $Z \rightarrow E$  azobenzene isomerization (chapter 3.1) we discovered by fluorescence correlation spectroscopy (FCS) that azobenzenes depopulate triplet states of fluorophores in covalent azobenzene fluorophore conjugates (reproduced in **Figure 24**, EY-AK vs EY-P) which led to much more photostable and brighter fluorophores.

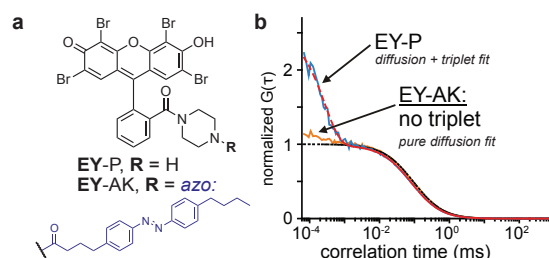


**Figure 24:** a) chemical structure of Eosin Y piperazine amide (EY-P) and Eosin Y - azobenzene AK conjugate (EY-AK); b) fluorescence correlation spectroscopy (FCS) of EY-P and EY-AK showing complete depopulated triplet state in EY-AK vs huge triplet contribution in EY-P.

Azobenzenes have medium-lying triplet state energies (**Figure 20a**) and ultra-short triplet state lifetimes ( $\tau_T \sim 10$  ps<sup>61</sup>,  $10^7$  less than the current state-of-the-art triplet state quencher COT  $\tau_T \sim 100$   $\mu$ s<sup>169</sup>). Current photostabilisation methods in single molecule localization microscopy (SMLM) experiments rely on oxygen-free conditions with huge excess of COT (2 mM), transition metal complexes, or cocktails of reducing and oxidizing agents, which are not compatible with live cell imaging.<sup>150,166</sup> We think that azobenzenes will be key to develop a novel class of super stable and bright fluorophores that can be applied as drug-like small-molecules, compatible with live cell settings.

**Intermolecular Stabilisation:** We were keen to study the impact of azobenzenes on fluorophore performance in single molecule experiments. We applied the water soluble azobenzene **PST-2S** (2 mM solution) to a Cy5 fluorophore that is attached as a DNA strand on a DNA origami surface and studied the absolute photon output number and time before bleaching in absence and presence of **PST-2S** (**Figure 25**). Single molecule fluorescence trajectories (**Figure 25b**) show a tremendous increase of Cy5 photon count rate and brightness, i.e. intermolecular solution-based stabilisation (**Figure 25c**).

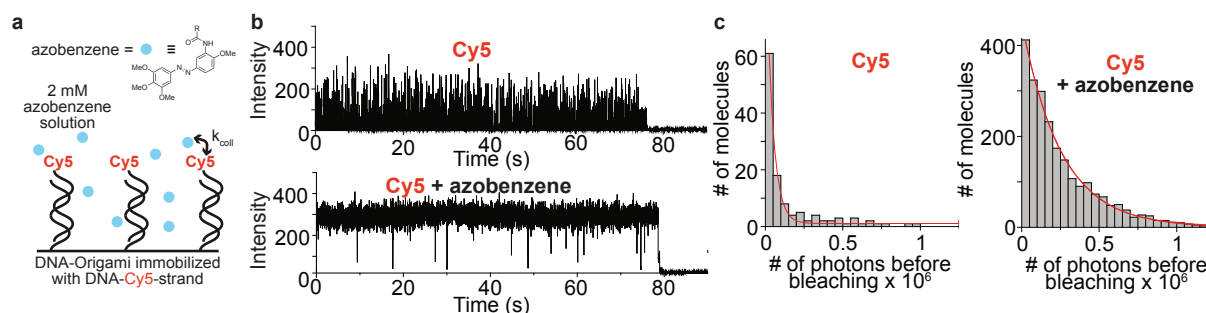


**Figure 25:** a) solution based single molecule experiment on photostabilization of Cy5 fluorophore by azobenzene **PST-2S** solution (2 mM); b) single molecule fluorescence trajectories of Cy5 in absence (top) and presence (bottom) of 2 mM **PST-2S**; c) quantification of Cy5 photon output in absence (left) and presence (right) of 2 mM **PST-2S**.

**1:1 Templated-Intermolecular Stabilisation:** In a next step we were keen to study how generalizable the concept of azobenzene stabilized fluorophores is. To screen different combinations of azobenzenes and fluorophores, we synthesized a small set of azobenzenes and stilbenes with a carboxylic acid attachment handle for coupling on 17 nt DNA oligos (**Figure 26**, for synthesis procedure, see supporting information). Having both azobenzene and fluorophore complementarily labelled on DNA oligos enables us to position the fluorophore and the azobenzene moieties in close proximity, to study the photostabilization properties of different photoswitches. The proximity docking site studies are currently ongoing.

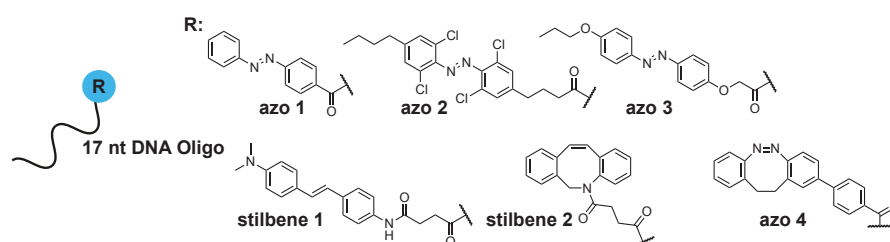


**Figure 26:** Chemical structures of azobenzenes and stilbenes attached to 17 nt DNA oligo for proximity docking site studies.

In the meantime, we tested the performance in DNA-PAINT super resolution microscopy. DNA-PAINT relies on transient binding of a fluorophore-labeled imager strand (8-10 nucleotides) to a docking strand that is e.g. attached to a target in live cell or a DNA origami surface. Transient binding events create blinking in DNA-PAINT and allow for subdiffractional limited resolution (< 5 nm is possible).<sup>145</sup> In our case, we studied one of the best-in-class super resolution microscopy fluorophores AbberiorStar635P and additionally added a photostabilizer strand (**azo 1** labeled 17 nt DNA oligo, **Figure 27a**). The azo strand gives drastically brighter images (**Figure 27b**), 5-fold better survival/tracking time, and 10-fold higher localisation rate (**Figure 27c**) compared with the parent fluorophore (oxygen-free).



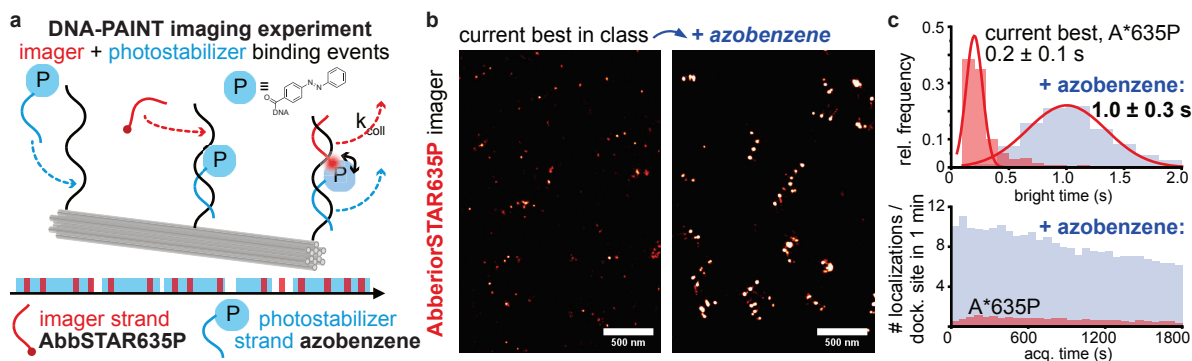


**Figure 27:** a) experimental setup of DNA-PAINT experiment with AbberiorStar635P imager strand and azobenzene photostabilizer strand; b) images in presence of azobenzene (right) are drastically brighter compared to absence of azobenzene (left); c) AbberiorStar645P shows 5-fold better survival/tracking time, and 10-fold higher localisation rate in presence of azobenzene (grey) compared to absence of azobenzene (red).

**1:1 Intramolecular Stabilisation:** The ultimate goal has been to reach a new class of self-healing fluorophores that can be applied as easily as current best-in-class fluorophores, but which have superior performance in survival time, brightness and localization rate. This implies that the photostabilizing agent needs to be covalently attached on the fluorophore molecule. Our first design concept for superstable fluorophores is shown in **Figure 28a**. We use the azobenzene as a linker, connecting the fluorophore and the attachment handle (fluorophores for super resolution imaging usually need attachment via a handle or targeting group, e.g. DBCO for copper free click chemistry or benzylguanine for SNAP-tag self-labeling protein ligation; we used DBCO as a standard handle in our work). Together with the results of the docking site studies, we aim to find the best suiting pair of azobenzene and fluorophore.

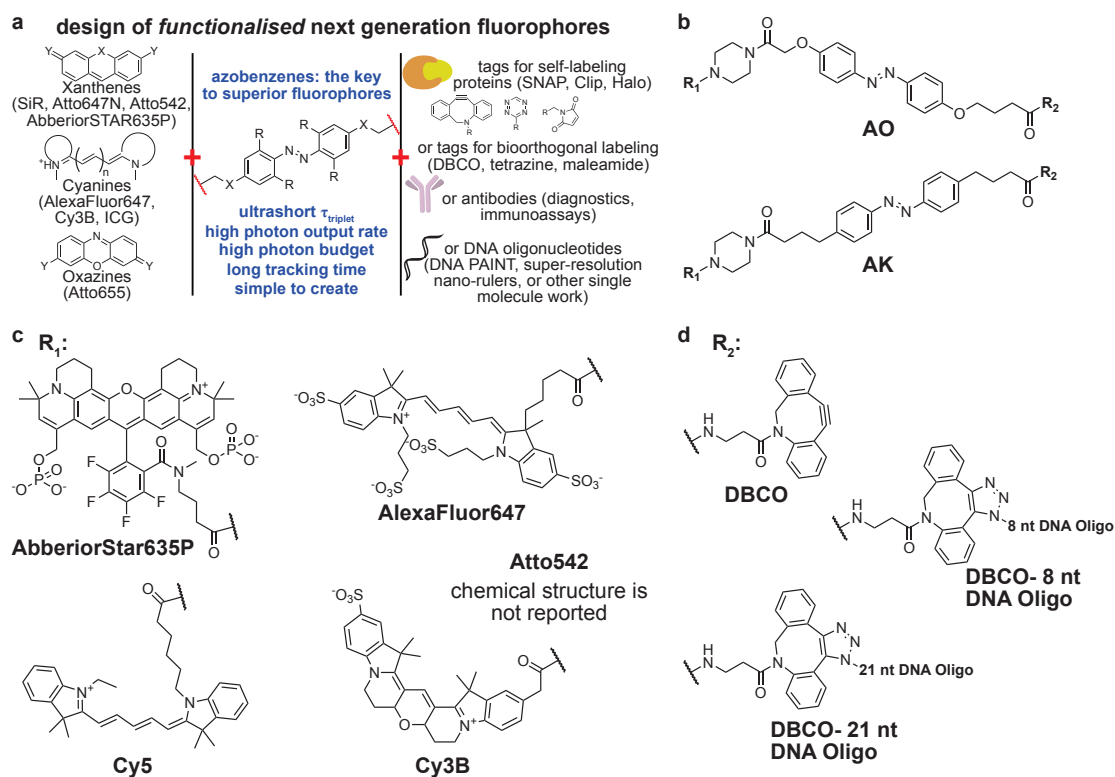


**Figure 28:** a) design concept of our functionalized next generation fluorophores; b) azobenzenes used for the initial library synthesis; c) state of the art super resolution and single molecule localization microscopy fluorophores used for the initial library synthesis; d) DBCO attachment handle used for bioorthogonal chemistry and labeling of 8 nt and 21 nt DNA oligos.

We started with the synthesis of a small library of 10 azobenzene-fluorophore conjugates using five state-of-the-art fluorophores for super resolution microscopy (**Figure 28c**), two azobenzenes with different substitution patterns (**Figure 28b**) and a DBCO attachment handle for DNA labeling and bioorthogonal chemistry (**Figure 28d**; for synthesis procedures, see supporting chapter).

#### single molecule mode performance

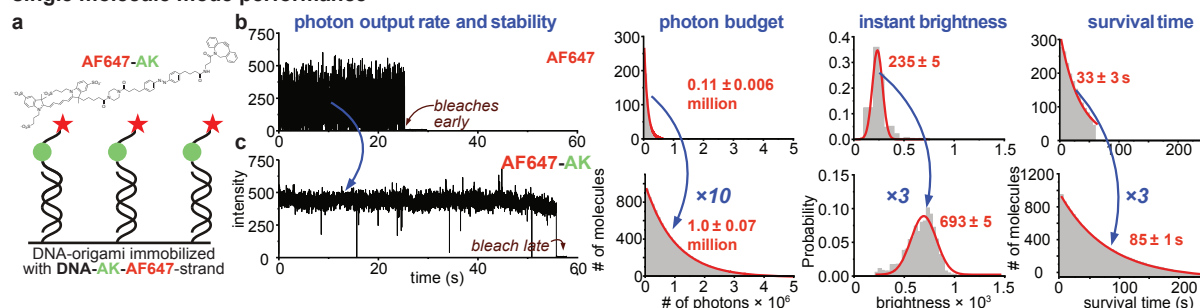


**Figure 29:** a) SMLM experimental setup for AF647-AK; b-c) photon output rate, photon budget, instant brightness and survival time in absence (AF647, b) and presence of azobenzene (AF647,AK, c). AF647-AK shows massively enhanced photon output & stability, 10-fold higher photon budget, 3-fold higher brightness during on-time, and 3-fold longer tracking time vs. AF647.

The 10 conjugates have been labeled to both 8 nt DNA oligos for transient labeling, and 21 nt DNA oligos for permanent labeling. We tested and evaluated the first conjugate AlexaFluor-AK-DBCO-21nt DNA oligo (**AF647-AK**) in single molecule localization microscopy immobilized on a DNA origami surface (**Figure 29**). **AF647-AK** shows 10-fold higher photon budget, 3-fold higher brightness and 3-fold longer survival time compared to **AF647** without stabilizer. For all other conjugates we show a summary of brightness and photon output normalized to the parent fluorophore (**Figure 30**). The extraordinary performance in stabilizing **AbberiorStar635P** by both azobenzene scaffolds is remarkable: > 5-fold increase in brightness and > 15-fold increase in photon output. **AO**-type conjugates outperform **AK** in photostabilizing **Atto542** and **Cy5**, although the **AK**-type is more efficient for **AF647**. The measurements of Cy3B conjugates and more detailed analysis are currently ongoing.

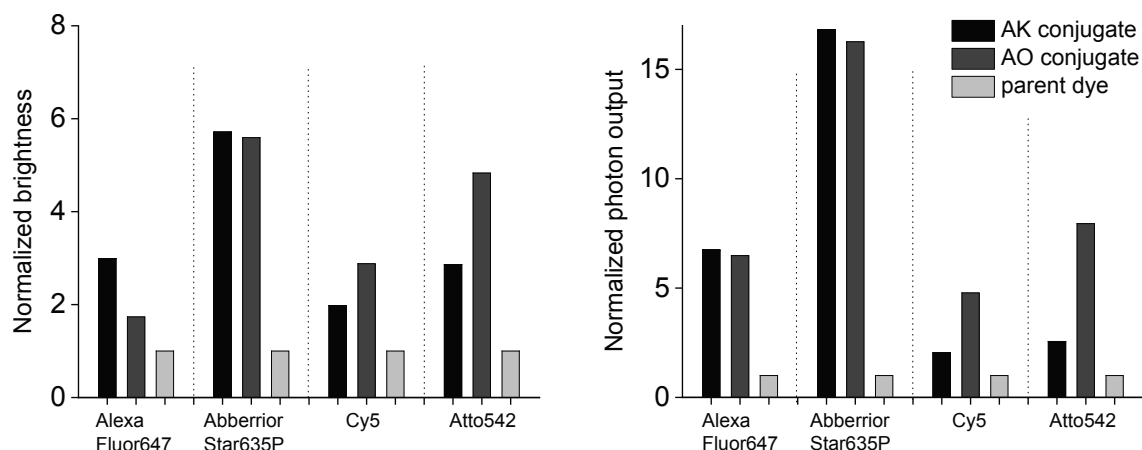


**Figure 30:** Brightness (photon count rate in the single-molecule imaging studies) and photon output (total number of photons until photobleaching) obtained for fluorophore-azobenzene conjugates normalized to the values of the parent fluorophore. All measurements performed under deoxygenated conditions.

After evaluation of the ongoing data and selection of best-matching pairs, we aim to investigate the impact on the triplet state quenching kinetics that is given by the length and flexibility of the linker connecting fluorophore and azobenzene. Furthermore, we aim to distribute our azobenzene stabilized fluorophores with attachment handles to leading imaging groups to get

realistic impressions of their performance benefits or drawbacks in high impact biological imaging settings. We believe that the current impressive fold-improvements are still not the limit, and we are confident that this new approach of super photostable fluorophores will increase the resolution of super resolution microscopy and single molecule localization microscopy so helping to tackle fundamental questions in biomedical research.

**Own contributions:** I designed the compounds, performed and supervised the synthesis of the azobenzene photoswitches and the azobenzene-fluorophore conjugates. I coordinated DNA oligo labeling with azobenzenes, fluorophores or azobenzene-fluorophore conjugates, which was done by Ella Biotech GmbH. I analyzed experimental data, coordinated results, and assembled data in figures. Single molecule localization- and super resolution microscopy experiments including photon budget, brightness and survival time analysis have been performed by Michael Scheckenbach and Niklas Kölbl and performed and supervised and analyzed by Viktorija Glembockyte in the lab of Philip Tinnefeld.

*This work is being prepared as a full paper in e.g. Nature Chemistry or JACS.*

## 5 Summary and Outlook

### 5.1 Summary

Azobenzene photoswitches are powerful tools in chemical biology and biomedical basic research. Within this interdisciplinary work we have developed two so far not available pathways for NIR-based (near-)quantitative  $Z \rightarrow E$  isomerization of azobenzenes that deliver intrinsic photoswitch performance properties by harnessing intramolecular mechanisms.

**In chapter 3.1** we have utilized **intramolecular energy transfer** from small-molecule organic fluorophores to azobenzene photoswitches, yielding near-quantitative  $Z \rightarrow E$  isomerization of azobenzenes. We have screened a library of azobenzene-fluorophore conjugates, including the most used azobenzene substitution patterns in photopharmacology and fluorophores that are widely used in biological imaging applications (xanthene, cyanine and oxazine core fluorophores) showing the generality of this method. Our mechanistic proposal is not fully conclusive but we show that efficient  $Z \rightarrow E$  photoswitching in the conjugate does not require a high intersystem crossing quantum yield of the isolated chromophore. Quite in contrast, photostable fluorophores with extremely low  $\phi_{ISC}$  like rhodamine B do show efficient energy transfer, which is contrary to a mechanism that is dependent on a high quantum yield for intersystem crossing of the fluorophore. Furthermore, we exclude photoredox as a mechanism, due to mismatching redox potentials. Based on our mechanistic analysis we propose exciplex formation driven by the high spin orbit coupling of azobenzenes. We characterized the conjugates by UV/Vis spectroscopy including action spectra, photoswitch kinetics and photostationary state quantification. We show for the best performing conjugates  $Z \rightarrow E$  photoswitching up to 98%  $E$  isomer at 660 nm, a wavelength where azobenzenes do not absorb. The photoswitch kinetics of intramolecular energy transfer-based  $Z \rightarrow E$  isomerization of azobenzenes are superior to direct excitation of the azobenzene. The proposed mechanism is supported by fluorescence correlation spectroscopy (FCS), femtosecond transient absorption spectroscopy (fs TAS), and fluorescence quantum yield ( $\phi_f$ ) determination.  $\phi_f$  and fs TAS showed that the singlet excited state of the fluorophores is not much affected compared to the parent fluorophore, while FCS proved that azobenzenes depopulate the triplet excited state of the fluorophore. Azobenzenes have low-lying, ultra-short lived triplet states. As soon as azobenzenes are in their triplet state they relax to a majority  $E$  isomer state (up to 99%  $E$  isomer, due to potential energy surface overlap of triplet and singlet ground state). Furthermore, we reevaluated a known hybrid PORTL system that was designed to allow the simultaneous photoinduced modulation of neuronal activity in the prefrontal cortex of mice and imaging of the modulated receptor. By that, we showed the first ever single photon NIR (up to 740 nm) photomodulation of biological activity in cell culture and acute brain slices by Cy5-triggered energy transfer. Thereby we could also investigate the linker length dependency on the efficiency of TET. Even a PEG12 linker between fluorophore and azobenzene only decreases the photoswitch rate by factor 2.

**In chapter 4.1** we extended this approach to see how far the photoresponse wavelength for energy transfer-based isomerization can be shifted. We applied the polymethine SWIR dye **NorCy7** ( $\lambda_{max} \sim 960$  nm) and conjugated it to an azobenzene. This approach allowed us to show single photon based  $Z \rightarrow E$  isomerization of azobenzenes above 1000 nm.

**In chapter 3.2** we describe singlet-manifold, **intramolecular photoredox catalysis** enabling quantitative, NIR-induced  $Z \rightarrow E$  isomerization of azobenzenes. We performed electrochemical measurements of  $\sim 30$  azobenzenes and  $\sim 10$  fluorophores/ photoredox catalysts yielding a library of oxidation and reduction potentials that allows us to predict whether photoredox is

possible. We identified the phenoxazine fluorophore nile blue as the ideal candidate to perform photoredox based isomerization with moderately electron-rich azobenzenes, due to its high excited state reduction potential (1.2 V vs Fc), the low  $\phi_{ISC}$  ( $\ll 0.03$ ; singlet manifold only) and the absorption maximum at  $\sim 635$  nm (no overlap with azobenzene absorption spectra). We synthesized the most promising conjugates **NB-AO** and **NB-AN** and showed for both quantitative  $Z \rightarrow E$  photoswitching at 635-660 nm. Our data show that if the excited state reduction potential of the fluorophore is larger than the ground state oxidation potential of the azobenzene photoredox-based isomerization is possible. We investigated the mechanism by fs TAS and  $\phi_{fl}$  determination. **NB-AO** showed a 2-fold lower  $\phi_{fl}$  compared to the parent fluorophore **NB** and the negative control **NB-AK** (which is not able to act *via* photoredox), clearly indicating that the singlet excited state is quenched. Furthermore, fs TAS of **NB-AO** showed an additional occurring absorption band in the spectral region where **NB<sup>\*</sup>** (determined by spectroelectrochemistry) is located, which strongly supports a mechanism by photoredox. Intermolecular photoredox-induced  $Z \rightarrow E$  azobenzene isomerization showed orders of magnitude slower kinetics compared to an intramolecular conjugate with a short flexible linker. As a fluorophore attached via a short-flexible linker might influence the binding properties of a photopharmaceutical, we were interested in how long a linker can be while still allowing efficient photoredox catalysis. We tested a fluorophore-azobenzene conjugate that was predicted to perform photoredox and measured PET-based photoswitch kinetics with different linker lengths ranging from PEG<sub>0</sub> to PEG<sub>24</sub>. By increasing the linker length by factor 5 the kinetic decreases by 6-fold, still allowing efficient isomerization. Based on these results, and the fact that so far, our method still relied on poorly tissue penetrating UV light for the  $E \rightarrow Z$  photoswitching direction, we were keen to test whether photoredox based isomerization is also compatible with techniques to red-shift  $E \rightarrow Z$  isomerization wavelengths, in the form of tetra-*ortho*-substitutions. We synthesized a 4,4'-bisalkoxy tetra-*ortho*-methoxy substituted azobenzene **AO(OMe)<sub>4</sub>** whose redox potential predicted suitability for photoredox-mediated isomerization by **NB** and coupled them. **NB-AO(OMe)<sub>4</sub>** shows efficient  $E \rightarrow Z$  photoisomerization at 525 nm and  $Z \rightarrow E$  at 660 nm: so being the first photostable, bidirectionally-fast-photoisomerisable, bidirectionally-visible-light-switched azobenzene. Our initial goal was to develop suitable pathways to modulate bioactivity in live cell/animal settings. Therefore, we used our known hybrid PORTL system, but exchanged its Cy5 fluorophore for **NB**, to allow for photoredox-mediated isomerization. Indeed, by applying **BANG** (benzylguanine azobenzene nile blue glutamate), we could show a switch-off of SNAP-mGluR2 activity in cell culture at 660 nm illumination, supporting proof-of-concept for NIR triggered photoredox based  $Z \rightarrow E$  isomerization of azobenzenes in biological environment.

Triplet state associated photobleaching is the major degradation pathway of fluorophores in modern imaging applications. The first intramolecular fluorophore photostabilizing strategies compatible with live cell imaging have been developed a decade ago, but until now never succeeded. These concepts rely on the small-molecule cyclooctatetraene (COT) which has an energetically low-lying triplet state with a relatively long triplet state lifetime. Azobenzenes triplet state energy is in the same range as COTs but it has  $10^7$  times shorter triplet state lifetime, enabling to quench orders of magnitude more triplet states of the fluorophore in the same time. However, azobenzenes have usually been thought to quench fluorescence of nearby fluorophores, so were almost unexplored for fluorescence *enhancement*. While studying triplet energy transfer between fluorophores and azobenzenes, we found that azobenzenes can depopulate the triplet state of organic fluorophores and so enhance their photostability, total photon output, and instantaneous brightness under high imaging intensity.



**In chapter 4.2** we show strong support that azobenzenes can thus be next-generation photostabilizing agents resulting in very photostable fluorophores for super resolution and single molecule localization microscopy. We show intermolecular photostabilisation in single molecule localization experiments and super resolution microscopy DNA-PAINT applications yielding in 5-fold better survival/tracking time, and 10-fold higher localisation rate for AbberiorStar635P in the presence of azobenzene photostabilizer. Furthermore, we are building a library of fluorophore-azobenzene-attachment handle conjugates for applications in biological imaging experiments. Currently, we are evaluating what combinations match best to give the most improved photostabilization. In one example for intramolecular stabilization, we show in single-molecule imaging experiments 10-fold higher photon budget, 3-fold higher brightness, and 3-fold longer survival time of AlexaFluor647 as its 1:1 azobenzene conjugate compared to AF647 without a stabilizer. After evaluation of all initial data, we aim to choose the best pairs with suitable attachment handles and distribute them to the world leading imaging labs to see how this method can perform in real world imaging experiments.

## 5.2 Outlook I: NIR triggered energy transfer enables $E \rightarrow Z$ photoisomerization of stilbene photoswitches for *in vivo* photopharmacology

We showed that assisted photoswitching, both based on energy transfer and based on photoredox, enable (near-)quantitative  $Z \rightarrow E$  isomerization of azobenzenes, at spectral regions where the parent azobenzene does not absorb. Furthermore, we used this powerful approach to demonstrate the first ever single photon modulation of bioactivity in the NIR in cell culture and in complex biological tissue (brain slice). Nevertheless, applying energy transfer or photoredox to trigger azobenzene  $Z \rightarrow E$  photoswitching, does not solve the problem that  $E \rightarrow Z$  isomerization still relies on poorly-penetrating UV or blue light. *In vivo* experiments in animals would therefore be restricted by e.g. fiber optics in the brains of mice for photocontrol of neuronal activity.

A system that would overcome these limitations includes (1) a photopharmaceutical that is bioinactive in the thermodynamically stable isomer; (2) activating photoisomerisation by NIR or SWIR light (biological window) to allow for illumination from outside of the animal (human) with no invasive interventions necessary; (3) fast and quantitative inactivation via thermal relaxation (as soon as the illumination stops); (4) sufficient metabolic stability for *in vivo* use.

So far, no azobenzene based photopharmaceutical is known to fulfill these criteria, so we are keen to investigate different classes of photoswitches.

The preparative organic chemistry literature holds dozens of reports for catalytic  $E \rightarrow Z$  isomerization of stilbenes by TET from small-molecule organic triplet sensitizers (intermolecular catalysis, reaction times under illumination typically 16-24 h, in presence of oxygen). Stilbenes have, compared to azobenzenes, higher triplet state energy ( $E_{T, E\text{-stilbene}} \sim 206$  kJ/mol and  $E_{T, Z\text{-stilbene}} \sim 227$  kJ/mol vs.  $E_{T, E\text{-azobenzene}} \sim 146$  kJ/mol and  $E_{T, Z\text{-azobenzene}} \sim 121$  kJ/mol).<sup>59,175</sup> Triplet energy transfer from a photosensitizer to the *E* isomer is efficient, but it is inefficient to the *Z* isomer (higher  $E_T$ ), leading to an accumulation of the *Z* isomer in a TET-SS (up to > 95% *Z* isomer).<sup>175</sup> This type of selective energy transfer catalysis for stilbene isomerization has almost never been applied in the field of photopharmacology, and convincing cellular examples are still missing<sup>176</sup>.

We hypothesize that (1) a suitable photosensitizer will enable NIR-triggered  $E \rightarrow Z$  isomerization of stilbenes that is not possible with azobenzenes; (2) a “fast”-relaxing stilbene will enable thermally  $Z \rightarrow E$  isomerization; (3) a fast-relaxing stilbene can be achieved, e.g. by pyridinium or thiazolium based stilbenes (**Figure 32b**); and (4) stilbene's metabolic stability can be made superior to that of azobenzenes.

Combining our expertise in fluorophore photoswitch conjugates, their evaluation and application in *in vivo* photopharmacology, we already performed proof-of-concept experiments investigating fluorophore-stilbene conjugates (**XX-DMS**) using rhodamine B (**RhB**) and **Cy5** fluorophores as energy donors (**Figure 31a**, synthesis and characterization in supporting chapter) and investigated their photoswitch properties.

Firstly, we tested the photoswitch properties of the stilbene **DMS** (**Figure 31b**). We started with the dark adapted all *E* isomeric state and screened 11 wavelengths ranging from 770 nm down to 365 nm for 2 min each to find where the photoresponse ( $E \rightarrow Z$  isomerization) starts. As expected **DMS** did not show any  $E \rightarrow Z$  photoswitching at wavelengths above 435 nm (**Figure 31b**, middle graph). Furthermore, we tested the thermal stability of the **DMSs** *Z* isomer, which showed no relaxation towards the *E* isomer over a timescale of 90 min at room temperature, after having been set to a *Z* enriched state by illumination with 365 nm light

(**Figure 31b**, right graph). We performed the same wavelength response screen for the stilbene fluorophore conjugates **RhB-DMS** and **Cy5-DMS**. To our satisfaction we could see a red-shifted photoresponse for both conjugates: starting at 525 nm for **RhB-DMS** and at 660 nm for **Cy5-DMS** (**Figure 31c-d**, mid graphs). As the illumination time at each wavelength was limited to 2 min per wavelength, we took both conjugates for further investigations at longer illumination experiments at the most red-shifted response wavelengths. Both conjugates showed progressive  $E \rightarrow Z$  photoswitching under continuing illumination of 525 nm and 660 nm, respectively (**Figure 31c-d**, right graph). **RhB-DMS** did not show any photochemical degradation at 525 nm illumination over 25 min, and **Cy5-DMS** did undergo some photobleaching over 20 min 660 nm illumination (decreasing  $A_{660}$  signal) but this is not surprising, due to the known limited photostability of Cy5. All measurements were performed in aqueous environment (1:1 water:acetonitrile) under oxygenated conditions. These data support the proof of hypothesis (1) that intramolecular red/NIR initiated energy transfer can trigger  $E \rightarrow Z$  photoisomerization of stilbenes at faster timescales compared to intermolecular energy transfer, reaching rates that can be useful in practical biocompatible settings (in accordance with what we saw for intra- vs intermolecular energy transfer with azobenzenes, chapter 3.1).

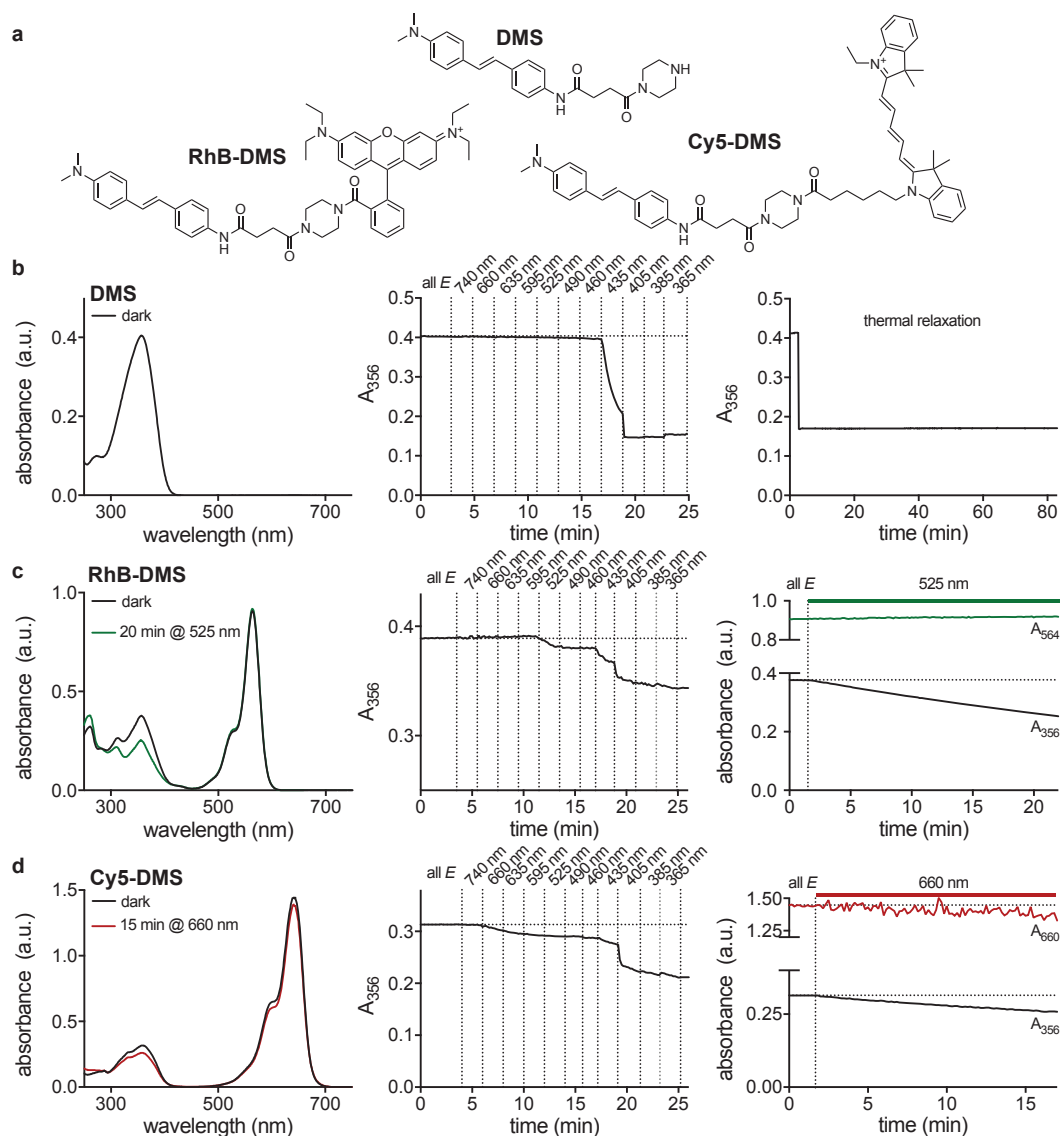


**Figure 31:** a) chemical structures of stilbene **DMS** and fluorophore stilbene conjugates **RhB-DMS** and **Cy5-DMS**; b-d) photocharacterization of **DMS** (b), **RhB-DMS** (c) and **Cy5-DMS** (d); left: UV/Vis absorption spectra; middle: evaluation of photoresponse wavelength for  $E \rightarrow Z$  isomerization; right: thermal stability of **Z-DMS** and kinetic for TET-based  $E \rightarrow Z$  isomerization of **RhB-DMS** at 525 nm and **Cy5-DMS** at 660 nm.

Nevertheless, these kinetics of assisted  $E \rightarrow Z$  switching are orders of magnitude slower than the timescale on which biology happens, or than the assisted azobenzene switching. These need to be part of further investigations, e.g. by screening for other stilbene fluorophore pairs that have better matching triplet energies, or fluorophores with higher intersystem crossing quantum yield. In contrast to azobenzene research on thermally fast-relaxing derivatives, the literature on fast relaxing stilbenes is poor, but there is one recent and promising report by Li Gao from our research group, describing methyl benzothiazolium-based heterostilbenes with  $Z \rightarrow E$  half-times in aqueous media at room temperature down to 4 min.<sup>177</sup> We expect that we can apply this behavior to enable fast thermal  $Z \rightarrow E$  relaxation at room temperature, and even faster at 37°C for *in vivo* work. To start with, we aim to try pyridinium and thiazolium based heterostilbenes (**Figure 32a**) and investigate the thermal stability of their Z isomer in cuvette.

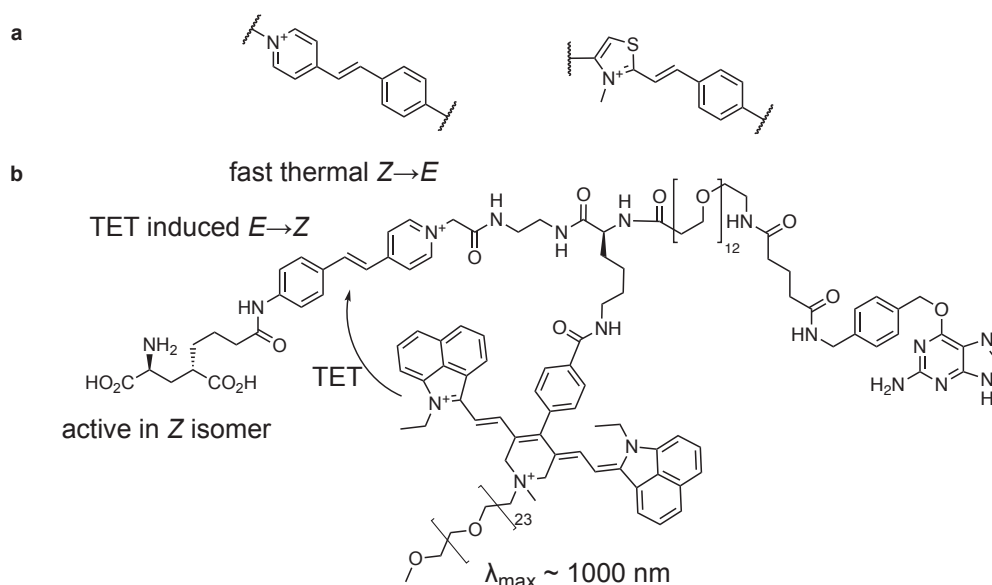


**Figure 32:** a) Chemical structures of proposed fast thermal relaxing stilbenes; b) chemical structure of a proposed 1000 nm activatable PORTL system for mGluR2 photomodulation that deactivates by fast thermal relaxation.

With satisfying pairs identified, we could then aim to apply energy transfer based  $E \rightarrow Z$  isomerization for *in vivo* NIR-triggered photomodulation of metabotropic glutamate channel activity in the prefrontal cortex of freely moving mice, with PORTL structures like those of **BGAG<sub>12,400</sub>-Cy5** and **BANG** (star compounds of chapter 3.1 and 3.2, respectively). We would keep the tethering motif (SNAPtag ligand), linker (PEG-12) and pharmacophore (glutamate), but exchange the azobenzene to a fast-relaxing stilbene, and exchange the fluorophore to a NIR/SWIR polymethine dye with absorption maximum around 1000 nm (**Figure 32b**) (e.g. **NorCy7**, that we have successfully used in chapter 4.1 to drive azobenzene  $Z \rightarrow E$  isomerization). If successful, this system would enable the first ever noninvasive photomodulation of biological activity in the brain of freely-moving mice based on illumination from outside of the body. This technique would pave the way for real *in vivo* applications of photopharmacology, enabling to solve unmet questions in biomedical basic research and bring photoswitchable drugs one step closer to the clinics.

### 5.3 Outlook II: Dual-colour photocaging for convenient red-light release of APIs

Red-shifting the photoresponse wavelength of small-molecule photocages to enable deep tissue penetration and *in vivo* applications without invasive surgical methods for light application is a very active field (see chapter 1.2.2) and has gained much attention in the last decades. Nevertheless, all progress that has been made yields light sensitive molecules that uncage (degrade) as soon as exposed to visible or NIR light. This makes precautions to exclude daylight or red-light during synthesis, purification, stock preparation/dilution and cell treatment necessary. Amber glass vials and flasks are not sufficient (because they are transparent in the yellow/red/NIR part of the spectrum), so tedious "truly dark" working conditions in the lab are required.

A convenient way to make visible/NIR photocages practicable for lab work under ambient light conditions (bench stable) would be, to do the preparation (synthesis, purification, dilutions) with a visible/NIR-inactive form, and activate it right before the cell treatment to limit the undesired uncaging to a minimum. After treatment only the cells would need to be protected from light and can conveniently be NIR-uncaged at the desired time point. A dual colour



photoinitiation pathway, as described by Hecht and coworkers in 2020 for 3D volumetric printing, might be adjusted to reach such an application in photouncaging (**Figure 33** and chapter 1.1).<sup>13</sup> Hecht and coworkers integrated benzophenone, a known photoinitiator for polymerization, into the structure of a spiropyran-merocyanine (SP-MC) photoswitch. The thermodynamically stable, closed SP isomer absorbs in the UV and is transparent in the visible/NIR spectral region, which makes it convenient to work with under ambient light conditions. As soon as illuminated with UV light it switches to the open MC form that has a broad absorption peak in the visible/NIR spectral region. Illumination with a second wavelength that hits the MC absorption peak can then initiate the polymerization by benzophenone radical mechanism.

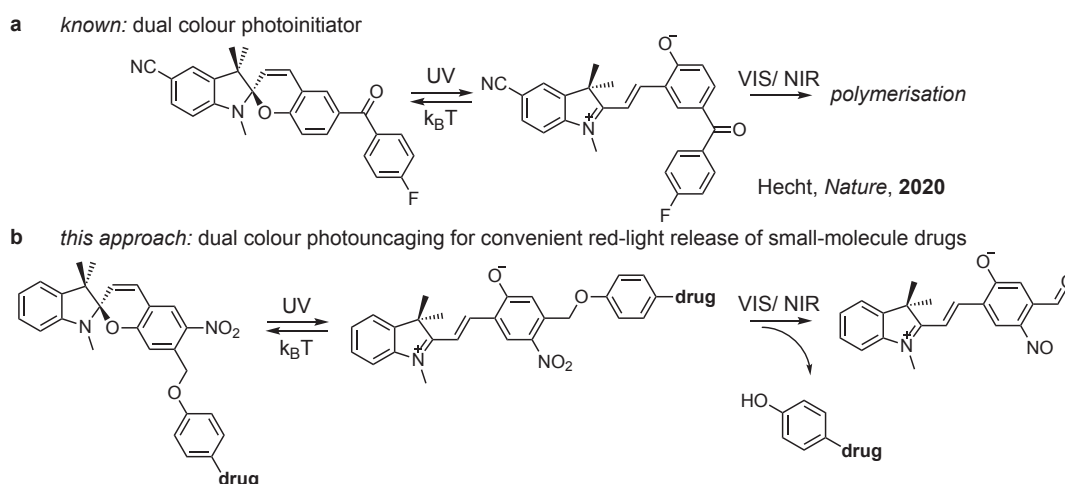


**Figure 33:** a) known system for dual colour photoinitiators consisting of SP-MC photoswitch and benzophenone photoinitiator. Photoinitiation requires activation with UV light to the open MC form before visible/NIR light can trigger polymerization<sup>13</sup>; b) proposed system for dual colour photouncaging: an ONB photocage is incorporated into a SP-MC photoswitch and enables practicable red light uncaging by initial UV activation step before cell treatment.

I propose that this strategy could be used for dual-colour-gated uncaging by incorporating an *ortho*-nitro benzyl (ONB) photocage (chapter 1.2.2) into the structure of a SP-MC photoswitch. ONBs are the most used photocages but suffer are limited by photouncaging that must happen in the UV. If successful, an SP-ONB spiro/caged small-molecule drug (**Figure 33b**) could be synthesized and prepared under ambient conditions without light protecting precautions more than amber glass vials and without unwanted uncaging/degradation. Right before cell or animal treatment the final dilution could be activated by UV light to the MC-ONB open/caged drug, which can then be uncaged to release the active drug in a cell or animal by deep tissue penetrating visible/NIR light at the desired time point (**Figure 33b**). Dual-colour activatable photocages could open new areas for deep tissue *in vivo* photouncaging in biomedical basic research.

## 6 References

- (1) Debenhofer, J.; Huber, R.; Michel, H. Die Strukturelle Grundlage Der Lichtreaktionen in Bakterien. *Nachrichten aus Chemie, Technik und Laboratorium* **1986**, *34* (5), 416–422. <https://doi.org/10.1002/nadc.19860340504>.
- (2) Boyer, P. D. The ATP Synthase - a Splendid Molecular Machine. *Annu. Rev. Biochem.* **1997**, *66* (1), 717–749. <https://doi.org/10.1146/annurev.biochem.66.1.717>.
- (3) Boyer, P. D. A Research Journey with ATP Synthase. *Journal of Biological Chemistry* **2002**, *277* (42), 39045–39061. <https://doi.org/10.1074/jbc.X200001200>.
- (4) Kassem, S.; van Leeuwen, T.; Lubbe, A. S.; Wilson, M. R.; Feringa, B. L.; Leigh, D. A. Artificial Molecular Motors. *Chem. Soc. Rev.* **2017**, *46* (9), 2592–2621. <https://doi.org/10.1039/C7CS00245A>.
- (5) Browne, W. R.; Feringa, B. L. Making Molecular Machines Work. *Nature Nanotech* **2006**, *1* (1), 25–35. <https://doi.org/10.1038/nnano.2006.45>.
- (6) Erbas-Cakmak, S.; Leigh, D. A.; McTernan, C. T.; Nussbaumer, A. L. Artificial Molecular Machines. *Chem. Rev.* **2015**, *115* (18), 10081–10206. <https://doi.org/10.1021/acs.chemrev.5b00146>.
- (7) Koumura, N.; Zijlstra, R. W. J.; van Delden, R. A.; Harada, N.; Feringa, B. L. Light-Driven Monodirectional Molecular Rotor. *Nature* **1999**, *401* (6749), 152–155. <https://doi.org/10.1038/43646>.
- (8) Kudernac, T.; Ruangsapapichat, N.; Parschau, M.; Maciá, B.; Katsonis, N.; Harutyunyan, S. R.; Ernst, K.-H.; Feringa, B. L. Electrically Driven Directional Motion of a Four-Wheeled Molecule on a Metal Surface. *Nature* **2011**, *479* (7372), 208–211. <https://doi.org/10.1038/nature10587>.
- (9) Balzani, V.; Credi, A.; Raymo, F. M.; Stoddart, J. F. Artificial Molecular Machines. *Angewandte Chemie International Edition* **2000**, *39* (19), 3348–3391. [https://doi.org/10.1002/1521-3773\(20001002\)39:19<3348::AID-ANIE3348>3.0.CO;2-X](https://doi.org/10.1002/1521-3773(20001002)39:19<3348::AID-ANIE3348>3.0.CO;2-X).
- (10) E. Mitscherlich. Ueber Das Stickstoffbenzid. *Annalen der Pharmazie* **1834**, *12* (2–3), 311–314. <https://doi.org/10.1002/jlac.18340120282>.
- (11) Hartley, G. S. The Cis-Form of Azobenzene. *Nature* **1937**, *140* (3537), 281–281. <https://doi.org/10.1038/140281a0>.
- (12) Liu, Z. F.; Hashimoto, K.; Fujishima, A. Photoelectrochemical Information Storage Using an Azobenzene Derivative. *Nature* **1990**, *347* (6294), 658–660. <https://doi.org/10.1038/347658a0>.
- (13) Regehly, M.; Garmshausen, Y.; Reuter, M.; König, N. F.; Israel, E.; Kelly, D. P.; Chou, C.-Y.; Koch, K.; Asfari, B.; Hecht, S. Xolography for Linear Volumetric 3D Printing. *Nature* **2020**, *588* (7839), 620–624. <https://doi.org/10.1038/s41586-020-3029-7>.
- (14) Borowiak, M.; Nahaboo, W.; Reynders, M.; Nekolla, K.; Jalinot, P.; Hasserodt, J.; Rehberg, M.; Delattre, M.; Zahler, S.; Vollmar, A.; Trauner, D.; Thorn-Seshold, O. Photoswitchable Inhibitors of Microtubule Dynamics Optically Control Mitosis and Cell Death. *Cell* **2015**, *162* (2), 403–411. <https://doi.org/10.1016/j.cell.2015.06.049>.
- (15) Klán, P.; Wirz, J. Molecular Photoswitches-Physicochemical Aspects of Photoswitching. In *Molecular Photoswitches-Physicochemical Aspects of Photoswitching*; Wiley, 2022. <https://doi.org/10.1002/9783527827626.fmatter>.
- (16) Meier, H. The Photochemistry of Stilbenoid Compounds and Their Role in Materials Technology. *Angewandte Chemie International Edition in English* **1992**, *31* (11), 1399–1420. <https://doi.org/10.1002/anie.199213993>.

- (17) Waldeck, D. H. Photoisomerization Dynamics of Stilbenes. *Chem. Rev.* **1991**, *91* (3), 415–436. <https://doi.org/10.1021/cr00003a007>.
- (18) Han, W.-G.; Lovell, T.; Liu, T.; Noodleman, L. Density Functional Studies of the Ground- and Excited-State Potential-Energy Curves of Stilbene Cis–Trans Isomerization. *ChemPhysChem* **2002**, *3* (2), 167–178. [https://doi.org/10.1002/1439-7641\(20020215\)3:2<167::AID-CPHC167>3.0.CO;2-G](https://doi.org/10.1002/1439-7641(20020215)3:2<167::AID-CPHC167>3.0.CO;2-G).
- (19) Gao, L.; Meiring, J. C. M.; Kraus, Y.; Wranik, M.; Weinert, T.; Pritzl, S. D.; Bingham, R.; Ntoulidou, E.; Jansen, K. I.; Olieric, N.; Standfuss, J.; Kapitein, L. C.; Lohmüller, T.; Ahlfeld, J.; Akhmanova, A.; Steinmetz, M. O.; Thorn-Seshold, O. A Robust, GFP-Orthogonal Photoswitchable Inhibitor Scaffold Extends Optical Control over the Microtubule Cytoskeleton. *Cell Chemical Biology* **2021**, *28* (2), 228–241.e6. <https://doi.org/10.1016/j.chembiol.2020.11.007>.
- (20) Wiedbrauk, S.; Dube, H. Hemithioindigo—an Emerging Photoswitch. *Tetrahedron Letters* **2015**, *56* (29), 4266–4274. <https://doi.org/10.1016/j.tetlet.2015.05.022>.
- (21) Sailer, A.; Meiring, J. C. M.; Heise, C.; Pettersson, L. N.; Akhmanova, A.; Thorn-Seshold, J.; Thorn-Seshold, O. Pyrrole Hemithioindigo Antimitotics with Near-Quantitative Bidirectional Photoswitching Photocontrol Cellular Microtubule Dynamics with Single-Cell Precision. *Angew. Chem. Int. Ed. n/a* (n/a). <https://doi.org/10.1002/anie.202104794>.
- (22) Kortekaas, L.; R. Browne, W. The Evolution of Spiropyran: Fundamentals and Progress of an Extraordinarily Versatile Photochrome. *Chemical Society Reviews* **2019**, *48* (12), 3406–3424. <https://doi.org/10.1039/C9CS00203K>.
- (23) Klajn, R. Spiropyran-Based Dynamic Materials. *Chem. Soc. Rev.* **2013**, *43* (1), 148–184. <https://doi.org/10.1039/C3CS60181A>.
- (24) Tang, Y.-Y.; Zeng, Y.-L.; Xiong, R.-G. Contactless Manipulation of Write–Read–Erase Data Storage in Diarylethene Ferroelectric Crystals. *J. Am. Chem. Soc.* **2022**, *144* (19), 8633–8640. <https://doi.org/10.1021/jacs.2c01069>.
- (25) Fleming, C. L.; Li, S.; Grøtli, M.; Andréasson, J. Shining New Light on the Spiropyran Photoswitch: A Photocage Decides between Cis–Trans or Spiro-Merocyanine Isomerization. *J. Am. Chem. Soc.* **2018**, *140* (43), 14069–14072. <https://doi.org/10.1021/jacs.8b09523>.
- (26) Goulet-Hanssens, A.; Eisenreich, F.; Hecht, S. Enlightening Materials with Photoswitches. *Advanced Materials* **2020**, *32* (20), 1905966. <https://doi.org/10.1002/adma.201905966>.
- (27) Bandara, H. M. D.; Burdette, S. C. Photoisomerization in Different Classes of Azobenzene. *Chem. Soc. Rev.* **2012**, *41* (5), 1809–1825. <https://doi.org/10.1039/C1CS15179G>.
- (28) Beharry, A. A.; Woolley, G. A. Azobenzene Photoswitches for Biomolecules. *Chem. Soc. Rev.* **2011**, *40* (8), 4422–4437. <https://doi.org/10.1039/C1CS15023E>.
- (29) Bléger, D.; Schwarz, J.; Brouwer, A. M.; Hecht, S. O -Fluoroazobenzenes as Readily Synthesized Photoswitches Offering Nearly Quantitative Two-Way Isomerization with Visible Light. *J. Am. Chem. Soc.* **2012**, *134* (51), 20597–20600. <https://doi.org/10.1021/ja310323y>.
- (30) Mourot, A.; Kienzler, M. A.; Banghart, M. R.; Fehrentz, T.; Huber, F. M. E.; Stein, M.; Kramer, R. H.; Trauner, D. Tuning Photochromic Ion Channel Blockers. *ACS Chem. Neurosci.* **2011**, *2* (9), 536–543. <https://doi.org/10.1021/cn200037p>.
- (31) Stricker, L.; Fritz, E.-C.; Peterlechner, M.; Doltsinis, N. L.; Ravoo, B. J. Arylazopyrazoles as Light-Responsive Molecular Switches in Cyclodextrin-Based

- Supramolecular Systems. *J. Am. Chem. Soc.* **2016**, *138* (13), 4547–4554. <https://doi.org/10.1021/jacs.6b00484>.
- (32) Weston, C. E.; Richardson, R. D.; Haycock, P. R.; White, A. J. P.; Fuchter, M. J. Weston\_error\_Richardson\_error\_Haycock\_error\_White\_error\_and\_Fuchter (Fuchter) 2014 *J. Am. Chem. Soc.* - Arylazopyrazoles: Azoheteroarene Photoswitches Offering Quantitative Isomerization and Long Thermal Half-Lives. *J. Am. Chem. Soc.* **2014**, *136* (34), 11878–11881. <https://doi.org/10.1021/ja505444d>.
- (33) Calbo, J.; Weston, C. E.; White, A. J. P.; Rzepa, H. S.; Contreras-García, J.; Fuchter, M. J. Tuning Azoheteroarene Photoswitch Performance through Heteroaryl Design. *J. Am. Chem. Soc.* **2017**, *139* (3), 1261–1274. <https://doi.org/10.1021/jacs.6b11626>.
- (34) Fortin, D. L.; Banghart, M. R.; Dunn, T. W.; Borges, K.; Wagenaar, D. A.; Gaudry, Q.; Karakossian, M. H.; Otis, T. S.; Kristan, W. B.; Trauner, D.; Kramer, R. H. Photochemical Control of Endogenous Ion Channels and Cellular Excitability. *Nat. Methods* **2008**, *5* (4), 331–338. <https://doi.org/10.1038/nmeth.1187>.
- (35) Reynders, M.; Matsuura, B. S.; Bérouti, M.; Simoneschi, D.; Marzio, A.; Pagano, M.; Trauner, D. PHOTACs Enable Optical Control of Protein Degradation. *Sci. Adv.* **6** (8), eaay5064. <https://doi.org/10.1126/sciadv.aay5064>.
- (36) König, K. Multiphoton Microscopy in Life Sciences. *Journal of Microscopy* **2000**, *200* (2), 83–104. <https://doi.org/10.1046/j.1365-2818.2000.00738.x>.
- (37) Hüll, K.; Morstein, J.; Trauner, D. In Vivo Photopharmacology. *Chem. Rev.* **2018**, *118* (21), 10710–10747. <https://doi.org/10.1021/acs.chemrev.8b00037>.
- (38) Szymański, W.; Beierle, J. M.; Kistemaker, H. A. V.; Velema, W. A.; Feringa, B. L. Reversible Photocontrol of Biological Systems by the Incorporation of Molecular Photoswitches. *Chem. Rev.* **2013**, *113* (8), 6114–6178. <https://doi.org/10.1021/cr300179f>.
- (39) Velema, W. A.; Szymanski, W.; Feringa, B. L. Photopharmacology: Beyond Proof of Principle. *J. Am. Chem. Soc.* **2014**, *136* (6), 2178–2191. <https://doi.org/10.1021/ja413063e>.
- (40) Fuchter, M. J. On the Promise of Photopharmacology Using Photoswitches: A Medicinal Chemist's Perspective. *J. Med. Chem.* **2020**, *63* (20), 11436–11447. <https://doi.org/10.1021/acs.jmedchem.0c00629>.
- (41) Gorostiza, P.; Volgraf, M.; Numano, R.; Szobota, S.; Trauner, D.; Isacoff, E. Y. Mechanisms of Photoswitch Conjugation and Light Activation of an Ionotropic Glutamate Receptor. *Proceedings of the National Academy of Sciences* **2007**, *104* (26), 10865–10870. <https://doi.org/10.1073/pnas.0701274104>.
- (42) Samanta, S.; Beharry, A. A.; Sadovski, O.; McCormick, T. M.; Babalhavaeji, A.; Tropepe, V.; Woolley, G. A. Photoswitching Azo Compounds in Vivo with Red Light. *J. Am. Chem. Soc.* **2013**, *135* (26), 9777–9784. <https://doi.org/10.1021/ja402220t>.
- (43) Konrad, D. B.; Frank, J. A.; Trauner, D. Synthesis of Redshifted Azobenzene Photoswitches by Late-Stage Functionalization. *Chem. Eur. J.* **2016**, *22* (13), 4364–4368. <https://doi.org/10.1002/chem.201505061>.
- (44) Müller-Deku, A.; Thorn-Seshold, O. Exhaustive Catalytic Ortho-Alkoxylation of Azobenzenes: Flexible Access to Functionally Diverse Yellow-Light-Responsive Photoswitches. *J. Org. Chem.* **2022**, *87* (24), 16526–16531. <https://doi.org/10.1021/acs.joc.2c02214>.
- (45) Konrad, D. B.; Savasci, G.; Allmendinger, L.; Trauner, D.; Ochsenfeld, C.; Ali, A. M. Computational Design and Synthesis of a Deeply Red-Shifted and Bistable Azobenzene. *J. Am. Chem. Soc.* **2020**, *142* (14), 6538–6547. <https://doi.org/10.1021/jacs.9b10430>.



- (46) Siewertsen, R.; Neumann, H.; Buchheim-Stehn, B.; Herges, R.; Näther, C.; Renth, F.; Temps, F. Highly Efficient Reversible Z–E Photoisomerization of a Bridged Azobenzene with Visible Light through Resolved S1(N $\pi^*$ ) Absorption Bands. *J. Am. Chem. Soc.* **2009**, *131* (43), 15594–15595. <https://doi.org/10.1021/ja906547d>.
- (47) Hammerich, M.; Schütt, C.; Stähler, C.; Lentens, P.; Röhricht, F.; Höppner, R.; Herges, R. Heterodiazocines: Synthesis and Photochromic Properties, Trans to Cis Switching within the Bio-Optical Window. *J. Am. Chem. Soc.* **2016**, *138* (40), 13111–13114. <https://doi.org/10.1021/jacs.6b05846>.
- (48) Maier, M. S.; Hüll, K.; Reynders, M.; Matsuura, B. S.; Leippe, P.; Ko, T.; Schäffer, L.; Trauner, D. Oxidative Approach Enables Efficient Access to Cyclic Azobenzenes. *J. Am. Chem. Soc.* **2019**, *141* (43), 17295–17304. <https://doi.org/10.1021/jacs.9b08794>.
- (49) Reynders, M.; Chaikuad, A.; Berger, B.-T.; Bauer, K.; Koch, P.; Laufer, S.; Knapp, S.; Trauner, D. Controlling the Covalent Reactivity of a Kinase Inhibitor with Light. *Angewandte Chemie International Edition* **2021**, *60* (37), 20178–20183. <https://doi.org/10.1002/anie.202103767>.
- (50) Herges, R.; Lentens, P. J. Molecular Photoswitches-4 Diazocines: Photoswitches with Excellent Photophysical Properties and Inverted Stabilities. In *Molecular Photoswitches-Physicochemical Aspects of Photoswitching*; Wiley, 2022. <https://doi.org/10.1002/9783527827626.fmatter>.
- (51) Ronayette, J.; Arnaud, R.; Lemaire, J. Isomérisation photosensibilisée par des colorants et photoréduction de l'azobenzène en solution. II. *Can. J. Chem.* **1974**, *52* (10), 1858–1867. <https://doi.org/10.1139/v74-265>.
- (52) Arnaud, R.; Lemaire, J. Isomérisation *cis* – *trans* de l'azobenzène catalysée par l'iode. III. *Can. J. Chem.* **1974**, *52* (10), 1868–1871. <https://doi.org/10.1139/v74-266>.
- (53) Shimomura, M.; Kunitake, T. Fluorescence and Photoisomerization of Azobenzene-Containing Bilayer Membranes. *J. Am. Chem. Soc.* **1987**, *109* (17), 5175–5183. <https://doi.org/10.1021/ja00251a022>.
- (54) Goulet-Hanssens, A.; Rietze, C.; Titov, E.; Abdullahu, L.; Grubert, L.; Saalfrank, P.; Hecht, S. Hole Catalysis as a General Mechanism for Efficient and Wavelength-Independent Z  $\rightarrow$  E Azobenzene Isomerization. *Chem* **2018**, *4* (7), 1740–1755. <https://doi.org/10.1016/j.chempr.2018.06.002>.
- (55) Isokuorrtti, J.; Kuntze, K.; Virkki, M.; Ahmed, Z.; Vuorimaa-Laukkanen, E.; Filatov, M. A.; Turshatov, A.; Laaksonen, T.; Priimagi, A.; Durandin, N. A. Expanding Excitation Wavelengths for Azobenzene Photoswitching into the Near-Infrared Range via Endothermic Triplet Energy Transfer. *Chem. Sci.* **2021**, *12* (21), 7504–7509. <https://doi.org/10.1039/D1SC01717A>.
- (56) Großkopf, J.; Kratz, T.; Rigotti, T.; Bach, T. Enantioselective Photochemical Reactions Enabled by Triplet Energy Transfer. *Chem. Rev.* **2022**, *122* (2), 1626–1653. <https://doi.org/10.1021/acs.chemrev.1c00272>.
- (57) Strieth-Kalthoff, F.; Glorius, F. Triplet Energy Transfer Photocatalysis: Unlocking the Next Level. *Chem* **2020**, *6* (8), 1888–1903. <https://doi.org/10.1016/j.chempr.2020.07.010>.
- (58) Bortolus, Pietro.; Monti, Sandra. Cis-Trans Photoisomerization of Azobenzene. Solvent and Triplet Donors Effects. *J. Phys. Chem.* **1979**, *83* (6), 648–652. <https://doi.org/10.1021/j100469a002>.
- (59) Monti, S.; Gardini, E.; Bortolus, P.; Amouyal, E. The Triplet State of Azobenzene. *Chem. Phys. Lett.* **1981**, *77* (1), 115–119. [https://doi.org/10.1016/0009-2614\(81\)85611-4](https://doi.org/10.1016/0009-2614(81)85611-4).



- (60) Monti, S.; Dellonte, S.; Bortolus, P. The Lowest Triplet State of Substituted Azobenzenes: An Energy Transfer Investigation. *J. Photochem.* **1983**, *23* (2), 249–256. [https://doi.org/10.1016/0047-2670\(83\)80065-3](https://doi.org/10.1016/0047-2670(83)80065-3).
- (61) Cembran, A.; Bernardi, F.; Garavelli, M.; Gagliardi, L.; Orlandi, G. On the Mechanism of the Cis–trans Isomerization in the Lowest Electronic States of Azobenzene:  $S_0$ ,  $S_1$ , and  $T_1$ . *J. Am. Chem. Soc.* **2004**, *126* (10), 3234–3243. <https://doi.org/10.1021/ja038327y>.
- (62) Holzmeister, P.; Wunsch, B.; Gietl, A.; Tinnefeld, P. Single-Molecule Photophysics of Dark Quenchers as Non-Fluorescent FRET Acceptors. *Photochem. Photobiol. Sci.* **2014**, *13* (6), 853–858. <https://doi.org/10.1039/C3PP50274K>.
- (63) Olesińska-Mönch, M.; Deo, C. Small-Molecule Photoswitches for Fluorescence Bioimaging: Engineering and Applications. *Chem. Commun.* **2023**, *59* (6), 660–669. <https://doi.org/10.1039/D2CC05870G>.
- (64) Crisalli, P.; Kool, E. T. Multi-Path Quenchers: Efficient Quenching of Common Fluorophores. *Bioconjugate Chem.* **2011**, *22* (11), 2345–2354. <https://doi.org/10.1021/bc200424r>.
- (65) Izquierdo-Serra, M.; Gascón-Moya, M.; Hirtz, J. J.; Pittolo, S.; Poskanzer, K. E.; Ferrer, È.; Alibés, R.; Busqué, F.; Yuste, R.; Hernando, J.; Gorostiza, P. Two-Photon Neuronal and Astrocytic Stimulation with Azobenzene-Based Photoswitches. *J. Am. Chem. Soc.* **2014**, *136* (24), 8693–8701. <https://doi.org/10.1021/ja5026326>.
- (66) Moreno, J.; Gerecke, M.; Grubert, L.; Kovalenko, S. A.; Hecht, S. Sensitized Two-NIR-Photon  $Z \rightarrow E$  Isomerization of a Visible-Light-Addressable Bistable Azobenzene Derivative. *Angew. Chem. Int. Ed.* **2016**, *55* (4), 1544–1547. <https://doi.org/10.1002/anie.201509111>.
- (67) Thorn-Seshold, O.; Trauner, D.; Borowiak, M.; Hasserodt, J. EP3137554 - Azoaryls as Reversibly Modulatable Tubulin Inhibitors.
- (68) Goulet-Hanssens, A.; Utecht, M.; Mutruc, D.; Titov, E.; Schwarz, J.; Grubert, L.; Bléger, D.; Saalfrank, P.; Hecht, S. Electrocatalytic  $Z \rightarrow E$  Isomerization of Azobenzenes. *J. Am. Chem. Soc.* **2017**, *139* (1), 335–341. <https://doi.org/10.1021/jacs.6b10822>.
- (69) Moreno, J.; Grubert, L.; Schwarz, J.; Bléger, D.; Hecht, S. Efficient Sensitized  $Z \rightarrow E$  Photoisomerization of an Iridium(III)-Azobenzene Complex over a Wide Concentration Range. *Chem. Eur. J.* **2017**, *23* (56), 14090–14095. <https://doi.org/10.1002/chem.201703376>.
- (70) Greenfield, J. L.; Gerkman, M. A.; Gibson, R. S. L.; Han, G. G. D.; Fuchter, M. J. Efficient Electrocatalytic Switching of Azoheteroarenes in the Condensed Phases. *J. Am. Chem. Soc.* **2021**, *143* (37), 15250–15257. <https://doi.org/10.1021/jacs.1c06359>.
- (71) Method of the Year 2010. *Nat Methods* **2011**, *8* (1), 1–1. <https://doi.org/10.1038/nmeth.f.321>.
- (72) Deisseroth, K. Optogenetics. *Nat Methods* **2011**, *8* (1), 26–29. <https://doi.org/10.1038/nmeth.f.324>.
- (73) Oesterhelt, D.; Stoekenius, W. Rhodopsin-like Protein from the Purple Membrane of Halobacterium Halobium. *Nature New Biology* **1971**, *233* (39), 149–152. <https://doi.org/10.1038/newbio233149a0>.
- (74) Mukohata, Y. Two Possible Roles of Bacteriorhodopsin; a Comparative Study of Strains of Halobacterium Halobium Differing in Pigmentation. *Biochemical and biophysical research communications* **1977**, *78* (1), 237–243.

- (75) Nagel, G.; Ollig, D.; Fuhrmann, M.; Kateriya, S.; Musti, A. M.; Bamberg, E.; Hegemann, P. Channelrhodopsin-1: A Light-Gated Proton Channel in Green Algae. *Science* **2002**, 296 (5577), 2395–2398. <https://doi.org/10.1126/science.1072068>.
- (76) Engelhard, C.; Chizhov, I.; Siebert, F.; Engelhard, M. Microbial Halorhodopsins: Light-Driven Chloride Pumps. *Chem. Rev.* **2018**, 118 (21), 10629–10645. <https://doi.org/10.1021/acs.chemrev.7b00715>.
- (77) Boyden, E. S.; Zhang, F.; Bamberg, E.; Nagel, G.; Deisseroth, K. Millisecond-Timescale, Genetically Targeted Optical Control of Neural Activity. *Nat Neurosci* **2005**, 8 (9), 1263–1268. <https://doi.org/10.1038/nn1525>.
- (78) Nagel, G.; Brauner, M.; Liewald, J. F.; Adeishvili, N.; Bamberg, E.; Gottschalk, A. Light Activation of Channelrhodopsin-2 in Excitable Cells of *Caenorhabditis Elegans* Triggers Rapid Behavioral Responses. *Current Biology* **2005**, 15 (24), 2279–2284. <https://doi.org/10.1016/j.cub.2005.11.032>.
- (79) Wietek, J.; Wiegert, J. S.; Adeishvili, N.; Schneider, F.; Watanabe, H.; Tsunoda, S. P.; Vogt, A.; Elstner, M.; Oertner, T. G.; Hegemann, P. Conversion of Channelrhodopsin into a Light-Gated Chloride Channel. *Science* **2014**, 344 (6182), 409–412. <https://doi.org/10.1126/science.1249375>.
- (80) Christie, J. M.; Reymond, P.; Powell, G. K.; Bernasconi, P.; Raibekas, A. A.; Liscum, E.; Briggs, W. R. Arabidopsis NPH1: A Flavoprotein with the Properties of a Photoreceptor for Phototropism. *Science* **1998**, 282 (5394), 1698–1701. <https://doi.org/10.1126/science.282.5394.1698>.
- (81) Möglich, A.; Yang, X.; Ayers, R. A.; Moffat, K. Structure and Function of Plant Photoreceptors. *Annu. Rev. Plant Biol.* **2010**, 61 (1), 21–47. <https://doi.org/10.1146/annurev-arplant-042809-112259>.
- (82) Losi, A.; Gardner, K. H.; Möglich, A. Blue-Light Receptors for Optogenetics. *Chem. Rev.* **2018**, 118 (21), 10659–10709. <https://doi.org/10.1021/acs.chemrev.8b00163>.
- (83) Jia, S.; Sletten, E. M. Spatiotemporal Control of Biology: Synthetic Photochemistry Toolbox with Far-Red and Near-Infrared Light. *ACS Chem. Biol.* **2022**, 17 (12), 3255–3269. <https://doi.org/10.1021/acscchembio.1c00518>.
- (84) Young, D. D.; Deiters, A. Photochemical Control of Biological Processes. *Org. Biomol. Chem.* **2007**, 5 (7), 999–1005. <https://doi.org/10.1039/B616410M>.
- (85) Bojtár, M.; Kormos, A.; Kis-Petik, K.; Kellermayer, M.; Kele, P. Green-Light Activatable, Water-Soluble Red-Shifted Coumarin Photocages. *Org. Lett.* **2019**, 21 (23), 9410–9414. <https://doi.org/10.1021/acs.orglett.9b03624>.
- (86) Umeda, N.; Takahashi, H.; Kamiya, M.; Ueno, T.; Komatsu, T.; Terai, T.; Hanaoka, K.; Nagano, T.; Urano, Y. Boron Dipyrromethene as a Fluorescent Caging Group for Single-Photon Uncaging with Long-Wavelength Visible Light. *ACS Chem. Biol.* **2014**, 9 (10), 2242–2246. <https://doi.org/10.1021/cb500525p>.
- (87) Egyed, A.; Németh, K.; Molnár, T. Á.; Kállay, M.; Kele, P.; Bojtár, M. Turning Red without Feeling Embarrassed—Xanthinium-Based Photocages for Red-Light-Activated Phototherapeutics. *J. Am. Chem. Soc.* **2023**, 145 (7), 4026–4034. <https://doi.org/10.1021/jacs.2c11499>.
- (88) Gorka, A. P.; Nani, R. R.; Zhu, J.; Mackem, S.; Schnermann, M. J. A Near-IR Uncaging Strategy Based on Cyanine Photochemistry. *J. Am. Chem. Soc.* **2014**, 136 (40), 14153–14159. <https://doi.org/10.1021/ja5065203>.
- (89) Alachouzos, G.; Schulte, A. M.; Mondal, A.; Szymanski, W.; Feringa, B. L. Computational Design, Synthesis, and Photochemistry of Cy7-PPG, an Efficient NIR-Activated Photolabile Protecting Group for Therapeutic Applications\*\*. *Angewandte*

- (90) Janeková, H.; Russo, M.; Ziegler, U.; Štacko, P. Photocaging of Carboxylic Acids from Cyanine Dyes with Near-Infrared Light\*\*. *Angewandte Chemie* **2022**, 134 (33), e202204391. <https://doi.org/10.1002/ange.202204391>.
- (91) Bandi, V. G.; Luciano, M. P.; Saccomano, M.; Patel, N. L.; Bischof, T. S.; Lingg, J. G. P.; Tsrunchev, P. T.; Nix, M. N.; Ruehle, B.; Sanders, C.; Riffle, L.; Robinson, C. M.; Difilippantonio, S.; Kalen, J. D.; Resch-Genger, U.; Ivanic, J.; Bruns, O. T.; Schnermann, M. J. Targeted Multicolor in Vivo Imaging over 1,000 Nm Enabled by Nonamethine Cyanines. *Nat Methods* **2022**, 19 (3), 353–358. <https://doi.org/10.1038/s41592-022-01394-6>.
- (92) Cosco, E. D.; Spearman, A. L.; Ramakrishnan, S.; Lingg, J. G. P.; Saccomano, M.; Pengshung, M.; Arús, B. A.; Wong, K. C. Y.; Glasl, S.; Ntziachristos, V.; Warmer, M.; McLaughlin, R. R.; Bruns, O. T.; Sletten, E. M. Shortwave Infrared Polymethine Fluorophores Matched to Excitation Lasers Enable Non-Invasive, Multicolour in Vivo Imaging in Real Time. *Nat. Chem.* **2020**, 12 (12), 1123–1130. <https://doi.org/10.1038/s41557-020-00554-5>.
- (93) Karginov, A. V.; Zou, Y.; Shirvanyants, D.; Kota, P.; Dokholyan, N. V.; Young, D. D.; Hahn, K. M.; Deiters, A. Light Regulation of Protein Dimerization and Kinase Activity in Living Cells Using Photocaged Rapamycin and Engineered FKBP. *J. Am. Chem. Soc.* **2011**, 133 (3), 420–423. <https://doi.org/10.1021/ja109630v>.
- (94) Velema, W. A.; van der Berg, J. P.; Szymanski, W.; Driessen, A. J. M.; Feringa, B. L. Orthogonal Control of Antibacterial Activity with Light. *ACS Chem. Biol.* **2014**, 9 (9), 1969–1974. <https://doi.org/10.1021/cb500313f>.
- (95) Banala, S.; Maurel, D.; Manley, S.; Johnsson, K. A Caged, Localizable Rhodamine Derivative for Superresolution Microscopy. *ACS Chem. Biol.* **2012**, 7 (2), 289–293. <https://doi.org/10.1021/cb2002889>.
- (96) Lämmle, C. A.; Varady, A.; Müller, T. G.; Sturtzel, C.; Riepl, M.; Mathes, B.; Eichhorst, J.; Sporbert, A.; Lehmann, M.; Kräusslich, H.-G.; Distel, M.; Broichhagen, J. Photocaged Hoechst Enables Subnuclear Visualization and Cell Selective Staining of DNA in Vivo. *ChemBioChem* **2021**, 22 (3), 548–556. <https://doi.org/10.1002/cbic.202000465>.
- (97) Gautier, A.; Deiters, A.; Chin, J. W. Light-Activated Kinases Enable Temporal Dissection of Signaling Networks in Living Cells. *J. Am. Chem. Soc.* **2011**, 133 (7), 2124–2127. <https://doi.org/10.1021/ja1109979>.
- (98) Klöcker, N.; Weissenboeck, F. P.; van Dülmen, M.; Špaček, P.; Hüwel, S.; Rentmeister, A. Photocaged 5' Cap Analogues for Optical Control of mRNA Translation in Cells. *Nat. Chem.* **2022**, 14 (8), 905–913. <https://doi.org/10.1038/s41557-022-00972-7>.
- (99) Hüll, K.; Benster, T.; Manookin, M. B.; Trauner, D.; Van Gelder, R. N.; Laprell, L. Photopharmacologic Vision Restoration Reduces Pathological Rhythmic Field Potentials in Blind Mouse Retina. *Scientific Reports* **2019**, 9 (1), 1–12. <https://doi.org/10.1038/s41598-019-49999-w>.
- (100) Zenker, J.; White, M. D.; Templin, R. M.; Parton, R. G.; Thorn-Seshold, O.; Bissiere, S.; Plachta, N. A Microtubule-Organizing Center Directing Intracellular Transport in the Early Mouse Embryo. *Science* **2017**, 357 (6354), 925–928. <https://doi.org/10.1126/science.aam9335>.
- (101) Müller-Deku, A.; Meiring, J. C. M.; Loy, K.; Kraus, Y.; Heise, C.; Bingham, R.; Jansen, K. I.; Qu, X.; Bartolini, F.; Kapitein, L. C.; Akhmanova, A.; Ahlfeld, J.; Trauner, D.; Thorn-Seshold, O. Photoswitchable Paclitaxel-Based Microtubule Stabilisers Allow Optical

- Control over the Microtubule Cytoskeleton. *Nat Commun* **2020**, *11* (1), 4640. <https://doi.org/10.1038/s41467-020-18389-6>.
- (102) Borowiak, M.; Küllmer, F.; Gegenfurtner, F.; Peil, S.; Nasufović, V.; Zahler, S.; Thorn-Seshold, O.; Trauner, D.; Arndt, H.-D. Optical Manipulation of F-Actin with Photoswitchable Small Molecules. *J. Am. Chem. Soc.* **2020**, *142* (20), 9240–9249. <https://doi.org/10.1021/jacs.9b12898>.
- (103) Küllmer, F.; Vepřek, N. A.; Borowiak, M.; Nasufović, V.; Barutzki, S.; Thorn-Seshold, O.; Arndt, H.-D.; Trauner, D. Next Generation Opto-Jasplakinolides Enable Local Remodeling of Actin Networks. *Angew. Chem. Int. Ed. n/a* (n/a). <https://doi.org/10.1002/anie.202210220>.
- (104) Broichhagen, J.; Damijonaitis, A.; Levitz, J.; Sokol, K. R.; Leippe, P.; Konrad, D.; Isacoff, E. Y.; Trauner, D. Orthogonal Optical Control of a G Protein-Coupled Receptor with a SNAP-Tethered Photochromic Ligand. *ACS Cent Sci* **2015**, *1* (7), 383–393. <https://doi.org/10.1021/acscentsci.5b00260>.
- (105) Tsai, Y.-H.; Essig, S.; James, J. R.; Lang, K.; Chin, J. W. Selective, Rapid and Optically Switchable Regulation of Protein Function in Live Mammalian Cells. *Nat. Chem* **2015**, *7* (7), 554–561. <https://doi.org/10.1038/nchem.2253>.
- (106) Banghart, M.; Borges, K.; Isacoff, E.; Trauner, D.; Kramer, R. H. Light-Activated Ion Channels for Remote Control of Neuronal Firing. *Nat Neurosci* **2004**, *7* (12), 1381–1386. <https://doi.org/10.1038/nn1356>.
- (107) Leippe, P.; Koehler Leman, J.; Trauner, D. Specificity and Speed: Tethered Photopharmacology. *Biochemistry* **2017**, *56* (39), 5214–5220. <https://doi.org/10.1021/acs.biochem.7b00687>.
- (108) Müller, M.; Niemeyer, K.; Urban, N.; Ojha, N. K.; Zufall, F.; Leinders-Zufall, T.; Schaefer, M.; Thorn-Seshold, O. BTDAzo: A Photoswitchable TRPC5 Channel Activator\*\*. *Angew. Chem. Int. Ed.* **2022**, *61* (36), e202201565. <https://doi.org/10.1002/anie.202201565>.
- (109) Frank, J. A.; Moroni, M.; Moshourab, R.; Sumser, M.; Lewin, G. R.; Trauner, D. Photoswitchable Fatty Acids Enable Optical Control of TRPV1. *Nat Commun* **2015**, *6* (1), 7118. <https://doi.org/10.1038/ncomms8118>.
- (110) Lam, P.-Y.; Thawani, A. R.; Balderas, E.; White, A. J. P.; Chaudhuri, D.; Fuchter, M. J.; Peterson, R. T. TRPswitch—A Step-Function Chemo-Optogenetic Ligand for the Vertebrate TRPA1 Channel. *J. Am. Chem. Soc.* **2020**, *142* (41), 17457–17468. <https://doi.org/10.1021/jacs.0c06811>.
- (111) Gutzeit, V. A.; Acosta-Ruiz, A.; Munguba, H.; Häfner, S.; Landra-Willm, A.; Mathes, B.; Mony, J.; Yarotski, D.; Börjesson, K.; Liston, C.; Sandoz, G.; Levitz, J.; Broichhagen, J. A Fine-Tuned Azobenzene for Enhanced Photopharmacology in Vivo. *Cell Chem. Biol.* **2021**, *28* (11), 1648–1663. <https://doi.org/10.1016/j.chembiol.2021.02.020>.
- (112) Donthamsetti, P. C.; Broichhagen, J.; Vyklicky, V.; Stanley, C.; Fu, Z.; Visel, M.; Levitz, J. L.; Javitch, J. A.; Trauner, D.; Isacoff, E. Y. Genetically Targeted Optical Control of an Endogenous G Protein-Coupled Receptor. *J. Am. Chem. Soc.* **2019**, *141* (29), 11522–11530. <https://doi.org/10.1021/jacs.9b02895>.
- (113) Levitz, J.; Broichhagen, J.; Leippe, P.; Konrad, D.; Trauner, D.; Isacoff, E. Y. Dual Optical Control and Mechanistic Insights into Photoswitchable Group II and III Metabotropic Glutamate Receptors. *Proc. Natl. Acad. Sci. U.S.A.* **2017**, *114* (17), E3546–E3554. <https://doi.org/10.1073/pnas.1619652114>.
- (114) Tochitsky, I.; Kienzler, M. A.; Isacoff, E.; Kramer, R. H. Restoring Vision to the Blind with Chemical Photoswitches. *Chem. Rev.* **2018**, *118* (21), 10748–10773. <https://doi.org/10.1021/acs.chemrev.7b00723>.



- (115) Van Gelder, R. N. Photochemical Approaches to Vision Restoration. *Vision Research* **2015**, *111*, 134–141. <https://doi.org/10.1016/j.visres.2015.02.001>.
- (116) Molecular Photoswitches - Chemistry, Properties and Applications. In *Molecular Photoswitches - Chemistry, Properties and Applications*; Wiley, 2022. <https://doi.org/10.1002/9783527827626.fmatter>.
- (117) Broichhagen, J.; Frank, J. A.; Trauner, D. A Roadmap to Success in Photopharmacology. *Acc. Chem. Res.* **2015**, *48* (7), 1947–1960. <https://doi.org/10.1021/acs.accounts.5b00129>.
- (118) Burslem, G. M.; Crews, C. M. Small-Molecule Modulation of Protein Homeostasis. *Chem. Rev.* **2017**, *117* (17), 11269–11301. <https://doi.org/10.1021/acs.chemrev.7b00077>.
- (119) Pfaff, P.; Samarasinghe, K. T. G.; Crews, C. M.; Carreira, E. M. Reversible Spatiotemporal Control of Induced Protein Degradation by Bistable PhotoPROTACs. *ACS Cent. Sci.* **2019**, *5* (10), 1682–1690. <https://doi.org/10.1021/acscentsci.9b00713>.
- (120) Jin, Y.-H.; Lu, M.-C.; Wang, Y.; Shan, W.-X.; Wang, X.-Y.; You, Q.-D.; Jiang, Z.-Y. Azo-PROTAC: Novel Light-Controlled Small-Molecule Tool for Protein Knockdown. *J. Med. Chem.* **2020**, *63* (9), 4644–4654. <https://doi.org/10.1021/acs.jmedchem.9b02058>.
- (121) Reynders, M.; Trauner, D. Optical Control of Targeted Protein Degradation. *Cell Chemical Biology* **2021**, *28* (7), 969–986. <https://doi.org/10.1016/j.chembiol.2021.05.010>.
- (122) Keppler, A.; Gendreizig, S.; Gronemeyer, T.; Pick, H.; Vogel, H.; Johnsson, K. A General Method for the Covalent Labeling of Fusion Proteins with Small Molecules in Vivo. *Nat Biotechnol* **2003**, *21* (1), 86–89. <https://doi.org/10.1038/nbt765>.
- (123) Gautier, A.; Juillerat, A.; Heinis, C.; Corrêa, I. R.; Kindermann, M.; Beaufile, F.; Johnsson, K. An Engineered Protein Tag for Multiprotein Labeling in Living Cells. *Chemistry & Biology* **2008**, *15* (2), 128–136. <https://doi.org/10.1016/j.chembiol.2008.01.007>.
- (124) Los, G. V.; Encell, L. P.; McDougall, M. G.; Hartzell, D. D.; Karassina, N.; Zimprich, C.; Wood, M. G.; Learish, R.; Ohana, R. F.; Urh, M.; Simpson, D.; Mendez, J.; Zimmerman, K.; Otto, P.; Vidugiris, G.; Zhu, J.; Darzins, A.; Klauert, D. H.; Bulleit, R. F.; Wood, K. V. HaloTag: A Novel Protein Labeling Technology for Cell Imaging and Protein Analysis. *ACS Chem. Biol.* **2008**, *3* (6), 373–382. <https://doi.org/10.1021/cb800025k>.
- (125) Broichhagen, J.; Trauner, D. The in Vivo Chemistry of Photoswitched Tethered Ligands. *Current Opinion in Chemical Biology* **2014**, *21*, 121–127. <https://doi.org/10.1016/j.cbpa.2014.07.008>.
- (126) Broichhagen, J.; Levitz, J. Advances in Tethered Photopharmacology for Precise Optical Control of Signaling Proteins. *Current Opinion in Pharmacology* **2022**, *63*, 102196. <https://doi.org/10.1016/j.coph.2022.102196>.
- (127) Sriram, K.; Insel, P. A. G Protein-Coupled Receptors as Targets for Approved Drugs: How Many Targets and How Many Drugs? *Mol Pharmacol* **2018**, *93* (4), 251–258. <https://doi.org/10.1124/mol.117.111062>.
- (128) Acosta-Ruiz, A.; Broichhagen, J.; Levitz, J. Optical Regulation of Class C GPCRs by Photoswitchable Orthogonal Remotely Tethered Ligands. *Methods Mol Biol* **2019**, *1947*, 103–136. [https://doi.org/10.1007/978-1-4939-9121-1\\_6](https://doi.org/10.1007/978-1-4939-9121-1_6).
- (129) Acosta-Ruiz, A.; Gutzeit, V. A.; Skelly, M. J.; Meadows, S.; Lee, J.; Parekh, P.; Orr, A. G.; Liston, C.; Pleil, K. E.; Broichhagen, J.; Levitz, J. Branched Photoswitchable Tethered Ligands Enable Ultra-Efficient Optical Control and Detection of G Protein-Coupled Receptors In Vivo. *Neuron* **2020**, *105* (3), 446–463.e13. <https://doi.org/10.1016/j.neuron.2019.10.036>.



- (130) Farrants, H.; Gutzeit, V. A.; Acosta-Ruiz, A.; Trauner, D.; Johnsson, K.; Levitz, J.; Broichhagen, J. SNAP-Tagged Nanobodies Enable Reversible Optical Control of a G Protein-Coupled Receptor via a Remotely Tethered Photoswitchable Ligand. *ACS Chem. Biol.* **2018**, *13* (9), 2682–2688. <https://doi.org/10.1021/acscchembio.8b00628>.
- (131) Gao, L.; Meiring, J. C. M.; Varady, A.; Ruider, I. E.; Heise, C.; Wranik, M.; Velasco, C. D.; Taylor, J. A.; Terni, B.; Weinert, T.; Standfuss, J.; Cabernard, C. C.; Llobet, A.; Steinmetz, M. O.; Bausch, A. R.; Distel, M.; Thorn-Seshold, J.; Akhmanova, A.; Thorn-Seshold, O. In Vivo Photocontrol of Microtubule Dynamics and Integrity, Migration and Mitosis, by the Potent GFP-Imaging-Compatible Photoswitchable Reagents SBTubA4P and SBTub2M. *J. Am. Chem. Soc.* **2022**, *144* (12), 5614–5628. <https://doi.org/10.1021/jacs.2c01020>.
- (132) Gao, L.; Meiring, J. C. M.; Heise, C.; Rai, A.; Müller-Deku, A.; Akhmanova, A.; Thorn-Seshold, J.; Thorn-Seshold, O. Photoswitchable Epothilone-Based Microtubule Stabilisers Allow GFP-Imaging-Compatible, Optical Control over the Microtubule Cytoskeleton\*\*. *Angewandte Chemie International Edition* **2022**, *61* (10), e202114614. <https://doi.org/10.1002/anie.202114614>.
- (133) Sailer, A.; Ermer, F.; Kraus, Y.; Lutter, F. H.; Donau, C.; Bremerich, M.; Ahlfeld, J.; Thorn-Seshold, O. Hemithioindigos for Cellular Photopharmacology: Desymmetrised Molecular Switch Scaffolds Enabling Design Control over the Isomer-Dependency of Potent Antimitotic Bioactivity. *ChemBioChem* **2019**, *20* (10), 1305–1314. <https://doi.org/10.1002/cbic.201800752>.
- (134) Sailer, A.; Ermer, F.; Kraus, Y.; Bingham, R.; Lutter, F. H.; Ahlfeld, J.; Thorn-Seshold, O. Potent Hemithioindigo-Based Antimitotics Photocontrol the Microtubule Cytoskeleton in Cellulo. *Beilstein J. Org. Chem.* **2020**, *16* (1), 125–134. <https://doi.org/10.3762/bjoc.16.14>.
- (135) Zeisel, L.; Felber, J. G.; Scholzen, K. C.; Poczka, L.; Cheff, D.; Maier, M. S.; Cheng, Q.; Shen, M.; Hall, M. D.; Arnér, E. S. J.; Thorn-Seshold, J.; Thorn-Seshold, O. Selective Cellular Probes for Mammalian Thioredoxin Reductase TrxR1: Rational Design of RX1, a Modular 1,2-Thiaselenane Redox Probe. *Chem* **2022**, *8* (5), 1493–1517. <https://doi.org/10.1016/j.chempr.2022.03.010>.
- (136) Lichtman, J. W.; Conchello, J.-A. Fluorescence Microscopy. *Nat Methods* **2005**, *2* (12), 910–919. <https://doi.org/10.1038/nmeth817>.
- (137) Weber, M.; Leutenegger, M.; Stoldt, S.; Jakobs, S.; Mihaila, T. S.; Butkevich, A. N.; Hell, S. W. MINSTED Fluorescence Localization and Nanoscopy. *Nat. Photonics* **2021**, *15* (5), 361–366. <https://doi.org/10.1038/s41566-021-00774-2>.
- (138) Schneider, J.; Zahn, J.; Maglione, M.; Sigrist, S. J.; Marquard, J.; Chojnacki, J.; Kräusslich, H.-G.; Sahl, S. J.; Engelhardt, J.; Hell, S. W. Ultrafast, Temporally Stochastic STED Nanoscopy of Millisecond Dynamics. *Nat Methods* **2015**, *12* (9), 827–830. <https://doi.org/10.1038/nmeth.3481>.
- (139) Coltharp, C.; Kessler, R. P.; Xiao, J. Accurate Construction of Photoactivated Localization Microscopy (PALM) Images for Quantitative Measurements. *PLOS ONE* **2012**, *7* (12), e51725. <https://doi.org/10.1371/journal.pone.0051725>.
- (140) Beyond the Diffraction Limit. *Nature Photon* **2009**, *3* (7), 361–361. <https://doi.org/10.1038/nphoton.2009.100>.
- (141) Fernández-Suárez, M.; Ting, A. Y. Fluorescent Probes for Super-Resolution Imaging in Living Cells. *Nat Rev Mol Cell Biol* **2008**, *9* (12), 929–943. <https://doi.org/10.1038/nrm2531>.

- (142) Hell, S. W.; Wichmann, J. Breaking the Diffraction Resolution Limit by Stimulated Emission: Stimulated-Emission-Depletion Fluorescence Microscopy. *Opt. Lett., OL* **1994**, *19* (11), 780–782. <https://doi.org/10.1364/OL.19.000780>.
- (143) Vicidomini, G.; Bianchini, P.; Diaspro, A. STED Super-Resolved Microscopy. *Nat Methods* **2018**, *15* (3), 173–182. <https://doi.org/10.1038/nmeth.4593>.
- (144) Lelek, M.; Gyparaki, M. T.; Beliu, G.; Schueder, F.; Griffié, J.; Manley, S.; Jungmann, R.; Sauer, M.; Lakadamyali, M.; Zimmer, C. Single-Molecule Localization Microscopy. *Nat Rev Methods Primers* **2021**, *1* (1), 1–27. <https://doi.org/10.1038/s43586-021-00038-x>.
- (145) Schnitzbauer, J.; Strauss, M. T.; Schlichthaerle, T.; Schueder, F.; Jungmann, R. Super-Resolution Microscopy with DNA-PAINT. *Nat Protoc* **2017**, *12* (6), 1198–1228. <https://doi.org/10.1038/nprot.2017.024>.
- (146) Betzig, E.; Patterson, G. H.; Sougrat, R.; Lindwasser, O. W.; Olenych, S.; Bonifacino, J. S.; Davidson, M. W.; Lippincott-Schwartz, J.; Hess, H. F. Imaging Intracellular Fluorescent Proteins at Nanometer Resolution. *Science* **2006**, *313* (5793), 1642–1645. <https://doi.org/10.1126/science.1127344>.
- (147) Rust, M. J.; Bates, M.; Zhuang, X. Sub-Diffraction-Limit Imaging by Stochastic Optical Reconstruction Microscopy (STORM). *Nat Methods* **2006**, *3* (10), 793–796. <https://doi.org/10.1038/nmeth929>.
- (148) Jungmann, R.; Steinhauer, C.; Scheible, M.; Kuzyk, A.; Tinnefeld, P.; Simmel, F. C. Single-Molecule Kinetics and Super-Resolution Microscopy by Fluorescence Imaging of Transient Binding on DNA Origami. *Nano Lett.* **2010**, *10* (11), 4756–4761. <https://doi.org/10.1021/nl103427w>.
- (149) Galbraith, C. G.; Galbraith, J. A. Super-Resolution Microscopy at a Glance. *Journal of Cell Science* **2011**, *124* (10), 1607–1611. <https://doi.org/10.1242/jcs.080085>.
- (150) Isselstein, M.; Zhang, L.; Glembockyte, V.; Brix, O.; Cosa, G.; Tinnefeld, P.; Cordes, T. Self-Healing Dyes—Keeping the Promise? *J. Phys. Chem. Lett.* **2020**, *11* (11), 4462–4480. <https://doi.org/10.1021/acs.jpcllett.9b03833>.
- (151) Kasper, R.; Harke, B.; Forthmann, C.; Tinnefeld, P.; Hell, S. W.; Sauer, M. Single-Molecule STED Microscopy with Photostable Organic Fluorophores. *Small* **2010**, *6* (13), 1379–1384. <https://doi.org/10.1002/smll.201000203>.
- (152) Ha, T.; Tinnefeld, P. Photophysics of Fluorescent Probes for Single-Molecule Biophysics and Super-Resolution Imaging. *Annual Review of Physical Chemistry* **2012**, *63* (1), 595–617. <https://doi.org/10.1146/annurev-physchem-032210-103340>.
- (153) Grimm, J. B.; English, B. P.; Choi, H.; Muthusamy, A. K.; Mehl, B. P.; Dong, P.; Brown, T. A.; Lippincott-Schwartz, J.; Liu, Z.; Lionnet, T.; Lavis, L. D. Bright Photoactivatable Fluorophores for Single-Molecule Imaging. *Nat Methods* **2016**, *13* (12), 985–988. <https://doi.org/10.1038/nmeth.4034>.
- (154) Grimm, J. B.; English, B. P.; Chen, J.; Slaughter, J. P.; Zhang, Z.; Revyakin, A.; Patel, R.; Macklin, J. J.; Normanno, D.; Singer, R. H.; Lionnet, T.; Lavis, L. D. A General Method to Improve Fluorophores for Live-Cell and Single-Molecule Microscopy. *Nat Methods* **2015**, *12* (3), 244–250. <https://doi.org/10.1038/nmeth.3256>.
- (155) Eiring, P.; McLaughlin, R.; Matikonda, S. S.; Han, Z.; Grabenhorst, L.; Helmerich, D. A.; Meub, M.; Beliu, G.; Luciano, M.; Bandi, V.; Zijlstra, N.; Shi, Z.-D.; Tarasov, S. G.; Swenson, R.; Tinnefeld, P.; Glembockyte, V.; Cordes, T.; Sauer, M.; Schnermann, M. J. Targetable Conformationally Restricted Cyanines Enable Photon-Count-Limited Applications\*\*. *Angewandte Chemie* **2021**, *133* (51), 26889–26897. <https://doi.org/10.1002/ange.202109749>.

- (156) Roßmann, K.; Akkaya, K. C.; Poc, P.; Charbonnier, C.; Eichhorst, J.; Gonschior, H.; Valavalkar, A.; Wendler, N.; Cordes, T.; Dietzek-Ivanšić, B.; Jones, B.; Lehmann, M.; Broichhagen, J. N-Methyl Deuterated Rhodamines for Protein Labelling in Sensitive Fluorescence Microscopy. *Chem. Sci.* **2022**, *13* (29), 8605–8617. <https://doi.org/10.1039/D1SC06466E>.
- (157) Grimm, J. B.; Xie, L.; Casler, J. C.; Patel, R.; Tkachuk, A. N.; Falco, N.; Choi, H.; Lippincott-Schwartz, J.; Brown, T. A.; Glick, B. S.; Liu, Z.; Lavis, L. D. A General Method to Improve Fluorophores Using Deuterated Auxochromes. *JACS Au* **2021**, *1* (5), 690–696. <https://doi.org/10.1021/jacsau.1c00006>.
- (158) Yanagida, T.; Nakase, M.; Nishiyama, K.; Oosawa, F. Direct Observation of Motion of Single F-Actin Filaments in the Presence of Myosin. *Nature* **1984**, *307* (5946), 58–60. <https://doi.org/10.1038/307058a0>.
- (159) Cordes, T.; Vogelsang, J.; Tinnefeld, P. On the Mechanism of Trolox as Antiblinking and Antibleaching Reagent. *J. Am. Chem. Soc.* **2009**, *131* (14), 5018–5019. <https://doi.org/10.1021/ja809117z>.
- (160) Dave, R.; Terry, D. S.; Munro, J. B.; Blanchard, S. C. Mitigating Unwanted Photophysical Processes for Improved Single-Molecule Fluorescence Imaging. *Biophysical Journal* **2009**, *96* (6), 2371–2381. <https://doi.org/10.1016/j.bpj.2008.11.061>.
- (161) Vogelsang, J.; Kasper, R.; Steinhauer, C.; Person, B.; Heilemann, M.; Sauer, M.; Tinnefeld, P. A Reducing and Oxidizing System Minimizes Photobleaching and Blinking of Fluorescent Dyes. *Angew. Chem. Int. Ed.* **2008**, *47* (29), 5465–5469. <https://doi.org/10.1002/anie.200801518>.
- (162) Liphardt, B.; Liphardt, B.; Lüttke, W. Laser Dyes III: Concepts to Increase the Photostability of Laser Dyes. *Optics Communications* **1983**, *48* (2), 129–133. [https://doi.org/10.1016/0030-4018\(83\)90372-3](https://doi.org/10.1016/0030-4018(83)90372-3).
- (163) Altman, R. B.; Terry, D. S.; Zhou, Z.; Zheng, Q.; Geggier, P.; Kolster, R. A.; Zhao, Y.; Javitch, J. A.; Warren, J. D.; Blanchard, S. C. Cyanine Fluorophore Derivatives with Enhanced Photostability. *Nat Methods* **2012**, *9* (1), 68–71. <https://doi.org/10.1038/nmeth.1774>.
- (164) Pati, A. K.; El Bakouri, O.; Jockusch, S.; Zhou, Z.; Altman, R. B.; Fitzgerald, G. A.; Asher, W. B.; Terry, D. S.; Borgia, A.; Holsey, M. D.; Batchelder, J. E.; Abeywickrama, C.; Huddle, B.; Rufa, D.; Javitch, J. A.; Ottosson, H.; Blanchard, S. C. Tuning the Baird Aromatic Triplet-State Energy of Cyclooctatetraene to Maximize the Self-Healing Mechanism in Organic Fluorophores. *Proc Natl Acad Sci USA* **2020**, *117* (39), 24305–24315. <https://doi.org/10.1073/pnas.2006517117>.
- (165) van der Velde, J. H. M.; Ploetz, E.; Hiermaier, M.; Oelerich, J.; de Vries, J. W.; Roelfes, G.; Cordes, T. Mechanism of Intramolecular Photostabilization in Self-Healing Cyanine Fluorophores. *ChemPhysChem* **2013**, *14* (18), 4084–4093. <https://doi.org/10.1002/cphc.201300785>.
- (166) Glembockyte, V.; Wieneke, R.; Gatterdam, K.; Gidi, Y.; Tampé, R.; Cosa, G. *Tris*-*N*-Nitriлотriacetic Acid Fluorophore as a Self-Healing Dye for Single-Molecule Fluorescence Imaging. *J. Am. Chem. Soc.* **2018**, *140* (35), 11006–11012. <https://doi.org/10.1021/jacs.8b04681>.
- (167) Zheng, Q.; Jockusch, S.; Rodríguez-Calero, G. G.; Zhou, Z.; Zhao, H.; Altman, R. B.; Abruña, H. D.; Blanchard, S. C. Intra-Molecular Triplet Energy Transfer Is a General Approach to Improve Organic Fluorophore Photostability. *Photochem. Photobiol. Sci.* **2016**, *15* (2), 196–203. <https://doi.org/10.1039/C5PP00400D>.
- (168) Romero, N. A.; Nicewicz, D. A. Organic Photoredox Catalysis. *Chem. Rev.* **2016**, *116* (17), 10075–10166. <https://doi.org/10.1021/acs.chemrev.6b00057>.

- (169) Schols, S.; Kadashchuk, A.; Heremans, P.; Helfer, A.; Scherf, U. Triplet Excitation Scavenging in Films of Conjugated Polymers. *ChemPhysChem* **2009**, *10* (7), 1071–1076. <https://doi.org/10.1002/cphc.200900054>.
- (170) Henrikus, S. S.; Tassis, K.; Zhang, L.; van der Velde, J. H. M.; Gebhardt, C.; Herrmann, A.; Jung, G.; Cordes, T. Characterization of Fluorescent Proteins with Intramolecular Photostabilization\*\*. *ChemBioChem* **2021**, *22* (23), 3283–3291. <https://doi.org/10.1002/cbic.202100276>.
- (171) Broichhagen, J.; Schönberger, M.; Cork, S. C.; Frank, J. A.; Marchetti, P.; Bugliani, M.; Shapiro, A. M. J.; Trapp, S.; Rutter, G. A.; Hodson, D. J.; Trauner, D. Optical Control of Insulin Release Using a Photoswitchable Sulfonylurea. *Nature Communications* **2014**, *5* (1), 1–11. <https://doi.org/10.1038/ncomms6116>.
- (172) Sarott, R. C.; Viray, A. E. G.; Pfaff, P.; Sadybekov, A.; Rajic, G.; Katritch, V.; Carreira, E. M.; Frank, J. A. Optical Control of Cannabinoid Receptor 2-Mediated Ca<sup>2+</sup> Release Enabled by Synthesis of Photoswitchable Probes. *J. Am. Chem. Soc.* **2021**, *143* (2), 736–743. <https://doi.org/10.1021/jacs.0c08926>.
- (173) Cheng, B.; Shchepakina, D.; Kavanaugh, M. P.; Trauner, D. Photoswitchable Inhibitor of a Glutamate Transporter. *ACS Chem. Neurosci.* **2017**, *8* (8), 1668–1672. <https://doi.org/10.1021/acschemneuro.7b00072>.
- (174) Frank, J. A.; Yushchenko, D. A.; Hodson, D. J.; Lipstein, N.; Nagpal, J.; Rutter, G. A.; Rhee, J.-S.; Gottschalk, A.; Brose, N.; Schultz, C.; Trauner, D. Photoswitchable Diacylglycerols Enable Optical Control of Protein Kinase C. *Nat Chem Biol* **2016**, *12* (9), 755–762. <https://doi.org/10.1038/nchembio.2141>.
- (175) Nevesely, T.; Wienhold, M.; Molloy, J. J.; Gilmour, R. Advances in the E → Z Isomerization of Alkenes Using Small Molecule Photocatalysts. *Chem. Rev.* **2022**, *122* (2), 2650–2694. <https://doi.org/10.1021/acs.chemrev.1c00324>.
- (176) Watson, E. E.; Russo, F.; Moreau, D.; Winssinger, N. Optochemical Control of Therapeutic Agents through Photocatalyzed Isomerization. *Angewandte Chemie International Edition* **2022**, *61* (28), e202203390. <https://doi.org/10.1002/anie.202203390>.
- (177) Gao, L.; Kraus, Y.; Stegner, A.; Wein, T.; Heise, C.; Brunn, L. von; Fajardo-Ruiz, E.; Thorn-Seshold, J.; Thorn-Seshold, O. Self-Reporting Styrylthiazolium Photopharmaceuticals: Mitochondrial Localisation as Well as SAR Drive Biological Activity. *Org. Biomol. Chem.* **2022**, *20* (39), 7787–7794. <https://doi.org/10.1039/D2OB00347C>.
- (178) Pisoni, D. S.; Todeschini, L.; Borges, A. C. A.; Petzhold, C. L.; Rodembusch, F. S.; Campo, L. F. Symmetrical and Asymmetrical Cyanine Dyes. Synthesis, Spectral Properties, and BSA Association Study. *J. Org. Chem.* **2014**, *79* (12), 5511–5520. <https://doi.org/10.1021/jo500657s>.
- (179) Gao, F.; Zhong, X.; Wang, Q.; Li, H.; Zhang, S. Excited State Intramolecular Proton Transfer of New Diphenyl- Ethylene Derivatives Bearing Imino Group: A Combination of Experimental and Theoretical Investigation. *Chinese Journal of Chemistry* **2010**, *28* (7), 1057–1068. <https://doi.org/10.1002/cjoc.201090186>.
- (180) Hanabusa, K.; Takata, S.; Fujisaki, M.; Nomura, Y.; Suzuki, M. Fluorescent Gelators for Detection of Explosives. *BCSJ* **2016**, *89* (11), 1391–1401. <https://doi.org/10.1246/bcsj.20160232>.
- (181) McNelles, S. A.; Pantaleo, J. L.; Adronov, A. Highly Efficient Multigram Synthesis of Dibenzoazacyclooctyne (DBCO) without Chromatography. *Org. Process Res. Dev.* **2019**, *23* (12), 2740–2745. <https://doi.org/10.1021/acs.oprd.9b00406>.
- (182) Xue, X.; Yang, J.; Huang, W.; Yang, H.; Jiang, B.; Li, F.; Jiang, Y. Dual Thermo- and Light-Responsive Nanorods from Self-Assembly of the 4-Propoxyazobenzene-



- Terminated Poly(N-Isopropylacrylamide) in Aqueous Solution. *Polymer* **2015**, 73, 195–204. <https://doi.org/10.1016/j.polymer.2015.07.035>.
- (183) Song, Y.; Park, S. Y.; Wu, Z.; Liu, K.-H.; Seo, Y. H. Hybrid Inhibitors of DNA and HDACs Remarkably Enhance Cytotoxicity in Leukaemia Cells. *Journal of Enzyme Inhibition and Medicinal Chemistry* **2020**, 35 (1), 1069–1079. <https://doi.org/10.1080/14756366.2020.1754812>.
- (184) Küllmer, F.; Gregor, L.; Arndt, H.-D. Systematic Modifications of Substitution Patterns for Property Tuning of Photoswitchable Asymmetric Azobenzenes. *Org. Biomol. Chem.* **2022**, 20 (20), 4204–4214. <https://doi.org/10.1039/D2OB00214K>.
- (185) Scheckenbach, M.; Schubert, T.; Forthmann, C.; Glembockyte, V.; Tinnefeld, P. Self-Regeneration and Self-Healing in DNA Origami Nanostructures. *Angewandte Chemie International Edition* **2021**, 60 (9), 4931–4938. <https://doi.org/10.1002/anie.202012986>.
- (186) Grabenhorst, L.; Trofymchuk, K.; Steiner, F.; Glembockyte, V.; Tinnefeld, P. Fluorophore Photostability and Saturation in the Hotspot of DNA Origami Nanoantennas. *Methods Appl. Fluoresc.* **2020**, 8 (2), 024003. <https://doi.org/10.1088/2050-6120/ab6ac8>.



## **7 Appendix**

### **7.1 Supporting Information to chapter 3.1**

## Supporting Information to

# A general method for near-infrared photoswitching in biology, demonstrated by the >700 nm photocontrol of GPCR activity in brain slices

Benedikt Baumgartner<sup>1</sup>, Viktorija Glembockyte<sup>2,3</sup>, Alberto Jesus Gonzalez-Hernandez<sup>4</sup>, Abha Valavalkar<sup>5</sup>, Robert Mayer<sup>2</sup>, Lucy Fillbrook<sup>6</sup>, Adrian Müller-Deku<sup>1</sup>, Jinhua Zhang<sup>7</sup>, Florian Steiner<sup>2,3</sup>, Christoph Gross<sup>2</sup>, Martin Reynders<sup>1</sup>, Hermany Munguba<sup>4</sup>, Iram Arefin<sup>4</sup>, Armin Ofial<sup>2</sup>, Jon Beves<sup>6</sup>, Theobald Lohmüller<sup>7</sup>, Benjamin Dietzek-Ivanšić<sup>5,8</sup>, Johannes Broichhagen<sup>9</sup>, Philip Tinnefeld<sup>2,3</sup>, Josh Levitz<sup>4</sup>, Oliver Thorn-Seshold<sup>1\*</sup>

\* Correspondence and request for materials to O.T.-S. (oliver.thorn-seshold@cup.lmu.de)

(1) Department of Pharmacy, Ludwig-Maximilians University of Munich, D-81377 Munich, Germany; (2) Department of Chemistry, Ludwig-Maximilians University of Munich, D-81377 Munich, Germany; (3) Center for NanoScience, Ludwig-Maximilians University of Munich, D-81377 Munich, Germany; (4) Department of Biochemistry, Weill Cornell Medicine, New York, NY 10065, USA; (5) Leibniz Institute for Photonic Technology Jena e.V. (Leibniz-IPHT), Research Department Functional Interfaces, D-07745 Jena, Germany; (6) School of Chemistry, The University of New South Wales, NSW-2052 Sydney, Australia; (7) Chair for Photonics and Optoelectronics, Nano-Institute Munich, Department of Physics, Ludwig-Maximilians University of Munich, D-80539 Munich, Germany; (8) Institute for Physical Chemistry (IPC), Friedrich Schiller University Jena, D-07743 Jena, Germany; (9) Leibniz Institute for Molecular Pharmacology, D-13125 Berlin, Germany.

## Table of Contents

1	Supporting Notes .....	4
	Note 1: $Z \rightarrow E$ switching incompleteness and slowness limit the impact of azobenzenes ...	4
	Note 2: Prior art in assisted $Z \rightarrow E$ isomerization of azobenzene by triplet sensitisation .....	5
	Note 3: Challenges for prior art in TET-isomerization of azobenzene .....	7
	Note 4: Discussion of Possible Mechanisms for the Intramolecular Energy Transfer .....	8
	Note 5: $E/Z$ potentials .....	12
	Note 6: Targets, features, and opportunities for azobenzene TET isomerisation dyads ..	13
	Note 7: Photoswitching Rates .....	14
	Note 8: Complex Switching .....	14
	Note 9: Scaffolded intermolecular sensitisation .....	15
	Note 10: $Z \rightarrow E$ limits to photopharmacology's translation from cells to <i>in vivo</i> .....	15
2	UV/VIS spectroscopy and bulk photoisomerisation .....	17
2.1	General Methods .....	17
2.1.1	UV/VIS setup .....	17
2.1.2	General Methods for UV/VIS and bulk photoisomerisation .....	19
2.1.3	Light Source Properties for bulk photoisomerisations .....	19
2.2	Thermal Relaxation .....	22
2.3	Bulk Population Photoswitching .....	23
2.3.1	$\epsilon(\lambda)$ and PSS composition (LED assessment) .....	23
2.3.2	Bulk photoswitching efficiency with moderate intensity LED light .....	23
2.3.3	Bulk photoswitching efficiency with low intensity monochromatic light .....	26
2.4	Physical Mixture Action spectrum .....	28
2.5	NBD-AK: benefits of assisted switching at typical azobenzene wavelengths .....	28
2.6	Extinction coefficient determination .....	29
2.7	Linker length-dependent photoswitch kinetics .....	31
2.8	Vesicle-Scaffolded Intermolecular Sensitisation .....	31

3	Fluorescence Excitation / Emission from fluorophores.....	34
4	Electrochemistry in ground and photoexcited states .....	35
4.1	Experimental reduction/oxidation potentials: chromophores.....	35
4.2	Redox in S <sub>0</sub> , S <sub>1</sub> , and T <sub>1</sub> states: chromophores .....	37
4.3	Experimental reduction/oxidation potentials in ground state: azobenzenes .....	38
5	PSS and photoswitch E/Z ratio determinations by UV/Vis and HPLC .....	40
5.1	PSS determination by HPLC .....	40
5.2	Calibration curves for action spectra calibration .....	42
5.3	HPLC accuracy .....	43
6	Fluorescence Lifetime measurement by TCSPC .....	43
7	Fluorescence Correlation Spectroscopy (FCS) .....	45
7.1	FCS Methods .....	45
7.2	FCS and FLCS results for EYpip and EY-AK.....	45
7.3	FCS: "total" triplet quenching in EY-AK; & 'weak coupling model' quantum yields	46
8	Transient absorption (TA) spectroscopy (TAS) .....	48
8.1	TAS Methods .....	48
8.2	TAS Results for NB, RhB, and EY conjugates.....	49
8.3	Worked example: analysing NB / NB-AK decay rates .....	51
8.4	Crude order-of-magnitude estimation of "E/Z-average $\phi_{\text{exciplex}}$ " for RhB-AK .....	52
9	Fluorescence Quantum Yields .....	53
9.1	Mostly-E fluorescence quantum yields (integrating sphere measurements).....	53
9.2	Sensitivity, technical precision, and accuracy, of cuvette/PMT measurements ...	53
9.3	Fluorescence of conjugates depends on E/Z ratio (cuvette/PMT measurements)	55
10	Photoswitch Modeling .....	57
11	Cell culture transfection and electrophysiology.....	58
12	Viral injections, <i>in vivo</i> labelling and slice electrophysiology.....	60
13	Chemical Synthesis.....	61
13.1	General .....	61
13.2	NMR spectroscopy.....	61
13.3	High-resolution mass spectrometry (HRMS).....	62
13.4	Synthesis.....	62
13.4.1	Azobenzene building blocks.....	62
13.4.2	Fluorophore building blocks .....	66
13.4.3	Azobenzene-Fluorophore conjugates .....	73
13.4.4	Lipidated fluorophores.....	85
14	Appendix: NMR Spectra.....	87
15	Appendix: HRMS.....	108
16	Supporting References .....	121

## Reuse/Overlap of Content

Chapter 4 (Electrochemistry) of this supporting information, and a few other smaller sub-parts, are shared between this manuscript and our parallel manuscript focusing on photoredox-based isomerisation<sup>1</sup>. All shared material is otherwise original and has not been submitted or posted elsewhere, except as part of lead author Benedikt Baumgartner's cumulative PhD Thesis (2024, LMU Munich). Material is included in both papers only where necessary to support a seamless presentation and analysis of the data (e.g. by excluding competing mechanisms) without requiring the reader to flip between separate manuscripts.

## Author Contributions

BB designed targets, performed synthesis, assembled UV/Vis setup, performed UV/Vis and fluorescence spectroscopy, HPLC analysis, analyzed and coordinated data, assembled figures and contributed to manuscript preparation. VG and FS performed fluorescence lifetime experiments. VG performed fluorescence correlation spectroscopy. AJGH, HM and IA performed cell culture and brain slice experiments. AV performed transient absorption spectroscopy and fluorescence quantum yield measurements. LF designed and wrote the python scripts for mechanism modeling. AMD and MR performed synthesis and photocharacterization. RM and CG performed electrochemical measurements. AO supervised electrochemical measurements. JBeeves supervised molecular modeling. BDI analyzed and supervised transient absorption spectroscopy and fluorescence quantum yield measurements. JBroichhagen synthesized BGAG<sub>12,400</sub>-Cy5.v1/2. PT supervised fluorescence lifetime experiments and fluorescence correlation spectroscopy. JL analyzed and supervised cell culture and brain slice experiments. OTS conceived the study, performed synthesis, UV/Vis, data analysis, supervised all other experiments, and wrote the manuscript with input from all authors.

## 1 Supporting Notes

### Note 1: $Z \rightarrow E$ switching incompleteness and slowness limit the impact of azobenzenes

**(Expanded from main text):** Azobenzenes are the major synthetic molecular photoswitches. They deliver powerful applications in many areas where chemical effectors must be actuated with high spatial and/or temporal precision. These range from photopatterning properties in materials, soft matter and surfaces;<sup>2,3</sup> across to photocontrolling biology, from targets and phenomena in cell culture (ion channels,<sup>4,5</sup> cytoskeleton<sup>6-8</sup>, protein degradation<sup>9,10</sup>, antibacterial activity<sup>11</sup>, kinases<sup>12</sup>, and G protein-coupled receptors (GPCRs)<sup>13-15</sup>), through to *in vivo* applications particularly for vision restoration, including a recently started human clinical trial.<sup>16,17</sup> In each use, an azobenzene scaffold is decorated with substituents so that its *E* and *Z* isomers affect the system differently. Locally photoswitching a sample between majority-*E* and majority-*Z* states patterns its activity: and due to this, the *incompleteness* of population photoswitching ultimately limits the activity-switching performance accessible to any chemical type of photoswitch.

There are two major limits on the performance that azobenzenes can currently reach or aspire to. First, population-level photoswitching is not binary (all-*E*  $\rightleftharpoons$  all-*Z*) but is incomplete, due to extensive overlap of *E/Z* absorption spectra (**Figure 1c**).  $Z \rightarrow E$  photoswitching is particularly incomplete, and is also photon-inefficient due to low extinction coefficients.<sup>16</sup> Since designs typically aim at *Z*-active reagents to minimise background activity before the first photoswitching round,<sup>18</sup> the incompleteness of  $Z \rightarrow E$  photoswitching directly limits the ability to "switch a reagent off again": this is the major limit on the *fold-change of activity* that can be applied in a system - giving "more-on/less-on" rather than "on/off" performance. Mathematically, the maximum fold-change of activity permitted by bidirectionally photoisomerising an azobenzene affinity photoswitch is given by its functional dynamic range (FDR:=  $\phi_F/\phi_B$  for the fractions  $\phi$  of the more active isomer established by "forward" (F) and remaining after "backward" (B) photoisomerisations); even azobenzenes considered as "good" switches rarely exceed 5-fold (see<sup>19</sup>). To achieve more powerful control, several times higher FDRs are needed: i.e., several times more complete  $Z \rightarrow E$  photoswitching. Second, no broadly-applicable biocompatible strategy to operate azobenzenes with well-penetrating red/NIR light is known: typically,  $\epsilon(\lambda)$  are significant only below 530 nm. These wavelengths are strongly absorbed and scattered in biological tissues and complex samples, which limits the depths at which photocontrol can be applied.<sup>16,20-22</sup>

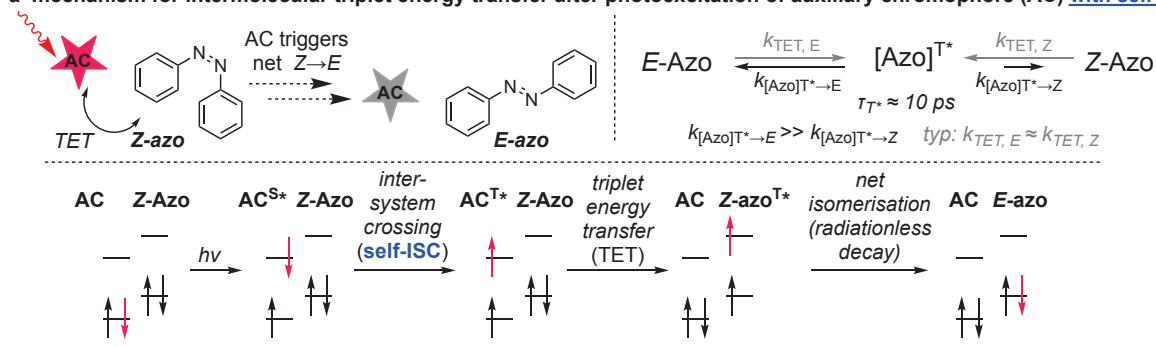
Strategies to improve the completeness and photon efficiency of  $Z \rightarrow E$  photoswitching with red/NIR light are therefore highly sought after. However, until now rather extreme substituent tuning has been needed to approach these goals, and still no generally useful, synthetically accessible, biocompatible designs have been found that do not compromise *Z*-isomer stability. Approaches for creating *Z*-stable azobenzenes with photoresponse up to 600 nm include the tetra-*ortho*-substitutions pioneered by Woolley, Hecht and others (incl. tetra-*ortho*-chloro<sup>23-25</sup>, -alkoxy<sup>26-28</sup>, -fluoro<sup>29,30</sup>, and mixed patterns<sup>28,31</sup>). The strained cyclic azobenzenes pioneered by Herges (diazocines<sup>32,33</sup> and diazonines<sup>34</sup>) also have notable mid-visible photoresponse. Both types can have better-complete switching than classical azobenzenes, due to wider separation between the *E/Z*-isomers' absorption bands; but their visible extinction coefficients are low (ca.  $< 1000 \text{ M}^{-1}\text{cm}^{-1}$ ), NIR photoswitching remains inaccessible, and these designs restrict the chemical and applications space available since they all rely on multiple substitutions around the diazene (a particular problem for uses as photoswitchable reagent pharmacophores, where these substituents are needed for specific interactions with target proteins; our view is that to allow uses in biology requires not compromising target binding, and therefore minimising changes in the molecular environment of the azobenzene scaffold: i.e. arguing against much substituent-based tuning of the diazene's absorption bands).



**Note 2: Prior art in assisted Z→E isomerization of azobenzene by triplet sensitisation**  
**(Text and figures reproduced from PhD Thesis, B. Baumgartner 2024, in submission):**

Besides auxochrome- or structure-based tuning of azobenzenes' "direct" photoswitching (where light is absorbed by the azoarene itself), methods for "assisted" or "indirect" isomerization have also been developed, where the energy required for isomerisation is initially harvested by another chromophore. These assisted methods enable photoswitching that is independent of the absorption spectra or direct quantum yields of the azobenzene itself. Two methods have gained most attention: Z→E isomerization by triplet energy transfer (TET), as discussed here; and Z→E isomerization by photoinduced electron transfer (PET).

**a mechanism for intermolecular triplet energy transfer after photoexcitation of auxiliary chromophore (AC) with self-ISC**



**b Prior art in intermolecular TET from self-ISC auxiliary chromophores**

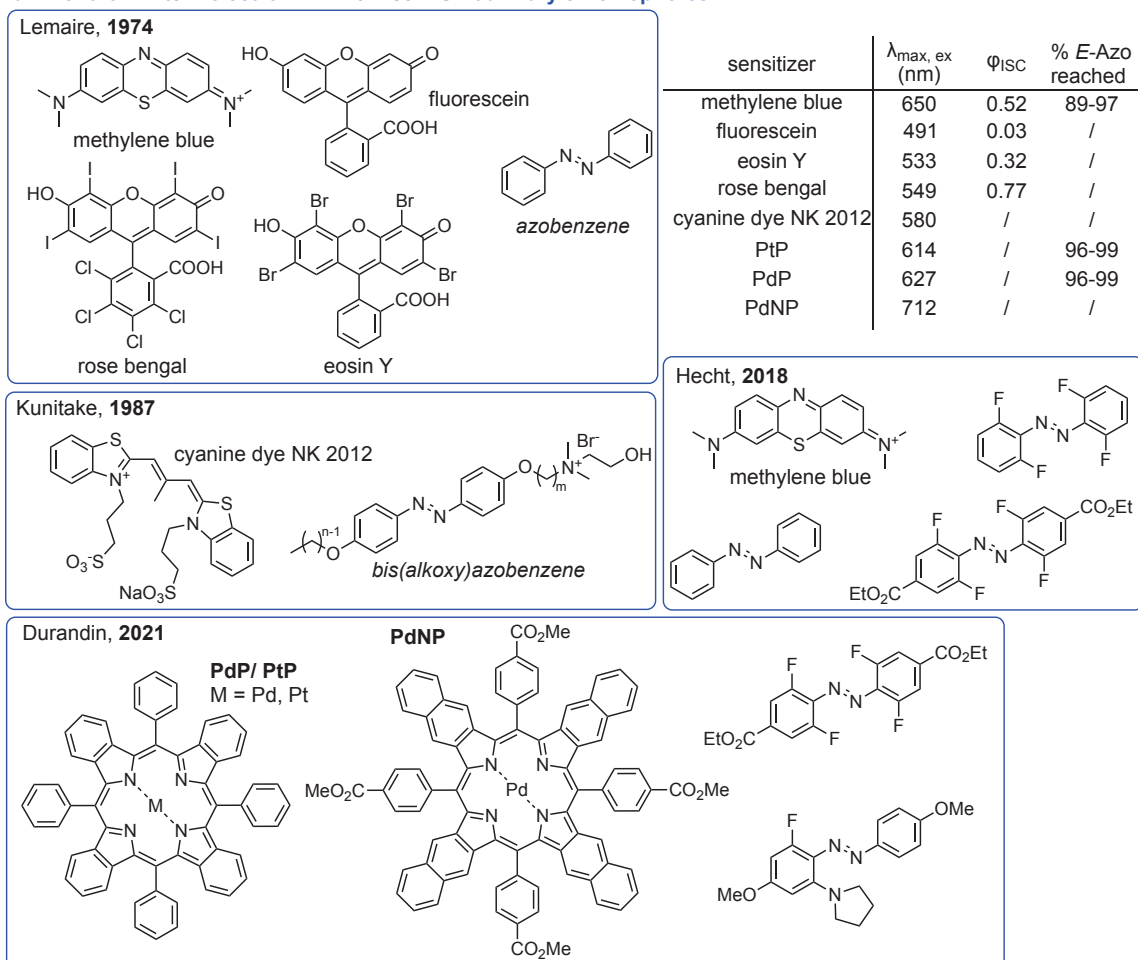


**Figure S1: (a)** a mechanism for TET-based Z→E isomerization of azobenzenes occurring after self-ISC on the auxiliary; **(b)** literature examples of azobenzene and triplet sensitizers: Lemaire, 1974<sup>35,36</sup>; Kunitake, 1987<sup>37</sup>; Hecht, 2018<sup>38</sup>; Durandin, 2021<sup>39</sup>; table (right) summarizes self-ISC  $\phi_{\text{ISC}}$  values for triplet sensitizers, and photostationary state % E values reached after sensitization ("/" indicates not tested, not reported, or not characterised).

TET is a prominent energy transfer pathway in photophysics and photochemistry. If intersystem crossing (ISC) on the antenna (which we call "self-ISC" in this paper) is efficient (high ISC quantum yield,  $\phi_{\text{ISC}}$ ), a triplet sensitizer can reach  $T_1$  after excitation from  $S_0$  to  $S_1$  (**Fig S1a**). Then, the  $T_1$  sensitizer can collide with and transfer its energy and spin to another molecule in its ground state (triplet acceptor), yielding the triplet sensitizer in its  $S_0$  ground state and the triplet acceptor in its triplet excited state  $T_1$ . The efficiency of TET is dependent on thermodynamics and collision rate<sup>39</sup>. TET is rapid if the triplet energy  $E_T$  of the triplet sensitizer is higher than that of the triplet acceptor (exergonic), but can also happen endergonically, if a subsequent reaction of the triplet acceptor occurs rapidly. Bimolecular sensitization rates will also depend on collision rates.<sup>40,41</sup>

Azobenzenes are known to have a low-lying triplet state ( $\sim 120\text{--}160$  kJ/mol)<sup>42,43</sup> and a very short triplet lifetime  $\tau_{\text{triplet}} \sim 10$  ps.<sup>42–45</sup> These properties have been exploited in several studies to control the isomeric ratio of azobenzenes by TET from triplet sensitizers (**Fig S1b**).<sup>35,37–39</sup> Once triplet energy has been transferred to a typical azobenzene, its  $T_1$  relaxes mainly to the *E* isomer ("TET-stationary-state" can contain e.g.  $\sim 90\text{--}98\%$  *E* isomer).

**Key Early Reports:** **Jones and Hammond's** 1965 communication reported a TET-PSS of ca. 98% *E*, achieved with 3-acetylpyrene or  $\beta$ -acetonaphthone sensitisation of unsubstituted azobenzene<sup>46</sup>. The next significant example of TET-based isomerization was by **Lemaire** in 1974 (**Fig S1b**),<sup>35</sup> showing that unsubstituted azobenzene's *Z*→*E* photoisomerization can be sensitized by organic small molecules with low-lying triplet-state-energy: xanthene-based chromophores Rose Bengal, Eosin Y, and fluorescein, and the thiazine-based Methylene Blue (MB). For example, Rose Bengal sensitized the photoisomerization under 546 nm to yield a TET-stationary state of 95% *E* isomer. Milestone mechanistic studies of azobenzene triplet processes were then delivered by **Bortolus and Monti** in the 1970s and 1980s,<sup>42,43</sup> and were added to by **Orlandi** who studied the mechanism of *Z*→*E* isomerization of azobenzenes in the 2000s and found that the  $T_1$  minimum of the potential energy surface (PES) is located at a twisted geometry that is below the ground state transition energy barrier between *Z* and *E* azobenzene (**Fig S2**, orange line represents PES of  $T_1$ , blue line represents PES of  $S_0$ ). The lower energy crossing point (red circle) of the  $T_1$  PES with the  $S_0$  PES is located on the side of the *E* isomer's energy minimum, close to the minimum of the  $T_1$  PES, favouring the decay of the triplet into the *E* isomer. This confirms the plausibility of quantum yields for TET-based *Z*→*E* isomerization close to 1 and *E*→*Z* isomerization around 0.02.<sup>45</sup> TET-based isomerization of azobenzenes thus enables a powerful pathway for near-quantitative *Z*→*E* isomerization, independent of the azobenzene's own spectral absorption or of the thermal stability of its *Z* isomer. These investigations were revisited from the 2020s onwards, notably by **Hecht**<sup>47</sup>.

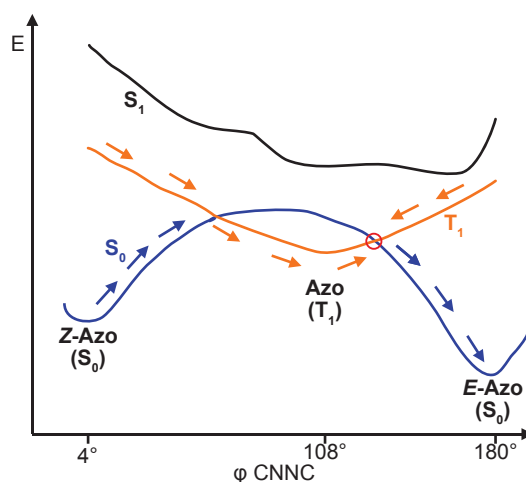


**Figure S2:** Potential energy surface of azobenzene's  $S_0$  ground state,  $S_1$  excited singlet state and  $T_1$  excited triplet state. Adapted from Orlandi, JACS, 2004<sup>45</sup>.

Perhaps the most forward-looking of the early studies of azobenzene triplet photochemistry was that of **Shimomura and Kunitake** in 1987, who investigated the photoswitching of azobenzene-lipid-containing bilayers in the presence of substoichiometric, membrane-bound thio-cyanine dye NK 2012 (**Fig S1b**).<sup>37</sup> The thiocyanine was able to catalyze  $Z \rightarrow E$  isomerization of the azobenzenes within the bilayer membrane, which was attributed to TET from the cyanine dye to the azobenzene.

This report was seminal, but lay seemingly forgotten for 30 years. In this time, hundreds of azobenzene-chromophore conjugates were developed, almost all of them being used as enzymatically unquenchable FRET probes,<sup>48–50</sup> plus a few fluorescently tagged azobenzenes for imaging the delivery of an azobenzene ligand.<sup>51,52</sup> It seems that only one observation of single-photon intramolecular TET-based isomerisation was published in this time (2014), although its basis was unexplained and applications were not demonstrated.<sup>53</sup>

**Key Recent Reports:** The topic was soundly resurrected with the 2018 work of **Hecht and coworkers**.<sup>38</sup> While studying photoinduced electron transfer-based isomerization of azobenzenes, they found that azobenzenes which could not be photooxidized to a radical cation by the triplet-manifold photooxidant MB were still isomerized towards the  $E$  isomer under MB excitation at 660 nm (**Fig S1b**), reaching TET-PSSs ranging from 89–97%  $E$  isomer, dependent on the electronic properties of the azobenzene. In 2021, **Durandin and Priimagi** shifted the wavelength used for TET-based  $Z \rightarrow E$  isomerization even further towards the NIR.<sup>39</sup> Applying Pd/Pt porphyrins (**Fig S1b**) as triplet sensitizers, they could reach up to 99%  $E$  isomer of a tetra-*ortho*-fluorinated azobenzene at up to 770 nm. Interestingly, they also reported that TET is also possible at endothermic conditions ( $E_T$  of the sensitizers  $>0.2$  eV lower than  $E_T$  of the azobenzenes, stated to be compensated by entropy).

However, both Hecht and Durandin showed that the triplet sensitizers used in their studies suffer photoinduced degradation (photobleaching) when TET-based isomerization was performed under air, which drastically limits the application of the systems. This is unsurprising since the sensitizers were available to solution and therefore oxygen could compete with azobenzene as a triplet acceptor.

*During the finalisation of this manuscript two new preprints were uploaded, giving new examples of triplet energy transfer based azobenzene isomerization:*

(1) **Klajn, Schapiro and coworkers** presented DESC (DisEquilibration by Sensitization under Confinement).<sup>54</sup> DESC is a supramolecular approach using a coordination cage with two binding sites; one is selective for a photosensitizer and the other for  $E$ -azobenzene. The  $Z$ -isomer cannot bind to the coordination cage. Even though the quantum yield of  $E \rightarrow Z$  isomerization by TET is about 1% they were able reach mixtures of ~95%  $Z$  isomer at TET-stationary state, since only the  $E$  isomer can bind the coordination cage then is isomerized to the  $Z$  and accumulates in solution where it is barely sensitised.

(2) **Durandin, Herges and coworkers** showed TET-based isomerization of diazocines. Triplet energies of diazocine  $E$  and  $Z$  isomers are more different than for classical azobenzenes, thus it was possible to selectively address the  $E$  and  $Z$  isomers with two different triplet sensitizers and show isomerization in both directions by TET at 530 nm ( $Z \rightarrow E$ ) and 740 nm ( $E \rightarrow Z$ ), respectively. The sensitizers used are both Pd/Pt porphyrins, therefore once again oxygen exclusion is necessary to avoid singlet oxygen-associated photobleaching. In the  $Z \rightarrow E$  direction, only up to 50%  $E$ -isomer is reached due to spectral overlap with direct absorption by the  $E$ -isomer (giving  $E \rightarrow Z$ ).<sup>37</sup>

### Note 3: Challenges for prior art in TET-isomerization of azobenzene

**Expanded from main text:** The desirability of near-complete TET-based  $Z \rightarrow E$  isomerisation at wavelengths decoupled from azobenzene's own absorption is clear,<sup>39</sup> but the systems developed so far (see above) could not be generally applied. This is mainly since they were **intermolecular** TET schemes, and intermolecularly seems impossible to translate to complex settings (expected: ~nM photoswitch) because its performance is *extrinsic*: it relies on the triplet donor colliding with the azobenzene and also not with any competitive quenchers ( $O_2$ ,

thiols, etc). Most studies needed O<sub>2</sub>-exclusion; e.g. by opening a cuvette to the air, Hecht observed triplet auxiliaries suffering a ca. 500-fold loss of isomerisation efficiency, as well as significant photobleaching even of the sensitiser<sup>38</sup> which highlights their danger of causing indiscriminate singlet oxygen-mediated photodamage in biology.

To overcome intermolecularity, we instead aimed to explore covalent dyads of auxiliaries with azobenzenes. Whether these dyads would ensure fully intramolecular triplet reactivity and so feature fully *intrinsic*, concentration- and environment-independent performance with full O<sub>2</sub>-tolerance, and whether they could avoid switch photodestruction or environment/target photobleaching, remained completely unknown.

Another problem for complex media is the inapplicability of the known extrinsic sensitisers: poorly-permeable heavy metal complexes >2000 Da<sup>39</sup> for absorption above 680 nm; or organic sensitisers that are biologically-partitioned redox cycling chromophores<sup>35,38</sup> or cell-excluded polyanionic dyes<sup>55</sup>. Additional problems include absorption by the sensitisers in the UV/blue region where azobenzenes require *E*→*Z* isomerisation, that greatly reduces *E*→*Z* yield<sup>38</sup>. Rather than maximising the triplet yield with organic synthetic photocatalysts, we expected that biological tractability and applicability would prove crucial for intrinsic systems. Therefore, despite their expected smaller values of  $\Phi_{ISC}$ , green/red/NIR auxiliary chromophores that are biologically validated fluorophores, such as rhodamines and cyanines, were inherently more interesting for this work. On top of this, our puzzling observation of very photon-efficient, near-complete *Z*→*E* azobenzene isomerization upon exciting a covalently-attached Rhodamine B auxiliary,<sup>53</sup> was particularly encouraging. The mechanism of this isomerisation was unknown (**section 1.4**), but, we wondered if proximity to the azobenzene with its large spin-orbit coupling coefficients was driving the energy of the singlet excited auxiliary ultimately into an azobenzene triplet, that then collapsed to give the mostly-*E* PSS observed. If this were true, low- $\Phi_{ISC}$  auxiliaries might have unique power for biocompatible TET switching: (a) when the azobenzene folds into molecular contact with it, even a typically low- $\Phi_{ISC}$  chromophore might pump azobenzene isomerisation via pushing it into the triplet state with high efficiency; but (b) when the azobenzene motif is not in molecular contact (e.g. linker-extended conformation), the chromophore should stay in a biocompatible singlet manifold photocycle. This might avoid the photodamage and O<sub>2</sub>-incompatibility of previous TET approaches, where a highly efficient photosensitiser generates triplet states continuously, irrespective of whether an azobenzene is nearby to accept them or not. It would also allow using validated fluorophores, optimised for high absorption and long excited state lifetimes (i.e. a relatively high chance to enter a relatively long-lived but biologically innocent excited state during which proximity/collision with the azobenzene might channel the energy through an isomerisation-competent azobenzene triplet state); with the major advantages of excellent biological tractability of the chromophores, that have known biodistribution, cell entry and localisation properties - unlike organic synthesis photocatalysts.

#### **Note 4: Discussion of Possible Mechanisms for the Intramolecular Energy Transfer**

This Note extends the discussion in the **main text sections 2.5-2.6**, by setting out and critiquing potential mechanisms of antenna-mediated isomerisation, to show why we believe that an induced-triplet energy transfer is the most likely process. The abbreviations AC (antenna chromophore) and MP (molecular photoswitch) are used.

#### **4.1 - Proximity-induced triplets that collapse to azobenzene triplets are a plausible route to isomerisation**

The azobenzene triplet state is isomerisation-competent and is at low energy above the S<sub>0</sub> state (energy gap equivalent to ca. 700-1000 nm): therefore it is energetically accessible to the long wavelength excitation we supply. If an isolated azobenzene enters its triplet state MP(T<sub>1</sub>), then it is expected to de-excite, optionally while isomerising, to give up to ca. 90-98% *E*-azobenzene<sup>46,56</sup>, which is indeed a typical outcome we observed for the sensitised process.

Uniquely, intramolecular entry to a triplet state via an *induced triplet / exciplex mechanism* can be isomer-dependent if one isomer is more efficient at inducing the ISC process than the



other (productive collisions have different  $E/Z$  likelihoods depending on the azo structure and its match to the chromophore). Consistent with this idea, even very similar conjugates (e.g. RhB-AN and RhB-AO) reached different sensitised PSSs (8% vs 2% remaining  $Z$ -isomer). Also consistent with biased entry, we observed that fluorescence quantum yields (which can be taken as a reporter of energy harvesting in the below-nanosecond timescale) could be  $\geq 3$ -fold lower for  $Z$  than  $E$  isomers (which ought to shift the sensitised PSS to higher  $E/Z$  ratio). These observations are consistent with biased induced entry, but they are inconsistent with self-ISC as an entry route to the triplet state (see **Note 4.2**).

*Note: Private communications from B.N. suggested to consider whether **singlet fission** might be a plausible mechanism for AC(S1)-MP(S0) to evolve to place a triplet state on the MP. Singlet fission would involve the steps: (1) AC(S1)-MP(S0)  $\rightarrow$  AC(T1)-MP(T1) [singlet fission]; (2)  $\rightarrow$  AC(T1)-MP(S0) [nonradiative MP(T1) collapse]; (3)  $\rightarrow$  AC(S0)-MP(T1) [TET]; (4)  $\rightarrow$  AC(T1)-MP(S0) [n.r.]. We do not consider this likely since step (1) is likely to be endergonic for most/all of the conjugates studied here (combined energy of chromophore T1 + azobenzene T1 states are higher-energy than the chromophore S1).*

#### **4.2 - self-generated AC triplet states are likely not *major* initiators of isomerisation:**

(4.2.1) If the major pathway for sensitised isomerisation is triplet energy transfer from a pre-formed, isolated auxiliary chromophore triplet AC\*(T1) to the photoswitch groundstate MP(S0), we would expect that ACs which have very different quantum yields of intersystem crossing to the triplet state  $\Phi_{ISC}$ , yet are relatively spectrally similar, would have very different **rates of sensitised isomerisation**: but we did not observe this. For example, consider Eosin Y (EY) and fluorescein (FI) as ACs. Eosin Y's  $\Phi_{ISC}$  is reported as ca. 0.3 according to conditions<sup>38</sup> under which fluorescein's  $\Phi_{ISC}$  is reported as ca. 30-fold less<sup>39</sup>. However, the rate of bulk sensitised photoisomerisation (assessed from PSS at 365 nm to PSS around 525 nm) is approximately only 3-fold less for FI-AK than EY-AK (**Figure 3d**, quantified in **Table S3**).

(4.2.2) Since the FCS data for **EY-AK** at low concentration (**Figure 4b**) support complete intramolecular funneling of chromophore triplet state energy into the azobenzene regardless of the isomer (which is more plausible than complete interception of **EY(S1)** motifs before they perform self-ISC to enter a triplet state, given that fluorescence quantum yield is only halved as compared to **EY**), it is plausible that *if* any triplet states had been pre-formed on any other chromophores, these would have been quenched quantitatively and intramolecularly by TET (no  $E/Z$  preference): forcing their azobenzene motifs into  $E/Z$  ratios at sensitised PSS that would be identical for any conjugate sharing the same azobenzene (not seen).

(4.2.3) It might be thought that the role of pre-formed AC\*(T1) could be tested by comparing isomerisation rates when additional triplet quenchers are present, to rates when additional triplet quenchers (such as oxygen) excluded: expecting that if rates increase when quenchers are excluded then this would imply that pre-formed AC\*(T1) is involved. This is reasonable when testing the role of *intermolecular* triplet sensitisation, and has been done for this before (e.g. Hecht, and Priimagi and Durandin, have reported sensitised isomerisation rates to be strongly depressed in the presence of oxygen<sup>44</sup>,). Here are two considerations why it is less reasonable in our case, where sensitisation is *intramolecular*.

(4.2.3a) We expect from hints in the literature as well as **EY-AK** FCS data (**Fig 4b**), that azobenzenes can be extremely rapid quenchers of triplet states<sup>43</sup>; and because azobenzene triplets decay on ultrafast timescales to S0, they are insensitive to additional triplet quenchers once the azobenzene triplet is formed. Since the conjugates enforce close proximity of the azobenzene and the AC, we consider it likely that *if* the AC\*(T1) state is entered, then the covalently attached azobenzene may substantially or entirely out-compete molecular oxygen, or other solution-state quenchers. Thus we do not expect additional intermolecular triplet quenchers to siphon off AC\*(T1); and we do not consider that excluding or adding triplet quenchers at reasonable concentrations would be able to change the chance of triplet-sensitised rates, so we think this experiment would not provide mechanistic insight.



(4.2.3b) However, we saw rapid sensitised isomerisation for a broad range of AC-MP conjugates, with half-powers [cf. rates per unit of photon energy] typically comparable to those of  $E \rightarrow Z$  photoisomerisation when directly illuminating azobenzenes in their well-absorbing  $\pi \rightarrow \pi^*$  near-UV band that has a quantum yield of isomerisation  $\Phi_{E \rightarrow Z}$  of ca. 0.3<sup>57</sup> (see **section 2.2** of the main article). To give a rough approximation, we note that the extinction coefficients of the ACs we use in the red/NIR are typically only five times that of the azobenzenes in the near-UV, and their  $\Phi_{ISC}$  are typically on the order of 1% or even very much less. Even in the case of 100%-efficient triplet sensitisation from  $AC^*(T1)$  to MP, at least  $\Phi_{ISC} = 8\%$  (multiplying the 5-fold higher extinction coefficient) would be needed for self-generated chromophore-sensitised isomerisation to be similar in rate to that of direct azobenzene isomerisation. Since this rough calculation is one or more orders of magnitude out of range, we do not think it leaves room for  $AC^*(T1)$  as the major initiating species.

### **4.3 - FRET from AC(S1) preferentially to Z-MP(S0) [ $\rightarrow$ MP(S1) $\rightarrow$ E] seems unlikely:**

Some azobenzenes are in wide use as intramolecular FRET quenchers that quench donor S1 states<sup>58</sup>: for example push-pull azobenzene DABCYL, as well as more complex systems (bis-azobenzenes BHQ-1 & BHQ-2; charged heteroarylazobenzene BHQ-3). The hundreds of literature reports leave no doubt that these azobenzenes can quench by rationally-designed FRET pairing, which emphasises overlap of e.g. the azobenzene's absorption band with the donor's emission band. (*However, to our knowledge, it remains unclear what happens with this FRET energy - we presume that the acceptor is isomerised by FRET, towards reaching a mixed E:Z PSS, but in practice remains present as mostly-E since all these quenchers should have (very) short thermal Z $\rightarrow$ E half-lives. It is unclear to us whether those quenchers can also engage in other mechanisms than FRET, for example in photoelectron transfer to quench the donors more efficiently than by FRET alone, if molecular contact is allowed*).

The situation is different for the AC-MP dyads we present, because the spectral overlap is in many cases too small to imagine for a classical FRET process - for example, when exciting the Cy5 of Cy5-AK at 640-740 nm, whereas both the *E* and *Z* azobenzenes' extinction coefficients drop monotonically below 200 M<sup>-1</sup>cm<sup>-1</sup> already by 520 nm. Therefore, classical FRET exciting the azobenzene's  $n \rightarrow \pi^*$  transition would appear to be an energetically- and overlap- forbidden process, that cannot be likely as the major isomerisation mechanism since the observed sensitised photon efficiency (that is comparable to UV direct  $E \rightarrow Z$  isomerisation) is far too high.

There are however several relevant observations.

(a) A FRET-type mechanism, with an appropriate energetically-matched donor, *could* provide a plausible route for selectively exciting the *Z* more than the *E* isomers of these bistable azobenzenes, since the *Z* isomer's  $n \rightarrow \pi^*$  band is bathochromically and hyperchromically shifted relative to that of the *E*.<sup>53</sup> The ratio of extinction coefficients in the long wavelength tail of the  $n \rightarrow \pi^*$  band is typically between 5:1 to 10:1 for *Z*:*E*, which approaches the *Z*-preference that would be required to set the observed PSSs of ca. 85-95%*E*). But it seems that the donors are not matched.

(b) FRET has a  $1/R^6$  through-space distance dependency; we do see distance-dependency but it is not as striking as FRET would have us expect (e.g. **BGAG<sub>12,400</sub>-Cy5.v1** is only 2.5 times as fast in sensitised isomerisation as **BGAG<sub>12,400</sub>-Cy5.v2** which should have a far larger distance separation between AC and MP).

(c) Aspects of photochemistry that occur in "classically forbidden" ways are still appearing. For example, Barner-Kowollik and coworkers<sup>59</sup> have shown experimentally that "*UV/vis spectra fail to act as a predictor for photochemical reactivity at a given wavelength in most of the examined reactions, with the photochemical reactivity being strongly red shifted in comparison to the absorption spectrum*". The reasons for this remain unclear, although in many cases some degree of reactant  $\pi$ -stacking appears possible (and such cannot be excluded for the AC-MPs either); but the generality of the observations is compelling.

Separately, calculations on azobenzene energies suggest that geometric distortions in

the electronic groundstate which cost only small energy penalties, can be accompanied by much more significant drops in Franck-Condon excited state energies, i.e. they lower the overall energy cost of isomerisation<sup>57,45</sup>. Perhaps related to this, it has been seen experimentally that bulk azobenzene isomerisations can be driven even at surprisingly long wavelengths, which was theorised to be due to small twisted-geometry subpopulations within the electronic groundstate population (though these subpopulations *must* be small, otherwise they would show up detectably e.g. by UV-Vis)<sup>24</sup>. We cannot exclude that a combination of these effects could allow azobenzenes to accept apparently-too-low energies for S0→S1, then isomerise. However, the extreme photon-efficiency of the isomerisations we see, makes it seem unlikely that only a small fraction of the conjugates is being addressed at any one time. Pritzl 24/68<sup>24</sup>; Ronayette 35/97<sup>35</sup>; Shimomura 37 / 56<sup>37</sup>; Goulet-Hanssens 38/59<sup>38</sup>; Isokuoritti 39/60<sup>39</sup>; Bortolus 43/63<sup>43</sup>; Monti 44/61<sup>44</sup>; Monti 42/45<sup>42\*</sup>; Cembran 46/67<sup>45</sup>

**4.4 - Dexter energy transfer seems unlikely:** As for FRET, the energy gap that would need to be covered by Dexter energy transfer from the chromophore S1 to excite the azobenzene to S1 seems greater than the energy available to the system (long-wavelength absorption). The relatively low degree of fluorescence quenching also seems insufficient for this to be a relevant mechanism (**Figure S23, Table S14**).

**4.5 - Photoredox of MP(S0) by AC\*(S1) or AC\*(T1) seems unlikely:**

**Design, 1:** In this study, the oxidation potentials of the *E*-MPs are chosen to be rather higher than the excited state reduction potential of the AC\*(S1) (see **section Electrochemistry**), thermodynamically blocking photooxidation. Note also that the triplet excited state reduction potential of AC\*(T1) is typically ~0.2 V lower than that of the singlet, so photooxidation from the AC triplet is thus also excluded.

**Results, 1:** Photooxidation would give the MP radical cation, that quantitatively relaxes to *E* before recombination.<sup>38</sup> However, the relaxation we see in this study is not quantitative; whereas the relaxation seen when the same MPs are matched within dyads to appropriate ACs with high enough AC\*(S1) reduction potentials, is indeed quantitative (see ref<sup>1</sup>).

**Alternatives, 1:** Although the *Z*-MP oxidation potentials are unknown (azobenzene *Z* isomers are thought to be only ~0.06 V easier to oxidise than *E* isomers, i.e. they too are inaccessible to photooxidation in this study: see **Supporting Note 5**), to conjecture that the *Z*-MP would be photooxidised while *E*-MP is mostly unaffected is not a better explanation of the data: since our highest long-wavelength isomerisation PSS is around 98% which matches expectations for similar triplet sensitisation of *E* and *Z* azobenzenes, without requiring an additional mechanism for enriching the *E*-isomer fraction, as *Z*-selective photoredox would provide.

**Design, 2:** Photoreduction would give the MP radical anion, that relaxes quantitatively to *E* before recombination.<sup>60</sup> Similarly as for **Design, 1**, we do not believe this is operating since the isomerisation is not quantitative. Furthermore, the azobenzenes used in this manuscript are rather electron rich (i.e. easy to oxidize: **AO, AN**) and if anything are therefore more prone to isomerize via an oxidation pathway, when in the presence of mostly cationic and relatively oxidising chromophores we use (**RhB, Cy**, etc). (Also, Hecht also showed the necessity of O<sub>2</sub>-free conditions in the electrocatalytic reductive pathway operating via the azobenzene radical anion,<sup>60</sup> but we never excluded O<sub>2</sub> and did not see any interruption of the assisted switching).

**4.6 - Multiphoton processes seem unlikely:**

We exclude multiphoton processes since we worked with very low intensity (≤mW/mm<sup>2</sup>) non-coherent nonfocussed LEDs, i.e., never approaching the power density required for sequential or concerted multiphoton absorption by small molecules, particularly as these ones have ~ns relaxation timescales on the chromophore and picosecond scales on the azobenzene.

**4.7 - Strong coupling in the ground state:**

(a) We would not expect the sensitised isomerisation to be such a general phenomenon (all MPs, all ACs) and yet to be so insensitive to linker lengths (not much slowing of rate when an additional PEG12 spacer is applied used) if strong coupling in the ground state were needed for isomerisation. (b) The dyads' absorption spectra were nearly the sum of the azobenzene and chromophore spectra, indicating no strong ground state coupling of their electronic systems, except that rhodamine conjugates of *cis*-AO/*cis*-AN had ca. 5% lower rhodamine absorption than expected (**Fig 2**).

**4.8 - Conclusions:**

We believe the major mechanism must be a net excited energy transfer from AC\*(S1), via some intermediate intramolecular pathway, to generate MP(T1), and where electron transfers are not involved. We refer to this simply as "[triplet] sensitisation" in the rest of the paper, but stress that (1) it is *absolutely general* across many molecular combinations in azobenzene dyads, including those with very low self-ISC quantum yields of the chromophores; and (2) that the *E/Z*-dependency and association-dependency leads us to believe that the triplet is being *induced* after collision of the azobenzene with the chromophore that has just absorbed before that chromophore can de-excite, including by fluorescing.

We believe that the apparently "energetically uphill" nature of this energy transfer has caused many previous researchers who have worked with covalently-bound azobenzene-chromophore dyads or tightly-associated systems to simply never even test whether this could operate. Indeed, we imagine that in many cases, puzzling older results will now make sense (e.g. in experiments with fluorophore-decorated azolipid vesicles) since significant long-wavelength pumping of azobenzene isomerisation may have been occurring.

Although it is unsatisfying to bring these results to the community without giving a satisfactory experimental mechanistic proof, we believe that due to the long-undisclosed, general, and powerful nature of this approach, disclosing this set of AC-MPs and their switching behaviour will productively draw attention to this high-performance possibility that can help address shortcomings of many previous photoswitch and photopharmaceutical concepts.

Finally, we note that in preparation for this project we have also tested AC-MP conjugates involving several other photoswitch types, e.g., heterostilbene, hemithioindigo, etc. So far, none of them have shown sensitised behaviour with *these* ACs. Firstly, that argues additionally against a "self-ISC" mechanism, since if that had operated, we would expect assisted switching of C=C photoswitches too: regardless of whether the self-ISC that initiates the process is then relayed to the MP indirectly e.g. by  $^1\text{O}_2$ , or directly by triplet energy transfer, or by photoredox (because these alternative MPs include representatives that are sensitive to those stimuli, but none responded in the dyads). With the knowledge of azobenzene's uniquely high spin-orbit coupling coefficients and unusual triplet chemistry, we thus feel confident that a triplet state is involved in our dyads' photocycle, in the sense that the azobenzenes have a special ability to *induce* the formation of that triplet and then harness it. We would be delighted to discuss other possibilities, and we are happy to share all remaining compound stocks from this study, with researchers wishing to make their own investigations.

**Note 5: *E/Z* potentials**

To test for conditional TET in auxiliary-azobenzene dyads, we first excluded dyads that can perform intramolecular singlet excited state photoredox. The process we needed to exclude is photooxidation of the azobenzene. We recently measured a dataset of highly absorbing organic chromophores with low  $\Phi_{\text{ISC}}$ , covering a range of excited state reduction potentials  $E_{\text{red}}^{\text{S}1}$  (key properties reproduced in **Table S9**, also incl. fluorescence excitation/emission (ex/em) spectra,  $\lambda_{\text{max}}$  ex/em,  $\phi_{\text{ISC}}$ , and  $E_{\text{red}}^{\text{S}0}$ ); as well as ground-state oxidation potentials for a range of *E*-azobenzenes (reproduced in **Tables S10-S11**).<sup>1</sup>

Although oxidation potentials for *Z*-azobenzenes were reported in older works, it is becoming clear that they may in fact not be measurable by voltammetry, and the best hypothesis is that they are a little lower than the corresponding *E*-potentials<sup>39</sup> (further discussion in ref<sup>1</sup>).

Therefore, these data allow choosing pairs of chromophores and azobenzenes that should *not* be able to perform photooxidation ( $E_{red}^{S^1}$  of the chromophore rather larger than  $-E_{ox}^{S^0}$  of the *E*-azobenzene, to give some buffer for the *Z*-oxidation that is expected to be slightly easier than *E*-oxidation (perhaps 0.06 V)<sup>1</sup>.

#### Note 6: Targets, features, and opportunities for azobenzene TET isomerisation dyads

Azobenzenes are considered generally bistable in photopharmacology if the half-life for their *Z*-isomer to spontaneously "relax" back to the thermodynamically preferred *E*-isomer under experimental conditions is hours or longer, since this is longer than most experimental timescales in biology. As a counterpart, azobenzenes with e.g. push-pull- or *para*, *para*-diamino patterns are "fast-relaxing" as their half-lives are < seconds, so they do not require photoswitching for *Z*→*E* isomerisation (but face many other challenges instead<sup>17</sup>). Bistable photoswitches however would greatly benefit from efficient mechanisms for *Z*→*E* photoisomerisation.<sup>8,29,61</sup> We focused on designing dyads for the three classes of "bistable" azobenzenes, here defined as those whose metastable *Z*-isomer spontaneously isomerises to the thermodynamic *E* isomer slower than typical experimental timescales (e.g. halflife > 12 hours). These bidirectionally-photoisomerisable switch types are the ones that have been the most useful in materials sciences and photopharmacology, and which would benefit the most from better *Z*→*E* completion.

Thus, we focus on dyads for bistable azobenzene switches bearing the three most common classes of substituents in 'classic' configurations (i.e. not tetra-*ortho*-substituted, which may change the electronics substantially): alkyl **AK**; *para*, *para*-bisalkoxylated **AO**; *para*, *para*-bisanilide **AN**. Electron-neutral **AK**-type azobenzenes are more difficult to oxidize ( $E_{1/2}(Az^+/Az) = E_{ox}^{S^0}$  ca. 1.7 V vs Fc), so, for TET, **AKs** could be paired with nearly all chromophores we measured ( $E_{red}^{S^1}$  typically 0.5 - 1.2 V vs Fc) without complications from photoredox-based processes. Electron-rich **AO** and **AN** ( $E_{ox}^{S^0}$  ca. 1 V vs Fc) can participate in photoredox-based switching with stronger photooxidants like the naphthoxazine Nile Blue (**NB**,  $E_{red}^{S^1} = 1.1$  V vs Fc), so such conjugates are also studied in the photoredox parallel article<sup>1</sup> to this paper; but simple **AOs/ANs** are compatible with e.g. xanthene and cyanine chromophore sensitisation.

Increasing the count of electron-rich substituents enables easier oxidation of the azobenzene (i.e. lower  $E_{ox}^{S^0}$ ) so allows weaker photooxidants e.g. xanthene and cyanine chromophores to operate them via a photoredox pathway. Not surprisingly, voltammetry indicates that *ortho* and *para* substituents contribute similarly (ca. 0.5 V lower for either *para-para* bisalkoxy [**CV-29** vs **CV-25**] and *ortho-ortho* bisalkoxy [**CV-20** vs **CV-25**], while *meta* substituents influence azobenzene oxidation potential rather less (ca. 0.15 V lower for **CV-6** vs **CV-2**). In a parallel paper<sup>1</sup> we are therefore using substituent tuning to make even xanthene-type dyes (**CPY**) suitable as photooxidizing auxiliaries for an electron rich-enough azobenzene (**CV-32**), to induce red-light triggered, quantitative *Z*→*E* isomerization.

However, bistable azobenzene scaffolds that have been used most in photopharmacology (see **Table S11**) should be able to be controlled by triplet energy transfer for photon-efficient, and optionally also near-quantitative *Z*→*E*, isomerization in the red/NIR region at least with xanthene and cyanine fluorophores.

Note that photoredox is distinguished from triplet energy transfer since photoredox is a quantitative isomerisation mechanism, suitable for reaching nearly 100% *E* isomer [may be minor residual energy transfer]. We use this as proof of which mechanism operates for a conjugate. Thus, we were careful to start photoresponse cycles always from an all-*E* state generated by thermal relaxation and *additionally verified by HPLC*, and to ensure that the first illumination phase was a long-wavelength phase (595-700 nm), before any UV phase: this is a sensitive way to determine whether the long-wavelength light gives quantitative *Z*→*E*



isomerisation (in which case, no change of absorption profile will be seen with the first long-wavelength phase, i.e. photoredox operates); or only gives mostly-complete isomerisation (i.e. sensitisation operates; see **Figure 2**).

### Note 7: Photoswitching Rates

Bulk photoisomerization rates were determined as described in **chapter 2.3**. To be able to compare bulk photoswitching rates we use and recommend half-power  $p_{1/2} = t_{1/2} \times I(\lambda)$ , with  $t_{1/2}$  being the isomerization half-time, and  $I(\lambda)$  the light intensity at wavelength  $\lambda$ .

$p_{1/2}$  makes the report of isomerisation rate *independent* of the light source and geometry used, and can comparably report photoisomerization efficiency. This compares more favourably than some current practice, which gives exhaustive parts lists and build descriptions for an apparatus but only reports switching half-times (or even worse, "switching took X minutes" without a definition of what was defined as completion), without intensity data.

We see that triplet energy transfer is somewhat faster than photoredox ( $p_{1/2} = 396$  mJ for **NB-AO**, photoredox vs  $p_{1/2} = 186$  mJ for **NB-AK**, triplet energy transfer).

We stress that the speed of the triplet energy transfer we observe is *not* directly dependent on the antenna chromophore's own intersystem crossing quantum yield. Eosin Y's  $\phi_{ISC}$  is ca. 100 times higher than those of fluorescein or rhodamine B ( $\phi_{ISC, \text{Eosin Y}} = 0.32$ ,  $\phi_{ISC, \text{Fluorescein}} = 0.03$ ,  $\phi_{ISC, \text{Rhodamine B}} = 0.0024$ ): but their triplet energy transfer-based isomerizations operate at similar half-powers at the chromophores' absorption maxima ( $p_{1/2, \text{EY-AK @ 533 nm}} = 3.9$  mJ,  $p_{1/2, \text{Fl-AK @ 508 nm}} = 4.6$  mJ,  $p_{1/2, \text{RhB-AK @ 564 nm}} = 4.6$  mJ). In fact, fluorophores from different structural classes, even if they have similar order of magnitude  $\phi_{ISC}$  ( $\phi_{ISC, \text{Rhodamine B}} = 0.0024$  and  $\phi_{ISC, \text{nile blue}} \ll 0.03$ ) are seen here to be able to operate at vastly different triplet energy transfer bulk switching rates ( $p_{1/2, \text{RhB-AK @ 564 nm}} = 4.6$  mJ,  $p_{1/2, \text{NB-AK @ 635 nm}} = 75$  mJ).

Bulk  $Z \rightarrow E$  isomerization rates based on triplet energy transfer for all conjugates are significantly faster compared to direct azobenzene photoisomerization ( $p_{1/2, \text{AK @ 490 nm}} = 209$  mJ).

Bulk  $E \rightarrow Z$  isomerization rates (@ 365 nm) are nearly not affected by attaching a fluorophore on the azobenzene ( $p_{1/2, \text{AK @ 365 nm}} = 20$  mJ,  $p_{1/2, \text{conjugates @ 365 nm}} = 13\text{-}24$  mJ).

### Note 8: Complex Switching

The photon-efficient, high-completeness, fully reversible long-wavelength photoresponse is the most important aspect of the dyads' behaviour. However, three minor, potentially interrelated features caught our attention (**Figure 2**). Firstly, **RhB-Z-AO** and **RhB-Z-AN** had ca. 5% lower absorption in the rhodamine peak than the corresponding  $E$  isomers. We assign this to similar strong interactions with the xanthene chromophore as has been reported intermolecularly from the 1970s<sup>35</sup>. Secondly, for a simple two-state  $E \rightleftharpoons Z$  photoswitching system, at high dilution so as to have near-constant illumination intensity throughout the sample at all times (carefully controlled: see **Supporting Information** at **Figure S1**), apparent first-order bulk population photoisomerisation kinetics should operate, so that each new illumination phase evolves to its PSS following an exponential. This was usually, but not always, observed. **RhB-AO**, **RhB-AN** (**Figure 2**) and **Cy5-AK** (**Figure 3**) are three cases where we observed apparently biphasic  $Z \rightarrow E$  kinetics for the long-wavelength sensitised process, regardless of the light source employed: a fast initial phase, then a slow drift. We did not pursue this phenomenon experimentally, since we were interested in the biological application of these dyads for fast and near-complete reversible switching, rather than how they resist or evolve under very prolonged illumination which is not physiologically relevant. We did however recover this feature during our modelling attempts (see **section 10**). We are happy to share our dyad stocks with researchers interested in pursuing this aspect further.



**Note 9: Scaffolded intermolecular sensitisation**

In general we consider *intermolecular* triplet energy transfer in solution as a photon-inefficient, concentration- and context-dependent (extrinsic) method for bulk photoswitching with poor prospects for applications to biology or materials.

However, there are cases where intermolecular proximity between sensitiser and photoswitch can be enforced, even if both are present at very low overall concentrations, and which might therefore overcome the disadvantages of *even self-ISC-triplet-based* switching that are associated to sensitiser triplet states not being quenched by the intended photoswitch (e.g. singlet oxygen generation and associated damage to biological and chemical components in the vicinity of the sensitiser as well as to the sensitiser itself). One such situation can be where the photoswitch forms a material that can advantageously be doped by substoichiometric amounts of the sensitiser, such that collisional triplet energy transfer from the sensitiser to the photoswitch is almost certain to out-compete other quenching routes. One biophysically relevant example of this would be doping azobenzene-lipid-membranes, that have been used for decades as biophysical model systems with rapidly-photomodulatable properties (permeability, thickness, fluidity, etc), with triplet sensitisers. During the preparation of this paper we identified the truly excellent 1987 report by Shimomura and Kunitake<sup>55</sup>, which had been sadly unknown to us. That paper studied quaternary ammonium (bisalkoxy)azobenzene lipid membranes in the presence of the thio-Cy3 sensitiser NK 2012 (ex/em 580/600). The paper is well worth reading in detail. As relevant to this work, they identified energy transfer from the thiocyanine to the azobenzene as a mechanism that alters the photostationary states otherwise reachable by direct azobenzene isomerisation (that paper's Figures 8, 10), due to sensitisation favouring the *cis-to-trans* photoconversion. They also postulated that the triplet energy transfer can propagate across *trans*-azobenzene monomers so that sensitised *cis-to-trans* isomerisation can effectively operate throughout the lipid bilayer with only a small sensitiser dopant percentage without requiring lateral diffusional mixing, which our data is not able to test, but which is an intriguing idea. The bulk of their results and interpretation are coherent with our study of vesicle-scaffolded intermolecular sensitised isomerisation in **chapter 2.8**.

**Note 10: Z→E limits to photopharmacology's translation from cells to *in vivo***

*This Note provides a fuller description of the limits on *in vivo* photopharmaceutical performance that are intrinsically imposed by the low-efficiency and substantial incompleteness of the direct green light Z→E photoisomerisation of usual azobenzenes (expands on the main text at **section 2.7**).*

Most *in vivo* photopharmacology studies in larger animals have not been able to harness *bidirectional* photoisomerisations, but have either (i) relied on separate administrations of all-*E*- vs of pre-isomerised, mostly-*Z*-reagent stocks; or (ii) relied on spontaneous *Z*→*E* switchoff; or else (iii) *have* been able to use typically implanted UV/violet light sources (fibre optic or LED) to perform the photon-efficient, more-complete all-*E*→partially-*Z* photoisomerisation step *in situ*, *but have not been able* to switch its biological effects back off again (the less-photon-efficient as well as less-complete *Z*→*E* direction). This last may seem counterintuitive, since the typically ~520 nm light used in the cuvette for mostly-*Z*→mostly-*E* isomerisation ("switching-mostly-off") penetrates tissues better than UV/violet light. However, due to the variety of light sources and illumination geometries that can be used, we consider that light penetration is typically **not** the problem that most limits photopharmacology (it is an *extrinsic* challenge for performance, that depends on the setting and equipment). Rather, we consider the two most severe problems instead to be the *intrinsic* photochemical limitations which no optics engineering can address:

**(1)** Azobenzene *Z*→*E* switching is incomplete. *In vivo*, inhomogeneous ligand concentrations as well as target expression levels may make it impossible for typical "best switch-off PSSs" (typically ca. 80:20 *E*:*Z*) to switch all cells off, even with ideal light penetration. This strongly relates to the mechanism of the photopharmaceutical: e.g.

(A) if using a freely-diffusing affinity switch [most common situation] where the *E* isomer is essentially non-binding, the problem will be severe, since that *E/Z ratio* implies very different absolute concentrations of *Z*-bound protein targets for high ligand exposure cells vs low exposure cells (PK), as well as for high-target-expression cells vs low-target-expression cells. Thus, even if violet light can switch nearly all cells from inactive all-*E* to an active partially-*Z* state, followup with even saturating green light may never return the whole cell population below the bioactivity threshold level of their *absolute Z* isomer concentration (it may even *raise* the overall amount of *Z* isomer, if the initial violet light isomerisation was strongly absorbed). The only way for an affinity switch reagent to ensure all cells can be switched off again, despite the inhomogeneity problem, is if the *Z*→*E* switching is nearly quantitative.

(B) However, if using an efficacy switch where both isomers have high-affinity binding but the *E* may be an antagonist while the *Z* is an agonist [rarest situation] then there may be no problem, since these systems are essentially concentration-independent in their action.

**(2)** Azobenzene *Z*→*E* photoswitching with green light is far less photon-efficient (here, we find typically 30 times less for **AK/AN/AO**-type switches) than its *E*→*Z* switching with violet light. Therefore, illuminations in the *Z*→*E* direction may run into problems of heating and phototoxicity if they are to be performed "as fast as" *E*→*Z* switching (especially near the emission point of fibre/LED sources). Light intensity can also be restricted by the power densities of the miniaturised sources that are compatible with free-moving small animals. The several practical and biological limits to illumination intensity thus hamper the ability to perform *Z*→*E* photoisomerisation on biologically appropriate timescales (or, isomerisations that would take 30 times longer than useful timescales, may simply have been missed).

These intrinsic limits on *Z*→*E* photoisomerisation performance have held back much of the promise of photopharmacology over its last twenty years, by limiting the translation of bidirectional photoisomerisations, especially of affinity switches, from cuvettes and cell culture (homogeneous ligand concentration and relatively well-controlled target expression) across to *in vivo* settings.

Here, we aimed to demonstrate that the sensitisation approach can *intrinsically* increase both photon efficiency and completeness of *Z*→*E* photoswitching, while leaving the satisfactory performance of the UV *E*→*Z* step untouched, and without requiring substantial redesign of the photoswitchable ligand (**Figures 5-6**). If so, this would provide proof of concept showing how to mend the bidirectionality of *in vivo* photopharmaceuticals by simple molecular retrofitting, rather than ever-more-complex illumination setups.

(As an aside: more reports have claimed to carry out *in vivo* bidirectional switching, than probably achieved it in practice. At least in some cases where the lack of appreciable absorption ought to have cautioned against interpreting isomerisation as being light-dependent, it would have been advisable to control that whenever light is applied with the aim to drive the *Z*→*E* direction, then, switching rates ought to increase linearly with applied light intensity, in order to rule out that spontaneous relaxation was the real driver of switch-off.)

Note also, that the choice of the sparsely labelled mGluR2 fusion receptor for cell work here has allowed us to prove stringently that the sensitisation is truly intramolecular (which the bulk solution measurements at 10 μM had supported, by comparison of the conjugate to the physical mixture), since reagent density at the cell surface, especially in the tissue slice setup, is likely to be far too low for intermolecular collisions to drive the assisted switching process. The "PORTL" photoswitchable tethered ligand approach used on mGluR2 has also been successful on e.g. dopamine receptor & serotonin receptor, and we believe it has an intrinsically much better match to the assisted switching paradigm than e.g. freely-diffusing ligands (including: avoids biodistribution problems in the case of strongly-localising auxiliary chromophores<sup>62</sup>).

## 2 UV/VIS spectroscopy and bulk photoisomerisation

### 2.1 General Methods

#### 2.1.1 UV/VIS setup

The UV/VIS setup used in this paper is shown in **Figure S3a**. UV/VIS experiments were performed with a Cary 60 spectrophotometer (Agilent Technologies). Experiments were done in a 1 cm optical path length, 2 mm wide High Precision Cell (Hellma Analytics 108-002-10-40) filling samples to typically 0.9 cm height (volume 180  $\mu$ L). Typically, 5 or 10 mM DMSO stocks were diluted in steps of 1:10 to reach 10  $\mu$ M solutions into a mixture of acetonitrile (HPLC grade) and distilled water (1/1 v/v). To exclude impurities from previous runs or dilution of the samples by residual solvent, the cuvettes were cleaned after each experiment by rinsing with MeCN (HPLC grade, 3 times) and drying under a stream of nitrogen or compressed air.

For medium-intensity sample illumination during UV/VIS, a pE-4000 LED light source (CoolLED; controlled by the open source software  *$\mu$ Manager* (version 1.4.22)) was used.<sup>63</sup> The light was guided towards the cuvette via a liquid light guide (AHF Analysetechnik AG L52-4LG3; length = 3 m; diameter = 3 mm). If not otherwise stated, the intensity of all LEDs was adjusted to give 50 mW/mm<sup>2</sup> output intensity at the liquid light guide exit. The spectral properties of the LEDs are given in **Chapter 2.1.3**.

For near-monochromatic illumination during UV/VIS, a Polychrom V Monochromator light source (Till Photonics; controlled by PolyCon 3.2.3 software) was used. The light was guided towards the cuvette via a liquid light guide (ThorLabs LLG05-4H; length = 1.2 m; diameter = 5 mm). The slitwidth was set to 5 nm and the intensity to 100% unless otherwise stated. The intensity at the exit of the liquid light guide was measured with a Thorlabs PM100USB Powermeter equipped with a Thorlabs S130VC sensor; intensity data are shown in **Chapter 2.1.3**.

For illumination during UV/VIS, our aim was to ensure reproducible incident intensity profiles throughout the whole sample volume, aiming at applying *homogeneous light intensity throughout the whole sample cell, and having homogeneous analyte concentration throughout the cell, under conditions that allow reliable extraction of photoisomerisation rates and timecourses* (incl. profiles of approaching PSS). For this we took precautions, including: (1) ensuring constant distance and angle from light guide exit to sample, and constant geometry within each run (over multiple wavelengths) as well as between runs (across multiple samples); and (2) minimising evaporation, so the sample concentrations stay constant and homogeneous throughout the sample cell, even in long experiments. For these, the cuvettes were used with a Teflon lid through which a centered hole (diameter = 4.9 mm or 6.9 mm, that tightly fits the exit head of the liquid light guides used) was bored. After inserting the light guides, which blocks the bore, the lids were additionally sealed onto the cuvettes using *Parafilm*<sup>®</sup>. The dimensions and setup for the cuvette and attached illumination sources are shown in **Figure S3b** (pE-4000 LED source) and **Figure S3c** (Polychrome V monochromatised source). We also made sure that (3) the light guides were positioned at such a distance, that the whole sample cell volume experiences similar light intensity; (4) stray incident light is blocked/minimised; (5) optical path length of illumination (typically 9 mm to bottom of cuvette, but only ca. 5 mm to bottom of optical window) was short enough, so that at the analyte concentrations and the applied illumination wavelengths used, typically less than 25% of the illumination beam intensity was lost through the sample (i.e. delivers relatively homogeneous illumination intensities, and no significant inner filter / shielding effects).

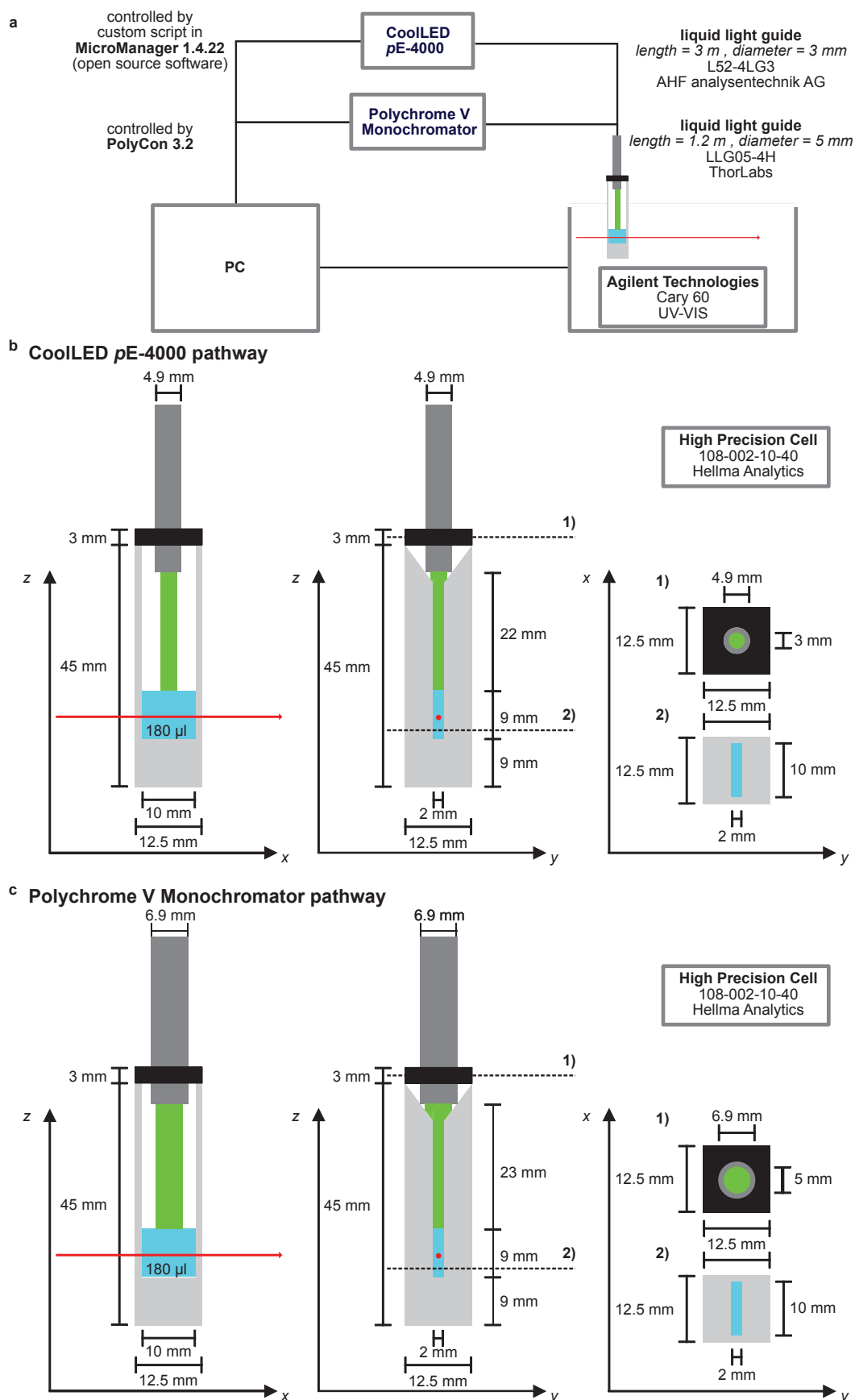


**Figure S3:** UV/Vis setup used in this study: a) Spectrophotometer, and light sources used. b) dimensions of cuvette, sample solvent and light supply for pE-4000 setup. c) dimensions of cuvette, sample solvent and light supply for Monochromator setup.

### 2.1.2 General Methods for UV/VIS and bulk photoisomerisation

**Action spectra** were recorded by measuring an UV/Vis spectrum (from 750 – 300 nm) every 10 s. Azobenzene containing samples (10  $\mu\text{M}$ , dilution prepare as mentioned in chapter 2.2.1) were applied in their all-*trans* state (enabled by keeping the DMSO stock at 60 °C overnight before measurements and taking precautions for light exclusion e.g. using amber glass vials and wrapping in aluminum foil. After measuring spectra of the all-*E* sample for 5 min and confirming no changes of absorption profile (can happen if compound aggregates / precipitates, if bubbles form, etc), the illumination protocol of the pE-4000 light source was started. Alternating cycles of 365 nm (1 min at 50 mW/mm<sup>2</sup>) and  $\lambda_2$  ( $\lambda_2$  = sequentially 770 nm, 740 nm, 660 nm, 635 nm, 595 nm, 525 nm, 490 nm, 460 nm, 435 nm, 405 nm, and 385 nm, each 5 min at 10 mW/mm<sup>2</sup>) were performed. The usual measurement time was 72 min. The data were analyzed by extracting the absorbance values at the absorption maximum of the azobenzene *E*-isomer over time. Isomeric ratios at two or three of the photostationary states were determined by HPLC analysis (see **chapter 5.1**), and these were used to transform absorbance values to %-*trans* values by a linear calibration curve (see **chapter 5.2**).

**Analysis:** Curve fitting (e.g. monoexponential fits for thermal relaxation or for illumination-stimulated photoisomerisations) was performed in Graphpad Prism 8 software for MacOS.

### 2.1.3 Light Source Properties for bulk photoisomerisations

By default, we wished to characterise *approximately* how compound bulk photoisomerisation rates *and* photostationary states depend on illumination wavelength, across the UV/VIS spectrum. These depend on the wavelength/intensity profiles of the light sources.

In most cases, we were content to use the pE-4000 as a cost-effective fixed array of LED wavelengths, most of which have acceptably narrow emission profiles ca. FWHM~20-30 nm (**Figure S4a**), making use of their relatively high intensities (**Figure S4b-c**) to rapidly approach PSSs during photoswitching and to study many compounds serially, and with calibrated and reproducible performance that is quite accurately intensity- and time-modulated through the control software. In this way we could profile relative rates of approaching PSS, and PSS composition, with values that were *technically reproducible* and which are informative for general performance in other chemical or biological applications, under either LED or narrower (laser, filtered, or monochromatised) light sources. (When incident intensity powers are quoted, these are understood as total optical power over the LED emission spectrum).

The "PSS" values obtained with LEDs are not truly reproducible single-wavelength values; but only in some settings were LED sources insufficient to characterise the *intrinsic performance of the conjugates*, and in all cases the LED sources were sufficient for characterising the responses to long-wavelength illuminations of the auxiliary chromophore which are the main interest of this work. [LED sources would be insufficient if illuminating at spectral regions where the photoisomerisation response changes *both rapidly and meaningfully* with wavelength; which is the case (1) between the photoswitch's  $\pi \rightarrow \pi^*$  and  $n \rightarrow \pi^*$  bands [typically in the region 360-430 nm], and/or (2) where the fraction of the absorption coefficient that is due to the photoswitch ("direct excitation") rather than the antenna chromophore is high *and* also changes rapidly with wavelength (typically also in the region 360-430 nm, but some photoswitch-antenna pairs have additional regions of sensitivity where the antenna absorption is comparable to the photoswitch's but one increases as the other decreases). For simplicity, only in such situations have we annotated the PSS values or rate data to indicate that either an LED or the monochromator was used (see e.g. **Table S1**).]

We also note that it will always be possible to find a monochromatic wavelength that gives *equal or greater completion* of photoisomerisation, than can any broader source (e.g. LED). Therefore, the PSS values obtained with the pE-4000 offer the *minimum* performance that a compound can achieve.

In some cases we used the Polychrome V monochromator as light source to deliver near-monochromatised light (typ. 5 nm bandwidth), either when we wished to (a) find true *intrinsic* PSS values that would be reproducible with e.g. laser illumination; or to (b) study the relative



bulk photoswitching rates at low incident intensity (compare **Figure S4d** vs **Figure S4b**). The Polychrome V does not have filters to eliminate first harmonic (half wavelength) light; but we confirmed by spectral measurement that no harmonics are present at LIG exit when the monochromator is set to wavelengths below 650 nm [arises since the *transmission* of the light guide is so low below 325 nm that it eliminates these harmonics]; but, the fractional intensity of first harmonic light above 680 nm setting (i.e. harmonic >340 nm) reaches ca. 10-20% of the intended >680 nm wavelength intensity. However, rather than install filters, we instead restricted ourselves to interpreting monochromator-reliant data for only the wavelength range below 650 nm, since wavelengths above 650 nm were easily accessed without a harmonic and without problematic interpretation by using the multi-LED source as written above.

The PSS values of most interest to know accurately are those established for red/NIR conjugates, under long wavelength excitation of the antenna moiety (>600 nm) at or near its absorption maximum, i.e. where the azobenzene has essentially zero absorption in both isomers and therefore measurements do not suffer from the "insufficiency of LED measurement" described above. To test how PSSs across the spectrum depend on the light source, standard PSS measurements with closest-fit wavelengths using the pE-4000 as source were compared to PSS measurements with illumination at the antenna absorption maxima using the monochromator as source. As expected, the PSS values were more source-dependent region at 365 nm than at long wavelengths (**Table S1**).

**Table S1:** PSS composition under monochromatic illuminations v.s. LED illuminations

Compound	pE-4000		Monochromator	
	PSS <sub>LED-365</sub> %E	PSS <sub>λ</sub> %E (nm)	PSS <sub>mono-365</sub> %E	PSS <sub>λ</sub> %E (nm)
	5	71.5 (490)	6	71 (490)
<b>RhB-AK</b>	42	89 (595)	38.5	88.5 (564)
<b>FI-AK</b>	29.5	67.5 (525)	19	66 (508)
<b>EY-AK</b>	36	76.5 (525)	42.5	87.5 (535)
<b>NB-AK</b>	18.5	98 (635)	28.5	96.5 (635)

**Table S1** shows that the true monochromatic PSS composition for the conjugates is well predicted by the pseudo-PSS compositions under illumination with LEDs with nearby emission maxima, when the antenna's absorption maximum is substantially lower in energy than the longest appreciable absorption of the azobenzene (note too the case of **EY-AK**, with 10% more complete PSS under longer-wavelength monochromatic illumination, illustrating the case of true monochromatic light being able to deliver more complete switching than broadband). The PSS or pseudo-PSS compositions at or around 365 nm where both photoswitch and antennas absorb strongly, are more dependent on the source profiles (**Figure S4**).

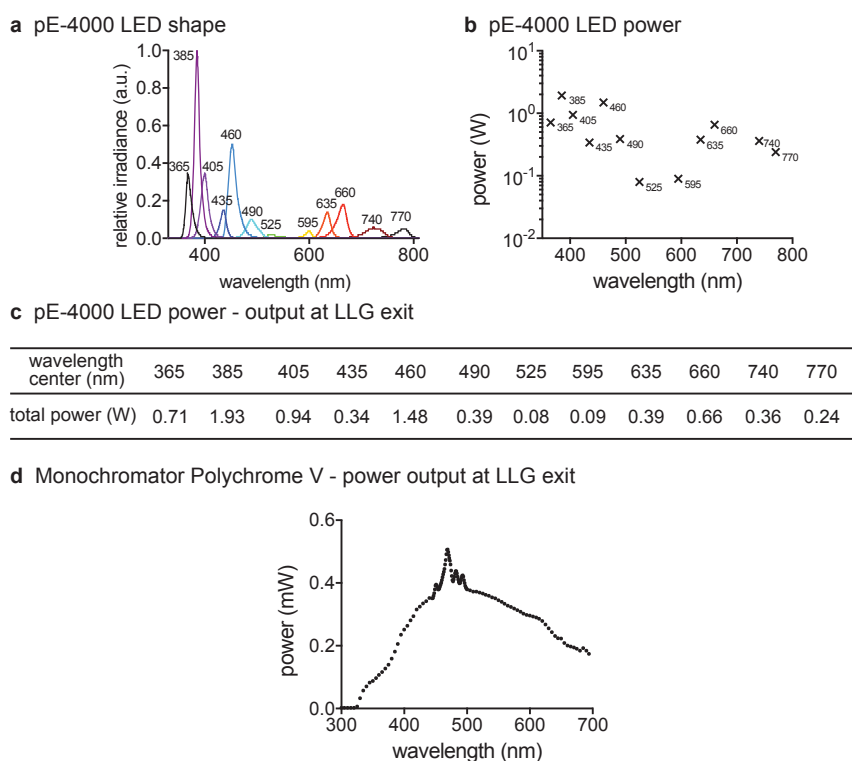


**Figure S4:** (a-c) Spectral and max total power from a pE-4000 as reported at the exit of a liquid light guide of same specifications as used in this work (data provided by *CoolLED Ltd*; our measurements match the relative total power; light guide diameter 3 mm [7 mm<sup>2</sup> exit]; 100% intensity setting). (d) Spectral intensity from the Polychrome V as measured at the exit of a liquid light guide of same specifications as used in this work (measured with a Thorlabs PM100USB Powermeter equipped with a ThorlabsS130VC sensor; light guide diameter 5 mm, i.e. surface area 20 mm<sup>2</sup>) in the wavelength range 300-694 nm, when set to 5 nm slit width and 100% intensity setting.

The coupling of each light source into its light guide sets different beam divergence profiles (the monochromator beam is more closely parallel than the LEDs); the light guide diameters are also different (so different proportions of the exit intensity will be lost when directed into the 2×10 mm cuvette). These result in different illumination profiles in the sample volume. However, we believe that due to divergence and reflections, the two light sources give comparably homogeneous illumination throughout the sample volumes. Since each guide probably has its own fraction of exit intensity that is transmitted to the sample (not measured), we expect that a given output power from one guide would give a different intensity in the sample surface area than the same nominal output power from the other: i.e. the in-sample intensities are probably a constant proportion of the nominal exit intensities. However, we note that the half-energy we found to be needed for 635 nm isomerisation of **NB-AK** from PSS-365 to PSS-635 with the pE-4000+guide (190 mJ nominal at exit) is very similar as with the monochromator+guide (60 mJ at exit), despite the two measurements being performed with different beam shapes and at exit intensities that can differ by a factor of ca. 400 (5.5 mW/mm<sup>2</sup> nominal exit for pE-4000 at 10%; 0.015 mW/mm<sup>2</sup> nominal exit for monochromator), which gives confidence in these assumptions and in the comparability of these data.

## 2.2 Thermal Relaxation

The three major azobenzenes used in this work all have far slower spontaneous relaxation under normal cell-free assay conditions than the rates of photoswitching (**Figure S5**). Thus we are confident in assigning the fast rates seen during illumination to photoswitching, without spontaneous relaxation as a confounding issue.

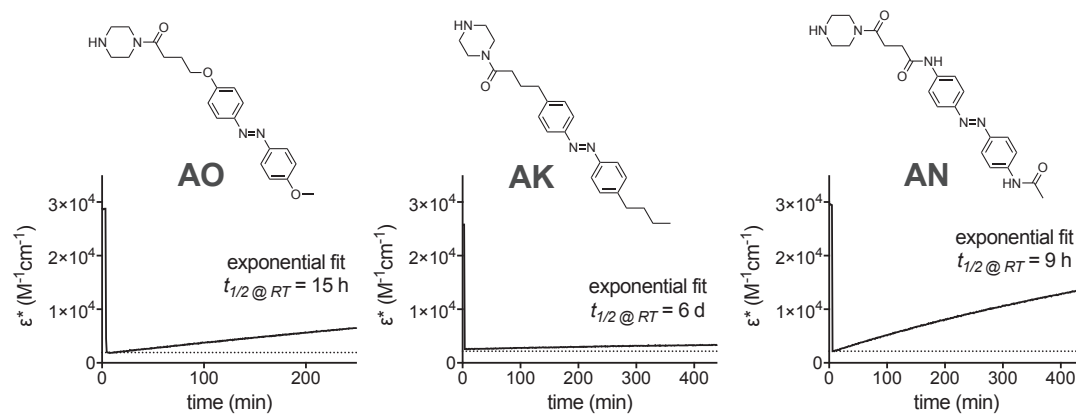


**Figure S5:** Thermal relaxation of photoswitches **AO**, **AK** and **AN** was performed at  $10 \mu\text{M}$  in water/acetonitrile (50/50) at room temperature.  $\text{PSS}_{\text{LED-365}}$  was reached by illumination with 365 nm LED ( $50 \text{ mW}/\text{mm}^2$ ) until constant absorption, then illumination was stopped and absorbance was monitored for long enough to perform an accurate first-order fit.  $\epsilon^*$  is the apparent molar extinction coefficient of the *E/Z* mixture.

## 2.3 Bulk Population Photoswitching

### 2.3.1 $\epsilon(\lambda)$ and PSS composition (LED assessment)

Data on significant azobenzenes, chromophores, and conjugates is tabulated in **Table S2**.

**Table S2:** (top) extinction coefficients at center wavelengths of the pE-4000 LED channels, for azobenzenes **AK**, **AO** and **AN**, as *E* and *Z* isomers (from pure isomer spectra extracted from the HPLC-DAD trace), and for selected fluorophores. (bottom) % trans values at PSS of those wavelengths, as extracted from photoswitching action spectra; "--" indicates *no change in the absorption spectrum, from a UV-PSS starting spectrum, during illumination at that wavelength* (i.e. there was no light response occurring); ">" indicates a lower bound in cases where the photostationary state was not reached during just the standard 5 min illumination cycle; "<" indicates that no significant extinction coefficient value could be extracted from the noise (i.e. absorption is essentially zero).

$\epsilon(\lambda)$ [ $10^2 \times \text{M}^{-1}\text{cm}^{-1}$ ]	770 nm	740 nm	660 nm	635 nm	595 nm	525 nm	490 nm	460 nm	435 nm	405 nm	385 nm	365 nm
<b>AK-E</b>	< 0.5	< 0.5	< 0.5	< 0.5	< 0.5	0.5	3	8	10	8	21	127
<b>AK-Z</b>	< 0.5	< 0.5	< 0.5	< 0.5	< 0.5	1	6	15	21	12	4	2
<b>AO-E</b>	< 0.5	< 0.5	< 0.5	< 0.5	< 0.5	1	4	14	29	65	168	255
<b>AO-Z</b>	< 0.5	< 0.5	< 0.5	< 0.5	< 0.5	4	15	31	32	14	6	8
<b>AN-E</b>	< 0.5	< 0.5	< 0.5	< 0.5	< 0.5	1	8	25	49	125	244	287
<b>AN-Z</b>	< 0.5	< 0.5	< 0.5	< 0.5	< 0.5	3	16	30	31	14	6	15
<b>RhBpip</b>	< 0.5	1	3	3	71	349	75	16	23	32	24	43
<b>Cy3</b>	1	1	1	1	3	594	250	62	18	9	6	7
<b>EYpip</b>	< 0.5	2	2	2	2	782	255	55	19	21	17	15
%-E at PSS( $\lambda_{\text{LED}}$ )	770 nm	740 nm	660 nm	635 nm	595 nm	525 nm	490 nm	460 nm	435 nm	405 nm	385 nm	365 nm
<b>AK</b>	--	--	--	--	--	77%	71%	74%	75%	65%	25%	3%
<b>AO</b>	--	--	--	--	--	91%	82%	68%	56%	14%	4%	3%
<b>AN</b>	--	--	--	--	--	86%	77%	66%	53%	12%	6%	6%
<b>RhB-AK</b>	--	--	--	> 83%	> 88%	92%	91%	85%	86%	83%	62%	40%
<b>RhB-AO</b>	--	--	--	> 85%	> 89%	97%	95%	82%	73%	42%	25%	25%
<b>RhB-AN</b>	--	--	--	> 87%	> 93%	95%	76%	76%	66%	29%	18%	22%
<b>Cy3-AK</b>	--	--	--	--	> 78%	79%	79%	77%	79%	70%	33%	9%
<b>Cy3-AO</b>	--	--	--	--	> 91%	95%	93%	81%	66%	24%	12%	11%
<b>Cy3-AN</b>	--	--	--	--	> 85%	87%	86%	75%	61%	25%	18%	19%

### 2.3.2 Bulk photoswitching efficiency with moderate intensity LED light

Kinetics for photoisomerizations of azobenzenes or conjugates were recorded by monitoring absorbance at a single wavelength (with **AO**: 358 nm; **AK**: 337 nm; **AN**: 369 nm), with one datapoint taken every 0.0375 s. To ensure that reproducible data were being acquired (e.g. negligible inner filter effect through the sample; negligible rate errors introduced by the time resolution limitation of 0.0375 s as data interval, in the case of fast isomerisations at high powers), we acquired multiple kinetic runs while stepping down the incident power over a 20-fold range (from 353 mW down to 18 mW, which is the minimum rated power for some LEDs in the pE-4000 source). Monoexponential fitting was used to extract half-times  $t_{1/2}$ ; after adjusting for the illumination power applied, the half-powers  $p_{1/2}$  were calculated. These parameters, with fit  $r^2$  values, are given in **Table S3** and fit curves are shown in **Figure S6**. As described above, for the half-power calculation, the total optical output power (OOPT, leftmost column, in mW) is assumed to irradiate the total cuvette surface area (2 mm  $\times$  10 mm) without loss, i.e.  $p_{1/2}$  is calculated as (OOPT  $\times$   $t_{1/2}$  / 20) mJ/mm<sup>2</sup>; while the LLG beam exit light is not collimated, we assume that the angular irradiance is approximately the same for all LED wavelengths due to standardisation of in-coupling within the light engine, so the loss factor between OOPT and power delivered to the sample should be the same for all wavelengths, making the half-powers comparable *between different wavelengths and compounds in the LED measurements* (as long as the  $\epsilon(\lambda)$  vs. LED bandwidth profiles are taken into account).

From experiences with stepping intensities here and in other work, we assume that data acquired with halftime  $\geq$ 5-10 s, at intermediate OOPT (35 or 71 mW, i.e. 3 - 10 mW/mm<sup>2</sup>), is most accurate; still, the good agreement between  $p_{1/2}$  values at different OOPTs is satisfying.

**Table S3:** pE-4000 power (at indicated wavelength), and the half-time, half-power, and goodness of fit parameter for monoexponential fitting of  $Z \rightarrow E$  and  $E \rightarrow Z$  photoisomerization time courses of selected compounds. Half-powers are the power *applied* (in a mostly-optically-transparent sample, since low concentration and path length), which gives a better description of the practical efficiency of photoswitching for a biological end-user than does the more typical "power *absorbed*". Note that these are experimentally convenient LED wavelengths, but are not the chromophores' best-absorbed wavelengths (and some of the LEDs have broad spectra), therefore these results should only be used to roughly compare rates between dyads with the same chromophore.

LLG optical output power, total [mW]	NB-AK [18.5% $E \rightarrow 98\% E$ ] @ 635 nm: $p_{1/2} \sim 9.8 \text{ J/mm}^2$			RhB-AN [28.5% $E \rightarrow 92.5\% E$ ] @ 595 nm: $p_{1/2} \sim 3 \text{ mJ/mm}^2$			RhB-AO [25% $E \rightarrow 97.5\% E$ ] @ 595 nm: $p_{1/2} \sim 2 \text{ mJ/mm}^2$		
	$t_{1/2}$ [s]	$p_{1/2}$ [ $\text{J/mm}^2$ ]	$R^2$	$t_{1/2}$ [s]	$p_{1/2}$ [ $\text{mJ/mm}^2$ ]	$R^2$	$t_{1/2}$ [s]	$p_{1/2}$ [ $\text{mJ/mm}^2$ ]	$R^2$
353.5	0.6	10	0.9592	[a]	-	-	[a]	-	-
176.8	1.1	10	0.9884	[a]	-	-	[a]	-	-
70.7	2.6	9	0.9985	0.9	3	0.9663	0.7	3	0.9047
35.4	5.6	10	0.9994	1.7	3	0.9764	1.3	2	0.9689
17.7	11.2	10	0.9998	3.3	3	0.9924	2.5	2	0.9956
	RhB-AK [42% $E \rightarrow 89\% E$ ] @ 595 nm: $p_{1/2} \sim 4 \text{ mJ/mm}^2$			FI-AK [29% $E \rightarrow 67\% E$ ] @ 525 nm: $p_{1/2} \sim 1 \text{ mJ/mm}^2$			* EY-AK [36% $E \rightarrow 76\% E$ ] @ 525 nm: $p_{1/2} \sim 0 \text{ mJ/mm}^2$ *		
OOPT [mW]	$t_{1/2}$ [s]	$p_{1/2}$ [ $\text{mJ/mm}^2$ ]	$R^2$	$t_{1/2}$ [s]	$p_{1/2}$ [ $\text{mJ/mm}^2$ ]	$R^2$	$t_{1/2}$ [s]	$p_{1/2}$ [ $\text{mJ/mm}^2$ ]	$R^2$
70.7	1.1	4	0.9697	0.3	0.9	0.9559	0.08	0.3	0.9515
35.4	2.1	4	0.9821	0.4	0.7	0.9872	0.11	0.2	0.9679
17.7	3.8	3	0.9969	0.7	0.6	0.9975	0.16	0.1	0.9716
	Cy3-AK [11% $E \rightarrow 79\% E$ ] @ 595 nm: $p_{1/2} \sim 92 \text{ mJ/mm}^2$			Cy3-AO [13% $E \rightarrow 91\% E$ ] @ 595 nm: $p_{1/2} \sim 70 \text{ mJ/mm}^2$			Cy3-AN [22% $E \rightarrow 85\% E$ ] @ 595 nm: $p_{1/2} \sim 93 \text{ mJ/mm}^2$		
OOPT [mW]	$t_{1/2}$ [s]	$p_{1/2}$ [ $\text{mJ/mm}^2$ ]	$R^2$	$t_{1/2}$ [s]	$p_{1/2}$ [ $\text{mJ/mm}^2$ ]	$R^2$	$t_{1/2}$ [s]	$p_{1/2}$ [ $\text{mJ/mm}^2$ ]	$R^2$
70.7	27.3	96.4	1.0000	20.7	73.1	0.9997	27.5	97	0.9999
35.4	51.5	91.0	1.0000	38.6	68.3	1.0000	52.6	93	0.9999
17.7	100.1	88.5	1.0000	76	67.1	1.0000	101.7	90	1.0000
	AO [6% $E \rightarrow 82\% E$ ] @ 490 nm: $p_{1/2} \sim 19 \text{ mJ/mm}^2$			AO [6% $E \rightarrow 91\% E$ ] @ 525 nm: $p_{1/2} \sim 38 \text{ mJ/mm}^2$			AO [91% $E \rightarrow 6\% E$ ] @ 365 nm: $p_{1/2} \sim 2 \text{ mJ/mm}^2$		
OOPT [mW]	$t_{1/2}$ [s]	$p_{1/2}$ [ $\text{mJ/mm}^2$ ]	$R^2$	$t_{1/2}$ [s]	$p_{1/2}$ [ $\text{mJ/mm}^2$ ]	$R^2$	$t_{1/2}$ [s]	$p_{1/2}$ [ $\text{mJ/mm}^2$ ]	$R^2$
353.5	1.3	23	0.9998	[a]	-	-	0.1	1.7	0.9886
176.8	2.2	20	0.9998	[a]	-	-	0.2	1.6	0.9953
70.7	4.9	18	0.9999	12.6	45	0.9999	0.5	1.7	0.9987
35.4	9.9	18	0.9999	20.6	36	1	1.2	2.0	0.9994
17.7	19.5	17	0.9999	36.6	32	1	2.7	2.4	0.9996
	AK [4.5% $E \rightarrow 77\% E$ ] @ 525 nm: $p_{1/2} \sim 89 \text{ mJ/mm}^2$			AN [8.5% $E \rightarrow 86\% E$ ] @ 525 nm: $p_{1/2} \sim 27 \text{ mJ/mm}^2$					
OOPT [mW]	$t_{1/2}$ [s]	$p_{1/2}$ [ $\text{mJ/mm}^2$ ]	$R^2$	$t_{1/2}$ [s]	$p_{1/2}$ [ $\text{mJ/mm}^2$ ]	$R^2$			
70.7	29.5	104.3	0.9999	8.9	31.4	0.9998			
35.4	48.5	85.8	1.0000	14.7	26.0	0.9998			
17.7	86.1	76.1	1.0000	26.3	23.3	0.9999			

[a] = not tested, since the maximum LED power is 10 mW/mm<sup>2</sup> (525 and 595 nm). \* EY-AK data has a shaded grey background since the halftimes under this illumination intensity were of similar size as the time interval between datapoints, so we considered these data as overestimates of the true half-powers. See **Table S5** for an evaluation under lower illumination powers, which is also performed at the wavelengths where the chromophores absorb maximally and therefore can better be compared between dyads involving different chromophores.



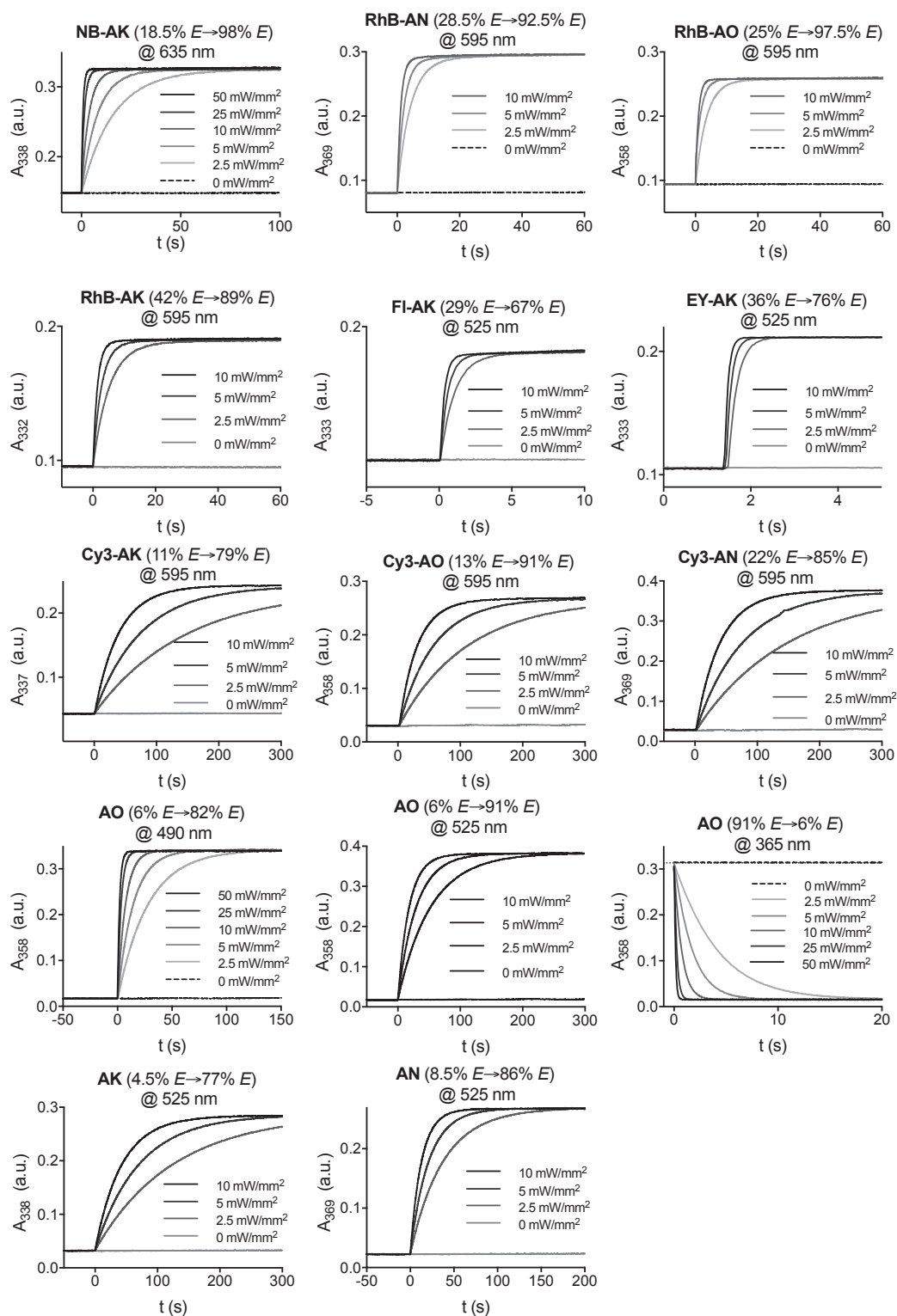


**Figure S6:**  $Z \rightarrow E$  and  $E \rightarrow Z$  isomerization of selected compounds at indicated light intensities (pE-4000 LEDs; here indicated as light intensities at liquid light guide exit, for 3 mm LLG).

### 2.3.3 Bulk photoswitching efficiency with low intensity monochromatic light

We also acquired similar isomerisation kinetics using the monochromator as light source, to have a near-monochromatic incident beam which is also at much lower intensity than that of the pE-4000 source (ca. 10-100 times lower, depending on wavelength and intensity setting used) and so allows longer acquisitions before reaching PSS, which gives more reliable bulk photoswitching rate fits that are less sensitive to early timing errors (**Figure S7**). Kinetic traces were recorded at 338 nm (absorption maximum of **AK**). % *E* isomer values were calculated using the calibration curves from **chapter 6.2**. We confirmed by independent measurements that the bandwidth set for the monochromator emission in the control software (here 5 nm FWHM), with the expected triangular emission intensity profile, were delivered at all wavelengths chosen for these studies.

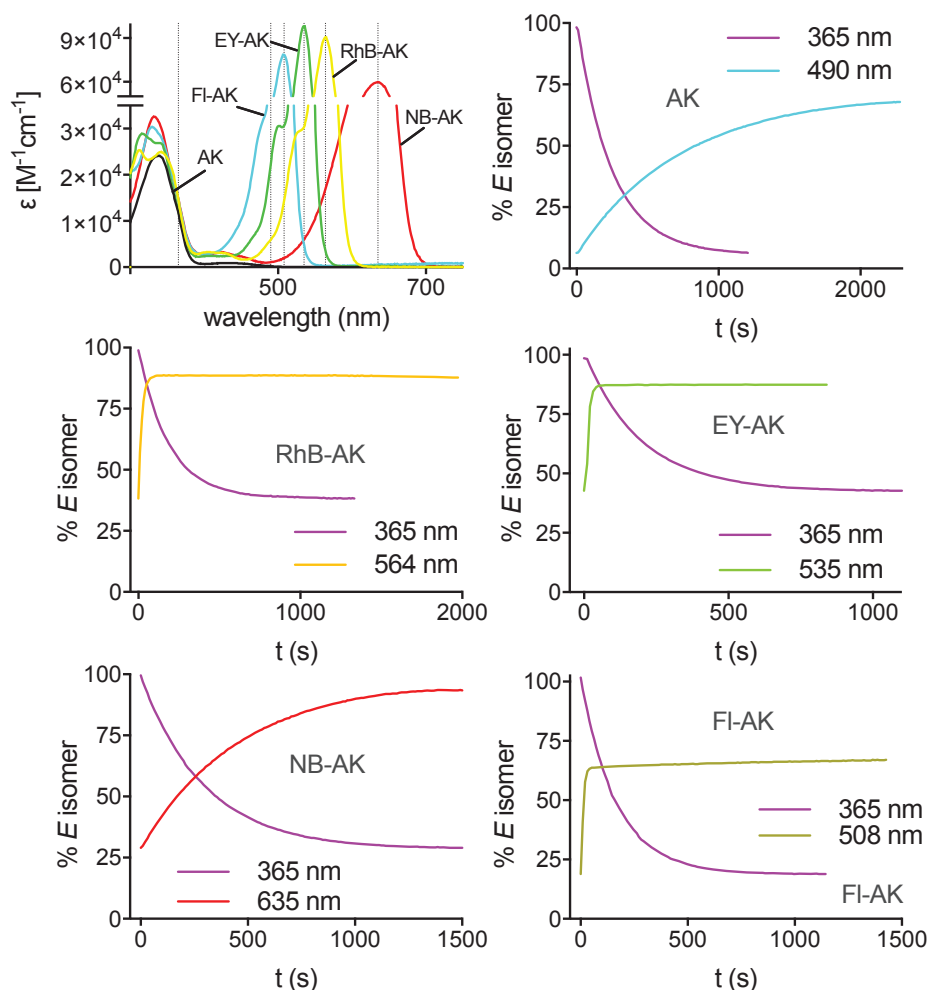


**Figure S7:** UV/Vis spectra of compounds used (top-left); kinetic traces for *E*→*Z* (365 nm) and *Z*→*E* (490 nm for **AK** or absorption maximum of the fluorophore) isomerization. For total optical output powers driving these isomerisations, see **Table S5**.

Kinetics of the monochromator-switched data were fitted by monoexponential fit in GraphPad Prism (one phase association) by equation:

$$Y = Y_0 + (\text{Plateau}-Y_0) * (1-\exp(-Kx))$$

Best-fit values are given in **Table S4** and power (at indicated wavelength), half-time, goodness of fit parameter and half power in **Table S5**.

**Table S4:** Best-fit values for photoswitch kinetics. For the optical powers for these isomerisations, see **Table S5**.

compounds	$\lambda_{\text{excitation}}$ (nm)	Y0	Plateau	K
AK	365	100.5	5.87	0.004053
	490	5.927	71.11	0.001352
RhB-AK	365	99.54	38.40	0.005350
	564	37.76	88.49	0.04961
EY-AK	365	100.5	42.50	0.004996
	533	39.90	87.48	0.06291
FI-AK	365	101.8	18.87	0.006023
	508	18.36	65.73	0.07197
NB-AK	365	99.50	28.48	0.003389
	635	28.23	96.64	0.002259

**Table S5:** Monochromator power (at indicated wavelength), half-time, goodness of fit parameter and half power for  $E \rightarrow Z$  and  $Z \rightarrow E$  isomerization of selected compounds.

AK [100% $E \rightarrow$ 6% $E$ ] @ 365 nm				AK [6% $E \rightarrow$ 71% $E$ ] @ 490 nm			
Power [mW]	$t_{1/2}$ [s]	$R^2$	$p_{1/2}$ [mJ/mm <sup>2</sup> ]	Power [mW]	$t_{1/2}$ [s]	$R^2$	$p_{1/2}$ [mJ/mm <sup>2</sup> ]
0.116	171.0	0.9999	0.99	0.407	512.6	1.0000	10.4
RhB-AK [100% $E \rightarrow$ 38.5% $E$ ] @ 365 nm				RhB-AK [38.5% $E \rightarrow$ 88.5% $E$ ] @ 564 nm			
Power [mW]	$t_{1/2}$ [s]	$R^2$	$p_{1/2}$ [mJ/mm <sup>2</sup> ]	Power [mW]	$t_{1/2}$ [s]	$R^2$	$p_{1/2}$ [mJ/mm <sup>2</sup> ]
0.116	129.6	0.9999	0.75	0.328	14.0	0.9966	0.23
EY-AK [100% $E \rightarrow$ 42.5% $E$ ] @ 365 nm				EY-AK [42.5% $E \rightarrow$ 87.5% $E$ ] @ 535 nm			
Power [mW]	$t_{1/2}$ [s]	$R^2$	$p_{1/2}$ [mJ/mm <sup>2</sup> ]	Power [mW]	$t_{1/2}$ [s]	$R^2$	$p_{1/2}$ [mJ/mm <sup>2</sup> ]
0.116	138.7	0.9997	0.81	0.359	11.0	0.9924	0.20
FI-AK [100% $E \rightarrow$ 19% $E$ ] @ 365 nm				FI-AK [19% $E \rightarrow$ 66% $E$ ] @ 508 nm			
Power [mW]	$t_{1/2}$ [s]	$R^2$	$p_{1/2}$ [mJ/mm <sup>2</sup> ]	Power [mW]	$t_{1/2}$ [s]	$R^2$	$p_{1/2}$ [mJ/mm <sup>2</sup> ]
0.116	115.1	0.9999	0.67	0.373	9.6	0.9928	0.23
NB-AK [100% $E \rightarrow$ 28.5% $E$ ] @ 365 nm				NB-AK [28.5% $E \rightarrow$ 96.5% $E$ ] @ 635 nm			
Power [mW]	$t_{1/2}$ [s]	$R^2$	$p_{1/2}$ [mJ/mm <sup>2</sup> ]	Power [mW]	$t_{1/2}$ [s]	$R^2$	$p_{1/2}$ [mJ/mm <sup>2</sup> ]
0.116	204.5	1.0000	1.19	0.244	306.9	0.9997	3.74

Recall that the powers quoted for monochromator data are not expected to match in an absolute sense to those of the pE-4000 data, due to the different beam profiles; but we did expect a relatively constant scaling factor between them (see **section 2.1.3**). Recall also that additional differences between the LED and monochromator rates can be expected when a broad LED profile preferentially hits "one side" of an absorption band, whereas the narrow monochromator emission profile either hits the band centrally or "misses" it. It is always the monochromator data that is more reliably intercomparable, due to its precision and accuracy. (Even so, the powers and half-powers listed are powers at beam exit, which therefore give an overestimate of the true applied energies for switching).

## 2.4 Physical Mixture Action spectrum

The action spectrum of an equimolar mixture of **NB-COOH** and **AK** (Figure S8) does not show significant enhancement of its red light switching kinetic, or red-shifting of the wavelength for *cis*→*trans* isomerization. The action spectrum was acquired as described in **chapter 2.1.2**, although without calibration of the %*E|Z*: this was not needed, since the qualitative result is clear, that intermolecular energy transfer is not occurring (i.e. the physical mixture "**NB+AK**" has essentially identical photoresponses as **AK** alone; the slightly slower 525 nm response is attributed to the optical inner filter effect at concentration 10 μM).

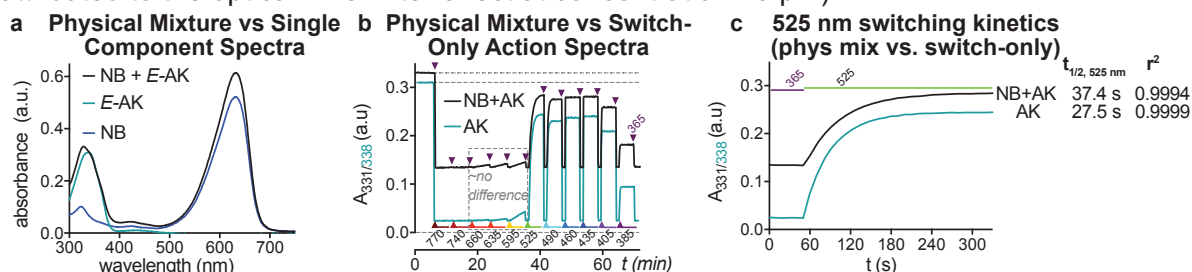


**Figure S8:** a) UV/Vis spectra of equimolar mixture of **NB-COOH** + **E-AK**, **E-AK**, and **NB-COOH**; b) Action spectra of equimolar mixture of **NB-COOH** + **AK** vs. **AK**; c) Photoswitch kinetics and half-times of an equimolar mixture of **NB-COOH** + **AK** and **AK** at 525 nm illumination (Intensity: 10 mW/mm<sup>2</sup>).

## 2.5 NBD-AK: benefits of assisted switching at typical azobenzene wavelengths

Another example of covalent azobenzene-fluorophore conjugate is **NBD-AK** (Figure S9). We have included this conjugate to illustrate *roughly* some features that result when the chromophore's absorption is in the region where the azobenzene itself is absorbing (even though, naturally, their absorptions are at quite different relative intensities, with the chromophore being more strongly-absorbing here than the azobenzene's weak  $n \rightarrow \pi^*$  bands). The action spectrum was acquired as described in **section 2.1.2** (Fig S9), and like in **section 2.4** this was done without calibrations to % *E|Z* isomer to simply show qualitative features.

As expected, **NBD-AK** shows assisted photoswitching like all other conjugates tested.

(a) The first important result is that assisted switching may also be used to boost the photon efficiency of photoswitching, without occupying an additional "channel" of light application: e.g. the 525 nm response of **NBD-AK** (half time here: 4 s) is much faster than for **AK** alone (halftime: 27 s), *despite* the optical inner filter effect (compare to **section 2.4**). This is only true if the efficiency of the assisted switching can be comparably high, or higher, than the efficiency of direct azobenzene isomerisation, *when both are run at the same wavelength* (we do also show a similar efficiency result elsewhere, but only comparing e.g. red light assisted efficiency to blue light azobenzene efficiency) - which is a non-obvious, but very pleasing, result.

(b) As expected, the PSS values reached show a different pattern to that of **AK** alone, e.g. all PSS values from 525 nm to 405 nm are almost the same %*E*; whereas for **AK**, they are, as expected, wavelength dependent (e.g. 77%*E* at 525 nm vs 65%*E* at 405 nm). We interpret the wavelength-independence of **NBD-AK** in this range as showing that the very much stronger **NBD** absorption drowns out the absorption strength of both *E*&*Z* azobenzene isomers (whose relative intensity is wavelength-dependent) such that the PSS values are set, over this entire range, by energy transfer from the strongly-absorbing and -transferring **NBD** chromophore. Therefore any researcher using an **NBD-AK**-based tool need only apply a wavelength in this 120 nm-broad range, to reach the same PSS%*E*. This makes the usually crucial choices or availability of "specific illumination wavelengths for specific, different PSS values" irrelevant: and can represent a real advantage for practical applications of assisted switching tools.

(c) Next we will discuss the PSSs established. Rough inspection of the UV-Vis spectra (Fig S9) vs. those for **AK** alone (Fig 3d) shows that the PSS-365 nm is roughly unchanged from that of **AK** alone (see e.g. epsilon values at 300 nm), i.e. ca. 97%*Z*. This means the PSSs across the **NBD** region of 525-405 nm are ca. 57%*E*. Thus, an experimenter could use illumination at 525 nm to rapidly drive all-*E* → 43%*Z* isomerisation, whereas long-wavelength

all-*E* → significant-%*Z* photoswitching of normal azobenzenes is usually both far slower (ca. 15 times less *E*→*Z* conversion per unit 525 nm light applied), and even if saturating light can be applied, it is much less complete at PSS (20%*Z*).

**Therefore, assisted triplet-switching conjugates have the potential to act as effective systems for visible-light *E*→*Z* photoswitching**, even on thoroughly "ordinary" azobenzenes such as **AK** for which visible light is usually seen as (at best) an inefficient wavelength for "*Z*→*E*" photoswitching.

This can make this mode of energy transfer an excellent complement to the assisted photoredox-switching mode (presented in our parallel paper<sup>1</sup>) which can only drive isomerisation towards the all-*E* population; and it will encourage the re-evaluation of how "ordinary" azobenzenes were or are handled in the presence of molecularly-associated chromophores (as we study further in the vesicle experiments).

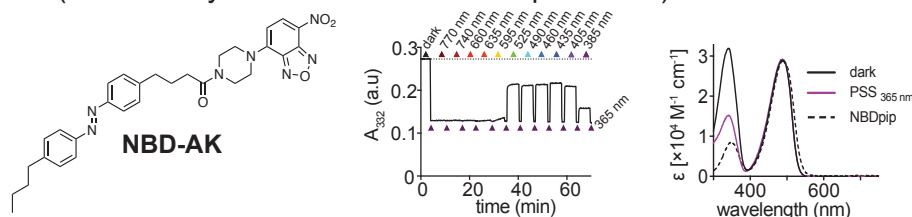


**Figure S9:** Structure, action spectrum, and UV/Vis spectra for "spectrally overlapped" conjugate **NBD-AK** (UV-Vis spectra in all-*E* dark state and at PSS-365 nm, vs the parental fluorophore **NBDpip** alone (no azobenzene)).

(d) Finally, a corollary of the wavelength-independent PSSs seen here is that, to linearly tune the assisted photoswitching rate, *the total chromophore-absorbed energy* should be tuned. Conventionally, in photopharmacology, one would do this by linearly varying (i) *illumination power at fixed wavelength*; or equivalently on a microscope, the dwell time per pixel for pixel-scanning illumination modes. However, here we show that the assisted switching allows to also do this by (ii) *changing the centre wavelength or beam profile of the illuminating beam to reduce/increase the switching rate by a reduction/increase in spectral overlap, without changing the equilibrium photoswitching outcome (PSS)*. We feel this is a significant result, particularly for microscopy where our experience has often been that direct photoswitching (360 - 515 nm) tends to cause unwanted photobleaching, since the direct wavelengths are also absorbed by fluorescent protein markers as well as endogenous chromophores. With assisted switching, if bleaching of a marker is caused at one wavelength (say, at 647 nm illumination which is intended for switching a Cy5 conjugate, but which is also absorbed by red fluorophore), then the relatively strong absorption of most potential antenna chromophores, coupled with the intrinsic efficiency of the assisted switching process, should allow more biologically innocent photoswitching instead at a range of other wavelengths, chosen to reduce background biological absorption: which will reduce photodamage to other chromophores, while reaching the same switching outcomes.

## 2.6 Extinction coefficient determination

*The data used for extinction coefficient determination were collected for this study and a parallel study, and are reported in both papers.*<sup>1</sup>

We determined the molar extinction coefficients  $\epsilon$  of *isolated fluorophores* in 1:1 MeCN:H<sub>2</sub>O mixtures. Two 10 mM DMSO stocks of each compound were prepared (compound weight > 1 mg). The stocks were diluted 1:100 (990  $\mu$ L 1:1 MeCN:H<sub>2</sub>O and 10  $\mu$ L DMSO stock) then 1:10 (900  $\mu$ L 1:1 MeCN:H<sub>2</sub>O and 100  $\mu$ L 1:100 dilution) to reach a final concentration of 10  $\mu$ M. Each stock was diluted 3 times independently, giving 6  $\epsilon$  values for each compound. **Figure S10** shows the mean and standard deviation of  $\epsilon$  from each stock; the six datapoints were then pooled for overall  $\epsilon$  values (**Table S6**). We assumed that the conjugates'  $\epsilon$  values at wavelengths >550 nm are essentially the same as the fluorophores; this was supported by the decent additivity of spectra [e.g.  $\epsilon(\lambda)_{E-NB-AK} \approx \epsilon(\lambda)_{NB} + \epsilon(\lambda)_{E-AK}$ ].



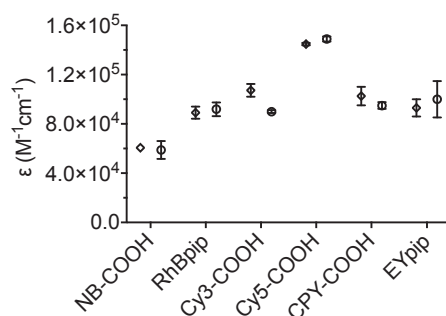


**Figure S10:** Experimentally determined molar extinction coefficients  $\epsilon$  (mean $\pm$ SD) for two independently prepared stocks for each compound, each evaluated in triplicates.

**Table S6:** Fluorophore molar extinction coefficients  $\epsilon$  at  $\lambda_{max}$  in 1:1 water:MeCN mixture with standard deviation, as a mean of 6 datapoints.

	$\lambda_{max}$	$\epsilon(\lambda_{max})$ ( $\times 10^3 M^{-1} cm^{-1}$ )	SD $\epsilon(\lambda_{max})$ ( $\times 10^3 M^{-1} cm^{-1}$ )	n
<b>NB-COOH</b>	634	59.8	4.8	6
<b>RhBpip</b>	564	90.6	4.9	6
<b>Cy3-COOH</b>	546	98.7	10.1	6
<b>Cy5-COOH</b>	643	147.0	2.7	6
<b>CPY-COOH</b>	608	98.9	6.6	6
<b>EYpip</b>	533	96.6	11.0	6

We then wished to assign *effective molar extinction coefficients* in the UV, at the  $\pi \rightarrow \pi^*$  band maximum wavelength for the *E*-azobenzene motifs within each conjugate (determined separately, **Fig S15**: e.g. maximum 338 nm for **AK**). The effective  $\epsilon$  for the azobenzene *moieties* within the azobenzene-fluorophore conjugates were then calculated as

$$\text{effective } \epsilon (\text{azobenzene}) = \epsilon (\text{fluorophore-azobenzene}) - \epsilon (\text{fluorophore}) \quad (\text{Table S7})$$

and "mean" values were found by averaging over values available (right column, **Table S7**).

**Table S7:** Effective molar extinction coefficients  $\epsilon$  of azobenzenes at  $\lambda_{max}$  in 1:1 water:MeCN calculated by subtracting  $\epsilon$  (fluorophore) from  $\epsilon$  (fluorophore-azobenzene) [mean of different conjugates, unless *not applicable*].

all $\epsilon$ : $\times 10^3 M^{-1} cm^{-1}$	$\epsilon$ (Cy3-X – Cy3-COOH)	$\epsilon$ (RhB-X – RhBpip)	$\epsilon$ (NB-X – NB-COOH)	$\epsilon$ (Cy5-X – Cy5-COOH)	$\epsilon$ (EY-X – EYpip)	$\epsilon$ (CPY-X – CPY-COOH)	mean $\epsilon(X)$ at $\lambda$
X = <b>AK</b>	20.1	21.6	21.5	35.6	21.9		<b>24</b> at 338 nm
X = <b>AO</b>	22.9	26.0	27.8	/	/		<b>25.5</b> at 358 nm
X = <b>AN</b>	26.7	28.4	31.6	/	/		<b>29</b> at 369 nm
X = <b>PST2</b>	/	/	/	/	/	29.3	<b>29</b> at 371 nm
X = <b>BAG /</b> <b>BGAG<sub>12,400</sub></b>	/	/	26.9	26.3 (v1) 29.4 (v2)	/	/	<b>27.5</b> at 377 nm
X = <b>AO(OMe)<sub>4</sub></b>	/	/	14.4	/	/	/	<b>14.5</b> at 331 nm

## 2.7 Linker length-dependent photoswitch kinetics

**BGAG<sub>12,400</sub>-Cy5-v1** and **BGAG<sub>12,400</sub>-Cy5-v2** differ only in the position where the **Cy5** fluorophore is attached (**Figure 5c**: **v2** places it further from the azobenzene by an additional PEG12 spacer, on top of the ca. 20 heavy atoms in the linker chain separating these motifs in **v1**). We compared how the distance between azobenzene and fluorophore influences the kinetics of energy transfer-based  $Z \rightarrow E$  isomerization (**Fig S11**).

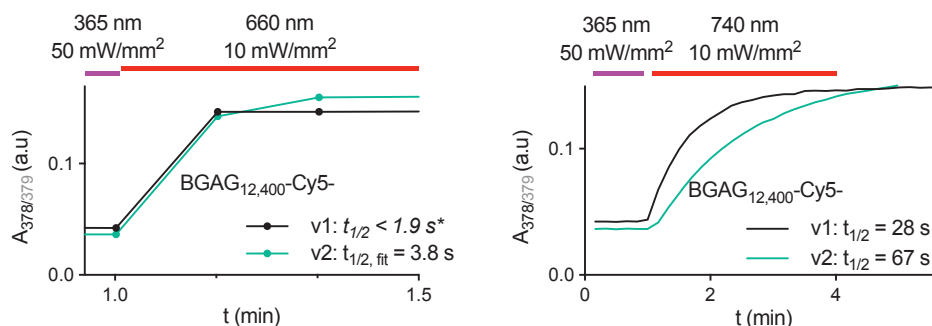


**Figure S11:** mostly- $Z \rightarrow$  mostly- $E$  photoswitch kinetics of **BGAG<sub>12,400</sub>-Cy5-v1** vs **BGAG<sub>12,400</sub>-Cy5-v2** under 660 nm and 740 nm illumination. Datapoints were acquired every 10 s, limiting the time resolution with 660 nm.

The **-v1** compound, where they are in closer proximity, had a sensitised switching rate that was only  $\sim 2.5$  times as fast as that of **v2** (calculated on the 740 nm data for reliability). We assume that this indicates its greater tendency for the two motifs to collide with each other during the  $\sim$ nanosecond excited state lifetime of the **Cy5** motif, which is reasonable, although the difference was smaller than we had expected for the structural change. From the interpretation discussed for **NBD-AK** that the chromophore must simply absorb light, for its driven PSS to be reached, we expect that the ratio of the assisted switching rates between **v1** and **v2** should be constant at any wavelength, as the conjugates feature the same antenna and photoswitch: thus we would expect this 2.5-fold ratio to have been the same at 660 nm, implying a half-time of 1.5 s for **v1** (as the maximum possible fitted half-time with the observed 10 s datapoint interval is 1.9 s, this is coherent with but not absolutely confirmable from data). We note also, that the half-powers for 660 nm photoswitching of the rather far-separated **v2** conjugate is not drastically greater than conjugates with much "shorter" chromophore-azobenzene distances. Here we measure "long" **BGAG<sub>12,400</sub>-Cy5-v2**  $t_{1/2} \sim 3.8$  s at 660 nm (56 heavy atoms in the linker chain; **Fig S11**); for a comparison to a "shorter" conjugate with a similar match between its  $\epsilon(\lambda)$  and the applied LED  $I(\lambda)$  [see **Fig 3** and **Fig S4a**] we consider the 635 nm isomerisation of **NB-AK** (14 heavy atoms in the linker chain), which at 10 mW/mm<sup>2</sup> performs 18.5%  $E \rightarrow 98\%$   $E$  with  $t_{1/2} \sim 2.6$  s (**Table S3**). Although this simplistic use of chain length as a proxy for distance ignores molecular folding and intrinsic association, etc, it can be argued that a 33% reduction of *what is actually a very photon-efficient* assisted switching rate (**NB-AK**), is a small penalty to pay for being able to much further separate the photoswitch from its antenna chromophore without losing the practical benefit of assisted switching [as is confirmed to still operate in cell and slice biology: **Figure 5-6**].

In passing, we note that although the thermal relaxation of unlabelled **BGAG<sub>12,400</sub>** was appreciable in the cell-free cuvette switching (**Fig 5e**), instead when it is conjugated to the receptor, it is bistable for the experimental timecourse (**Fig 5g**), matching previous results. This simplifies the analysis of unlabelled and labelled **BGAGs** in cellular electrophysiology.

## 2.8 Vesicle-Scaffolded Intermolecular Sensitisation

We had set out to test (**Supporting Note 1.8**) whether anchoring a catalytic amount of a triplet sensitiser chromophore to azobenzene lipid bilayer vesicles would allow photocatalytic, red/NIR-sensitised,  $Z \rightarrow$  *nearly-all-E* photoswitching even in intermolecular mode, due to molecular proximity (**Fig S12**).

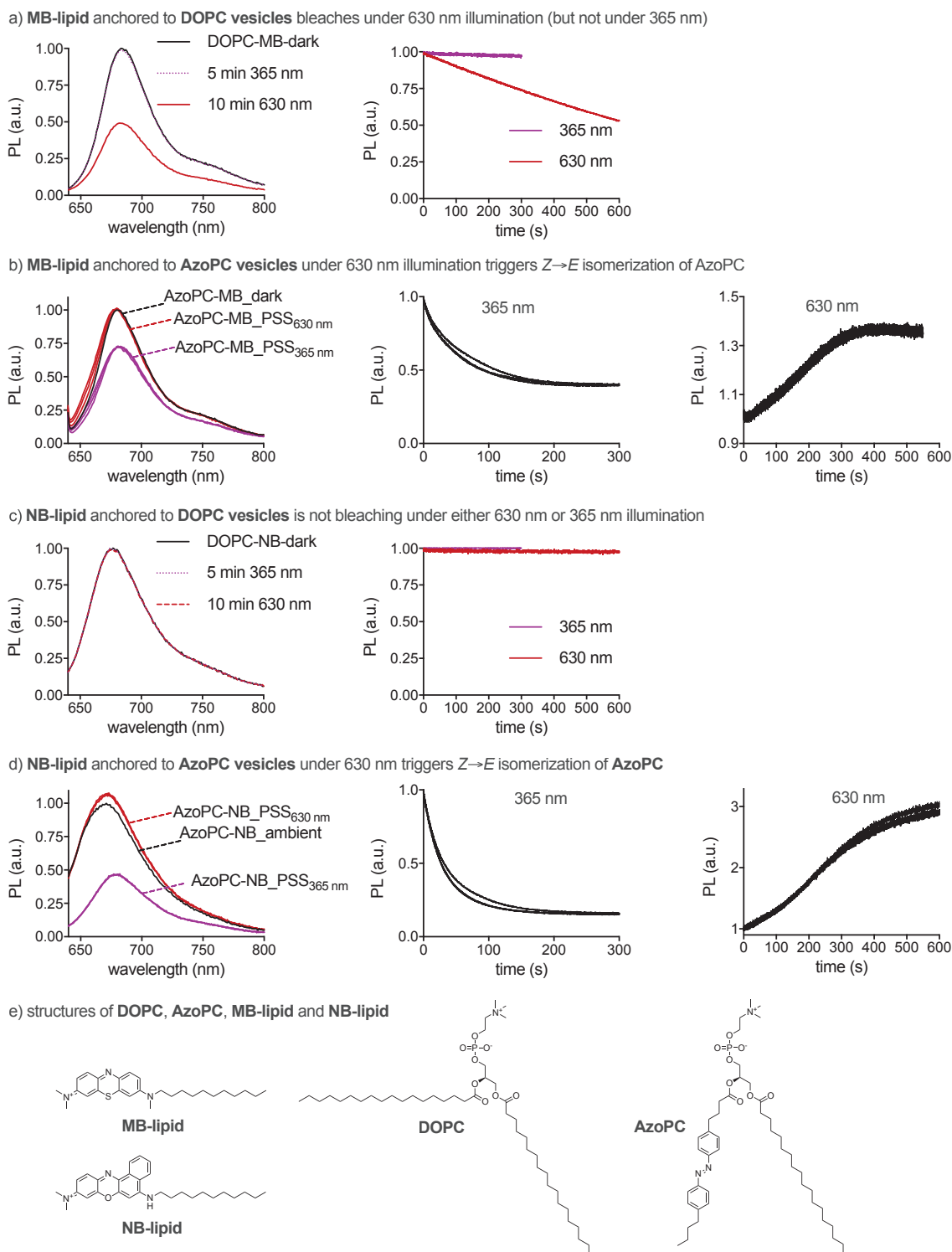


**Figure S12: vesicle-anchored sensitised photoswitching** as an intermediate scenario between intermolecular sensitisation in free solution, and intramolecular sensitisation. All graphs in panels (b) and (d) show two or three traces per illumination condition (experiment: dark state → 365 nm → 630 nm → 365 nm → 630 nm with one optional additional 365/630 nm cycle). PL (a.u.) is photoluminescence [fluorescence] intensity measured in arbitrary units, although the intensity scaling is kept constant during each experiment (so curves on the same graph are quantitatively comparable). Left-side graphs in each panel show PL spectra at discrete timepoints during the illumination sequences; right-hand graphs in each panel show continuously sampled PL kinetics during the annotated illumination phases, with the PL value at the start of each phase reset to a value of 1.0: so, the overlap of these traces highlights the photoreversibility of the switching processes and the absence of photobleaching.

We synthesised  $C_{11}$ -alkylated chromophores **NB-lipid** and **MB-lipid** and assembled lipid bilayer vesicles from either the well-studied commercially available photoswitchable "AzoPC"

(Avanti Polar Lipids, USA) or else the saturated lipid DOPC (**Fig S12e**). We doped the vesicles with 1 mol% of the chromophores relative to lipid, and irradiated the vesicles during absorbance and fluorescence measurements, following standard vesicle preparations and photoisomerisation procedures as already reported<sup>3,64</sup>. Several features stand out:

**(1)** Coherent with the mechanisms proposed by Shimomura and Kunitake<sup>55</sup> (see **Supporting Note 9**) and with the results in this paper and its companion photoredox paper<sup>1</sup>, we saw that the fluorescence intensity of the chromophore is strongly affected by the azolipid's isomer state (**Fig S12b,d**), so can be used as a sensitive readout for azobenzene isomer state if and only if the chromophore is not photobleached during the experiment (which was confirmed, see legend to **Fig S12**). This isomer-dependency also matches our solution-state fluorescence studies of molecularly dissolved dyads with intramolecular assisted switching, that show *E/Z*-dependent fluorescence intensity (**Fig S24**).

Thus, a large *E/Z*-dependency of fluorescence in a system is probably a proxy readout for the presence of strong assisted switching that is also stronger for one isomer relative to another, i.e. an indication (though, not a necessary indication) of efficient assisted switching.

**(2)** Similarly to the solution state intermolecular measurements, the **MB-lipid** photobleaches under 630 nm light with DOPC vesicles, that feature no azobenzenes (**Fig S12a**). However, similarly to the photostability and cyclical reversibility of switching observed for e.g. intramolecularly-operable **EY-AK**, when **MB-lipid** is anchored to AzoPC vesicles it no longer photobleaches under 630 nm illumination, but instead the azolipid is isomerised to a nearly-all-*E* state; and multiple cycles of 365 nm ( $\rightarrow$ mostly-*Z*) and 630 nm ( $\rightarrow$ mostly-*E*) can be used to photoreversibly switch the azolipid (**Fig S12b**). These are coherent with the energy of the self-ISC **MB-lipid** triplet state being harvested by templated intermolecular transfer to the azobenzene lipid it is associated thanks to partitioning *before* photodamage can occur (and, after harvesting, it is expected to trigger *Z* $\rightarrow$ mostly-*E* isomerisation).

**(3)** Also consistent with intermolecular and intramolecular results in this paper and its companion photoredox paper<sup>1</sup>, we saw that: (i) **NB-lipid** was photostable even with DOPC vesicles (**Fig S12c**), coherent with its photochemistry *as an isolated chromophore* being overwhelmingly within the singlet manifold (no self-ISC), unlike that of **MB**; (ii) **NB-lipid**-doping left similar *E* $\rightarrow$ *Z* photoswitching kinetics at 365 nm as doping with **MB-lipid** (**Fig S12b/d**), coherent with both dopant chromophores being nearly optically transparent at 365 nm compared to the azobenzene lipid that they dope; (iii) **MB** and **NB** were similarly photon-efficient in sensitising *Z* $\rightarrow$ *E* photoswitching under 630 nm where the azobenzene is transparent (**Fig S12b/d**; note: the bimodal kinetics match observations from Shimomura and Kunitake<sup>55</sup> concerning a "lag phase" in photocatalytic sensitised photoswitching, which we did not expect to see in dyads, and indeed did not see in that context).

**Thus**, partitioning of a sensitiser chromophore to force molecular proximity with an excess of azobenzene enables driving photocatalytic intermolecular sensitised photoswitching [catalytic with respect to chromophore loading] with performance that mirrors that of the intrinsic intramolecular conjugates used elsewhere in this paper. We believe that similar intermolecular systems may find many uses from materials through to biophysics and biology, allowing e.g. to read out proximity, or to exploit it to write isomer-dependent functions.

**We also note that** photoswitchable azobenzene-based lipid membrane constituents have been used for years with great success at up to 100% membrane constitution. In our opinion, the azobenzenes' success is not just because photoresponsive lipids are a powerful idea, because photouncaged or other photoswitch-chemotype lipids have never approached such percentages. We contend that their success is because they, highly unusually, both quench and do not produce triplet manifold photochemistry (Antonenko and Pohl have published a strong cautionary tale showing that photo-effects of another switch chemotype on membranes, that were previously assumed to be mechanical, are almost certainly due to simple phototoxicity and attack on (poly)unsaturated lipids)<sup>65</sup>. Therefore we are sure that biological lipid membranes are one context where azobenzene switches are *irreplaceable*.

### 3 Fluorescence Excitation / Emission from fluorophores

Excitation and emission spectra were recorded with a Cary Eclipse Spectrophotometer from Agilent Technologies (**Figure S13**). Experiments were performed in a 1 cm × 3 mm fluorescence cuvette (Hellma Analytics, 105-251-15-40). 10 mM DMSO stocks of respective compounds were diluted to 1 μM samples in acetonitrile (HPLC grade), except fluorescein and quinacrin which were measured at 10 μM.

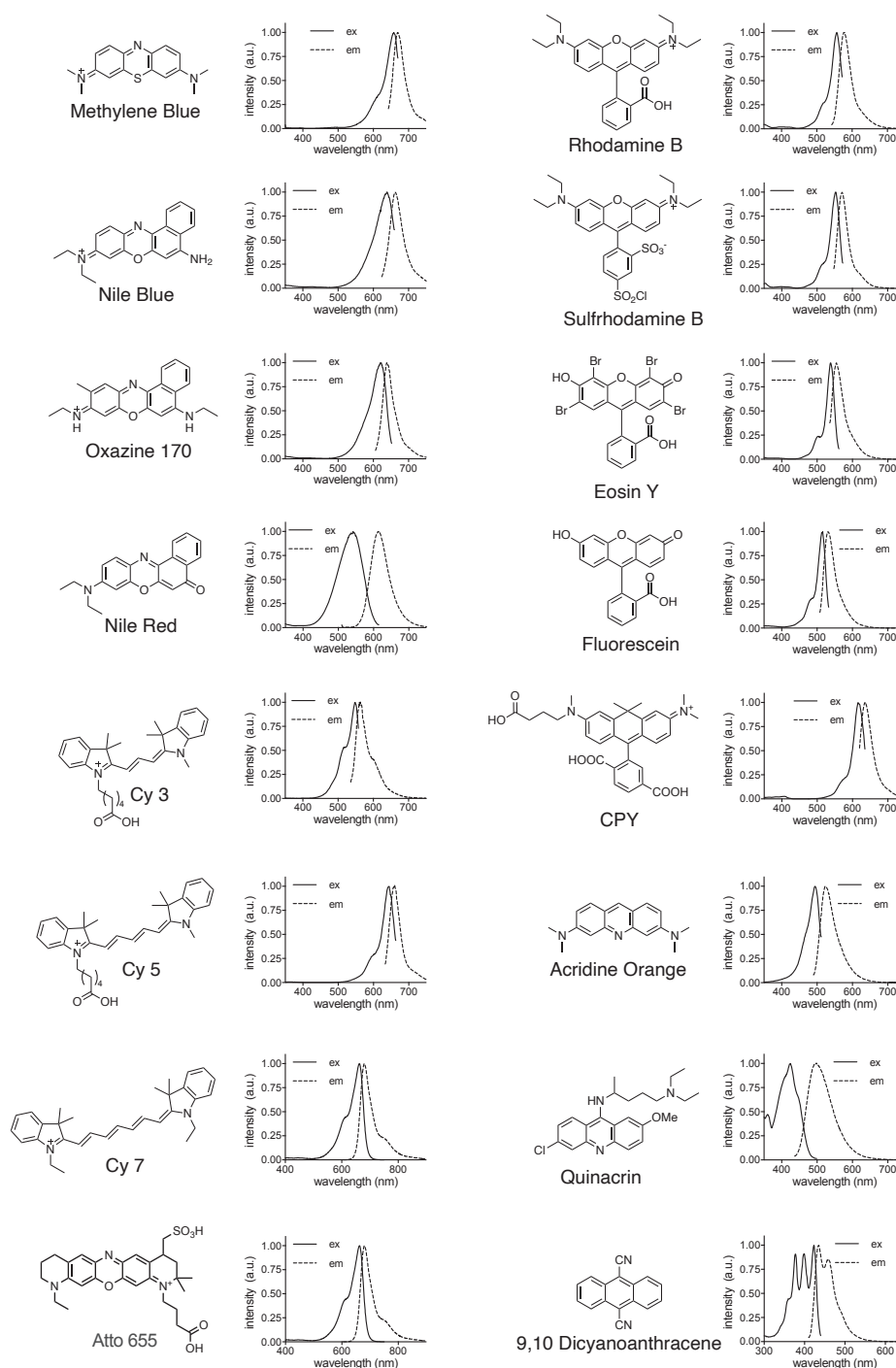


**Figure S13:** excitation / emission spectra measured for common fluorophores selected from **Supporting Table S9** (except: extinction / emission spectra of Atto 655 that were taken from <https://www.atto-tec.com/ATTO-655.html>, measured in PBS, last visited 15.09.2022). Excitation and emission data were normalized to 1 at maxima.



## 4 Electrochemistry in ground and photoexcited states

### 4.1 Experimental reduction/oxidation potentials: chromophores

**Ground state electrochemistry** was determined on three setups:

**(Setup 1, CV & SWV)** Redox potentials were determined in acetonitrile on a CH Instruments 630E electrochemical analyzer using a 2 mm diameter platinum working electrode, a platinum wire counter electrode, and an Ag wire pseudo-reference electrode. Ground state reduction and oxidation potentials of all compounds were determined in MeCN under argon with 0.1 M NBu<sub>4</sub>ClO<sub>4</sub> unless otherwise stated. Both cyclic voltammetry (CV, scan rate: 0.5 V/s) and square wave voltammetry (SWV, frequency: 15 Hz, increment E: 0.004 V, amplitude: 0.025 V) were used, applying ferrocene as an internal standard. Where the oxidation was found to be irreversible in CV, only peak potentials ( $E_p$ ) could be determined by both CV and SWV; but the reduction was reversible in most cases so reduction potentials  $E_{1/2}$  could usually be determined. Such cases are annotated.

**(Setup 2, CV)** was performed using a PGSTAT 128N, Deutsche Metrohm GmbH & Co. KG (Filderstadt, Germany) and software: NOVA 1.10. for data evaluation. A three-electrode configuration contained in a nondivided cell consisting of a platinum disc ( $d = 1$  mm) as the working electrode, a platinum plate as the counter electrode, and a saturated calomel electrode (SCE) with an agar-agar plug in a Luggin capillary with a diaphragm as the reference electrode, was used. Measurements were carried out in acetonitrile (HPLC-grade, dried over calcium hydride and distilled) containing 0.1 M Bu<sub>4</sub>NPF<sub>6</sub> using a scan rate of  $dE/dt = 1$  V s<sup>-1</sup> or 0.1 V s<sup>-1</sup>. The data is given in reference to the ferrocene redox couple (Fc/Fc<sup>+</sup>), which was used as an external standard.

**(Setup 3, Spectroelectrochemistry [SEC]):** An SEC-C Thin Layer Quartz Glass Spectroelectrochemical cell, 0.5 mm optical path length, with platinum mesh electrode as a working electrode (scan rate of  $dE/dt = 10$  mV s<sup>-1</sup>), with counter electrode: platinum wire, and reference electrode: non aqueous reference electrode Ag/Ag<sup>+</sup> (0.01 M AgNO<sub>3</sub> in 0.1 M Bu<sub>4</sub>NPF<sub>6</sub> acetonitrile; ALS Co., Ltd (Tokyo, Japan)) were used for SEC; with an AvaSpec-2048x14 spectrometer with AvaLight-DH-S-BAL, using AvaSoft 7.7.2 (Avantes; Apeldoorn, Netherlands); and with a PGSTAT 128N potentiostat (Deutsche Metrohm GmbH & Co. KG; Filderstadt, Germany) on NOVA 1.10 software.

All results are collected in **Table S8**.

**Table S8:** Ground state redox properties which were measured experimentally in this work, for selected chromophores / fluorophores. Underline highlights a matched pair of redox potentials for Cy 5 that are numbered differently between the study methods (see **Appendix: CV and SWV**).

	CV vs. Fc				SWV vs. Fc			
	$E_{ox,1}$	$E_{ox,2}$	$E_{red,1}$	$E_{red,2}$	$E_{p,ox1}$	$E_{p,ox2}$	$E_{p,red1}$	$E_{p,red2}$
Sulforhodamine B	0.79 <sup>[a]</sup>		-1.15 <sup>[b]</sup>	-1.36 <sup>[a]</sup>	0.78		-1.07	-1.36
Cy 5	0.35 <sup>[b]</sup>	<u>0.48<sup>[b]</sup></u>	-1.28 <sup>[b]</sup>		<u>0.46</u>	1.79	-1.22	
Acridine Orange	0.32 <sup>[b]</sup>	0.77 <sup>[b]</sup>	[d]	-2.40 <sup>[b]</sup>	0.36	0.68	[d]	-2.34
Methylene Blue	0.85 <sup>[b]</sup>		-0.72 <sup>[a]</sup>		0.82	1.56	-0.76	-1.48
Cy 7	[c]		-1.14 <sup>[b]</sup>		1.78		-1.07	
Oxazine 170	0.75 <sup>[a]</sup>		-0.81 <sup>[a]</sup>	-1.66 <sup>[a]</sup>	0.75		-0.83	-1.66
CPY	0.66 <sup>[b]</sup>		-1.09 <sup>[b]</sup>		0.63		-1.04 <sup>[d]</sup>	-1.64 <sup>[d]</sup>
Cy 3	0.63 <sup>[a]</sup>		-1.37 <sup>[b]</sup>	-1.48 <sup>[b]</sup>	0.63		-1.30	-1.44
Rhodamine B, Cl <sup>-</sup> salt	0.78 <sup>[a]</sup>		-1.02 <sup>[b]</sup>	-1.58 <sup>[a]</sup>	0.79		-0.94	-1.58
<i>Rhodamine B, PF<sub>6</sub><sup>-</sup> salt*</i>	0.82 <sup>[a]</sup>		-1.26 <sup>[b]</sup>					
<i>Rhodamine B piperazinamide, Cl salt*</i>	0.81 <sup>[b]</sup>		-1.25 <sup>[a]</sup>					
<i>Rhodamine B methyl ester, PF<sub>6</sub><sup>-</sup> salt*</i>	0.86 <sup>[a]</sup>		-1.27 <sup>[a]</sup>					
<i>Nile Blue, ClO<sub>4</sub><sup>-</sup> salt*</i>	0.81 <sup>[b]</sup>		-0.80 <sup>[b]</sup>					
<i>Fluorescein methyl ester*</i>	0.98 <sup>[b]</sup>		-1.61 <sup>[b]</sup>					

[a] reversible, value corresponds to  $E_{1/2}$ . [b] peak potential. [c] not resolved. [d] possible lower lying reduction potential not clearly resolved. \* data measured with scan rate = 1 V/s, in 0.1 M Bu<sub>4</sub>NPF<sub>6</sub> in acetonitrile.

Regarding **Table S9**, note that where literature values in V vs. SCE were used, these have been converted using (V vs. Fc) = (V vs. SCE) – 0.40 V according to Connelly and Geiger<sup>66</sup>. Though they give corrections for Fc that are electrolyte-dependent (e.g. 0.40 V with [NBu<sub>4</sub>][PF<sub>6</sub>] but 0.38 V with [NBu<sub>4</sub>][ClO<sub>4</sub>]), slightly different correction values are given elsewhere<sup>67</sup>, and the differences are small relative to the values of interest in this work: so we are content to keep the correction simple here.

### **Excited state redox properties:**

Excitation and emission maxima were extracted from fluorescence spectra (**Fig S13**). The optical gap  $E_{00}$  was calculated from the intersection of excitation and emission spectra. Excited state reduction potentials were calculated by the Rehm-Weller equation:

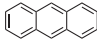
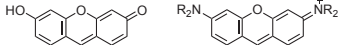
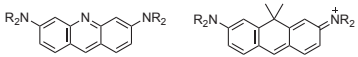
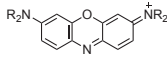
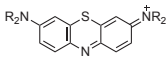
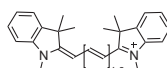
$$E_{red}^{S1} = E_{red}^{S0} + E_{00}$$

with  $E_{red}^{S1}$ : excited state reduction potential,  $E_{red}^{S0}$ : ground state reduction potential, and  $E_{00}$ : energy difference between the ground and first excited neutral states as calculated from the intersection of the normalized excitation and emission spectra (corresponds to optical gap [eV] in **Table S9**).<sup>68–70</sup> Triplet excited state redox properties are listed in **Table S9** as described.

## 4.2 Redox in S0, S1, and T1 states: chromophores

Excited state reduction ( $E_{red}^{S1}$ ) and oxidation ( $E_{ox}^{S1}$ ) potentials were calculated from ground state potentials by the Rehm-Weller equation:  $E_{red}^{S1} = E_{red}^{S0} + E_{00}$  and  $E_{ox}^{S1} = E_{ox}^{S0} - E_{00}$ ,<sup>68–70</sup> where  $E_{00}$  is the energy difference between the ground and first excited states, that can be calculated from the intersection ("ex/em cross") of the normalized fluorescence excitation and emission spectra (which were measured at 1  $\mu$ M in acetonitrile). The ground state (S0) reduction and oxidation potentials were taken from CV data measured in acetonitrile with  $\text{NBu}_4\text{ClO}_4$  (0.1 M) vs. Fc (see **Section 4.1**).

**Table S9:** Ground and excited state redox, and  $\Phi_{ISC}$ , of common chromophores / fluorophores.

Core Scaffolds & examples	$\lambda_{max, ex}$ [nm]	$\lambda_{max, em}$ [nm]	ex/em cross [nm]	$\rightarrow E_{00}$ [eV]	$\Phi_{ISC}$ [lit. values]	$E_{red}^{S0}$ [V vs. Fc]	$E_{red}^{S1}$ { $E^{T1}_{red}$ } <sup>[c]</sup> [V vs. Fc]	$E_{ox}^{S0}$ [V vs. Fc]	$E_{ox}^{S1}$ { $E^{T1}_{ox}$ } <sup>[c]</sup> [V vs. Fc]
<b>Anthracenes</b> 									
9,10 dicyanoanthracene (DCA)	423	435	428	2.90	0.0085 <sup>[h]</sup>	-1.31 <sup>[f]</sup>	1.59 <sup>[f]</sup>	[g]	[g]
<b>Xanthenes</b> 									
Fluorescein	516	531	521	2.38	0.03 <sup>[h]</sup>	-1.61 <sup>[d]</sup>	0.85 <sup>[f]</sup>	0.98 <sup>[d]</sup>	-1.95 <sup>[f]</sup>
Eosin Y	538	555	545	2.27	<b>0.32</b> <sup>[h]</sup>	-1.48 <sup>[f]</sup>	0.83 <sup>[f]</sup> { <b>0.43</b> } <sup>[f]</sup>	0.76 <sup>[f]</sup>	-1.98 <sup>[f]</sup> { <b>-1.55</b> } <sup>[f]</sup>
Rhodamine B	557	577	566	2.19	0.0024 <sup>[h]</sup>	-1.26 <sup>[d]</sup>	0.93	0.82 <sup>[d]</sup>	-1.37
Sulforhodamine B	553	571	561	2.21	[a]	-1.36	0.85	0.79	-1.42
<b>Acridines, Carbopyronines</b> 									
Acridine Orange	425	525	509	2.44	[a]	-2.40	0.04	0.77	-1.67
Carbopyronine <b>CPY</b>	616	635	627	1.98	[a]	-1.09	0.89	0.66	-1.32
<b>Phenoxazines</b> 									
Oxazine 170	620	638	631	1.96	[a]	-0.81	1.15	0.75	-1.21
Atto 655	663 <sup>[i]</sup>	680 <sup>[i]</sup>	672 <sup>[i]</sup>	1.86 <sup>[j]</sup>	[a]	-0.82 <sup>[f]</sup>	1.04	0.91 <sup>[f]</sup>	-0.55
Nile Blue <b>NB</b>	639	663	652	1.90	<<0.03 <sup>[k]</sup>	-0.80 <sup>[d]</sup>	1.10	0.81 <sup>[d]</sup>	-1.09
Nile Red	542	613	582	2.13	[a]	[b]	[b]	[b]	[b]
<b>Phenothiazines</b> 									
Methylene Blue <b>MB</b>	658	669	664	1.87	<b>0.52</b> <sup>[h]</sup>	-0.72	1.15 <sup>[f]</sup> { <b>1.20</b> } <sup>[f]</sup>	0.85	-1.02 <sup>[f]</sup> { <b>-1.08</b> } <sup>[f]</sup>
<b>Cyanines</b> 									
Cy 3	549	560	555	2.23	[a]	-1.37	0.86	0.63	-1.60
Cy 5	644	659	653	1.90	0.025 <sup>[i]</sup>	-1.28	0.62	0.48	-1.42
Cy 7	746	766	756	1.64	[a]	-1.14	0.50	[e]	[e]

[a] no appropriate literature  $\Phi_{ISC}$  found. [b]  $E_{red/ox}^{S0}$  values for Nile Red are not given since its solubility in MeCN was too poor for measurement under our standard conditions (MeCN with 0.1 M  $\text{NBu}_4\text{ClO}_4$ ); this also prevents giving  $E_{red/ox}^{S1}$  values. However, we assume them to be close to those of structurally similar Oxazine 170. [c]  $E_{red}^{T1}$  and  $E_{ox}^{T1}$  are only indicated for Eosin Y and Methylene Blue, since only they have high enough  $\Phi_{ISC}$  for plausible triplet photoredox. [d] CV data measured with  $\text{NBu}_4\text{PF}_6$  (0.1 M) instead of  $\text{NBu}_4\text{ClO}_4$ . [e] We did not resolve  $E_{ox}^{S0}$  during measurement, so no value is given, and  $E_{ox}^{S1}$  cannot be calculated. [f] reported in V vs. SCE, converted to (V vs. Fc) = (V vs. SCE) – 0.40 V<sup>66</sup>. [g] not measured, and no appropriate literature  $E_{ox}^{S0}$  found. [h] value from ref<sup>71</sup>. [i] value from ref<sup>72</sup>. [j] value from ref<sup>73</sup>. [k] value from ref<sup>74</sup>. [l] value from ref<sup>75</sup>.

### 4.3 Experimental reduction/oxidation potentials in ground state: azobenzenes

Ground state redox properties of a set of azobenzene chemotypes (**Figure S14**) on the next page) were measured in electrochemistry as for the chromophores detailed in **Section 4.1**. As discussed in the **Supporting Note**, we interpret all their redox properties measured under these conditions as belonging to the *E* isomer of the azobenzenes, that can be formed locally then catalytically propagate around the electrode. We assume the oxidation potential of the *Z*-isomer to be somewhat lower than of the *E*-isomers, perhaps by ~0.06 V.

**Table S10:** Ground state reduction and oxidation potentials of a library of 33 *E*-azobenzenes determined by cyclic voltammetry and square wave voltammetry. Data are given in V vs Fc. Chemical structures shown in **Fig S14**.

Azo	CV, vs. Fc				SWV, vs. Fc				
	$E_{ox,1}$	$E_{ox,2}$	$E_{red,1}$	$E_{red,2}$	$E_{p,ox1}$	$E_{p,ox2}$	$E_{p,ox3}$	$E_{p,red1}$	$E_{p,red2}$
CV-1	0.23 <sup>[b]</sup>	0.74 <sup>[b]</sup>	-2.16 <sup>[b]</sup>		0.20	0.66		-2.11	
CV-2	0.94 <sup>[b]</sup>	1.08 <sup>[b]</sup>	-1.88 <sup>[a]</sup>		0.74	1.04	1.76	-1.88	
CV-3	0.66 <sup>[b]</sup>	0.83 <sup>[b]</sup>	-1.76 <sup>[a]</sup>		0.66	0.84	1.60	-1.76	
CV-4	0.55 <sup>[b]</sup>	0.82 <sup>[b]</sup>	-1.97 <sup>[a]</sup>		0.83	[d]		-1.96	
CV-5	0.83 <sup>[b]</sup>	0.93 <sup>[b]</sup>	-1.78 <sup>[b]</sup>		0.79	0.96	1.80	-1.74	
CV-6	0.89 <sup>[b]</sup>		-1.86 <sup>[a]</sup>		0.89	0.97		-1.87	
CV-7	0.93 <sup>[b]</sup>		-1.83 <sup>[a]</sup>		0.96			-1.85	
CV-8	1.00 <sup>[b]</sup>		-1.78 <sup>[a]</sup>		1.05	1.77		-1.79	
CV-9	1.04 <sup>[b]</sup>		-1.67 <sup>[a]</sup>		1.05			-1.71	
CV-10	0.99 <sup>[b]</sup>		-1.77 <sup>[a]</sup>		1.02	1.74		-1.77	
CV-11	0.95 <sup>[b]</sup>		-1.75 <sup>[a]</sup>		1.00	1.81		-1.75	-1.99
CV-12	0.82 <sup>[b]</sup>	1.03 <sup>[b]</sup>	-1.71 <sup>[a]</sup>		0.84	1.04	1.85	-1.71	
CV-13	0.45 <sup>[b]</sup>	1.04 <sup>[b]</sup>	-1.94 <sup>[a]</sup>		0.44	1.07		-1.96	
CV-14	0.98 <sup>[b]</sup>	1.99 <sup>[b]</sup>	-1.78 <sup>[a]</sup>						
CV-15	0.77 <sup>[b]</sup>		-1.78 <sup>[a]</sup>		0.80			-1.78	
CV-16	0.64 <sup>[b]</sup>	0.83 <sup>[b]</sup>	-1.85 <sup>[a]</sup>		0.65	0.94		-1.87	
CV-17	[c]		[d]	-1.37 <sup>[a]</sup>	[c]			-1.04	-1.70
CV-18	0.49 <sup>[b]</sup>	0.72 <sup>[b]</sup>	-1.96 <sup>[a]</sup>		0.45	0.75		-1.96	
CV-19	1.34 <sup>[b]</sup>		-1.07 <sup>[b]</sup>	-1.97 <sup>[a]</sup>	1.33			-1.16	-1.96
CV-20	1.08 <sup>[b]</sup>		-1.81 <sup>[a]</sup>		1.11			-1.81	
CV-21	0.96 <sup>[b]</sup>		-1.80 <sup>[b]</sup>		1.00			-1.76	
CV-22	0.47 <sup>[b]</sup>	0.82 <sup>[b]</sup>	-2.09 <sup>[b]</sup>		0.45	0.76		-2.05	
CV-23	[c]		[d]	-1.61 <sup>[a]</sup>	1.64			-1.30	-1.61
CV-24	0.43 <sup>[b]</sup>		-2.04 <sup>[b]</sup>		0.42	0.79		-2.01	
CV-25	1.59 <sup>[b]</sup>		-1.78 <sup>[a]</sup>		1.57			-1.82	
CV-26	[c]		[d]	-1.87 <sup>[a]</sup>	1.71			-1.30	-1.89
CV-27	0.97 <sup>[b]</sup>		-1.81 <sup>[a]</sup>		0.98	1.61		-1.81	
CV-28	1.07 <sup>[b]</sup>		-1.96 <sup>[a]</sup>		1.07			-1.98	
CV-29	1.04 <sup>[b]</sup>		[c]		1.07			-1.12	-2.02
CV-30	1.56 <sup>[b]</sup>		[d]	-1.40 <sup>[a]</sup>	[c]			-1.02	-1.38
CV-31	0.73 <sup>[b]</sup>	0.85 <sup>[b]</sup>	[c]		0.74	0.80		-2.34	
CV-32	0.92 <sup>[b]</sup>		[c]		0.99			-1.82	
CV-33	1.25 <sup>[b]</sup>		[c]		1.24			-1.76	

[a] reversible, value corresponds to  $E_{1/2}$ . [b] peak potential. [c] not resolved. [d] possible lower-lying reduction potential not clearly resolved.

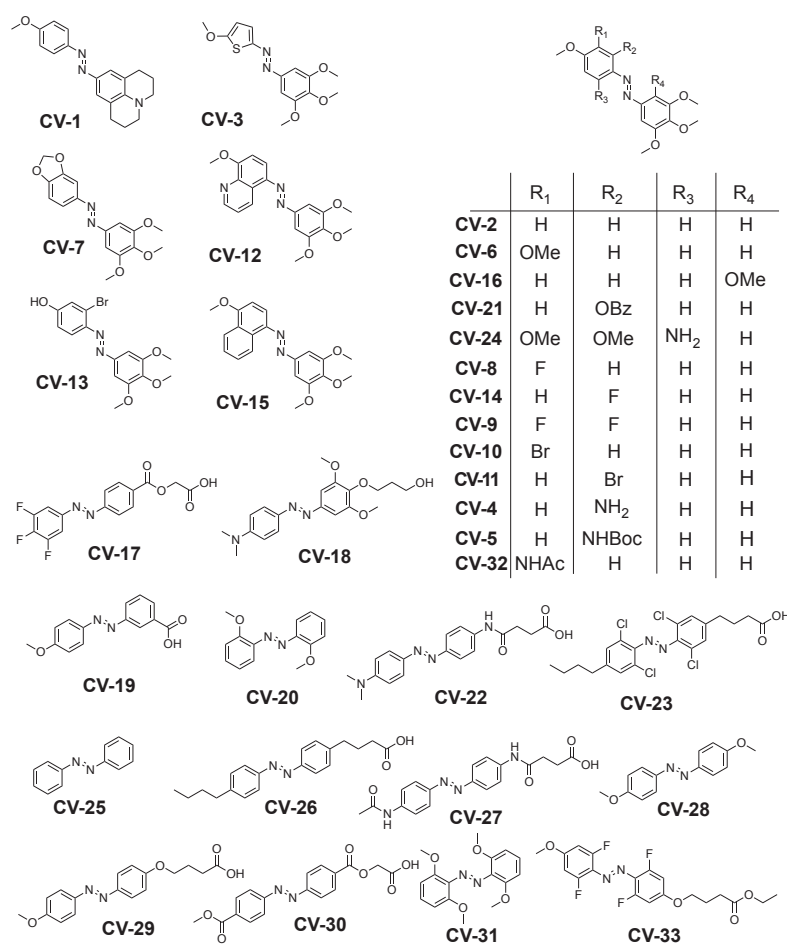


Figure S14: Structures of the 33 azobenzenes whose ground state redox properties were measured.

Table S11: Ground state oxidation potentials &amp; photopharmacology use examples of common azobenzene types.

Structure (R = alkyl, not H/aryl)	$E_{1/2}(Az^+/Az) = E_{ox}^{S0}$ [V vs. Fc] [a]	Biological use example	Structure	$E_{ox}^{S0}$ [V vs Fc]	Biological use example
	1.71	PKC <sup>76</sup> , TRPV1 <sup>30</sup> , lipids <sup>3,78</sup> our example: <b>AK</b>		1.07	cell adhesion <sup>79</sup> our example: <b>AO</b>
	0.97	glutamate receptors <sup>80</sup> our example: <b>AN</b>		1.08	Nav and K <sub>v</sub> <sup>81</sup>
	0.82	K <sub>v</sub> , HCN <sup>82</sup>		0.73	none yet
	1.25	none yet		0.94	microtubules <sup>6,53,83</sup> , actin <sup>84</sup>
	1.64	TRPV1 <sup>23</sup> , lipids <sup>85,86</sup>		0.89	none yet

[a] All potentials determined in MeCN with 0.1 M NBu<sub>4</sub>ClO<sub>4</sub>. Both cyclic voltammetry (CV, scan rate: 0.5 V/s) and square wave voltammetry (SWV) were used, with ferrocene as an internal standard. Values given in V vs. Fc. R in structures represents general alkyl substituents (not aryl, H, or heteroatoms).



## 5 PSS and photoswitch E/Z ratio determinations by UV/Vis and HPLC

### 5.1 PSS determination by HPLC

Photostationary states (PSSs; **Table S12**) were determined by HPLC analysis. Samples were prepared from a 5 or 10 mM stock of the compound in DMSO, diluted to 500  $\mu$ M in 1:1 vol:vol acetonitrile (HPLC grade):distilled water in 1.5 mL amber glass vials, with sample volume 70  $\mu$ L. PSSs were reached by illumination from the top into the open vials for 5 min using the pE-4000 light source at LED intensity of 50 mW/mm<sup>2</sup> (exception: for 595 nm, illumination was at 10 mW/mm<sup>2</sup>). HPLC was then performed at 1 mL/min with a 10%→100% gradient of acetonitrile in water (both with 0.1% formic acid) over 27 min on a Zorbax C18 column (250 mm  $\times$  4.6 mm, 10  $\mu$ m particle size, Agilent); for each run, the column was equilibrated at starting conditions (10% MeCN) for 5 min, then 10  $\mu$ L sample were injected. Quantification was performed by integrating the area under the curve of DAD traces at selected wavelengths: 220 nm for azobenzenes (~isosbestic area: **Fig S15**), and a wavelength at the isosbestic curve region (fluorophore absorption peak) for conjugates.

**Table S12:** Isomer ratios *determined directly by HPLC measurements* at selected photostationary states (PSS) for a set of azobenzene-fluorophore conjugates (of which none have the right redox potential match for photoredox-based isomerisation), and azobenzenes alone.

entry	$\lambda$ DAD trace [nm]	PSS-I ( $\lambda$ [nm], %-trans isomer)	PSS-II ( $\lambda$ [nm], %-trans isomer)	PSS-III ( $\lambda$ [nm], %-trans isomer)
NB-AK	635	365, 18.5%	385, 40.5%	635, 98%
RhB-AO	560	365, 25%	435, 73%	595, 97.5%
RhB-AN	560	365, 28.5%	435, 59.5%	595, 92.5%
RhB-AK	560	365, 42%	385, 59.5%	595, 89%
SRhB-AK	560	365, 41%	385, 60%	
Cy5-AK	660	365, 18%	385, 47.5%	
FI-AK	490	365, 29.5%	435, 77.5%	
EY-AK	560	365, 36%	435, 77%	
Cy3-AK	548	365, 10.5 %	435, 72%	
Cy3-AO	548	365, 13.5 %	435, 60 %	
Cy3-AN	548	365, 15.5%	435, 62.5%	
AK	220	365, 4.5 %	385, 23%	490, 71%
AN	220	365, 8.5%	435, 48.5%	490, 76%
AO	220	365, 6%	435, 47.5%	

We find this HPLC method robust (see **chapter 5.3**) and we feel it is much easier to get right, as well as faster, cheaper, more convenient, and photochemically more appropriate, than more sophisticated and time-expensive NMR measurements typically used in this field<sup>31,87</sup>:

- NMR has limited sensitivity & accuracy at small isomer percentages (e.g. the critical difference of 98% vs 99.7% here) even if near-prohibitively long acquisitions are used.
- With high molecular complexity, NMR can be difficult to analyze (large conjugates).
- High concentrations that are quick to measure by NMR take long times to reach PSS during switching, due to optical shielding: so long illumination times and care to minimise optical path lengths are needed. Low concentrations that allow quickly reaching PSS instead require long measurement times by NMR. In both ways, acquiring reliable action spectra by NMR can be time-prohibitive.
- Illuminations can be done outside the NMR, but this allows changes in PSS before measurement due to thermal relaxation or surrounding light that must be controlled for, and it is tediously manual. Alternatively, illuminations can be done within the NMR e.g. via fiber optic (no spinning possible / bad sample quality; it takes out machine time to set up & run; most do not have access to it; typically the mixing that is key for bulk isomerisation speed at high concentration is missing; typically also the light intensities

that can be applied within NMR are much smaller than those outside it, and the intensity is usually not homogeneous throughout, so apparent rates can be misleading). To avoid potential errors in NMR illumination, and to run the right controls for  $\lambda$ -independent homogeneity of intensity, seems much harder than to use HPLC.

The isosbestic points/regions for azobenzenes **AK**, **AN** and **AO**, were confirmed by UV/Vis determination in HPLC eluent (Fig S15).

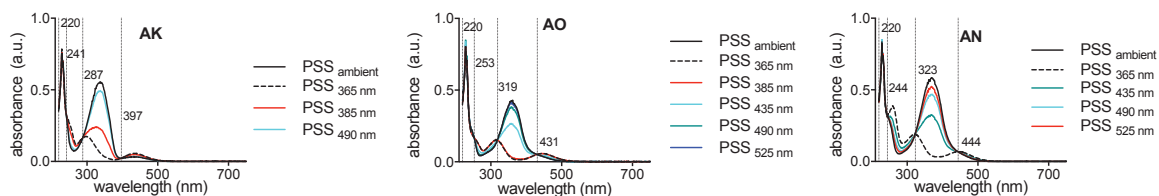


**Figure S15:** Isosbestic points of azobenzenes **AK**, **AO** and **AN** determined by UV-Vis in HPLC eluent mix (50:50 MeCN:water with 0.1% HCOOH): e.g. 241, 287, 397 nm for **AK**, in addition to its  $\sim$ isosbestic region around 220 nm.

## 5.2 Calibration curves for action spectra calibration

To show the current isomer ratios during different illumination periods during *in cuvette* photoswitching monitored by UV-Vis, we aimed to transform measured absorbance values into %*trans*-isomer values. Therefore we used the selected PSS values from HPLC (**chapter 5.1**) with the corresponding absorbance values from UV/Vis "action spectra" (**chapter 2.1.2**) to set up calibration curves (**Fig S16**). Linear fits were determined in the software GraphPad Prism 8 and were satisfying; these linear fits were then used to interpolate/extrapolate %*E* values during the photoswitching action spectra timecourses measured on UV-Vis.

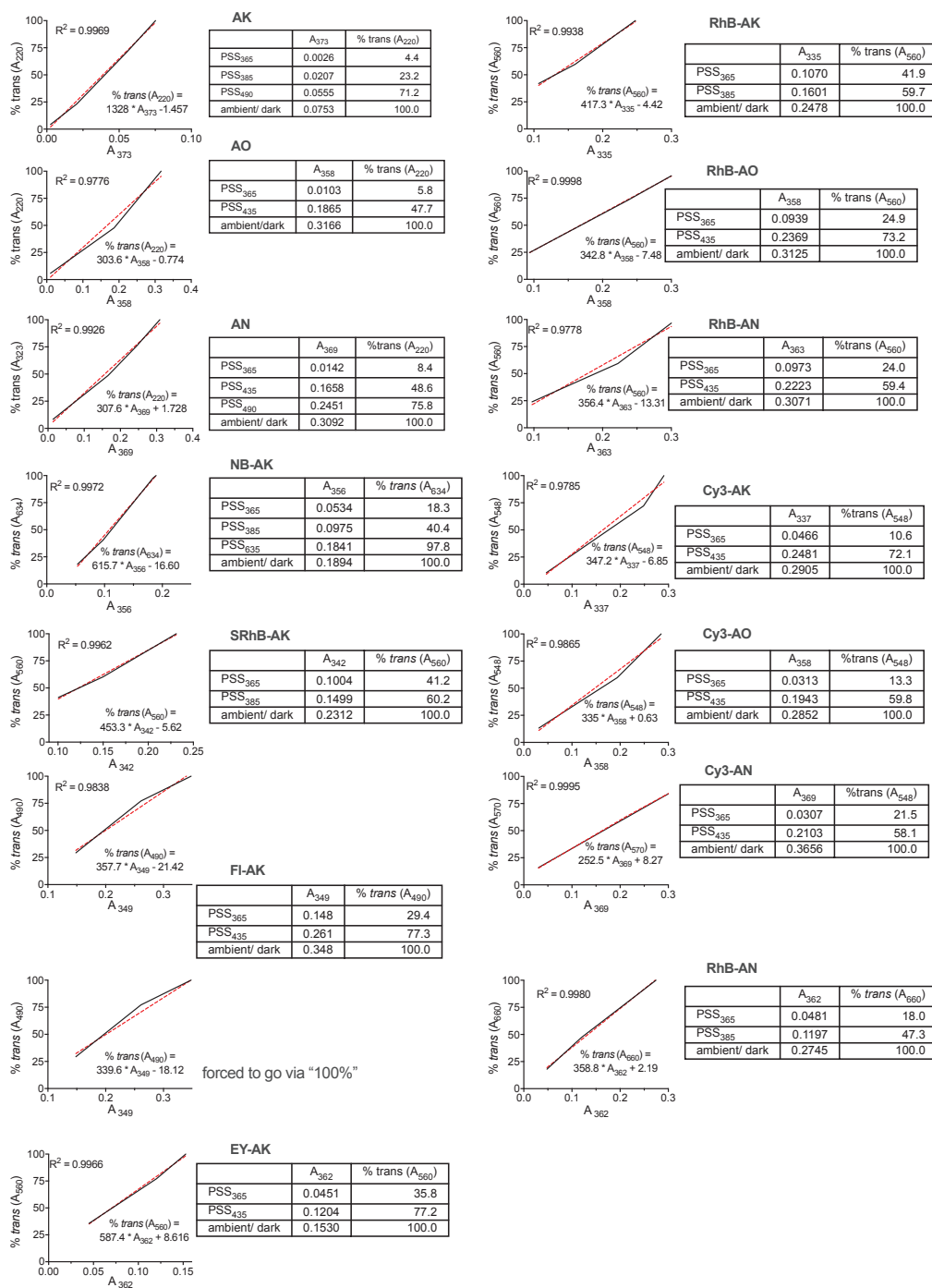
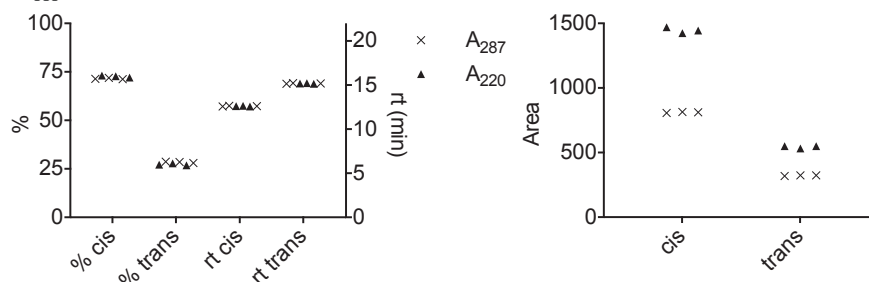


**Figure S16:** Data tables of the absorbance and %*trans*-isomer values used for generating the plotted calibration curves, with linear fits and goodness of fit, for a set of azobenzenes and azobenzene-fluorophore dyads.

### 5.3 HPLC accuracy

For testing the precision of the PSS quantification by HPLC (**chapter 5.1**), a sample of azobenzene **AK** (500  $\mu\text{M}$  in 1:1 water: acetonitrile) was set to PSS<sub>385</sub> by illumination (385 nm LED, 50 mW/mm<sup>2</sup>) and injected three times. **Fig S17** summarizes the retention times of *cis* and *trans* isomers, and their relative quantification by the areas under the curve near an isosbestic point (287 nm) or near an  $\sim$ isosbestic curve region (preferred; here, 220 nm).

**a** Comparison of isomer ratios, retention time and area under the curve of HPLC analysis of **AK** (PSS<sub>385</sub>) at DAD trace 220 and 287 nm. Statistical analysis of 3 measurements.



	A287			A220		
	Mean	SD	N	Mean	SD	N
% cis	71.5	0.29	3	72.7	0.46	3
Area cis	811.1	3.40	3	1447.3	21.78	3
rt cis	12.6	0.04	3	12.6	0.04	3
% trans	28.5	0.29	3	27.3	0.46	3
Area trans	322.7	3.44	3	544.5	10.14	3
rt trans	15.2	0.03	3	15.2	0.03	3

**b** Spectra of **AK** *cis* and *trans* isomers extracted from HPLC and normalized to isosbestic point at 287 nm (left); Zoom towards the isosbestic point 287 nm and the isosbestic region around 220 nm.

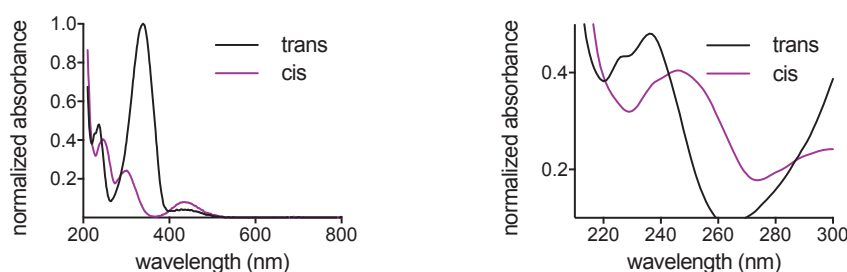


**Figure S17: (a)** Comparison of isomer ratio, retention time and area under curve of 3 HPLC runs of **AK** at PSS<sub>385</sub> (from DAD traces at 220 and 287 nm) including statistics. **(b)** UV-Vis spectra (extracted from HPLC) showing isosbestic region around 220 nm and isosbestic point at 287 nm.

We were therefore satisfied that this HPLC quantification is suitably reproducible for use.

## 6 Fluorescence Lifetime measurement by TCSPC

Fluorescence lifetime analysis was performed on a custom-built inverted confocal microscope based on an Olympus IX-71 body (Olympus Deutschland GmbH). The Rhodamine B and eosin conjugates were excited with 532 nm laser (532 nm, LDH-P-FA-530B, PicoQuant GmbH) while Nile Blue conjugates were excited with a 639 nm pulsed laser, all with a repetition rate of 80 MHz. After passing a single-mode fiber (P3-488PM-FC, Thorlabs GmbH), the laser light was circularly polarized by a linear polarizer (LPVISE100-A, Thorlabs GmbH) and a quarter-wave plate (AQWP05M-600, Thorlabs GmbH). The laser power was adjusted to 10  $\mu\text{W}$  for 532 nm and 20  $\mu\text{W}$  for 639 nm lasers at the entrance of the microscope body by means of a neutral-density filter (ND06A, Thorlabs GmbH). The light was focused onto the

sample by an oil-immersion objective (UPLSAPO100XO, NA 1.40, Olympus Deutschland GmbH). The emission was separated from the excitation beam by a dichroic beam splitter (zt532/640rpc, Chroma Technologies) and focused onto a 50  $\mu\text{m}$  diameter pinhole (Thorlabs GmbH). The emission light was split into a green channel and a red channel with a dichroic mirror (640 LPXR, Chroma Technologies) and spectrally cleaned by filters (HC582/75, AHF; RazorEdge LP 532, Semrock for green channel and SP 750, ThorLabs; RazorEdge LP 647, Semrock for red channel). The photons were detected on avalanche photodiodes (SPCM-AQRH-14-TR, Excelitas) and signals registered by a time-correlated single-photon counting (TCSPC) unit (HydraHarp400, PicoQuant GmbH). For controlling the microscope and data analysis a commercial software package was used (SymPhoTime64, Picoquant GmbH). The fluorescence lifetimes were measured in Nunc Lab-Tek II Chambered Slides (Thermo Fisher Scientific) which were cleaned with 1M KOH for 1 h, washed with 1 $\times$  phosphate buffered saline (PBS) buffer four times, and passivated with 1 mg/mL BSA-biotin (Thermo Fisher Scientific). Measurements were performed in 50/50 water/acetonitrile solution at 1-10 nM concentrations. As the molecules are excited with high intensity 532 / 639 nm light to pump their antenna chromophores, we take the lifetimes as corresponding essentially to the *E*-isomer, and we do not conclude about the *Z*-isomer from these data. Decay curves and fits are shown in **Fig S18**, extracted parameters in **Table S13**.

**Table S13:** Fluorescence lifetimes from TCSPC, with goodness of fit (local  $X^2$ ) for monoexponential decay.

compound (mostly <i>E</i> )	fluorescence lifetime $\tau_{\text{fl}}$ [ns]	local $X^2$ for fit
<b>NB-COOH</b>	1.26	1.44
<b>NB-E-AK</b>	1.44	1.29
<b>RhBpip</b>	1.53	1.16
<b>RhB-E-AO</b>	1.55	1.56
<b>RhB-E-AK</b>	1.41	1.68
<b>EYpip</b>	2.66	1.26
<b>EY-E-AK</b>	1.16	1.22

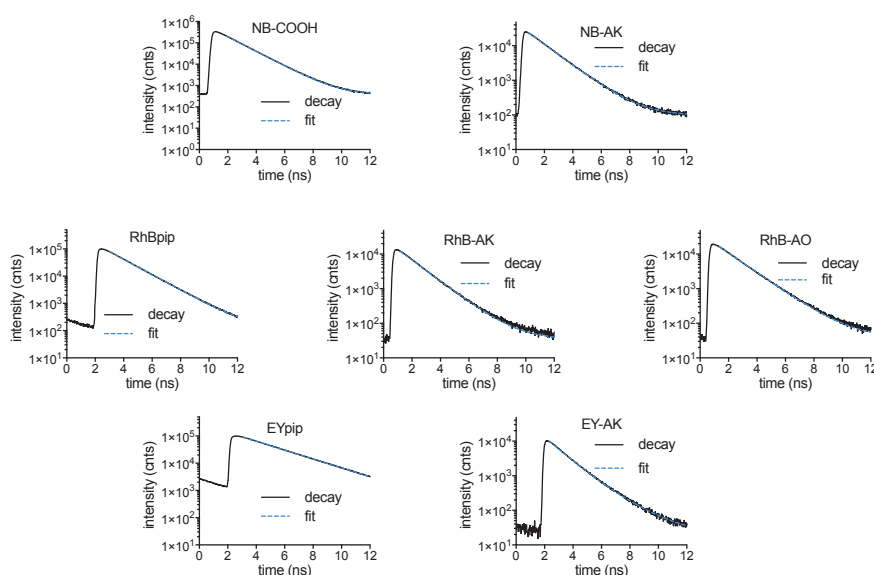


**Figure S18:** Decay kinetics and monoexponential fits.



## 7 Fluorescence Correlation Spectroscopy (FCS)

### 7.1 FCS Methods

Fluorescence correlation analysis was performed comparing **EYpip** and **EY-AK**, using a custom-built inverted confocal microscope based on Olympus IX-71 body (Olympus Deutschland GmbH). Samples were excited with 532 nm laser (532 nm, LDH-P-FA-530B, PicoQuant GmbH) pulsed laser with a repetition rate of 80 MHz. After passing a single-mode fibre (P3-488PM-FC, Thorlabs GmbH), the laser light was circularly polarized by a linear polarizer (LPVISE100-A, Thorlabs GmbH) and a quarter-wave plate (AQWP05M-600, Thorlabs GmbH). The excitation power used for each measurement was adjusted and measured at the entrance of the microscope body by means of a neutral-density filter (ND06A, Thorlabs GmbH). The light was focused onto the sample by water immersion objective (UPlanSApo, 60XWO, NA 1.20, Olympus Deutschland GmbH). The emission was separated from the excitation beam by a dichroic beam splitter (zt532/640rpc, Chroma Technologies) and focused onto a 50  $\mu\text{m}$  diameter pinhole (Thorlabs GmbH). The emission light was separated from scattered excitation light by a long pass filter (RazorEdge LP 532, Semrock) and split into two detection channels by a nonpolarizing 50:50 beam splitter (CCM1-BS013/M, Thorlabs GmbH). In each detection channel, the afterglow luminescence of the avalanche photodiode was blocked by a 750 nm short-pass filter (FES0750, Thorlabs GmbH). Emission was focused onto avalanche photodiodes (SPCM-AQRH-14-TR, Excelitas Technologies GmbH & Co. KG), and the signals were registered by a multichannel picosecond event timer (HydraHarp 400, PicoQuant GmbH). SymphoTime 64 (PicoQuant GmbH, Germany) was used as control and analysis software. The fluorescence correlation measurements were performed in Nunc Lab-Tek II Chambered Slides (Thermo Fisher Scientific) which were cleaned with 1M KOH for 1h, washed with 1 $\times$  phosphate buffered saline (PBS) buffer four times, and passivated with 1 mg/mL BSA-biotin (Thermo Fisher Scientific). Measurements were performed in 50/50 water/acetonitrile solution at  $\sim$ 200 pM concentrations, under air and without deoxygenation, without precautions to protect the azobenzene conjugate from ambient light since the samples are anyway isomerised to PSS by the 532 nm excitation laser (note: for **EY-AK**, the 525 nm LED gave ca. 80% *E* : 20% *Z* isomer ratio, see **Figure 3d**).

The cross-correlation function ( $G(\tau)$ ) of the signals recorded on two avalanche photodiodes was calculated with SymphoTime 64. The software computes the cross-correlation of each of the two channels with the other channel, respectively, using the formula

$$G(\tau) = \frac{\langle I(t)I(t + \tau) \rangle}{\langle I(t) \rangle^2} - 1$$

and then averages the result of both calculations to yield an averaged correlation function, which we normalize across species so that the diffusion-only component (correlation time range 0.01 - 1 ms) overlaps, with a pure-diffusion fit intercepting  $G(0)=1$ .

### 7.2 FCS and FLCS results for EYpip and EY-AK

The averaged  $G(\tau)$  for eosin (**EYpip**; **Figure S19**) fitted the “diffusion+triplet” model which describes diffusion of one fluorescing species in the presence of one dark (triplet) state:

$$G(\tau) = \frac{(1 + T(e^{-\frac{t}{\tau_{trip}}} - 1))}{N \left(1 + \frac{t}{\tau_{diff}}\right) \left(1 + \frac{t}{\tau_{diff}\kappa^2}\right)^{1/2}}$$

*Note:  $N$  = average number of molecules in the focal volume,  $\tau_{diff}$  = diffusion time of diffusing species,  $\tau_{trip}$  = lifetime of the dark triplet state,  $T$  = dark (triplet) fraction of molecules,  $\kappa$  = length to diameter ratio of the focal volume.*

The **EYpip** fit had a diffusion time constant of 88  $\mu\text{s}$  that was independent of excitation power; and its triplet fits were power-dependent (increasing triplet fraction, and decreasing triplet lifetime, as intensity is raised; observed range: 31-61% triplet, 1.2-0.3  $\mu\text{s}$  lifetime; **Figure S19**).

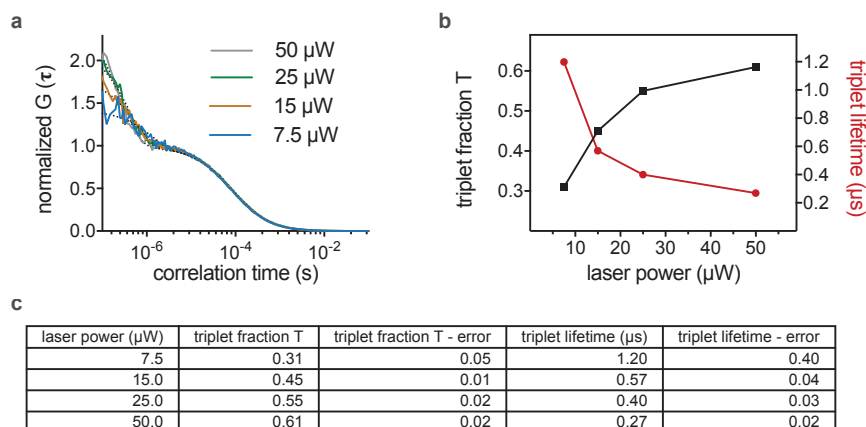


**Figure S19: EYpip.** (a) Fluorescence correlation function normalized to the diffusion component obtained for **EY-P** recorded at varying excitation powers; (b) triplet fraction as well as the lifetime of the dark triplet state obtained from fitting the fluorescence correlation curves obtained at varying excitation intensities; (c) table of data from panel **b** adding the fit errors of triplet fraction and triplet lifetimes.

The averaged  $G(\tau)$  for **EY-AK** fitted the “pure diffusion” model which assumes that exclusively diffusion contribution is present in the cross-correlation curve (no triplet state, no other dark species):

$$G(\tau) = \frac{1}{N \left(1 + \frac{t}{\tau_{diff}}\right) \left(1 + \frac{t}{\tau_{diff} \kappa^2}\right)^{1/2}}$$

This returned a **EY-AK** diffusion time constant of 95 μs. It seems logical that this is slightly slower than for **EYpip** since the molecule is larger.

### 7.3 FCS: "total" triplet quenching in EY-AK; & 'weak coupling model' quantum yields

Eosin has a high intersystem crossing yield ("self-ISC") to enter a long-lived dark triplet state, which can relax slowly spontaneously (lifetimes ca. 100 μs), or can be depleted e.g. by collision with oxygen or by photoexcitation to a higher excited state particularly with higher intensity imaging.

The **EYpip** data show the triplet state is a highly relevant species (30-60% of sample), and its depletion by oxygen collision, and/or by photodepletion (observed lifetime 0.27 μs at 50 μW, or 1.2 μs at 7.5 μW, since less photodepletion of the triplet at this lower intensity) are very significant, as expected.

By contrast, the absence of a detectable long-lived dark state FCS component for **EY-AK** suggests that the triplet states arising from excitation of its eosin EY motif are very efficiently quenched by its own azobenzene AK motif in either *E* or *Z* isomer (since the low concentration of 200 pM should preclude collisional annihilation between two dye triplets).

Since the EY triplet reduction potential ( $E^\circ = 0.43$  V vs Fc) is not sufficient to oxidise ground state AK ( $E^\circ = 1.7$  V vs Fc), nor can EY triplet reduce ( $E^\circ = -1.55$  V vs Fc) AK ( $-1.9$  V vs Fc), we discount redox as a quenching mechanism.

Under a weak coupling model for **EY-AK** where EY and AK motifs access electronic states exactly as they would if they were molecularly isolated, we could thus conclude that the EY self-ISC triplet energy transfers intramolecularly **to either E- or Z- AK** (since the conjugate is highly dilute but present in both isomers) much more rapidly than its usual decay time (i.e. reaching 100% depletion very rapidly): which would give *E-AK*\*(T1) and *Z-AK*\*(T1) states that nonradiatively relax to AK ground state [optionally with isomerisation].

If we also assume that (1) no **EY-AK** is simultaneously engaged in the assisted switching mechanism that bypasses the need for self-ISC generation of the triplet state (which we are confident is not true, since all other chromophores were photon-efficiently in engaging with it,

and since **EY-AK** has 2.3-fold *E/Z*-dependent fluorescence intensity (**Fig S23**) which supports that an isomer-dependent assisted switching mechanism is highly present in **EY-AK** just as in all other conjugates); and furthermore assume also that (2) direct absorption of 532 nm light by the azobenzene motif ( $\epsilon < 200 \text{ M}^{-1}\text{cm}^{-1}$  and  $\Phi < 0.5$ ) has negligible impact on the isomer ratio (which seems reasonable, as compared to the self-ISC pathway ( $\epsilon$  ca.  $60,000 \text{ M}^{-1}\text{cm}^{-1}$  and  $\Phi_{\text{ISC}} \sim 30\%$ ), then we might conclude that **EY-AK**'s intrinsic ratio of quantum yields for *intramolecularly-EY-triplet-sensitised isomerisations* (i.e. when both *E* and *Z* isomers are equally likely to intramolecularly acquire triplet energy) is:

$$\text{PSS@532 nm} = 80\%E : 20\%Z \rightarrow \Phi^{\text{iT}}(\text{EY,AK})_{E \rightarrow Z} / \Phi^{\text{iT}}(\text{EY,AK})_{Z \rightarrow E} = 0.25$$

Although we remind the reader that we consider assumption 1 flawed, nevertheless, a ratio on the order of 0.25 would compare reasonably to the *intermolecular EY-triplet-sensitised isomerisation* reported by Lemaire in 1974<sup>35</sup> as nearing PSS of 86%*E*:14%*Z*, albeit under somewhat different conditions of solvent, wavelength, and azobenzene nature; but under vastly different concentration regimes (ca. 100  $\mu\text{M}$ ). A necessary condition for inter- and intramolecular PSS values to be strictly comparable is that all triplet energy transfers should be effectively collision-limited, rather than exhibiting preference for one isomer over the other; this seems<sup>44</sup> to be true for intermolecular systems as for the weakly coupled model; and in this specific case, **EY-AK** may have a much more significant self-ISC pathway than any other dyad due to its high  $\Phi_{\text{ISC}}$ , so it may also be that its assisted switching is in fact dominated by the self-ISC pathway and therefore mimics the outcomes of the intermolecular self-ISC case; but we recall that in general, the assisted switching indicates strong coupling outside the self-ISC pathway will necessarily skew or even completely override this kind of interpretation of the triplet isomerisation quantum yield ratio for other dyads.

**Note also: even if** we assume that  $\Phi_{\text{ISC}}$  is the same in **EY-AK** as in **EYpip**, which is not necessarily true, this still does not allow conclusions about the absolute magnitude of  $\Phi_{\text{ISC}}\Phi^{\text{iT}}(\text{EY,AK})$  yield products. These would require either actinometry, or the relative rates of triplet-based **EY-AK** vs direct **AK** photoisomerisation. However, since it seems clear from data for other donors like Cy5, RhB, etc, that a strong coupling model for assisted switching (where their effective  $\Phi_{\text{ISC}}$  drastically depends on if they are *E/Z*-azobenzene-conjugated or not) is the only explanation that is supported by the data (on *E/Z* variable fluorescence as well as chromophore-dependent sensitised PSSs), we do not seek to engage these methods to draw further conclusions.

In that context, we note also, that proximity-driven electronic strong coupling has been reported for azobenzene chromophores,<sup>35</sup> and that there are additional reasons to expect that the weak coupling model cannot capture the full behaviour of even the rich self-ISC system of **EY-AK** (as its absorption spectrum is not the strict sum of that for **EYpip** and **AK**, for example, which Lemaire also observed in related intermolecular experiments with fluorescein<sup>35</sup>).

## 8 Transient absorption (TA) spectroscopy (TAS)

### 8.1 TAS Methods

The femtosecond-TA data were acquired on a custom-built setup. Briefly, a regenerative Ti:sapphire amplifier (Astrella, Coherent, USA) is used as the pump laser, delivering pulses of 5 mJ pulse energy at 1 kHz pulse repetition rate. The output of the laser is then divided by a beam splitter. The first part is focused into a rotating CaF<sub>2</sub> plate to generate a broadband white light supercontinuum beam covering the spectral range 300 to 700 nm. This broadband pulse is subsequently split into two parts, which are used as reference and probe pulse. A second fraction of the Ti:sapphire output is used to pump an optical parametric amplifier (TOPAS prime, Light conversion, Lithuania) for generating pulses of about 100 fs pulse duration. The output of the amplifier is tunable across the UV-Vis-NIR spectral range. The repetition rate of the **pump pulses** is then reduced to **500 Hz** by a mechanical chopper. A Berek compensator and a polarizer are used to adjust the polarization difference of pump and the white light probe pulse to the magic angle of 54.7°. The probe pulse is focused into a quartz cuvette (pump/probe optical path length 10 mm, width 10 mm) by a concave mirror of 500 mm focal length. The spectra of probe and reference pulses are acquired by a 150 mm focal length Czerny-Turner spectrograph (SP2150, Princeton Instruments) equipped with two CCD arrays (Pascher Instruments AB, Sweden). Since strong contributions of coherent artifact signals<sup>88</sup> are observed during pump-probe pulse overlap, the transient absorption data recorded at delay times in the range  $-150 \text{ fs} < \Delta t < 150 \text{ fs}$  are removed from data analysis, because the multiexponential fitting algorithms cannot be applied. The TA data analysis of the remaining data includes a spectral preprocessing to correct for the chirp of the broadband pulse. Afterwards, a sum of exponential functions is fitted to the data using a least squares regression analysis for optimization using a software tool from Pascher AG. Solutions were prepared with an OD between 0.1 and 0.2 (**NB-COOH** and **NB-AK** at 630 nm; **RhBpip**, **RhB-AK** and **RhB-AO** at 560 nm; **EY-COOH** and **EY-AK** at 530 nm) in 1:1 acetonitrile: water.



**Figure S20: TA setup.** The 365 nm LED illuminating constantly from the side is seen as a bright white-blue light.

A pump pulse of 630 nm, 560 nm or 530 nm and a pulse energy of 1.8  $\mu\text{J}$  is used to excite the sample. The spatial profile of the pump pulse was slightly elliptical with a 700  $\mu\text{m}$  long axis and a 558  $\mu\text{m}$  short axis. Further geometric optics details are described in the parallel photoredox paper.<sup>1</sup>

The goal of these TAS measurements was to see if plausible intermediates along the major photoisomerisation path of interest (sensitised Z $\rightarrow$ E) could be observed, even if (in retrospect) we might have assumed that any dyad that enters into the sensitised switching pathway (e.g. exciplex that collapses to the azobenzene triplet) might evolve so rapidly after entry that the concentration of exciplex intermediates always remains below the threshold for detection; and, given how rapidly triplet azobenzene returns to the ground state (<5 ps lifetime), if its entry to the triplet state is staggered on the  $\sim$ nanosecond timescale of the singlet excited state, then



there would likewise never be enough accumulation of excited azobenzene to surpass the detection threshold.

Experimentally however, our design was to apply the dyads in the mainly-*Z* isomer state in the bulk solution, by irradiating the solutions with a LED at 365 nm at 90° to the pump/probe axis under constant stirring (**NB-COOH**, **RhBpip**, and **EY-COOH** were not irradiated). However, although the bulk solution in the cuvette was kept at *Z*-rich PSS-365 nm (confirmed by UV-Vis), in retrospect it seems probable that the higher light intensities in the pump/probe beam path enforced typically 90%*E* (pump-wavelength-sensitised PSS) in the measured fraction. This would be consistent with the observation that all dyads' TAS spectra seemed to return towards baseline (i.e. no overall *Z*→*E* isomerisation), even though analyses elsewhere (UV PSS fit, *E/Z*-dependency of fluorescence, etc) would have indicated that ca. 15 - 50% of the initially absorbing *Z*-dyad would be expected to undergo assisted isomerisation to the *E*-isomer, which should have been visible in the TAS. For reference, the 365 nm PSS values to be expected in the bulk solution were: 82% *Z*-**NB-AK**; 58% *Z*-**RhB-AK**; 75% *Z*-**RhB-AO**; 64% *Z*-**EY-AK**. In the future, a control TAS experiment repeating these measurements under e.g. 500 nm LED illumination (or without LED illumination) could be performed, expecting to see identical TAS profiles if indeed the pump/probe beam zone is at pump-PSS despite the external illumination. Our conclusion is that it would be very tricky and time-consuming to attempt TAS on a mostly-*Z* sample (would need powerful interleaved *E*→*Z* pulses between each measurement).

The absorbance was recorded before and after the experiment, confirming that the chromophores did not degrade during measurement.

## 8.2 TAS Results for NB, RhB, and EY conjugates

**Note:** *We do not consider these studies mechanistically conclusive; but, we have tried to highlight aspects that might be helpful in testing hypotheses either on the basis of this data, or with the addition of future experimental results.*

**Initial Impressions (summarised as point 2 in main text section 2.6):** TAS data are returned as  $\Delta\text{Abs}(t,\lambda)$  datasets (time-delay-series of absorption spectra differences between the ground state and post-pumped sample). These can be spectrally plotted for selected representative delay times (e.g. **Figure S21a**); or intercept traces at fixed wavelengths (typically, strongly-evolving wavelengths that can also be maxima or minima) can be taken to temporally plot the molecular evolution (e.g. **Figure S21b**). These already show that **NB-AK** returns to the NB ground state without distinguishable differences of rate or form as compared to **NB-COOH** (**Figure S21d-e**); there is slightly faster return to ground state for **RhB-AO** than for **RhB-AK** than for **RhBpip** (**Figure S21b**); and there is much faster return to ground state for **EY-AK** than for **EY-COOH** (**Figure S21h**), with that difference being bigger than that for RhB conjugates. We interpret this to reflect a significant percentage of excited dyad undergoing triplet energy transfer for **EY-AK**; a moderate percentage for **RhB-AO**; small for **RhB-AK**; and very small for **NB-AK**; which reflects their relative half-powers needed for assisted photoisomerisation (in order: smallest for **EY-AK** through to largest for **NB-AK**).

**Data Processing (worked example mainly for NB; similar processing is done for RhB and EY species):** We normalise the  $\Delta\text{Abs}(t,\lambda)$  datasets of **NB-AK** and **NB-COOH** by multiplying all points by a constant, such that  $\Delta^*\text{Abs}(t_{\text{norm}}, 518 \text{ nm})$  is one. 518 nm is chosen since it is close to the differential absorption maximum for the **NB**<sup>(S1)</sup> moiety whose decay we wish to study. This normalisation time  $t_{\text{norm}}$  can be chosen freely, typically "late" ( $t_{\text{norm}} \sim 500 \text{ ps}$ ) or "early" (e.g.  $t_{\text{norm}} \sim 2 \text{ ps}$ ) are chosen, to visually highlight different features: "late" normalisation (e.g. 562 ps traces, **Figure S21e**) highlights if any different pathways have been taken up until the normalisation time, even if the differences are minor: which is useful when comparing molecules bearing the same chromophore (e.g. **NB-AK** vs **NB-COOH**; no differences



detected,  $t_{\text{norm}}=562$  ps traces, **Fig 4h**). By contrast, "early" normalisation highlights if molecules evolve with substantially different overall rates after the normalisation time, i.e. soon after excitation (**NB**: no differences in  $t_{\text{norm}}=2$  ps traces, **Fig S21e,f**; but note the differences in the **RhB** 2 ps traces in **Figure S21b**).

To supply the decay time constant(s), we also give unbiased monoexponential fits to the early-normalised data at times  $t > 5$  ps (and if this does not converge then also biexponential fits, to highlight which fit is more appropriate). In the case of **NB**, a monoexponential decay is preferred (**Figure S21e**); for **RhB/EY** the monoexponential decays fit poorly but biexponentials fit well (**Figure S21b,h**). We also subtract e.g.  $\Delta^*\text{Abs}(t,\lambda)_{\text{NB}}$  from  $\Delta^*\text{Abs}(t,\lambda)_{\text{NB-AK}}$  to give the subtraction spectral series  $\Delta(\Delta^*\text{Abs}(t,\lambda))$ ; and plot the subtraction's single-wavelength projections  $\Delta(\Delta^*\text{Abs}(t,527 \text{ nm}))$  for early and/or late normalisations as needed (**NB**: **Figure S21f**; **RhB**: **Figure S21c**). This highlights if pathway/rate differences are significant: and for **NB** they are not; while for **RhB** they are).

**NB-AK**: TAS traces show essentially no detectable differences in the evolution of the excited state between *E/Z*-**NB-AK** and parent **NB-COOH**. This is easiest seen in the single-wavelength projection (527 nm) of the subtraction spectral series (**Figure S21f**), which are horizontal lines almost at  $y=0$  for both late- and early-normalised data. We conclude that the assisted switching mechanism(s) operating for **NB-E-AK** are relatively insignificant (e.g.  $<10\%$ ) compared to the usual singlet-state processes accessible to **NB-COOH**: i.e. energy transfer to the azobenzene is not efficient.

**RhB-AO/AK**: **RhBpip**, **RhB-AO** and **RhB-AK** were fitted well by biexponential (but not by monoexponential) fits (**Figure S21b**). The slow (both ca. 840 ps) and fast (both ca. 100 ps) decay time constants for **RhB-AO** and **RhB-AK** are essentially identical; the difference in overall evolution speed between **RhB-AO** and **RhB-AK** arises simply since **RhB-AO** has a higher proportion of the fast decay component in its overall kinetic than does **RhB-AK** (visible in the single-wavelength projection (455 nm) of the subtraction spectral series (**Figure S21c**)). The dual components are not due to the *E/Z*-azobenzene, since **RhBpip** itself has both of them: although **RhBpip** decays are significantly slower than the conjugates', indicating moderately efficient energy transfer in the **RhB** conjugates.

**EY**: Like the rhodamine, these data were only well-fitted by a biexponential. Both fast and slow decay components are significantly quicker in **EY-AK** than in **EY-COOH**, indicating efficient energy transfer (**Figure S21h**).

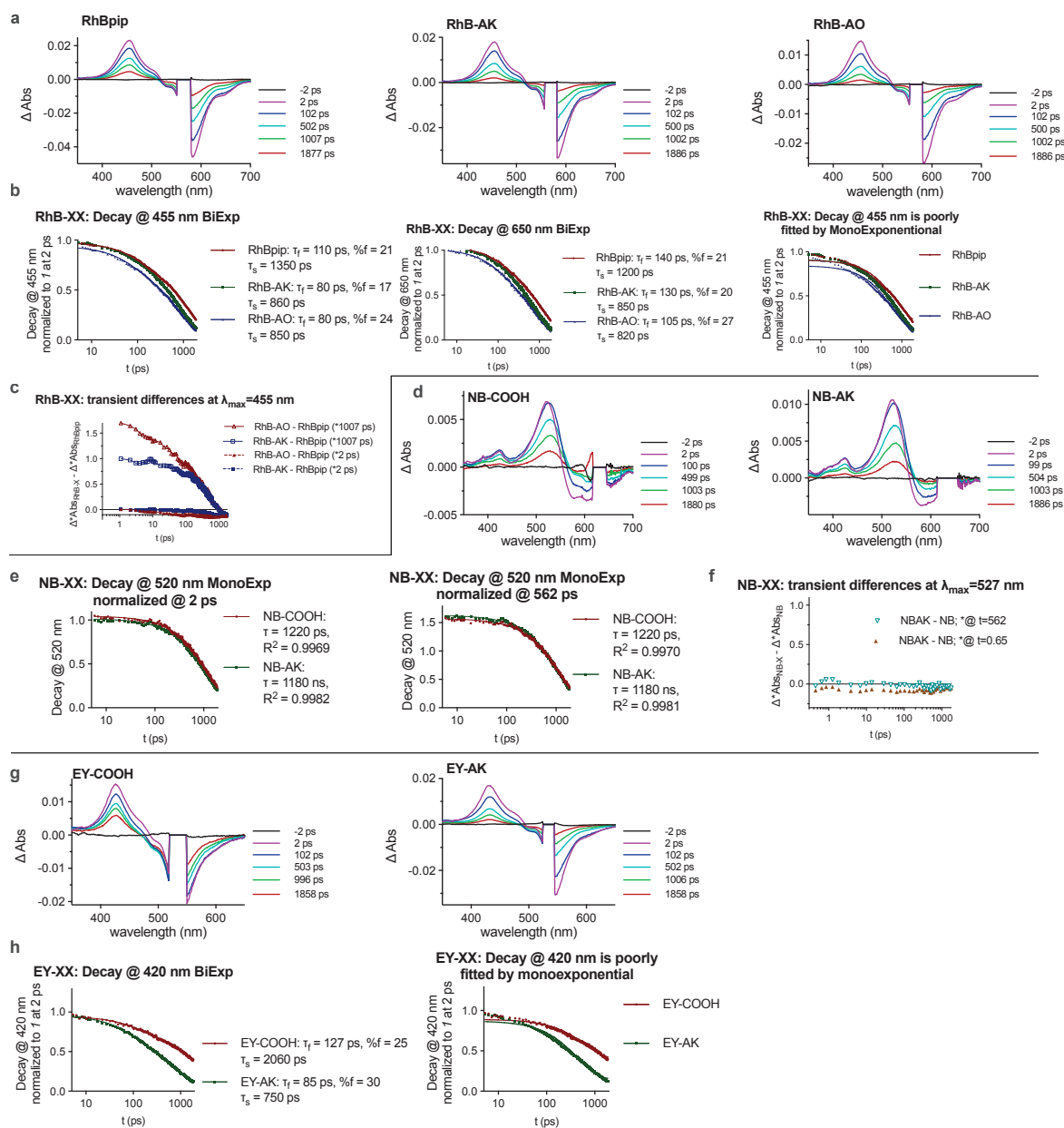


**Figure S21: TAS data**, as described in the text. Note the significant differences between RhBpip and RhB-AK, whereas NB-COOH and NB-AK are almost identical.

### 8.3 Worked example: analysing NB / NB-AK decay rates

The singlet excited states of the NB moiety evolve almost identically in both **NB-COOH** and **NB-E-AK**. This supports that there is no *significant* photoredox in **NB-AK** (expected, since mismatched potentials; for a counterexample, see the TAS analysis of related dyad **NB-AO** which has matched potentials and which is discussed in the parallel photoredox paper,<sup>1</sup> where approximately 25% of the initially excited **NB-AO** evolves within ca. 1 ps by photoredox to **NB<sup>-</sup>-AO<sup>+</sup>** which then decays with ca. 70 ps half-life), and that there is no *significant* ISC to **NB<sup>\*</sup>(T1)** (where "significant" is defined as a process that is detectable under these TAS conditions, i.e. one that builds up to, or captures, ca.  $\geq 5\%$  of the molecules after pump excitation). Thus, TA spectra show **NB-COOH** and **NB-E-AK** being excited to **NB<sup>\*</sup>(S1)-COOH** and **NB<sup>\*</sup>(S1)-E-AK** respectively within 1-2 ps, then after a delay of ca. 10 ps, decaying monoexponentially to the groundstate by a mixture of radiative and non-radiative decay processes. We note their almost identical overall decay times; and that their fluorescence quantum yields determined

elsewhere (**NB-COOH**:  $0.15 \pm 0.01$ ; mostly-*E*-**NB-AK**:  $0.17 \pm 0.01$ ; *E/Z* QY ratio for **NB-AK** only 1.2) were almost identical within expected experimental error; and we note that the fluorescence lifetimes  $\tau_{fl}$  measured by time-correlated single-photon counting (TCSPC, **Chapter S6**) (**NB-COOH**: 1.26 ns; **NB-AK**: 1.44 ns) were similar (ca.  $1.35 \pm 0.1$  ns, i.e. within the same margin of error as the quantum yields). We could combine these data to assign "typical" rates for  $\text{NB}^{*(S1)}$  moiety decay, whether it is present alone or as an *E*-azobenzene conjugate:

$$k_{\text{rad}}(\text{NB}^{*(S1)}) = 0.16 / 1.35 \times 10^{-9} \text{ s} = \mathbf{1.2 \times 10^8 \text{ s}^{-1}}$$

$$k_{\text{non-rad}}(\text{NB}^{*(S1)}) = (1 / 1.25 \times 10^{-9} \text{ s}) - k_{\text{rad}}(\text{NB}^{*(S1)}) = \mathbf{6.8 \times 10^8 \text{ s}^{-1}}$$

These rates might be useful elsewhere, e.g. for model-building.

#### 8.4 Crude order-of-magnitude estimation of "*E/Z*-average $\phi_{\text{exciplex}}$ " for RhB-AK

*This section expands on the summary given in point (5) of the main text section 2.6.*

We attempted to use the dyads' higher %*E* fraction at UV PSSs, compared to the UV PSSs of the isolated azobenzenes, to estimate a rough "average  $\phi_{\text{exciplex}}$ " value by a calculation that only involves the experimental PSSs, typical azobenzene isomerisation quantum yields, and partial extinction coefficients for the moieties (e.g. partial  $\epsilon$  for the **RhB** moiety considered separately from the partial  $\epsilon$  of the *E*-**AK** or *Z*-**AK** moiety; some of these assumptions have limited accuracy, and the answer should be seen as having  $\times/\div$  factor of 2 accuracy at best).

To estimate an average  $\phi_{\text{exciplex}}$  crudely, we compare PSSs reached under 365 nm for **AK** alone ( $\epsilon_E = 12700 \text{ M}^{-1}\text{cm}^{-1}$ ,  $\epsilon_Z \sim 500 \text{ M}^{-1}\text{cm}^{-1}$ , **Table S2**; PSS ca. 95%*Z*, **Table S5**) with the combination of direct and sensitised isomerisation in dyad **RhB-AK** ( $\epsilon_{365, \text{RhB}} = 4300 \text{ M}^{-1}\text{cm}^{-1}$ , **Table S2**; dyad PSS<sub>365</sub> ca. 61%*Z*, **Table S5**).

Assuming the dyad can either absorb on the **AK** motif (then undergo its usual photochemistry), or on the **RhB** motif (then undergo the exciplex→triplet mechanism *in the same way* as operates under long-wavelength excitation of **RhB-AK** i.e. ultimately giving a 90:10 *E*:*Z* ratio at equilibrium, with quantum yield of entering this mechanism of  $\phi_{\text{exciplex}}$  (\*though, see discussion below)), we can include the known quantum yields for direct *E*→*Z* and *Z*→*E* UV isomerisations of the **AK** motif (ca. 0.2 and 0.35), to set the *E*→*Z* and *Z*→*E* rates of **RhB-AK** at PSS<sub>365</sub> to be equal, which leaves only one unknown (the average  $\phi_{\text{exciplex, avg}}$ ):

$$E \rightarrow Z \text{ rate is } 0.39 \times (0.2 \times 12700 + \phi_{\text{exciplex}} \times 0.1 \times 4300)$$

$$Z \rightarrow E \text{ rate is } 0.61 \times (0.35 \times 500 + \phi_{\text{exciplex}} \times 0.9 \times 4300)$$

This returns an ***E/Z*-averaged  $\phi_{\text{exciplex}} = 0.46$** . Analysing other dyads like this, or using UV-PSS data at different wavelengths, yields results with a similar order of magnitude (0.05-0.5).

\*Discussion: this *E/Z*-averaged  $\phi_{\text{exciplex}}$  is not a physical quantity, since this method assumed that  $\phi_{\text{exciplex}}$  is the same for RhB-*E*-AK as RhB-*Z*-AK (which we do not believe is physically reasonable: we rather believe that  $\phi_{\text{exciplex, E}}$  and  $\phi_{\text{exciplex, Z}}$  are at least as different from each other as their fluorescence quantum yields, i.e. >2-fold). However, we believe that its order of magnitude is similar to each of the real  $\phi_{\text{exciplex, E/Z}}$  values. We do not invest more into this approach since we know the assumption of spectral additivity of absorption spectra is also flawed (spectra are e.g. 5% isomer-dependent), added to which the values for the partial extinction coefficients used here are not strictly accurate.

However, we feel confident in the conclusion that the real  $\phi_{\text{exciplex, E/Z}}$  values, that should roughly bracket this *E/Z*-averaged  $\phi_{\text{exciplex}}$ , will thus be of comparable size to the quantum yields for direct photoisomerisations of isolated azobenzenes (which is coherent with the bulk sensitised isomerisation kinetics being much faster than those for azobenzene, even after correcting for the long-wavelength extinction coefficients being rather higher for the auxiliary chromophore): thus supporting the important conclusion of this work, that assisted photoswitching can be highly photon-efficient at the antenna chromophore's absorption wavelengths.

## 9 Fluorescence Quantum Yields

### 9.1 Mostly-*E* fluorescence quantum yields (integrating sphere measurements)

We first determined absolute quantum yields for fluorophore-azobenzene *conjugates* (in **mostly-*E*** isomer state) compared to *parent fluorophores* **EY-COOH**, **RhBpip**, and **NB-COOH**, and to *physical mixtures* of the parents and mostly-*E*-azobenzenes (as a control against intermolecular inner filter effects reducing the detected fluorescence), by fluorimetry employing an integrating sphere (**Table S14**) (stocks made in the dark, few precautions to block ambient light, measured under mostly-*E* conditions).

The solutions were made up to an absorbance of 0.1 at 495 nm for EY species, 530 nm for RhB species, and at 600 nm for NB species, all in 1:1 acetonitrile:water, in spectroscopy-grade solvents without degassing and under air atmosphere. The steady state absorbance was measured on a Specord S600 (Analytik Jena) in 1 cm cuvettes. The emission spectra for quantum yield were measured on an Edinburgh FLS980 emission spectrofluorometer equipped with an integrating sphere in a 1 cm cuvette at 90° angle. Absorbance profiles did not change significantly during measurements (i.e. negligible direct photoisomerisation; low light energy applied for excitation). We estimate an error of ca. ±3% in the  $\Phi_{fl}$  measurements.

**Table S14:** Fluorescence quantum yields (measured using an integrating sphere), excitation wavelengths and integrated emission ranges, for two separate measurements / acquisitions annotated "1" and "2".

compound, mostly- <i>E</i>	$\lambda_{ex, 1}$ [nm]	emission range 1 [nm]	$\Phi_{fl, 1}$ [%]	$\lambda_{ex, 2}$ [nm]	emission range 2 [nm]	$\Phi_{fl, 2}$ [%]
<b>NB-COOH</b>	600	620-800	14	600	625-850	16
<b>NB-AK</b>	600	620-800	16	600	625-850	17
physical mixture <b>NB + AK</b>	600	620-850	17	<i>not repeated</i>		
<b>RhBpip</b>	530	550-770	36	530	545-730	33
<b>RhB-AO</b>	530	550-770	35	530	545-730	32
physical mixture <b>RhBpip + AO</b>	530	545-730	31	<i>not repeated</i>		
<b>RhB-AK</b>	530	550-770	33	530	545-730	28
physical mixture <b>RhBpip + AK</b>	530	545-730	31	<i>not repeated</i>		
<b>EY-COOH</b>	495	505-770	71	495	505-730	65
<b>EY-AK</b>	495	505-770	38	495	505-730	23
physical mixture <b>EY-COOH + AK</b>	495	505-700	67	<i>not repeated</i>		

**EY-E-AK** was the only *E*-conjugate with a high change of fluorescence quantum yield from that of its parent fluorophore or physical mixture.

### 9.2 Sensitivity, technical precision, and accuracy, of cuvette/PMT measurements

It would have been convenient if we could use fluorescence excitation/emission intensity at the ex/em maxima as a sensitive and robust readout for concentration of the conjugates [in fact, fluorophore-azobenzene conjugates have previously been imaged in biology to follow their biodistribution, presumably assuming that the *E/Z*-intensities are similar]. However, we observed that separately-prepared solutions of *conjugates*, even when adjusted to the same absorbance intensity in the fluorophore portion of the spectrum (**Figure S22**), had noticeably different fluorescence ex/em intensities (sometimes higher, sometimes lower), which often were >10% different from those of their parents at ostensibly the same concentrations.

## Supplementary Information - Section Fluorescence Quantum Yields

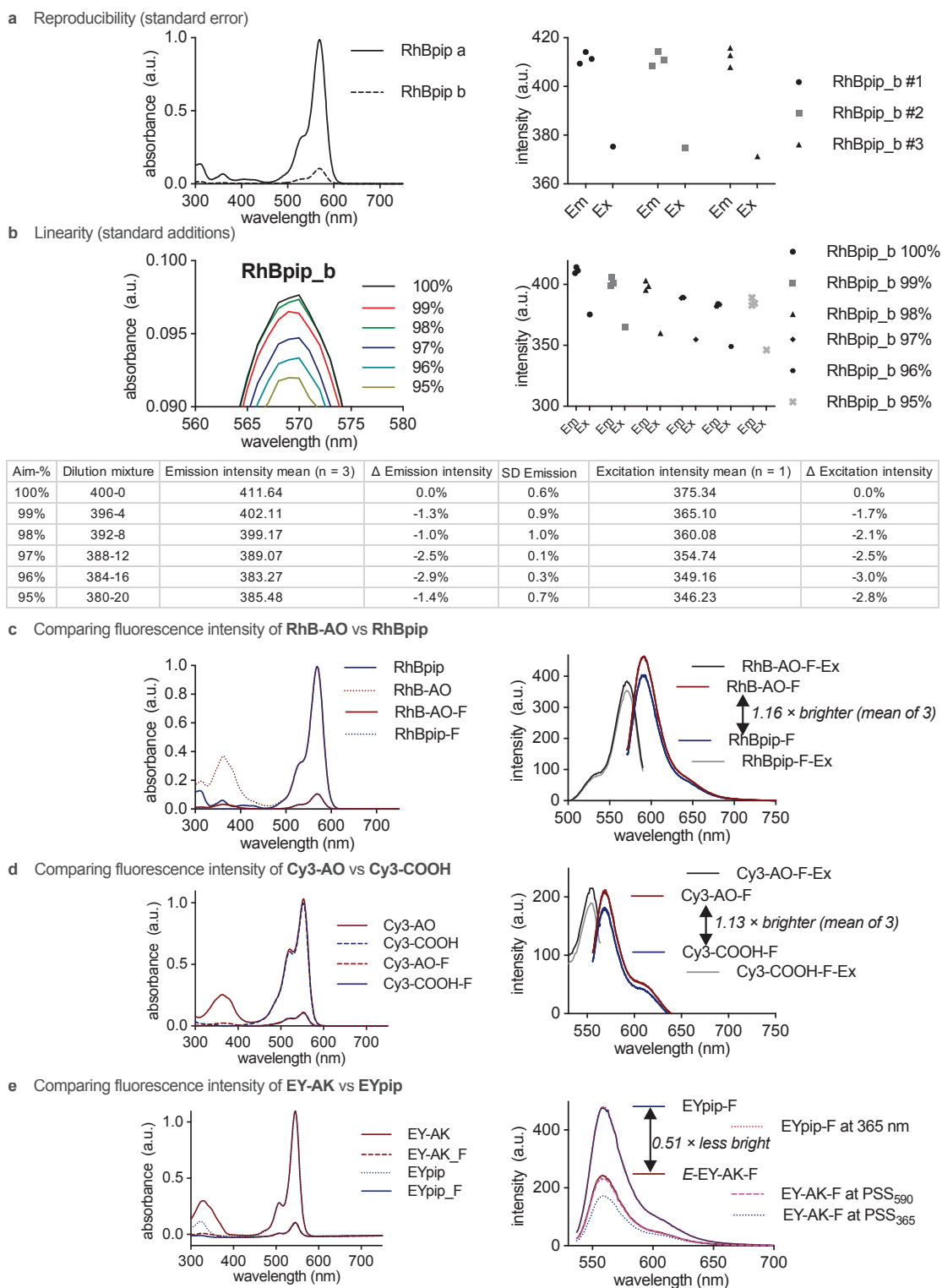


**Figure S22: Sensitivity, linearity, and technical precision/accuracy of cuvette/PMT fluorimetry.** (a) (left) UV/Vis spectra of stock **RhBpip<sub>a</sub>** and one of the 1:10 dilutions **RhBpip<sub>b</sub>**; (right) fluorescence emission and excitation intensities (at excitation/emission maximum) for technical replicates. (b) Method of standard addition: (left) UV/Vis absorbances and (right) fluorescence emission/excitation intensities (at excitation/emission maxima) for an **RhBpip<sub>b</sub>** solution and its independent 1-5% dilutions; table shows the changes of fluorescence intensity relative to expected values for linear response (ideal value: 0% difference). (c-e) Comparison of fluorescence and excitation intensities of conjugate and parent, after adjusting concentrations to give the same UV/Vis absorption (~1.0) at the fluorophore motif abs. max. (c) **RhB-AO** and **RhBpip**. (d) **Cy3-AO** and **Cy3-COOH**; since the UV/Vis absorptions differed by 3% (left), the fluorescence ex/em intensities have been adjusted by 3% to compensate. (e) **EY-AK** and **EYpip**. The differences in fluorescence according to *E/Z* ratio are explored further below.



Assuming that these fluorescence intensity deviations could be related to quantum yield changes during photoisomerisation of the conjugates, we first wished to see what magnitude of change is significant on our setup, before attempting to measure these changes. We therefore tested the reproducibility and linearity of fluorescence excitation / emission intensities between technical replicate samples (separately- but identically-prepared) of nearly-all-*E* conjugates against their parents.

All measurements were performed in a mixture of 9:1 DMSO/PBS buffer (pH = 7.4). Parent (**RhBpip** or **Cy3-COOH**) and conjugate (**RhB-AO** or **Cy3-AO**) stock solutions were adjusted so the absorbance value of the fluorophore motif at its  $\lambda_{\text{max}}$  was 1.00 ( $\pm 0.03$ ) in a 1.00 cm cuvette; then for fluorescence/excitation intensity measurements these solutions were diluted by ratio 1.00:10.0. All measurements were performed on the fluorimeter described in section 3 and all acquisition parameters within conjugate/parent pairs were kept the same.

**(1) Dilution precision and accuracy, and reproducibility of handling and acquisition:** A single stock solution **RhBpip\_a** was diluted tenfold, in three independent repetitions giving technical replicate dilutions **RhBpip\_b#1-3**. Their UV/Vis absorbances and their fluorescence emission intensities were acquired three times each (and excitation once), with the standard cuvette washing / drying procedures between changing the samples. These show excellent technical precision and accuracy for the emission intensities, and argue against any significant degree of photoisomerisation during prep and handling (see discussion at **Figure S23**), i.e. expected technical error is <2%, well within our desired scope (**Figure S22a**).

**(2) Sensitivity and reproducibility of linearly quantifying changes to emission intensity:** To establish what change in fluorescence intensity can be interpreted as a *significant* difference, we then performed a series of independent standard addition dilutions (1→0.99, 1→0.98, 1→0.97, 1→0.96, 1→0.95) of a single "b" solution. We split each dilution to measure UV/Vis absorbance and fluorescence separately. UV/Vis absorbances were satisfying (est. <2% error; **Figure S22b** left panel). The precision of repeated emission measurements was again very good (SD  $\leq 1\%$ ) and their accuracy match to expected linearity was good (deviation <3%; (**Figure S22b** right panel). These indicate no significant extra errors (e.g. from small volume handling) convoluted with the <2% technical errors established in paragraph (1).

We therefore consider that we can interpret any detected differences in fluorescence intensity of >3% as being significant.

**(3) Fluorescence intensities of parent vs *E*-conjugate at matched UV/Vis absorptions:** We compared fluorescence emission and excitation intensities at concentrations with the same UV/Vis absorption, by absorption matching at the parent's maximum at Abs~1.00 then performing 10.0-fold dilution ("-F" solutions) and measuring fluorescence.

*E*-**RhB-AO** had 1.16 times the emission intensity of its parent **RhB-pip** at 590 nm (as well as 1.10 times the excitation intensity at 571 nm) (**Figure S22c**).

*E*-**Cy3-AO** had 1.13 times the emission intensity (569 nm) and 1.10 times the excitation intensity (554 nm) of its parent **Cy3-COOH** (**Figure S22d**).

In the integrating sphere measurements (**Table S14**), the mostly-*E*-conjugates' quantum yields were indistinguishable from those of the parents (within 3%, except for **EY-AK**, note below). We believe that the *E*-conjugate vs parent fluorophore fluorescence quantum yield ratios determined on the PMT setup more accurately represent the pure *E*-dyads, since the *E/Z* ratio affects fluorescence yield, and the integrating sphere ratios would match an expected ambient ca. 90%-*E* proportion (see below).

Note: *E*-**EY-AK** had 0.51 times the emission intensity (558 nm) of its parent **EYpip** (**Figure S22e**): a close match to the 0.54-fold ratio of the integrating sphere measurements.

### 9.3 Fluorescence of conjugates depends on *E/Z* ratio (cuvette/PMT measurements)

Since the cuvette/PMT measurements were rapid and had good precision and technical accuracy, we used this method to test fluorescence emission from the conjugates during photoisomerisation between *E/Z* isomers, which already had clearly noticeable differences

(Figure S22e, right panel). We therefore performed repeated photoisomerisations between PSS values between fluorescence measurements, using dilute solutions (Figure S23 left panels) to avoid potential for inner filter absorption of fluorescence emission before exiting the cuvette (although the significant and *E/Z*-dependent absorption from the azobenzenes is anyway at wavelengths far shorter than the emission, so is unlikely to be relevant).

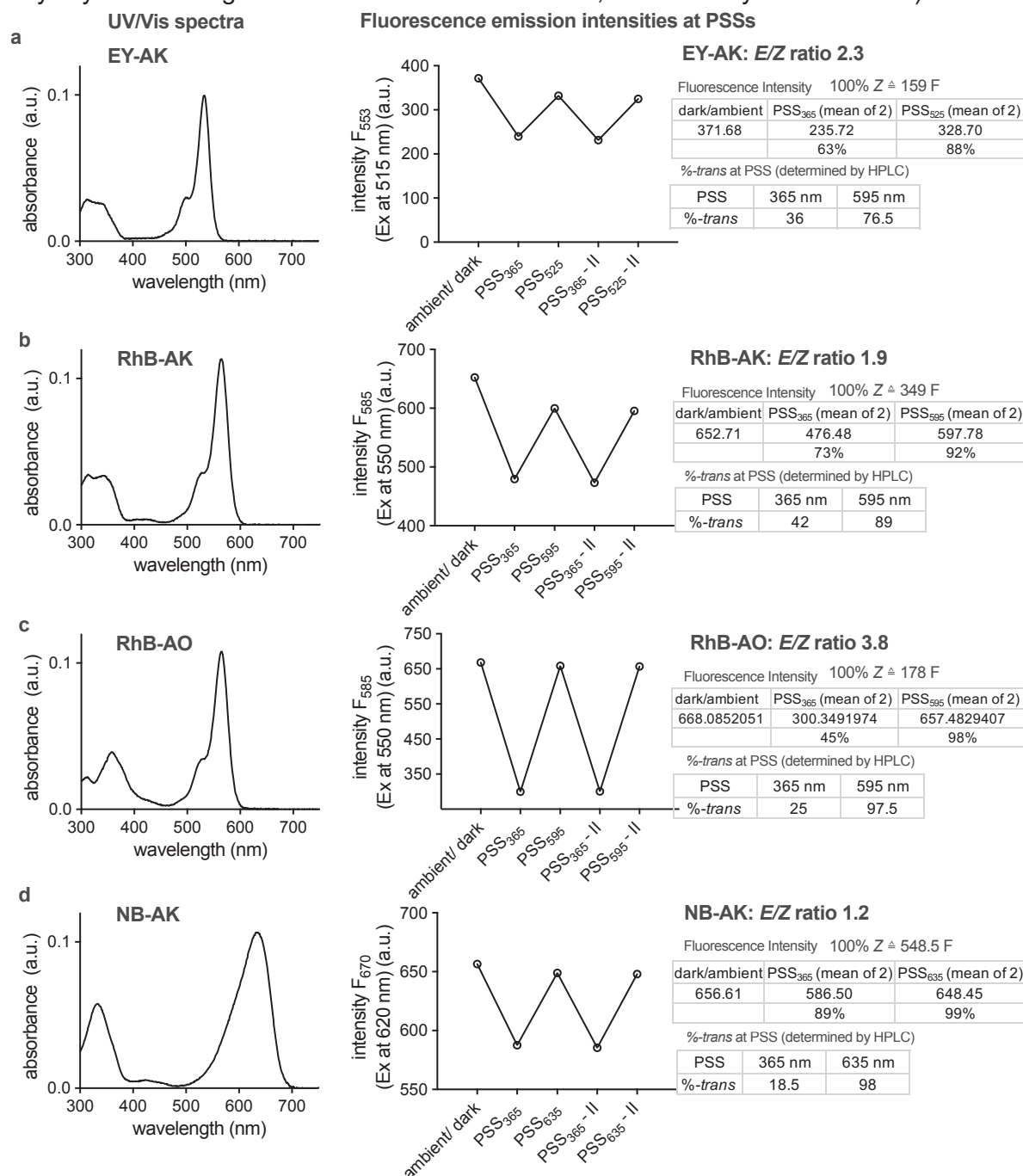


**Figure S23: Fluorescence dependency on *E/Z* ratio.** UV/Vis spectra are for dark state (nearly all-*E*) conjugates; other PSS absorption spectra are given in Fig 3, but *E/Z* absorption differences are not large and are localised in the near-UV/violet. %*E*(PSS) values from HPLC were used to analyse the FL(PSS) intensities and extract relative ratios between the pure-*E* and pure-*Z* conjugates' fluorescence intensities. Note that these are not determined at the same excitation wavelengths as used in integrating sphere quantum yield measurement or in FCS, although in all cases except **EY** they are comparable, and the outcomes should be the same.

The *E/Z*-dependent differences of fluorescence intensity are striking; and for these conjugates the *Z*-isomers are all much less fluorescent than the *E*-isomers (see PSS at 365 nm vs PSS at long wavelength or mostly-*E*/mostly-dark state). By using the %*E* composition of the PSSs

known from HPLC measurements, we perform two-component analysis with the PSS-365 and the dark/PSS-long-wavelength fluorescence values, and extract *E* and *Z* isomer fluorescence intensities (in a.u.).

The *E* to *Z* ratios of the conjugates' fluorescence intensities are thus:

**NB-AK:** 1.2, **RhB-AK:** 1.9, **EY-AK:** 2.3, **RhB-AO:** 3.8 (**Figure S23**, right panels).

Without wishing to over-interpret, we note that a conjugate that we tested in the parallel photoredox paper, **NB-AO**, which undergoes photoredox, had a higher fluorescence emission intensity as its *Z*-isomer<sup>1</sup>: i.e. the reverse trend from the more-fluorescent sensitisation dyads we report here. Whether that is a chance effect or more general, remains to be seen.

## 10 Photoswitch Modeling

Here we define the antenna chromophore as **ant**, and photoswitch as *E/Z-azo*.

We trialled several mathematical models for assisted switching, to examine whether they could be constrained using observed system behaviour (wavelength-dependent isomerisation rates and PSS values) in order to converge towards values for the unknown quantities of the assisted switching process that we wished to discover: for example, the relative or absolute quantum efficiencies of entering the sensitised energy transfer process from e.g. red-excited ant\*-*E*-Azo vs from ant\*-*Z*-azo across a range of ant-azo dyads, and ideally finding this quantity relative to the quantum efficiencies of direct photoswitching of the azo motifs (using e.g. UV/blue light that should be directly absorbed by the azo).

We had originally expected that assisted switching would deliver the same or similar PSS values for a range of azos when driven by the same ant, based on the ant's tendency to undergo self-ISC and quantitatively sensitise its attached azo partner (enforced, isomer-independent collision). This would have allowed us to compare a range of ant-azo dyads to extract quantum yields.

Then, realising that requiring self-ISC to initiate the energy transfer is incompatible with the high rates and variation of PSSs observed, and settling on the interpretation that the entry to the assisted isomerisable state is based on strong coupling that is *E/Z*-isomer-dependent with vastly different *E/Z*-dependencies across different ant-azos (without shared features, even when the same ant or the same azo are present on pairs or sets of dyads being considered), we found it difficult to set enough system constraints to rule out a broad range of fitted values, including value sets that we consider unphysical.

We have been unable to set up an instructive and robust model to use in numerical analysis of the data we have acquired. We present our final model iteration below, in the hope that it may be instructive or directly useful to readers some day; or that a reader may be able to find reasonable assumptions or data constraints to allow robustly solving such a model system.

(0) Conditions: Our model assumed high dilution and no spontaneous relaxation, so that the only photoprocesses relevant are absorption by molecules in an ensemble, without fluorescence emission that may influence neighbours and without optical shielding (i.e. optically transparent solution at infinite dilution).

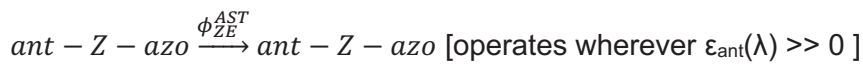
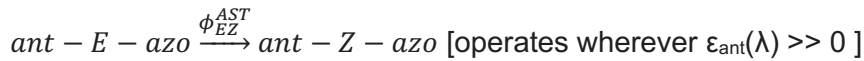
(1a): Direct absorption "DIR": Irradiation may be directly absorbed by the azo motif within an ant-*E*-azo or ant-*Z*-azo dyad, and may trigger direct isomerization to the other isomer:

$ant - E - azo \xrightarrow{\phi_{EZ}^{DIR}} ant - Z - azo$  [operates on the basis of  $\epsilon_{E-azo}(\lambda)$  (where  $\epsilon_{E-azo} \gg 0$ )]

$ant - Z - azo \xrightarrow{\phi_{ZE}^{DIR}} ant - E - azo$  [operates on the basis of  $\epsilon_{Z-azo}(\lambda)$  (where  $\epsilon_{Z-azo} \gg 0$ )]

As known, these quantum yields are wavelength dependent due to wavelength-dependent overlap of the  $\pi \rightarrow \pi^*$  and  $n \rightarrow \pi^*$  bands, which have different quantum yields.

(1b): Assisted switching "AST": Irradiation can be absorbed by the ant motif within an ant-*E*-azo or ant-*Z*-azo dyad, and may trigger assisted isomerization to the other isomer:



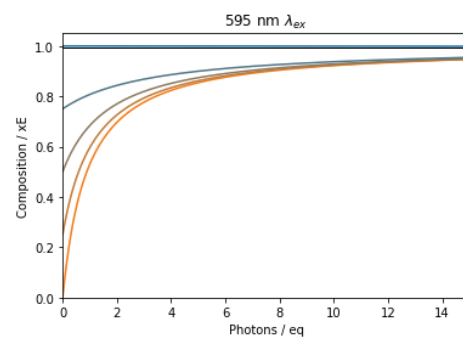
We assumed that these quantum yields are wavelength independent (assisted switching is initiated from the antenna S1 state regardless how it is generated).

(2) Absorptions: we assumed that  $\epsilon_{\text{ant}}(\lambda)$  is independent of the *E/Z*-isomer state of the ant-azo dyad and can be taken from the free antenna; and likewise that  $\epsilon_{\text{azo}}(\lambda)$  can be taken from the free photoswitch spectra as *E* and *Z*.

Thus, at long wavelengths (example below: 595 nm), where  $\epsilon_E^{azo} = \epsilon_Z^{azo} = 0$ , the PSS mole fraction of *E* should be given by:

$$x_E^{PSS_{595}} = \frac{\phi_{ZE}^{AST}}{\phi_{EZ}^{AST} + \phi_{ZE}^{AST}}$$

(3) Observation: We found that this left us with too many unknown parameters, where variations in one parameter could be compensated by the others to reproduce experimental behaviour, i.e. unique fits could not be generated. However, as a general principle, with reasonable values we noted that long-wavelength illumination kinetics appear to capture an experimental feature that had concerned us: the *apparently biphasic* assisted isomerisation kinetics of some dyads, from *Z*-rich mixes back towards their *E*-rich PSSs: where the initial isomerisation progress was very rapid, but then slowed to give near-flat-line kinetics: so that after long time periods the composition may appear to have reached PSS but is in fact still changing at a very slow rate (see panel, which shows a sample model fit, intended for **RhB-AO**, using experimental absorption data with fitted unknown assisted quantum yields, that captures the experimental UV-PSS value ca. 40%*E*, nearly captures the experimental long wavelength PSS (here, ~99%, instead of ca. 97.5%*E*), and matches the experimental direct photoswitching behaviour of **AO**: which predicts a rapid isomerisation phase that is followed by a slow approach to equilibrium).



## 11 Cell culture transfection and electrophysiology

HEK293 cells were cultured in Dulbecco's Modified Eagle Medium (DMEM; Corning) supplemented with 10% fetal bovine serum (FBS) and maintained at 37°C and 5% CO<sub>2</sub> in a humidified incubator. For experiments, cells were plated at low density on poly-L-lysine coated 18 mm coverslips and transfected the following day with Lipofectamine 2000 (Thermo Fisher Scientific). SNAP-mGluR2<sup>89</sup>, GIRK1-F137S<sup>90</sup> and tdTomato as a transfection marker were cotransfected in a 1:1:0.2 ratio.

Whole cell patch clamp recordings were performed 24 h after transfection as previously described<sup>91</sup> using an Axopatch 200B amplifier and a Digidata 1550B interface controlled by pClamp software (Molecular Devices). Voltage clamp recordings at -60 mV were performed in a high potassium solution (120 mM) to enable large inward currents upon receptor activation. Bath solution contained (in mM): 120 KCl, 25 NaCl, 10 HEPES, 2 CaCl<sub>2</sub>, 1 MgCl<sub>2</sub>. Pipettes of 3-5 MΩ resistance were filled with intracellular solution (in mM: 140 KCl, 10 HEPES, 5 EGTA, 3 MgCl<sub>2</sub>, 3 Na<sub>2</sub>ATP, 0.2 Na<sub>2</sub>GTP).

For labeling, cells were incubated with 1 μM **BGAG<sub>12,400</sub>**, **BGAG<sub>12,400</sub>-Cy5.v1**, or **BGAG<sub>12,400</sub>-Cy5.v2** 60 min at 37°C as described previously.<sup>91</sup> For photoswitching, a computer controlled CoolLED pE-4000 was used as illumination source and light was applied through a 40X



objective. Light intensities at the focal plane were approximately (in  $\text{mW}/\text{mm}^2$ ): 9.6 for 385 nm, 4.9 for 525 nm, 5.1 for 660 nm, 1.7 for 740 nm and 2.8 for 770 nm. The photostimulation protocol was: (a) 2 s of 385 nm light allowing receptor activation and then (b) maintenance in the dark, until evoked GIRK current reached the steady-state (plateau; "on" level); then (c) 10 s of 525 nm, 660 nm, 740 nm, or 770 nm "photo-switch-off" light immediately followed by (d) 10 s of 525 nm light to finish the switch-off. 5-15 measurement cycles per cell were used to generate one datapoint in **Figure S24** and **Figure 5**, and each cell was screened over all switchoff wavelengths, with 6-10 cells per wavelength per compound being used to make the dataset.

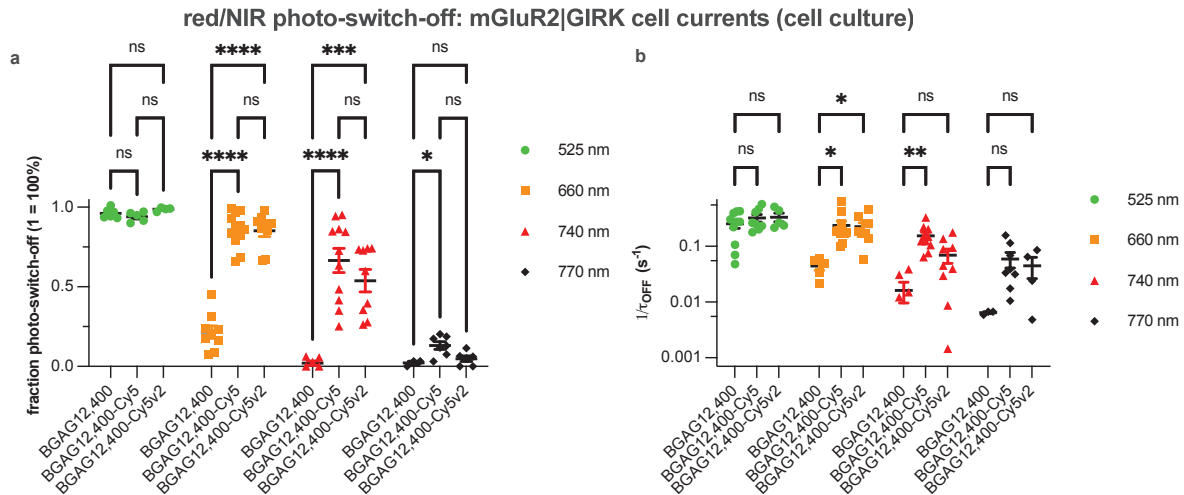


**Figure S24: (a) Photo-switch-off percentages. (b) Photo-switch-off rates.**  $p$ -values for Student's two-tailed  $t$ -test are shown on comparison brackets (\*\*\* =  $p < 0.001$ ; \* =  $p < 0.1$ ; etc).

Data was analyzed using Clampfit (Molecular Devices) and Prism 9 (GraphPad). To quantify the photo-switch-off, the reduction (from the maximum steady-state 385 nm-evoked GIRK current) after the end of the 10 s switch-off period (typically this is at or near a plateau in the timecourse) was measured, normalized to the baseline, and expressed as a percentage relative to switchoff by  $2 \times 10$  s of 525 nm switch-off (that was set to 100%; **Figure S24a**). Since this percentage is just an equilibrium value after a high light dose, we also fitted the photo-switch-off rates to provide an estimate of the *photon-efficiency* of the switching process (**Fig 24b**), which is increasingly important as the light dose is limited (e.g. in deep tissue).

The trend is that **Cy5-BGAG** conjugates could be photoswitched-off by red light (presumably, for the "740 nm" LED, the effective spectral portion is the  $<700$  nm fraction; **Fig 5i**) whereas BGAG without the **Cy5** is essentially low- or non-responsive to red light.

*We have no explanation for the small apparent photo-switch-off of BGAG<sub>12,400</sub> by the "660 nm" phase (Fig 5f), which is highly anomalous in that it has an exponential fit plateauing at 10-20% recovery. This could be consistent with either: (1) some emission portion from the nominal 660 nm LED continuously photo-driving a PSS that is slightly less Z-rich than the PSS-385 nm by direct absorption by the BGAG azobenzene (which seems very unlikely, since it would have to be UV emission); or (2) with a transient (e.g. 0.1 s) burst of light around 400 - 540 nm being passed to the sample only at the start of the "660 nm switchoff" phase, which causes a partial back-isomerisation, following which GIRK currents reach a new steady state corresponding to ca. 15% switchoff (this would seem most likely - perhaps e.g. the mechanical switching between 385 and 660 LED couplings transiently passes the emission of the 525 nm LED or some other white light into the light guide, although that would be an unexpected design flaw in the light engine; alternatively, there might be a "switch-on" effect with high voltage driving higher-energy emission from the 660 LED while the current stabilises); (3) or maybe that tdTomato absorption plays a role (this also seems unlikely).*



## 12 Viral injections, *in vivo* labelling and slice electrophysiology

BGAG<sub>12,400</sub> and BGAG<sub>12,400</sub>-Cy5-v1 were used in brain slices as described recently.<sup>91</sup> Male Grm2-Cre mice<sup>13</sup> of p60-p70 were bilaterally injected in the dentate gyrus (DG; coordinates: ML +/- 2.8, AP -3.5, DV -3.2) with 500 nL per hemisphere of AAV9-EF1a-FLEX-SNAP-mGluR2-WPRE-hGH and AAV9-CAG-FLEX-GFP<sup>92</sup> (3:1 ratio), using a Kopf motorized stereotaxic and a microinjection syringe pump from World Precision Instruments coupled to a 10  $\mu$ L syringe. Slice recordings were performed after 2-4 weeks of virus expression.

Slice preparations was performed as previously described<sup>91</sup>. Briefly, the viral-expressing mice were microinfused with 10  $\mu$ M BGAG<sub>12,400</sub> or BGAG<sub>12,400</sub>-Cy5-v1 in the DG. 4-12 hrs later, mice were anaesthetized with isoflurane and perfused with cold NMDG-based aCSF (in mM): 93 NMDG, 2.5 KCl, 1.2 NaH<sub>2</sub>PO<sub>4</sub>, 30 NaHCO<sub>3</sub>, 20 HEPES, 25 glucose, 5 sodium ascorbate, 2 thiourea, 3 sodium pyruvate, 10 MgSO<sub>4</sub>, 0.5 CaCl<sub>2</sub> (pH 7.4, 300-310 mOsm). Brains were extracted and 300  $\mu$ m horizontal slices were collected in NMDG solution and left for recovery for 30 min at 35 °C. Slices were then transferred to HEPES aCSF (in mM): 92 NaCl, 2.5 KCl, 1.2 NaH<sub>2</sub>PO<sub>4</sub>, 30 NaHCO<sub>3</sub>, 20 HEPES, 25 glucose, 5 sodium ascorbate, 2 thiourea, 3 sodium pyruvate, 2 MgSO<sub>4</sub>, 2 CaCl<sub>2</sub> (pH 7.4, 300-305 mOsm) for at least 45 minutes.

Hyperpolarization evoked by mGluR2 photo-activation was recorded at 30° C in aCSF solution (in mM): 124 NaCl, 2.5 KCl, 1.2 NaH<sub>2</sub>PO<sub>4</sub>, 24 NaHCO<sub>3</sub>, 5 HEPES, 12.5 glucose, 1.3 MgSO<sub>4</sub>, 2.5 CaCl<sub>2</sub> (pH 7.4, 300-305 mOsm). Whole-cell patch clamp recordings were acquired with a MultiClamp 700B amplifier (Molecular Devices) and a Digidata 1550B (Molecular Devices) in current-clamp mode. Pipettes between 3-6 M $\Omega$  resistance were filled with pipette solution (in mM): 130 K-gluconate, 4 KCl, 10 HEPES, 0.3 EGTA, 10 Na<sub>2</sub>-phosphocreatine, 4 Mg-ATP, 0.3 Na<sub>2</sub>-GTP (pH 7.35, 280-290 mOsm).

Photoswitching with the pE-4000 LED source was performed as described in **section 11**. Analogously, photo-switch-off percentage (degree of return from hyperpolarized to normal state) during 10 s long-wavelength illumination was plotted (**Fig 6d**); as was the rate of photo-switch-off [given as  $1/\tau$ , where  $\tau$  is the time constant of monoexponential fit to the kinetic of return from hyperpolarized (lowest possible value) towards depolarized (highest possible value) GIRK currents, wherein this fit was forced to start from the 385-then-dark-adapted (lowest plateau) value and forced to reach high plateau set to the current measured after an extended 525 nm period was applied (this corrects for auto-fitting errors with slow/zero kinetics of return)]. These parameters were analysed with Clampfit; data were plotted and statistically analysed with Prism 9 (GraphPad) (**Figure 6**). 5 measurement cycles per cell were recorded for each switchoff wavelength (representative trace overlays in **Figure 6c**), and the five switch-off percentages / rates were averaged to generate one datapoint in the data underlying **Figure 6d-e**. 1 or 2 cells were patched per brain slice, with a minimum of three slices per compound used to generate the full dataset represented as mean with SEM in **Fig 6d-e**.

## 13 Chemical Synthesis

### 13.1 General

All **chemicals**, which were obtained from Sigma-Aldrich, TCI, Alfa Aesar, Acros, abcr or Carbolution were used as received and without purification. Tetrahydrofuran (THF), dichloromethane (DCM) and dimethylformamide (DMF) were provided by Acros and were stored under argon atmosphere and dried over molecular sieves. TLC control, extractions and column chromatography were conducted using distilled, technical grade solvents. "Hexane" indicates a mixture of isomeric hexanes (e.g. 2-methylpentane, 3-methylpentane, 2,2-dimethylbutane, 2,3-dimethylbutane).

Unless stated otherwise, all **reactions** were performed without precautions in regard of potential air- and moisture-sensitivity and were stirred with Teflon-coated magnetic stir bars. Flash column **chromatography** was conducted under positive nitrogen pressure using Ceduran® Si60 silica gel from Merck GmbH. Reactions were monitored by thin layer chromatography (TLC) on Si60 F254 aluminium-backed sheets (Merck GmbH) and visualised by UV irradiation and/or KMnO<sub>4</sub> (3.0 g KMnO<sub>4</sub>, 20 g K<sub>2</sub>CO<sub>3</sub>, 0.30 g KOH, 0.30 L H<sub>2</sub>O).

**Analytical high performance liquid chromatography** coupled to mass spec analysis (HPLC-MS) was conducted using an Agilent 1100 system, through a Hypersil Gold HPLC column from ThermoFisher Scientific GmbH, with a DAD detector and a unit resolution Agilent LC/MSD IQ mass spectrometer (ESI mode). Mixtures of water (analytical grade, 0.1% formic acid) and MeCN (analytical grade, 0.1% formic acid) were used as eluent systems.

**Compound purity and isomer ratios** were determined by analytical HPLC with an Agilent 1100 system equipped with a DAD detector, using an Agilent Zorbax Eclipse Plus C18 column (4.6 mm × 250 mm, particle size 10 μm). Mixtures of water (analytical grade, 0.1% formic acid) and MeCN (analytical grade, 0.1% formic acid) were used as eluent systems. Typical gradient used was from 10% to 100% MeCN over 27 min.

**Preparative HPLC** purification was performed with an Agilent 1260 equipped with a DAD detector, using an Agilent Zorbax Eclipse Plus C18 column (21.4 mm × 250 mm, particle size 10 μm). Mixtures of water (analytical grade, 0.1% formic acid) and MeCN (analytical grade, 0.1% formic acid) were used as eluent systems.

**Abbreviations:** DCM (dichloromethane), DMF (dimethylformamide), MeOH (methanol), MeCN (acetonitrile), HBTU ((2-(1H-benzotriazol-1-yl)-1,1,3,3-tetramethyluronium hexafluorophosphate), DIPEA (diisopropylethylamine), TEA (triethylamine), EA (ethyl acetate), TFA (trifluoroacetic acid), AcOH (acetic acid), Boc (*tert*-butyloxycarbonyl), TSTU (*N,N,N',N'*-tetramethyl-*O*-(*N*-succinimidyl)uronium tetrafluoroborate).

### 13.2 NMR spectroscopy

Nuclear magnetic resonance (**NMR**) spectroscopy was performed using *Bruker Avance III HD Biospin* (<sup>1</sup>H: 400 MHz/<sup>13</sup>C: 100 MHz, with BBFO cryoprobeTM; or <sup>1</sup>H: 500 MHz/<sup>13</sup>C: 126 MHz) or *Bruker Avance III* (<sup>1</sup>H: 800 MHz/<sup>13</sup>C: 201 MHz, with TCI cryoprobe) spectrometers. NMR spectra were measured at 298 K, unless stated otherwise, and were analysed with MestreNova 12. H-NMR spectra chemical shifts (δ) in parts per million (ppm) relative to tetramethylsilane (δ = 0 ppm) are reported using the residual protic solvent (CHCl<sub>3</sub> in CDCl<sub>3</sub>: δ = 7.26 ppm, DMSO-d<sub>5</sub> in DMSO-d<sub>6</sub>: δ = 2.50 ppm, CHD<sub>2</sub>OD in CD<sub>3</sub>OD: δ = 3.31 ppm, CHDCl<sub>2</sub> in CD<sub>2</sub>Cl<sub>2</sub>: δ = 5.32 ppm, and CHD<sub>2</sub>CN in CD<sub>3</sub>CN: δ = 1.94 ppm,) as an internal reference. For <sup>13</sup>C-NMR spectra, chemical shifts in ppm relative to tetramethylsilane (δ = 0 ppm) are reported using the central resonance of the solvent signal (CDCl<sub>3</sub>: δ = 77.2 ppm, DMSO-d<sub>6</sub>: δ = 39.5 ppm, CD<sub>3</sub>OD: δ = 49.0 ppm, CD<sub>2</sub>Cl<sub>2</sub>: δ = 54.0 ppm, CD<sub>3</sub>CN: δ = 118.3 ppm) as an internal reference. For <sup>1</sup>H-NMR spectra in addition to the chemical shift the following data is reported in parentheses: multiplicity, coupling constant(s) and number of hydrogen atoms. The abbreviations for multiplicities and related descriptors are s = singlet, d = doublet, t = triplet, q = quartet, or combinations thereof, m = multiplet and br = broad. Where known products matched literature analysis data, reference for literature is given.

### 13.3 High-resolution mass spectrometry (HRMS)

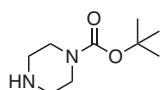
High resolution mass spectrometry (**HRMS**) was conducted using a Thermo Finnigan LTQ FT Ultra Fourier Transform ion cyclotron resonance spectrometer, applying electron spray ionisation (ESI) with a spray capillary voltage of 4 kV at temperature 250 °C with a method dependent range from 50 to 2000 u. All reported  $m/z$  values refer to positive ionization mode, unless stated otherwise.

### 13.4 Synthesis

Any requests for materials or raw/additional analytical data, please reference our internal lab book numbers which are given for all compounds (e.g. **BW063**).

#### 13.4.1 Azobenzene building blocks

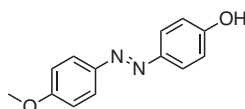
*tert*-butyl piperazine-1-carboxylate (**S1**, **BW063**; known compound)



**S1** was synthesized according to literature.<sup>93</sup>

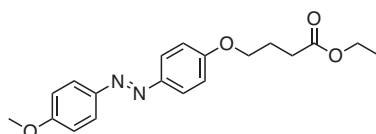
A solution of di-*tert*-butyl dicarbonate (6.43 g, 29.5 mmol, 1 eq.) in DCM (20 mL) was added to a solution of piperazine (5.06 g, 58.8 mmol, 2 eq.) in DCM (50 mL) at 0 °C. The reaction mixture was allowed to warm to room temperature and stirred at room temperature for 16 h. The suspension was filtered, and the filtrate was concentrated under reduced pressure. The resulting white solid was suspended in ice-cold water (100 mL), filtered, and the filtrate was basified to pH 12 with a saturated solution of potassium carbonate. The aqueous phase was extracted with methyl *tert*-butyl ether (3 x 100 mL). The combined organics were washed with brine (100 mL), dried (MgSO<sub>4</sub>) and concentrated under reduced pressure to yield **S1** (2.07 g, 11.1 mmol, 19%) as a colorless solid. Analytical data (H-NMR) match literature.<sup>93</sup>

4-((4-methoxyphenyl)diazenyl)phenol (**S2**, **BW192**; known compound)



Sodium nitrite (2M aqueous solution, 3.65 mL, 7.3 mmol) were added to a solution of 4-methoxyaniline (824 mg, 6.69 mmol, 1 eq.) in MeOH (20 mL) and hydrochloric acid (2M aqueous solution, 20 mL) at 0 °C and stirred at 0 °C for 30 min. The reaction mixture was added slowly to a solution of phenol (678 mg, 7.30 mmol, 1.1 eq.) in MeOH (20 mL) and dipotassium hydrogen phosphate (0.5M aqueous solution, 20 mL) at 0 °C and stirred at 0 °C for 1 h. During the addition pH was adjusted to 10 with potassium hydroxide (1M aqueous solution). The reaction mixture was allowed to warm to room temperature, pH was adjusted to 7 with hydrochloric acid (2M aqueous solution) and extracted with EA (3 x 100 ml). The combined organics were dried (MgSO<sub>4</sub>), concentrated under reduced pressure and purified by silica gel column chromatography (5-25% ethyl acetate in hexane) to yield **S2** (1.10 g, 4.82 mmol, 72 %) as an orange solid. Analytical data (H-NMR) match literature.<sup>94</sup>

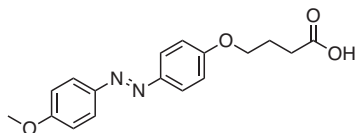
ethyl 4-(4-((4-methoxyphenyl)diazenyl)phenoxy)butanoate (**S3**, **BW257**; known compound)



Ethyl 4-bromobutyrate (0.62 mL, 848 mg, 4.34 mmol, 2 eq.) were added to a solution of **S2** (496 mg, 2.17 mmol, 1 eq.) and potassium carbonate (902 mg, 6.52 mmol, 3 eq.) in acetone

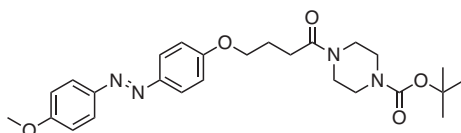
(20 mL) and refluxed for 16 h. The reaction mixture was quenched with water (50 mL) and extracted with EA (3 x 50 mL). The combined organics were dried (MgSO<sub>4</sub>), concentrated under reduced pressure and purified by silica gel column chromatography (0-10% EA in hexane) to yield **S3** (400 mg, 1.17 mmol, 54%) as an orange solid. Analytical data (H-NMR) match literature.<sup>95</sup>

4-(4-((4-methoxyphenyl)diazenyl)phenoxy)butanoic acid (**S4**, **AO-COOH**, **BW265**; **known**)



Potassium hydroxide (328 mg, 5.84 mmol, 5 eq.) was added to a solution of **S3** (400 mg, 1.17 mmol, 1 eq.) in MeOH (20 mL) and stirred at 50 °C for 16 h. The reaction mixture was concentrated under reduced pressure. The solid residue was suspended in hydrochloric acid (2M aqueous solution, 50 mL) and extracted with DCM (5 x 50 mL). The combined organics were dried (MgSO<sub>4</sub>) and concentrated under reduced pressure to yield **AO-COOH** (345 mg, 1.10 mmol, 94%) as an orange solid. Analytical data (H-NMR) match literature.<sup>95</sup>

*tert*-butyl-4-(4-(4-((4-methoxyphenyl)diazenyl)phenoxy)butanoyl)piperazine-1-carboxylate (**S5**, **BW270**, **BEW338**; **novel**)



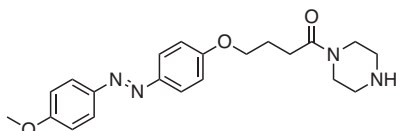
**AO-COOH** (100 mg, 0.32 mmol, 1 eq.), **S1** (88.9 mg, 0.48 mmol, 1.5 eq.), HBTU (145 mg, 0.38 mmol, 1.2 eq.) and TEA (134 μL, 96.6 mg, 0.95 mmol, 3 eq.) were dissolved in DMF (3 mL) and stirred at room temperature for 16 h. The reaction mixture was concentrated under reduced pressure. The resulting solid was dissolved in EA (50 mL) and washed with a saturated aqueous solution of sodium hydrogen carbonate (5 x 50 mL). The organic phase was dried (MgSO<sub>4</sub>), concentrated under reduced pressure and purified by silica gel column chromatography (20-80% EA in hexane) to yield **S5** (132 mg, 0.27 mmol, 86%) as an orange solid.

<sup>1</sup>H-NMR (400 MHz; CDCl<sub>3</sub>): δ = 7.91 – 7.83 (m, 4H), 7.04 – 6.96 (m, 4H), 4.12 (t, *J* = 5.8 Hz, 2H), 3.89 (s, 3H), 3.63 – 3.57 (m, 2H), 3.49 – 3.38 (m, 6H), 2.57 (t, *J* = 7.2 Hz, 2H), 2.18 (p, *J* = 6.7 Hz, 2H), 1.47 (s, 9H).

<sup>13</sup>C-NMR (101 MHz; CDCl<sub>3</sub>): δ = 174.5, 171.0, 161.0, 156.0, 147.2, 140.5, 124.6, 124.5, 114.8, 114.3, 80.5, 67.4, 59.4, 55.7, 45.4, 29.6, 28.5, 24.9.

HR-MS (ESI) *m/z*: calculated for C<sub>26</sub>H<sub>35</sub>N<sub>4</sub>O<sub>5</sub><sup>+</sup>: 483.2620; found: 483.26028, (M + H)<sup>+</sup>.

4-(4-((4-methoxyphenyl)diazenyl)phenoxy)-1-(piperazin-1-yl)butan-1-one (**S6**, **AOpip**, **BW274**, **BEW337**; **novel**)



TFA (2 mL) was added dropwise to a solution of **S5** (130 mg, 0.27 mmol, 1 eq.) in DCM (2 mL) at 0 °C and stirred at 0 °C for 2 h. The reaction mixture was allowed to warm to room temperature and quenched with a saturated aqueous solution of sodium hydrogen carbonate (50 mL). The reaction mixture was extracted with DCM (3 x 50 mL). The combined organics

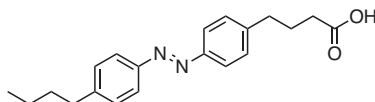
were dried ( $\text{MgSO}_4$ ) and concentrated under reduced pressure to yield **AOpip** (100 mg, 0.26 mmol, 97%) as an orange solid.

**$^1\text{H-NMR}$**  (400 MHz;  $\text{CDCl}_3$ ):  $\delta$  = 7.91 – 7.83 (m, 4H), 7.04 – 6.96 (m, 4H), 4.12 (t,  $J$  = 5.9 Hz, 2H), 3.89 (s, 3H), 3.66 (s, 2H), 3.55 – 3.50 (m, 2H), 2.92 – 2.83 (m, 4H), 2.56 (t,  $J$  = 7.2 Hz, 2H), 2.18 (p,  $J$  = 6.5 Hz, 2H).

**$^{13}\text{C-NMR}$**  (101 MHz;  $\text{CDCl}_3$ ):  $\delta$  = 170.9, 161.7, 161.0, 147.2, 146.7, 124.5, 124.5, 114.8, 114.3, 67.4, 55.7, 46.0, 45.6, 42.1, 25.0.

**HR-MS** (ESI)  $m/z$ : calculated for  $\text{C}_{21}\text{H}_{26}\text{N}_4\text{O}_3$ : 382.20777; found: 383.20799,  $\text{M}^+$ .

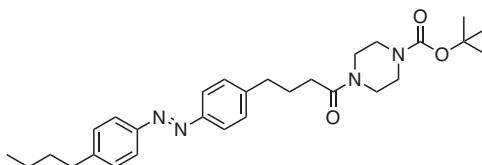
4-(4-((4-butylphenyl)diazenyl)phenyl)butanoic acid (**S7**, **AK-COOH**, **BW029**; **known**)



Known compound **AK-COOH** was synthesized according to literature.<sup>77</sup>

A solution of Oxone<sup>®</sup> (18.4 g, 59.8 mmol, 9 eq.) in water (150 mL) was added to a solution of 4-butylaniline (1.60 mL, 1.52 g, 10.1 mmol, 1.5 eq.) in DCM (150 mL) and stirred at room temperature for 16 h. The phases were separated, and the aqueous phase was extracted with DCM (2 x 50 mL). The combined organics were washed with hydrochloric acid (1M aqueous solution, 50 mL), a saturated aqueous solution of sodium hydrogen carbonate (50 mL) and water (50 mL). 4-(4-aminophenyl)butanoic acid (1.20 g, 6.70 mmol, 1 eq.) and AcOH (100 mL) were added to the organic phase, DCM was evaporated under reduced pressure and the resulting mixture was stirred at room temperature for 16 h. The reaction mixture was concentrated under reduced pressure, azeotroped with toluene (3 x 5 mL) and purified by silica gel column chromatography (3% MeOH in DCM + 0.5% AcOH) to yield **AK-COOH** (1.46 g, 4.50 mmol, 67%) as a red/orange solid. Analytical data ( $^1\text{H-NMR}$ ) match literature.<sup>77</sup>

*tert*-butyl 4-(4-(4-((4-butylphenyl)diazenyl)phenyl)butanoyl)piperazine-1-carboxylate (**S8**, **BW281**, **BEW336**; **novel**)



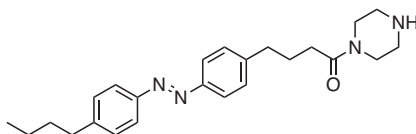
**AO-COOH** (100 mg, 0.31 mmol, 1 eq.), **S1** (86.1 mg, 0.46 mmol, 1.5 eq.), HBTU (140 mg, 0.37 mmol, 1.2 eq.) and TEA (130  $\mu\text{L}$ , 93.6 mg, 0.95 mmol, 3 eq.) were dissolved in DMF (3 mL) and stirred at room temperature for 16 h. Water (30 mL) was added, and the reaction mixture was extracted with DCM (5 x 50 mL). The combined organics were dried ( $\text{MgSO}_4$ ), concentrated under reduced pressure and purified by silica gel column chromatography (20-50% EA in hexane) to yield **S8** (119 mg, 0.24 mmol, 78%) as an orange solid.

**$^1\text{H-NMR}$**  (400 MHz;  $\text{CDCl}_3$ ):  $\delta$  = 7.83 (dd,  $J$  = 8.4, 2.6 Hz, 4H), 7.32 (dd,  $J$  = 8.4, 3.6 Hz, 4H), 3.59 (s, 2H), 3.46 – 3.32 (m, 6H), 2.77 (t,  $J$  = 7.4 Hz, 2H), 2.69 (t,  $J$  = 7.8 Hz, 2H), 2.35 (t,  $J$  = 7.4 Hz, 2H), 2.03 (p,  $J$  = 7.5 Hz, 2H), 1.69 – 1.61 (m, 2H), 1.46 (s, 9H), 1.38 (dq,  $J$  = 14.7, 7.3 Hz, 2H), 0.94 (t,  $J$  = 7.3 Hz, 3H).

**$^{13}\text{C-NMR}$**  (101 MHz;  $\text{CDCl}_3$ ):  $\delta$  = 171.4, 154.7, 151.4, 151.1, 146.5, 144.9, 129.3, 129.2, 123.0, 122.9, 80.5, 45.4, 41.5, 35.7, 35.3, 33.6, 32.4, 28.5, 26.5, 22.5, 14.1.

**HR-MS** (ESI)  $m/z$ : calculated for  $\text{C}_{29}\text{H}_{41}\text{N}_4\text{O}_3^+$ : 493.31732; found: 493.31742, ( $\text{M} + \text{H}$ )<sup>+</sup>.



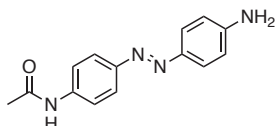
4-(4-((4-butylphenyl)diazenyl)phenyl)-1-(piperazin-1-yl)butan-1-one (**S9**, **AKpip**, **BW283**, **BEW339**; *novel*)

TFA (5 mL) was added dropwise to a solution of **S8** (110 mg, 0.22 mmol, 1 eq.) in DCM (5 mL) at 0 °C and stirred at 0 °C for 2 h. The reaction mixture was allowed to warm to room temperature, saturated aqueous solution of sodium hydrogen carbonate (50 mL) was added, and the mixture was extracted with DCM (3 x 50 mL). The combined organics were dried (MgSO<sub>4</sub>) and concentrated under reduced pressure to yield **AKpip** (84 mg, 0.21 mmol, 96%) as an orange solid.

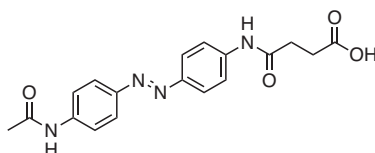
<sup>1</sup>H-NMR (400 MHz; CDCl<sub>3</sub>):  $\delta$  = 7.83 (dd,  $J$  = 8.4, 2.8 Hz, 4H), 7.32 (dd,  $J$  = 8.4, 4.1 Hz, 4H), 3.66 (t,  $J$  = 5.1 Hz, 2H), 3.44 (t,  $J$  = 5.1 Hz, 2H), 3.16 (bs, 1H), 2.89 (q,  $J$  = 4.6 Hz, 4H), 2.76 (t,  $J$  = 7.4 Hz, 2H), 2.69 (t,  $J$  = 7.7 Hz, 2H), 2.33 (t,  $J$  = 7.5 Hz, 2H), 2.03 (p,  $J$  = 7.5 Hz, 2H), 1.73 – 1.58 (m, 2H), 1.38 (h,  $J$  = 7.3 Hz, 2H), 0.94 (t,  $J$  = 7.3 Hz, 3H).

<sup>13</sup>C-NMR (101 MHz; CDCl<sub>3</sub>):  $\delta$  = 171.2, 151.4, 151.1, 146.5, 144.9, 129.3, 129.2, 123.0, 122.9, 45.5, 41.8, 35.7, 35.3, 33.6, 32.2, 26.5, 22.5, 14.1.

HR-MS (ESI) m/z: calculated for C<sub>24</sub>H<sub>33</sub>N<sub>4</sub>O<sup>+</sup>: 393.26489; found: 393.26516, (M + H)<sup>+</sup>.

N-(4-((4-aminophenyl)diazenyl)phenyl)acetamide (**S10**, **BW050**; *known*)

Sodium nitrite (2M aqueous solution, 5.50 mL, 11 mmol) was added to a solution of 4-aminoacetanilide (1.50 g, 10.0 mmol, 1 eq.) in MeOH (90 ml) and hydrochloric acid (2M aqueous solution, 30 mL) at 0 °C and stirred at 0 °C for 30 min. Sulfamic acid (131 mg, 1.35 mmol, 0.14 eq.) was added to the reaction mixture and stirred at 0 °C for 3 min. Subsequently, AcOH (30 mL) and aniline (1.20 mL, 1.22 g, 13.1 mmol, 1.3 eq.) were added before sodium acetate (13.7 g, 101 mmol, 10 eq.) was added portion wise and stirred at 0 °C for another 30 min. The reaction mixture was allowed to warm to room temperature, pH was adjusted to 7 with hydrochloric acid (2M aqueous solution) and extracted with EA (3 x 150 mL). The combined organics were dried (MgSO<sub>4</sub>), concentrated under reduced pressure and purified by silica gel column chromatography (10-50% EA in hexane) to yield **S10** (265 mg, 1.04 mmol, 10%) as an orange solid. Analytical data (H-NMR) match literature.<sup>96</sup> For better yields, aniline-formaldehyde-bisulfite adduct could probably be used instead.

4-((4-((4-acetamidophenyl)diazenyl)phenyl)amino)-4-oxobutanoic acid (**S11**, **AN-COOH**, **BW351**, **BEW442**; *novel*)

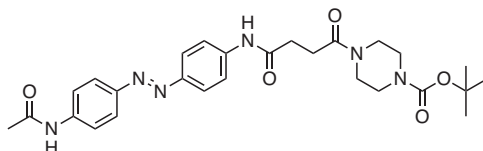
**S10** (80 mg, 0.315 mmol, 1 eq.), succinic anhydride (49.5 mg, 0.495 mmol, 1.6 eq.) and pyridine (40.5  $\mu$ L, 29.9 mg, 0.38 mmol, 1.2 eq.) were dissolved in anhydrous acetone (5 mL) under nitrogen atmosphere and heated to 60 °C for 16 h. The red precipitate was filtered and washed with cold acetone and diethyl ether to yield **AN-COOH** (59 mg, 0.17 mmol, 53%) as a red solid.

**<sup>1</sup>H-NMR** (400 MHz; D<sub>3</sub>COD):  $\delta$  = 7.86 (dd,  $J$  = 8.9, 1.2 Hz, 4H), 7.74 (dd,  $J$  = 9.0, 2.3 Hz, 4H), 2.74 – 2.63 (m, 4H), 2.17 (s, 3H).

**<sup>13</sup>C-NMR** (101 MHz; D<sub>3</sub>COD):  $\delta$  = 173.3, 171.8, 163.6, 157.3, 150.2, 148.9, 142.8, 124.5, 124.5, 121.0, 121.0, 32.9, 30.6, 24.0.

**HR-MS** (ESI)  $m/z$ : calculated for C<sub>18</sub>H<sub>19</sub>N<sub>4</sub>O<sub>4</sub><sup>+</sup>: 355.14008; found: 355.14007, (M + H)<sup>+</sup>.

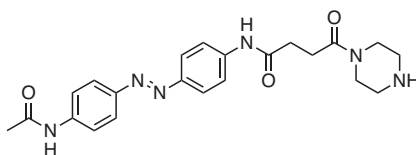
*tert*-butyl 4-(4-((4-((4-acetamidophenyl)diazenyl)phenyl)amino)-4-oxobutanoyl) piperazine-1-carboxylate (**S12**, **BW358**; **novel**)



**AN-COOH** (55 mg, 0.16 mmol, 1 eq.), **S1** (57.8 mg, 0.31 mmol, 2. eq.), HBTU (70.6 mg, 0.19 mmol, 1.2 eq.) and TEA (87.3  $\mu$ L, 62.8 mg, 0.62 mmol, 4 eq.) were dissolved in DMF (3 mL) and stirred at room temperature for 16 h. The reaction mixture was concentrated under reduced pressure and purified by silica gel column chromatography (10% MeOH in DCM) to yield **S12** (75.0 mg, 0.14 mmol, 93 %) as an orange solid that was immediately passed on for deprotection without NMR characterisation.

**HR-MS** (ESI)  $m/z$ : calculated for C<sub>27</sub>H<sub>35</sub>N<sub>6</sub>O<sub>5</sub><sup>+</sup>: 523.26634; found: 523.26634, (M + H)<sup>+</sup>.

*N*-(4-((4-acetamidophenyl)diazenyl)phenyl)-4-oxo-4-(piperazin-1-yl)butanamide (**S13**, **ANpip**, **BW366**, **BEW444**; **novel**)



TFA (2 mL) was added dropwise to a solution of **S12** (70.0 mg, 0.13 mmol, 1 eq.) in DCM (2 mL) at 0 °C and stirred at 0 °C for 2 h. The reaction mixture was allowed to warm to room temperature, saturated aqueous solution of sodium hydrogen carbonate (50 mL) was added, and the mixture was extracted with a 3:1 mixture of DCM and propanol (3 x 50 mL). The combined organics were dried (MgSO<sub>4</sub>) and concentrated under reduced pressure to yield **ANpip** (55 mg, 0.13 mmol, 97%) as an orange solid

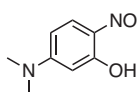
**<sup>1</sup>H-NMR** (400 MHz; CD<sub>3</sub>OD):  $\delta$  = 7.86 (dd,  $J$  = 9.0, 1.5 Hz, 4H), 7.74 (dd,  $J$  = 8.9, 3.8 Hz, 4H), 3.64 – 3.55 (m, 4H), 2.98 – 2.87 (m, 2H), 2.82 (t,  $J$  = 5.1 Hz, 2H), 2.81 – 2.70 (m, 4H), 2.17 (s, 3H).

**<sup>13</sup>C-NMR** (101 MHz; CD<sub>3</sub>OD):  $\delta$  = 173.4, 172.6, 171.8, 150.2, 150.1, 142.8, 142.6, 124.5, 124.5, 121.0, 120.9, 46.1, 43.3, 32.7, 28.8, 24.0.

**HR-MS** (ESI)  $m/z$ : calculated for C<sub>22</sub>H<sub>27</sub>N<sub>6</sub>O<sub>3</sub><sup>+</sup>: 423.21392; found: 423.21385, (M + H)<sup>+</sup>.

### 13.4.2 Fluorophore building blocks

5-(dimethylamino)-2-nitrosophenol (**S14**, **BW260**; **known**)

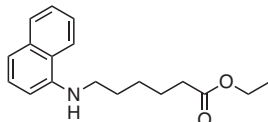


**S14** was synthesized according to literature.<sup>97</sup>

A solution of sodium nitrite (251 mg, 3.64 mmol; 1 eq.) in water (3 mL) was added to a solution of 3-(dimethylamino) phenol (500 mg, 3.64 mmol; 1 eq.) in hydrochloric acid (12M aqueous

solution, 3 mL) and water (1 mL) at 0 °C and stirred at 0 °C for 1 h. The resulting red precipitate was filtered, washed with a saturated, aqueous solution of sodium acetate and recrystallized from acetone to yield **S14** (342 mg, 2.06 mmol; 57%) as a red solid. Analytical data (H-NMR) match literature.<sup>97</sup>

ethyl 6-(naphthalen-1-ylamino)hexanoate (**S15**, **BW297**, **BEW326**; *novel*)



**S15** was synthesized similarly to a procedure adapted from the literature.<sup>98</sup>

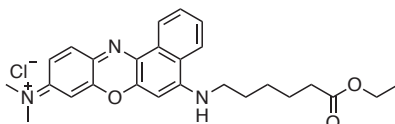
1-naphthalenamine (732 mg, 5.11 mmol, 1 eq.), ethyl 6-bromohexanoate (1.00 mL, 1.25 g, 5.26 mmol, 1.1 eq.) and potassium carbonate (2.12 g, 15.3 mmol, 3 eq.) were dissolved in MeCN (30 mL) and heated to reflux for 16 h. The reaction mixture was filtered and concentrated under reduced pressure. The crude material was purified by silica gel column chromatography (10% EA in hexane) to yield **S15** (320 mg, 1.12 mmol, 22 %) as a colorless oil.

**<sup>1</sup>H-NMR** (400 MHz; CDCl<sub>3</sub>):  $\delta$  = 7.96 – 7.62 (m, 2H), 7.47 – 7.41 (m, 2H), 7.35 (t,  $J$  = 7.9 Hz, 1H), 7.23 (d,  $J$  = 8.2 Hz, 1H), 6.62 (d,  $J$  = 7.6 Hz, 1H), 4.14 (q,  $J$  = 7.1 Hz, 2H), 3.30 (t,  $J$  = 7.1 Hz, 2H), 2.35 (t,  $J$  = 7.4 Hz, 2H), 1.81 (p,  $J$  = 14.7, 7.3 Hz, 2H), 1.72 (p,  $J$  = 7.6 Hz, 2H), 1.26 (t,  $J$  = 7.1 Hz, 3H).

**<sup>13</sup>C-NMR** (101 MHz; CDCl<sub>3</sub>):  $\delta$  = 173.8, 134.5, 128.8, 126.8, 126.6, 125.8, 124.8, 123.5, 119.9, 118.6, 117.4, 60.4, 55.2, 34.4, 29.2, 27.0, 24.9, 14.4.

**HR-MS** (ESI)  $m/z$ : calculated for C<sub>18</sub>H<sub>24</sub>NO<sub>2</sub><sup>+</sup>: 286.18016; found: 286.18030, (M + H)<sup>+</sup>.

*N*-(5-((6-ethoxy-6-oxohexyl)amino)-9*H*-benzo[*a*]phenoxazin-9-ylidene)-*N*-methylmethanaminium chloride (**S16**, **BW301**, **BEW332**; *novel*)



**S16** was synthesized similarly to a procedure adapted from the literature.<sup>99</sup>

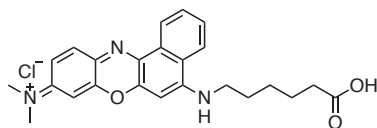
Hydrochloric acid (12M aqueous solution, 1.17 mL, 1.39 g, 14.2 mmol, 15 eq.) and **S14** (157 mg, 0.95 mmol, 1 eq.) were added to a solution of **S15** (270 mg, 0.95 mmol, 1 eq.) in ethanol (40 mL) at 0 °C. The reaction mixture was stirred at 0 °C for 10 min, allowed to warm to room temperature and heated to reflux for 16 h. The solvent was removed under reduced pressure and the crude material was purified by dry column chromatography (side products were eluted with EA and the desired product with 5% MeOH in DCM) to yield **S16** (74.3 mg, 0.16 mmol, 17 %) as a blue solid.

**<sup>1</sup>H-NMR** (500 MHz; CD<sub>3</sub>OD):  $\delta$  = 8.90 (d,  $J$  = 8.2 Hz, 1H), 8.35 (d,  $J$  = 8.5 Hz, 1H), 7.93 (ddt,  $J$  = 8.1, 7.1, 1.0 Hz, 1H), 7.88 – 7.81 (m, 2H), 7.28 – 7.24 (m, 1H), 6.99 (s, 1H), 6.91 – 6.86 (m, 1H), 4.10 (q,  $J$  = 7.2 Hz, 2H), 3.75 (t,  $J$  = 7.3 Hz, 2H), 3.32 (s, 6H), 2.39 (t,  $J$  = 7.3 Hz, 2H), 1.90 (p,  $J$  = 7.5 Hz, 2H), 1.74 (p,  $J$  = 7.4 Hz, 2H), 1.62 – 1.49 (m, 2H), 1.22 (t,  $J$  = 7.1 Hz, 3H).

**<sup>13</sup>C-NMR** (126 MHz; CD<sub>3</sub>OD):  $\delta$  = 175.3, 159.7, 157.4, 153.5, 149.4, 135.5, 133.8, 133.1, 132.7, 131.5, 131.1, 125.8, 124.9, 123.9, 116.5, 97.1, 94.6, 61.5, 45.7, 41.1, 34.8, 29.4, 27.5, 25.7, 14.5.

**HR-MS** (ESI)  $m/z$ : calculated for C<sub>26</sub>H<sub>30</sub>N<sub>3</sub>O<sub>3</sub><sup>+</sup>: 432.22799; found: 432.22817, M<sup>+</sup>.

*N*-(5-((5-carboxypentyl)amino)-9*H*-benzo[*a*]phenoxazin-9-ylidene)-*N*-methylmethanaminium chloride (**S17**, **NB-COOH**, **BW303**, **BEW333**; *novel*)



**NB-COOH** was synthesized similarly to a procedure adapted from the literature.<sup>100</sup>

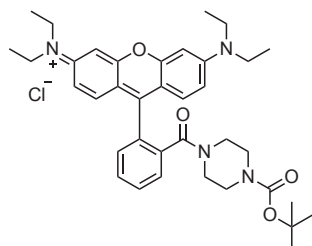
**S16** (71.0 mg, 0.15 mmol, 1 eq.) was dissolved in hydrochloric acid (1M aqueous solution, 15 mL) and heated to reflux for 2 h. The reaction mixture was concentrated under reduced pressure to yield **NB-COOH** (65.0 mg, 0.15 mmol, 97 %) as a blue solid.

<sup>1</sup>H-NMR (500 MHz; CD<sub>3</sub>OD):  $\delta$  = 8.95 – 8.88 (m, 1H), 8.55 – 8.12 (m, 1H), 7.97 – 7.90 (m, 1H), 7.91 – 7.80 (m, 2H), 7.30 – 7.23 (m, 1H), 7.03 – 6.98 (m, 1H), 6.93 – 6.87 (m, 1H), 3.76 (t, *J* = 7.6 Hz, 2H), 3.32 (d, *J* = 1.4 Hz, 6H), 2.40 (t, *J* = 7.3 Hz, 2H), 1.90 (p, *J* = 7.6 Hz, 2H), 1.74 (p, *J* = 7.4 Hz, 2H), 1.61 – 1.49 (m, 2H).

<sup>13</sup>C-NMR (126 MHz; CD<sub>3</sub>OD):  $\delta$  = 175.8, 159.8, 157.4, 153.6, 149.4, 135.6, 133.8, 133.1, 132.7, 131.5, 131.1, 125.8, 124.9, 123.9, 116.5, 97.2, 94.6, 45.7, 41.1, 34.5, 29.4, 27.5, 25.6.

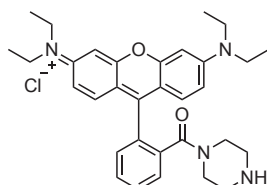
**HR-MS** (ESI) *m/z*: calculated for C<sub>24</sub>H<sub>25</sub>N<sub>3</sub>O<sub>3</sub><sup>+</sup>: 404.19687; found: 404.19677, M<sup>+</sup>.

*N*-(9-(2-(4-(*tert*-butoxycarbonyl)piperazine-1-carbonyl)phenyl)-6-(diethylamino)-3*H*-xanthen-3-ylidene)-*N*-ethylethanaminium chloride (**S18**, **BW040**; *known*)



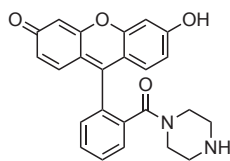
*N*-(9-(2-carboxyphenyl)-6-(diethylamino)-3*H*-xanthen-3-ylidene)-*N*-ethylethanaminium chloride (3.30 g, 6.95 mmol, 1 eq.), **S1** (2.50 g, 13.4 mmol, 1.9 eq.), HBTU (2.81 g, 7.41 mmol, 1.1 eq.) and TEA (2.80 mL, 2.02 g, 19.9 mmol, 2.9 eq.) were dissolved in DMF (15 mL) and stirred at room temperature for 16 h. The reaction mixture was diluted with water (150 mL) and extracted with EA (3 x 180 mL). The combined organic phases were washed with a saturated aqueous solution of sodium chloride (3 x 100 mL), dried (MgSO<sub>4</sub>) and concentrated under reduced pressure. The crude material was purified by silica gel column chromatography (8% MeOH in DCM) to yield known compound **S18** (2.95 g, 66%, 4.56 mmol) as a pink solid. Analytical data (H-NMR) match literature.<sup>101</sup>

*N*-(6-(diethylamino)-9-(2-(piperazine-1-carbonyl)phenyl)-3*H*-xanthen-3-ylidene)-*N*-ethylethanaminium chloride (**RhBpip**, **BW043**, **S19**; *known*)



Hydrochloric acid (2M solution in ethanol, 10 mL) was added to a solution of **S18** (2.95 g, 4.56 mmol, 1 eq.) in ethanol (90 mL) and heated to reflux for 3 h. The reaction mixture was concentrated under reduced pressure to yield known compound **RhBpip** (2.66 g, 4.55 mmol, 99%) as a pink solid. Analytical data (H-NMR) match literature.<sup>101</sup>

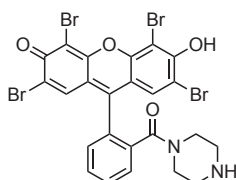
6-hydroxy-9-(2-(piperazine-1-carbonyl)phenyl)-3*H*-xanthen-3-one (**S20**, **Flpip**, **BW073**; **known**)



Known compound **Flpip** was synthesized according to literature.<sup>102</sup>

*N,N'*-dicyclohexylcarbodiimide (315 mg, 1.53 mmol, 1.5 eq.) and *N*-hydroxysuccinimide (146 mg, 1.27 mmol, 1.3 eq.) were added to a solution of disodium 2-(6-oxido-3-oxo-3*H*-xanthen-9-yl)benzoate (379 mg, 1.01 mmol, 1 eq.) in anhydrous DMF (1.5 mL) under nitrogen atmosphere and heated to 80°C for 1 h. The reaction mixture was allowed to cool to room temperature. Piperazine (183 mg, 2.12 mmol, 2.11 eq.) and TEA (0.45 mL, 324 mg, 3.20 mmol, 3.2 eq.) were added and the mixture was stirred at room temperature for 16 h. The reaction mixture was concentrated under reduced pressure and purified by silica gel column chromatography (20-33% MeOH in DCM) to yield **Flpip** (101 mg, 25%, 0.25 mmol) as a red solid. Analytical data (H-NMR) match literature.<sup>102</sup>

2,4,5,7-tetrabromo-6-hydroxy-9-(2-(piperazine-1-carbonyl)phenyl)-3*H*-xanthen-3-one (**S21**, **EYpip** **BW080**, **BEW375**; **novel**)



*N,N'*-dicyclohexylcarbodiimide (631 mg, 3.06 mmol, 1.54 eq.) and *N*-hydroxysuccinimide (305 mg, 2.65 mmol, 1.3 eq.) were added to a solution of disodium 2-(6-oxido-3-oxo-3*H*-xanthen-9-yl)benzoate (1372 mg, 1.98 mmol, 1 eq.) in anhydrous DMF (6 mL) under nitrogen atmosphere and heated to 80°C for 1 h. The reaction mixture was allowed to cool to room temperature. Piperazine (372 mg, 4.32 mmol, 2.2 eq.) and TEA (0.90 mL, 648 mg, 6.40 mmol, 3.2 eq.) were added and the mixture was stirred at room temperature for 16 h. The reaction mixture was concentrated under reduced pressure and purified by silica gel column chromatography (20-33% MeOH in DCM) to yield **EYpip** (800 mg, 56%, 1.12 mmol) as a red solid.

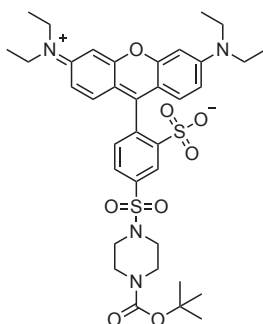
<sup>1</sup>**H-NMR** (500 MHz; (CD<sub>3</sub>)<sub>2</sub>SO):  $\delta$  = 7.74 – 7.68 (m, 2H), 7.70 – 7.64 (m, 1H), 7.54 – 7.47 (m, 1H), 7.05 (s, 2H), 3.50 – 3.43 (m, 4H), 2.94 – 2.83 (m, 4H).

<sup>13</sup>**C-NMR** (126 MHz; (CD<sub>3</sub>)<sub>2</sub>SO):  $\delta$  = 172.8, 168.4, 166.5, 152.8, 148.4, 134.7, 131.1, 130.5, 129.8, 129.6, 127.3, 118.4, 109.5, 99.5, 44.8, 43.3.

**HR-MS** (ESI) *m/z*: calculated for C<sub>24</sub>H<sub>17</sub>Br<sub>4</sub>N<sub>2</sub>O<sub>4</sub><sup>+</sup>: 716.78754; found: 716.78786, (M + H)<sup>+</sup>.



5-((4-(*tert*-butoxycarbonyl)piperazin-1-yl)sulfonyl)-2-(6-(diethylamino)-3-(diethyliminio)-3*H*-xanthen-9-yl)benzenesulfonate (**S22**, **BW066**, **BEW411**; *novel*)



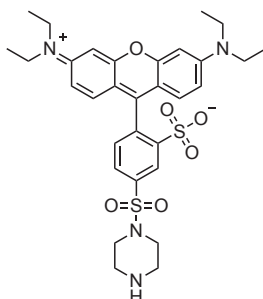
5-(chlorosulfonyl)-2-(6-(diethylamino)-3-(diethyliminio)-3*H*-xanthen-9-yl)benzenesulfonate (99.2 mg, 0.17 mmol, 1 eq.), **S1** (72.3 mg, 0.39 mmol, 2.3 eq.) and TEA (50  $\mu$ L, 36.0 mg, 0.36 mmol, 2.1 eq.) were dissolved in DCM (5 mL) and stirred at room temperature for 16 h. The reaction mixture was concentrated under reduced pressure and purified by silica gel column chromatography (10% MeOH in DCM) to yield **S22** (90.0 mg, 72%, 0.12 mmol) as a pink solid.

**<sup>1</sup>H-NMR** (500 MHz; CDCl<sub>3</sub>):  $\delta$  = 8.74 (d,  $J$  = 1.9 Hz, 1H), 7.87 (dd,  $J$  = 7.9, 1.9 Hz, 1H), 7.28 – 7.21 (m, 3H), 6.81 (dd,  $J$  = 9.5, 2.5 Hz, 2H), 6.68 (d,  $J$  = 2.5 Hz, 2H), 3.70 – 3.41 (m, 12H), 3.50 – 3.33 (m, 4H), 1.48 (d,  $J$  = 4.9 Hz, 9H), 1.30 (t,  $J$  = 7.1 Hz, 12H).

**<sup>13</sup>C-NMR** (126 MHz; CDCl<sub>3</sub>):  $\delta$  = 158.1, 155.7, 154.5, 148.8, 137.4, 134.5, 133.6, 129.9, 128.3, 127.8, 114.5, 113.7, 95.8, 80.7, 46.2, 46.0, 28.5, 28.5, 21.5, 12.7.

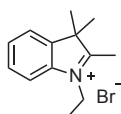
**HR-MS** (ESI)  $m/z$ : calculated for C<sub>36</sub>H<sub>47</sub>N<sub>4</sub>O<sub>8</sub>S<sub>2</sub><sup>+</sup>: 727.28298; found: 727.28380, (M+H)<sup>+</sup>.

2-(6-(diethylamino)-3-(diethyliminio)-3*H*-xanthen-9-yl)-5-(piperazin-1-ylsulfonyl)benzenesulfonate (**S23**, **SRhBpip**, **BW070**; *known*)



TFA (2 mL) was added to a solution of **S22** (85.0 mg, 0.12 mmol, 1 eq.) in DCM (2 mL) at 0°C. The reaction mixture was allowed to warm to room temperature and stirred at room temperature for 3 h. The reaction mixture was diluted with a saturated aqueous solution of NaHCO<sub>3</sub> (50 mL) and extracted with DCM (3 x 50 mL). The combined organic phases were dried (MgSO<sub>4</sub>) and concentrated under reduced pressure to yield known compound **SRhBpip** (57.0 mg, 78%, 90.7  $\mu$ mol) as a violet solid. Analytical data (H-NMR) match literature.<sup>103</sup>

1-ethyl-2,3,3-trimethyl-3*H*-indol-1-ium bromide (**S24**, **BW076**; *known*)

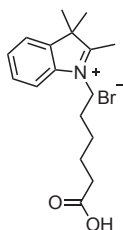


**S13** was synthesized according to literature.<sup>104</sup>

2,3,3-trimethylindolenine (1.50 g, 9.42 mmol, 1 eq.) and bromoethane (1 mL, 1.46 g, 13.4 mmol, 1.4 eq.) were dissolved in 1,2-dichlorobenzene (10 mL) and heated to 120°C for 24 h. The reaction mixture was allowed to cool to room temperature. The precipitate was

filtered, washed with hexane (3 x 50 mL) and diethyl ether (3 x 50 mL) to yield **S24** (2.07 g, 82%, 7.70 mmol) as a dark red solid. Analytical data (H-NMR) match literature.<sup>104</sup>

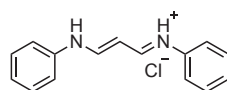
1-(5-carboxypentyl)-2,3,3-trimethyl-3*H*-indol-1-ium (**S25**, **BW077**; *known*)



**S25** was synthesized according to literature.<sup>104</sup>

2,3,3-trimethylindolenine (1.50 g, 9.42 mmol, 1 eq.) and 6-bromohexanoic acid (2.62 g, 13.5 mmol, 1.4 eq.) were dissolved in 1,2-dichlorobenzene (10 mL) and heated to 120°C for 24 h. The reaction mixture was allowed to cool to room temperature. The precipitate was filtered, washed with hexane (3 x 50 mL) and diethyl ether (3 x 50 mL) to yield **S25** (2.05 g, 61%, 5.77 mmol) as a light red solid. Analytical data (H-NMR) match literature.<sup>104</sup>

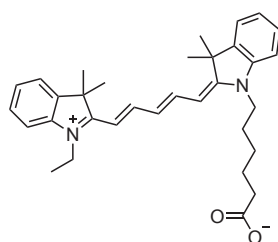
*N*-3-(phenylamino)allylidene)benzenaminium chloride (**S26**, **BW088**; *known*)



**S26** was synthesized according to literature.<sup>105</sup>

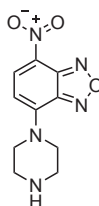
A solution of aniline (3.70 mL, 3.77 g, 40.3 mmol, 1.3 eq.) in water (70 mL) and hydrochloric acid (12M aqueous solution, 5 mL) was added dropwise to a solution of malonaldehydebis(dimethylacetal) (5 mL, 4.99 g, 30.4 mmol, 1 eq.) in water (85 mL) and hydrochloric acid (12M aqueous solution, 4.3 mL) at 50°C. The reaction mixture was stirred at 50°C for 4 h. The precipitate was filtered and washed with water (3 x 50 mL) to yield **S26** (2.91 g, 37%, 11.2 mmol) as a red/orange solid. Analytical data (H-NMR) match literature.<sup>105</sup>

6-((*E*)-2-((2*E*,4*E*)-5-(1-ethyl-3,3-dimethyl-3*H*-indol-1-ium-2-yl)penta-2,4-dien-1-ylidene)-3,3-dimethylindolin-1-yl)hexanoate (**S27**, **Cy5-COOH**, **BW089**; *known*)



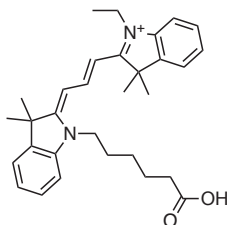
**Cy5-COOH** was synthesized according to literature.<sup>104</sup>

A solution of **S24** (500 mg, 1.86 mmol, 1 eq.) and **S26** (594 mg, 2.3 mmol, 1.2 eq.) in acetic anhydride (5 mL) was heated to 125°C for 2 h. The reaction mixture was allowed to cool to room temperature and was concentrated under reduced pressure. The residue was re-dissolved in anhydrous ethanol (25 mL) under nitrogen atmosphere and **S15** (660 mg, 1.86 mmol, 1 eq.) and sodium acetate (350 mg, 4.27 mmol, 2.3 eq.) were added. The reaction mixture was heated to reflux for 4 h and subsequently concentrated under reduced pressure. The crude material was purified by silica gel column chromatography (10-20% MeOH in DCM) to yield **Cy5-COOH** (564 mg, 61%, 1.14 mmol) as a blue metallic foam. Analytical data (H-NMR) match literature.<sup>104</sup>

4-nitro-7-(piperazin-1-yl)benzo[c][1,2,5]oxadiazole (**S28**, **NBDpip**, **S17**; known)

**NBDpip** was synthesized according to literature.<sup>106</sup>

A solution of 4-chloro-7-nitrobenzofurazan (526 mg, 2.64 mmol, 1 eq.) in MeOH (20 mL) was added dropwise to a solution of piperazine (678 mg, 7.88 mmol, 3 eq.) in MeOH (15 mL) at 0°C. The reaction mixture was stirred at 0°C for 30 min and subsequently concentrated under reduced pressure. The residue was suspended in a 1:4 mixture of saturated aqueous solution of NaHCO<sub>3</sub> and water (25 mL) and stirred at 0°C for 2 min. The precipitate was filtered and washed with ice-cold water (2 x 30 mL), ice-cold MeOH (1 x 30 mL) and diethyl ether (2 x 30 mL) to yield **NBDpip** (600 mg, 91%, 2.41 mmol) as a red solid. Analytical data (H-NMR) match literature.<sup>106</sup>

2-((*E*)-3-((*Z*)-1-(5-carboxypentyl)-3,3-dimethylindolin-2-ylidene)prop-1-en-1-yl)-1-ethyl-3,3-dimethyl-3*H*-indol-1-ium (**S29**, **Cy3-COOH**, **BW508**; known)

**Cy3-COOH** was synthesized according to literature.<sup>104</sup>

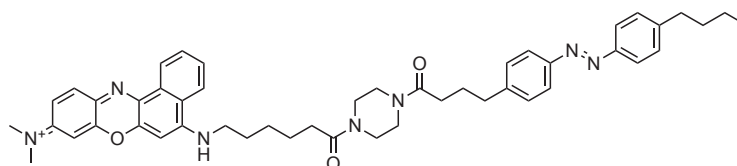
A solution of **S24** (189 mg, 0.71 mmol, 1 eq.) and *N,N'*-Diphenylformamidin (202 mg, 0.87 mmol, 1.2 eq) in acetic anhydride (3 mL) was heated to 125°C for 2 h. The reaction mixture was allowed to cool to room temperature and was concentrated under reduced pressure. The residue was re-dissolved in anhydrous ethanol (10 mL) under nitrogen atmosphere and 250 mg (0.71 mmol, 1 eq.) **S25** and sodium acetate (132 mg, 1.61 mmol, 2.3 eq.) were added. The reaction mixture was heated to reflux for 4 h and subsequently concentrated under reduced pressure. The crude material was purified by reverse phase flash column chromatography (20-70% MeCN + 0.1% formic acid in water + 0.1% formic acid) to yield **Cy3-COOH** (66 mg, 20%, 0.14 mmol) as a pink metallic foam. Analytical data (H-NMR) match literature.<sup>107</sup>

### 13.4.3 Azobenzene-Fluorophore conjugates

#### General procedure A for conjugate coupling

1 eq. carboxylic acid, 1 eq. amine, 1.2 eq. HBTU and 5 eq. TEA were dissolved in DMF (10 mg/mL) and stirred at room temperature for 16 h. The reaction mixture was diluted with 12.5 vol-% water and 5 vol-% acetic acid and purified by reversed phase preparative HPLC. Typical gradient used for preparative HPLC: 9:1 water (0.1% formic acid) / MeCN (0.1% formic acid) to MeCN (0.1 % formic acid) over 27 min.

*N*-(5-((6-(4-(4-(4-((4-butylphenyl)diazenyl)phenyl)butanoyl)piperazin-1-yl)-6-oxohexyl)amino)-9*H*-benzo[*a*]phenoxazin-9-ylidene)-*N*-methylmethanaminium chloride (**S30**, **NB-AK**, **BW284**, **BEW342**; *novel*)



**NB-AK** was synthesized according to *General procedure A*.

Carboxylic acid: **NB-COOH** (10 mg, 22.7  $\mu\text{mol}$ ) Amine: **AKpip** (8.9 mg, 22.7  $\mu\text{mol}$ )

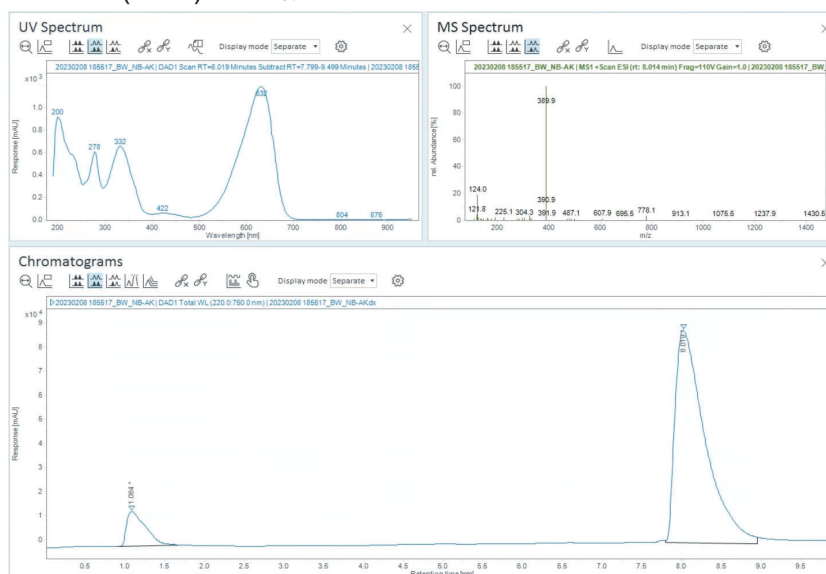
Yield: 8,2 mg (10.2  $\mu\text{mol}$ , 44%) as a blue solid.

$^1\text{H-NMR}$  (400 MHz;  $(\text{CD}_3)_2\text{SO}$ ):  $\delta$  = 10.07 (s, 1H), 8.80 (d,  $J$  = 8.1 Hz, 1H), 8.52 (d,  $J$  = 8.2 Hz, 1H), 7.95 (d,  $J$  = 7.9 Hz, 1H), 7.87 (t,  $J$  = 7.9 Hz, 2H), 7.79 (t,  $J$  = 7.2 Hz, 4H), 7.47 – 7.34 (m, 4H), 7.25 (s, 1H), 7.07 (s, 1H), 6.88 (s, 1H), 3.73 (t,  $J$  = 7.1 Hz, 2H), 3.51 – 3.36 (m, 8H), 3.27 (s, 6H), 2.68 (q,  $J$  = 7.4 Hz, 4H), 2.34 (q,  $J$  = 6.1, 5.4 Hz, 4H), 1.85 (p,  $J$  = 7.6 Hz, 2H), 1.77 (p,  $J$  = 7.4 Hz, 2H), 1.66 – 1.54 (m, 4H), 1.45 (p,  $J$  = 7.5 Hz, 2H), 1.33 (h,  $J$  = 7.3 Hz, 2H), 0.91 (t,  $J$  = 7.3 Hz, 3H).

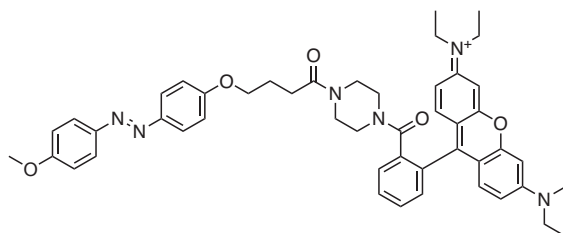
$^{13}\text{C-NMR}$  (201 MHz;  $\text{D}_3\text{COD}$ ):  $\delta$  = 176.0, 169.3, 159.8, 157.4, 153.6, 152.2, 149.5, 147.9, 146.6, 133.8, 133.1, 132.8, 132.4, 131.5, 131.1, 130.4, 130.2, 129.9, 125.8, 125.5, 123.9, 123.9, 116.4, 114.7, 97.2, 94.7, 46.6, 45.7, 42.8, 41.1, 36.5, 34.9, 34.7, 33.1, 30.2, 27.7, 27.6, 27.5, 25.9, 23.4, 14.3.

**HR-MS** (ESI)  $m/z$ : calculated for  $\text{C}_{48}\text{H}_{56}\text{N}_7\text{O}_3^+$ : 778.44392; found: 778.44385,  $\text{M}^+$ .

**HPLC-MS**:  $m/z$ : = 390 ( $\text{M}+\text{H}$ ) $^{2+}$  at  $t_{\text{ret}}$  = 8.0 min



*N*-(6-(diethylamino)-9-(2-(4-(4-(4-((4-methoxyphenyl)diazenyl)phenoxy)butanoyl)piperazine-1-carbonyl)phenyl)-3*H*-xanthen-3-ylidene)-*N*-ethylethanaminium chloride (**S31**, **RhB-AO**, **BW279**, **PhMaPh-NMR 1H**, (**13C** @ (800MHz) ; *novel*)



**RhB-AO** was synthesized according to *General procedure A*.

Carboxylic acid: **AO-COOH** (8 mg, 20.9  $\mu\text{mol}$ ) Amine: **RhBpip** (10 mg, 20.9  $\mu\text{mol}$ )

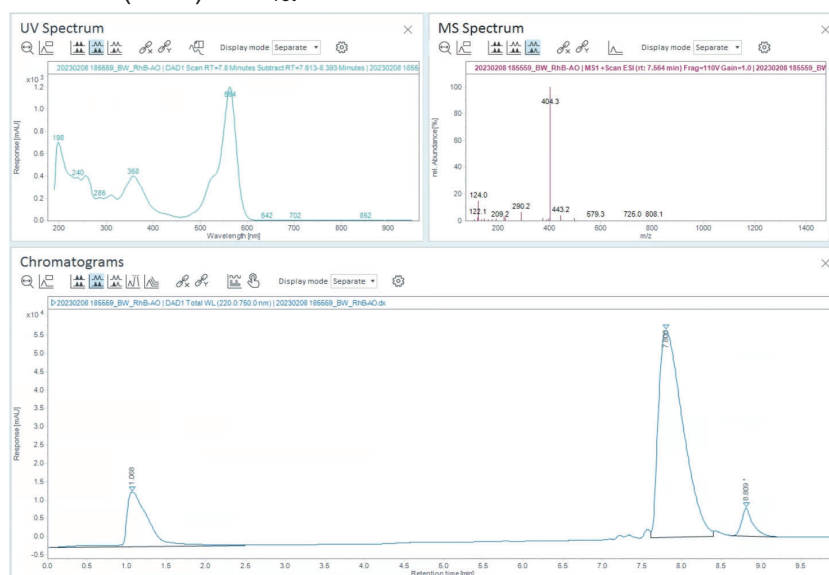
Yield: 11.7 mg (13.9  $\mu\text{mol}$ , 66%) as a pink solid.

**$^1\text{H-NMR}$**  (400 MHz;  $\text{CD}_3\text{OD}$ ):  $\delta$  = 7.88 – 7.80 (m, 4H), 7.78 – 7.74 (m, 2H), 7.70 – 7.63 (m, 1H), 7.54 – 7.48 (m, 1H), 7.27 (td,  $J$  = 7.0, 3.5 Hz, 2H), 7.07 (dt,  $J$  = 9.4, 1.7 Hz, 4H), 7.01 (d,  $J$  = 8.6 Hz, 2H), 6.93 (d,  $J$  = 2.4 Hz, 2H), 4.11 – 4.05 (m, 2H), 3.89 (s, 3H), 3.67 (q,  $J$  = 7.1 Hz, 8H), 3.41 (s, 8H), 2.57 (t,  $J$  = 7.2 Hz, 2H), 2.07 (p,  $J$  = 6.6 Hz, 2H), 1.29 (t,  $J$  = 7.1 Hz, 12H).

**$^{13}\text{C-NMR}$**  (201 MHz;  $\text{CD}_3\text{OD}$ ):  $\delta$  = 173.6, 173.4, 169.3, 163.4, 163.4, 162.4, 159.3, 157.2, 157.0, 148.3, 136.5, 133.6, 132.4, 131.8, 131.3, 129.9, 128.9, 125.3, 115.8, 115.4, 115.3, 114.9, 97.3, 68.4, 56.1, 48.2, 46.9, 45.5, 30.2, 26.0, 12.8.

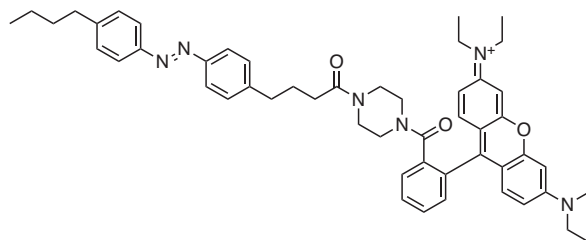
**HR-MS** (ESI)  $m/z$ : calculated for  $\text{C}_{49}\text{H}_{55}\text{N}_6\text{O}_5^+$ : 807.42285; found: 807.42166,  $\text{M}^+$ .

**HPLC-MS**:  $m/z$ : = 404 ( $\text{M}+\text{H}$ ) $^{2+}$  at  $t_{\text{ret}}$  = 7.6 min





*N*-(9-(2-(4-(4-(4-(4-butylphenyl)diazenyl)phenyl)butanoyl)piperazine-1-carbonyl)phenyl)-6-(diethylamino)-3*H*-xanthen-3-ylidene)-*N*-ethylethanaminium chloride (**S32**, **RhB-AK**, **BW045**, **BEW340**, **1H**, **13C** @ 800MHz; *novel*)



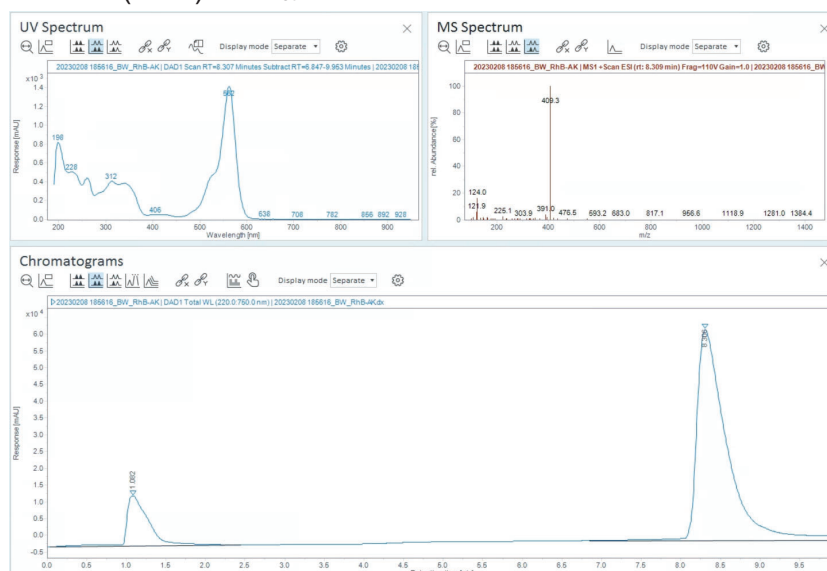
**RhBpip** (51.3 mg, 0.16 mmol, 1 eq.), **S1** (178 mg, 0.31 mmol, 2 eq.), HBTU (64.0 mg, 0.17 mmol, 1.1 eq.) and TEA (0.11 mL, 79.2 mg, 0.783 mmol, 5 eq.) were dissolved in DMF (3 mL) and stirred at room temperature for 16 h. The reaction mixture was diluted with a saturated aqueous solution of NH<sub>4</sub>Cl (40 mL) and extracted with EA (3 x 40 mL). The combined organic phases were washed with a saturated aqueous solution of sodium chloride (3 x 40 mL), dried (MgSO<sub>4</sub>) and concentrated under reduced pressure. The crude material was purified by silica gel column chromatography (3% MeOH in DCM) to yield **RhB-AK** (100 mg, 74%, 0.12 mmol) as a pink solid.

<sup>1</sup>H-NMR (400 MHz; CD<sub>3</sub>OD):  $\delta$  = 7.86 – 7.75 (m, 6H), 7.70 (t, *J* = 4.6 Hz, 1H), 7.53 (s, 1H), 7.41 – 7.34 (m, 4H), 7.28 (s, 2H), 7.09 (dd, *J* = 10.0, 2.0 Hz, 2H), 6.99 – 6.94 (m, 2H), 3.67 (q, *J* = 6.4 Hz, 8H), 3.44 – 3.40 (m, 8H), 2.74 (t, *J* = 6.4 Hz, 4H), 2.40 (t, *J* = 7.4 Hz, 2H), 1.99 – 1.86 (m, 2H), 1.67 (p, *J* = 8.0 Hz, 2H), 1.42 (d, *J* = 7.4 Hz, 2H), 1.30 (t, *J* = 7.0 Hz, 12H), 0.99 (t, *J* = 7.3 Hz, 3H).

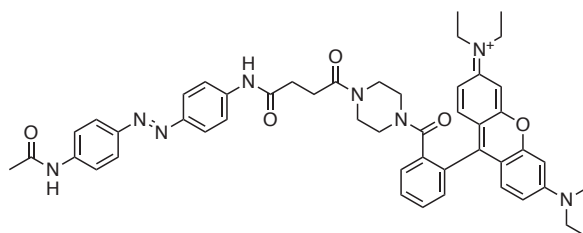
<sup>13</sup>C-NMR (201 MHz; CD<sub>3</sub>OD):  $\delta$  = 173.9, 173.7, 169.3, 159.3, 157.2, 152.3, 147.9, 146.5, 136.5, 133.6, 133.2, 132.4, 131.8, 131.3, 130.4, 130.3, 129.9, 128.9, 125.5, 123.8, 115.4, 114.9, 97.3, 48.3, 46.9, 42.8, 36.5, 34.9, 34.8, 33.1, 27.8, 23.4, 14.3, 12.8.

HR-MS (ESI) *m/z*: calculated for C<sub>52</sub>H<sub>61</sub>N<sub>6</sub>O<sub>3</sub>: 817.47997; found: 817.47864, M<sup>+</sup>.

HPLC-MS: *m/z*: = 409 (M+H)<sup>2+</sup> at *t*<sub>ret</sub> = 8.3 min



*N*-(9-(2-(4-(4-((4-((4-acetamidophenyl)diazenyl)phenyl)amino)-4-oxobutanoyl)piperazine-1-carbonyl)phenyl)-6-(diethylamino)-9a,10a-dihydro-3*H*-xanthen-3-ylidene)-*N*-ethylethanaminium chloride (**S33**, **RhB-AN**, **BW-KF11**, **BEW383**; novel)



**RhB-AN** was synthesized according to *General procedure A*.

Carboxylic acid: **AN-COOH** (15 mg, 42.3  $\mu\text{mol}$ ), Amine: **RhBpip**, (21.7 mg, 42.3  $\mu\text{mol}$ )  
Yield 26.0 mg (30.7  $\mu\text{mol}$ , 72%) as a pink solid.

$^1\text{H-NMR}$  (500 MHz;  $\text{CD}_3\text{CN}$ ):  $\delta$  = 8.83 (s, 1H), 8.71 (s, 1H), 7.81 (dd,  $J$  = 8.9, 6.8 Hz, 4H), 7.77 – 7.68 (m, 6H), 7.63 – 7.57 (m, 1H), 7.42 (s, 1H), 7.17 (d,  $J$  = 9.6 Hz, 2H), 6.94 (dd,  $J$  = 9.6, 2.6 Hz, 1H), 6.78 (d,  $J$  = 2.5 Hz, 1H), 3.59 (q,  $J$  = 7.3 Hz, 8H), 3.41 – 3.23 (m, 8H), 2.61 (dd,  $J$  = 13.7, 5.5 Hz, 4H), 2.09 (s, 3H), 1.23 (t,  $J$  = 7.1 Hz, 12H).

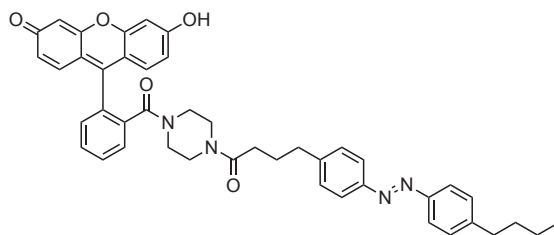
$^{13}\text{C-NMR}$  (126 MHz;  $\text{CD}_3\text{CN}$ ):  $\delta$  = 172.6, 171.5, 170.1, 168.3, 158.8, 156.9, 156.7, 149.3, 149.3, 142.8, 142.7, 136.5, 132.9, 131.9, 131.2, 130.9, 130.7, 128.5, 124.4, 124.4, 120.6, 120.2, 115.1, 114.6, 96.9, 48.0, 46.7, 32.6, 31.4, 28.6, 24.5, 12.8.

**HR-MS** (ESI)  $m/z$ : calculated for  $\text{C}_{50}\text{H}_{55}\text{N}_6\text{O}_3^+$ : 847.42899; found: 847.42884,  $\text{M}^+$ .

**HPLC-MS**:  $m/z$ : = 847 ( $\text{M}^+$ ) at  $t_{\text{ret}}$  = 6.1.0 min



9-(2-(4-(4-(4-((4-butylphenyl)diazenyl)phenyl)butanoyl)piperazine-1-carbonyl)phenyl)-6-hydroxy-3*H*-xanthen-3-one (**S34**, **FI-AK**, **BW402**, **BEW441**; novel)



**FI-AK** was synthesized according to *General procedure A*.

Carboxylic acid: **AK-COOH** (25 mg, 77.1  $\mu\text{mol}$ ), Amine: **Flpip** (30.9 mg, 77.1  $\mu\text{mol}$ )

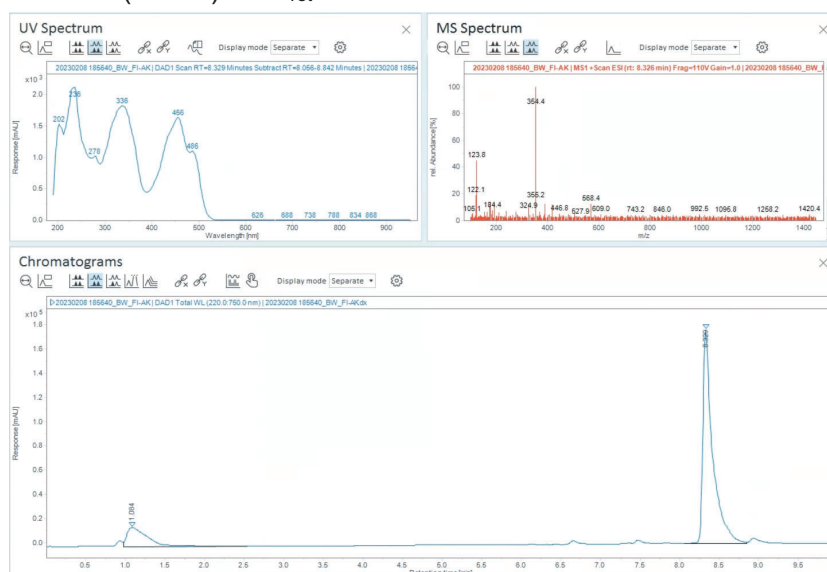
Yield 24.5 mg (34.7  $\mu\text{mol}$ , 45%) as an orange solid.

**$^1\text{H-NMR}$**  (400 MHz;  $(\text{CD}_3)_2\text{SO}$ ):  $\delta$  = 7.79 (d,  $J$  = 8.3 Hz, 4H), 7.72 – 7.65 (m, 2H), 7.65 – 7.59 (m, 1H), 7.49 (dd,  $J$  = 5.8, 3.1 Hz, 1H), 7.39 (dd,  $J$  = 8.7, 6.8 Hz, 4H), 6.97 (d,  $J$  = 9.1 Hz, 2H), 6.65 – 6.52 (m, 4H), 3.30 (s, 4H), 2.72 – 2.62 (m, 4H), 2.31 (t,  $J$  = 7.2 Hz, 2H), 1.81 (p,  $J$  = 7.3 Hz, 2H), 1.60 (tt,  $J$  = 7.7, 6.5 Hz, 2H), 1.33 (h,  $J$  = 7.3 Hz, 2H), 0.91 (t,  $J$  = 7.3 Hz, 3H).

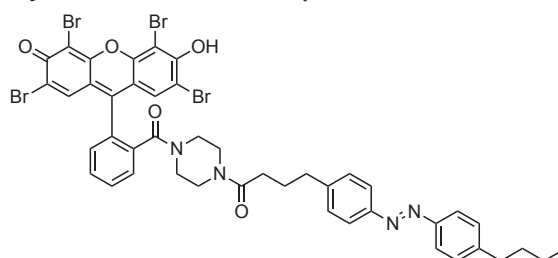
**$^{13}\text{C-NMR}$**  (101 MHz;  $(\text{CD}_3)_2\text{SO}$ ):  $\delta$  = 170.4, 150.3, 150.6, 148.8, 146.3, 145.7, 145.7, 139.6, 135.4, 131.1, 131.0, 130.4, 129.6, 129.3, 129.3, 129.1, 127.4, 123.5, 122.6, 122.5, 120.5, 103.2, 102.2, 44.7, 40.9, 34.7, 34.4, 32.9, 31.5, 26.2, 21.8, 13.8.

**HR-MS** (ESI)  $m/z$ : calculated for  $\text{C}_{44}\text{H}_{43}\text{N}_4\text{O}_5^+$ : 707.32280; found: 707.32328,  $(\text{M} + \text{H})^+$ .

**HPLC-MS**:  $m/z$ : = 354  $(\text{M} + 2\text{H})^{2+}$  at  $t_{\text{ret}}$  = 8.3 min



2,4,5,7-tetrabromo-9-(2-(4-(4-(4-((4-butylphenyl)diazenyl)phenyl)butanoyl)piperazine-1-carbonyl)phenyl)-6-hydroxy-3H-xanthen-3-one (**S35**, **EY-AK**, **BW403**, **BEW439**; *novel*)



**EY-AK** was synthesized according to *General procedure A*.

Carboxylic acid: **AK-COOH** (25 mg, 77.1  $\mu\text{mol}$ ), Amine: **EYpip** (55.2 mg, 77.1  $\mu\text{mol}$ )

Yield 30.0 mg (29.3  $\mu\text{mol}$ , 38%) as an orange solid.

**$^1\text{H-NMR}$**  (500 MHz;  $(\text{CD}_3)_2\text{SO}$ ):  $\delta$  = 7.83 – 7.76 (m, 4H), 7.73 – 7.67 (m, 2H), 7.63 (s, 1H), 7.52 – 7.47 (m, 1H), 7.39 (dd,  $J$  = 8.7, 6.7 Hz, 4H), 7.04 (d,  $J$  = 8.1 Hz, 2H), 3.28 (s, 4H), 2.71 – 2.62 (m, 4H), 2.38 – 2.28 (m, 2H), 1.85 – 1.78 (m, 1H), 1.65 – 1.55 (m, 2H), 1.33 (h,  $J$  = 7.4 Hz, 2H), 0.91 (t,  $J$  = 7.4 Hz, 3H).

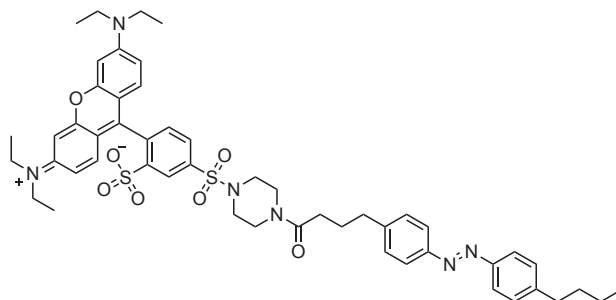
**$^{13}\text{C-NMR}$**  (126 MHz;  $(\text{CD}_3)_2\text{SO}$ ):  $\delta$  = 170.4, 168.3, 166.6, 166.5, 162.5, 154.4, 152.8, 150.3, 150.2, 148.7, 146.2, 145.8, 135.0, 129.7, 129.3, 129.3, 127.3, 122.6, 122.5, 120.1, 118.3, 109.6, 99.5, 46.8, 41.1, 34.7, 34.4, 32.9, 31.5, 26.2, 21.7, 13.8.

**HR-MS** (ESI)  $m/z$ : calculated for  $\text{C}_{44}\text{H}_{39}\text{Br}_4\text{N}_4\text{O}_5$ : 1022.96075; found: 1022.96134, ( $\text{M} + \text{H}$ ) $^+$ .

**HPLC-MS**:  $m/z$ : = 512 ( $\text{M} + 2\text{H}$ ) $^{2+}$  Z-isomer at  $t_{\text{ret}}$  = 7.1 min &  $m/z$ : = 1023 ( $\text{M} + \text{H}$ ) $^+$  E-isomer at  $t_{\text{ret}}$  = 10.2 min



5-((4-(4-(4-((4-butylphenyl)diazenyl)phenyl)butanoyl)piperazin-1-yl)sulfonyl)-2-(6-(diethylamino)-3-(diethyliminio)-3*H*-xanthen-9-yl)benzenesulfonate (**S36**, **SRhB-AK**, **BW072**, **BEW372**; *novel*)



**SRhB-AK** was synthesized according to *General procedure A*.

Carboxylic acid: **AK-COOH** (10 mg, 30.8  $\mu\text{mol}$ ) Amine: **SRhBpip** (19.3 mg, 30.8  $\mu\text{mol}$ )

Yield 27.0 mg (28.9  $\mu\text{mol}$ , 94%) as a violet solid.

**$^1\text{H-NMR}$**  (500 MHz;  $(\text{CD}_3)_2\text{SO}$ ):  $\delta$  = 8.29 (d,  $J$  = 1.9 Hz, 1H), 7.90 (dd,  $J$  = 7.9, 2.0 Hz, 1H), 7.76 (d,  $J$  = 8.3 Hz, 4H), 7.54 (d,  $J$  = 8.0 Hz, 1H), 7.39 (dd,  $J$  = 8.5, 2.9 Hz, 4H), 6.99 (s, 4H), 6.91 (s, 2H), 3.62 (d,  $J$  = 8.0 Hz, 12H), 3.05 (d,  $J$  = 22.0 Hz, 4H), 2.67 (t,  $J$  = 7.5 Hz, 4H), 2.37 (t,  $J$  = 7.3 Hz, 2H), 1.82 (p,  $J$  = 7.5 Hz, 2H), 1.60 (p,  $J$  = 7.6 Hz, 2H), 1.33 (h,  $J$  = 7.4 Hz, 2H), 1.19 (t,  $J$  = 7.0 Hz, 12H), 0.91 (t,  $J$  = 7.3 Hz, 3H).

**$^{13}\text{C-NMR}$**  (126 MHz;  $(\text{CD}_3)_2\text{SO}$ ):  $\delta$  = 170.5, 157.1, 157.0, 155.0, 150.3, 150.2, 148.2, 146.3, 145.7, 136.0, 134.1, 132.8, 131.1, 129.3, 129.3, 127.6, 126.5, 122.5, 122.5, 113.7, 113.4, 95.4, 45.8, 45.3, 44.2, 34.7, 34.4, 32.9, 31.5, 26.2, 21.8, 13.8, 12.5.

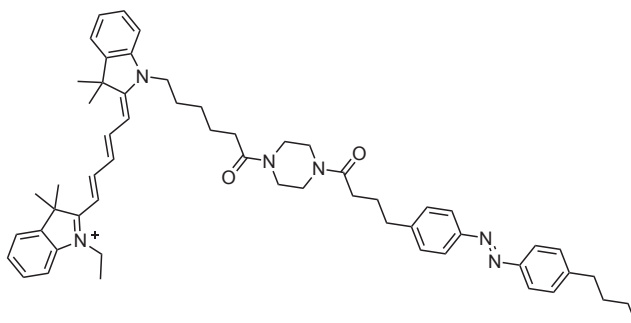
**HR-MS** (ESI)  $m/z$ : calculated for  $\text{C}_{51}\text{H}_{61}\text{N}_6\text{O}_7\text{S}_2^+$ : 933.40377; found: 933.40420,  $(\text{M}+\text{H})^+$ .

**HPLC-MS**:  $m/z$ : = 467  $(\text{M}+2\text{H})^{2+}$  at  $t_{\text{ret}} = 11.3$  min





2-((1*E*,3*E*)-5-((*E*)-1-(6-(4-(4-(4-((*E*)-(4-butylphenyl)diazenyl)phenyl)butanoyl)piperazin-1-yl)-6-oxohexyl)-3,3-dimethylindolin-2-ylidene)penta-1,3-dien-1-yl)-1-ethyl-3,3-dimethyl-3*H*-indol-1-ium (**S37**, **Cy5-AK**, **BW384**, **BEW405**; *novel*)



**Cy5-AK** was synthesized according to *General procedure A*.

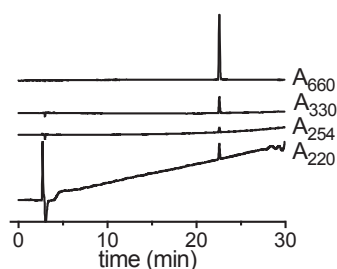
Carboxylic acid: **Cy5-COOH** (19 mg, 38.2  $\mu\text{mol}$ ), Amine: **AKpip** (15 mg, 38.2  $\mu\text{mol}$ )

Yield: 19.0 mg (21.8  $\mu\text{mol}$ , 57%) as a blue solid.

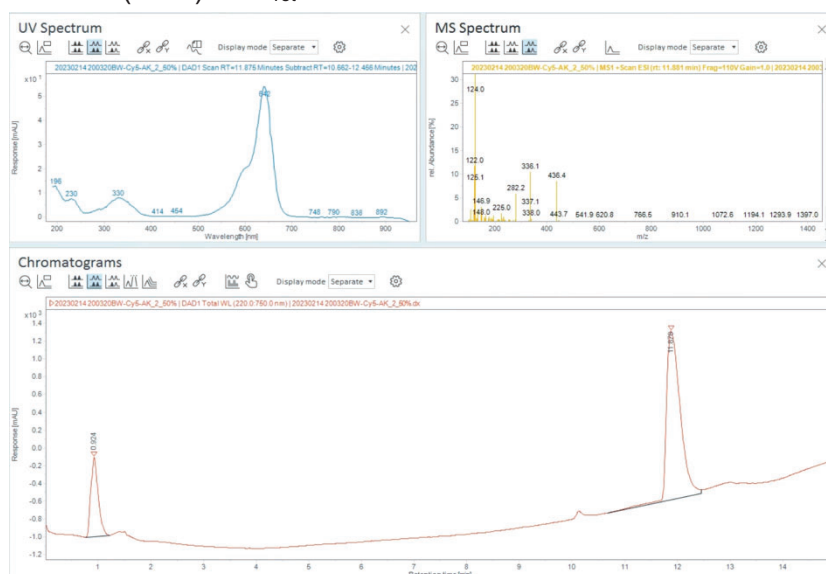
**$^1\text{H-NMR}$**  (400 MHz;  $\text{CD}_3\text{OD}$ ):  $\delta$  =  $^1\text{H NMR}$  (400 MHz, Methanol- $d_4$ )  $\delta$  8.23 (t,  $J$  = 13.0 Hz, 2H), 7.81 (d,  $J$  = 8.2 Hz, 4H), 7.48 (t,  $J$  = 7.5 Hz, 2H), 7.37 (ddd,  $J$  = 12.4, 8.0, 6.3 Hz, 7H), 7.26 (ddd,  $J$  = 17.4, 8.9, 6.2 Hz, 3H), 6.62 (t,  $J$  = 12.3 Hz, 1H), 6.28 (dd,  $J$  = 13.7, 5.3 Hz, 2H), 4.18 – 4.05 (m, 4H), 3.61 – 3.43 (m, 8H), 2.73 (dt,  $J$  = 19.1, 7.7 Hz, 6H), 2.43 (t,  $J$  = 6.7 Hz, 4H), 2.04 – 1.90 (m, 4H), 1.84 (t,  $J$  = 7.7 Hz, 2H), 1.71 (d,  $J$  = 2.2 Hz, 12H), 1.70 – 1.61 (m, 4H), 1.38 (m, 3H), 0.96 (t,  $J$  = 7.4 Hz, 3H).

**HR-MS** (ESI)  $m/z$ : calculated for  $\text{C}_{57}\text{H}_{71}\text{N}_6\text{O}_2^+$ : 871.56330; found: 871.56324,  $\text{M}^+$ .

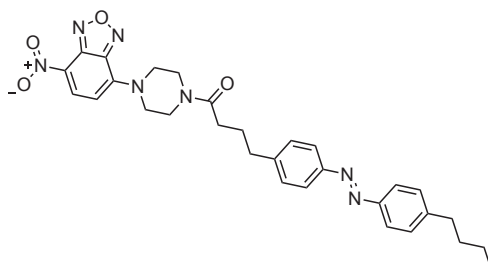
**HPLC DAD trace:**



**HPLC-MS:**  $m/z$  = 436 ( $\text{M}+\text{H}$ ) $^{2+}$  at  $t_{\text{ret}}$  = 11.9 min



4-(4-((4-butylphenyl)diazenyl)phenyl)-1-(4-(7-nitrobenzo[c][1,2,5]oxadiazol-4-yl)piperazin-1-yl)butan-1-one (**S38**, **NBD-AK**, **BW064**, **BEW371**; *novel*)



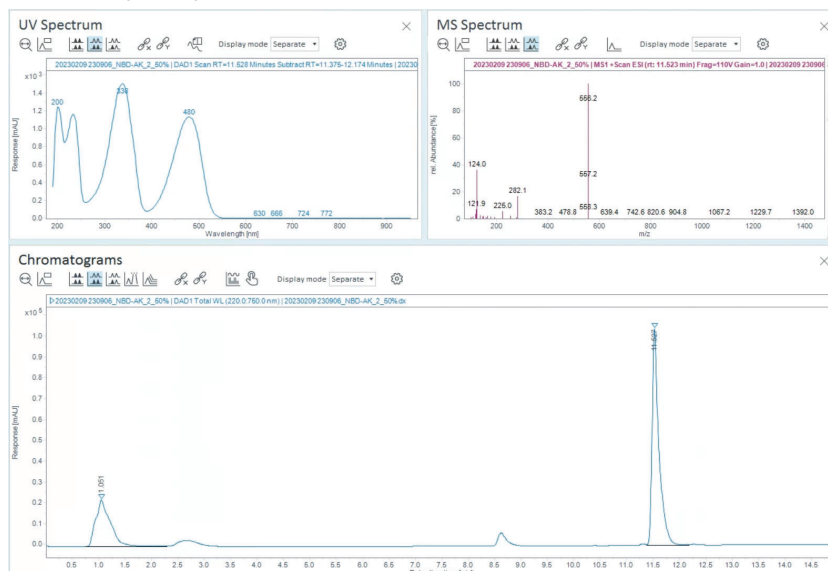
**AK-COOH** (32.6 mg, 0.1 mmol, 1 eq.), **NBDpip** (51.0 mg (0.21 mmol, 2 eq.)), HBTU (42.5 mg, 0.11 mmol, 1.1 eq.) and TEA (50  $\mu$ L, 36.0 mg, 0.36 mmol, 3.5 eq.) were dissolved in DMF (1.5 mL) and stirred at room temperature for 16 h. The reaction mixture was diluted with a saturated aqueous solution of  $\text{NH}_4\text{Cl}$  (15 mL) and extracted with EA (3 x 20 mL). The combined organic phases were washed with a saturated aqueous solution of sodium chloride (3 x 15 mL), dried ( $\text{MgSO}_4$ ) and concentrated under reduced pressure. The crude material was purified via silica gel column chromatography (70% EA in hexane) to yield **NBD-AK** (48.0 mg, 86%, 86.4  $\mu$ mol) as an orange solid.

**$^1\text{H-NMR}$**  (500 MHz;  $(\text{CD}_3)_2\text{SO}$ ):  $\delta$  = 8.52 (d,  $J$  = 9.1 Hz, 1H), 7.80 (t,  $J$  = 8.1 Hz, 4H), 7.42 (dd,  $J$  = 11.0, 8.2 Hz, 4H), 6.61 (d,  $J$  = 9.2 Hz, 1H), 4.19 (d,  $J$  = 32.7 Hz, 4H), 3.76 (s, 4H), 2.73 (t,  $J$  = 7.7 Hz, 2H), 2.68 (t,  $J$  = 7.6 Hz, 2H), 2.43 (t,  $J$  = 7.4 Hz, 2H), 1.89 (p,  $J$  = 7.5 Hz, 2H), 1.60 (p,  $J$  = 7.4 Hz, 2H), 1.33 (h,  $J$  = 7.3 Hz, 2H), 0.91 (t,  $J$  = 7.3 Hz, 3H).

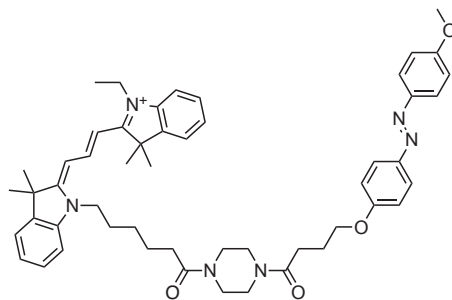
**$^{13}\text{C-NMR}$**  (126 MHz;  $(\text{CD}_3)_2\text{SO}$ ):  $\delta$  = 170.8, 150.4, 150.3, 146.3, 145.7, 145.5, 144.8, 136.4, 129.4, 129.3, 122.6, 122.5, 121.2, 103.2, 48.6, 43.5, 34.7, 34.5, 32.9, 31.6, 26.1, 21.8, 13.8.

**HR-MS** (ESI)  $m/z$ : calculated for  $\text{C}_{30}\text{H}_{34}\text{N}_7\text{O}_4^+$ : 556.26668; found: 556.26712,  $(\text{M} + \text{H})^+$ .

**HPLC-MS**:  $m/z$ : = 556  $(\text{M} + \text{H})^+$  at  $t_{\text{ret}}$  = 11.5 min



1-ethyl-2-(3-((Z)-1-(6-(4-(4-(4-((E)-4-methoxyphenyl)diazenyl)phenoxy)butanoyl)piperazin-1-yl)-6-oxohexyl)-3,3-dimethylindolin-2-ylidene)propyl)-3,3-dimethyl-3H-indol-1-ium (**Cy3-AO**, **BW513/BW479**, **BEW506**, **S39**; *novel*)



**Cy3-AO** was synthesized according to *General procedure A*.

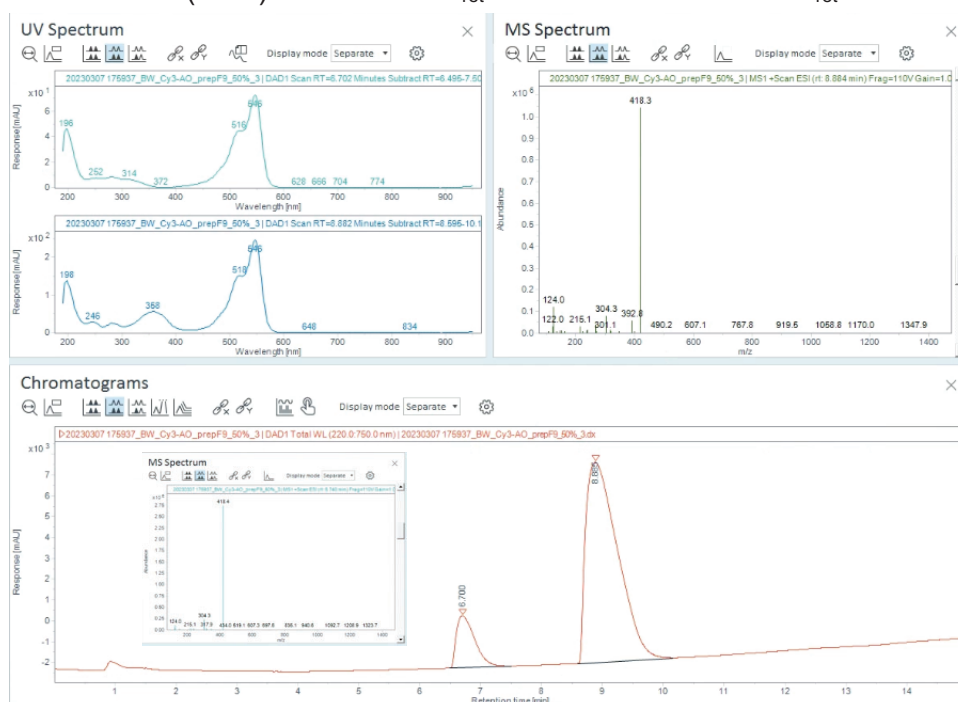
Carboxylic acid: **Cy3-COOH** (12.4 mg, 26.1  $\mu\text{mol}$ ), Amine: **AOpip** (10 mg, 26.1  $\mu\text{mol}$ ), Yield 6.0 mg (7.3  $\mu\text{mol}$ , 28%) as a pink solid.

**$^1\text{H-NMR}$**  (500 MHz;  $\text{CD}_2\text{Cl}_2$ ):  $\delta$  = 8.45 (t,  $J$  = 13.4 Hz, 2H), 7.86 (dd,  $J$  = 9.0, 3.3 Hz, 4H), 7.70 (dd,  $J$  = 5.7, 3.3 Hz, 1H), 7.55 (dd,  $J$  = 5.7, 3.3 Hz, 1H), 7.43 (t,  $J$  = 5.8 Hz, 4H), 7.29 (t,  $J$  = 7.4 Hz, 2H), 7.18 (d,  $J$  = 8.2 Hz, 2H), 7.01 (dd,  $J$  = 9.0, 2.1 Hz, 4H), 4.22 – 4.13 (m, 4H), 4.15 – 4.05 (m, 4H), 3.57 – 3.44 (m, 12H), 2.59 – 2.52 (m, 2H), 2.39 (dd,  $J$  = 14.0, 6.7 Hz, 2H), 2.32 (t,  $J$  = 7.5 Hz, 2H), 2.14 (p,  $J$  = 6.6 Hz, 2H), 1.74 (s, 12H), 1.45 (t,  $J$  = 7.0 Hz, 3H).

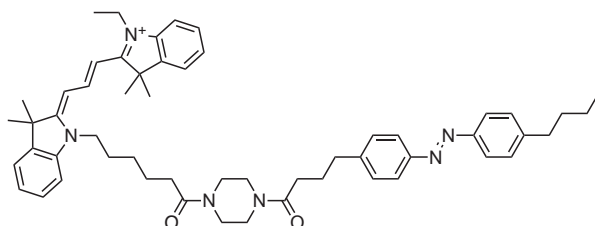
**$^{13}\text{C-NMR}$**  (126 MHz;  $\text{CD}_2\text{Cl}_2$ ):  $\delta$  = 162.3, 147.5, 142.6, 141.4, 131.5, 129.5, 129.3, 126.1, 124.8, 124.8, 122.9, 115.2, 114.7, 111.4, 68.6, 68.0, 56.1, 40.2, 39.4, 32.5, 30.9, 30.6, 30.3, 29.9, 29.5, 28.5, 28.4, 25.3, 24.3, 23.6, 23.3, 14.4, 14.4, 12.9, 11.3.

**HR-MS** (ESI)  $m/z$ : calculated for  $\text{C}_{52}\text{H}_{63}\text{N}_6\text{O}_4^+$ : 835.49053; found: 835.49245,  $\text{M}^+$ .

**HPLC-MS**:  $m/z$ : = 418 ( $\text{M}+\text{H}$ ) $^{2+}$  Z-isomer at  $t_{\text{ret}}$  = 6.7 min & E-isomer at  $t_{\text{ret}}$  = 8.9 min



2-(3-((Z)-1-(6-(4-(4-(4-((E)-4-butylphenyl)diazenyl)phenyl)butanoyl)piperazin-1-yl)-6-oxohexyl)-3,3-dimethylindolin-2-ylidene)propyl)-1-ethyl-3,3-dimethyl-3H-indol-1-ium (S40, **Cy3-AK**, **BW514**, **BEW505**; *novel*)



**Cy3-AK** was synthesized according to *General procedure A*.

Carboxylic acid: **Cy3-COOH** (12.1 mg, 25.5  $\mu\text{mol}$ ), Amine: **AKpip** (12.4 mg, 25.5  $\mu\text{mol}$ )

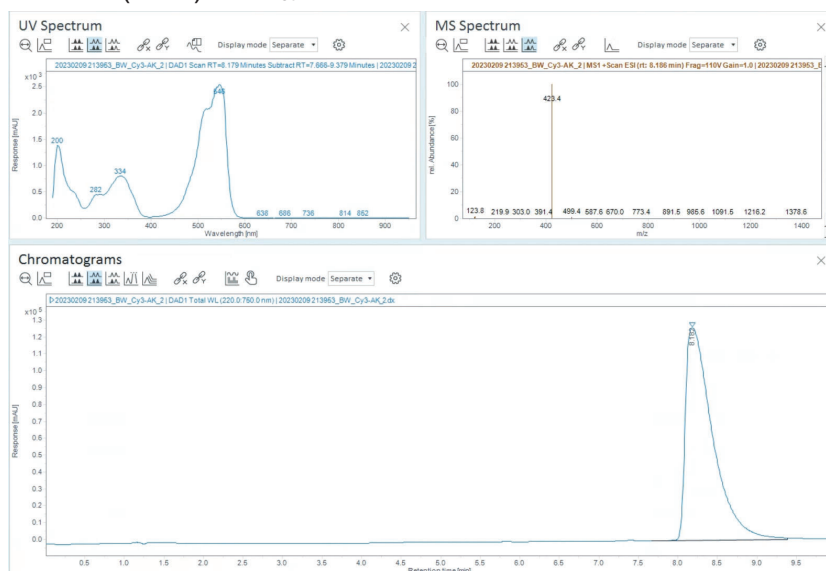
Yield 8.3 mg (9.5  $\mu\text{mol}$ , 38%) as a pink solid.

**$^1\text{H-NMR}$**  (500 MHz;  $\text{CD}_2\text{Cl}_2$ ):  $\delta$  = 8.49 – 8.40 (m, 2H), 7.86 – 7.79 (m, 4H), 7.46 – 7.39 (m, 4H), 7.35 (dd,  $J$  = 10.5, 8.2 Hz, 4H), 7.29 (td,  $J$  = 7.4, 4.8 Hz, 2H), 7.19 (d,  $J$  = 7.9 Hz, 2H), 6.69 – 6.52 (m, 2H), 4.17 (q,  $J$  = 7.3 Hz, 2H), 4.09 (t,  $J$  = 7.8 Hz, 2H), 3.64 – 3.34 (m, 10H), 2.75 (t,  $J$  = 7.6 Hz, 2H), 2.73 – 2.66 (m, 2H), 2.36 (td,  $J$  = 15.7, 13.8, 7.8 Hz, 4H), 1.98 (p,  $J$  = 7.5 Hz, 2H), 1.88 (p,  $J$  = 8.5, 8.1 Hz, 2H), 1.79 – 1.67 (m, 12H), 1.68 – 1.61 (m, 2H), 1.59 – 1.52 (m, 2H), 1.45 (t,  $J$  = 7.2 Hz, 3H), 1.43 – 1.36 (m, 2H), 0.95 (t,  $J$  = 7.4 Hz, 3H).

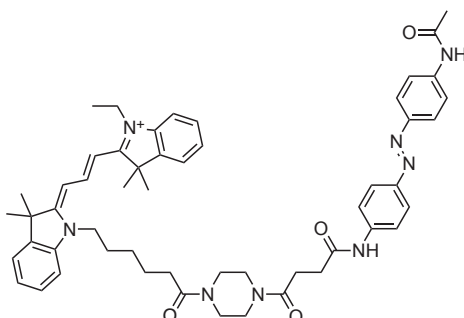
**$^{13}\text{C-NMR}$**  (126 MHz;  $\text{CD}_2\text{Cl}_2$ ):  $\delta$  = 174.7, 174.5, 171.8, 171.6, 163.5, 151.7, 151.5, 151.4, 147.2, 142.6, 142.1, 141.4, 141.3, 129.8, 129.7, 129.4, 129.4, 126.2, 126.1, 123.3, 123.2, 122.9, 122.8, 111.6, 111.4, 103.6, 103.5, 65.0, 49.8, 42.0, 41.8, 40.3, 36.1, 35.7, 34.1, 30.3, 28.5, 28.4, 27.8, 27.1, 27.0, 26.5, 25.3, 22.9, 14.3, 12.9, 10.5.

**HR-MS** (ESI)  $m/z$ : calculated for  $\text{C}_{55}\text{H}_{69}\text{N}_6\text{O}_2^+$ : 845.54765; found: 845.54984,  $\text{M}^+$ .

**HPLC-MS**:  $m/z$ : = 423 ( $\text{M}+\text{H}$ ) $^{2+}$  at  $t_{\text{ret}}$  = 8.2 min



2-(3-((Z)-1-(6-(4-(4-((E)-4-acetamidophenyl)diazenyl)phenyl)amino)-4-oxobutanoyl)piperazin-1-yl)-6-oxohexyl)-3,3-dimethylindolin-2-ylidene)propyl)-1-ethyl-3,3-dimethyl-3*H*-indol-1-ium (**S41**, **Cy3-AN**, **BW523**, **BEW510**; *novel*)



**Cy3-AN** was synthesized according to *General procedure A*.

Carboxylic acid: **Cy3-COOH** (6.7 mg, 14.2  $\mu\text{mol}$ ), Amine: **ANpip** (6 mg, 14.2  $\mu\text{mol}$ ),

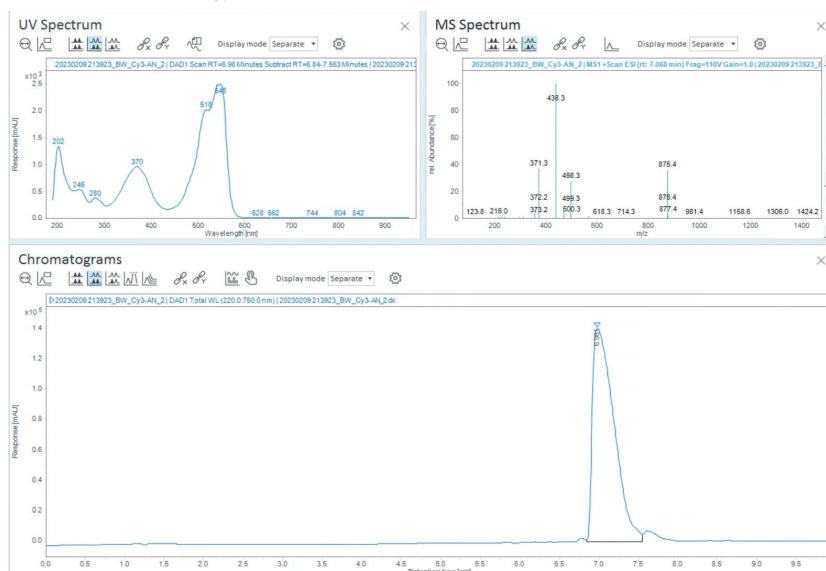
Yield 9.0 mg (10.3  $\mu\text{mol}$ , 72%) as a pink solid.

**<sup>1</sup>H-NMR** (400 MHz;  $\text{CD}_2\text{Cl}_2$ ):  $\delta$  = 9.62 (d,  $J$  = 51.4 Hz, 1H), 9.15 (s, 1H), 8.55 (s, 1H), 8.41 (t,  $J$  = 13.4 Hz, 1H), 7.76 (d,  $J$  = 4.4 Hz, 7H), 7.45 – 7.37 (m, 4H), 7.28 (t,  $J$  = 7.5 Hz, 2H), 7.15 (d,  $J$  = 8.0 Hz, 2H), 6.29 (q,  $J$  = 15.2 Hz, 2H), 4.08 (q,  $J$  = 7.2 Hz, 2H), 3.99 (t,  $J$  = 7.8 Hz, 2H), 3.66 – 3.37 (m, 8H), 2.75 (s, 4H), 2.31 (d,  $J$  = 7.5 Hz, 2H), 2.18 (s, 3H), 1.82 (p,  $J$  = 7.8 Hz, 2H), 1.71 (d,  $J$  = 1.9 Hz, 12H), 1.53 – 1.43 (m, 2H), 1.40 (t,  $J$  = 7.3 Hz, 3H).

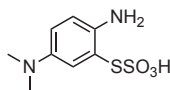
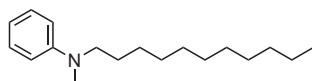
**<sup>13</sup>C-NMR** (101 MHz;  $\text{CD}_2\text{Cl}_2$ ):  $\delta$  = 174.6, 174.5, 171.7, 171.1, 169.5, 168.0, 166.7, 166.7, 151.0, 148.8, 142.3, 142.1, 141.9, 141.2, 141.1, 132.8, 131.4, 129.3, 129.1, 126.0, 123.8, 123.8, 122.8, 119.9, 119.8, 114.9, 111.5, 111.3, 102.7, 68.3, 45.7, 45.5, 44.8, 39.9, 33.0, 29.3, 28.8, 28.2, 28.1, 27.5, 26.9, 25.0, 24.6, 23.4, 12.6.

**HR-MS** (ESI)  $m/z$ : calculated for  $\text{C}_{53}\text{H}_{63}\text{N}_8\text{O}_4^+$ : 875.49668; found: 875.49903,  $\text{M}^+$ .

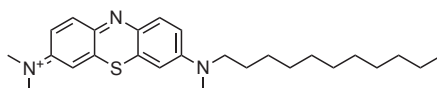
**HPLC-MS**:  $m/z$ : = 875  $\text{M}^+$  at  $t_{\text{ret}}$  = 7.0 min





**13.4.4 Lipidated fluorophores**2-amino-5-(dimethylamino)benzenesulfonoperoxothioic O-acid (**S44**, **BW250**; **known**)**S44** was synthesized according to literature.<sup>108</sup>*N*-methyl-*N*-undecylaniline (**S45**, **BW306**; **known**)

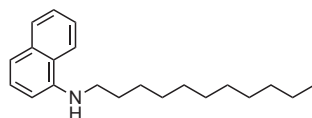
*N*-methylaniline (0.75 mL, 742 mg, 6.93 mmol, 1 eq.), 1-bromoundecane (1.6 mL, 1.63 g, 6.93 mmol, 1 eq.) and potassium carbonate (3.1 g, 22.4 mmol, 3.2 eq.) were dissolved in DMF (5 mL) and stirred at 90 °C for 16 h. The reaction mixture was concentrated under reduced pressure. The crude material was purified *via* silica gel column chromatography (0-5% EA in hexane) to yield **S45** (1.2 g, 4.4 mmol, 64%) as a yellow oil. Analytical data (H-NMR) match literature.<sup>108,109</sup>

*N*-methyl-*N*-(7-(methyl(undecyl)amino)-3*H*-phenothiazin-3-ylidene)methanaminium (**S46**, **MB-lipid**, **BW313**, **BEW354**; **novel**)

**MB-lipid** was synthesized by adapting a literature procedure for a similar substrate<sup>108</sup>. Silver carbonate (50 wt% on celite, 333 mg, 1.21 mmol, 3 eq.) was added portion wise to a solution of **S44** (50 mg, 0.20 mmol, 1 eq.) and **S45** (52.6 mg, 0.20 mol, 1 eq.) were dissolved methanol (4 mL) and water (1.6 ml) at 60 °C. The reaction mixture was heated to reflux for 4 h. The reaction mixture was directly loaded and purified by dry column chromatography (side products were eluted with DCM and the desired product with 3-10% MeOH in DCM) to yield **MB-lipid** (6.6 mg, 14 μmol, 7%) as a blue solid.

<sup>1</sup>H-NMR (500 MHz; CD<sub>3</sub>OD): δ = 7.96 (d, *J* = 9.6 Hz, 2H), 7.56 – 7.45 (m, 2H), 7.41 – 7.29 (m, 2H), 3.75 (t, *J* = 7.6 Hz, 2H), 3.40 (s, 6H), 3.37 (s, 3H), 1.76 (t, *J* = 7.1, 6.5 Hz, 1H), 1.44 – 1.40 (m, 2H), 1.33 – 1.25 (m, 10H), 0.88 (t, *J* = 7.0 Hz, 2H).

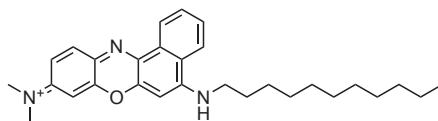
HR-MS (ESI) *m/z*: calculated for C<sub>26</sub>H<sub>38</sub>N<sub>3</sub>S<sup>+</sup>: 424.27810; found: 424.27947, M<sup>+</sup>.

*N*-undecylnaphthalen-1-amine (**S42**, **BW309**; **novel**)**S42** was synthesized by adapting a literature procedure for a similar substrate.<sup>110</sup>

1-naphthalenamine (500 mg, 3.5 mmol, 1 eq. and 1-bromoundecane (1.1 mL, 1.15 g, 4.89 mmol, 1.4 eq.) were dissolved in ethanol (5 mL) and heated to reflux for 16 h. The reaction mixture was concentrated under reduced pressure. The crude material was purified *via* silica gel column chromatography (2-5% EA in hexane) to yield **S42** (182 mg, 0.61 mmol, 18%) as a yellow oil that was immediately passed on without NMR characterisation.

HR-MS (ESI) *m/z*: calculated for C<sub>21</sub>H<sub>32</sub>N<sup>+</sup>: 298.25293; found: 298.25332, (M+H)<sup>+</sup>.

*N*-methyl-*N*-(5-(undecylamino)-9*H*-benzo[*a*]phenoxazin-9-ylidene)methanaminium (S43, NB-lipid, BW310, BEW351; *novel*)



**NB-lipid** was synthesized by adapting a literature procedure for a similar substrate.<sup>99</sup>

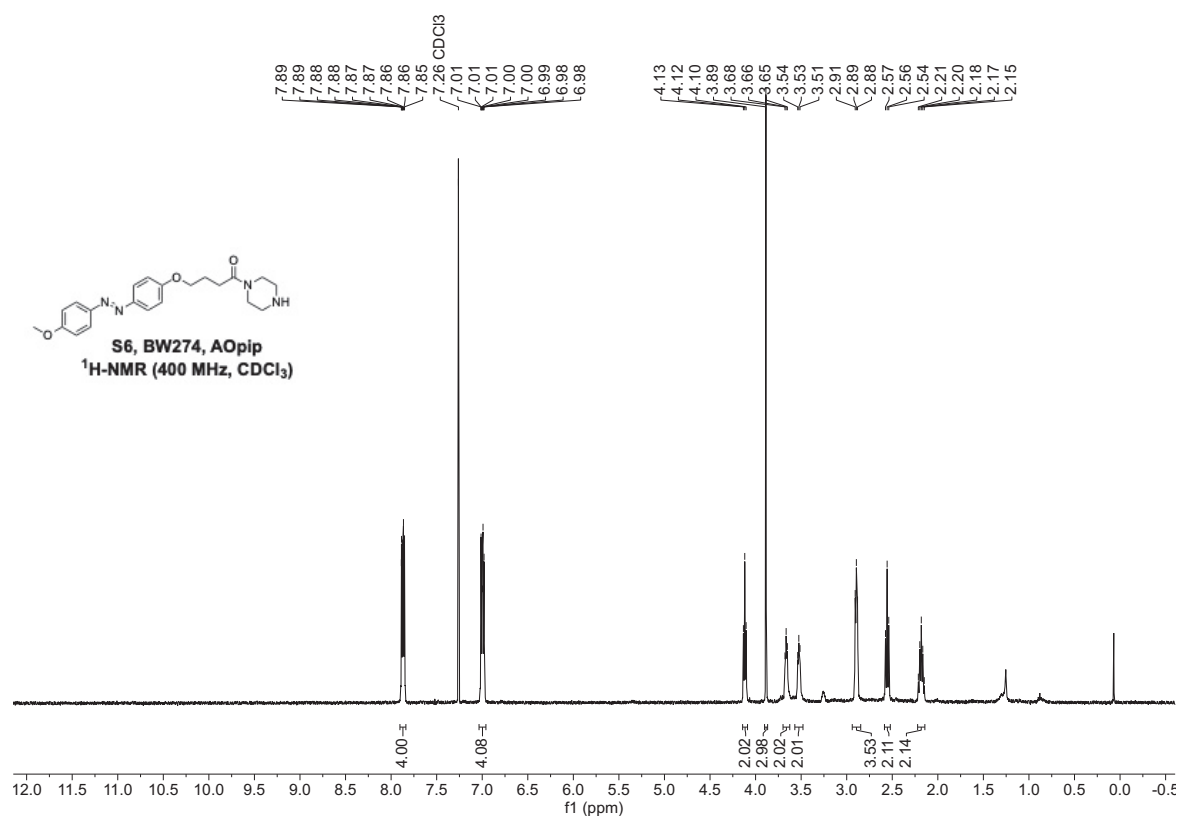
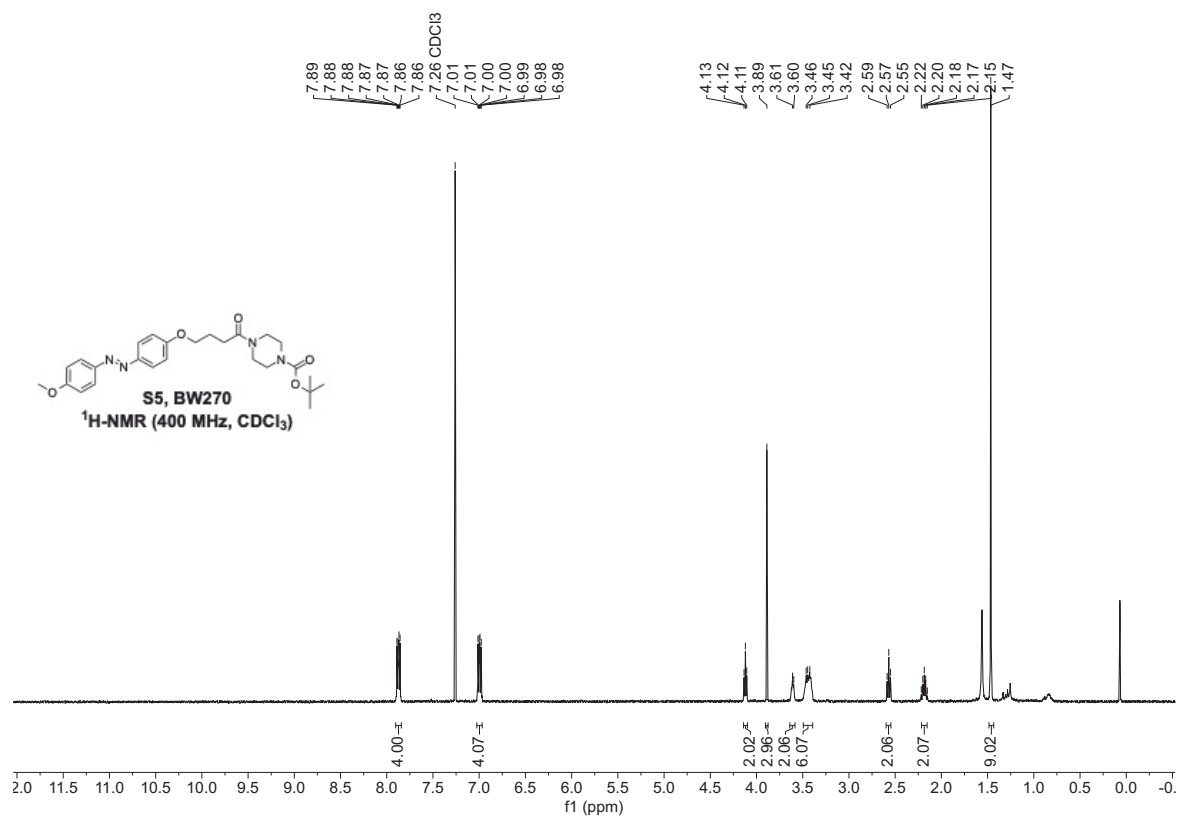
Hydrochloric acid (12M aqueous solution, 1 mL, 1.2 g, 12.2 mmol, 24 eq.) and **S14** (84 mg, 0.51 mmol, 1 eq.) were added to a solution of **S42** (150 mg, 0.51 mmol, 1 eq.) in ethanol (20 mL) at 0 °C. The reaction mixture was stirred at 0 °C for 10 min, allowed to warm to room temperature and heated to reflux for 16 h. The solvent was removed under reduced pressure and the crude material was purified by dry column chromatography (side products were eluted with EA and the desired product with 10% MeOH in DCM) to yield **NB-lipid** (139 mg, 0.31 mmol, 62%) as a blue solid.

<sup>1</sup>H-NMR (400 MHz; CD<sub>3</sub>OD):  $\delta$  = 8.90 (d, *J* = 7.9 Hz, 1H), 8.34 (d, *J* = 8.2 Hz, 1H), 7.92 (t, *J* = 7.6 Hz, 1H), 7.89 – 7.77 (m, 2H), 7.25 (dd, *J* = 9.3, 2.4 Hz, 1H), 6.98 (s, 1H), 6.88 (d, *J* = 2.5 Hz, 1H), 3.74 (t, *J* = 7.3 Hz, 2H), 1.88 (t, *J* = 7.4 Hz, 2H), 1.52 (dt, *J* = 22.3, 7.2 Hz, 2H), 1.47 – 1.38 (m, 2H), 1.37 – 1.20 (m, 12H), 0.87 (t, *J* = 7.0, 6.2 Hz, 3H).

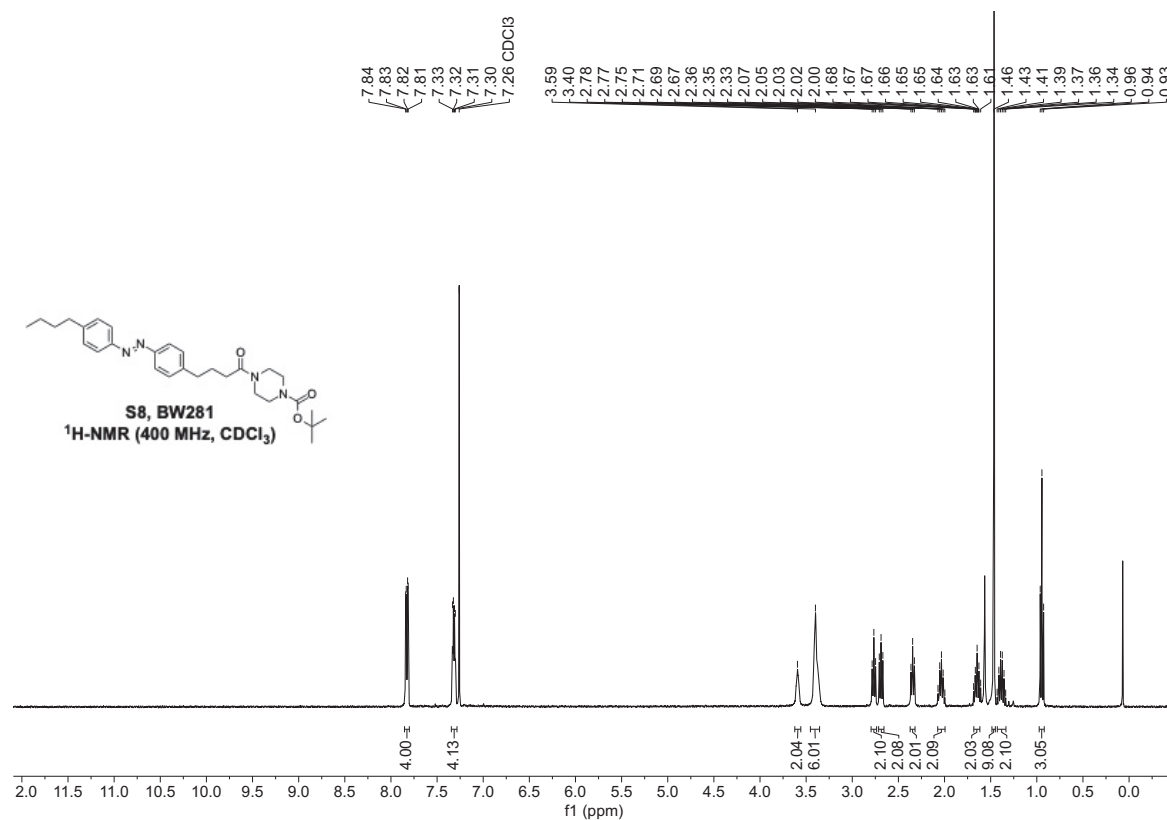
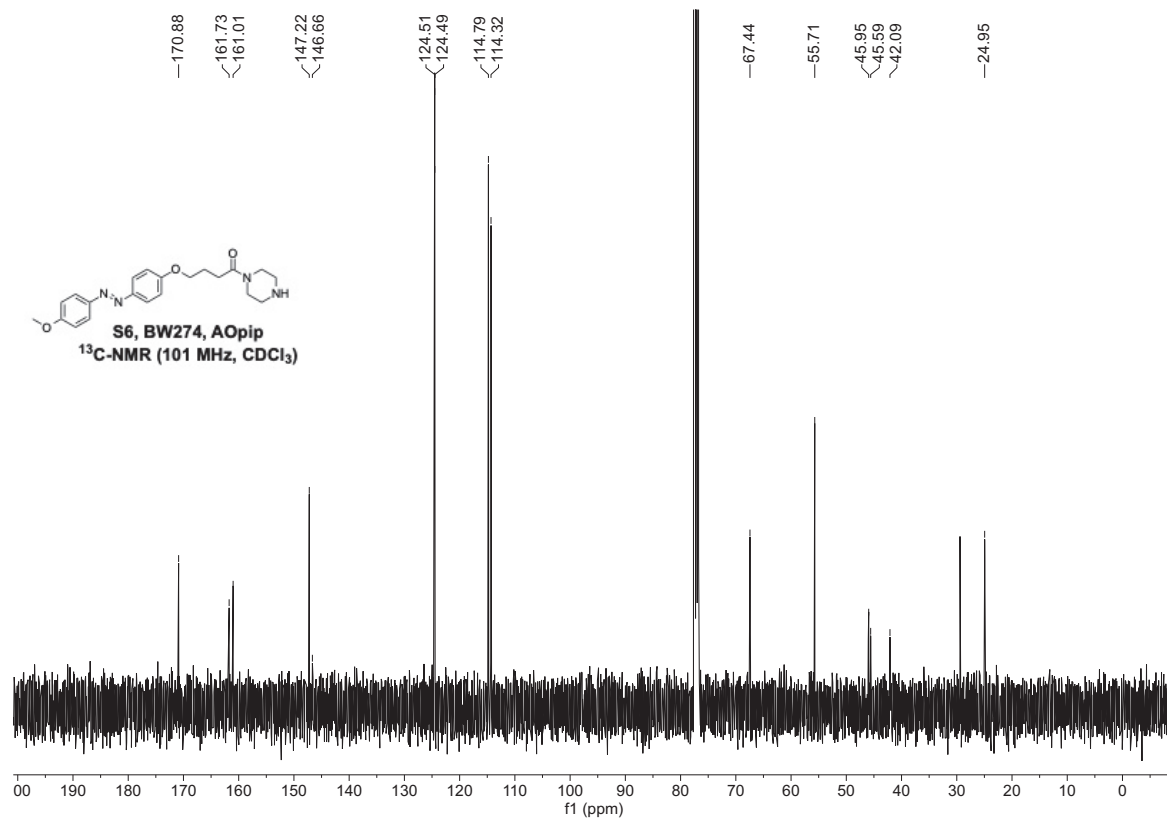
<sup>13</sup>C-NMR (101 MHz; CD<sub>3</sub>OD):  $\delta$  = 159.7, 157.3, 153.5, 149.4, 135.6, 133.8, 133.1, 132.7, 131.4, 131.1, 125.8, 124.9, 123.9, 116.4, 97.2, 94.6, 45.9, 41.1, 33.1, 30.7, 30.7, 30.6, 30.5, 30.4, 29.7, 28.1, 23.7, 14.4.

**HR-MS** (ESI) *m/z*: calculated for C<sub>29</sub>H<sub>38</sub>N<sub>3</sub>O<sup>+</sup>: 444.30094; found: 444.30085, M<sup>+</sup>.

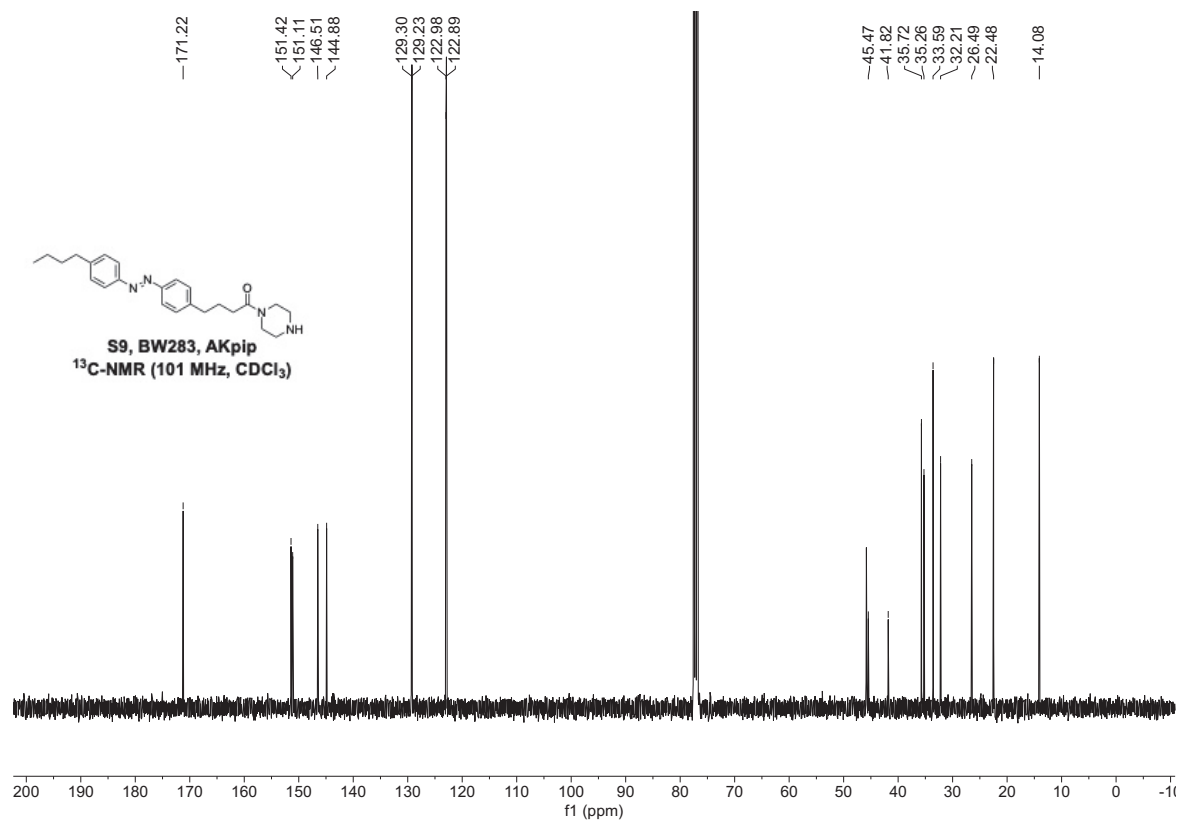
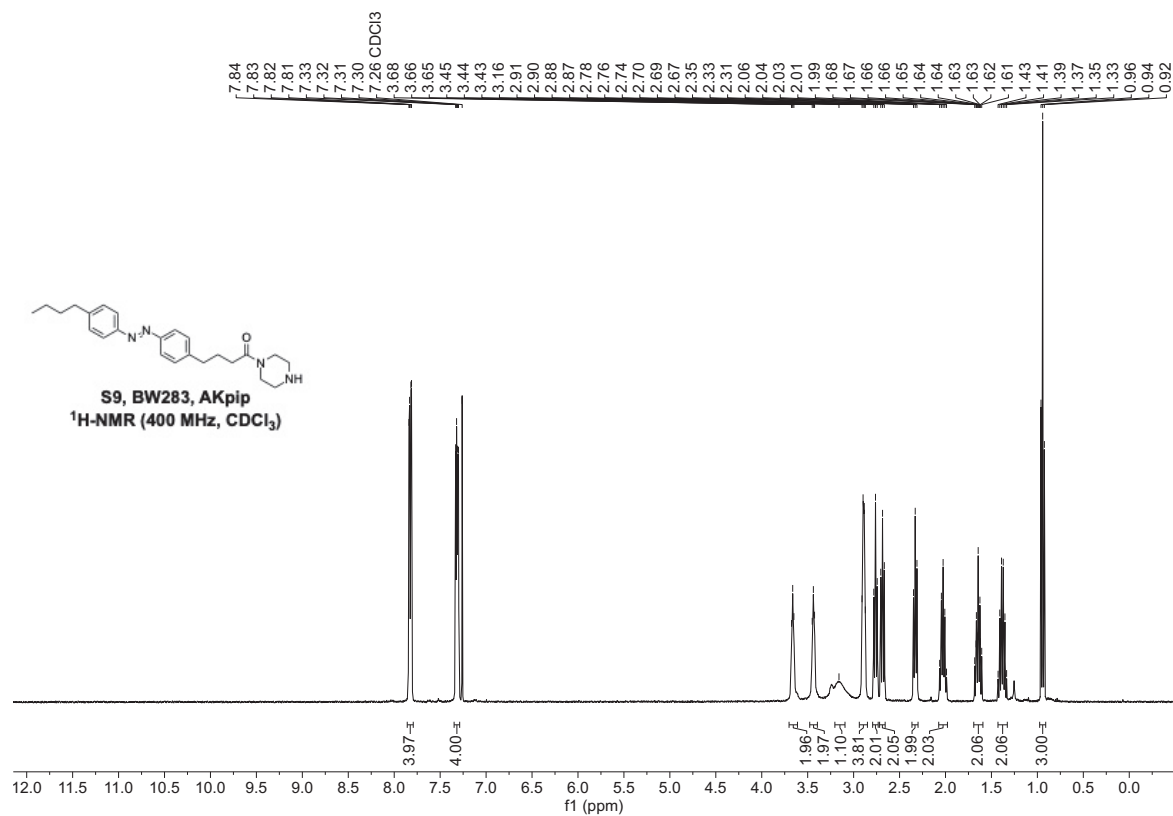
## 14 Appendix: NMR Spectra

*H-NMRs for precursors, H- and C-NMRs for pre-final-step amines/acids and conjugates*

Supplementary Information - Section Appendix: NMR Spectra

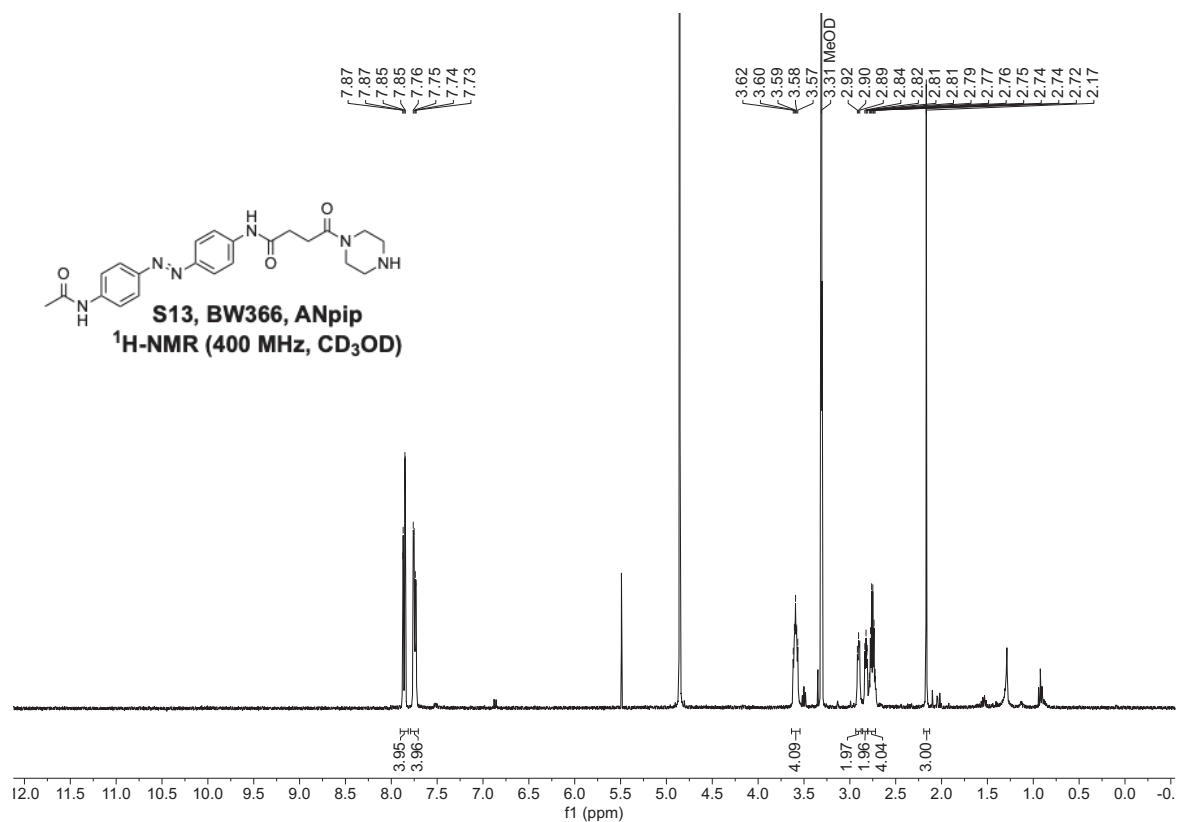
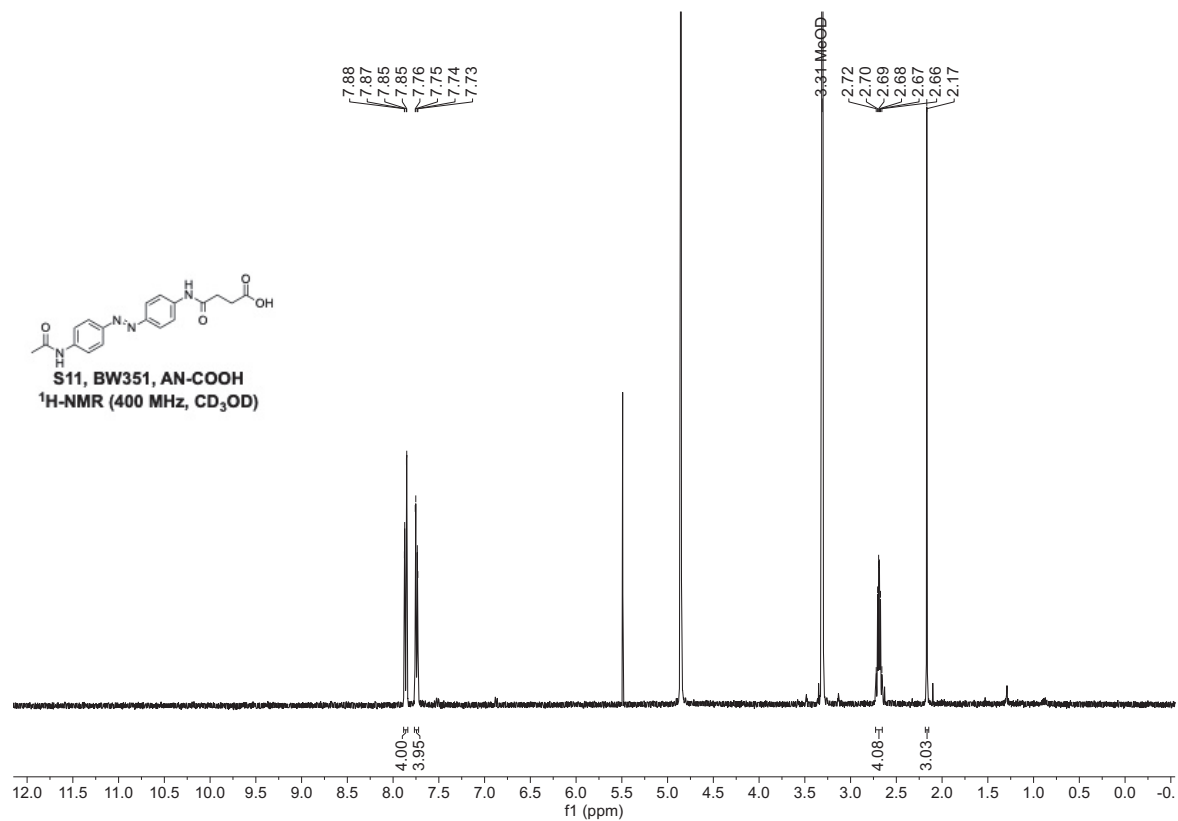


Supplementary Information - Section Appendix: NMR Spectra

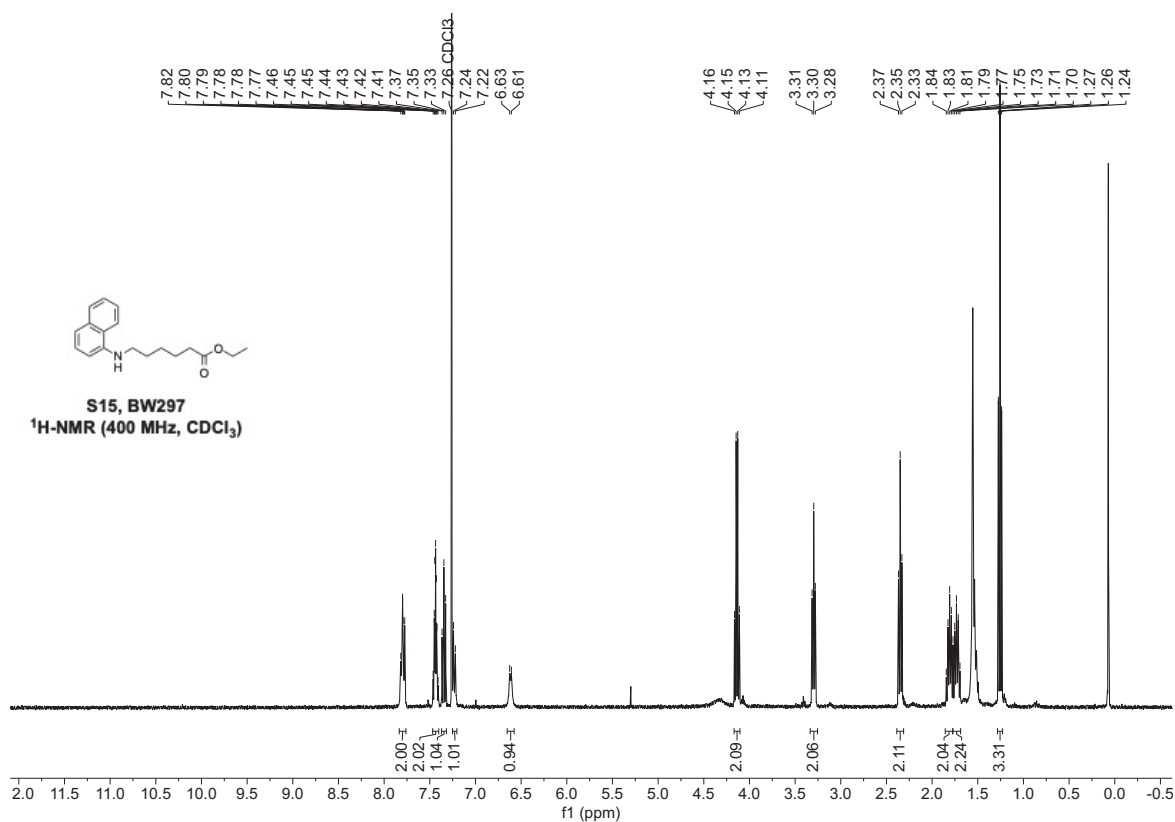
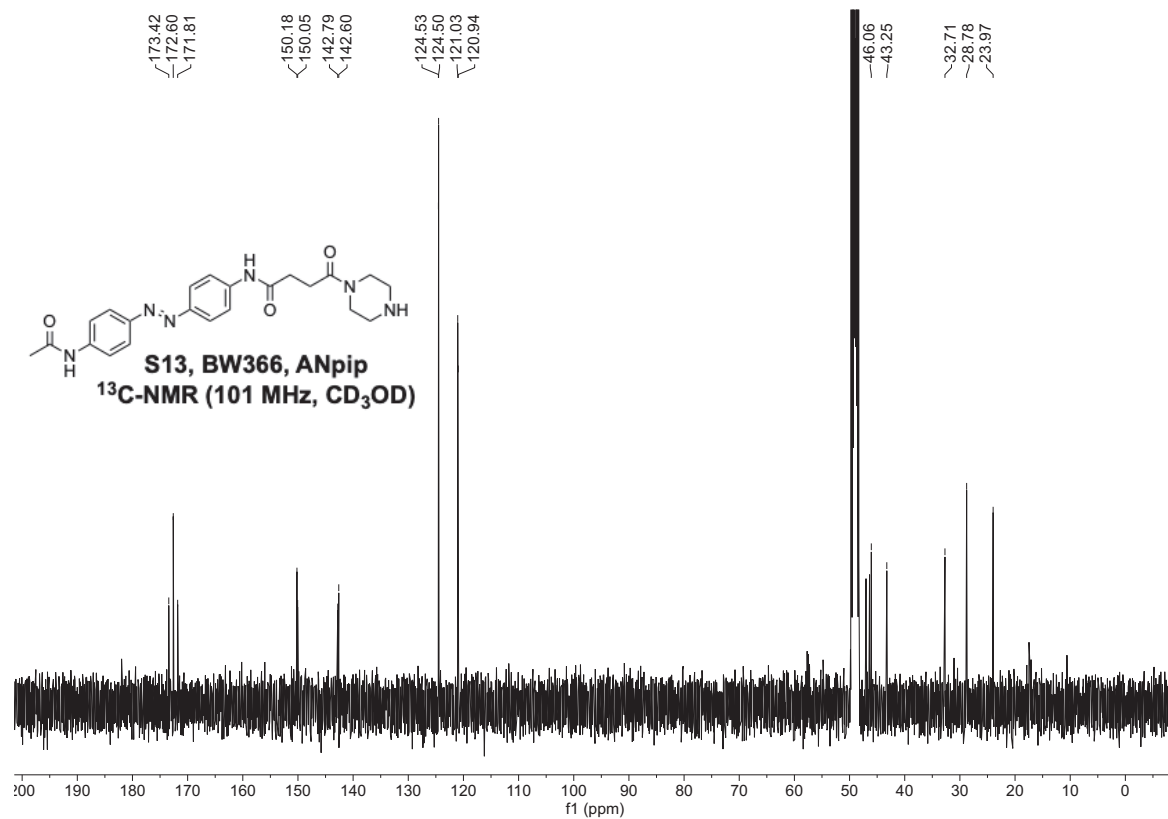




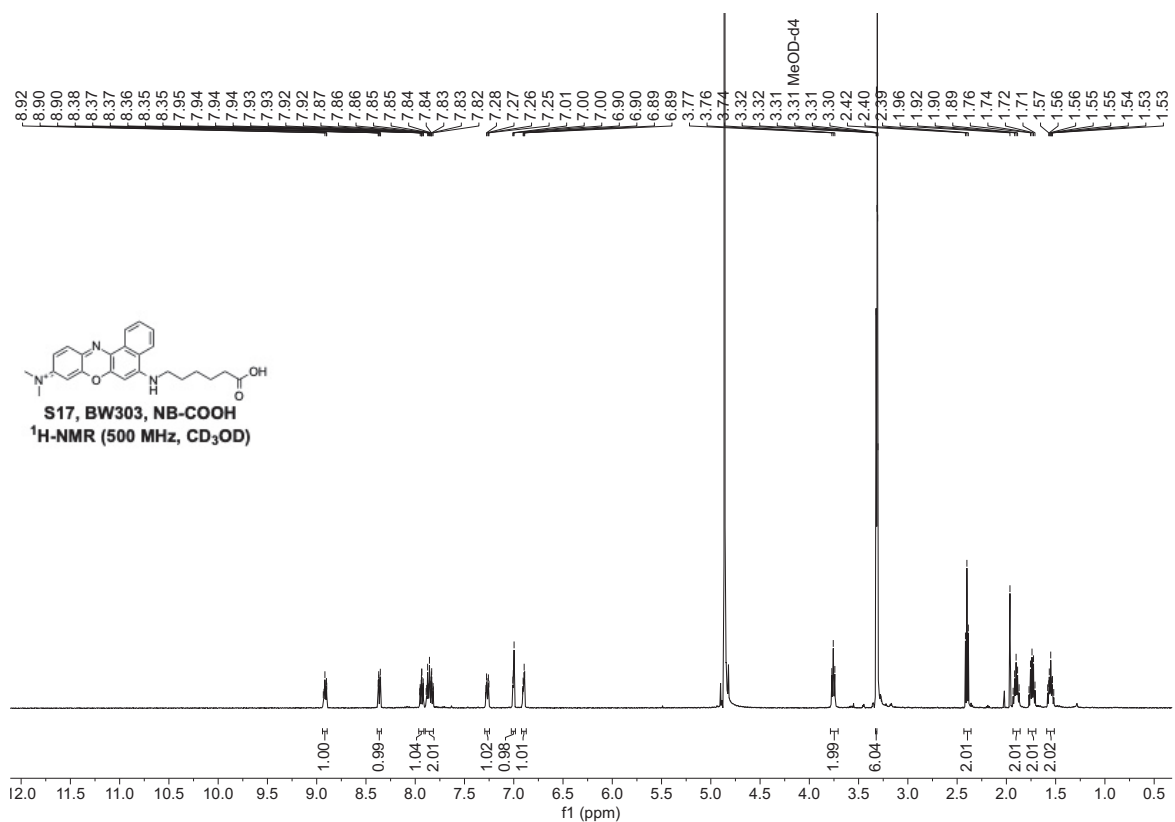
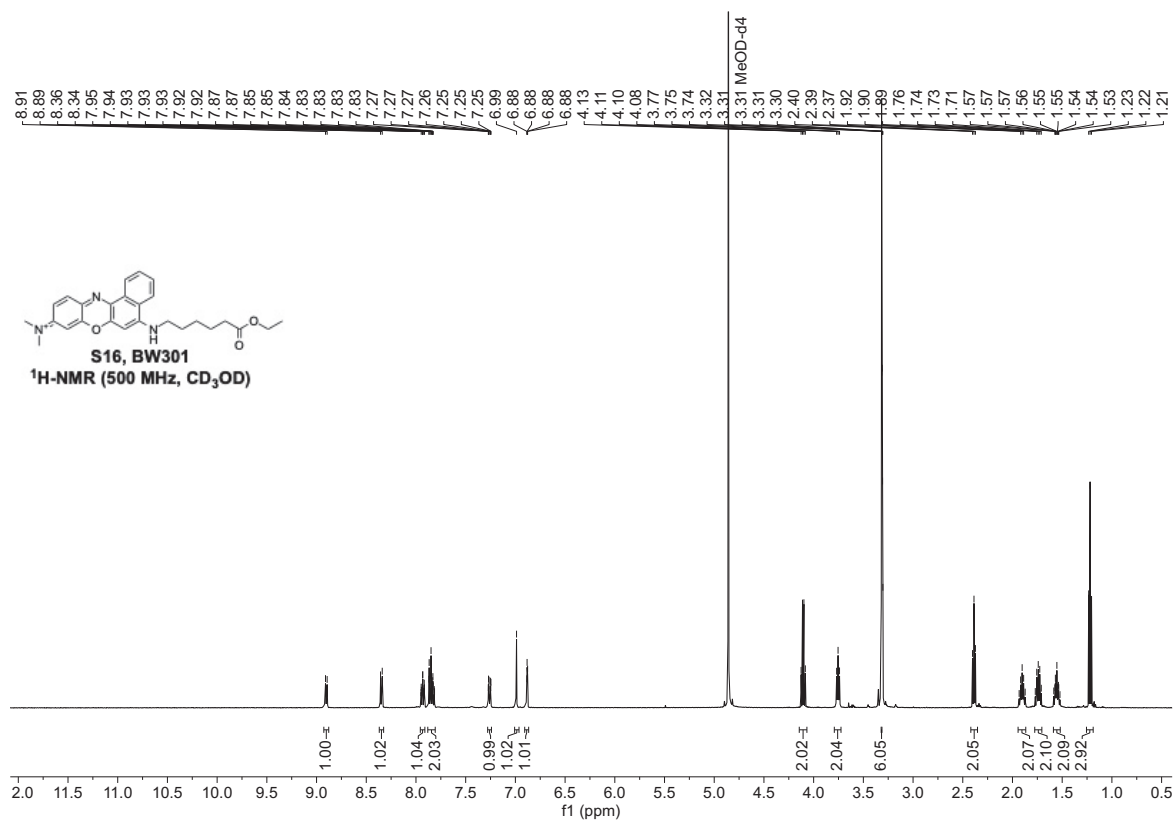
Supplementary Information - Section Appendix: NMR Spectra



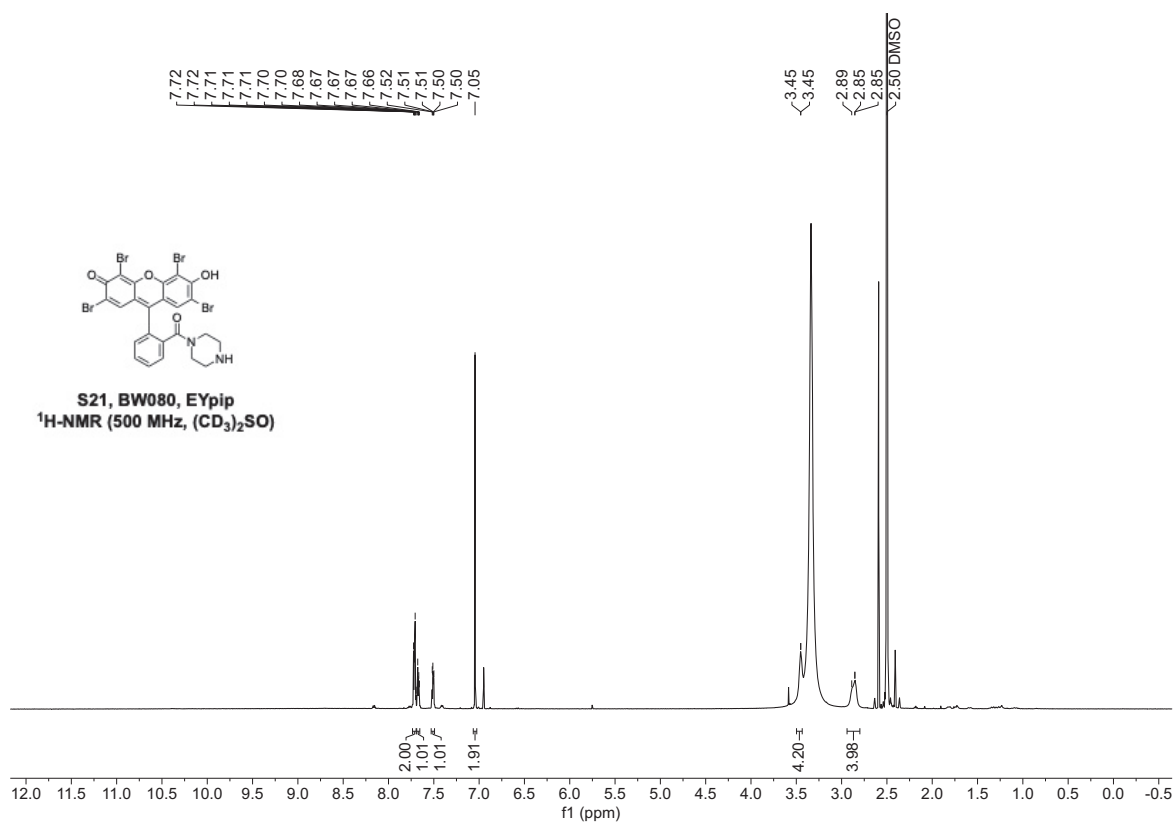
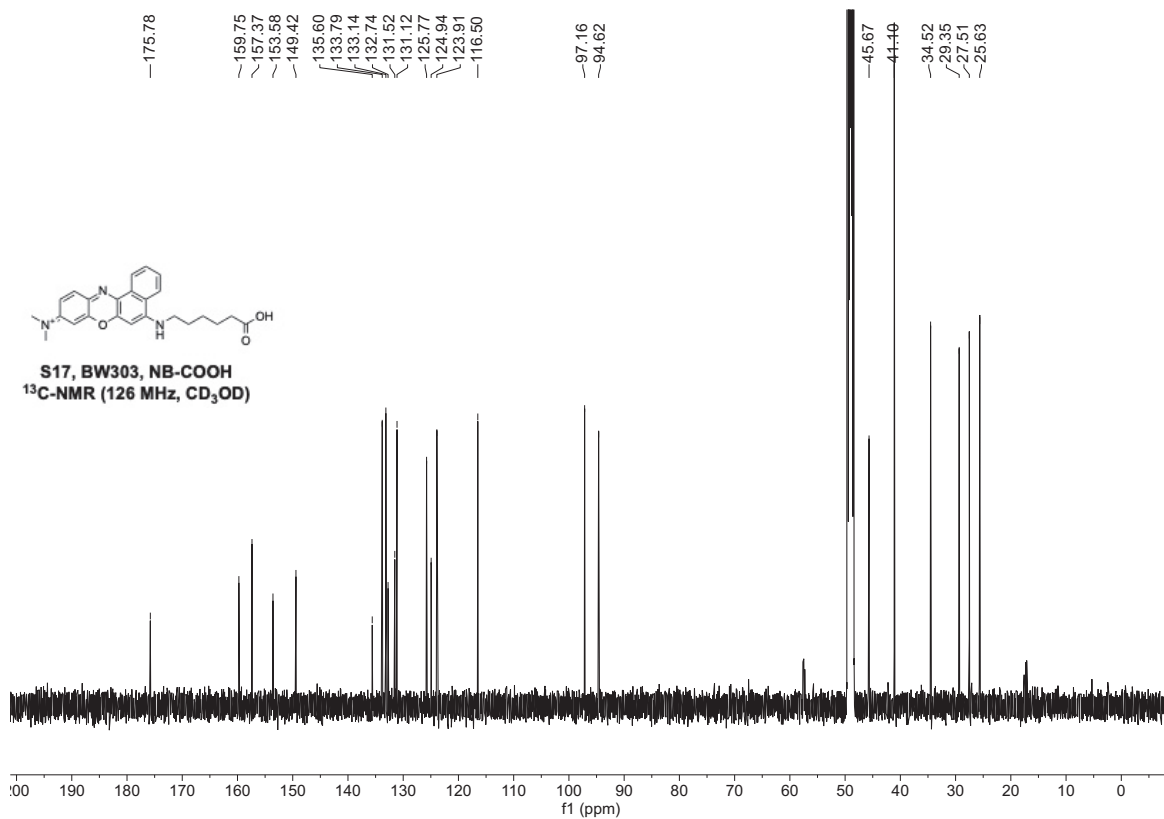
Supplementary Information - Section Appendix: NMR Spectra



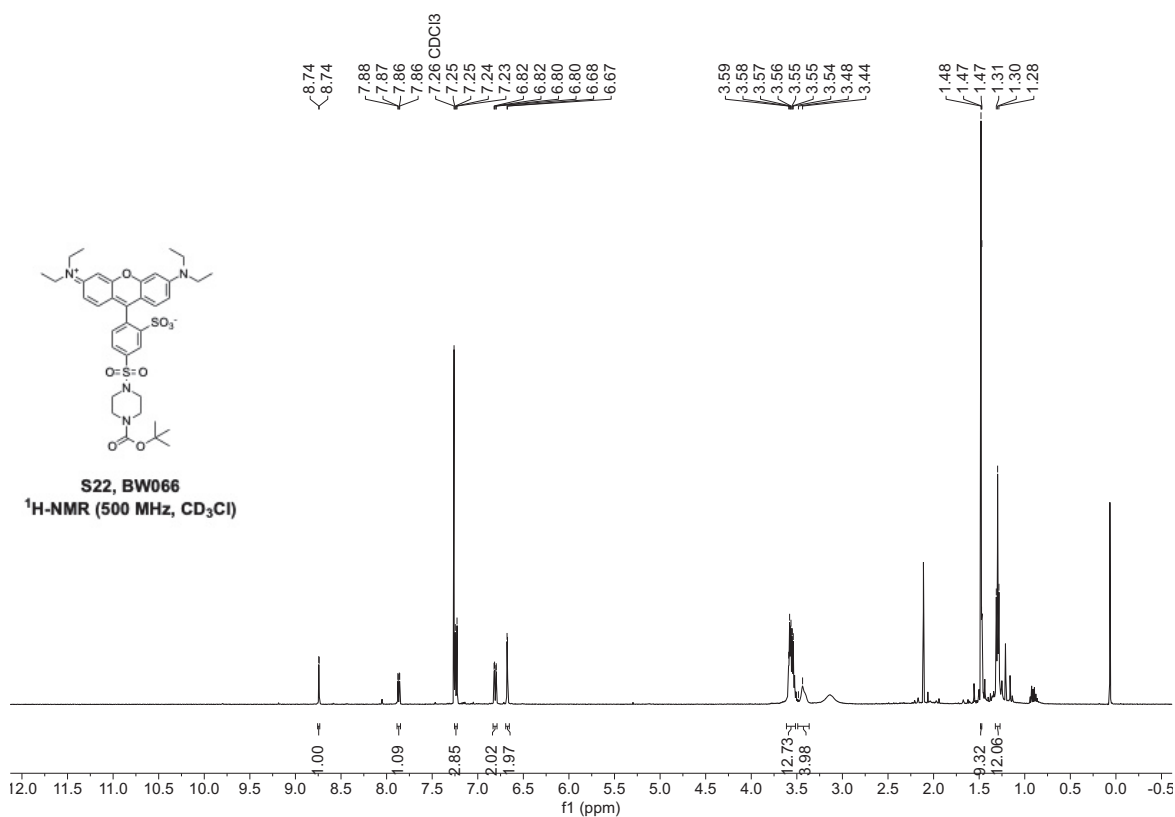
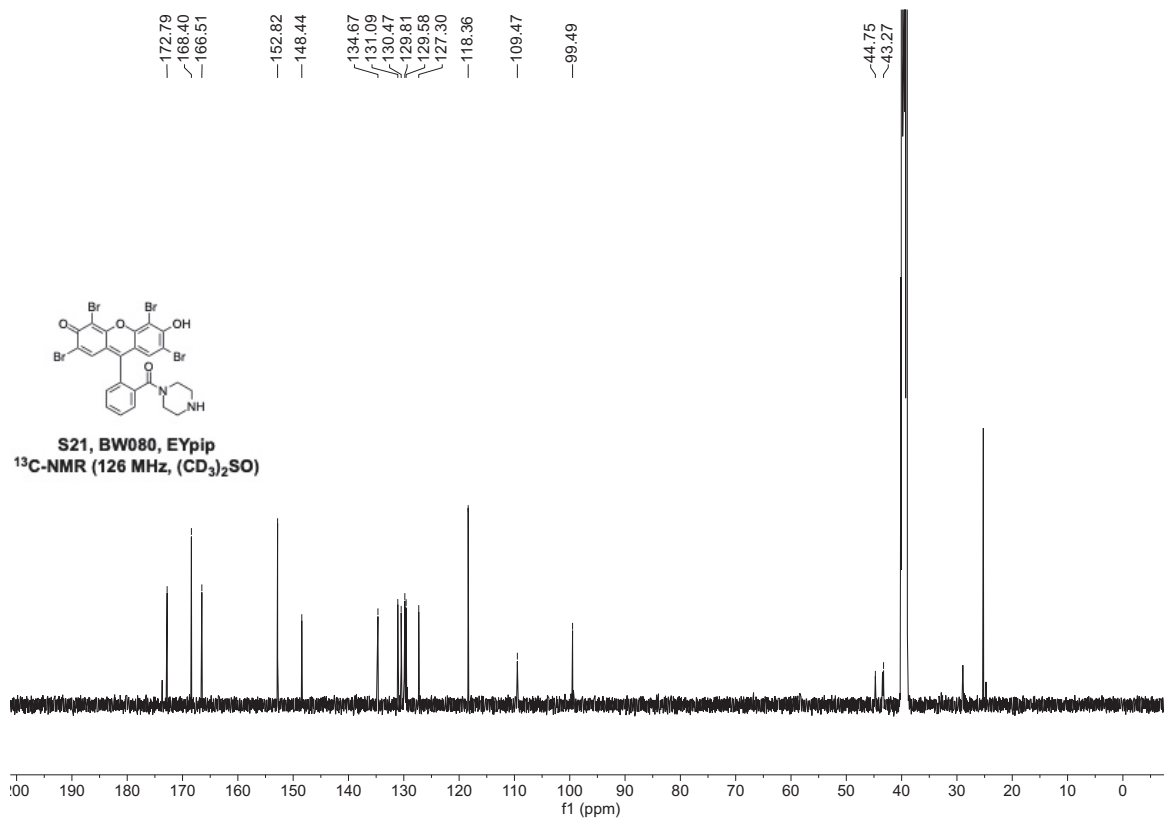
Supplementary Information - Section Appendix: NMR Spectra



Supplementary Information - Section Appendix: NMR Spectra

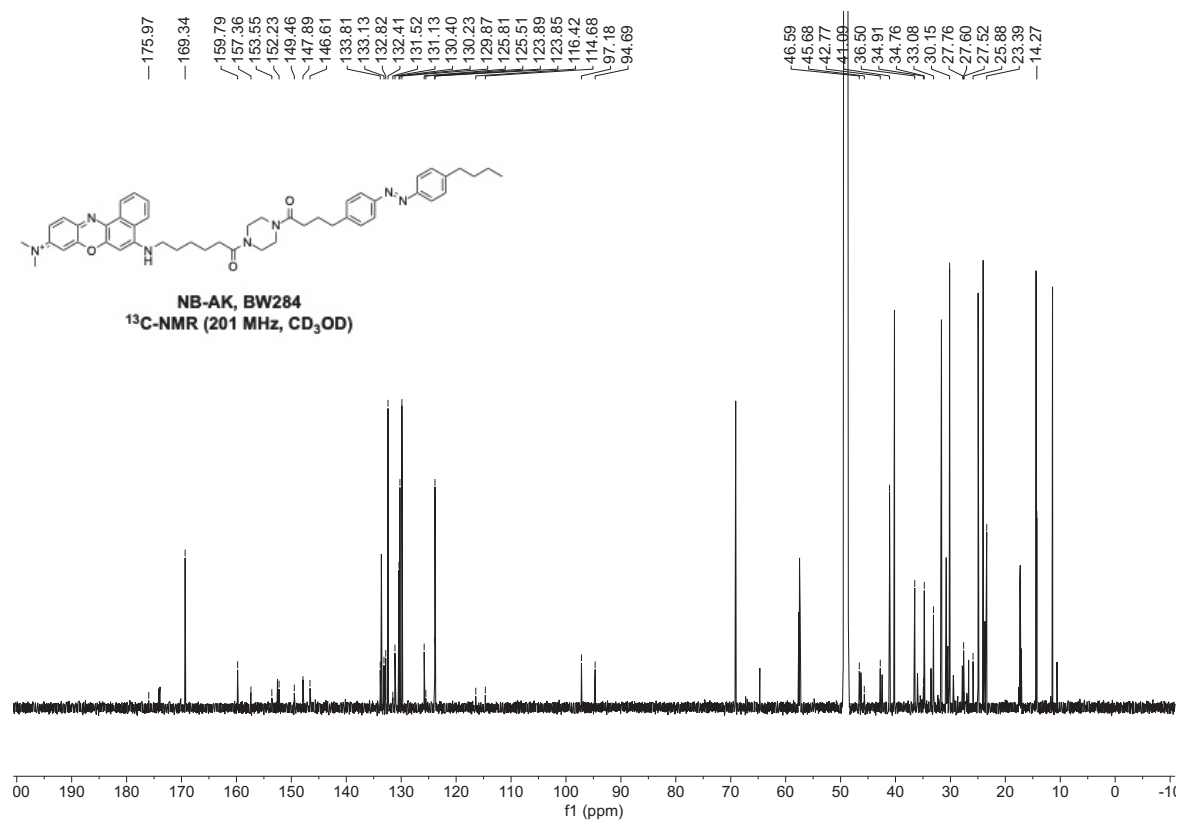
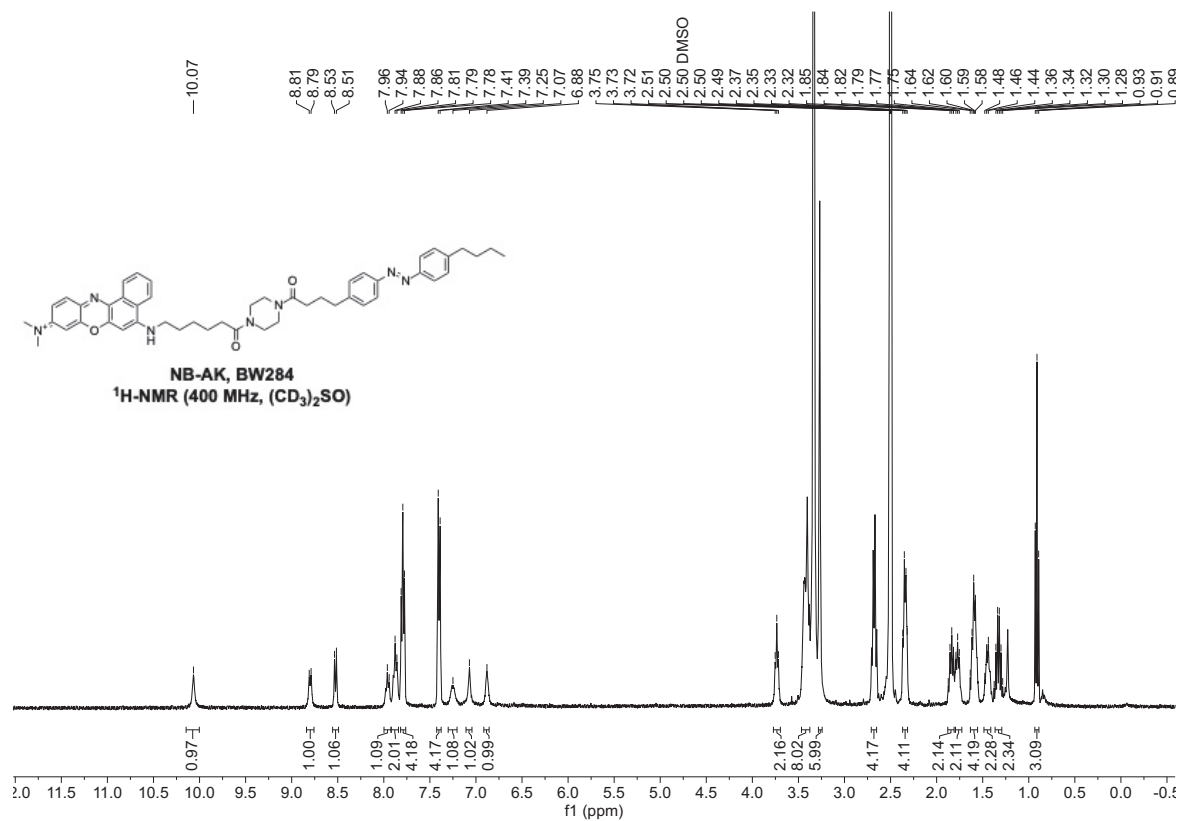


Supplementary Information - Section Appendix: NMR Spectra





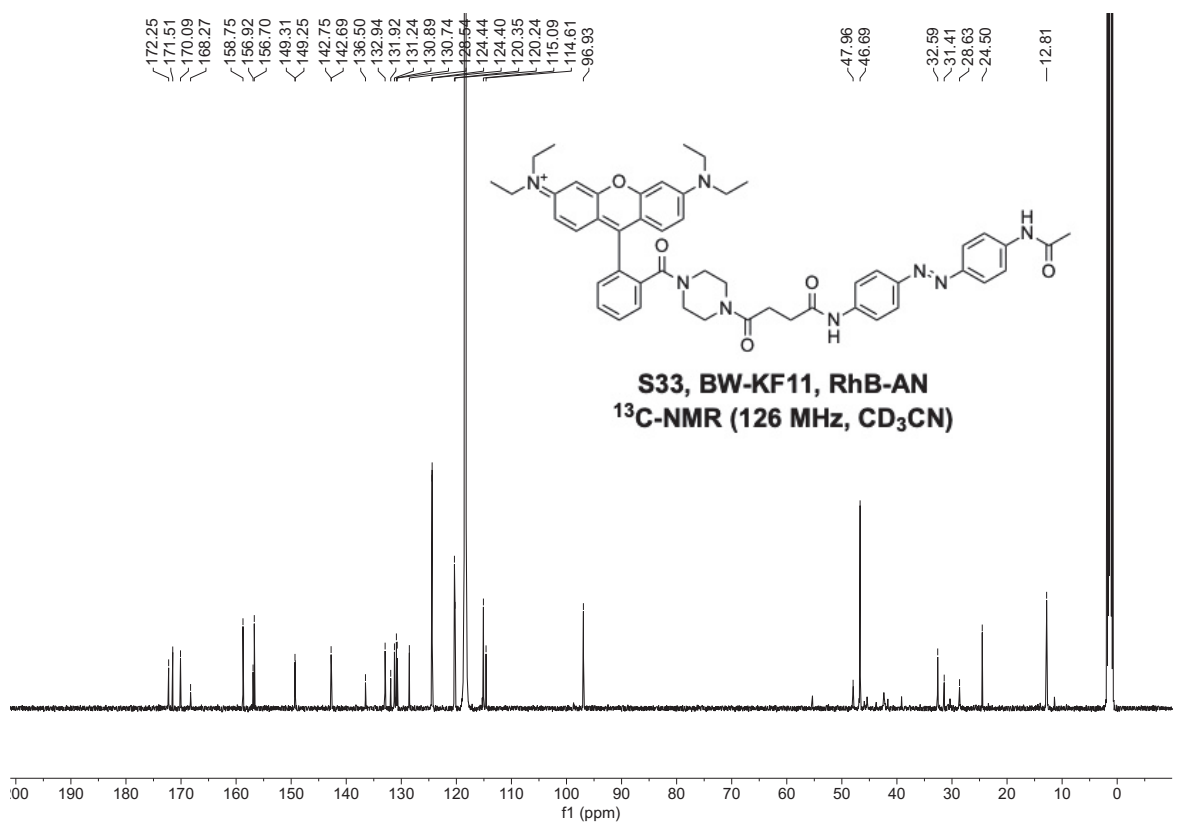
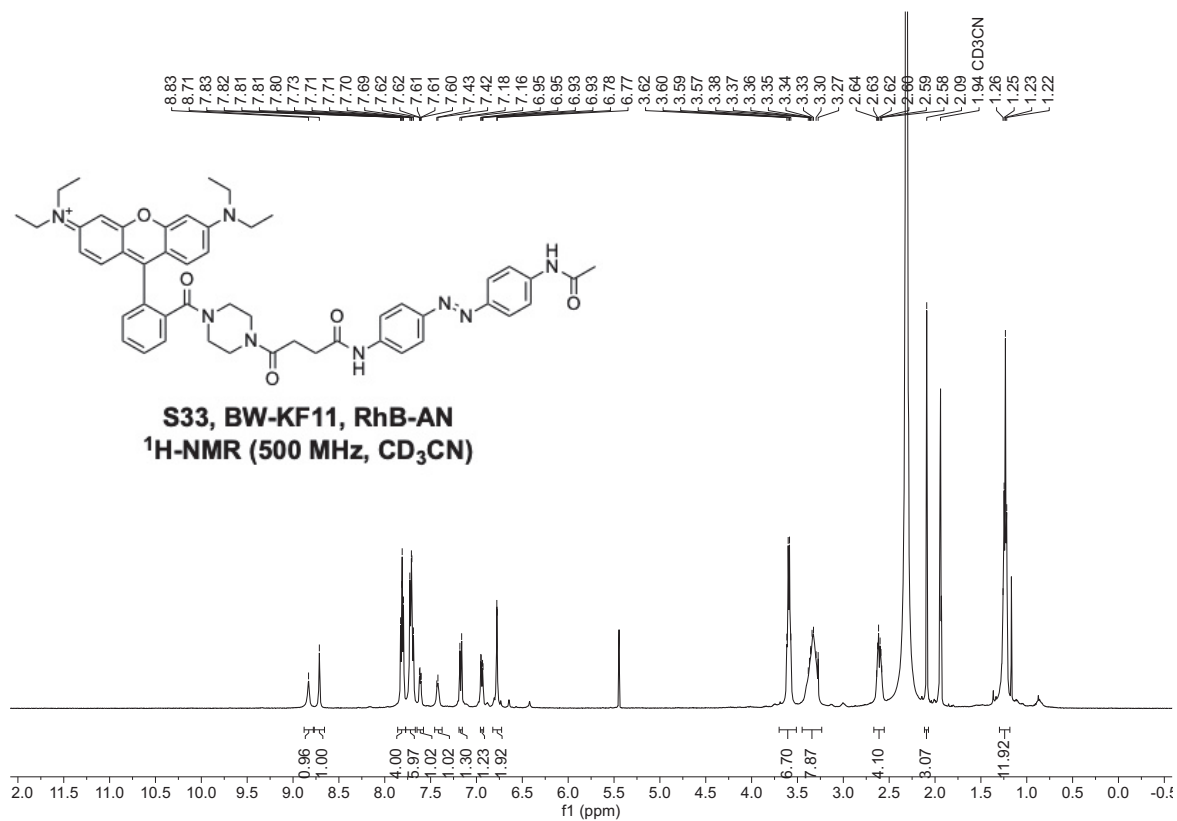
Supplementary Information - Section Appendix: NMR Spectra



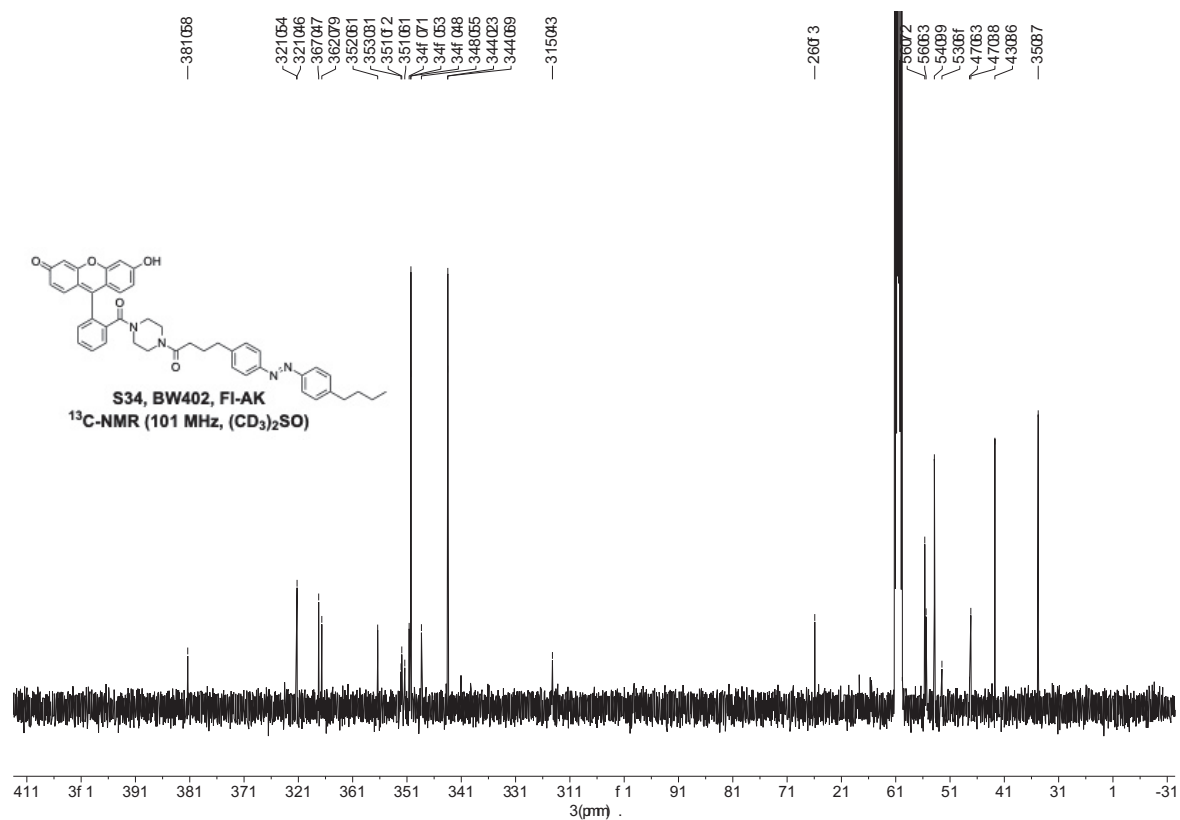
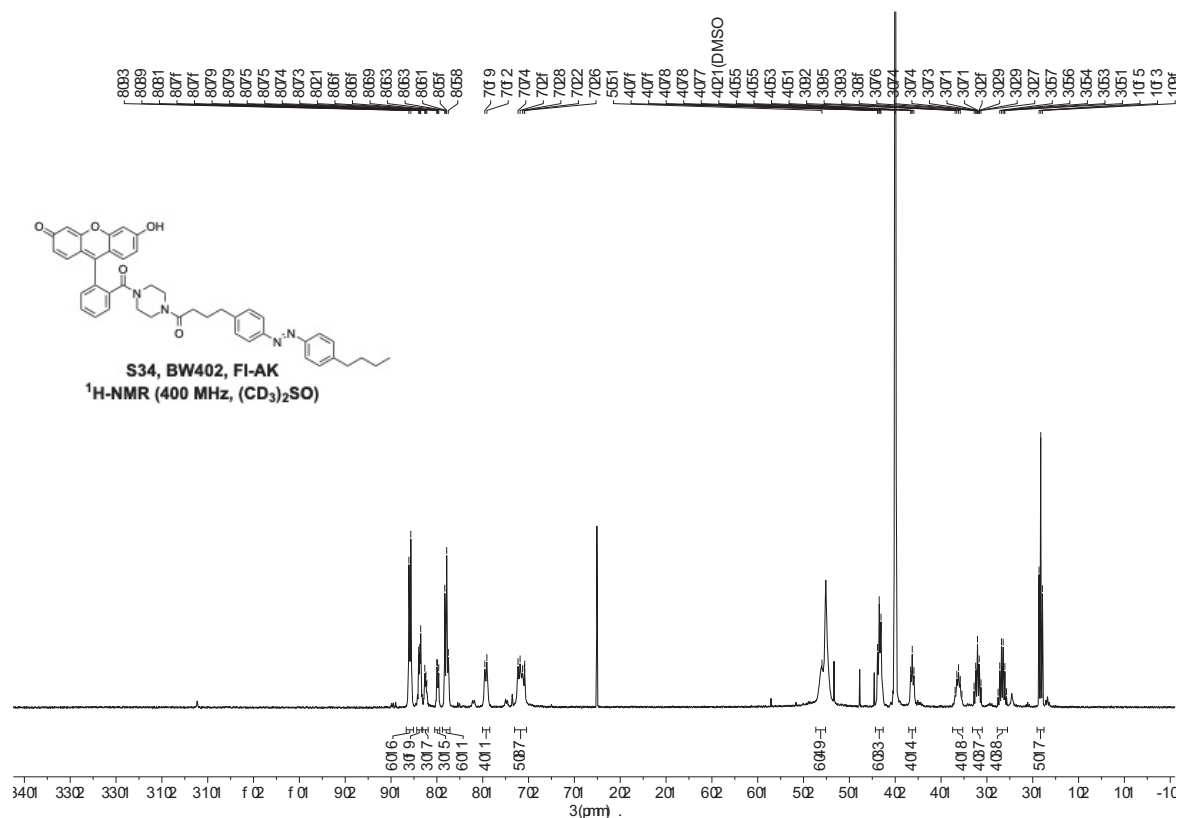




Supplementary Information - Section Appendix: NMR Spectra

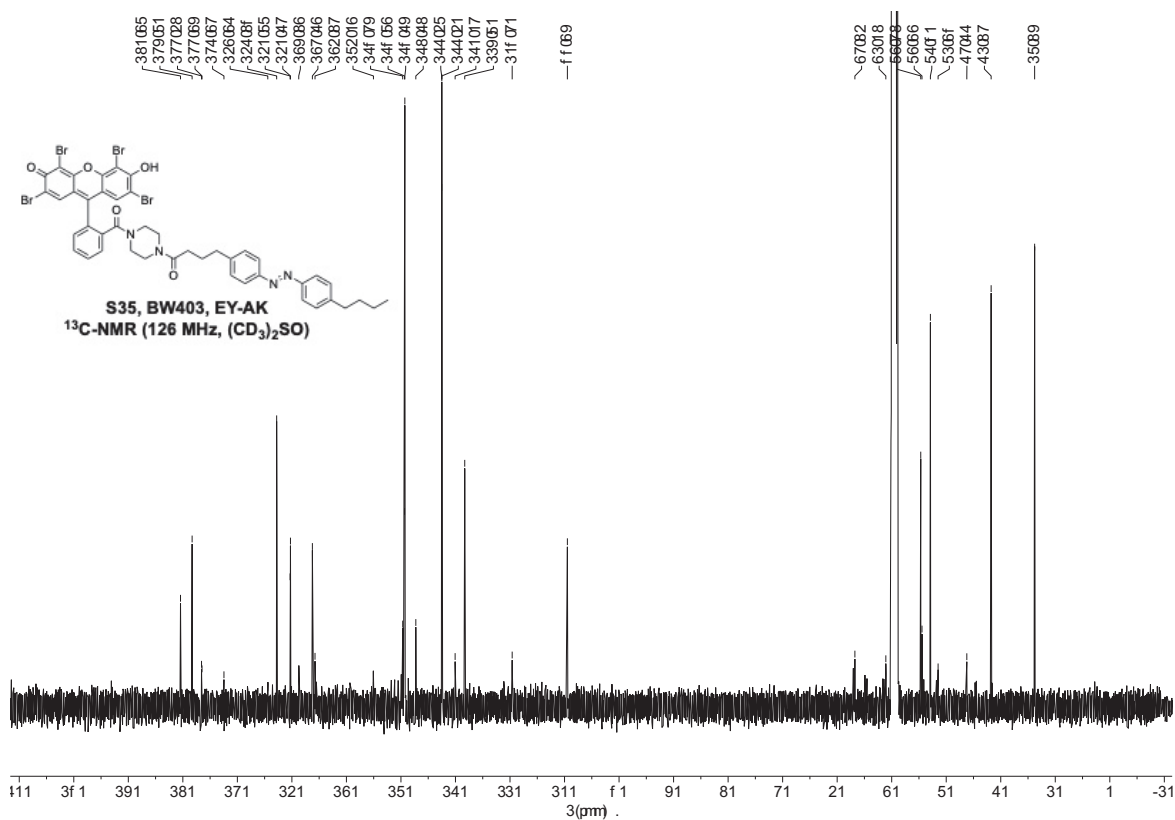
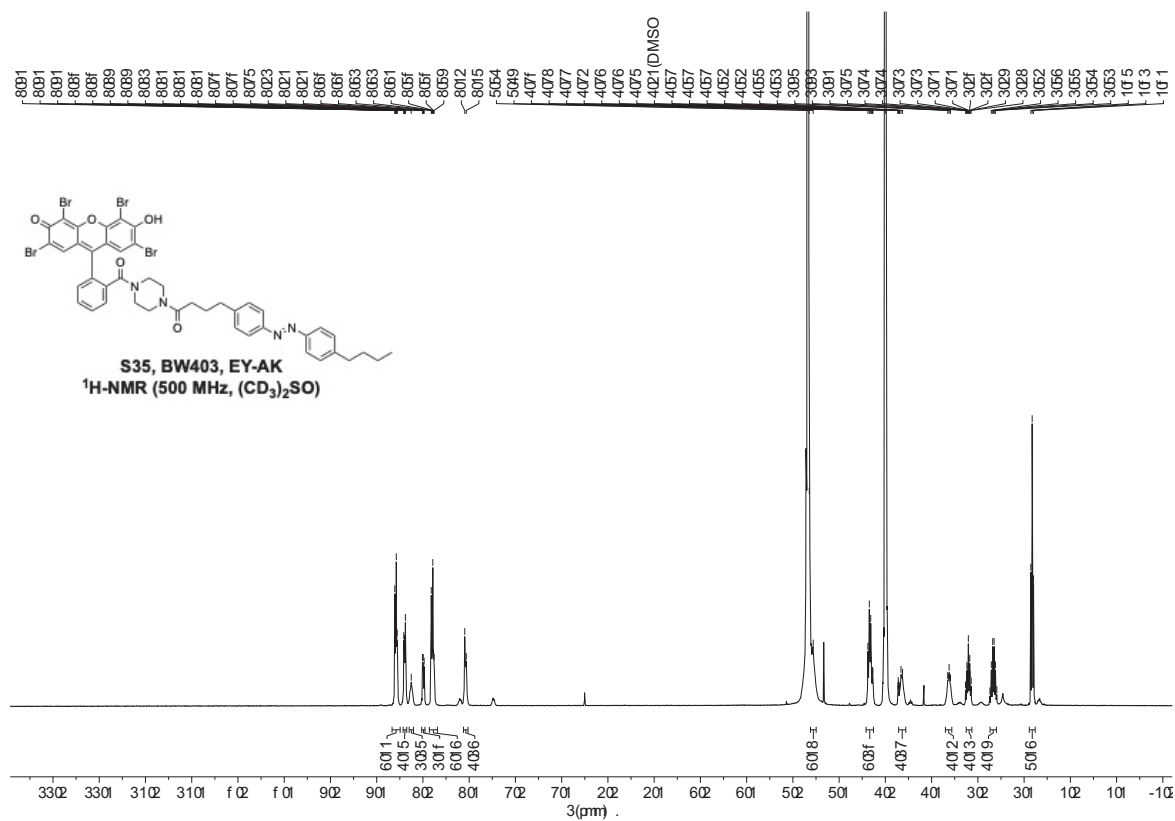


Supplementary Information - Section Appendix: NMR Spectra

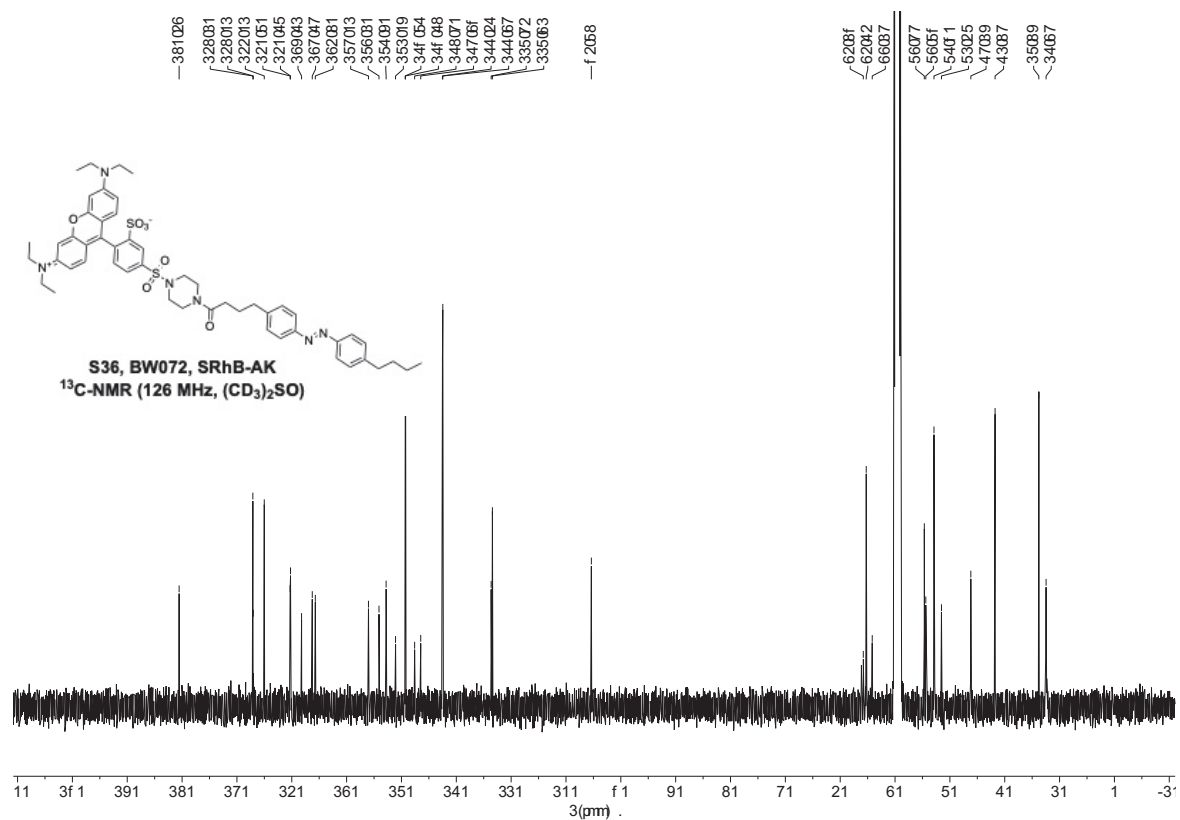
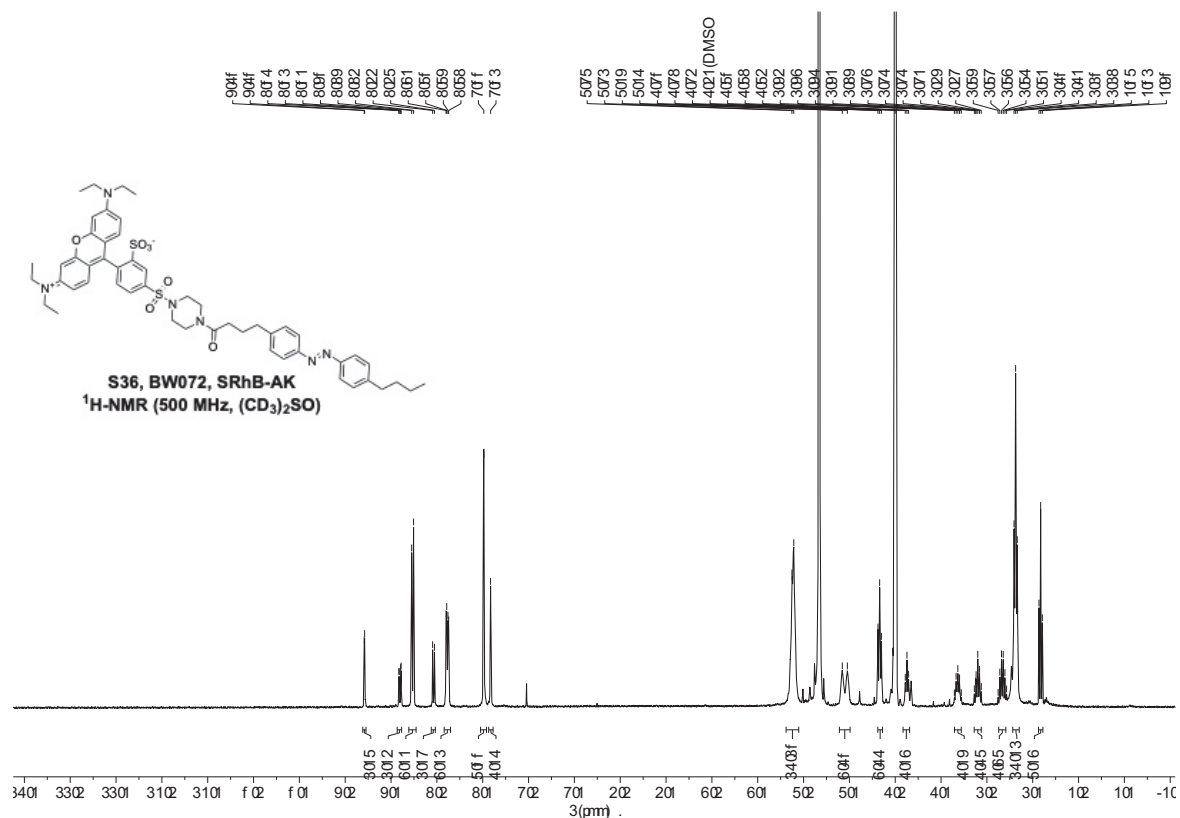




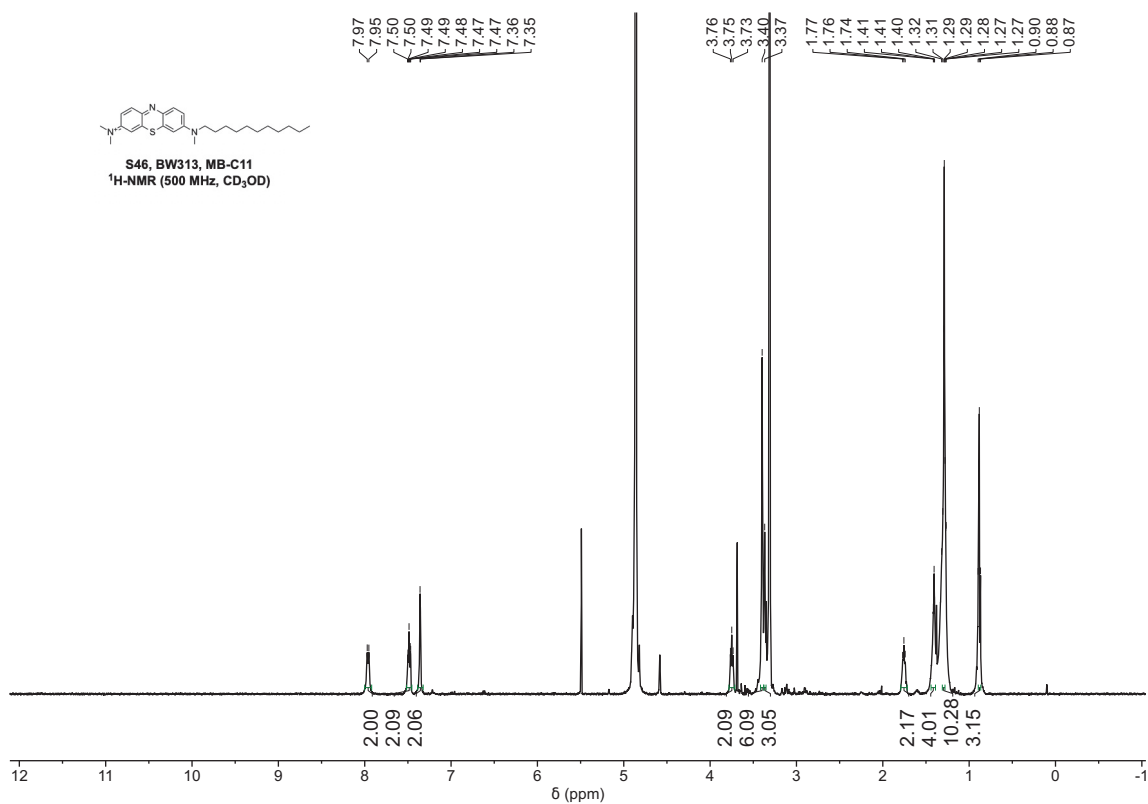
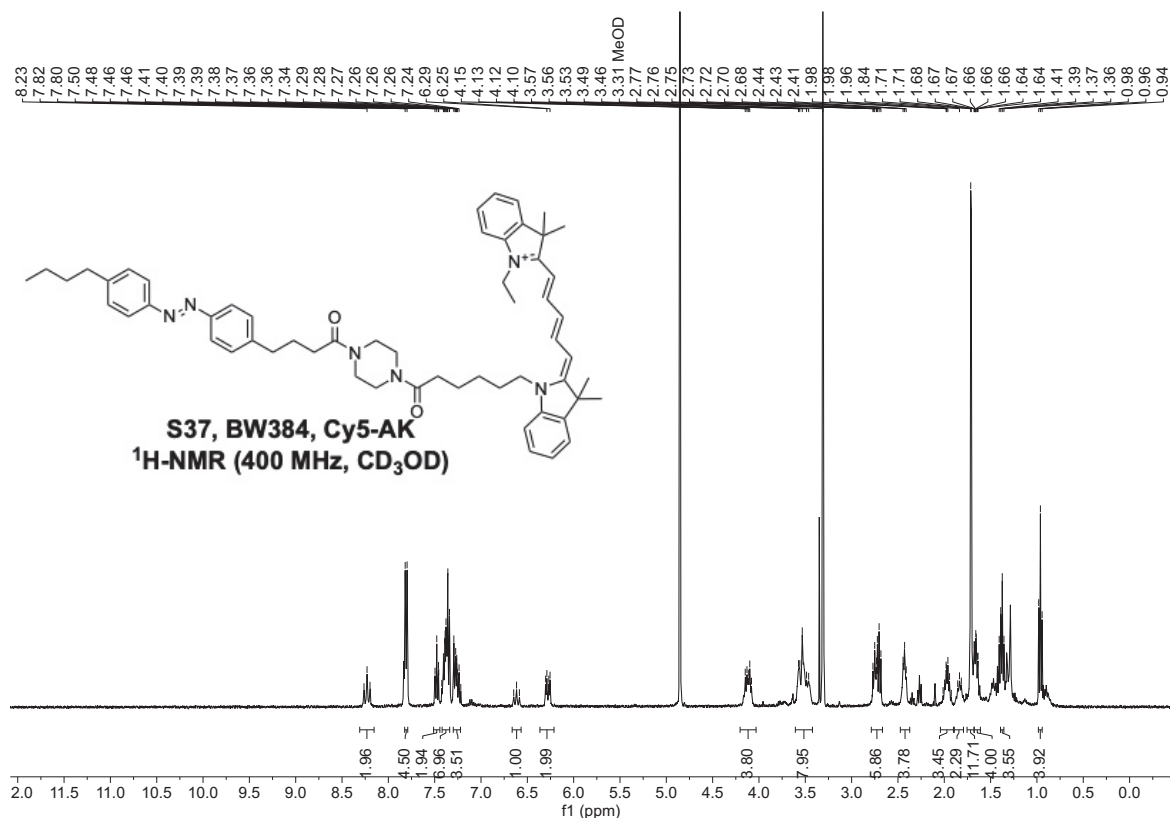
Supplementary Information - Section Appendix: NMR Spectra



Supplementary Information - Section Appendix: NMR Spectra

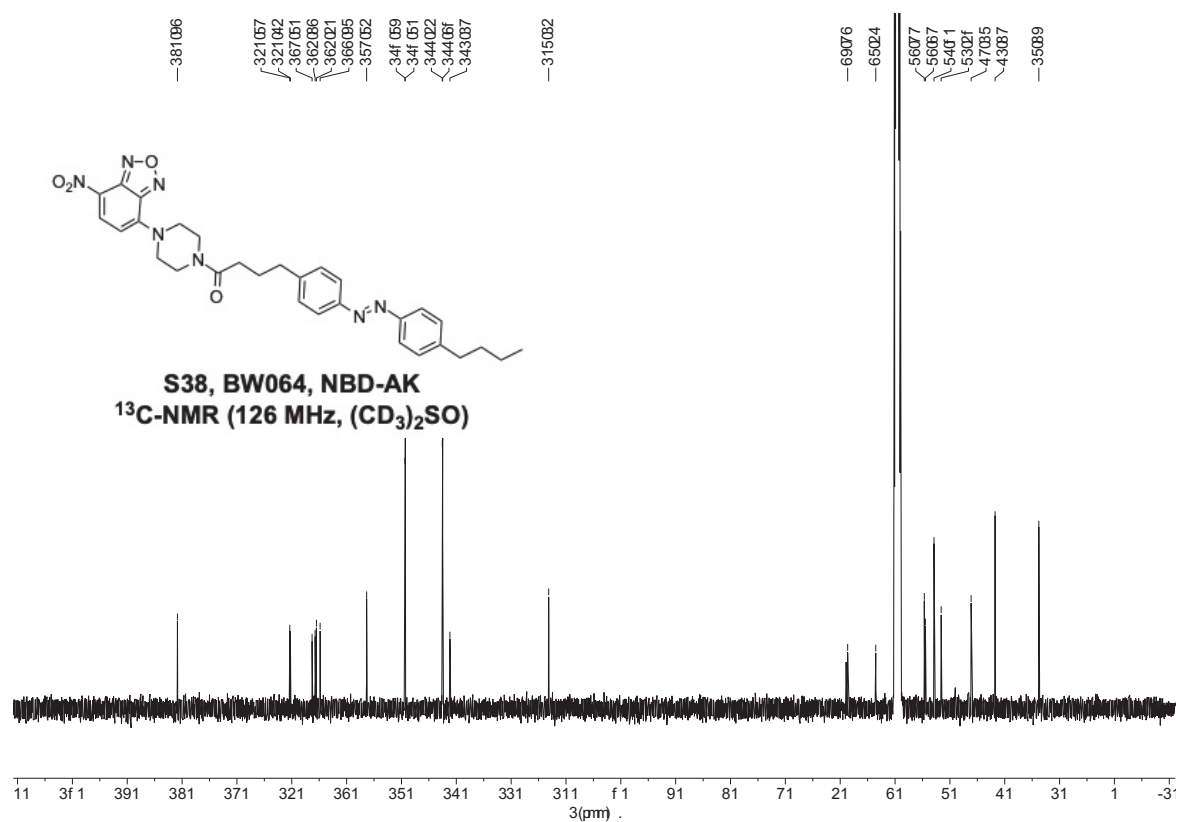
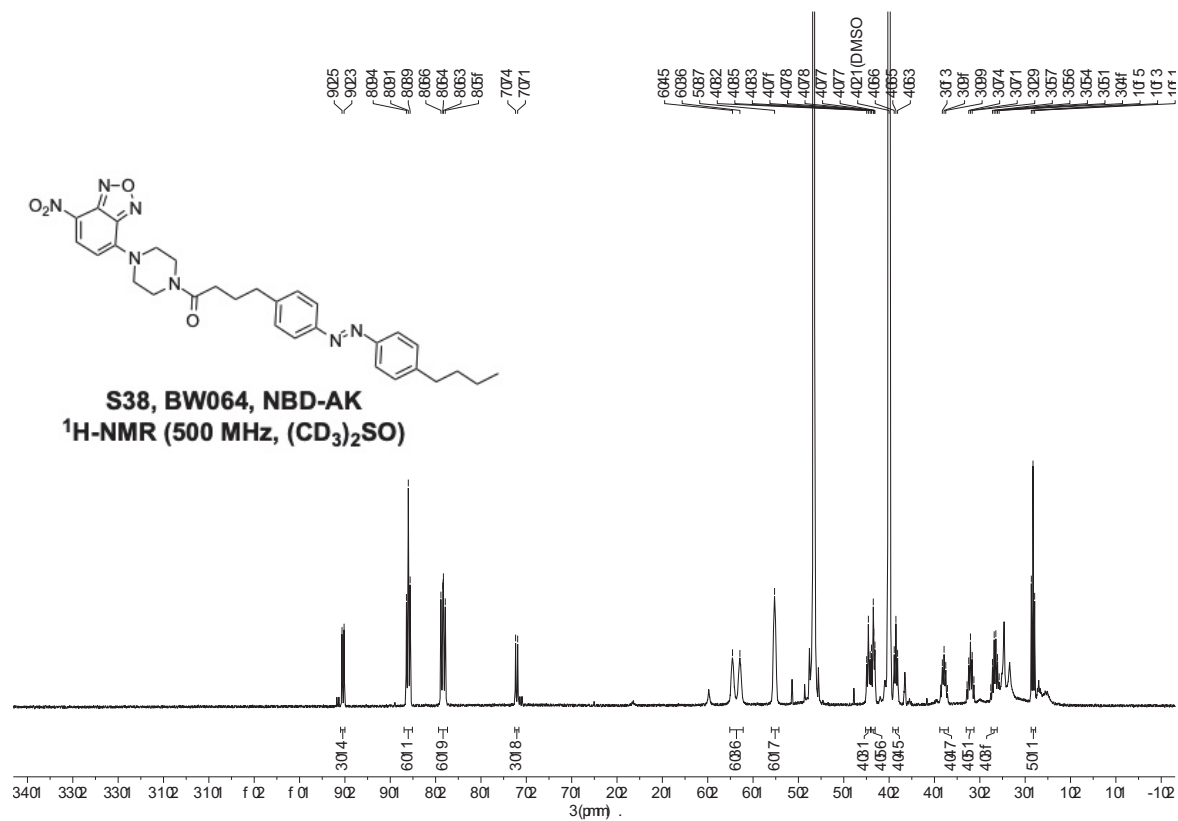


Supplementary Information - Section Appendix: NMR Spectra



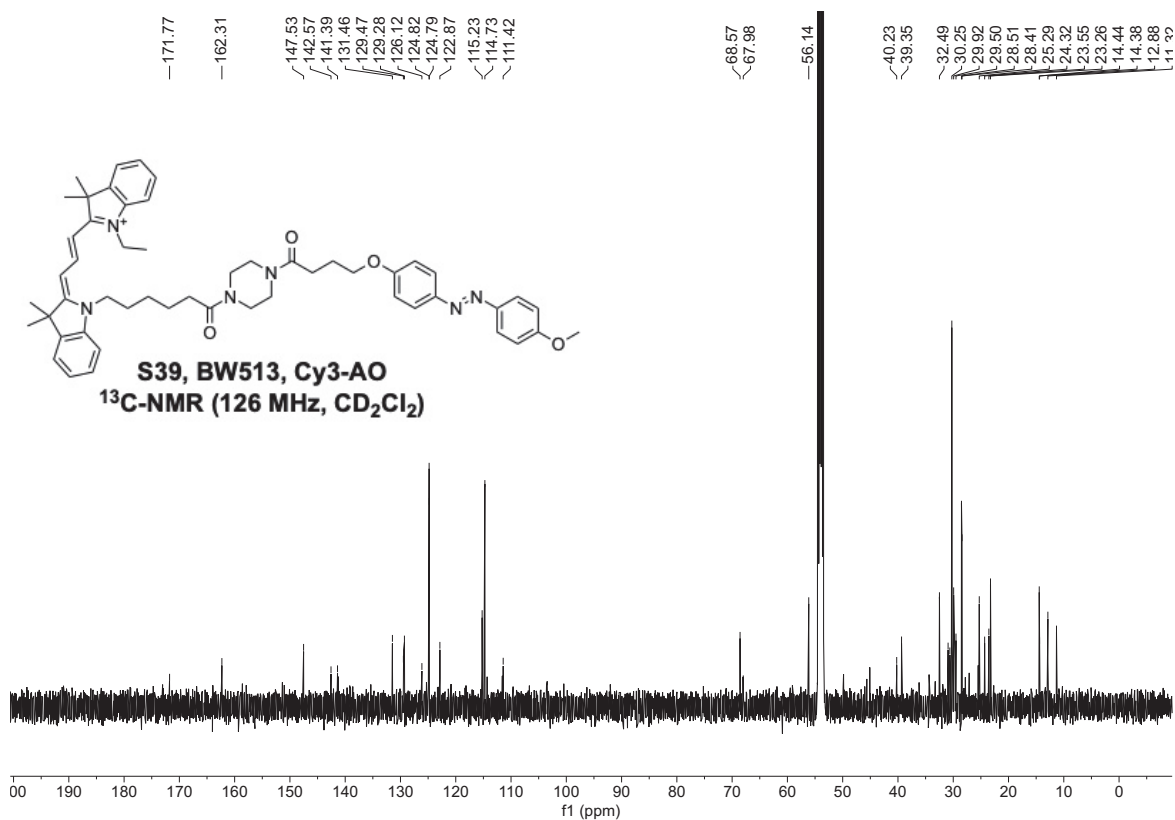
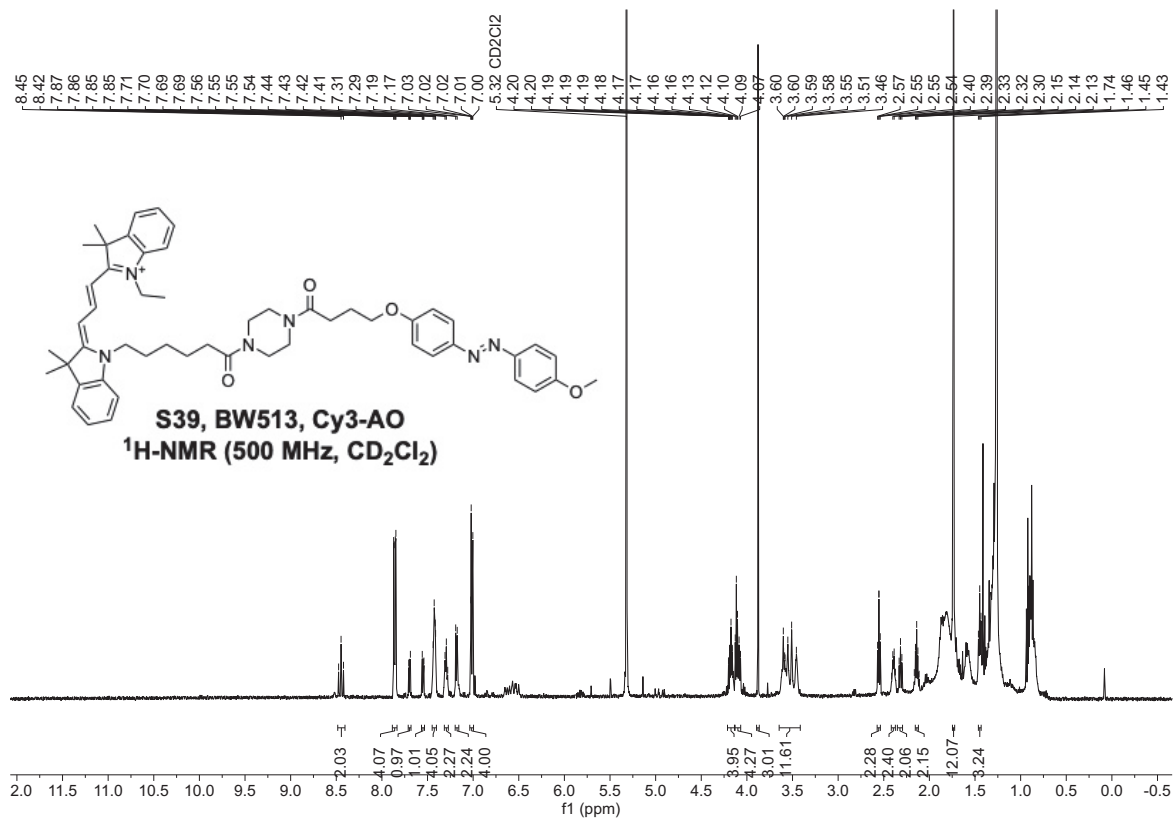


Supplementary Information - Section Appendix: NMR Spectra



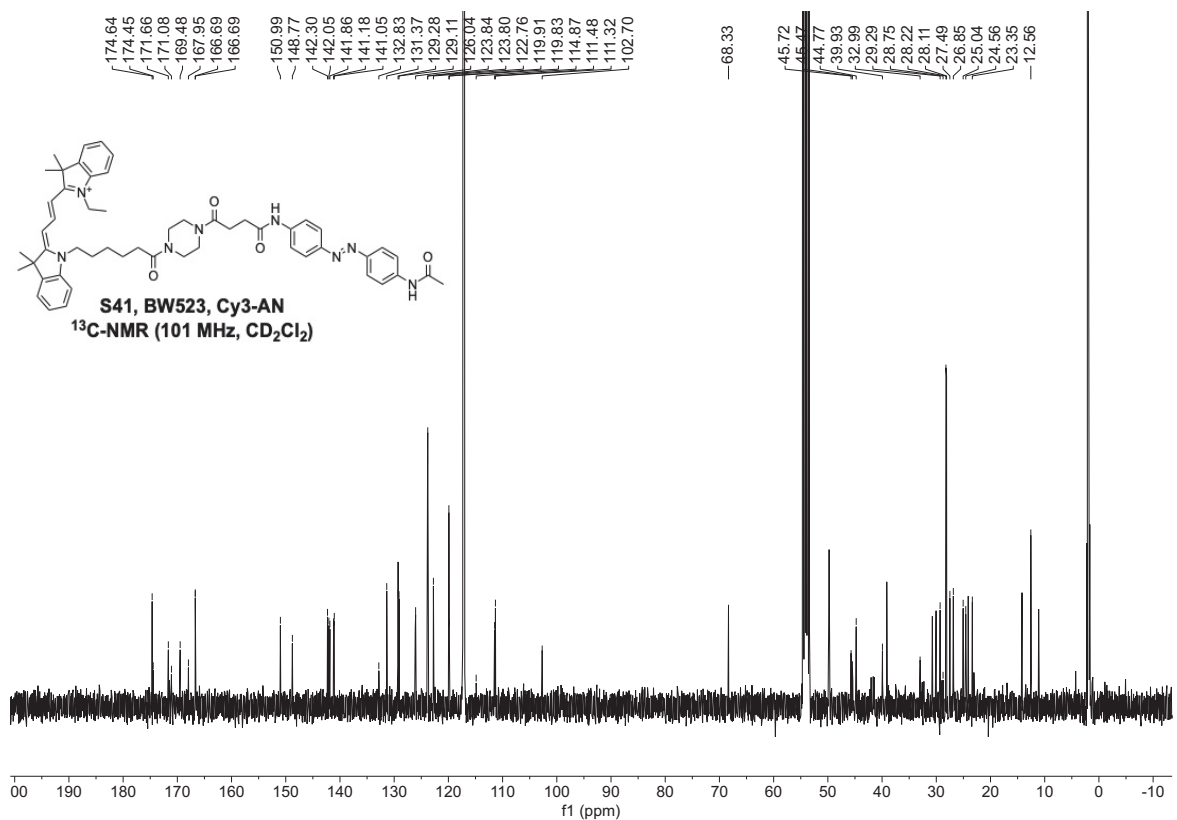
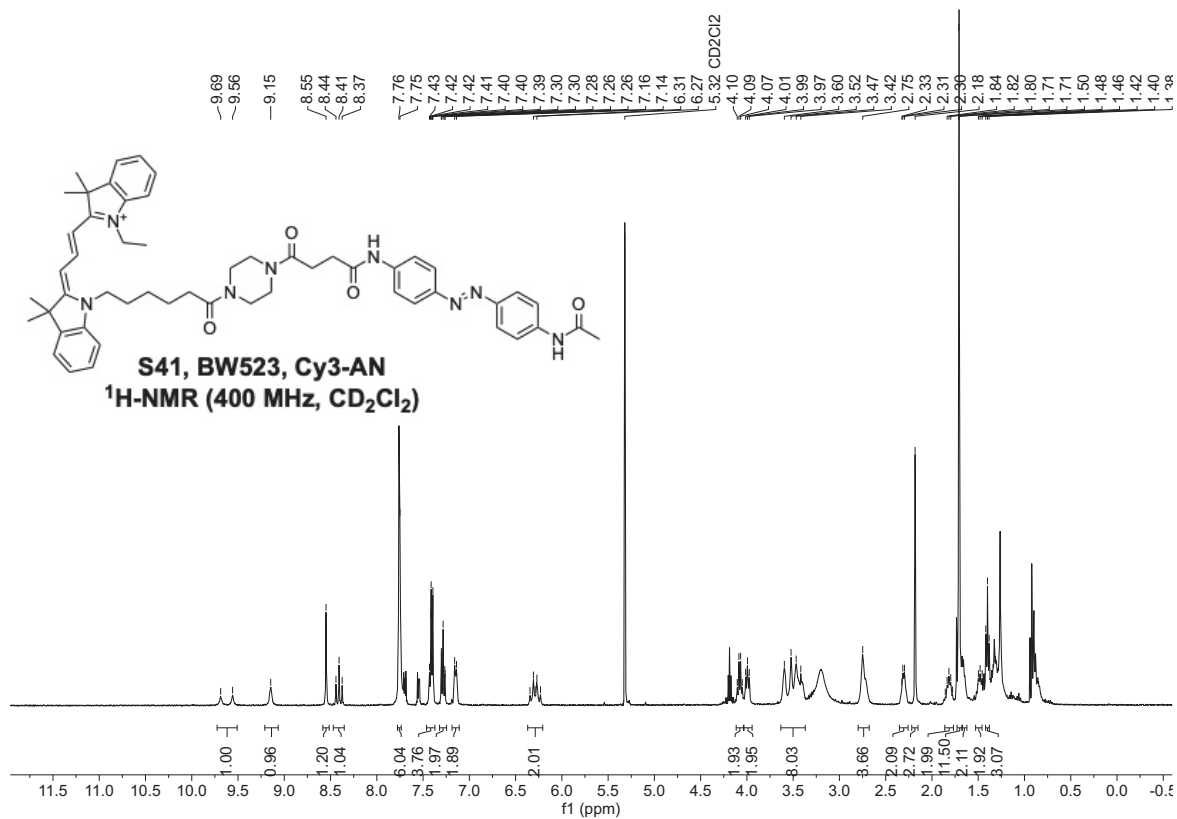


Supplementary Information - Section Appendix: NMR Spectra



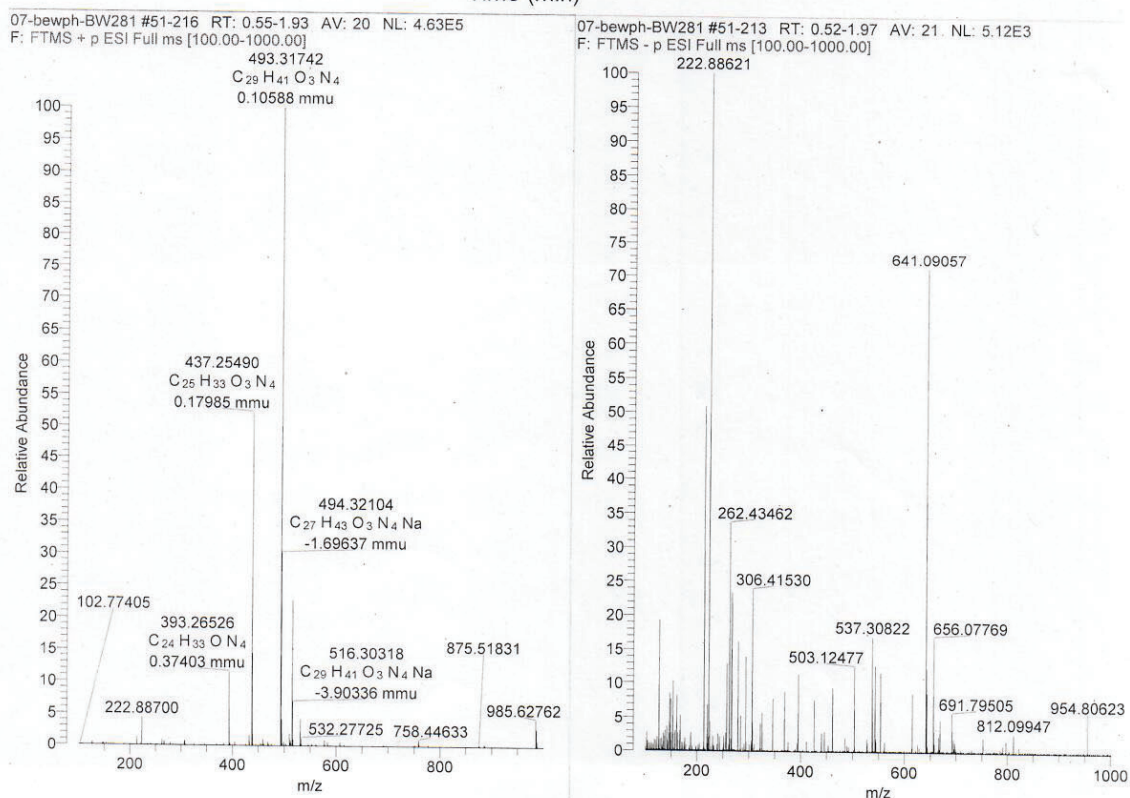
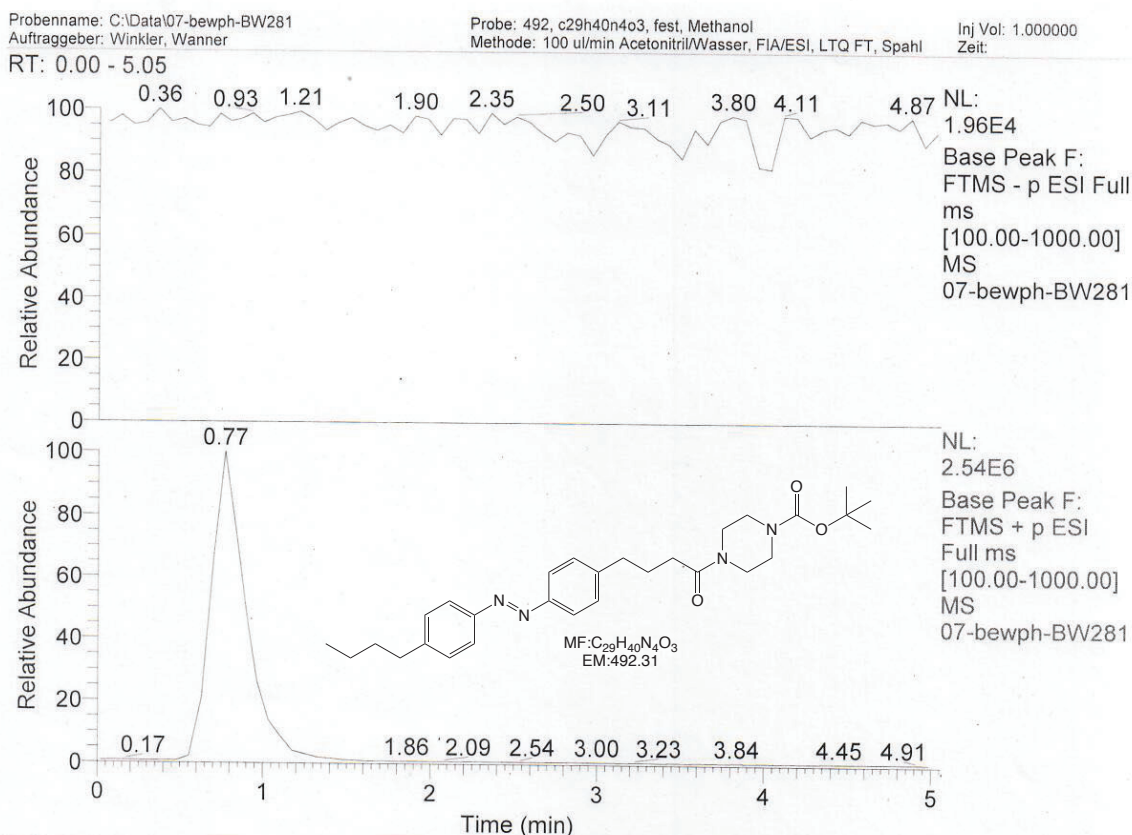


Supplementary Information - Section Appendix: NMR Spectra



## 15 Appendix: Selected HRMS

Intermediates: S8, S9, S21, S22; Conjugates: S30 (NB-AK), S31 (RhB-AO), S32 (RhB-AK), S33 (RhB-AN), S34 (FI-AK), S35 (EY-AK), S36 (SRhB-AK), S37 (Cy5-AK), S38 (NBD-AK).



S8, BW281 / BEW336

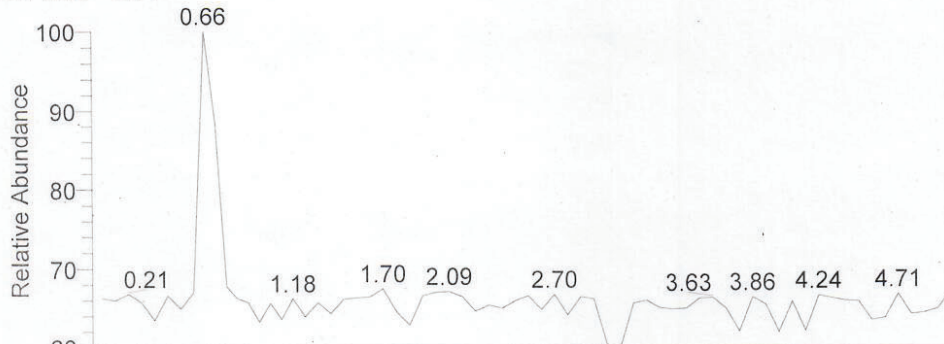
Supplementary Information - Section Appendix: Selected HRMS

Probenname: C:\Data\07-bewph-BW283  
 Auftraggeber: Winkler, Wanner

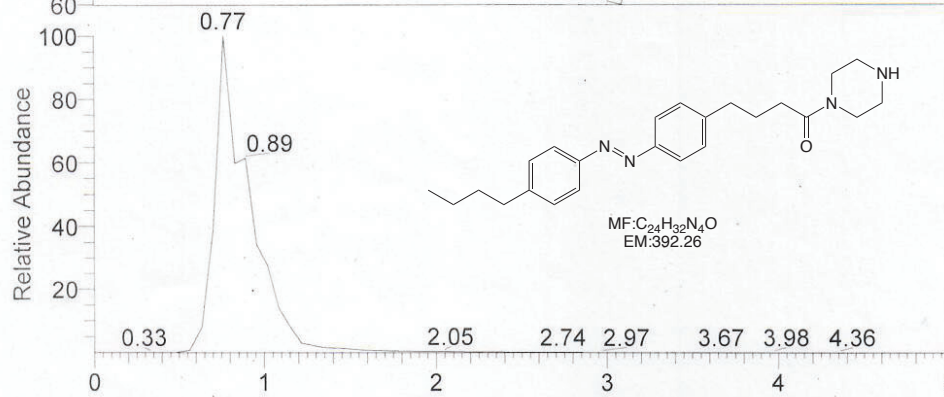
Probe: 392, c24h32n4o, fest, Methanol  
 Methode: 100 ul/min Acetonitril/Wasser, FIA/ESI, LTQ FT, Spahl

Inj Vol: 1.000000  
 Zeit:

RT: 0.00 - 5.04

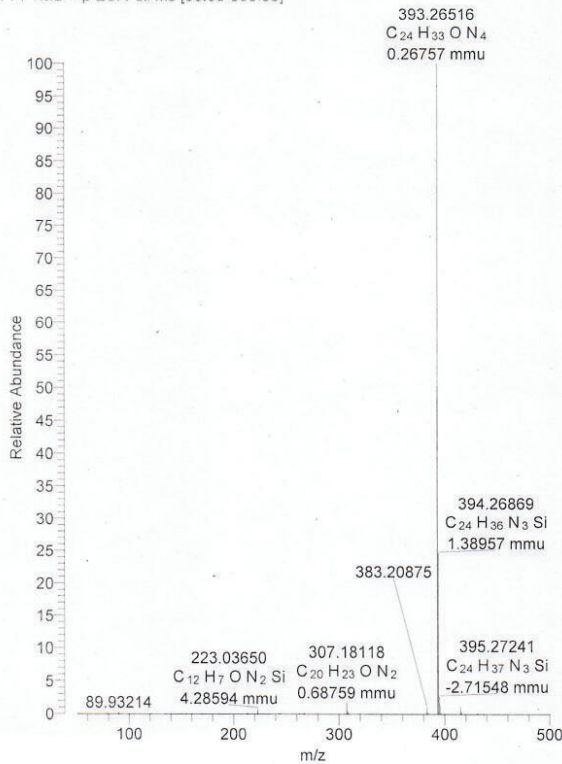


NL:  
 3.01E4  
 Base Peak F:  
 FTMS - p ESI  
 Full ms  
 [50.00-500.00]  
 MS  
 07-bewph-BW283

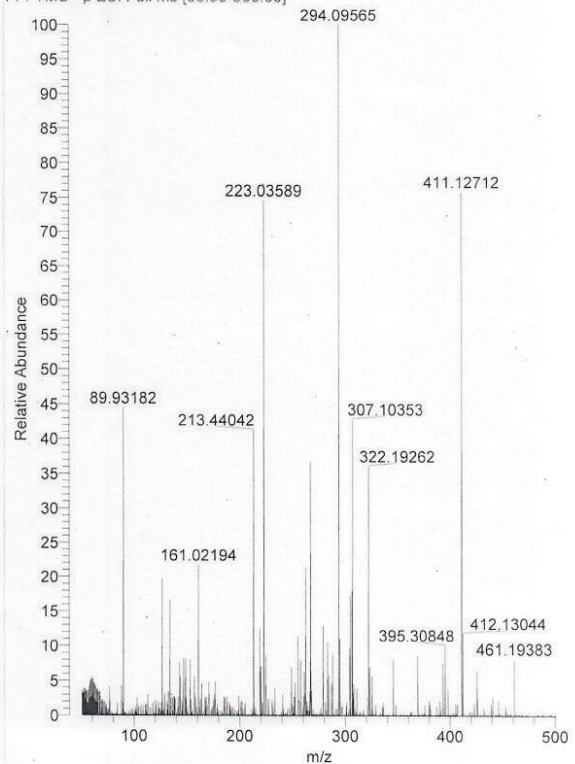


NL:  
 1.13E8  
 Base Peak F:  
 FTMS + p ESI  
 Full ms  
 [50.00-500.00]  
 MS  
 07-bewph-BW283

07-bewph-BW283 #49-219 RT: 0.48-1.97 AV: 22 NL: 1.80E7  
 F: FTMS + p ESI Full ms [50.00-500.00]



07-bewph-BW283 #48-217 RT: 0.52-1.93 AV: 21 NL: 6.79E3  
 F: FTMS - p ESI Full ms [50.00-500.00]



S9 (AK-H), BW283 / BEW339

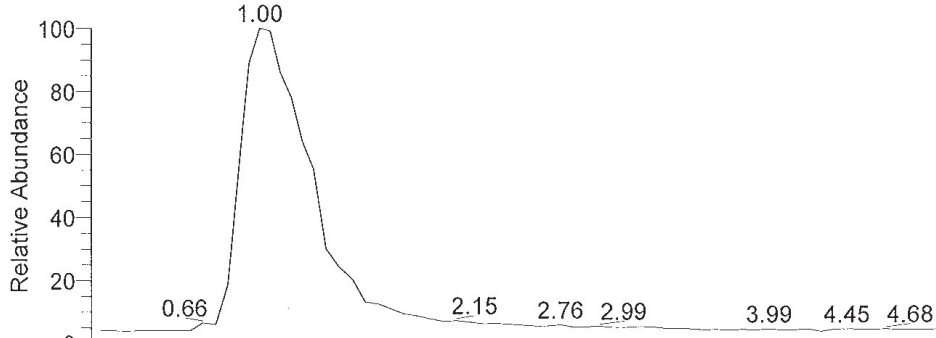


Supplementary Information - Section Appendix: Selected HRMS

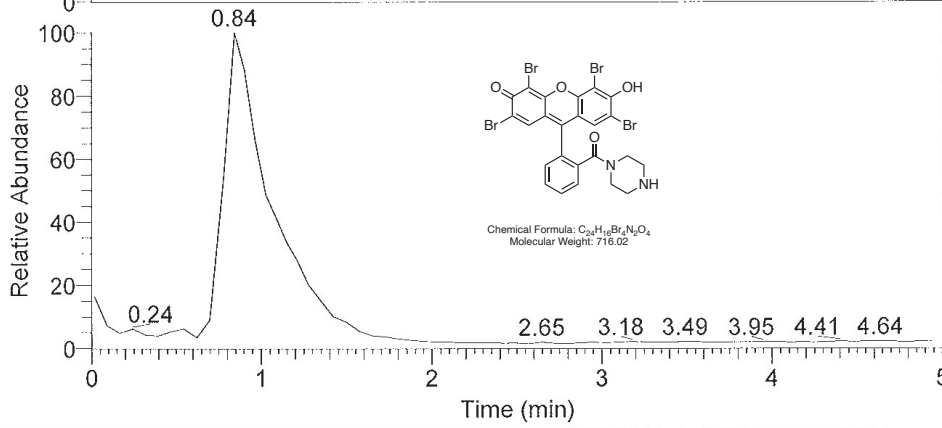
Probenname: C:\Data\03-bewph-BW080  
 Auftraggeber: Winkler, Thorn-Seshold  
 RT: 0.00 - 5.01

Probe: 716, c24h16brn2o4, fest, Methanol  
 Methode: 100 ul/min Acetonitril/Wasser, FIA/ESI, LTQ FT, Spahl

Inj Vol: 10.000000  
 Zeit:

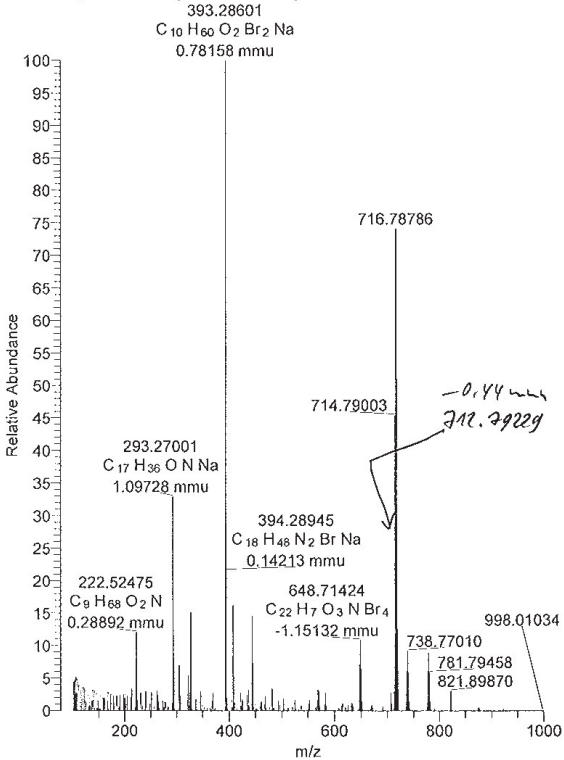


NL:  
 4.55E5  
 Base Peak F:  
 FTMS - p ESI Full  
 ms  
 [100.00-1000.00]  
 MS  
 03-bewph-BW080

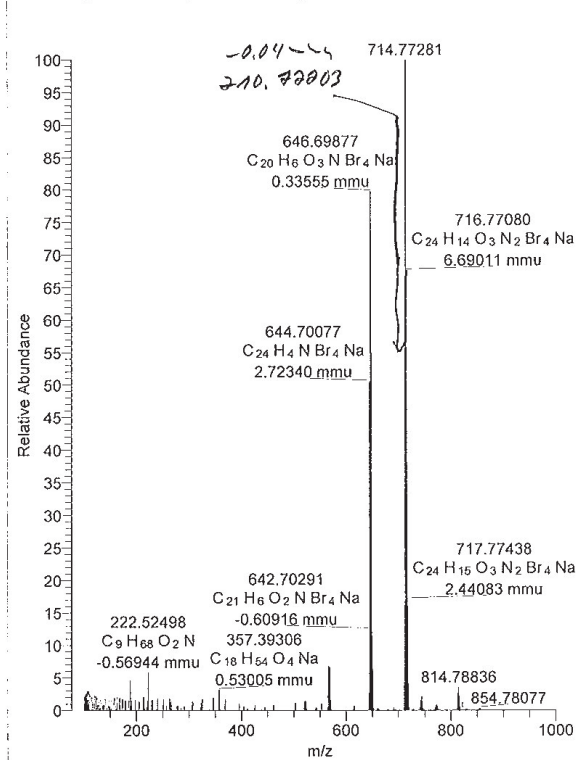


NL:  
 8.96E5  
 Base Peak F:  
 FTMS + p ESI  
 Full ms  
 [100.00-1000.00]  
 MS  
 03-bewph-BW080

03-bewph-BW080 #52-221 RT: 0.55-1.95 AV: 21 NL: 1.87E5  
 F: FTMS + p ESI Full ms [100.00-1000.00]



03-bewph-BW080 #52-219 RT: 0.51-1.92 AV: 21 NL: 1.62E5  
 F: FTMS - p ESI Full ms [100.00-1000.00]



S21, EYpip, BW080 / BEW375

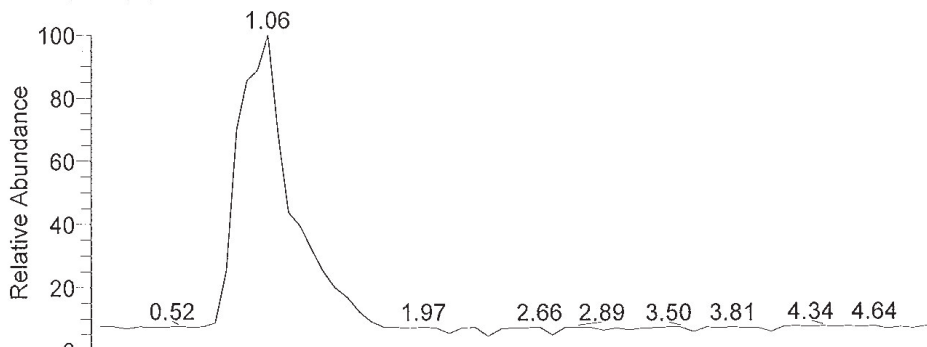
Supplementary Information - Section Appendix: Selected HRMS

Probenname: C:\Data\03-bewph-BW066  
 Auftraggeber: Winkler, Thorn-Seshold

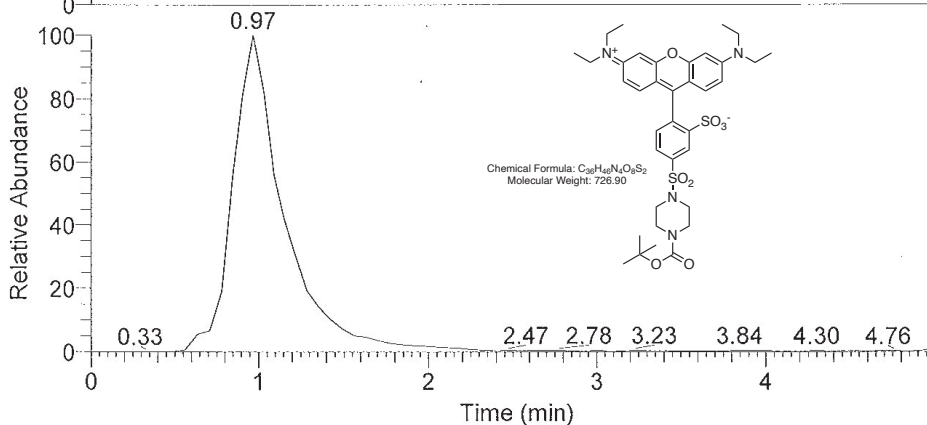
Probe: 726, c36h46n4o8s2, fest, Methanol  
 Methode: 100 ul/min Acetonitril/Wasser, FIA/ESI, LTQ FT, Spahl

Inj Vol: 10.000000  
 Zeit:

RT: 0.00 - 5.05

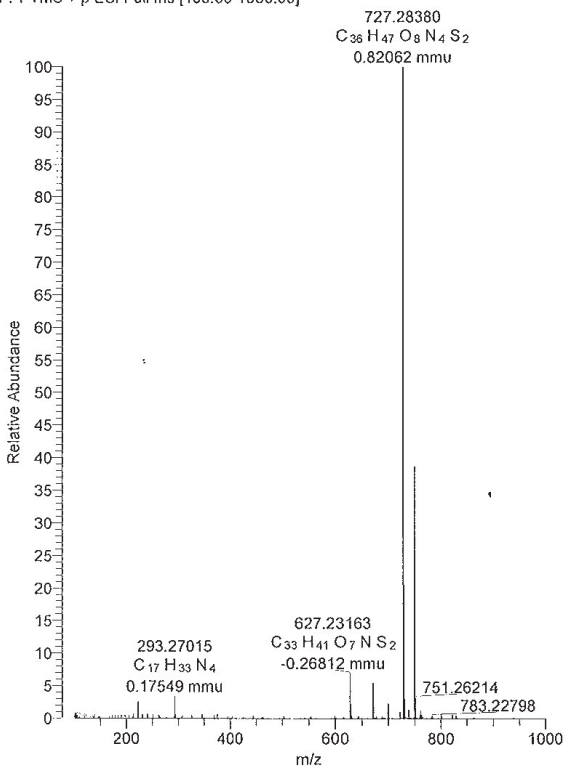


NL:  
 2.40E5  
 Base Peak F:  
 FTMS - p ESI Full  
 ms  
 [100.00-1000.00]  
 MS  
 03-bewph-BW066

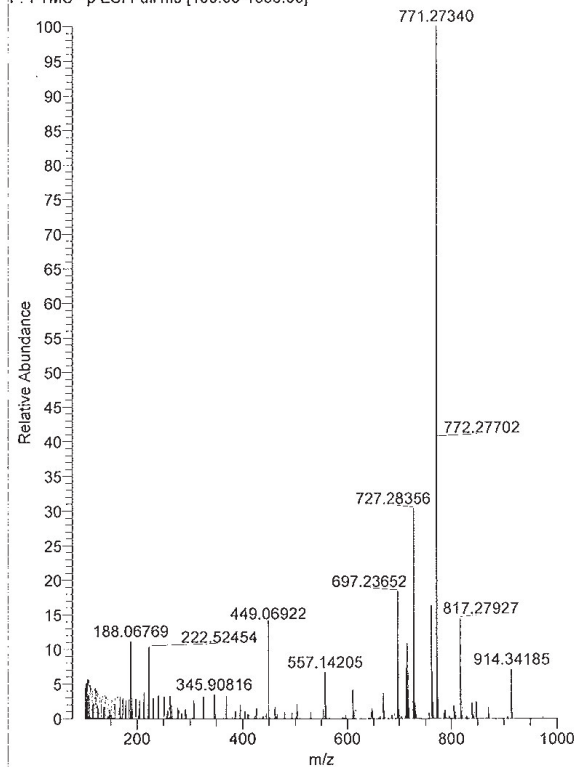


NL:  
 1.37E7  
 Base Peak F:  
 FTMS + p ESI  
 Full ms  
 [100.00-1000.00]  
 MS  
 03-bewph-BW066

03-bewph-BW066 #50-224 RT: 0.56-1.93 AV: 21 NL: 3.43E6  
 F: FTMS + p ESI Full ms [100.00-1000.00]



03-bewph-BW066 #50-221 RT: 0.52-1.97 AV: 22 NL: 7.06E4  
 F: FTMS - p ESI Full ms [100.00-1000.00]



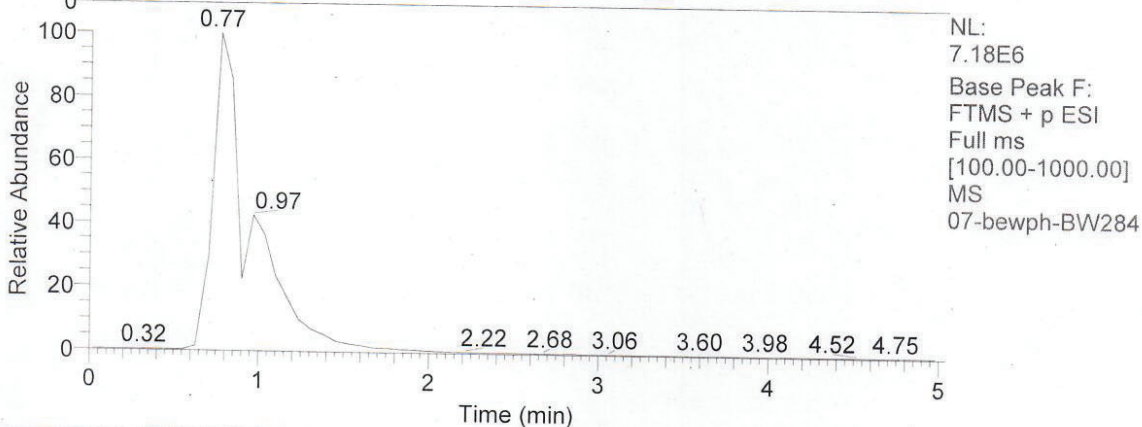
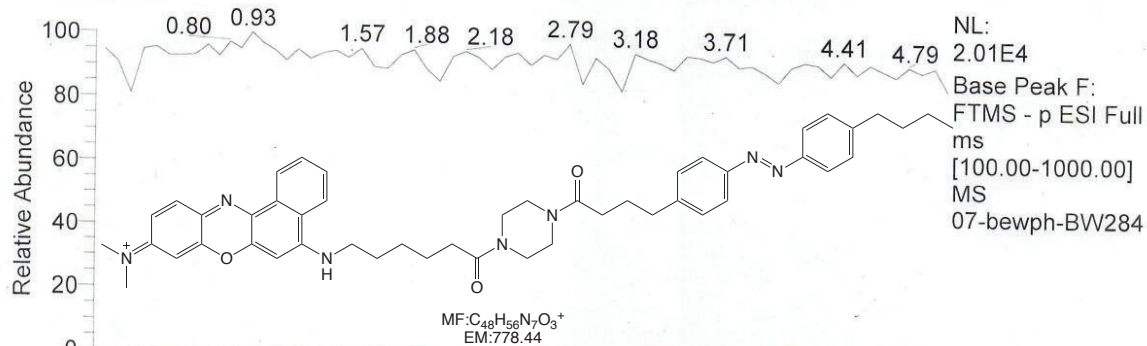
S22, BW066 / BEW411

Supplementary Information - Section Appendix: Selected HRMS

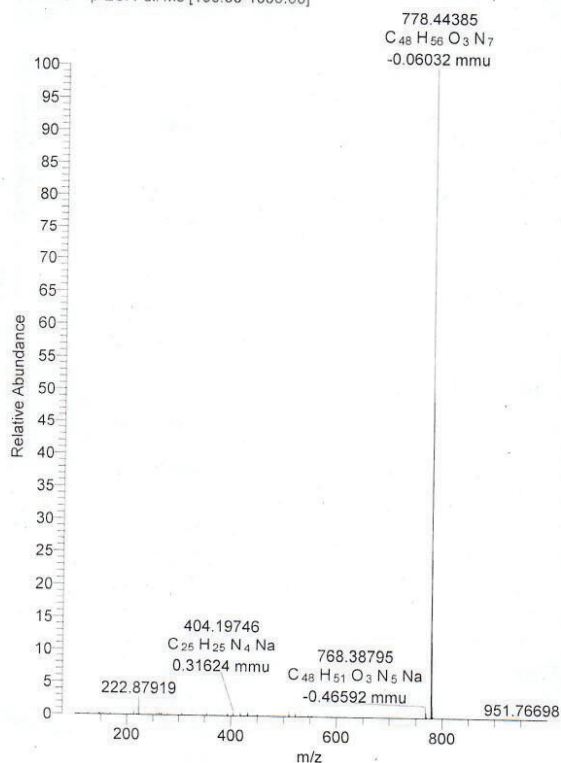
Probenname: C:\Data\07-bewph-BW284  
 Auftraggeber: Winkler, Wanner  
 RT: 0.00 - 5.04

Probe: 778, c48h56n7o3, fest, Methanol  
 Methode: 100 ul/min Acetonitril/Wasser, FIA/ESI, LTQ FT, Spahl

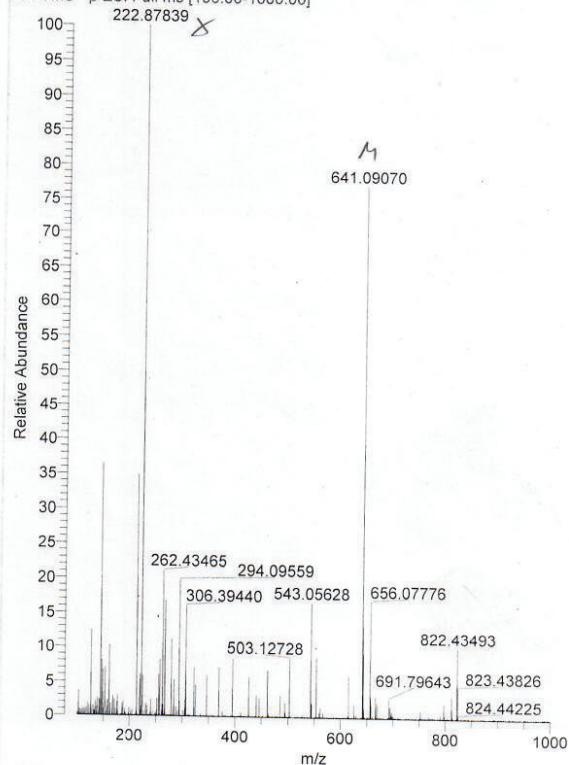
Inj Vol: 1.000000  
 Zeit:



07-bewph-BW284 #51-217 RT: 0.55-1.99 AV: 21 NL: 1.29E6  
 F: FTMS + p ESI Full ms [100.00-1000.00]



07-bewph-BW284 #51-215 RT: 0.52-1.95 AV: 21 NL: 7.51E3  
 F: FTMS - p ESI Full ms [100.00-1000.00]



S30, NB-AK, BW284 / BEW342

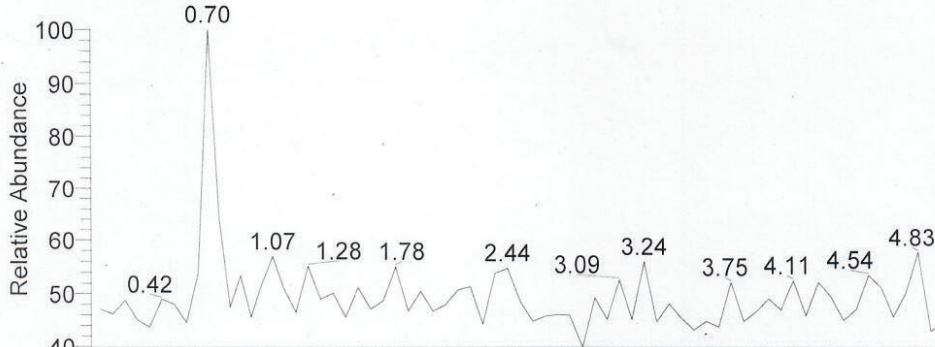
Supplementary Information - Section Appendix: Selected HRMS

Probenname C:\Data\07-bewph-BW279  
 Auftraggeber: Winkler, Wanner

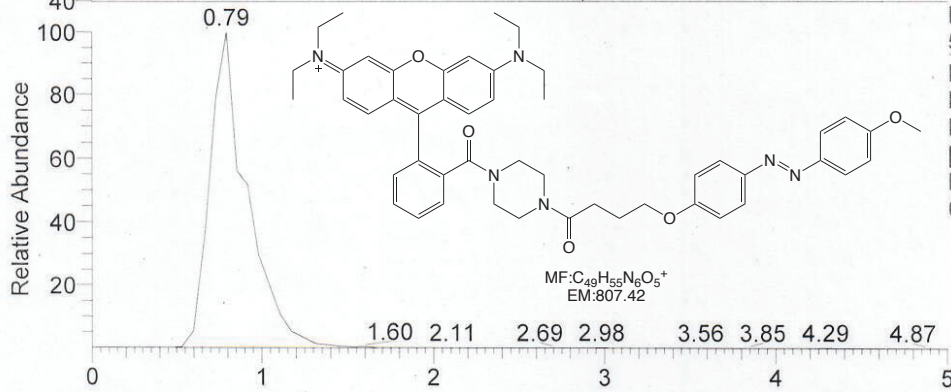
Probe: 807, c49h55n6o5, fest, Methanol  
 Methode: 100 ul/min Acetonitril/Wasser, FIA/ESI, LTQ FT, Spahl

Inj Vol: 1.000000  
 Zeit:

RT: 0.00 - 5.00



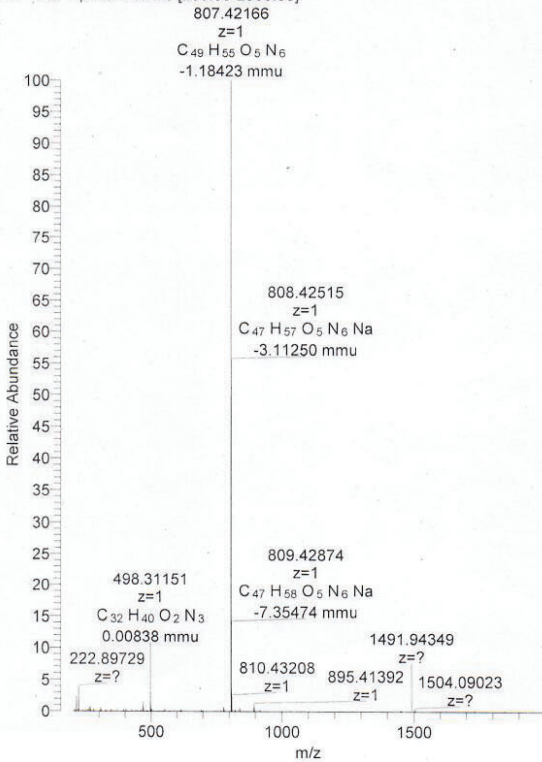
NL:  
 2.53E4  
 Base Peak F:  
 FTMS - p ESI Full  
 ms  
 [200.00-2000.00]  
 MS  
 07-bewph-BW279



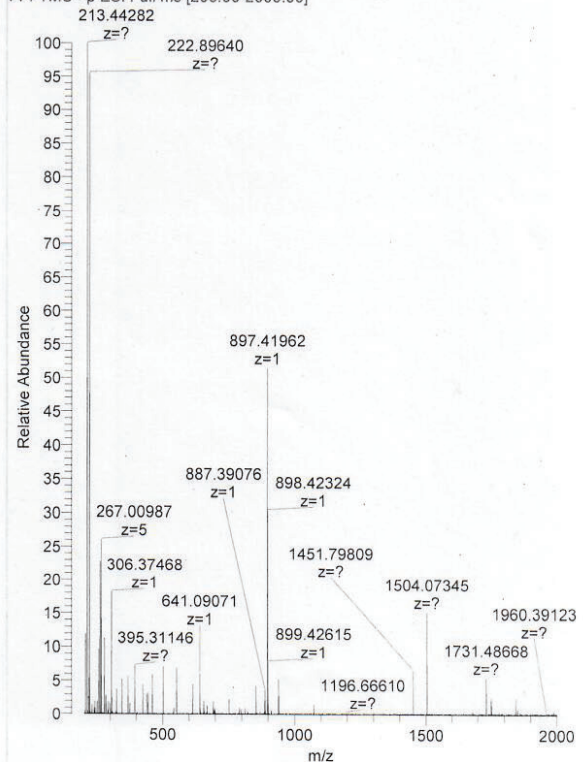
NL:  
 5.90E6  
 Base Peak F:  
 FTMS + p ESI  
 Full ms  
 [200.00-2000.00]  
 MS  
 07-bewph-BW279

MF: C<sub>49</sub>H<sub>55</sub>N<sub>6</sub>O<sub>5</sub><sup>+</sup>  
 EM: 807.42

07-bewph-BW279 #54-281 RT: 0.53-2.47 AV: 29 NL: 7.60E5  
 F: FTMS + p ESI Full ms [200.00-2000.00]



07-bewph-BW279 #52-281 RT: 0.49-2.44 AV: 29 NL: 7.08E3  
 F: FTMS - p ESI Full ms [200.00-2000.00]



S31, RhB-AO, BW279

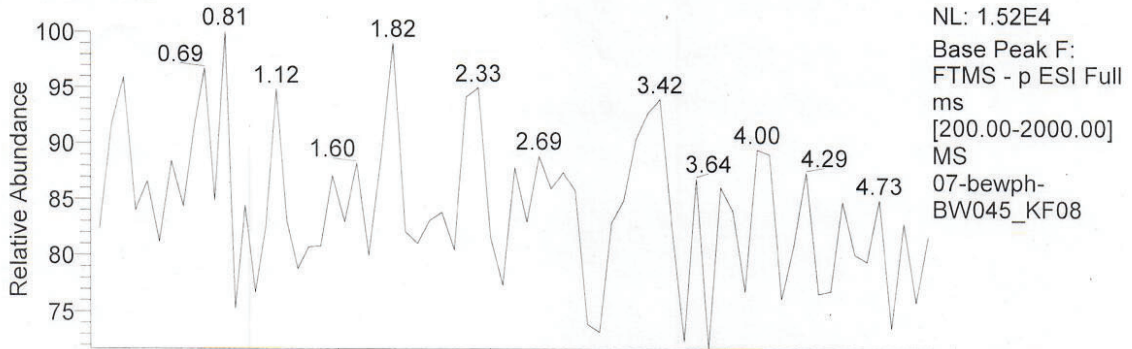


Supplementary Information - Section Appendix: Selected HRMS

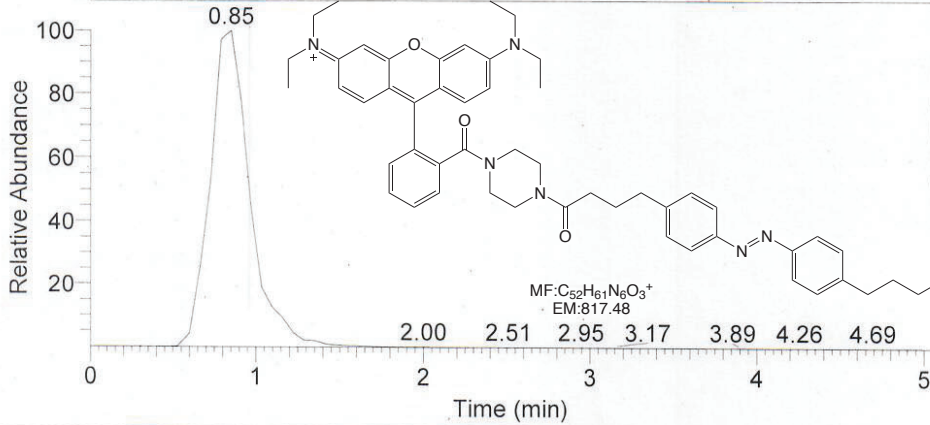
Probenname C:\Data\07-bewph-BW045\_KF08  
 Auftraggeber: Winkler, Wanner  
 RT: 0.00 - 5.05

Probe: 817, c52h61n6o3, fest, Methanol  
 Methode: 100 ul/min Acetonitril/Wasser, FIA/ESI, LTQ FT, Spahl

Inj Vol: 1.000000  
 Zeit:

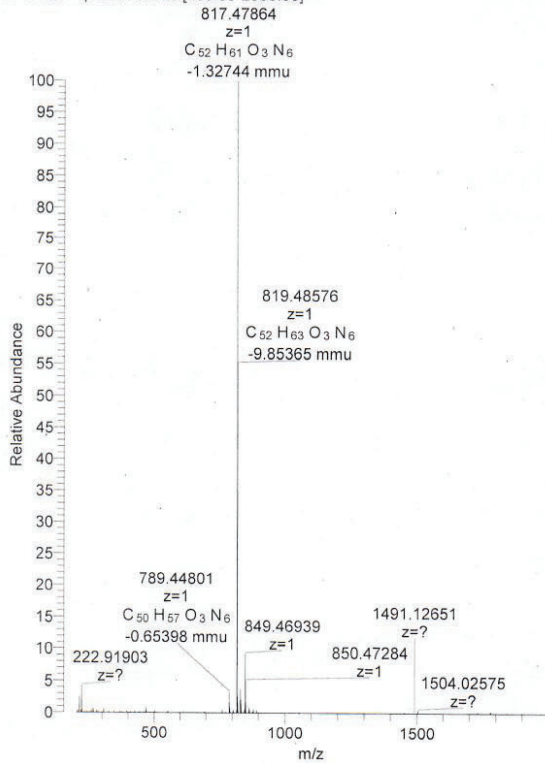


NL: 1.52E4  
 Base Peak F:  
 FTMS - p ESI Full  
 ms  
 [200.00-2000.00]  
 MS  
 07-bewph-  
 BW045\_KF08

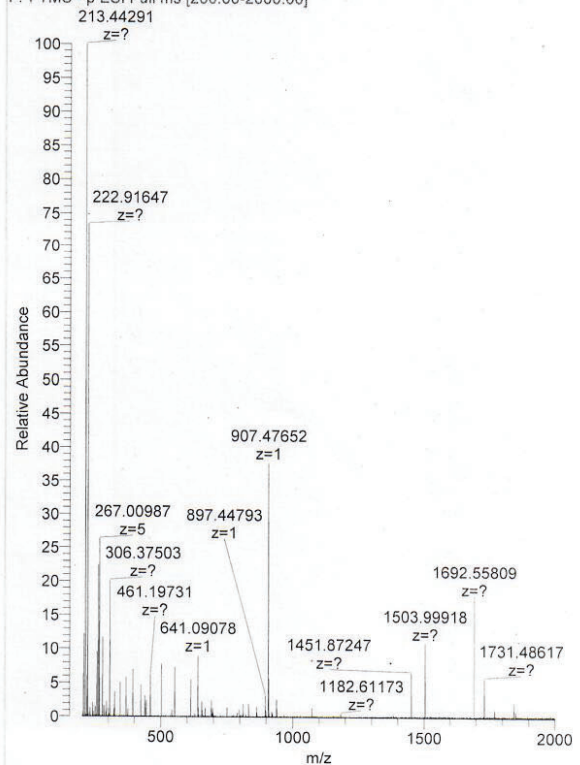


NL: 1.39E7  
 Base Peak F:  
 FTMS + p ESI Full  
 ms  
 [200.00-2000.00]  
 MS  
 07-bewph-  
 BW045\_KF08

07-bewph-BW045\_KF08 #54-285 RT: 0.53-2.44 AV: 29 NL: 2.10E6  
 F: FTMS + p ESI Full ms [200.00-2000.00]



07-bewph-BW045\_KF08 #52-285 RT: 0.49-2.47 AV: 30 NL: 7.04E3  
 F: FTMS - p ESI Full ms [200.00-2000.00]



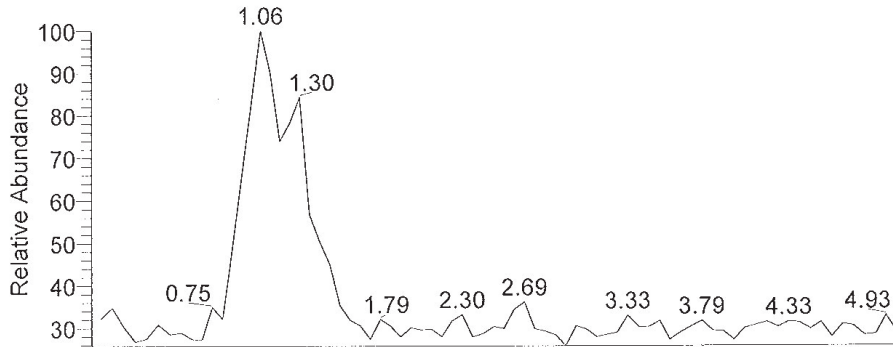
S32, RhB-AK, BW045 / BEW340



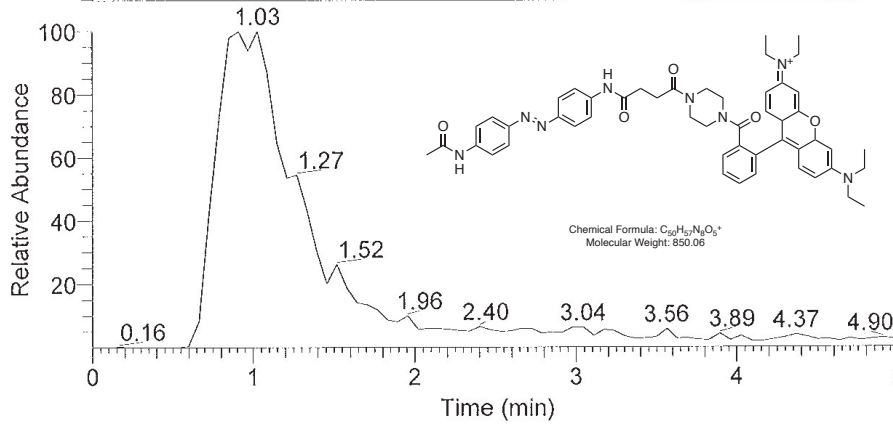
Supplementary Information - Section Appendix: Selected HRMS

Probenname C:\Data\03-bewph-BW\_KF11\_220318105221  
 Auftraggeber: Winkler, Thorn-Seshold  
 RT: 0.00 - 5.02

Probe: 848, c50h55n8o5, fest, Methanol  
 Methode: 100 ul/min Acetonitril/Wasser, FIA/ESI, LTQ FT, Spahl  
 Inj Vol: 10.000000  
 Zeit:

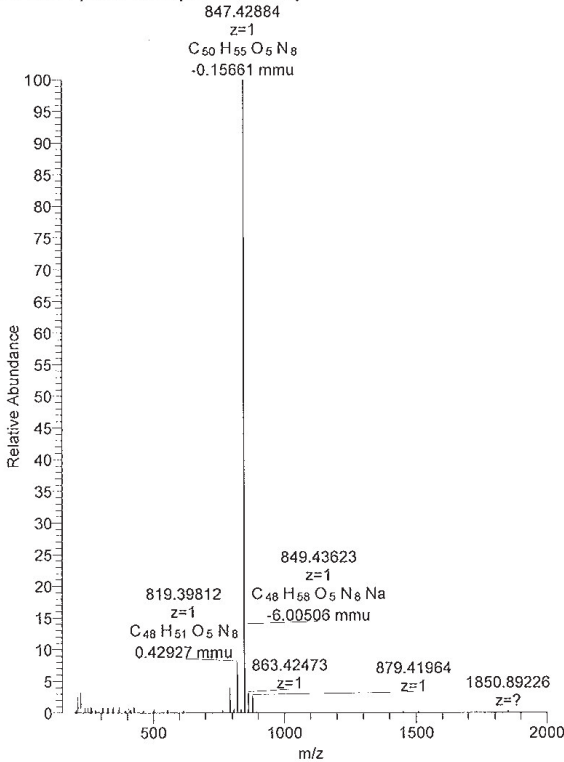


NL: 3.91E4  
 Base Peak F: FTMS -  
 p ESI Full ms  
 [200.00-2000.00] MS  
 03-bewph-  
 BW\_KF11\_22031810  
 5221

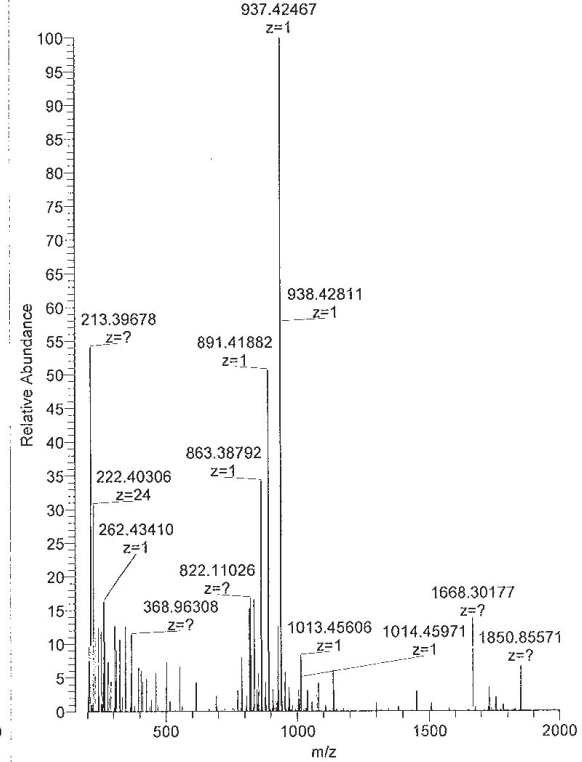


NL: 1.36E7  
 Base Peak F: FTMS  
 + p ESI Full ms  
 [200.00-2000.00] MS  
 03-bewph-  
 BW\_KF11\_22031810  
 5221

03-bewph-BW\_KF11\_220318105221 #54-307 RT: 0.52-2.47 AV: 32 NL:  
 F: FTMS + p ESI Full ms [200.00-2000.00]



03-bewph-BW\_KF11\_220318105221 #52-307 RT: 0.49-2.43 AV: 32 NL:  
 F: FTMS - p ESI Full ms [200.00-2000.00]



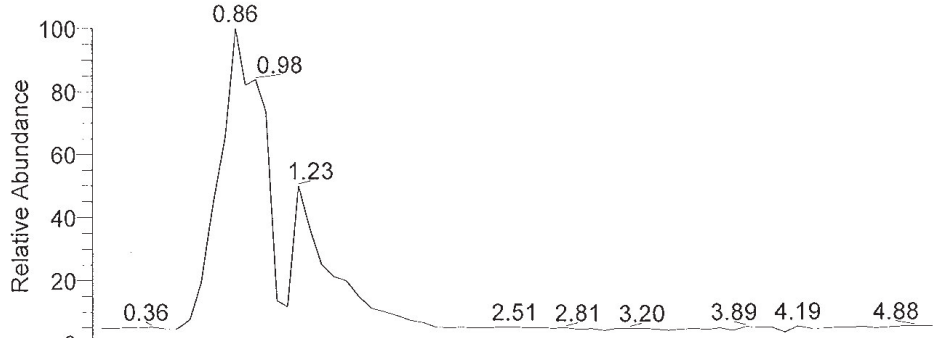
S33, RhB-AN, BW-KF11 / BEW383

Supplementary Information - Section Appendix: Selected HRMS

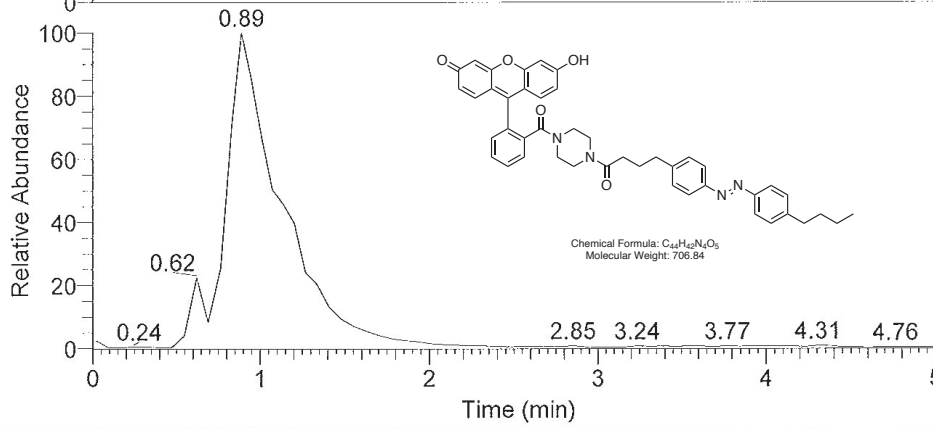
Probenname: C:\Data\03-bewph-BW402  
 Auftraggeber: Winkler, Thorn-Seshold  
 RT: 0.00 - 5.06

Probe: 706\_c44h42n4o5\_fest, Methanol  
 Methode: 100 ul/min Acetonitril/Wasser, FIA/ESI, LTQ FT, Spahl

Inj Vol: 10.000000  
 Zeit:

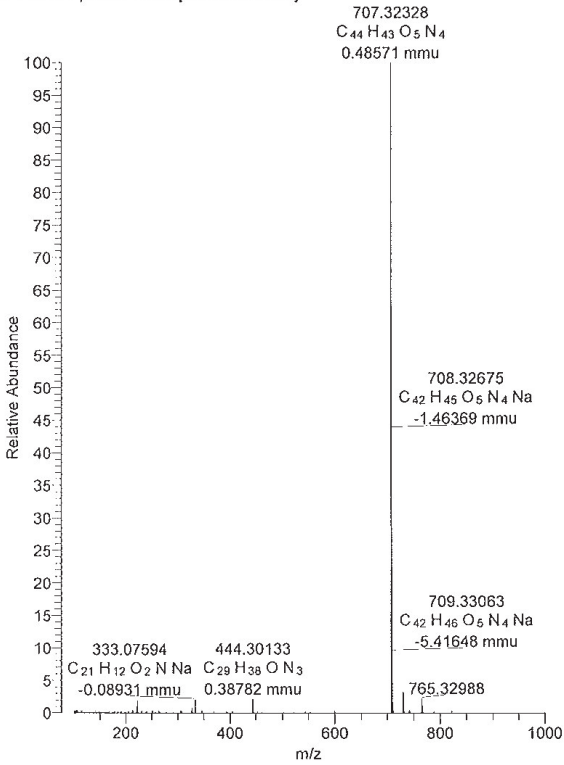


NL:  
 3.62E5  
 Base Peak F:  
 FTMS - p ESI Full  
 ms  
 [100.00-1000.00]  
 MS  
 03-bewph-BW402

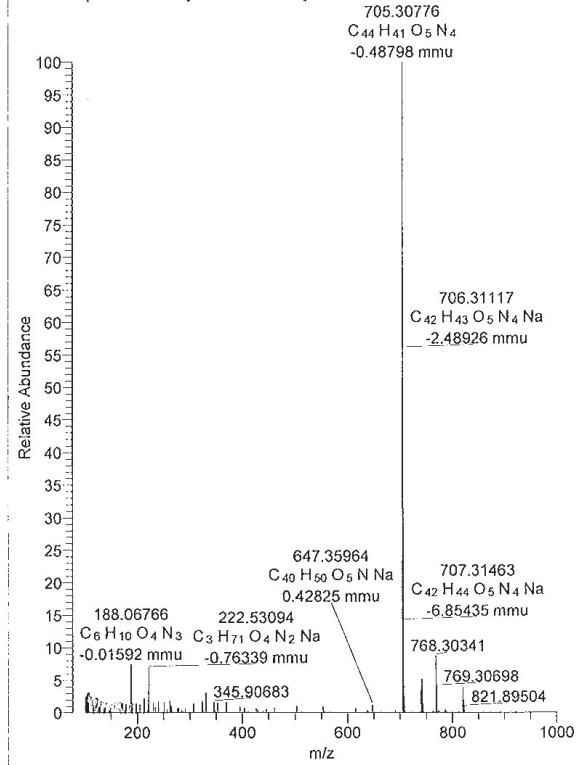


NL:  
 7.40E6  
 Base Peak F:  
 FTMS + p ESI  
 Full ms  
 [100.00-1000.00]  
 MS  
 03-bewph-BW402

03-bewph-BW402 #52-224 RT: 0.55-1.93 AV: 21 NL: 2.11E6  
 F: FTMS + p ESI Full ms [100.00-1000.00]



03-bewph-BW402 #52-221 RT: 0.51-1.97 AV: 22 NL: 1.13E5  
 F: FTMS - p ESI Full ms [100.00-1000.00]



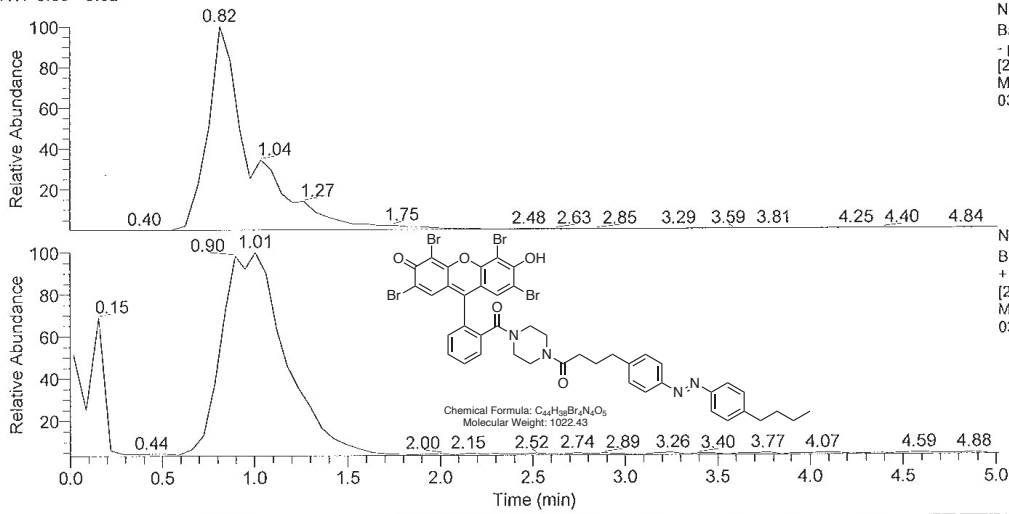
S34, FI-AK, BW402 / BEW441

Supplementary Information - Section Appendix: Selected HRMS

Probennamen: C:\Data\03-bewph-BW403  
 Auftraggeber: Winkler, Thorn-Seshold  
 RT: 0.00 - 5.02

Probe: 1022, c44h68br4n4o5, fest, Melhanol  
 Methode: 100 ul/min Acetonitril/Wasser, FIA/ESI, LTQ FT, Spahl

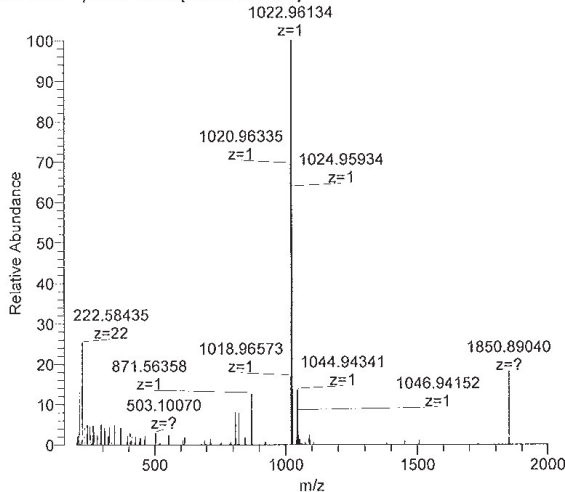
Inj Vol: 10.000000  
 Zeit:



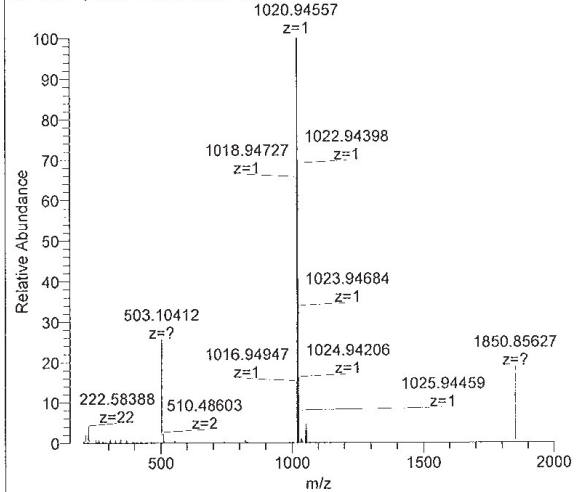
NL: 7.73E6  
 Base Peak F: FTMS  
 - p ESI Full ms  
 [200.00-2000.00]  
 MS  
 03-bewph-BW403

NL: 3.41E5  
 Base Peak F: FTMS  
 + p ESI Full ms  
 [200.00-2000.00]  
 MS  
 03-bewph-BW403

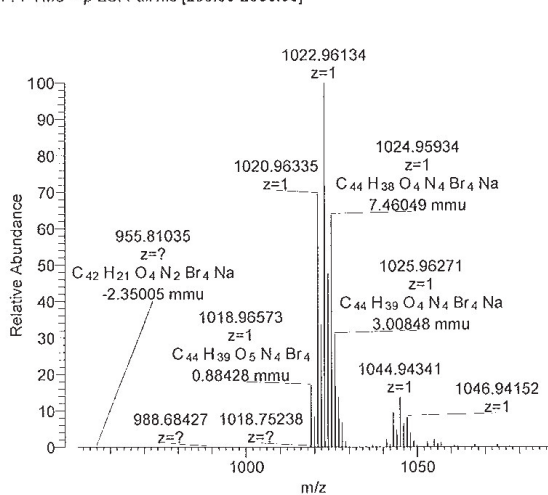
03-bewph-BW403 #56-293 RT: 0.52-2.45 AV: 30 NL: 8.31E4  
 F: FTMS + p ESI Full ms [200.00-2000.00]



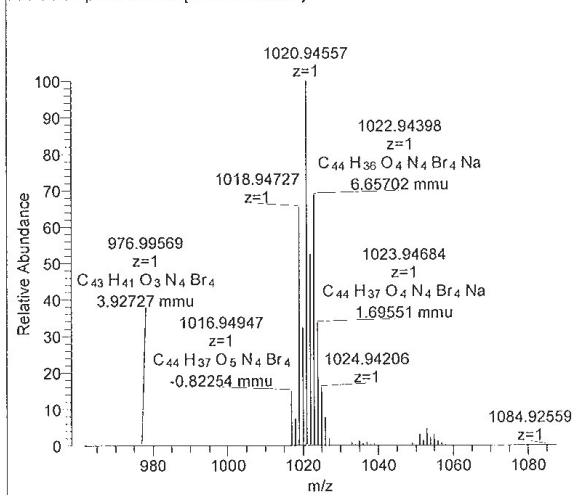
03-bewph-BW403 #53-293 RT: 0.48-2.48 AV: 31 NL: 1.16E6  
 F: FTMS - p ESI Full ms [200.00-2000.00]



03-bewph-BW403 #56-293 RT: 0.52-2.45 AV: 30 NL: 8.31E4  
 F: FTMS + p ESI Full ms [200.00-2000.00]



03-bewph-BW403 #53-293 RT: 0.48-2.48 AV: 31 NL: 1.16E6  
 F: FTMS - p ESI Full ms [200.00-2000.00]



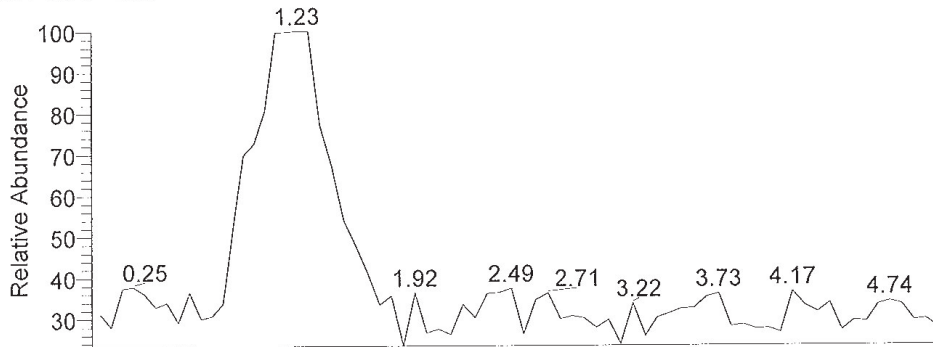
S35, EY-AK, BW403 / BEW439

Supplementary Information - Section Appendix: Selected HRMS

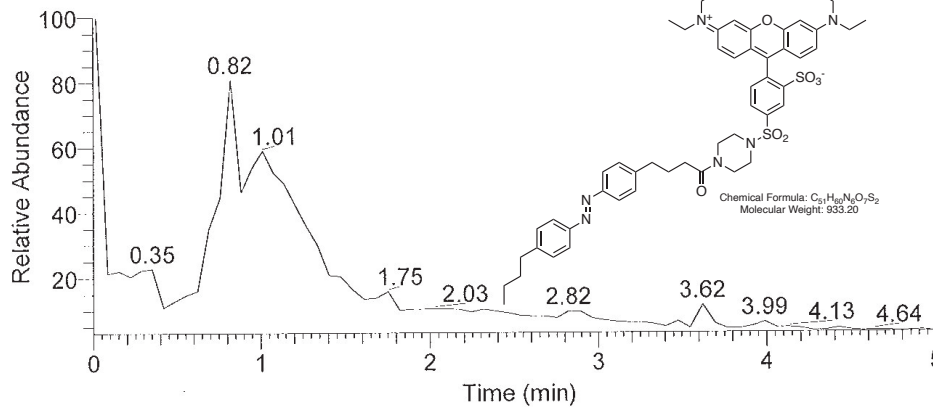
Probenname C:\Data\03-bewph-BW072  
 Auftraggeber: Winkler, Thorn-Seshold  
 RT: 0.00 - 5.05

Probe: 933, c51h60n6o7s2, fest, Methanol  
 Methode: 100 ul/min Acetonitril/Wasser, FIA/ESI, LTQ FT, Spahl

Inj Vol: 10.000000  
 Zeit:

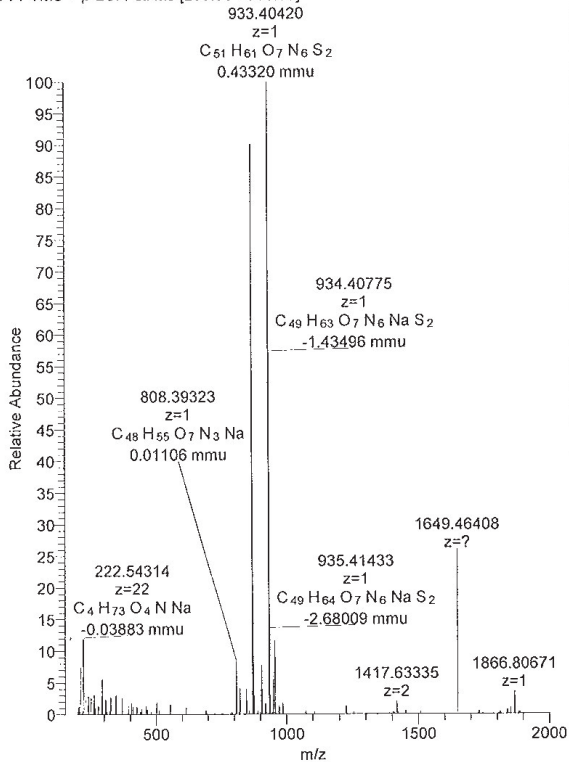


NL:  
 4.02E4  
 Base Peak F:  
 FTMS - p ESI Full  
 ms  
 [200.00-2000.00]  
 MS  
 03-bewph-BW072

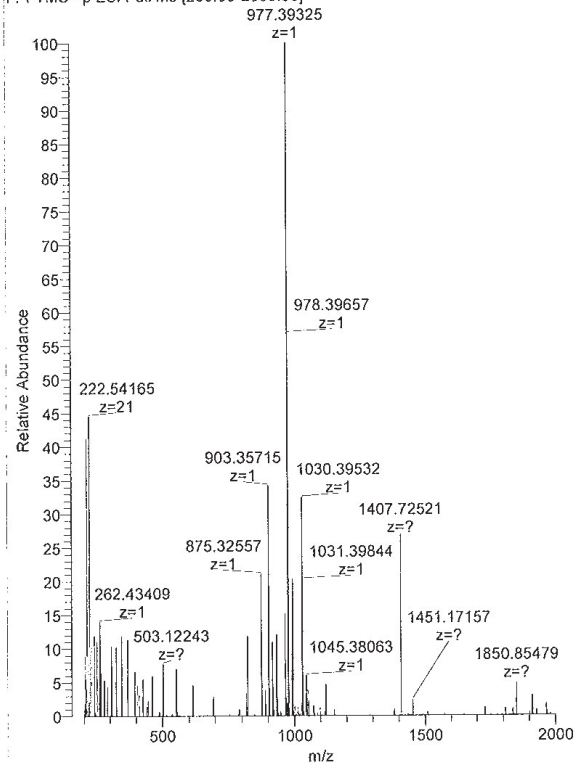


NL:  
 1.14E6  
 Base Peak F:  
 FTMS + p ESI  
 Full ms  
 [200.00-2000.00]  
 MS  
 03-bewph-BW072

03-bewph-BW072 #60-292 RT: 0.55-2.46 AV: 29 NL: 2.31E5  
 F: FTMS + p ESI Full ms [200.00-2000.00]



03-bewph-BW072 #56-292 RT: 0.52-2.42 AV: 29 NL: 1.49E4  
 F: FTMS - p ESI Full ms [200.00-2000.00]



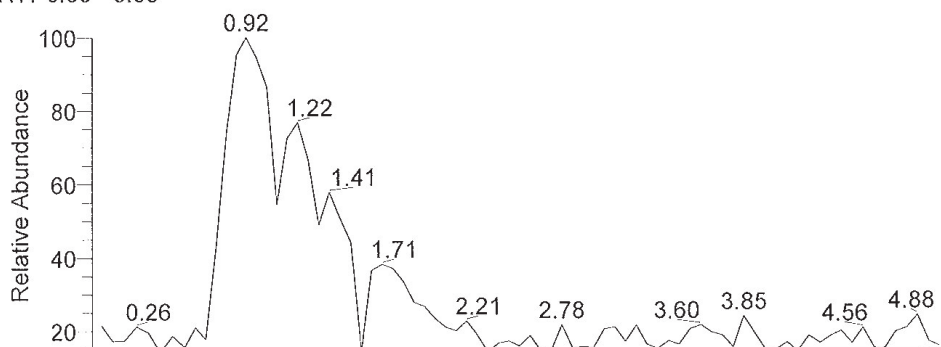
S36, SRhB-AK, BW072 / BEW372

Supplementary Information - Section Appendix: Selected HRMS

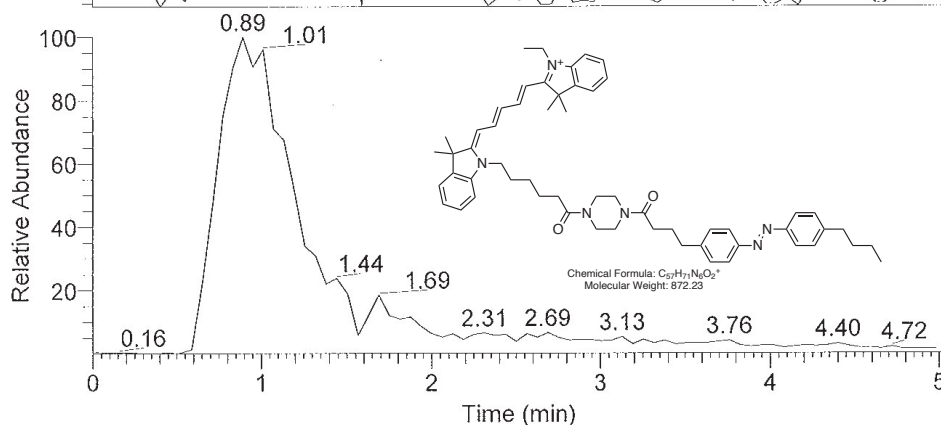
Probenname C:\Data\03-bewph-BW384  
 Auftraggeber: Winkler, Thorn-Seshold  
 RT: 0.00 - 5.03

Probe: 872, c57h71n6o2, fest, Methanol  
 Methode: 100 ul/min Acetonitril/Wasser, FIA/ESI, LTQ FT, Spahl

Inj Vol: 10.000000  
 Zeit:

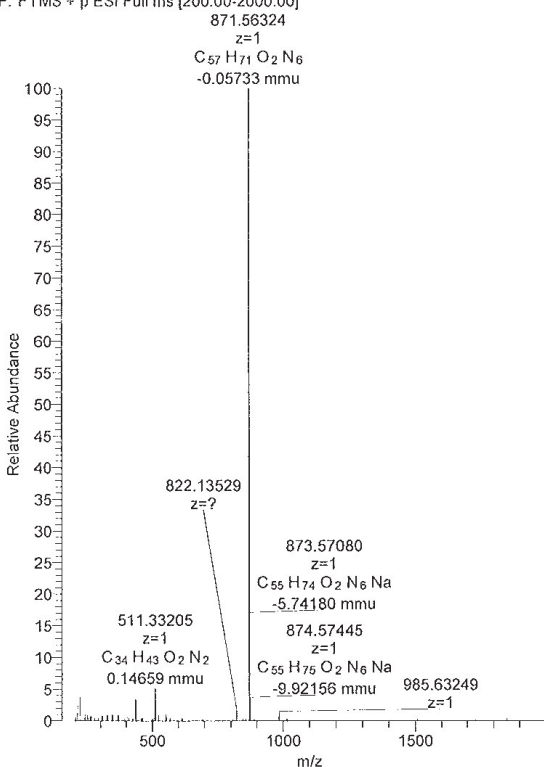


NL: 6.87E4  
 Base Peak F:  
 FTMS - p ESI Full  
 ms  
 [200.00-2000.00]  
 MS  
 03-bewph-BW384

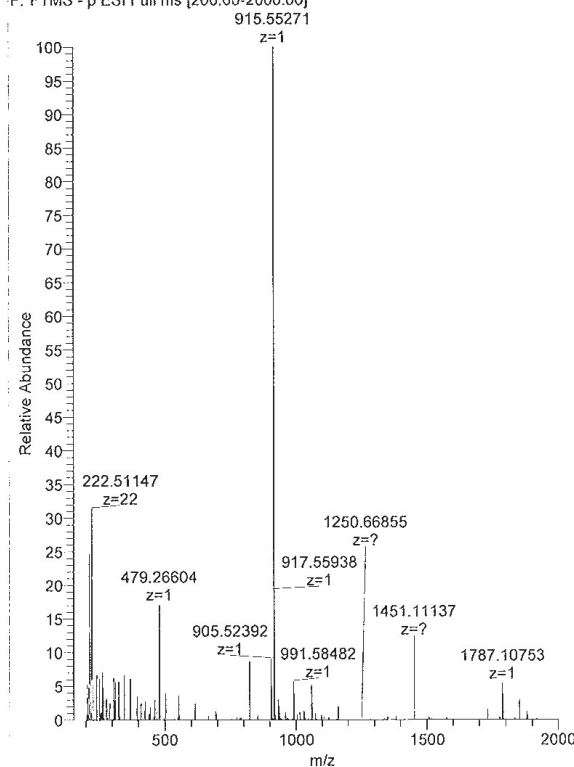


NL: 3.49E7  
 Base Peak F:  
 FTMS + p ESI  
 Full ms  
 [200.00-2000.00]  
 MS  
 03-bewph-BW384

03-bewph-BW384 #56-310 RT: 0.52-2.44 AV: 32 NL: 1.03E7  
 F: FTMS + p ESI Full ms [200.00-2000.00]



03-bewph-BW384 #53-310 RT: 0.48-2.46 AV: 33 NL: 2.61E4  
 F: FTMS - p ESI Full ms [200.00-2000.00]



S37, Cy5-AK, BW384 / BEW405

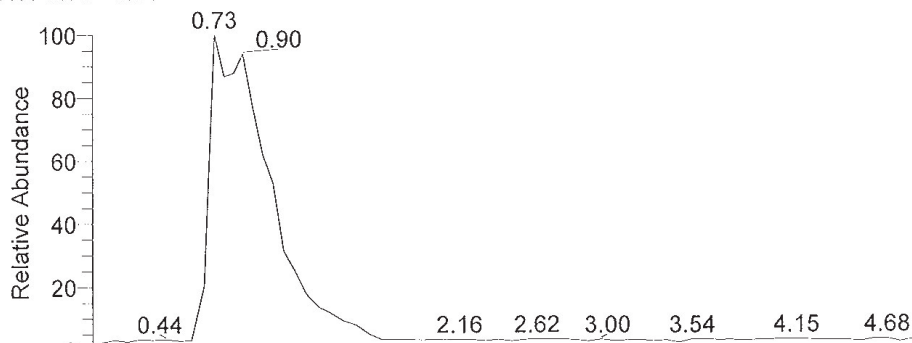


Supplementary Information - Section Appendix: Selected HRMS

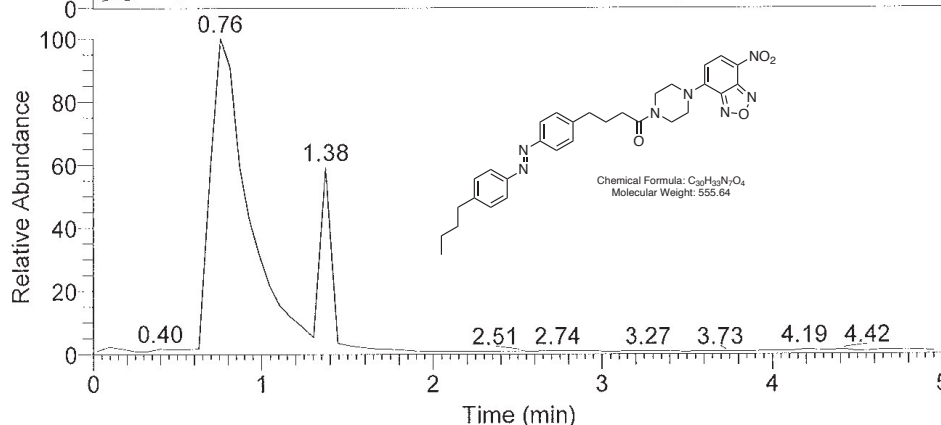
Probename: C:\Data\03-bewph-BW064  
 Auftraggeber: Winkler, Thorn-Seshold  
 RT: 0.00 - 5.01

Probe: 555, c30h33n7o4, fest, Methanol  
 Methode: 100 ul/min Acetonitril/Wasser, FIA/ESI, LTQ FT, Spahl

Inj Vol: 10.000000  
 Zeit:

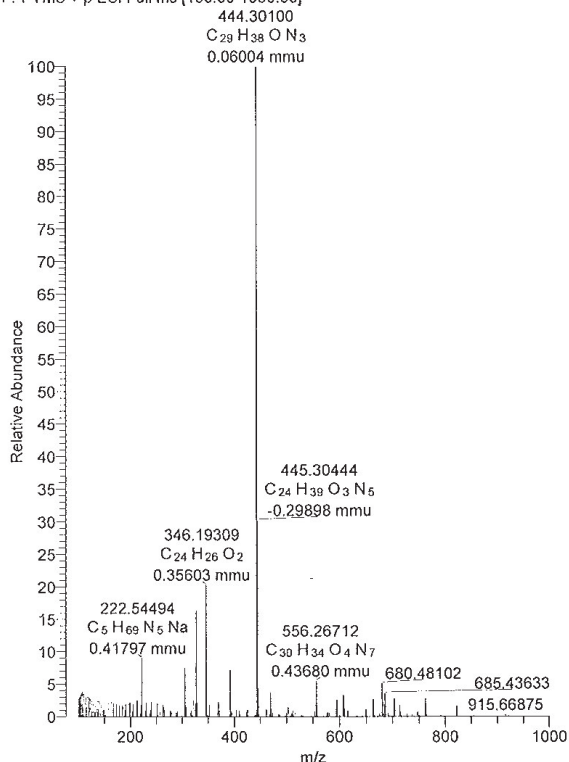


NL:  
 5.57E5  
 Base Peak F:  
 FTMS - p ESI Full  
 ms  
 [100.00-1000.00]  
 MS  
 03-bewph-BW064

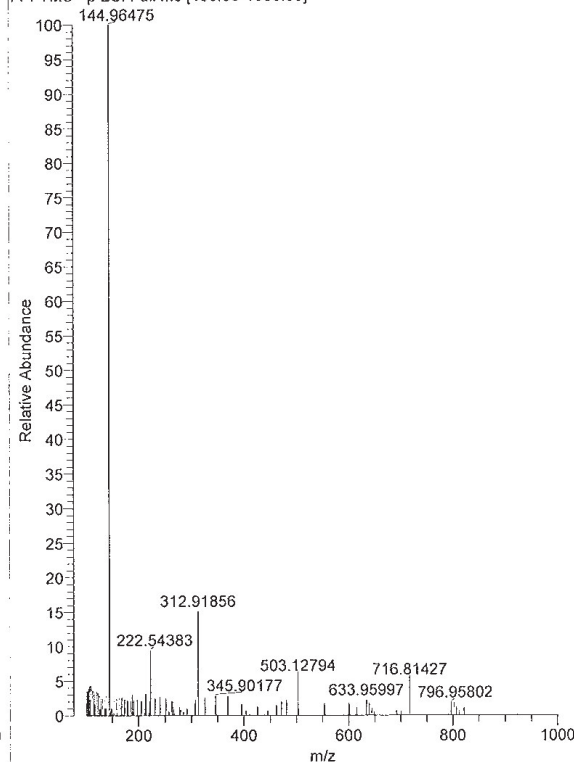


NL:  
 2.00E6  
 Base Peak F:  
 FTMS + p ESI  
 Full ms  
 [100.00-1000.00]  
 MS  
 03-bewph-BW064

03-bewph-BW064 #52-228 RT: 0.55-1.97 AV: 22 NL: 4.11E5  
 F: FTMS + p ESI Full ms [100.00-1000.00]



03-bewph-BW064 #52-225 RT: 0.51-1.93 AV: 22 NL: 1.74E5  
 F: FTMS - p ESI Full ms [100.00-1000.00]



S38, NBD-AK, BW064 / BEW371

## 16 Supporting References

- (1) Baumgartner, B.; Glembockyte, V.; Mayer, R.; Gonzalez-Hernandez, A.; Kindler, R.; Valavalkar, A.; Wiegand, A.; Müller-Deku, A.; Grubert, L.; Steiner, F.; Gross, C.; Reynders, M.; Grenier, V.; Broichhagen, J.; Hecht, S.; Tinnefeld, P.; Ofial, A.; Dietzek-Ivansic, B.; Levitz, J.; Thorn-Seshold, O. Azobenzenes Can Achieve Near-Infrared Photocontrol in Biological Systems, with Quantitative Z→E Photoisomerization, via Singlet Manifold Photoredox. *ChemRxiv* **2023**. <https://doi.org/10.26434/chemrxiv-2023-37sv4>.
- (2) Merino, E. Synthesis of Azobenzenes: The Coloured Pieces of Molecular Materials. *Chem. Soc. Rev.* **2011**, *40* (7), 3835–3853.
- (3) Pernpeintner, C.; Frank, J. A.; Urban, P.; Roeske, C. R.; Pritzl, S. D.; Trauner, D.; Lohmüller, T. Light-Controlled Membrane Mechanics and Shape Transitions of Photoswitchable Lipid Vesicles. *Langmuir* **2017**, *33* (16), 4083–4089. <https://doi.org/10.1021/acs.langmuir.7b01020>.
- (4) Volgraf, M.; Gorostiza, P.; Szobota, S.; Helix, M. R.; Isacoff, E. Y.; Trauner, D. Reversibly Caged Glutamate: A Photochromic Agonist of Ionotropic Glutamate Receptors. *J. Am. Chem. Soc.* **2007**, *129* (2), 260–261. <https://doi.org/10.1021/ja067269o>.
- (5) Müller, M.; Niemeyer, K.; Urban, N.; Ojha, N. K.; Zufall, F.; Leinders-Zufall, T.; Schaefer, M.; Thorn-Seshold, O. BTDAzo: A Photoswitchable TRPC5 Channel Activator\*\*. *Angew. Chem. Int. Ed.* **2022**, *61* (36), e202201565. <https://doi.org/10.1002/anie.202201565>.
- (6) Borowiak, M.; Nahaboo, W.; Reynders, M.; Nekolla, K.; Jalinot, P.; Hasserodt, J.; Rehberg, M.; Delattre, M.; Zahler, S.; Vollmar, A.; Trauner, D.; Thorn-Seshold, O. Photoswitchable Inhibitors of Microtubule Dynamics Optically Control Mitosis and Cell Death. *Cell* **2015**, *162* (2), 403–411. <https://doi.org/10.1016/j.cell.2015.06.049>.
- (7) Müller-Deku, A.; Meiring, J. C. M.; Loy, K.; Kraus, Y.; Heise, C.; Bingham, R.; Jansen, K. I.; Qu, X.; Bartolini, F.; Kapitein, L. C.; Akhmanova, A.; Ahlfeld, J.; Trauner, D.; Thorn-Seshold, O. Photoswitchable Paclitaxel-Based Microtubule Stabilisers Allow Optical Control over the Microtubule Cytoskeleton. *Nat Commun* **2020**, *11* (1), 4640. <https://doi.org/10.1038/s41467-020-18389-6>.
- (8) Küllmer, F.; Vepřek, N. A.; Borowiak, M.; Nasufović, V.; Barutzki, S.; Thorn-Seshold, O.; Arndt, H.-D.; Trauner, D. Next Generation Opto-Jasplakinolides Enable Local Remodeling of Actin Networks. *Angewandte Chemie International Edition* **2022**, *61* (48), e202210220. <https://doi.org/10.1002/anie.202210220>.
- (9) Reynders, M.; Matsuura, B. S.; Bérouti, M.; Simoneschi, D.; Marzio, A.; Pagano, M.; Trauner, D. PHOTACs Enable Optical Control of Protein Degradation. *Sci. Adv.* **2022**, *8* (8), eaay5064. <https://doi.org/10.1126/sciadv.aay5064>.
- (10) Pfaff, P.; Samarasinghe, K. T. G.; Crews, C. M.; Carreira, E. M. Reversible Spatiotemporal Control of Induced Protein Degradation by Bistable PhotoPROTACs. *ACS Cent. Sci.* **2019**, *5* (10), 1682–1690. <https://doi.org/10.1021/acscentsci.9b00713>.
- (11) Wegener, M.; Hansen, M. J.; Driessen, A. J. M.; Szymanski, W.; Feringa, B. L. Photocontrol of Antibacterial Activity: Shifting from UV to Red Light Activation. *J. Am. Chem. Soc.* **2017**, *139* (49), 17979–17986. <https://doi.org/10.1021/jacs.7b09281>.
- (12) Tsai, Y.-H.; Essig, S.; James, J. R.; Lang, K.; Chin, J. W. Selective, Rapid and Optically Switchable Regulation of Protein Function in Live Mammalian Cells. *Nat. Chem* **2015**, *7* (7), 554–561. <https://doi.org/10.1038/nchem.2253>.
- (13) Acosta-Ruiz, A.; Gutzeit, V. A.; Skelly, M. J.; Meadows, S.; Lee, J.; Parekh, P.; Orr, A. G.; Liston, C.; Pleil, K. E.; Broichhagen, J.; Levitz, J. Branched Photoswitchable Tethered Ligands Enable Ultra-Efficient Optical Control and Detection of G Protein-Coupled Receptors In Vivo. *Neuron* **2020**, *105* (3), 446–463. <https://doi.org/10.1016/j.neuron.2019.10.036>.
- (14) Westphal, M. V.; Schafroth, M. A.; Sarott, R. C.; Imhof, M. A.; Bold, C. P.; Leippe, P.; Dhopeswarkar, A.; Grandner, J. M.; Katritch, V.; Mackie, K.; Trauner, D.; Carreira, E. M.; Frank, J. A. Synthesis of Photoswitchable  $\Delta^9$ -Tetrahydrocannabinol Derivatives Enables Optical Control of Cannabinoid Receptor 1 Signaling. *J. Am. Chem. Soc.* **2017**, *139* (50), 18206–18212. <https://doi.org/10.1021/jacs.7b06456>.
- (15) Levitz, J.; Pantoja, C.; Gaub, B.; Janovjak, H.; Reiner, A.; Hoagland, A.; Schoppik, D.; Kane, B.; Stawski, P.; Schier, A. F.; Trauner, D.; Isacoff, E. Y. Optical Control of Metabotropic Glutamate Receptors. *Nat Neurosci* **2013**, *16* (4), 507–516. <https://doi.org/10.1038/nn.3346>.
- (16) Fuchter, M. J. On the Promise of Photopharmacology Using Photoswitches: A Medicinal Chemist's Perspective. *J. Med. Chem.* **2020**, *63* (20), 11436–11447. <https://doi.org/10.1021/acs.jmedchem.0c00629>.
- (17) Thorn-Seshold, O. Photoswitchable Cytotoxins. In *Molecular Photoswitches*; 2022; pp 873–919. <https://doi.org/10.1002/9783527827626.ch36>.
- (18) Matsuo, K.; Tamaoki, N. Rational Design and Development of a Lit-Active Photoswitchable Inhibitor Targeting CENP-E. *Org. Biomol. Chem.* **2021**, *19* (32), 6979–6984. <https://doi.org/10.1039/D1OB01332G>.
- (19) Sailer, A.; Meiring, J. C. M.; Heise, C.; Pettersson, L. N.; Akhmanova, A.; Thorn-Seshold, J.; Thorn-Seshold, O. Pyrrole Hemithioindigo Antimitotics with Near-Quantitative Bidirectional Photoswitching Photocontrol

- Cellular Microtubule Dynamics with Single-Cell Precision. *Angewandte Chemie International Edition* **2021**, *60* (44), 23695–23704. <https://doi.org/10.1002/anie.202104794>.
- (20) Hüll, K.; Morstein, J.; Trauner, D. In Vivo Photopharmacology. *Chem. Rev.* **2018**, *118* (21), 10710–10747. <https://doi.org/10.1021/acs.chemrev.8b00037>.
- (21) Velema, W. A.; Szymanski, W.; Feringa, B. L. Photopharmacology: Beyond Proof of Principle. *J. Am. Chem. Soc.* **2014**, *136* (6), 2178–2191. <https://doi.org/10.1021/ja413063e>.
- (22) Beharry, A. A.; Woolley, G. A. Azobenzene Photoswitches for Biomolecules. *Chem. Soc. Rev.* **2011**, *40* (8), 4422–4437. <https://doi.org/10.1039/C1CS15023E>.
- (23) Konrad, D. B.; Frank, J. A.; Trauner, D. Synthesis of Redshifted Azobenzene Photoswitches by Late-Stage Functionalization. *Chem. Eur. J.* **2016**, *22* (13), 4364–4368. <https://doi.org/10.1002/chem.201505061>.
- (24) Pritzl, S. D.; Konrad, D. B.; Ober, M. F.; Richter, A. F.; Frank, J. A.; Nickel, B.; Trauner, D.; Lohmüller, T. Optical Membrane Control with Red Light Enabled by Red-Shifted Photolipids. *Langmuir* **2022**, *38* (1), 385–393. <https://doi.org/10.1021/acs.langmuir.1c02745>.
- (25) Lameijer, L. N.; Budzak, S.; Simeth, N. A.; Hansen, M. J.; Feringa, B. L.; Jacquemin, D.; Szymanski, W. General Principles for the Design of Visible-Light-Responsive Photoswitches: Tetra-Ortho-Chloro-Azobenzenes. *Angew. Chem. Int. Ed.* **2020**, *132* (48), 21847–21854. <https://doi.org/10.1002/ange.202008700>.
- (26) Hansen, M. J.; Lerch, M. M.; Szymanski, W.; Feringa, B. L. Direct and Versatile Synthesis of Red-Shifted Azobenzenes. *Angew. Chem. Int. Ed.* **2016**, *55* (43), 13514–13518. <https://doi.org/10.1002/anie.201607529>.
- (27) Dong, M.; Babalhavaeji, A.; Samanta, S.; Beharry, A. A.; Woolley, G. A. Red-Shifting Azobenzene Photoswitches for in Vivo Use. *Acc. Chem. Res.* **2015**, *48* (10), 2662–2670. <https://doi.org/10.1021/acs.accounts.5b00270>.
- (28) Müller-Deku, A.; Thorn-Seshold, O. Exhaustive Catalytic Ortho-Alkoxylation of Azobenzenes: Flexible Access to Functionally Diverse Yellow-Light-Responsive Photoswitches. *J. Org. Chem.* **2022**, *87* (24), 16526–16531. <https://doi.org/10.1021/acs.joc.2c02214>.
- (29) Bléger, D.; Schwarz, J.; Brouwer, A. M.; Hecht, S. O-Fluoroazobenzenes as Readily Synthesized Photoswitches Offering Nearly Quantitative Two-Way Isomerization with Visible Light. *J. Am. Chem. Soc.* **2012**, *134* (51), 20597–20600. <https://doi.org/10.1021/ja310323y>.
- (30) Knie, C.; Utecht, M.; Zhao, F.; Kulla, H.; Kovalenko, S.; Brouwer, A. M.; Saalfrank, P.; Hecht, S.; Bléger, D. Ortho-Fluoroazobenzenes: Visible Light Switches with Very Long-Lived Z Isomers. *Chem. Eur. J.* **2014**, *20* (50), 16492–16501. <https://doi.org/10.1002/chem.201404649>.
- (31) Konrad, D. B.; Savasci, G.; Allmendinger, L.; Trauner, D.; Ochsenfeld, C.; Ali, A. M. Computational Design and Synthesis of a Deeply Red-Shifted and Bistable Azobenzene. *J. Am. Chem. Soc.* **2020**, *142* (14), 6538–6547. <https://doi.org/10.1021/jacs.9b10430>.
- (32) Trads, J. B.; Hüll, K.; Matsuura, B. S.; Laprell, L.; Fehrentz, T.; Gördlt, N.; Kozek, K. A.; Weaver, C. D.; Klöcker, N.; Barber, D. M.; Trauner, D. Sign Inversion in Photopharmacology: Incorporation of Cyclic Azobenzenes in Photoswitchable Potassium Channel Blockers and Openers. *Angew. Chem. Int. Ed.* **2019**, *58* (43), 15421–15428. <https://doi.org/10.1002/anie.201905790>.
- (33) Siewertsen, R.; Neumann, H.; Buchheim-Stehn, B.; Herges, R.; Näther, C.; Renth, F.; Temps, F. Highly Efficient Reversible Z–E Photoisomerization of a Bridged Azobenzene with Visible Light through Resolved S1(Nπ\*) Absorption Bands. *J. Am. Chem. Soc.* **2009**, *131* (43), 15594–15595. <https://doi.org/10.1021/ja906547d>.
- (34) Maier, M. S.; Hüll, K.; Reynders, M.; Matsuura, B. S.; Leippe, P.; Ko, T.; Schäffer, L.; Trauner, D. Oxidative Approach Enables Efficient Access to Cyclic Azobenzenes. *J. Am. Chem. Soc.* **2019**, *141* (43), 17295–17304. <https://doi.org/10.1021/jacs.9b08794>.
- (35) Ronayette, J.; Arnaud, R.; Lemaire, J. Isomérisation photosensibilisée par des colorants et photoréduction de l'azobenzène en solution. II. *Can. J. Chem.* **1974**, *52* (10), 1858–1867. <https://doi.org/10.1139/v74-265>.
- (36) Arnaud, R.; Lemaire, J. Isomérisation *cis* – *trans* de l'azobenzène catalysée par l'iode. III. *Can. J. Chem.* **1974**, *52* (10), 1868–1871. <https://doi.org/10.1139/v74-266>.
- (37) Shimomura, M.; Kunitake, T. Fluorescence and Photoisomerization of Azobenzene-Containing Bilayer Membranes. *J. Am. Chem. Soc.* **1987**, *109* (17), 5175–5183. <https://doi.org/10.1021/ja00251a022>.
- (38) Goulet-Hanssens, A.; Rietze, C.; Titov, E.; Abdullahu, L.; Grubert, L.; Saalfrank, P.; Hecht, S. Hole Catalysis as a General Mechanism for Efficient and Wavelength-Independent Z → E Azobenzene Isomerization. *Chem* **2018**, *4* (7), 1740–1755. <https://doi.org/10.1016/j.chempr.2018.06.002>.
- (39) Isokuoritti, J.; Kuntze, K.; Virkki, M.; Ahmed, Z.; Vuorimaa-Laukkanen, E.; Filatov, M. A.; Turshatov, A.; Laaksonen, T.; Priimagi, A.; Durandin, N. A. Expanding Excitation Wavelengths for Azobenzene Photoswitching into the Near-Infrared Range via Endothermic Triplet Energy Transfer. *Chem. Sci.* **2021**, *12* (21), 7504–7509. <https://doi.org/10.1039/D1SC01717A>.
- (40) Großkopf, J.; Kratz, T.; Rigotti, T.; Bach, T. Enantioselective Photochemical Reactions Enabled by Triplet Energy Transfer. *Chem. Rev.* **2022**, *122* (2), 1626–1653. <https://doi.org/10.1021/acs.chemrev.1c00272>.
- (41) Strieth-Kalthoff, F.; Glorius, F. Triplet Energy Transfer Photocatalysis: Unlocking the Next Level. *Chem* **2020**, *6* (8), 1888–1903. <https://doi.org/10.1016/j.chempr.2020.07.010>.

- (42) Monti, S.; Dellonte, S.; Bortolus, P. The Lowest Triplet State of Substituted Azobenzenes: An Energy Transfer Investigation. *Journal of Photochemistry* **1983**, *23* (2), 249–256. [https://doi.org/10.1016/0047-2670\(83\)80065-3](https://doi.org/10.1016/0047-2670(83)80065-3).
- (43) Bortolus, Pietro.; Monti, Sandra. Cis-Trans Photoisomerization of Azobenzene. Solvent and Triplet Donors Effects. *J. Phys. Chem.* **1979**, *83* (6), 648–652. <https://doi.org/10.1021/j100469a002>.
- (44) Monti, S.; Gardini, E.; Bortolus, P.; Amouyal, E. The Triplet State of Azobenzene. *Chem. Phys. Lett.* **1981**, *77* (1), 115–119. [https://doi.org/10.1016/0009-2614\(81\)85611-4](https://doi.org/10.1016/0009-2614(81)85611-4).
- (45) Cembran, A.; Bernardi, F.; Garavelli, M.; Gagliardi, L.; Orlandi, G. On the Mechanism of the Cis–trans Isomerization in the Lowest Electronic States of Azobenzene:  $S_0$ ,  $S_1$ , and  $T_1$ . *J. Am. Chem. Soc.* **2004**, *126* (10), 3234–3243. <https://doi.org/10.1021/ja038327y>.
- (46) Jones, L. B.; Hammond, G. S. Mechanisms of Photochemical Reactions in Solution. XXX.1 Photosensitized Isomerization of Azobenzene. *J. Am. Chem. Soc.* **1965**, *87* (18), 4219–4220. <https://doi.org/10.1021/ja01096a059>.
- (47) Reimann, M.; Teichmann, E.; Hecht, S.; Kaupp, M. Solving the Azobenzene Entropy Puzzle: Direct Evidence for Multi-State Reactivity. *J. Phys. Chem. Lett.* **2022**, *13* (46), 10882–10888. <https://doi.org/10.1021/acs.jpcclett.2c02838>.
- (48) Fang, B.; Shen, Y.; Peng, B.; Bai, H.; Wang, L.; Zhang, J.; Hu, W.; Fu, L.; Zhang, W.; Li, L.; Huang, W. Small-Molecule Quenchers for Förster Resonance Energy Transfer: Structure, Mechanism, and Applications. *Angew. Chem. Int. Ed.* **2022**, *61* (41), e202207188. <https://doi.org/10.1002/anie.202207188>.
- (49) Olesińska-Mönch, M.; Deo, C. Small-Molecule Photoswitches for Fluorescence Bioimaging: Engineering and Applications. *Chem. Commun.* **2023**, *59* (6), 660–669. <https://doi.org/10.1039/D2CC005870G>.
- (50) Crisalli, P.; Kool, E. T. Multi-Path Quenchers: Efficient Quenching of Common Fluorophores. *Bioconjugate Chem.* **2011**, *22* (11), 2345–2354. <https://doi.org/10.1021/bc200424r>.
- (51) Izquierdo-Serra, M.; Gascón-Moya, M.; Hirtz, J. J.; Pittolo, S.; Poskanzer, K. E.; Ferrer, È.; Alibés, R.; Busqué, F.; Yuste, R.; Hernandez, J.; Gorostiza, P. Two-Photon Neuronal and Astrocytic Stimulation with Azobenzene-Based Photoswitches. *J. Am. Chem. Soc.* **2014**, *136* (24), 8693–8701. <https://doi.org/10.1021/ja5026326>.
- (52) Moreno, J.; Gerecke, M.; Grubert, L.; Kovalenko, S. A.; Hecht, S. Sensitized Two-NIR-Photon  $Z \rightarrow E$  Isomerization of a Visible-Light-Addressable Bistable Azobenzene Derivative. *Angew. Chem. Int. Ed.* **2016**, *55* (4), 1544–1547. <https://doi.org/10.1002/anie.201509111>.
- (53) Thorn-Seshold, O.; Trauner, D.; Borowiak, M.; Hasserodt, J. EP3137554 - Azoaryls as Reversibly Modulatable Tubulin Inhibitors.
- (54) Gemen, J.; Church, J. R.; Ruoko, T.-P.; Durandin, N.; Bialek, M. J.; Weißenfels, M.; Feller, M.; Kazes, M.; Odaybat, M.; Borin, V. A.; Kalepu, R.; Diskin-Posner, Y.; Oron, D.; Fuchter, M. J.; Priimagi, A.; Schapiro, I.; Klajn, R. Disequilibrating Azobenzenes by Visible-Light Sensitization under Confinement. *Science* **2023**, *381* (6664), 1357–1363. <https://doi.org/10.1126/science.adh9059>.
- (55) Shimomura, M.; Kunitake, T. Fluorescence and Photoisomerization of Azobenzene-Containing Bilayer Membranes. *J. Am. Chem. Soc.* **1987**, *109* (17), 5175–5183. <https://doi.org/10.1021/ja00251a022>.
- (56) Bortolus, Pietro.; Monti, Sandra. Cis-Trans Photoisomerization of Azobenzene. Solvent and Triplet Donors Effects. *J. Phys. Chem.* **1979**, *83* (6), 648–652. <https://doi.org/10.1021/j100469a002>.
- (57) Knoll, H. Ch. 89 - Photoisomerism of Azobenzenes. In *CRC Handbook of Organic Photochemistry and Photobiology, Volumes 1 & 2*; CRC Press: Boca Raton, 2003.
- (58) Chevalier, A.; Renard, P.-Y.; Romieu, A. Straightforward Synthesis of Bioconjugatable Azo Dyes. Part 1: Black Hole Quencher-1 (BHQ-1) Scaffold. *Tetrahedron Lett.* **2014**, *55* (50), 6759–6763. <http://dx.doi.org/10.1016/j.tetlet.2014.10.053>.
- (59) Irshadeen, I. M.; Walden, S. L.; Wegener, M.; Truong, V. X.; Frisch, H.; Blinco, J. P.; Barner-Kowollik, C. Action Plots in Action: In-Depth Insights into Photochemical Reactivity. *J. Am. Chem. Soc.* **2021**, *143* (50), 21113–21126. <https://doi.org/10.1021/jacs.1c09419>.
- (60) Goulet-Hanssens, A.; Utecht, M.; Mutruc, D.; Titov, E.; Schwarz, J.; Grubert, L.; Bléger, D.; Saalfrank, P.; Hecht, S. Electrocatalytic  $Z \rightarrow E$  Isomerization of Azobenzenes. *J. Am. Chem. Soc.* **2017**, *139* (1), 335–341. <https://doi.org/10.1021/jacs.6b10822>.
- (61) Kienzler, M. A.; Reiner, A.; Trautman, E.; Yoo, S.; Trauner, D.; Isacoff, E. Y. A Red-Shifted, Fast-Relaxing Azobenzene Photoswitch for Visible Light Control of an Ionotropic Glutamate Receptor. *J. Am. Chem. Soc.* **2013**, *135* (47), 17683–17686. <https://doi.org/10.1021/ja408104w>.
- (62) Reynders, M.; Borowiak, M.; Müller-Deku, A.; Wranik, M.; Krauskopf, K.; de la Osa de la Rosa, L.; Schaffer, K.; Rode, A.; Stierle, V.; Kraus, Y.; Baumgartner, B.; Ali, A.; Bubeneck, A.; Seal, T.; Steinmetz, M.; Paulitschke, P.; Thorn-Seshold, O. A Photo-SAR Study of Azobenzene-Based Photoswitchable Antimitotics Identifying a General Method for near-Quantitative Photocontrol. *in submission* **2024**.
- (63) Edelstein, A. D.; Tsuchida, M. A.; Amodaj, N.; Pinkard, H.; Vale, R. D.; Stuurman, N. Advanced Methods of Microscope Control Using  $\mu$ Manager Software. *J Biol Methods* **2014**, *1* (2), e10. <https://doi.org/10.14440/jbm.2014.36>.
- (64) Urban, P.; Pritzl, S. D.; Ober, M. F.; Dirscherl, C. F.; Pernpeintner, C.; Konrad, D. B.; Frank, J. A.; Trauner, D.; Nickel, B.; Lohmueller, T. A Lipid Photoswitch Controls Fluidity in Supported Bilayer Membranes. *Langmuir* **2020**, *36* (10), 2629–2634. <https://doi.org/10.1021/acs.langmuir.9b02942>.



- (65) Firsov, A. M.; Pfeffermann, J.; Benditkis, A. S.; Rokitskaya, T. I.; Kozlov, A. S.; Kotova, E. A.; Krasnovsky, A. A.; Pohl, P.; Antonenko, Y. N. Photodynamic Activity Rather than Drilling Causes Membrane Damage by a Light-Powered Molecular Nanomotor. *Journal of Photochemistry and Photobiology B: Biology* **2022**, 112633. <https://doi.org/10.1016/j.jphotobiol.2022.112633>.
- (66) Connelly, N. G.; Geiger, W. E. Chemical Redox Agents for Organometallic Chemistry. *Chem. Rev.* **1996**, 96 (2), 877–910. <https://doi.org/10.1021/cr940053x>.
- (67) Aranzaes, J. R.; Daniel, M.-C.; Astruc, D. Metallocenes as References for the Determination of Redox Potentials by Cyclic Voltammetry - Permethylated Iron and Cobalt Sandwich Complexes, Inhibition by Polyamine Dendrimers, and the Role of Hydroxy-Containing Ferrocenes. *Can. J. Chem.* **2006**, 84 (2), 288–299. <https://doi.org/10.1139/v05-262>.
- (68) Jones, W. E.; Fox, M. A. Determination of Excited-State Redox Potentials by Phase-Modulated Voltammetry. *J. Phys. Chem.* **1994**, 98 (19), 5095–5099. <https://doi.org/10.1021/j100070a025>.
- (69) Rehm, D.; Weller, A. Kinetics of Fluorescence Quenching by Electron and H-Atom Transfer. *Isr. J. Chem.* **1970**, 8 (2), 259–271. <https://doi.org/10.1002/ijch.197000029>.
- (70) Narayanan, M.; Kodali, G.; Singh, V. R.; Velvadapu, V.; Stanley, R. J. Oxidation and Reduction Potentials of 8-Vinyladenosine Measured by Cyclic Voltammetry: Implications for Photoinduced Electron Transfer Quenching of a Fluorescent Adenine Analog. *J. Photochem. Photobiol. A* **2012**, 249, 9–14. <https://doi.org/10.1016/j.jphotochem.2012.08.018>.
- (71) Romero, N. A.; Nicewicz, D. A. Organic Photoredox Catalysis. *Chem. Rev.* **2016**, 116 (17), 10075–10166. <https://doi.org/10.1021/acs.chemrev.6b00057>.
- (72) values taken from <https://www.atto-tec.com/ATTO-655.html> (measured in PBS), last visited 15.09.2022.
- (73) Vogelsang, J.; Cordes, T.; Forthmann, C.; Steinhauer, C.; Tinnefeld, P. Controlling the Fluorescence of Ordinary Oxazine Dyes for Single-Molecule Switching and Superresolution Microscopy. *Proc. Natl. Acad. Sci. U.S.A.* **2009**, 106 (20), 8107–8112. <https://doi.org/10.1073/pnas.0811875106>.
- (74) Becker, R. S.; Chakravorti, S.; Das, S. The Photosensitizers Benzophenoxazine and Thiazines: Comprehensive Investigation of Photophysical and Photochemical Properties. *Photochem Photobiol* **1990**, 51 (5), 533–538. <https://doi.org/10.1111/j.1751-1097.1990.tb01962.x>.
- (75) Zhao, X.; Yao, Q.; Long, S.; Chi, W.; Yang, Y.; Tan, D.; Liu, X.; Huang, H.; Sun, W.; Du, J.; Fan, J.; Peng, X. An Approach to Developing Cyanines with Simultaneous Intersystem Crossing Enhancement and Excited-State Lifetime Elongation for Photodynamic Antitumor Metastasis. *J. Am. Chem. Soc.* **2021**, 143 (31), 12345–12354. <https://doi.org/10.1021/jacs.1c06275>.
- (76) Frank, J. A.; Yushchenko, D. A.; Hodson, D. J.; Lipstein, N.; Nagpal, J.; Rutter, G. A.; Rhee, J.-S.; Gottschalk, A.; Brose, N.; Schultz, C.; Trauner, D. Photoswitchable Diacylglycerols Enable Optical Control of Protein Kinase C. *Nat Chem Biol* **2016**, 12 (9), 755–762. <https://doi.org/10.1038/nchembio.2141>.
- (77) Frank, J. A.; Moroni, M.; Moshourab, R.; Sumser, M.; Lewin, G. R.; Trauner, D. Photoswitchable Fatty Acids Enable Optical Control of TRPV1. *Nat Commun* **2015**, 6 (1), 7118. <https://doi.org/10.1038/ncomms8118>.
- (78) Urban, P.; Pritzl, S. D.; Konrad, D. B.; Frank, J. A.; Pernpeintner, C.; Roeske, C. R.; Trauner, D.; Lohmüller, T. Light-Controlled Lipid Interaction and Membrane Organization in Photolipid Bilayer Vesicles. *Langmuir* **2018**, 34 (44), 13368–13374. <https://doi.org/10.1021/acs.langmuir.8b03241>.
- (79) Weber, T.; Chandrasekaran, V.; Stamer, I.; Thygesen, M. B.; Terfort, A.; Lindhorst, T. K. Switching of Bacterial Adhesion to a Glycosylated Surface by Reversible Reorientation of the Carbohydrate Ligand. *Angew. Chem. Int. Ed.* **2014**, 53 (52), 14583–14586. <https://doi.org/10.1002/anie.201409808>.
- (80) Broichhagen, J.; Damijonaitis, A.; Levitz, J.; Sokol, K. R.; Leippe, P.; Konrad, D.; Isacoff, E. Y.; Trauner, D. Orthogonal Optical Control of a G Protein-Coupled Receptor with a SNAP-Tethered Photochromic Ligand. *ACS Cent Sci* **2015**, 1 (7), 383–393. <https://doi.org/10.1021/acscentsci.5b00260>.
- (81) Fehrentz, T.; Kuttruff, C. A.; Huber, F. M. E.; Kienzler, M. A.; Mayer, P.; Trauner, D. Exploring the Pharmacology and Action Spectra of Photochromic Open-Channel Blockers. *ChemBioChem* **2012**, 13 (12), 1746–1749. <https://doi.org/10.1002/cbic.201200216>.
- (82) Tochitsky, I.; Polosukhina, A.; Degtyar, V. E.; Gallerani, N.; Smith, C. M.; Friedman, A.; Van Gelder, R. N.; Trauner, D.; Kaufner, D.; Kramer, R. H. Restoring Visual Function to Blind Mice with a Photoswitch That Exploits Electrophysiological Remodeling of Retinal Ganglion Cells. *Neuron* **2014**, 81 (4), 800–813. <https://doi.org/10.1016/j.neuron.2014.01.003>.
- (83) Reynders, M.; Oliver Thorn-Seshold. PST2. *in preparation*.
- (84) Borowiak, M.; Küllmer, F.; Gegenfurtner, F.; Peil, S.; Nasufovic, V.; Zahler, S.; Thorn-Seshold, O.; Trauner, D.; Arndt, H.-D. Optical Manipulation of F-Actin with Photoswitchable Small Molecules. *J. Am. Chem. Soc.* **2020**, 142 (20), 9240–9249. <https://doi.org/10.1021/jacs.9b12898>.
- (85) Pritzl, S. D.; Konrad, D. B.; Ober, M. F.; Richter, A. F.; Frank, J. A.; Nickel, B.; Trauner, D.; Lohmüller, T. Optical Membrane Control with Red Light Enabled by Red-Shifted Photolipids. *Langmuir* **2022**, 38 (1), 385–393. <https://doi.org/10.1021/acs.langmuir.1c02745>.
- (86) Chander, N.; Morstein, J.; Bolten, J. S.; Shemet, A.; Cullis, P. R.; Trauner, D.; Witzigmann, D. Optimized Photoactivatable Lipid Nanoparticles Enable Red Light Triggered Drug Release. *Small* **2021**, 17 (21), 2008198. <https://doi.org/10.1002/sml.202008198>.



- (87) Stadler, E.; Tassoti, S.; Lentès, P.; Herges, R.; Glasnov, T.; Zangger, K.; Gescheidt, G. In Situ Observation of Photoswitching by NMR Spectroscopy: A Photochemical Analogue to the Exchange Spectroscopy Experiment. *Anal. Chem.* **2019**, *91* (17), 11367–11373. <https://doi.org/10.1021/acs.analchem.9b02613>.
- (88) Dobryakov, A. L.; Kovalenko, S. A.; Ernsting, N. P. Coherent and Sequential Contributions to Femtosecond Transient Absorption Spectra of a Rhodamine Dye in Solution. *J. Chem. Phys.* **2005**, *123* (4), 044502. <https://doi.org/10.1063/1.1948383>.
- (89) Doumazane, E.; Scholler, P.; Zwier, J. M.; Trinquet, E.; Rondard, P.; Pin, J.-P. A New Approach to Analyze Cell Surface Protein Complexes Reveals Specific Heterodimeric Metabotropic Glutamate Receptors. *The FASEB Journal* **2011**, *25* (1), 66–77. <https://doi.org/10.1096/fj.10-163147>.
- (90) Vivaudou, M.; Chan, K. W.; Sui, J.-L.; Jan, L. Y.; Reuveny, E.; Logothetis, D. E. Probing the G-Protein Regulation of GIRK1 and GIRK4, the Two Subunits of the KACH Channel, Using Functional Homomeric Mutants. *J Biol Chem* **1997**, *272* (50), 31553–31560. <https://doi.org/10.1074/jbc.272.50.31553>.
- (91) Gutzeit, V. A.; Acosta-Ruiz, A.; Munguba, H.; Häfner, S.; Landra-Willm, A.; Mathes, B.; Mony, J.; Yarotski, D.; Börjesson, K.; Liston, C.; Sandoz, G.; Levitz, J.; Broichhagen, J. A Fine-Tuned Azobenzene for Enhanced Photopharmacology in Vivo. *Cell Chem. Biol.* **2021**, *28* (11), 1648–1663. <https://doi.org/10.1016/j.chembiol.2021.02.020>.
- (92) Oh, S. W.; Harris, J. A.; Ng, L.; Winslow, B.; Cain, N.; Mihalas, S.; Wang, Q.; Lau, C.; Kuan, L.; Henry, A. M.; Mortrud, M. T.; Ouellette, B.; Nguyen, T. N.; Sorensen, S. A.; Slaughterbeck, C. R.; Wakeman, W.; Li, Y.; Feng, D.; Ho, A.; Nicholas, E.; Hirokawa, K. E.; Bohn, P.; Joines, K. M.; Peng, H.; Hawrylycz, M. J.; Phillips, J. W.; Hohmann, J. G.; Wohnoutka, P.; Gerfen, C. R.; Koch, C.; Bernard, A.; Dang, C.; Jones, A. R.; Zeng, H. A Mesoscale Connectome of the Mouse Brain. *Nature* **2014**, *508* (7495), 207–214. <https://doi.org/10.1038/nature13186>.
- (93) Bartole, E.; Littmann, T.; Tanaka, M.; Ozawa, T.; Buschauer, A.; Bernhardt, G. [3H]UR-DEBa176: A 2,4-Diaminopyrimidine-Type Radioligand Enabling Binding Studies at the Human, Mouse, and Rat Histamine H4 Receptors. *J. Med. Chem.* **2019**, *62* (17), 8338–8356. <https://doi.org/10.1021/acs.jmedchem.9b01342>.
- (94) Ishiba, K.; Morikawa, M.; Chikara, C.; Yamada, T.; Iwase, K.; Kawakita, M.; Kimizuka, N. Photoliquefiable Ionic Crystals: A Phase Crossover Approach for Photon Energy Storage Materials with Functional Multiplicity. *Angew. Chem. Int. Ed.* **2015**, *54* (5), 1532–1536. <https://doi.org/10.1002/anie.201410184>.
- (95) Cui, K.; Lu, X.; Cui, W.; Wu, J.; Chen, X.; Lu, Q. Fluorescent Nanoparticles Assembled from a Poly(Ionic Liquid) for Selective Sensing of Copper Ions. *Chem. Commun.* **2010**, *47* (3), 920–922. <https://doi.org/10.1039/C0CC03900D>.
- (96) Banghart, M.; Mourot, A.; Fortin, D.; Yao, J.; Kramer, R.; Trauner, D. Photochromic Blockers of Voltage-Gated Potassium Channels. *Angew. Chem. Int. Ed.* **2009**, *48* (48), 9097–9101. <https://doi.org/10.1002/anie.200904504>.
- (97) Hu, M.; Fan, J.; Li, H.; Song, K.; Wang, S.; Cheng, G.; Peng, X. Fluorescent Chemodosimeter for Cys/Hcy with a Large Absorption Shift and Imaging in Living Cells. *Org. Biomol. Chem.* **2011**, *9* (4), 980–983. <https://doi.org/10.1039/C0OB00957A>.
- (98) Fei, M.; Wai-Yee, L.; Ching-Ying, C. Fluorescent Pyrene Compounds. US 2011/0097735A I.
- (99) Scilimati, A.; Ferorelli, S.; Iaselli, M. C.; Miciaccia, M.; Pati, M. L.; Fortuna, C. G.; Aleem, A. M.; Marnett, L. J.; Perrone, M. G. Targeting COX-1 by Mofezolac-Based Fluorescent Probes for Ovarian Cancer Detection. *Eur. J. Med. Chem.* **2019**, *179*, 16–25. <https://doi.org/10.1016/j.ejmech.2019.06.039>.
- (100) Yan, X.; Yuan, P. M. Sulfonated [8,9]Benzophenoxazine Dyes and the Use of Their Labelled Conjugates. WO 01/83621 A2.
- (101) Yuan, L.; Lin, W.; Cao, Z.; Wang, J.; Chen, B. Development of FRET-Based Dual-Excitation Ratiometric Fluorescent pH Probes and Their Photocaged Derivatives. *Chem. Eur. J.* **2012**, *18* (4), 1247–1255. <https://doi.org/10.1002/chem.201101434>.
- (102) Huang, C.; Yin, Q.; Meng, J.; Zhu, W.; Yang, Y.; Qian, X.; Xu, Y. Versatile Probes for the Selective Detection of Vicinal-Dithiol-Containing Proteins: Design, Synthesis, and Application in Living Cells. *Chem. Eur. J.* **2013**, *19* (24), 7739–7747. <https://doi.org/10.1002/chem.201300567>.
- (103) Yan, Y.; Krishnakumar, S.; Yu, H.; Ramishetti, S.; Deng, L.-W.; Wang, S.; Huang, L.; Huang, D. Nickel(II) Dithiocarbamate Complexes Containing Sulforhodamine B as Fluorescent Probes for Selective Detection of Nitrogen Dioxide. *J. Am. Chem. Soc.* **2013**, *135* (14), 5312–5315. <https://doi.org/10.1021/ja401555y>.
- (104) Pisoni, D. S.; Todeschini, L.; Borges, A. C. A.; Petzhold, C. L.; Rodembusch, F. S.; Campo, L. F. Symmetrical and Asymmetrical Cyanine Dyes. Synthesis, Spectral Properties, and BSA Association Study. *J. Org. Chem.* **2014**, *79* (12), 5511–5520. <https://doi.org/10.1021/jo500657s>.
- (105) Brun, M. A.; Tan, K.-T.; Nakata, E.; Hinner, M. J.; Johnsson, K. Semisynthetic Fluorescent Sensor Proteins Based on Self-Labeling Protein Tags. *J. Am. Chem. Soc.* **2009**, *131* (16), 5873–5884. <https://doi.org/10.1021/ja900149e>.
- (106) Waalboer, D. C. J.; Muns, J. A.; Sijbrandi, N. J.; Schasfoort, R. B. M.; Haselberg, R.; Somsen, G. W.; Houthoff, H.-J.; van Dongen, G. A. M. S. Platinum(II) as Bifunctional Linker in Antibody-Drug Conjugate Formation: Coupling of a 4-Nitrobenzo-2-Oxa-1,3-Diazole Fluorophore to Trastuzumab as a Model. *ChemMedChem* **2015**, *10* (5), 797–803. <https://doi.org/10.1002/cmdc.201402496>.
- (107) Wang, Q.; Wang, X.; Sun, Y.; Yang, X.; Zhang, L.; Zhang, Q.; Hu, Z.-Q.; Hu, H.-Y. Ratiometric Fluorescent Probes for Selective and Sensitive Visualization of Bacterial Microenvironment Protease Activity. *Chem. Commun.* **2019**, *55* (35), 5064–5067. <https://doi.org/10.1039/C9CC00953A>.

- (108) Pheaney, C. G.; Barton, J. K. DNA Electrochemistry with Tethered Methylene Blue. *Langmuir* **2012**, *28* (17), 7063–7070. <https://doi.org/10.1021/la300566x>.
- (109) Tang, Z.-L.; Ouyang, X.-H.; Song, R.-J.; Li, J.-H. Decarboxylative C(Sp<sup>3</sup>)–N Cross-Coupling of Diacyl Peroxides with Nitrogen Nucleophiles. *Org. Lett.* **2021**, *23* (3), 1000–1004. <https://doi.org/10.1021/acs.orglett.0c04203>.
- (110) Alves, C. M. A.; Naik, S.; Coutinho, P. J. G.; Gonçalves, M. S. T. Novel Long Alkyl Side Chain Benzo[a]Phenoxazinium Chlorides: Synthesis, Photophysical Behaviour and DNA Interaction. *Tetrahedron* **2009**, *65* (50), 10441–10452. <https://doi.org/10.1016/j.tet.2009.10.017>.

## 7.2 Supporting Information to chapter 3.2

## **Azobenzenes can achieve near-infrared photocontrol in biological systems, with quantitative $Z \rightarrow E$ photoisomerization, via singlet manifold photoredox**

Benedikt Baumgartner<sup>1</sup>, Viktorija Glembockyte<sup>2,3</sup>, Robert J. Mayer<sup>2</sup>, Alberto Jesus Gonzalez-Hernandez<sup>4</sup>, Robert O. Kindler<sup>5</sup>, Abha Valavalkar<sup>6</sup>, Alexander J. Wiegand<sup>1</sup>, Adrian Müller-Deku<sup>1</sup>, Lutz Grubert<sup>7</sup>, Florian Steiner<sup>2,3</sup>, Christoph Gross<sup>2</sup>, Martin Reynders<sup>1</sup>, Vincent Grenier<sup>5</sup>, Johannes Broichhagen<sup>10</sup>, Stefan Hecht<sup>7,8</sup>, Philip Tinnefeld<sup>2,3</sup>, Armin R. Ofial<sup>2</sup>, Benjamin Dietzek-Ivanšić<sup>6,9</sup>, Joshua Levitz<sup>4</sup>, Oliver Thorn-Seshold<sup>1\*</sup>

\* Correspondence and request for materials to O.T.-S. (oliver.thorn-seshold@cup.lmu.de)

(1) Department of Pharmacy, LMU Munich, 81377 Munich, Germany; (2) Department of Chemistry, LMU Munich, 81377 Munich, Germany; (3) Center for NanoScience, LMU Munich, 81377 Munich, Germany; (4) Department of Biochemistry and Department of Psychiatry, Weill Cornell Medicine, New York, NY 10065, USA; (5) Department of Chemical Biology, Max Planck Institute for Medical Research, 69120 Heidelberg, Germany; (6) Leibniz Institute for Photonic Technology Jena e.V. (Leibniz-IPHT), Research Department Functional Interfaces, 07745 Jena, Germany; (7) Department of Chemistry & Center for the Science of Materials Berlin, Humboldt-Universität zu Berlin, 12489 Berlin, Germany; (8) DWI – Leibniz Institute for Interactive Materials, 52074 Aachen, Germany; (9) Institute for Physical Chemistry (IPC), Friedrich Schiller University Jena, 07743 Jena, Germany; (10) Leibniz-Forschungsinstitut für Molekulare Pharmakologie, 13125 Berlin, Germany.

### **Table of Contents**

1	Supporting Notes .....	3
1.1	Note 1 - State of the Art in bioactive molecular switches for photopharmacology ..	3
1.2	Note 2 - <i>E/Z</i> redox potentials for azobenzenes .....	4
1.3	Note 3 - Full Figure Legends.....	4
1.4	Note 4 - Photoredox vs triplet energy transfer as dyad switching mechanisms.....	5
1.5	Note 5 - Biological aspects of singlet photoredox for <i>Z</i> -actives (eg BGAG-mGluR)	6
2	UV-VIS spectroscopy and bulk photoisomerisation.....	8
2.1	UV-VIS, General Methods.....	8
2.1.1	UV-VIS setup.....	8
2.1.2	General Methods for UV-VIS and bulk photoisomerisation.....	9
2.1.3	Light Source Properties for bulk photoisomerisations .....	9
2.2	Thermal Relaxation .....	10
2.3	Bulk Population Photoswitching .....	11
2.4	UV-Vis spectra and action spectra of non-photoredox control NB-AK.....	13
2.5	Extinction coefficient determination.....	14
3	Fluorophores: fluorescence excitation / emission spectra.....	15
4	Electrochemistry in ground and photoexcited states .....	16
4.1	Experimental reduction/oxidation potentials in ground state: chromophores.....	16
4.2	Experimental reduction/oxidation potentials in ground state: azobenzenes .....	17
5	PSS and photoswitch <i>E/Z</i> ratio determinations by UV-Vis and HPLC.....	19
5.1	PSS determination by HPLC.....	19
5.2	Calibrations for UV-Vis photoswitching action spectra.....	20
5.3	HPLC precision .....	21

6	Fluorescence lifetime measurement (mostly- <i>E</i> PSS at 639 nm) by TCSPC .....	22
7	Spectroelectrochemistry and transient absorption (TA) spectroscopy (TAS).....	23
7.1	Spectroelectrochemistry ( <i>E</i> and <i>Z</i> azobenzene oxidations and NB reduction).....	23
7.2	TAS Methods .....	24
7.3	TAS Results .....	25
8	Fluorescence Quantum Yields .....	28
8.1	Mostly- <i>E</i> fluorescence quantum yields (integrating sphere measurements).....	28
8.2	Fluorescence of conjugates depends on their <i>E/Z</i> isomer state .....	29
9	Cell culture transfection and electrophysiology .....	30
10	Chemical Synthesis.....	31
10.1	General .....	31
10.2	NMR spectroscopy.....	31
10.3	High-resolution mass spectrometry (HRMS).....	32
10.4	Synthesis.....	33
10.4.1	Azobenzene building blocks.....	33
10.4.2	Fluorophore building blocks .....	38
10.4.3	NB-Azobenzene conjugates for in cuvette studies.....	41
10.4.4	Bioactive Photoswitches BAG and BANG.....	45
10.4.5	CPY-PEG <sub>n</sub> -Azobenzene conjugates.....	51
11	References.....	55
12	Appendices .....	59
12.1	Cyclic voltammetry and square wave voltammetry spectra: azobenzenes.....	59
12.2	Cyclic voltammetry and square wave voltammetry spectra: fluorophores .....	70
12.3	NMR spectra .....	75

### Author Contributions

BB designed targets, performed synthesis, UV/Vis and fluorescence spectroscopy, HPLC analysis, analyzed and assembled data. AJW, AMD and MR performed synthesis and photocharacterisation. VGlembockyte and FS performed fluorescence lifetime experiments. AJGH performed mGluR2 electrophysiology. RK synthesised PST-PEG-CPY dyads, supervised by VGrenier. RJM, CG and LG performed electrochemistry. AV determined fluorescence quantum yields and performed transient absorption spectroscopy, supervised by BDI. JB performed synthesis and supplied building blocks. JL performed and supervised mGluR2 electrophysiology. SH and ARO supervised electrochemical measurements. PT supervised fluorescence lifetime experiments. OTS conceived the study, analyzed data, and supervised all other experiments. BB and OTS wrote the manuscript with input from all authors.



## 1 Supporting Notes

### 1.1 Note 1 - State of the Art in bioactive molecular switches for photopharmacology

Azobenzenes are the dominant photoswitch class; and beyond their uses in photoresponsive materials, they are driving the frontiers of photopharmacology from cellular applications in neuroscience, cytoskeleton, and signaling, through to *in vivo* clinical trials.<sup>1-4</sup> High demand biological targets in the field of chemical neuroscience<sup>5-10</sup>, cytoskeleton<sup>11-14</sup>, targeted protein degradation<sup>15,16</sup>, antibacterial activity<sup>17</sup>, kinases<sup>18</sup>, TRP channels<sup>19-21</sup>, and GPCRs<sup>22-28</sup> have all been successfully controlled by azobenzene based photopharmaceuticals.

The last decade has witnessed major efforts to solve two major problems: that (1) population-level photoswitching is not binary (all-*E*↔all-*Z*) but is incomplete, especially in the *Z*→*E* direction (that also is less photon-efficient); and (2) no broadly applicable strategy to operate azobenzenes with well-penetrating red/NIR light is known (typically,  $\epsilon(\lambda)$  are significant only below 530 nm). Excluding the approaches that are intrinsically not applicable for biological photocontrol, e.g. those relying on Brønsted or Lewis acid coordination to a diazene nitrogen (these typically need pH far below 5 to work,<sup>29</sup> or have fast *Z*→*E* relaxation,<sup>30</sup> or are hydrolytically unstable in water<sup>31</sup>), there were two major approaches pursued so far:

Firstly, tetra-*ortho*-substitution of azobenzenes can shift and can better separate the  $n\rightarrow\pi^*$  bands of the *E* and *Z* isomers, in some cases allowing for redshifted photoresponse (up to 600 nm) and near-quantitative bidirectional photoswitching. Early milestones in scaffold design by Woolley (chloro, methoxy<sup>32</sup>) and Hecht (fluoro<sup>33</sup>) were followed by some (catalytic) synthetic procedures enabling easier access to tetra-*ortho*-substituted azobenzenes (also by late stage introduction of motifs such as Cl<sub>4</sub><sup>21,34</sup>, F<sub>2</sub>Cl<sub>2</sub><sup>35</sup>, OMe<sub>4</sub><sup>36</sup>).

A second approach is based on cyclic azobenzene derivatives such as diazocines pioneered by Herges<sup>37,38</sup> and augmented by Trauner<sup>39</sup>, that can be bidirectionally isomerized by visible light. These also have inverted isomer stabilities (*Z* thermodynamically more stable).

Tetra-*ortho*-substitutions and diazocines share the limitation that both have low molar extinction coefficients in the well tissue penetrating red/NIR spectral region<sup>40</sup>, resulting in slow and inefficient photoswitching. Furthermore, if one of these methods should be applied to an arbitrarily chosen azobenzene photopharmaceutical, this usually entails substantial steric changes to the photoswitch, that can result in dramatic changes of bioactivity.

Two alternative routes to photocontrol azobenzenes' isomeric ratios with high switching completion and efficient red/NIR response, without complex redesign, have recently emerged in materials sciences. Both triplet energy transfer<sup>41-45</sup> (which we cover in a parallel manuscript<sup>46</sup>) and electro/photoredox catalysis<sup>45,47-49</sup> that are independent on the photoresponse wavelength and overlap of *E* and *Z* absorption spectra. Hecht and coworkers developed that azobenzenes can be quantitatively isomerized from *Z* to *E* isomer by electrocatalysis (a similar study has been showed recently by Fuchter for azoheteroarenes<sup>49</sup>). Depending on the electronic nature of the azobenzene this can happen by a radical anion mechanism<sup>47,48</sup> (electron poor azobenzenes, easy to reduce) or a radical cation mechanism<sup>45</sup> (electron rich azobenzenes, easy to oxidize). In both cases the azobenzene is reduced or oxidized to its radical anion/cation; then a rapid and quantitative (100%) thermal relaxation to the *E* isomer (that is 10<sup>13</sup> times faster than for the neutral species) occurs; then either propagation or back-electron-transfer restores the neutral state, now as the *E* isomer. In the work most relevant to this paper, Hecht showed<sup>45</sup> that hole catalysis (via radical cation) can be induced by triplet manifold, intermolecular photooxidative catalysis, by methylene blue (MB) operating on electron rich azobenzenes (whose oxidation potential is lower than the excited state reduction potential of MB). Thus, MB excitation at 660 nm can drive complete *Z*→*E* population switching in relatively concentrated, oxygen-free conditions.

Two of the limitations preventing these triplet concepts from being used in biology are given in the main text: (1) intermolecular catalysis is not suitable in cellular systems due to the limits of collisional reaction rates (at high dilution, the azobenzene cannot outcompete other reactive species); and (2) triplet photoredox catalysts produce reactive oxygen species that

not only yield in photobleaching of the catalyst, but also in damage of biological tissue, under biologically appropriate conditions where oxygen is available. Several more limitations and considerations are presented in the text and Supporting Notes of reference<sup>46</sup>.

Note also that photooxidation of the azobenzene is likely to be more biocompatible and robust against degradation, than photoreduction; see e.g. ref<sup>45,47-49</sup>. Therefore this paper concentrates only on azobenzene photooxidation as the redox route.

## 1.2 Note 2 - E/Z redox potentials for azobenzenes

While oxidation potentials for Z-azobenzenes have been reported in older works, or have been stated to be identical to those of E-azobenzenes, it is becoming accepted in the field that oxidation potentials for Z-azobenzenes have *not* actually been determined, and may in fact *never* be found by voltammetry; although they are likely somewhat lower than the E-potentials:

**Experimental measurements aiming to find Z-potentials in bulk solution**, e.g. by standard cyclic voltammetry are difficult. As soon as the Z isomer is oxidized or reduced yielding the respective Z<sup>•+</sup> or Z<sup>•-</sup> radical ion it undergoes rapid isomerization towards the E<sup>•+</sup> or E<sup>•-</sup> radical ion (the Z → E isomerization rates at room temperature can be 14 – 17 orders of magnitude faster for the radical ions compared to the neutral isomers<sup>45,47,49</sup>). Then, in an intermolecular reaction, the E<sup>•+</sup> or E<sup>•-</sup> radical ion is reduced or oxidised to the neutral E isomer by oxidizing or reducing another Z isomer, which propagates an electrocatalytic cycle that very rapidly builds up a "sheath" of E isomer surrounding the working electrode, such that at usual scan rates e.g. <2V/s the main species being measured is always the E, irrespective of what isomer was present before CV started (see for example the experimental potentials in the CRC Handbook, which are identical for E and Z isomers of the same azobenzene).

Laviron and Mugnier instead investigated the reduction potential of Z azobenzene with cyclic voltammetry in 1978, with an increased scan rate of up to 1000 V/s at temperatures down to -36°C, intended to be fast enough to out-compete (Z<sup>•-</sup>→E<sup>•-</sup> | propagation) cycles and measure substantial contribution from the Z isomer. They saw a cathodic shift of the peak potential of up to 60 mV compared to that for the pure E isomer (which was -1.33V vs SCE at those conditions),<sup>50</sup> indicating that the redox potentials are (as expected) isomer-dependent.

Although we found no such studies of E/Z azobenzene oxidation, we believe that in typical azobenzenes, the thermodynamic penalty for electron abstraction is lower in Z-S0 than in E-S0, due to Z having greater lone pair - lone pair repulsion on nitrogens; similar arguments are used to explain the Z's bathochromic shift of the n→π\* band (relative to E).

Oxidation and reduction potentials given in this manuscript are measured at a scan rate of 0.5 V/s at room temperature. Although this would prevent us from measuring the Z isomers' oxidation potential, we are satisfied with accepting that the Z isomers' oxidation potential is slightly lower than those of the E isomers which we *could* measure accurately, and that reproducible and accessible measurements of the E isomers' potential is therefore predictive of whether Z → E (photo)redox isomerization is an accessible pathway, since this matched to the PSS values reached experimentally (>99.5%E when oxidation was possible by this criterion; but when oxidation was not allowed, <98%E (more typically 90%) is observed, as well as different kinetics, and different isomer-dependency of fluorescence intensity (we postulate a triplet mechanism for that energy transfer - see e.g. **NB-AK** in **Fig S5** and **Fig S17**; a study of the triplet mechanism is being preprinted<sup>46</sup> in parallel to this study)).

## 1.3 Note 3 - Full Figure Legends

**Full Legend to Figure 2:** Spectroscopic studies of singlet photoredox switching driven by **NB**. (a) proposed **NB<sup>•+</sup>-AO** decay pathways (nonradiative decay not shown). (b) Spectroelectrochemistry in 100% MeCN showing (**left panel**) spectral and intensity ratio changes during ~100% reduction of **NB** moiety to radical anion **NB<sup>•-</sup>** (as **NB-COOH**), and (**right panel**) overall difference spectrum for **NB**→**NB<sup>•-</sup>** reduction. The difference band maximum in 100% MeCN is at 505 nm (here with ΔAbs = 0.030), the difference band minimum is at 635 nm (corresponds to ΔAbs = -0.054), and the zero-crossing point is at 547 nm. (c) transient absorption spectroscopy (**TAS**) traces during decay of **NB-AO** and **NB-COOH** after excitation at 630 nm.

(d) the TAS subtraction spectral series  $\Delta(\Delta^*Abs(t<520\text{ ps},\lambda))$  for **NB-AO** minus **NB**, normalised "late" (562 ps), in 50:50 MeCN:H<sub>2</sub>O. Note the band maximum for  $t = 0.5\text{-}10\text{ ps}$  at ca. 520 nm, and zero crossing point at ca. 555 nm. (e) Excited state decay kinetics of **NB-COOH**, **NB-AO** and **NB-AK**, read out at 520 nm, each normalized to unity at 2 ps, with lifetime fits. (f)  $\Delta(\Delta^*Abs(t,\lambda))$  for (**NB-AO** minus **NB**) and for (**NB-AK** minus **NB**), at late (562 ps) normalisation (see also full data in Fig S13-S15). (g) Fluorescence lifetimes ( $\tau_{fl}$ ) and quantum yields ( $\Phi_{fl}$ ) for **NB-COOH**, **NB-AO** and **NB-AK** and their physical mixtures.

**Extended Legend to Figure 4j:** **BANG** allows NIR photocontrol over SNAP-mGluR activity in live cells. Relative photo-switch-off rates  $k_{\text{photo-off}}$  were defined as the reciprocal of the *time to 50% switch-off* of cellular GIRK currents during photoswitching phases, where this time was found by direct measurement for shorter times (up to 20 s), or for longer times by extrapolating from a linear fit to the rate of the last four seconds of photo-switch-off (thus  $k_{\text{photo-off}}$  values below  $0.05\text{ s}^{-1}$  are systematically over-estimated, and the true switching rate ratios are higher than the  $\times 6$  and  $\times 74$  shown on the graph). The light source used was unfiltered pE-4000 LED emission, adjusted to constant power.  $k_{\text{photo-off}}$  was not modified to account for spontaneous [thermal] switch-off rates, as these are known to be much slower on the receptor-bound BGAGs than might be expected from protein-free results,<sup>25</sup> and indeed the 740 nm phase **BAG** switchoff was almost undetectable, which establishes an upper bound for the thermal rate as being almost undetectably slow. Data are shown as individual data points, with box and whisker plot (25th-75th percentiles boxed, full max/min range whiskered, thick black line at the geometric mean of the datapoints). Statistical test used: unpaired two-sample t-test, parametric (Gaussian distribution assumed), with no assumption of consistent SDs (Welch t-test) since the magnitude of the error of  $k_{\text{photo-off}}$  strongly depends on its absolute value.

#### 1.4 Note 4 - Photoredox vs triplet energy transfer as dyad switching mechanisms

We classify a dyad as being in one of two conformer types when its chromophore absorbs: "**proximal**", where the motifs are near enough to each other so that the azobenzene HOMO and the  $\pi$ -system of the excited chromophore can overlap (as needed for electron transfer or excited-state reactivity to be efficient); or "**distant**", i.e. too far for overlap. Simplistically, **for singlet-manifold chromophores**, we suggest that re-folding of a conformer between proximal and distant states is unlikely enough within the typical excited state lifetime  $\leq 1\text{ ns}$ , so that we need only consider proximal conformations to understand their entry into the two possible assisted switching pathways, that go via either (a) **photoredox**, or (b) **triplet energy transfer**, which we propose in the parallel paper to this one<sup>46</sup> to proceed in that: (i) the chromophore singlet excited state reacts with the azobenzene to give an exciplex, (ii) the exciplex mediates efficient intersystem crossing (ISC), (iii) the triplet exciplex collapses to an azobenzene triplet (e.g. **NB-AK**<sup>\*T1</sup>), (iv) this triplet can isomerise, giving a mostly-*E* population.

**Note 4.1: By which mechanism will a dyad switch?** (or, "why might **NB-AO** not undergo a triplet mechanism even though **NB-AK** does?") We find that redox potentials predict whether  $\sim 100\%E$  isomerisation is seen or not, supporting that redox compatibility is the priority consideration to determine which mechanism these dyads undergo (we also considered e.g. whether [mis]matching the isolated triplet energies of the azobenzene and chromophore might be determinant, but found that was not consistent with the scope of assisted switching<sup>46</sup>).

Our hypothesis is that in these dyads with **singlet-manifold chromophores**, understanding the population level evolution of the chromophore<sup>\*S1</sup>-Z-Azo needs us to consider the proximal and distant conformation subpopulations separately:

**(1) Distant conformations:** overlap-based mechanisms are not possible; the chromophore singlet excited state decays back to the ground state by its typical mixture of radiative and nonradiative mechanisms. (One corollary is that as the linker becomes longer, the likelihood of distant states increases, so assisted switching will be less probable: **Fig 3c**).

**(2a) Proximal conformations, photoredox is energetically favoured [e.g. NB-AO]:** electron transfer is so fast (TAS suggests  $< 2\text{ ps}$ ; **Fig S14**) that it happens preferentially compared to any exciplex formation (bulk UV-Vis results support that for **NB-AO**, photoredox must be at least  $> 3$ -fold more likely than the triplet pathway, since the experimental long-wavelength

PSSs are >99.5%*E* in **NB-AO** but <98.2%*E* in **NB-AK**; **Fig 3ab**). Redox may even happen for nearly all proximal states, quenching the chromophore<sup>\*S1</sup>: both *E*&*Z*-**NB-AO** fluorescence quantum yields are ca. 8%, not ca. 16% as for **NB-COOH** (**Table S8, Fig S17**), so up to 50% of **NB-AO** may be proximal conformers that undergo redox (*E* & *Z*: cf. **Supporting Note 2**).

**(2b) Proximal conformations, photoredox is not favoured [e.g. NB-AK]:** without redox to quench the proximal states, the intrinsically slower exciplex formation can occur competitively to typical radiative and non-radiative decays. Since neither the *E*/*Z*-**NB-AK** fluorescence quantum yields (**Table S8, Fig S17**) nor its molecular evolution seen in TAS (**Fig S14**) differ greatly from those of **NB-COOH**, we consider that entry to the exciplex/triplet pathway is slow (i.e. occurs to a marginal degree, over the whole lifetime of the singlet excited state) but evolution of the exciplex to its triplet that then collapses is very rapid (i.e. the concentration of exciplex is never higher than e.g. 1-2% of total, which hides it from these TAS measurements).

**Note 4.2, overall switching rates:** Even though our analysis suggests that the entry of *Z*-**NB-AO** into the photoredox route (here estimated at ~25%) is more efficient than entry of *Z*-**NB-AK** into the triplet route (estimated at <8%<sup>46</sup>), the bulk population kinetics of long wavelength isomerisation *from singlet excited state chromophores* are 50-100% faster for what we assign as triplet pathway species than for photoredox species (e.g. **NB-AK** vs **NB-AO**: **Table S1**). Thus we suggest that the route to dyad *Z*→*E* isomerisation is ≥5-fold more efficient from the exciplex than from the radical ion pair. We suggest it is plausible that this is because the azobenzene triplet isomerisation rate is intrinsically fast (literature data: isolated azobenzene triplet *Z*→*E*: <10 ps with  $\Phi \sim 0.98$ ) with no other significantly competitive relaxation pathways, but the intrinsic azobenzene radical cation isomerisation rate is slower enough to compete poorly with electron back-transfer (TAS: ~70 ps half-life, **Fig S14**; such that  $\Phi \leq 0.2$  is seen from the radical ion pair). (*Steric effects could have been proposed instead of intrinsic rates, i.e. that the photoredox radical ion pair e.g. NB<sup>-</sup>-AO<sup>+</sup> might have more restriction on the molecular motions it needs to isomerise than does the spin-collapsed azo-centred triplet e.g. NB-AK<sup>\*T1</sup>, for both in their proximal conformations: but we do not consider this plausible.*)

Testing these two hypotheses will be crucial as part of the campaign to understand and optimise practical dyad switching performance. We are finding them challenging to probe, and we will report the outcomes of those currently ongoing studies at a later date.

**Note 4.3: Caveat triplet-manifold chromophores (high  $\Phi_{ISC}$ ):** if the isolated chromophore has a high chance to enter a triplet with a typical lifetime (e.g. 100  $\mu$ s, i.e. long enough to allow molecular re-folding from a distant to a proximal conformation), then the chromophore-centred triplet may sensitise the photoswitch by triplet energy transfer without needing proximal exciplex-mediated ISC, or it may sensitise any other acceptor (e.g. molecular oxygen): so the simple picture in **Note 4.1** considering only the priorities of photoredox vs triplet pathways in proximal states, must be heavily modified. This is why the high-ISC chromophores, that so far were always used in the "triplet by design" systems outlined in **Supporting Note 1**, bring liabilities: their **distant conformations** obligatorily drive photodamage e.g. by singlet oxygen formation due to competitive transfer to O<sub>2</sub>, so we recommend against them.

**Note 4.4: Caveat spectroelectrochemistry:** we do not consider the time resolution of the spectroelectrochemistry (**Fig 2b**) to be fast enough that its difference spectrum can be unequivocally assigned as (**NB<sup>-</sup> - NB**), given that the reversibility of reduction observed in CV measurement was not ideal (**Appendix 12.1**). Therefore, using this spectrum to assign the peakshape seen in TAS (**Fig 2d**) should not be taken over-confidently. However, we feel that the conclusion of **NB-AO** being able to access photoredox is a robust one, due to the many qualitative differences of **NB-AO** photoswitching and photophysics compared to the non-photoredox control, plus its reasonable timescale.

### 1.5 Note 5 - Biological aspects of singlet photoredox for *Z*-actives (eg BGAG-mGluR)

The field's justified emphasis on developing *Z*-bioactive reagents requires particularly photon-efficient and high-completion *Z*→*E* photoswitching to avoid background activity. However, as outlined in many reports operating at the frontiers of photopharmacology<sup>36,45,46</sup> as well as briefly in the main text, this is the switching direction in which direct azobenzene



photoswitching is photon-inefficient both *intrinsically* (especially due to low  $\epsilon$ ) and *extrinsically* in practice (wavelengths for this switching direction are  $<550$  nm and are strongly scattered and absorbed in biological tissues). This explains the experimentally well-reported need for much longer or more intense periods of cyan/green light  $Z \rightarrow E$  photoswitching, or else for limited-scope fast-relaxing compounds, to shut down bioactivity of these compounds in *practical biological experiments in strongly-scattering environments* (not just 2D cell/slice culture or in retinal applications)<sup>23,25–28</sup>; or still more tellingly, the absence of bidirectional photoswitching applications in true deep tissue settings.

**These three chemical and extrinsic challenges** are all solved by NIR singlet photoredox  $Z \rightarrow E$  switching (photon efficiency, completion, deep tissue penetrance). Relatedly, photoredox switching also solves the **fourth problem** of *avoiding partial compound **activation** in non-targeted areas during attempted off-switching* (which green light illumination unavoidably causes, by scattering driving evolution to the green PSS of typically ca. 20% Z, even in areas that had previously been all-E). The relevance of this effect during tissue-level switching is clear; but it may also be relevant to high-precision neuroscience, in that diffusion of Z-switched receptors out of a target zone (e.g. synaptic cleft) may raise spatial-background signaling levels yet be impossible to fix by typical green light photoswitching: so the *theoretically optimal* (quantitative) switching that photoredox now brings, broadly throughout a sample, should allow steeper spatiotemporal gradients of bioactivity to be maintained over time, in the face of diffusion. A more theoretical picture is given in refs<sup>51,52</sup>.



## 2 UV-VIS spectroscopy and bulk photoisomerisation

### 2.1 UV-VIS, General Methods

#### 2.1.1 UV-VIS setup

The UV-VIS setup used in this paper is shown in **Fig S1a**. UV-VIS experiments were performed with a Cary 60 spectrophotometer (Agilent Technologies). Experiments were done in a 1 cm optical path length, 2 mm wide High Precision Cell (Hellma Analytics 108-002-10-40) filling samples to typically 0.9 cm height (volume 180  $\mu$ L). Typically, 5 or 10 mM DMSO stocks were diluted to 10  $\mu$ M solutions with a mixture of acetonitrile (HPLC grade) and distilled water (1/1 v/v). To exclude impurities from previous runs or dilution of the samples the cuvettes were cleaned after each experiment by rinsing with MeCN (HPLC grade, 3 times) and drying under a stream of nitrogen or compressed air.

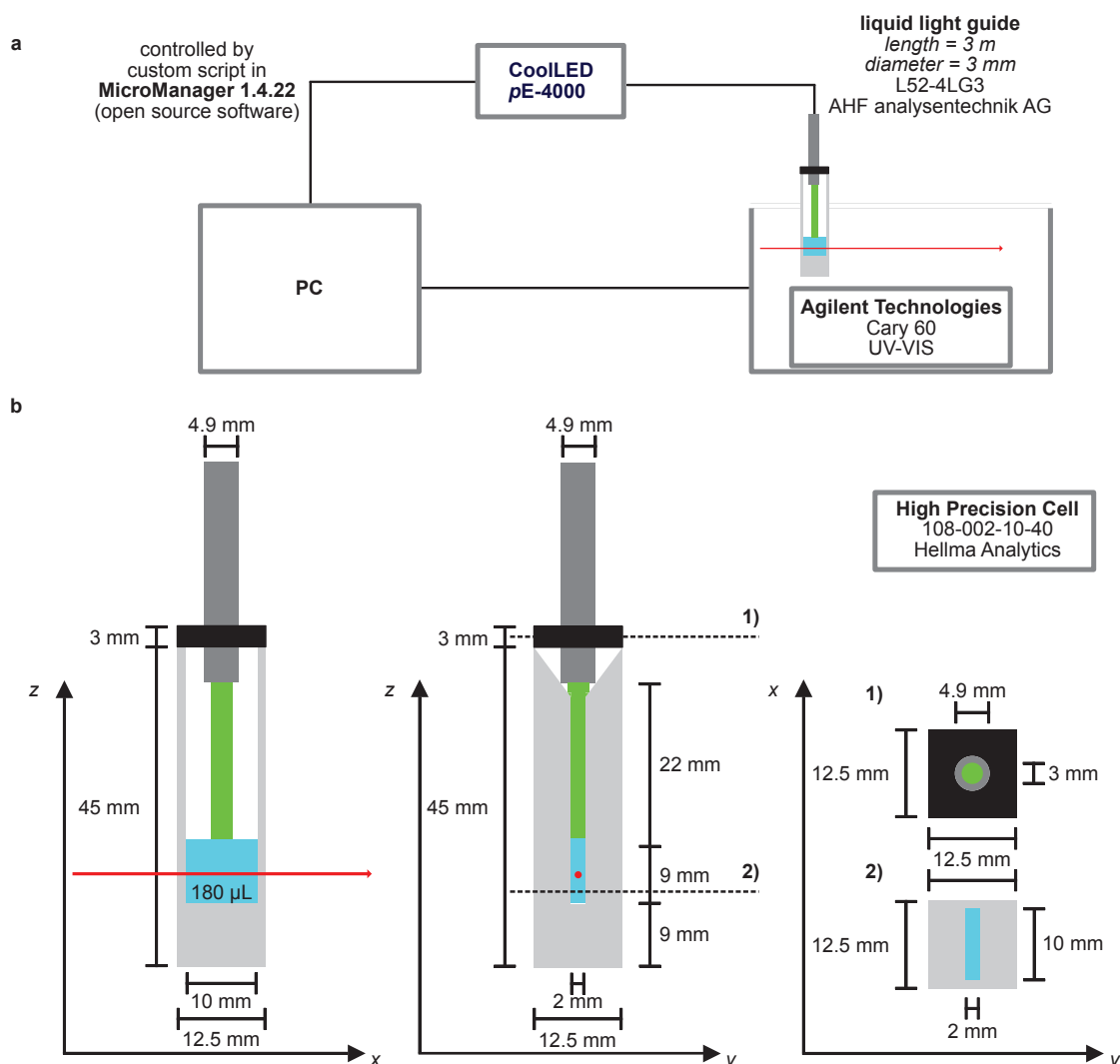


**Figure S1:** UV-Vis setup used in this study: (a) Spectrophotometer and light sources used. (b) Geometric features for illumination during UV-VIS: incl. dimensions of cuvette, sample volume, and light supply from pE-4000.

For medium-intensity sample illumination during UV-VIS, a pE-4000 LED light source was used (CoolLED), controlled through open source software  $\mu$ Manager (version 1.4.22).<sup>53</sup> The light was guided into the cuvette via a liquid light guide (LLG: AHF Analysetechnik AG L52-4LG3; length = 3 m; diameter = 3 mm). If not otherwise stated, the intensity of the LEDs was adjusted to 50 mW/mm<sup>2</sup> at LLG exit. Spectra of the LEDs are given in **Chapter 2.1.3**.

For illumination during UV-VIS, our aim was to ensure reproducible incident intensity profiles throughout the whole sample volume, aiming at applying *homogeneous light intensity throughout the whole sample cell, and having homogeneous analyte concentration throughout*

the cell, under conditions that allow reliable extraction of photoisomerisation rates and timecourses (incl. profiles of approaching PSS). For this we took precautions, including: (1) ensuring constant distance and angle from light guide exit to sample, and constant geometry within each run (over multiple wavelengths) as well as between runs (across multiple samples); and (2) minimising evaporation, so the sample concentrations stay constant and homogeneous throughout the sample cell, even in long experiments. For these, the cuvettes were used with a Teflon lid through which a centered hole (diameter = 4.9 mm, that tightly fits the exit head of the liquid light guide used) was bored. After inserting the light guide, which blocks the bore, the lids were additionally sealed onto the cuvettes using *Parafilm*<sup>®</sup>. The dimensions and setup for the cuvette and attached illumination sources are shown in **Fig S1b** (pE-4000 LED source). We also made sure that (3) the light guide was positioned at such a distance, that the whole sample cell volume experiences similar light intensity; (4) stray incident light is blocked/minimised; (5) optical path length (typically 9 mm to bottom of cuvette, but only ca. 5 mm to bottom of optical window) was small enough, so that at the analyte concentrations and the applied illumination wavelengths used, typically less than 25% of the illumination beam intensity was lost through the sample (i.e. relatively homogeneous illumination intensities, and no significant inner filter / shielding effects).

### 2.1.2 General Methods for UV-VIS and bulk photoisomerisation

**Action spectra** were recorded by measuring an UV-Vis spectrum (from 750 – 300 nm) every 10 s. Azobenzene-containing samples (10  $\mu$ M, dilution prepared as detailed in chapter 2.2.1) were applied in their all-*trans* state (enabled by keeping the DMSO stock at 60 °C overnight before measurements, then taking precautions for light exclusion by the usage of amber glass vials and aluminum foil). After measuring spectra of the all-*E* sample for 5 min (to ensure constant absorption), the illumination protocol of the pE-4000 light source was started. Alternating cycles of 365 nm (1 min at 50 mW/mm<sup>2</sup>) and  $\lambda_2$  ( $\lambda_2 = 770$  nm, 740 nm, 660 nm, 635 nm, 595 nm, 525 nm, 490 nm, 460 nm, 435 nm, 405 nm, and 385 nm, each 5 min at 10 mW/mm<sup>2</sup>) were performed. The usual total measurement time was 72 min. The data were analyzed by extracting the absorbance values over time at the absorption maximum of the azobenzene *E*-isomer. Isomeric ratios at 2 or 3 photostationary states were determined orthogonally by HPLC analysis (see **chapter 5.1**) and those HPLC data were used to transform UV-Vis absorbance values into %-*trans* values by calibration (see **chapter 5.2**).

**Analysis:** Curve fitting (e.g. monoexponential fits for thermal relaxation or illumination-stimulated photoisomerisations) was performed in Graphpad Prism 8 software for MacOS.

### 2.1.3 Light Source Properties for bulk photoisomerisations

By default, we wished to characterise *approximately* how not only the compound photostationary states, but also their bulk photoisomerisation rates, depend on illumination wavelength, across the UV-VIS spectrum. These in turn depend on the wavelength/intensity profiles of the [LED] light sources used.

In all cases, we were content to use the pE-4000 as a cost-effective fixed array of LED wavelengths, most of which have acceptably narrow emission profiles ca. FWHM~20-30 nm (**Fig S2a**), making use of their relatively high intensities (**Fig S2b-c**) to rapidly approach PSSs during photoswitching and to study many compounds serially, and with calibrated and reproducible performance that is quite accurately intensity- and time-modulated through the control software. In this way we could profile relative rates of approaching PSS, and PSS composition, with values that were *technically reproducible* and which are informative for general performance in other chemical or biological applications, under either LED or narrower (laser, filtered, or monochromatised) light sources. (When incident intensity powers are quoted, these are understood as total optical power over the LED emission spectrum).

The "PSS" values obtained with LEDs are not truly reproducible single-wavelength values; but only in some settings were LED sources insufficient to characterise the *intrinsic performance of the conjugates*. Principally this occurs when LED sources illuminate at spectral regions where the photoisomerisation response changes *both rapidly and meaningfully* with wavelength; which is the case (1) between the photoswitch's  $\pi \rightarrow \pi^*$  and  $n \rightarrow \pi^*$  bands [typically

in the region 360-430 nm], and/or (2) where the fraction of the absorption coefficient that is due to the photoswitch ("direct excitation") rather than the antenna chromophore is high, but changes rapidly with wavelength (typically also in the region 360-430 nm, but some photoswitch-antenna pairs have additional regions of sensitivity where the antenna absorption is comparable to the photoswitch's but one increases as the other decreases).

We also note that it will always be possible to find a monochromatic wavelength that gives *equal or greater completion* of photoisomerisation, than can any broader source (e.g. LED). Therefore, the PSS values obtained with the pE-4000 offer the *minimum* performance that a compound can achieve.

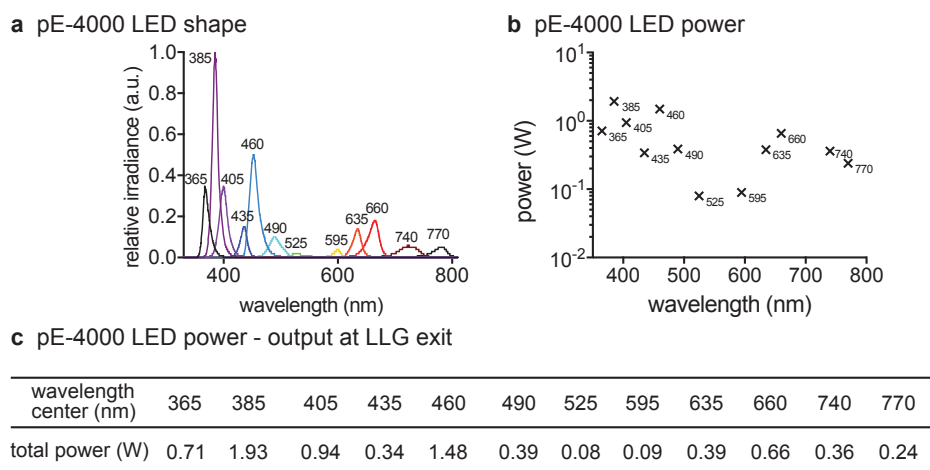


**Figure S2:** (a) Spectral power and (b-c) maximum optical output power from a pE-4000 as reported at the exit of a liquid light guide of same specifications as used in this work (data provided by *CoolLED Ltd*; our measurements matched the relative total powers; light guide diameter 3 mm [7 mm<sup>2</sup> exit] ; 100% intensity setting).

## 2.2 Thermal Relaxation

Other than the BGAGs, the major azobenzenes in this work all have far slower spontaneous relaxation under normal cell-free assay conditions than any rates of photoswitching (**Fig S3**).

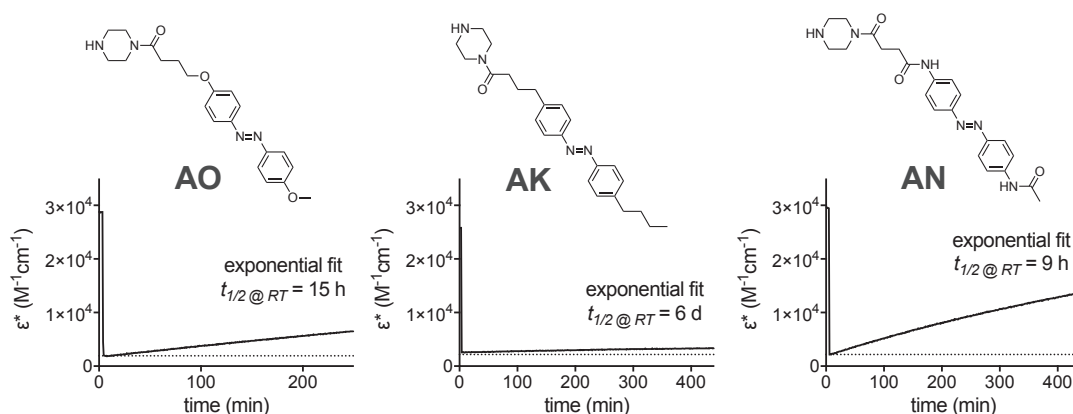


**Figure S3:** Thermal relaxation of photoswitches **AO**, **AK** and **AN** was performed at 10 μM in water/acetonitrile (50/50) at room temperature. PSS<sub>LED-365</sub> was reached by illumination with 365 nm LED (50 mW/mm<sup>2</sup>) until constant absorbance, then illumination was stopped and absorbance was monitored for long enough to perform an accurate first-order fit.  $\epsilon^*$  is the apparent molar extinction coefficient of the *E/Z* mixture (see **chapter 2.5**).

These results are particularly relevant for intermolecular measurements, as they argue that the quantitative *Z*→*all-E* isomerization observed with red light illumination of the **NB+AO** physical mixture (experimental half-time ca. 10 min) was not spontaneous thermal relaxation of the **AO**, nor is it likely, under these dilute settings at room temperature, to be photothermal relaxation: thus supporting the intermolecular singlet photoredox-based mechanism (**Fig 1c**).

### 2.3 Bulk Population Photoswitching

Kinetics for photoisomerizations were recorded by monitoring absorbance at a single wavelength (e.g. **AO**: 358 nm; **AK**: 337 nm; **AN**: 369 nm) with one datapoint every 0.0375 s. For physical mixture kinetics of **NB-COOH** and **AO**, one datapoint was taken every 30 s.

To ensure that reproducible data were being acquired (e.g. negligible inner filter effect through the sample; negligible rate errors introduced by the resolution limitation of 0.0375 s as data interval, that could reduce accuracy for analysing fast isomerisations at high powers), we acquired multiple kinetic runs while stepping down the incident power over a 20-fold range (from 353 down to 18 mW, which is the minimum rated power for some LEDs in the pE-4000 source). Monoexponential fitting was used to extract half-time  $t_{1/2}$ ; after adjusting for the illumination power applied, the half-powers  $p_{1/2}$  were calculated. Fits are shown in **Fig S4**, and the parameters, with fit  $r^2$  values, are given in **Table S1**. From our experience with stepping intensities here and in other work, we assume that data acquired with half-time  $\geq 5$ -10 s, and at intermediate powers  $\sim 35$  - 70 mW/mm<sup>2</sup>, is most likely to be accurate; however, we note that the agreement between values is rather satisfying.

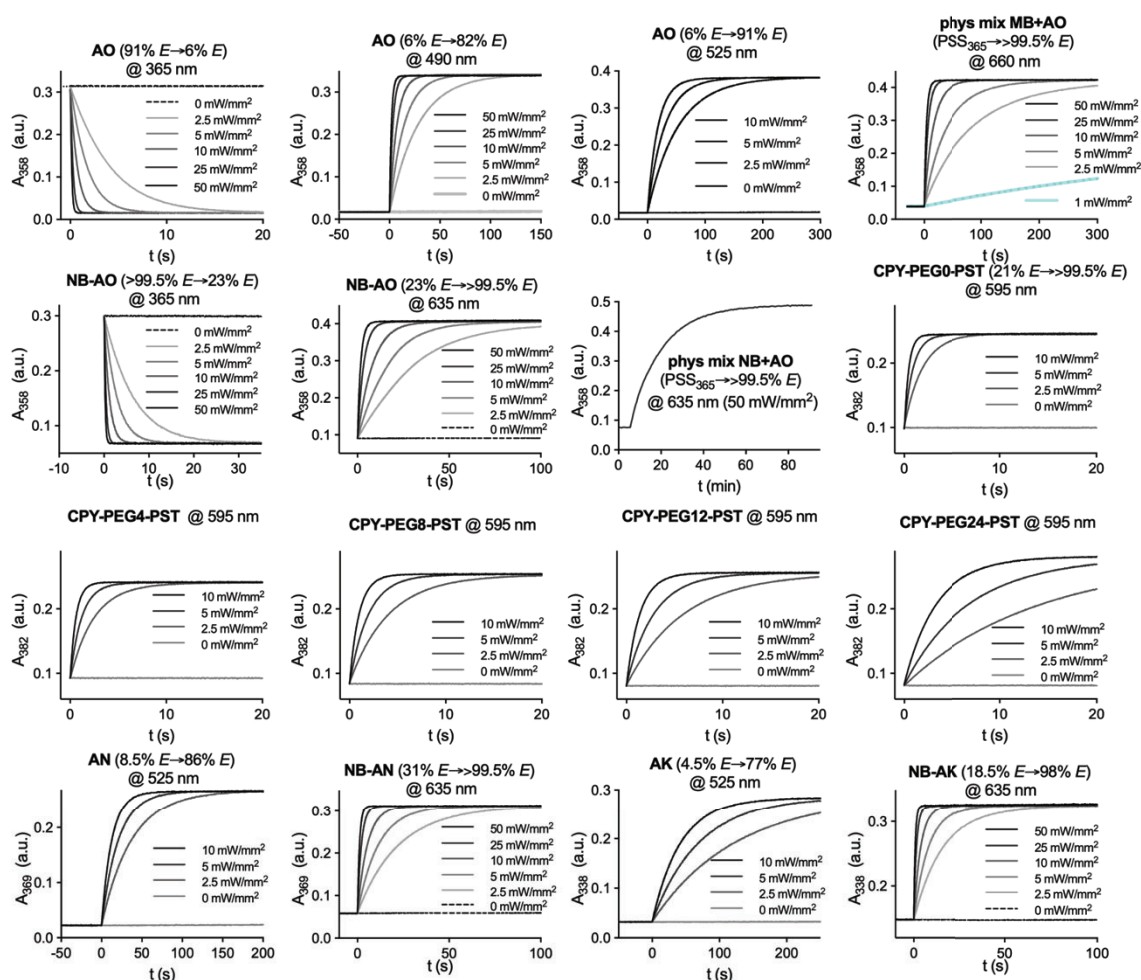


**Figure S4:** *Cis*→*trans* and *trans*→*cis* isomerization of selected compounds at different illumination powers (here indicated as light intensities at liquid light guide exit, for 3 mm LLG). For the **CPY-PEG<sub>n</sub>** series, HPLC calibration of %E was performed only for **PEG0**, but we assume from the good match between their absorbance data that the other series members' isomerisation plots under 595 nm are also for ca. 21%→99.5%E (**Table S1**).

Note: based on the Stern-Volmer equation, intermolecular excited state quenching rates depend on (i) the excited state lifetime, and (ii) the local concentration of the quencher: thus a 250-fold slower kinetic for a singlet-manifold (**NB**:  $\tau_{fl} = 1.3$  ns) than triplet-manifold (**MB**:  $\tau_T = 65$   $\mu$ s) intermolecular reaction is plausible (the rate ratio should not be directly proportional to the lifetime ratio however, since beyond a certain lifetime limit, quenching by either azobenzene or O<sub>2</sub> is practically ensured, thus there are diminishing returns for long  $\tau_T$ ).<sup>54–56</sup>

**Table S1:** pE-4000 output power (at indicated wavelength), and the half-time, half-power, and goodness of fit parameter for *cis*→*trans* and *trans*→*cis* isomerizations of selected mixes / compounds. Half-powers are the power applied (in a mostly-optically-transparent sample, since low concentration and path length), which gives a better description of the practical efficiency of photoswitching for the user than does the more typical "power absorbed". Note that the efficiency of isomerisation at 365 nm is similar between **AO** and **NB-AO**.

LLG Optical Output Power, Total [mW]	phys mix NB+AO [PSS <sub>365</sub> → >99.5% E] @ 635 nm: p <sub>1/2</sub> ~ 11 J/mm <sup>2</sup>			phys mix MB+AO [PSS <sub>365</sub> → >99.5% E] @ 660 nm: p <sub>1/2</sub> ~ 45 mJ/mm <sup>2</sup>			AK [4.5% E → % 77% E] @ 525 nm: p <sub>1/2</sub> ~ 89 mJ/mm <sup>2</sup>		
	t <sub>1/2</sub> [s]	p <sub>1/2</sub> [J/mm <sup>2</sup> ]	R <sup>2</sup>	t <sub>1/2</sub> [s]	p <sub>1/2</sub> [mJ/mm <sup>2</sup> ]	R <sup>2</sup>	t <sub>1/2</sub> [s]	p <sub>1/2</sub> [mJ/mm <sup>2</sup> ]	R <sup>2</sup>
353.5	609.5	11	0.9997	2.6	46	0.9995	[a]	-	-
176.8	-	-	-	4.5	40	0.9997	[a]	-	-
70.7	-	-	-	11.2	40	0.9998	29.5	104	0.9999
35.4	-	-	-	28.3	50	0.9997	48.5	86	1.0000
17.7	-	-	-	58	51	0.9999	86.1	76	1.0000
<b>NB-AO</b> [23% E → >99.5% E] @ 635 nm: p <sub>1/2</sub> ~ 20 mJ/mm <sup>2</sup>			<b>NB-AN</b> [31% E → >99.5% E] @ 635nm: p <sub>1/2</sub> ~ 14 mJ/mm <sup>2</sup>			<b>NB-AK</b> [18.5% E → 98% E] @ 635 nm: p <sub>1/2</sub> ~ 10 mJ/mm <sup>2</sup>			
OOPT [mW]	t <sub>1/2</sub> [s]	p <sub>1/2</sub> [mJ/mm <sup>2</sup> ]	R <sup>2</sup>	t <sub>1/2</sub> [s]	p <sub>1/2</sub> [mJ/mm <sup>2</sup> ]	R <sup>2</sup>	t <sub>1/2</sub> [s]	p <sub>1/2</sub> [mJ/mm <sup>2</sup> ]	R <sup>2</sup>
353.5	1.3	22	0.9839	0.8	14	0.9965	0.6	10	0.9592
176.8	2.3	21	0.9959	1.5	13	0.9982	1.1	10	0.9884
70.7	5.6	20	0.9995	3.7	13	0.9996	2.6	9	0.9985
35.4	11.1	20	0.9994	7.9	14	0.9998	5.6	10	0.9994
17.7	21	19	0.9995	15.7	14	0.9949	11.2	10	0.9998
<b>NB-AO</b> [>99.5% E → 23% E] @ 365 nm: p <sub>1/2</sub> ~ 3 mJ/mm <sup>2</sup>			<b>AO</b> [91% E → 6% E] @ 365 nm: p <sub>1/2</sub> ~ 2 mJ/mm <sup>2</sup>			<b>AN</b> [8.5% E → 86% E] @ 525 nm: p <sub>1/2</sub> ~ 27 mJ/mm <sup>2</sup>			
OOPT [mW]	t <sub>1/2</sub> [s]	p <sub>1/2</sub> [mJ/mm <sup>2</sup> ]	R <sup>2</sup>	t <sub>1/2</sub> [s]	p <sub>1/2</sub> [mJ/mm <sup>2</sup> ]	R <sup>2</sup>	t <sub>1/2</sub> [s]	p <sub>1/2</sub> [mJ/mm <sup>2</sup> ]	R <sup>2</sup>
353.5	0.2	2.9	0.9797	0.1	1.7	0.9886	[a]	-	-
176.8	0.3	2.6	0.9913	0.2	1.6	0.9953	[a]	-	-
70.7	0.8	2.8	0.9967	0.5	1.7	0.9987	8.9	31	0.9998
35.4	1.9	3.3	0.9985	1.2	2.0	0.9994	14.7	26	0.9998
17.7	4.3	3.8	0.9992	2.7	2.4	0.9996	26.3	23	0.9999
<b>AO</b> [6% E → 82% E] @ 490 nm: p <sub>1/2</sub> ~ 19 mJ/mm <sup>2</sup>			<b>AO</b> [6% E → 91% E] @ 525 nm: p <sub>1/2</sub> ~ 38 mJ/mm <sup>2</sup>			<b>CPY-PEG0-PST</b> [21% E → >99.5% E] @ 595 nm: p <sub>1/2</sub> ~ 1 mJ/mm <sup>2</sup>			
OOPT [mW]	t <sub>1/2</sub> [s]	p <sub>1/2</sub> [mJ/mm <sup>2</sup> ]	R <sup>2</sup>	t <sub>1/2</sub> [s]	p <sub>1/2</sub> [mJ/mm <sup>2</sup> ]	R <sup>2</sup>	t <sub>1/2</sub> [s]	p <sub>1/2</sub> [mJ/mm <sup>2</sup> ]	R <sup>2</sup>
353.5	1.3	23	0.9998	[a]	-	-	[a]	-	-
176.8	2.2	20	0.9998	[a]	-	-	[a]	-	-
70.7	4.9	18	0.9999	12.6	45	0.9999	0.3	1.1	0.9854
35.4	9.9	18	0.9999	20.6	36	1	0.7	1.2	0.9889
17.7	19.5	17	0.9999	36.6	32	1	1.4	1.2	0.9978
<b>CPY-PEG4-PST</b> @ 595 nm: p <sub>1/2</sub> ~ 1 mJ/mm <sup>2</sup>			<b>CPY-PEG8-PST</b> @ 595 nm: p <sub>1/2</sub> ~ 3 mJ/mm <sup>2</sup>			<b>CPY-PEG12-PST</b> @ 595 nm: p <sub>1/2</sub> ~ 4 mJ/mm <sup>2</sup>			
OOPT [mW]	t <sub>1/2</sub> [s]	p <sub>1/2</sub> [mJ/mm <sup>2</sup> ]	R <sup>2</sup>	t <sub>1/2</sub> [s]	p <sub>1/2</sub> [mJ/mm <sup>2</sup> ]	R <sup>2</sup>	t <sub>1/2</sub> [s]	p <sub>1/2</sub> [mJ/mm <sup>2</sup> ]	R <sup>2</sup>
353.5	[a]	-	-	[a]	-	-	[a]	-	-
176.8	[a]	-	-	[a]	-	-	[a]	-	-
70.7	0.4	1.4	0.9967	0.7	2.5	0.9903	1	3.5	0.9967
35.4	0.8	1.4	0.9985	1.4	2.5	0.9976	2	3.5	0.9978
17.7	1.7	1.5	0.9993	2.9	2.6	0.9991	4.2	3.7	0.9991
<b>CPY-PEG24-PST</b> @ 595 nm: p <sub>1/2</sub> ~ 9 mJ/mm <sup>2</sup>									
Power [mJ]	t <sub>1/2</sub> [s]	p <sub>1/2</sub> [mJ/mm <sup>2</sup> ]	R <sup>2</sup>						
353.5	[a]	-	-						
176.8	[a]	-	-						
70.7	2.4	8.5	0.999						
35.4	4.9	8.7	0.9995						
17.7	10.2	9.0	0.9997						

[a] = not tested, since the maximum 525 / 595 nm LED power at light guide output is 10 mW/mm<sup>2</sup> with 3 mm LLG.



## 2.4 UV-Vis spectra and action spectra of non-photoredox control NB-AK

We characterized non-photoredox control **NB-AK** (mismatched potentials) and azobenzene moiety **AK** in a parallel study,<sup>46</sup> but data are reproduced here for comparison:

Action spectra showed red-light response for **NB-AK** of up to 98% *trans* isomer at 660 nm, although none for **AK**. Nevertheless, the difference between 98% (**NB-AK**) and >99.5% *trans* isomer completion (e.g. **NB-AO**) is conclusive - it demarcates the mechanisms of singlet-manifold photoredox-induced isomerization reported here (~complete), and the triplet energy transfer induced isomerization in the other study (at best, near-complete).

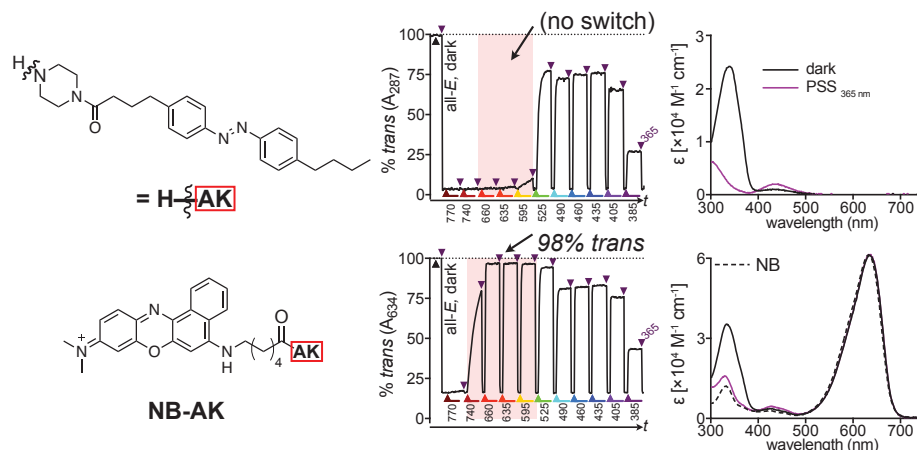


**Figure S5:** Structure, action spectra and UV-Vis spectra of azobenzene **AK** and non-photoredox control azobenzene-fluorophore conjugate **NB-AK**; reprinted from our parallel paper on photosensitization.

## 2.5 Extinction coefficient determination

The data used for extinction coefficient determination were collected for this study and a parallel study, and are shown in both.<sup>46</sup>

We determined the molar extinction coefficients  $\epsilon$  of isolated fluorophores in 1:1 MeCN:H<sub>2</sub>O mixtures. Two 10 mM DMSO stocks of each compound were prepared (compound weight > 1 mg). The stocks were diluted 1:100 (990  $\mu$ L 1:1 MeCN:H<sub>2</sub>O and 10  $\mu$ L DMSO stock) then 1:10 (900  $\mu$ L 1:1 MeCN:H<sub>2</sub>O and 100  $\mu$ L 1:100 dilution) to reach a final concentration of 10  $\mu$ M. Each stock was diluted 3 times independently, giving 6  $\epsilon$  values for each compound. **Fig S6a** shows the mean and standard deviation of  $\epsilon$  from each stock; the six datapoints were then pooled for overall  $\epsilon$  values (**Table S2**). We assumed that the conjugates'  $\epsilon$  values at wavelengths >550 nm are essentially the same as the fluorophores; this was supported by the additivity of spectra [e.g.  $\epsilon(\lambda)_{E-NB-AO} \approx \epsilon(\lambda)_{NB} + \epsilon(\lambda)_{E-AO}$ ; **Fig S6b**].

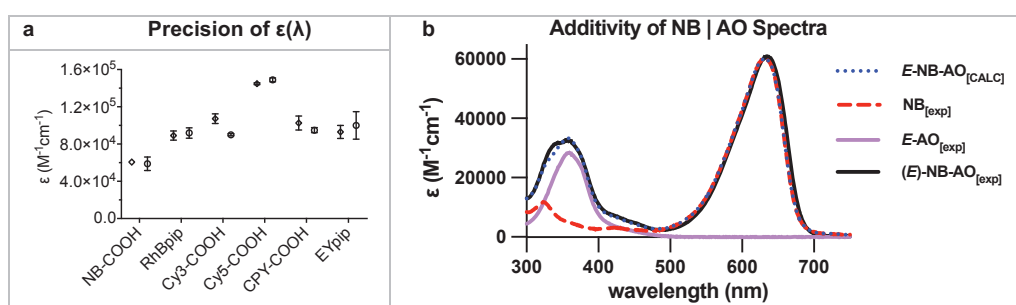


**Figure S6:** (a) Experimentally determined molar extinction coefficients  $\epsilon$ , with errors, for 2 independently prepared stocks for each compound, each evaluated in triplicates; (b) spectral additivity shown for NB-AO.

**Table S2:** Fluorophore molar extinction coefficients  $\epsilon$  at  $\lambda_{max}$  in 1:1 water:MeCN mixture with standard deviation as a mean of 6 datapoints.

	$\lambda_{max}$	$\epsilon(\lambda_{max})$ ( $\times 10^3 M^{-1} cm^{-1}$ )	SD $\epsilon(\lambda_{max})$ ( $\times 10^3 M^{-1} cm^{-1}$ )	n
<b>NB-COOH</b>	634	60	5	6
<b>RhBpip</b>	564	91	5	6
<b>Cy3-COOH</b>	546	99	10	6
<b>Cy5-COOH</b>	643	147	3	6
<b>CPY-COOH</b>	608	99	6.5	6
<b>EYpip</b>	533	97	11	6

We then wished to assign *effective molar extinction coefficients* in the UV, at the  $\pi \rightarrow \pi^*$  band maximum wavelength for the *E*-azobenzene motifs within each conjugate (determined separately, **Fig S9**: e.g. maximum 338 nm for **AK**). The effective  $\epsilon$  for the azobenzene *moieties* within the azobenzene-fluorophore conjugates were then calculated as

$$\text{effective } \epsilon (\text{azobenzene}) = \epsilon (\text{fluorophore-azobenzene}) - \epsilon (\text{fluorophore})$$

and "mean" values were found by averaging over values available (**Table S3**).

**Table S3:** Effective calculated extinction coefficients  $\epsilon$  of azobenzene **moieties** at  $\lambda_{max}$  in 1:1 water:MeCN (means from different fluorophores where possible).

$\epsilon$ ( $\times 10^3 M^{-1} cm^{-1}$ )	$\epsilon$ (Cy3-X – Cy3-COOH)	$\epsilon$ (RhB-X – RhBpip)	$\epsilon$ (NB-X – NB-COOH)	$\epsilon$ (Cy5-X – Cy5-COOH)	$\epsilon$ (EY-X – EYpip)	$\epsilon$ (CPY-X – CPY-COOH)	mean $\epsilon(X)$ at $\lambda$
X = <b>AK</b>	20.1	21.6	21.5	35.6	21.9		<b>24</b> at 338 nm
X = <b>AO</b>	22.9	26.0	27.8	/	/		<b>25.5</b> at 358 nm
X = <b>AN</b>	26.7	28.4	31.6	/	/		<b>29</b> at 369 nm
X = <b>PST2</b>	/	/	/	/	/	29.3	29 at 371 nm
X = <b>BAG / BGAG<sub>12,400</sub></b>	/	/	26.9	26.3 (v1) 29.4 (v2)	/	/	<b>27.5</b> at 377 nm
X = <b>AO(OMe)<sub>4</sub></b>	/	/	14.4	/	/	/	14 at 331 nm

### 3 Fluorophores: fluorescence excitation / emission spectra

Excitation and emission spectra were recorded with a Cary Eclipse Spectrophotometer from Agilent Technologies. Experiments were performed in a 1 cm × 3 mm fluorescence cuvette (Hellma Analytics, 105-251-15-40). 10 mM DMSO stocks were diluted to 1  $\mu$ M samples in acetonitrile (HPLC grade), except fluorescein and quinacrin which were measured at 10  $\mu$ M.

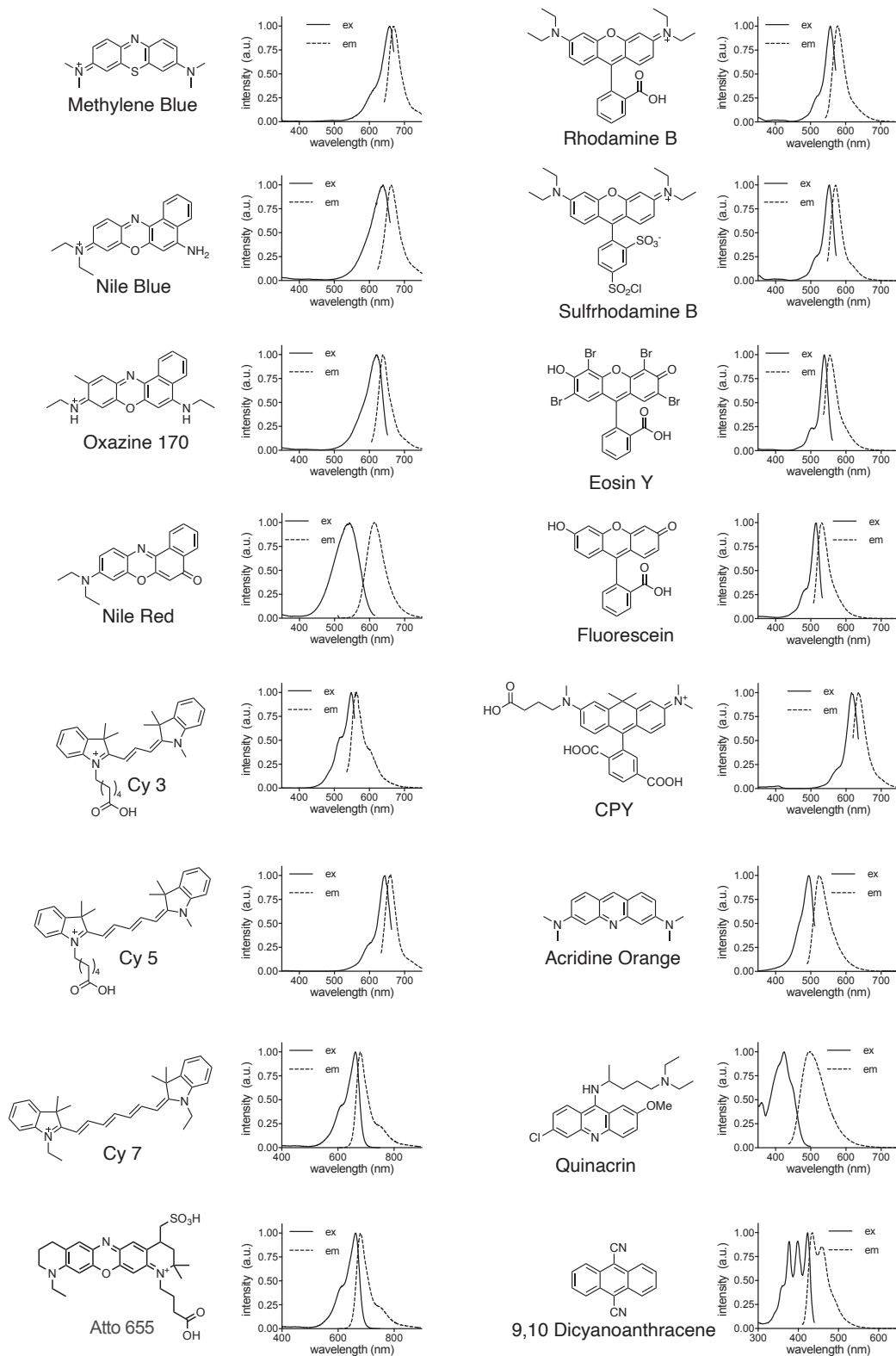


**Figure S7:** excitation / emission spectra measured for common fluorophores selected from **Table 1** (except the extinction and emission spectra of Atto 655 which were taken from <https://www.atto-tec.com/ATTO-655.html>, data measured in PBS, last visited 15.09.2022). Excitation and emission data were normalized to 1 at maxima.

## 4 Electrochemistry in ground and photoexcited states

### 4.1 Experimental reduction/oxidation potentials in ground state: chromophores

Redox potentials were determined in acetonitrile on a CH Instruments 630E electrochemical analyzer using a 2 mm diameter platinum working electrode, a platinum wire counter electrode, and an Ag wire pseudo-reference electrode. Ground state reduction and oxidation potentials of all compounds were determined in MeCN under argon with 0.1 M NBu<sub>4</sub>CIO<sub>4</sub> unless otherwise stated. Both cyclic voltammetry (CV, scan rate: 0.5 V/s) and square wave voltammetry (SWV, frequency: 15 Hz, increment E: 0.004 V, amplitude: 0.025 V) were used, applying ferrocene as an internal standard. Where the oxidation was found to be irreversible in CV, only peak potentials ( $E_p$ ) could be determined by both CV and SWV; but the reduction was reversible in most cases so reduction potentials  $E_{1/2}$  could usually be determined. Such cases are annotated.

Excitation and emission maxima were extracted from fluorescence spectra (**Fig S7**). The optical gap  $E_{00}$  was calculated from the intersection of excitation and emission spectra. Excited state reduction potentials were calculated by the Rehm-Weller equation:

$$E_{\text{red}}^{\text{S1}} = E_{\text{red}}^{\text{S0}} + E_{00}$$

with  $E_{\text{red}}^{\text{S1}}$ : excited state reduction potential,  $E_{\text{red}}^{\text{S0}}$ : ground state reduction potential, and  $E_{00}$ : energy difference between the ground and first excited neutral states as calculated from the intersection of the normalized excitation and emission spectra (corresponds to optical gap [eV] in **Table 1**).<sup>57–59</sup> All results are collected in **Table S4**, selected results in **Table 1**.

**Table S4:** Ground state redox properties which were measured experimentally in this work, for selected chromophores / fluorophores. Underline highlights a matched pair of redox potentials for Cy 5 that are numbered differently between the study methods (see **Appendix: CV and SWV**).

	CV vs. Fc				SWV vs. Fc			
	$E_{\text{ox},1}$	$E_{\text{ox},2}$	$E_{\text{red},1}$	$E_{\text{red},2}$	$E_{p,\text{ox}1}$	$E_{p,\text{ox}2}$	$E_{p,\text{red}1}$	$E_{p,\text{red}2}$
Sulforhodamine B	0.79 <sup>[a]</sup>		-1.15 <sup>[b]</sup>	-1.36 <sup>[a]</sup>	0.78		-1.07	-1.36
Cy 5	0.35 <sup>[b]</sup>	<u>0.48<sup>[b]</sup></u>	-1.28 <sup>[b]</sup>		<u>0.46</u>	1.79	-1.22	
Acridine Orange	0.32 <sup>[b]</sup>	0.77 <sup>[b]</sup>	[d]	-2.40 <sup>[b]</sup>	0.36	0.68	[d]	-2.34
Methylene Blue	0.85 <sup>[b]</sup>		-0.72 <sup>[a]</sup>		0.82	1.56	-0.76	-1.48
Cy 7	[c]		-1.14 <sup>[b]</sup>		1.78		-1.07	
Oxazine 170	0.75 <sup>[a]</sup>		-0.81 <sup>[a]</sup>	-1.66 <sup>[a]</sup>	0.75		-0.83	-1.66
CPY	0.66 <sup>[b]</sup>		-1.09 <sup>[b]</sup>		0.63		-1.04 <sup>[d]</sup>	-1.64 <sup>[d]</sup>
Cy 3	0.63 <sup>[a]</sup>		-1.37 <sup>[b]</sup>	-1.48 <sup>[b]</sup>	0.63		-1.30	-1.44
Rhodamine B, Cl <sup>-</sup> salt	0.78 <sup>[a]</sup>		-1.02 <sup>[b]</sup>	-1.58 <sup>[a]</sup>	0.79		-0.94	-1.58
<i>Rhodamine B, PF<sub>6</sub><sup>-</sup> salt*</i>	0.82 <sup>[a]</sup>		-1.26 <sup>[b]</sup>					
<i>Rhodamine B piperazinamide, Cl salt*</i>	0.81 <sup>[b]</sup>		-1.25 <sup>[a]</sup>					
<i>Rhodamine B methyl ester, PF<sub>6</sub><sup>-</sup> salt*</i>	0.86 <sup>[a]</sup>		-1.27 <sup>[a]</sup>					
<i>Nile Blue, ClO<sub>4</sub><sup>-</sup> salt*</i>	0.81 <sup>[b]</sup>		-0.80 <sup>[b]</sup>					
<i>Fluorescein methyl ester*</i>	0.98 <sup>[b]</sup>		-1.61 <sup>[b]</sup>					

[a] reversible, value corresponds to  $E_{1/2}$ . [b] peak potential. [c] not resolved. [d] possible lower lying reduction potential not clearly resolved. \* data measured with scan rate = 1 V/s, in 0.1 M Bu<sub>4</sub>NPF<sub>6</sub> in acetonitrile.

Regarding **Table 1**, note that where literature values in V vs. SCE were used, these have been converted using (V vs. Fc) = (V vs. SCE) – 0.40 V according to Connelly and Geiger<sup>60</sup>. They also note that corrections for Fc are electrolyte-dependent (e.g. 0.40 V with [NBu<sub>4</sub>][PF<sub>6</sub>] but 0.38 V with [NBu<sub>4</sub>][ClO<sub>4</sub>]); however, (a) slightly different correction values are given elsewhere<sup>61</sup>, and (b) the differences are small relative to the values of interest in this work: so we are content to keep the correction simple, practical, and fit for purpose.

## 4.2 Experimental reduction/oxidation potentials in ground state: azobenzenes

Ground state redox properties of a set of azobenzene chemotypes (**Fig S8** on the next page) were measured in electrochemistry as for the chromophores detailed in **Section 4.1**. As discussed in **Supporting Note 2**, we interpret all their redox properties measured under these conditions (**Table S5**) as belonging to the *E* isomer of the azobenzenes, that can be formed locally then catalytically propagate around the electrode. We assume the oxidation potential of the *Z*-isomer to be somewhat lower than of the *E*-isomers, perhaps by ~0.06 V.

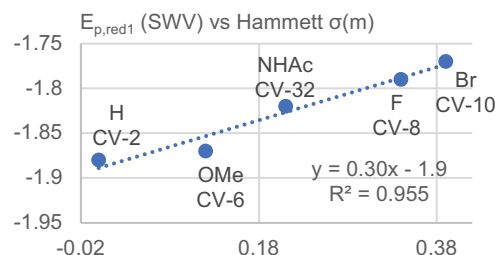
**Table S5:** Ground state reduction and oxidation potentials of a library of 33 *E*-azobenzenes determined by cyclic voltammetry and square wave voltammetry. Data are given in V vs Fc. Chemical structures shown in **Fig S8**.

Azo	CV, vs. Fc				SWV, vs. Fc				
	$E_{ox,1}$	$E_{ox,2}$	$E_{red,1}$	$E_{red,2}$	$E_{p,ox1}$	$E_{p,ox2}$	$E_{p,ox3}$	$E_{p,red1}$	$E_{p,red2}$
CV-1	0.23 <sup>[b]</sup>	0.74 <sup>[b]</sup>	-2.16 <sup>[b]</sup>		0.20	0.66		-2.11	
CV-2	0.94 <sup>[b]</sup>	1.08 <sup>[b]</sup>	-1.88 <sup>[a]</sup>		0.74	1.04	1.76	-1.88	
CV-3	0.66 <sup>[b]</sup>	0.83 <sup>[b]</sup>	-1.76 <sup>[a]</sup>		0.66	0.84	1.60	-1.76	
CV-4	0.55 <sup>[b]</sup>	0.82 <sup>[b]</sup>	-1.97 <sup>[a]</sup>		0.83	[d]		-1.96	
CV-5	0.83 <sup>[b]</sup>	0.93 <sup>[b]</sup>	-1.78 <sup>[b]</sup>		0.79	0.96	1.80	-1.74	
CV-6	0.89 <sup>[b]</sup>		-1.86 <sup>[a]</sup>		0.89	0.97		-1.87	
CV-7	0.93 <sup>[b]</sup>		-1.83 <sup>[a]</sup>		0.96			-1.85	
CV-8	1.00 <sup>[b]</sup>		-1.78 <sup>[a]</sup>		1.05	1.77		-1.79	
CV-9	1.04 <sup>[b]</sup>		-1.67 <sup>[a]</sup>		1.05			-1.71	
CV-10	0.99 <sup>[b]</sup>		-1.77 <sup>[a]</sup>		1.02	1.74		-1.77	
CV-11	0.95 <sup>[b]</sup>		-1.75 <sup>[a]</sup>		1.00	1.81		-1.75	-1.99
CV-12	0.82 <sup>[b]</sup>	1.03 <sup>[b]</sup>	-1.71 <sup>[a]</sup>		0.84	1.04	1.85	-1.71	
CV-13	0.45 <sup>[b]</sup>	1.04 <sup>[b]</sup>	-1.94 <sup>[a]</sup>		0.44	1.07		-1.96	
CV-14	0.98 <sup>[b]</sup>	1.99 <sup>[b]</sup>	-1.78 <sup>[a]</sup>						
CV-15	0.77 <sup>[b]</sup>		-1.78 <sup>[a]</sup>						
CV-16	0.64 <sup>[b]</sup>	0.83 <sup>[b]</sup>	-1.85 <sup>[a]</sup>		0.80			-1.78	
CV-17	[c]		[d]	-1.37 <sup>[a]</sup>	0.65	0.94		-1.87	
CV-18	0.49 <sup>[b]</sup>	0.72 <sup>[b]</sup>	-1.96 <sup>[a]</sup>		[c]			-1.04	-1.70
CV-19	1.34 <sup>[b]</sup>		-1.07 <sup>[b]</sup>	-1.97 <sup>[a]</sup>	0.45	0.75		-1.96	
CV-20	1.08 <sup>[b]</sup>		-1.81 <sup>[a]</sup>		1.33			-1.16	-1.96
CV-21	0.96 <sup>[b]</sup>		-1.80 <sup>[b]</sup>		1.11			-1.81	
CV-22	0.47 <sup>[b]</sup>	0.82 <sup>[b]</sup>	-2.09 <sup>[b]</sup>		1.00			-1.76	
CV-23	[c]		[d]	-1.61 <sup>[a]</sup>	0.45	0.76		-2.05	
CV-24	0.43 <sup>[b]</sup>		-2.04 <sup>[b]</sup>		1.64			-1.30	-1.61
CV-25	1.59 <sup>[b]</sup>		-1.78 <sup>[a]</sup>		0.42	0.79		-2.01	
CV-26	[c]		[d]	-1.87 <sup>[a]</sup>	1.57			-1.82	
CV-27	0.97 <sup>[b]</sup>		-1.81 <sup>[a]</sup>		1.71			-1.30	-1.89
CV-28	1.07 <sup>[b]</sup>		-1.96 <sup>[a]</sup>		0.98	1.61		-1.81	
CV-29	1.04 <sup>[b]</sup>		[c]		1.07			-1.98	
CV-30	1.56 <sup>[b]</sup>		[d]	-1.40 <sup>[a]</sup>	1.07			-1.12	-2.02
CV-31	0.73 <sup>[b]</sup>	0.85 <sup>[b]</sup>	[c]		[c]			-1.02	-1.38
CV-32	0.92 <sup>[b]</sup>		[c]		0.74	0.80		-2.34	
CV-33	1.25 <sup>[b]</sup>		[c]		0.99			-1.82	
			[c]		1.24			-1.76	

[a] reversible, value corresponds to  $E_{1/2}$ . [b] peak potential. [c] not resolved. [d] possible lower-lying reduction potential not clearly resolved.

For future work, we are interested in exploiting switches that can be used for photoredox, so polyalkoxylated compounds featured strongly in our test set (see table within **Figure S8**). We note that over small structural variations,  $E_{red}$  trends correlate well with Hammett constants:

	$R_1$	Hammett $\sigma(m)^{62}$	CV		SWV
			$E_{ox,1}$	$E_{red,1}$	$E_{p,red1}$
CV-2	H	0	0.94	-1.88	-1.88
CV-6	OMe	0.12	0.89	-1.86	-1.87
CV-8	F	0.34	1	-1.78	-1.79
CV-10	Br	0.39	0.99	-1.77	-1.77
CV-32	NHAc	0.21	0.92	-	-1.82



Such trends can be helpful for predicting the properties of further azo switches.



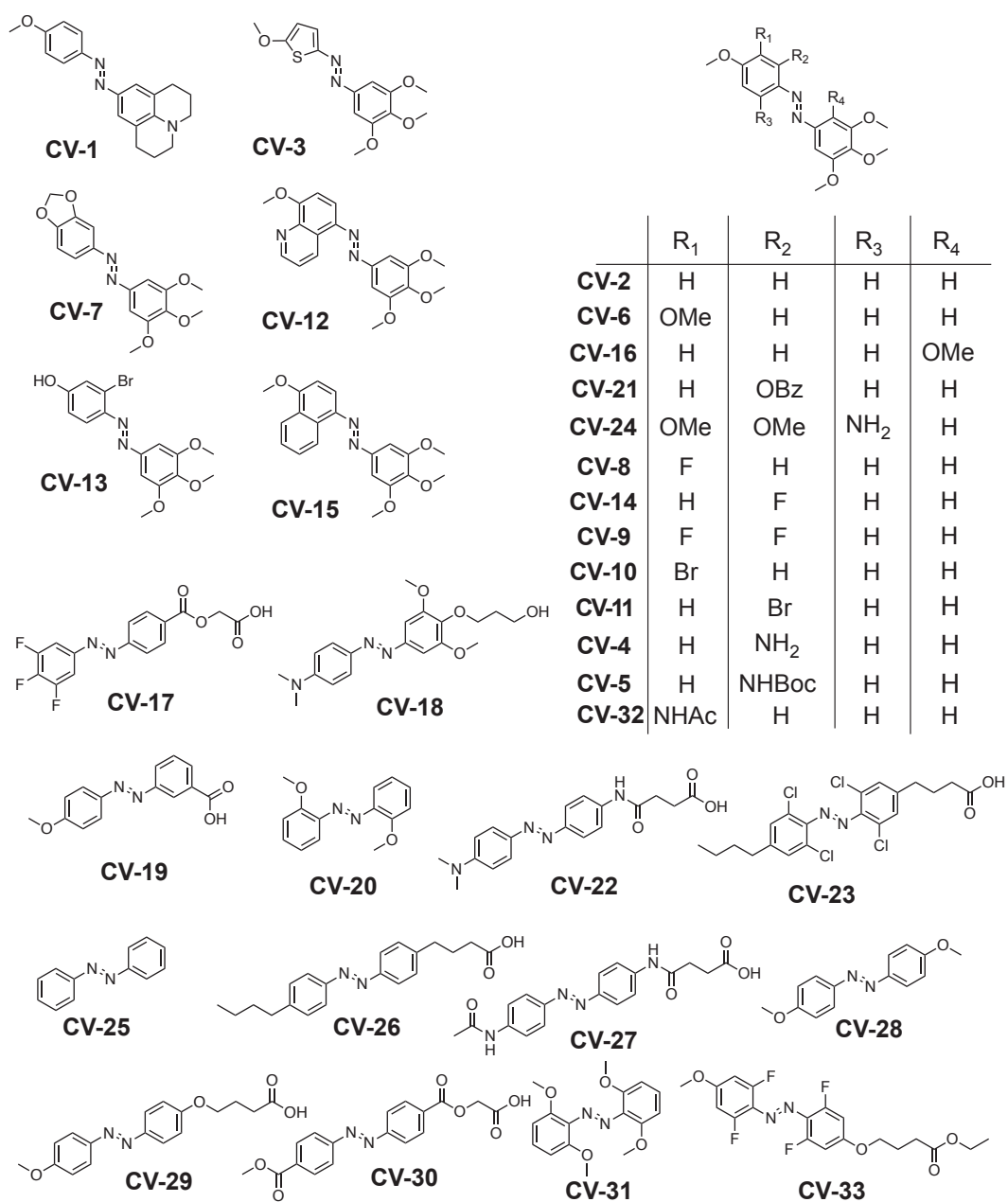


**Figure S8:** Structures of the 33 azobenzenes whose ground state redox properties were measured.

## 5 PSS and photoswitch E/Z ratio determinations by UV-Vis and HPLC

### 5.1 PSS determination by HPLC

Photostationary states (PSSs; **Table S6**) were determined by HPLC analysis. Samples were prepared from a 5 or 10 mM stock of the compound in DMSO, diluted to 500  $\mu$ M in 1:1 vol:vol acetonitrile (HPLC grade):distilled water in 1.5 mL amber glass vials, with sample volume 70  $\mu$ L. PSSs were reached by illumination from the top into the open vials for 5 min using the pE-4000 light source at LED intensity of 50 mW/mm<sup>2</sup> (see chapter **UV-VIS spectroscopy**; for 595 nm, illumination was at 10 mW/mm<sup>2</sup>). HPLC was then performed at 1 mL/min with a 10%→100% gradient of acetonitrile in water (both with 0.1% formic acid) over 27 min on a Zorbax C18 column (250 mm  $\times$  4.6 mm, 10  $\mu$ m particle size, Agilent); for each run, the column was equilibrated at starting conditions (10% MeCN) for 5 min, then 10  $\mu$ L sample were injected. Quantification was performed by integrating the area under the curve of DAD traces at selected wavelengths: 220 nm for azobenzenes (~isosbestic area: **Fig S9**, **Fig S11**), and a wavelength at the isosbestic curve region (fluorophore absorption peak) for conjugates.

**Table S6:** Isomer ratios at different photostationary states (PSS) for a set of azobenzene-fluorophore conjugates and azobenzenes alone, determined by HPLC measurements.

entry	$\lambda$ DAD trace [nm]	PSS-1 ( $\lambda$ [nm], %-trans isomer)	PSS-2 ( $\lambda$ [nm], %-trans isomer)	PSS-3 ( $\lambda$ [nm], %-trans isomer)
<b>NB-AK</b>	635	365, 18.5%	385, 40.5%	635, 98%
<b>NB-AO</b>	635	365, 23%	435, 71%	635, 99.8%
<b>NB-AN</b>	635	365, 31%	435, 69%	635, 99.7%
<b>CPY-PST</b>	615	365, 21%	385, 59.5%	595, 99.8%
<b>AK</b>	220	365, 4.5 %	385, 23%	490, 71%
<b>AN</b>	220	365, 8.5%	435, 48.5%	490, 76%
<b>AO</b>	220	365, 6%	435, 47.5%	

We find this HPLC method robust (see **chapter 5.3**) and we feel it is much easier to get right, as well as faster, cheaper, more convenient, and photochemically more appropriate, than more sophisticated and time-expensive NMR measurements typically used in this field<sup>35,63</sup>.

- NMR has limited sensitivity & accuracy at small isomer percentages (e.g. the critical difference of 98% vs 99.7% here) even if near-prohibitively long acquisitions are used.
- Depending on molecular complexity, NMR can be difficult to analyze (see **CPY-PST**).
- High concentrations that are quick to measure by NMR take long times to reach PSS during switching, due to optical shielding: so long illumination times and care to minimise optical path lengths are needed. Low concentrations that allow quickly reaching PSS instead require long measurement times by NMR. In both ways, acquiring reliable action spectra by NMR can be time-prohibitive.
- Illuminations can be done outside the NMR, but this allows changes in PSS before measurement due to thermal relaxation or surrounding light that must be controlled for, and it is tediously manual. Alternatively, illuminations can be done within the NMR e.g. via fiber optic (no spinning possible / bad sample quality; it takes out machine time to set up & run; most do not have access to it; typically the mixing that is key for bulk isomerisation speed at high concentration is missing; typically also the light intensities that can be applied within NMR are much smaller than those outside it, and the intensity is usually not homogeneous throughout, so apparent rates can be misleading). To avoid potential errors in NMR illumination, and to run the right controls for  $\lambda$ -independent homogeneity of intensity, seems much harder than to use HPLC.

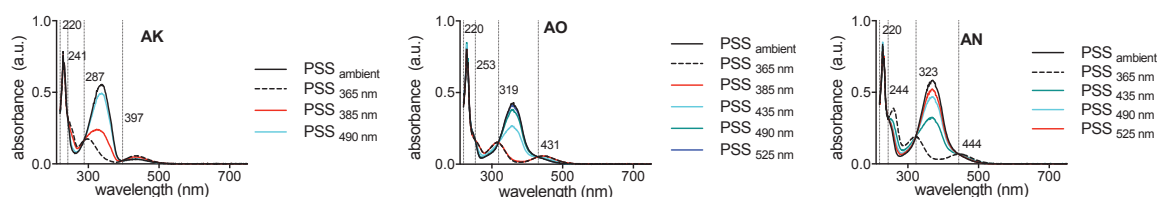


**Figure S9:** Isosbestic points of azobenzenes **AK**, **AO** and **AN** determined by UV-Vis in HPLC eluent mix (50:50 MeCN:water with 0.1% HCOOH); e.g. 241, 287, 397 nm for **AK**, in addition to its ~isosbestic region around 220 nm.

## 5.2 Calibrations for UV-Vis photoswitching action spectra

To show the current isomer ratios during different illumination periods during *in cuvette* photoswitching monitored by UV-Vis, we aimed to transform measured absorbance values into %*trans*-isomer values. Therefore we used the selected PSS values from HPLC (**chapter 5.1**) with their absorbance values from UV-Vis "action spectra" (**chapter 2.1.2**) to set up calibration curves (**Fig S10**). Linear fits (determined with software *GraphPad Prism 8*) were satisfying, and were used to interpolate/extrapolate %*E* values during the UV-Vis photoswitching action spectra timecourses.

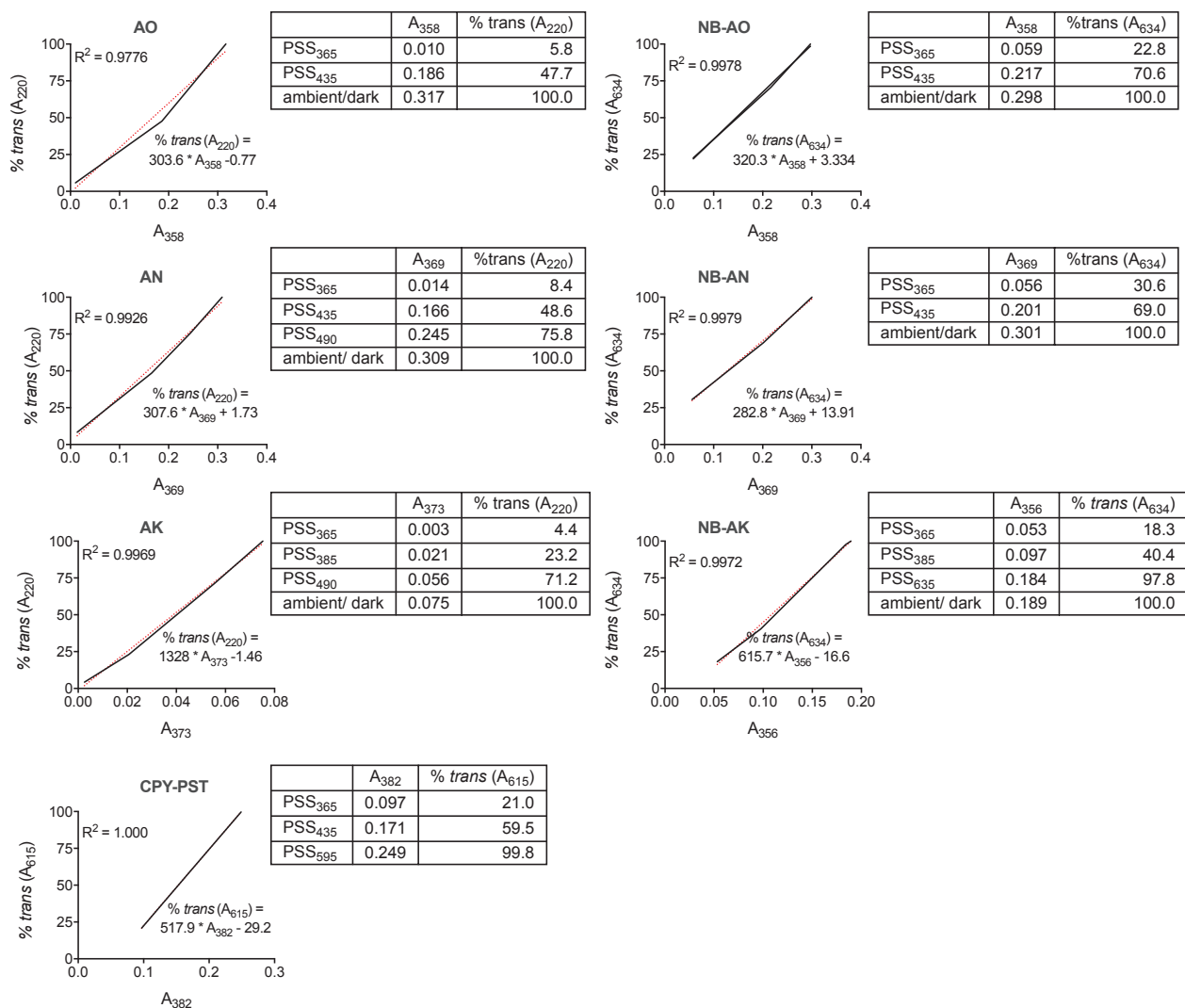
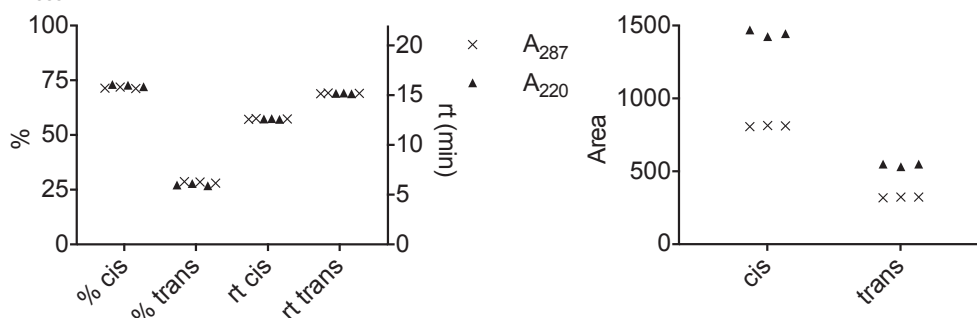


**Figure S10:** Data tables of the absorbance and %*trans*-isomer values used for generating the plotted calibration curves, with linear fits and goodness of fit, for a set of azobenzenes and azobenzene-fluorophore dyads.

### 5.3 HPLC precision

For testing the precision of the PSS quantification by HPLC (**chapter 5.1**), a sample of azobenzene **AK** (500  $\mu\text{M}$  in 1:1 water: acetonitrile) was set to PSS<sub>385</sub> by illumination (385 nm LED, 50 mW/mm<sup>2</sup>) and injected three times. **Fig S11** summarizes the retention times of *cis* and *trans* isomers, and their quantification by the areas under the curve of DAD traces near an isosbestic point (287 nm) or near an  $\sim$ isosbestic region (preferred; here, 220 nm).

**a** Comparison of isomer ratios, retention time and area under the curve of HPLC analysis of **AK** (PSS<sub>385</sub>) at DAD trace 220 and 287 nm. Statistical analysis of 3 measurements.



	A287			A220		
	Mean	SD	N	Mean	SD	N
% cis	71.5	0.29	3	72.7	0.46	3
Area cis	811.1	3.40	3	1447.3	21.78	3
rt cis	12.6	0.04	3	12.6	0.04	3
% trans	28.5	0.29	3	27.3	0.46	3
Area trans	322.7	3.44	3	544.5	10.14	3
rt trans	15.2	0.03	3	15.2	0.03	3

**b** Spectra of **AK** *cis* and *trans* isomers extracted from HPLC and normalized to isosbestic point at 287 nm (left); Zoom towards the isosbestic point 287 nm and the isosbestic region around 220 nm.

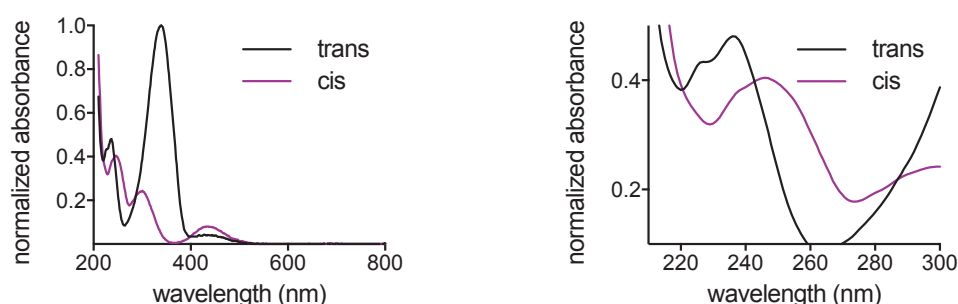


**Figure S11:** (a) Comparison of isomer ratio, retention time and area under curve of 3 HPLC runs of **AK** at PSS<sub>385</sub> (from DAD traces at 220 and 287 nm) including statistics. (b) UV-Vis spectra (extracted from HPLC) showing isosbestic region around 220 nm and isosbestic point at 287 nm.

We were therefore satisfied that this HPLC quantification is suitably reproducible for use.

## 6 Fluorescence lifetime measurement (mostly-*E* PSS at 639 nm) by TCSPC

Fluorescence lifetime analysis was performed on a custom-built inverted confocal microscope based on an Olympus IX-71 body (Olympus Deutschland GmbH). The Nile Blue conjugates were excited with a 639 nm pulsed laser, with a repetition rate of 80 MHz. After passing a single-mode fiber (P3-488PM-FC, Thorlabs GmbH), the laser light was circularly polarized by a linear polarizer (LPVISE100-A, Thorlabs GmbH) and a quarter-wave plate (AQWP05M-600, Thorlabs GmbH). The 639 nm laser power was adjusted to 20  $\mu$ W at the entrance of the microscope body by means of a neutral-density filter (ND06A, Thorlabs GmbH). The light was focused onto the sample by an oil-immersion objective (UPLSAPO100XO, NA 1.40, Olympus Deutschland GmbH). The emission was separated from the excitation beam by a dichroic beam splitter (zt532/640rpc, Chroma Technologies) and focused onto a 50  $\mu$ m diameter pinhole (Thorlabs GmbH). The emission light passed a dichroic mirror (640 LPXR, Chroma Technologies) and was spectrally cleaned by filters (SP 750, ThorLabs; RazorEdge LP 647, Semrock). The photons were detected on avalanche photodiodes (SPCM-AQRH-14-TR, Excelitas) and signals were registered by a time-correlated single-photon counting (TCSPC) unit (HydraHarp400, PicoQuant GmbH). For controlling the microscope and data analysis a commercial software package was used (SymPhoTime64, Picoquant GmbH). The fluorescence lifetimes were measured in Nunc Lab-Tek II Chambered Slides (Thermo Fisher Scientific) which were cleaned with 1M KOH for 1 h, washed with 1 $\times$  phosphate buffered saline (PBS) buffer four times, and passivated with 1 mg/mL BSA-biotin (Thermo Fisher Scientific). Measurements were performed in 50/50 water/acetonitrile solution at 1-10 nM concentrations. As the molecules are excited with high intensity 639 nm light, we take the lifetimes as corresponding to the *E*-isomer, and we do not conclude about the *Z*-isomer from these data. Decay curves and fits are shown in **Fig S12**, extracted parameters in **Table S7**.

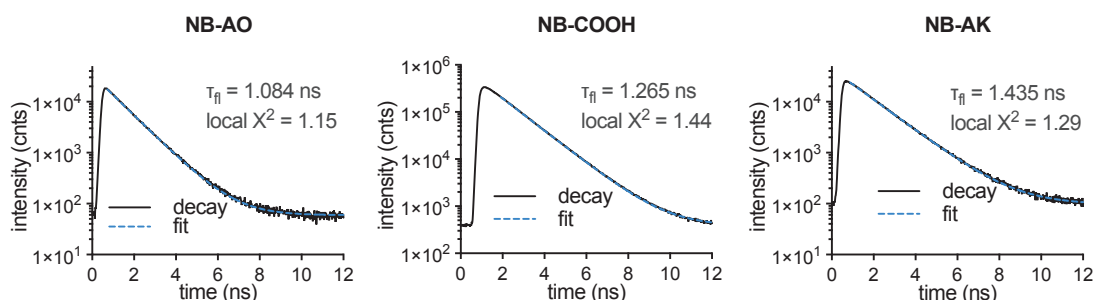


**Figure S12:** Decay kinetics and monoexponential fits.

**Table S7:** Fluorescence lifetimes from TCSPC, with goodness of fit (local  $\chi^2$ ) for monoexponential decay.

compound	fluorescence lifetime $\tau_{fit}$ [ns]	local $\chi^2$
<b>mostly-<i>E</i></b>		
<b>NB-COOH</b>	1.27	1.44
<b>NB-AO</b>	1.08	1.15
<b>NB-AK</b>	1.44	1.29



## 7 Spectroelectrochemistry and transient absorption (TA) spectroscopy (TAS)

### 7.1 Spectroelectrochemistry (*E* and *Z* azobenzene oxidations and NB reduction)

To understand if the TAS showed redox, we first needed to estimate how  $\text{NB}^{\cdot-}$ - $\text{AO}^{\cdot+}$  would contribute to TA spectra. We therefore wished to measure the radical ions' absorption profiles relative to those of their respective neutral species, that we had measured by UV-Vis (Tables S2-S3): so we aimed to perform spectroelectrochemistry during  $\text{AO} \rightarrow \text{AO}^{\cdot+}$  and  $\text{NB} \rightarrow \text{NB}^{\cdot-}$  redox reactions. We used a SEC-C Thin-Layer Quartz Glass Spectroelectrochemical cell, with Pt working and counter electrodes and Ag/Ag<sup>+</sup> reference electrode using a Gamry Interface 1010 Potentiostat. Absorbance spectra were measured in a 0.1 M solution of  $\text{NBu}_4\text{ClO}_4$  in acetonitrile (conduction salt solution). Concentration was dependent on compound solubility in conducting salt solution. Spectra were measured every 10 s, from 300 - 750 nm.

Fig 2b showed the spectral timecourse and difference spectra for ~100% NB reduction, which could be considered straightforward to interpret since only one band per species (NB and product) is involved (reproduced as Fig S15b-c below). However, as discussed in Supporting Note 4.4, the CV data do not support that this reduction should necessarily have been reversible, so doubt remains about whether the spectroelectrochemical difference corresponds to  $\text{NB} \rightarrow \text{NB}^{\cdot-}$  or rather the evolution to a consecutive product. Despite this caveat, it is instructive to follow the assumption of spectroelectrochemical  $\text{NB} \rightarrow \text{NB}^{\cdot-}$ , as we will do in this chapter. Then, given that NB has  $\epsilon \sim 60,000 \text{ M}^{-1}\text{cm}^{-1}$  at 635 nm, we could assign to  $\text{NB}^{\cdot-}$  a value of  $\epsilon \sim 40,000 \text{ M}^{-1}\text{cm}^{-1}$  at 510 nm, for use in TAS quantitation (continued below).

For the azobenzene, we initially oxidised *E*-AO; however, the spectral pattern and shifting isosbestic points indicated that the radical cation was not formed quantitatively, but was continuously accompanied by a second oxidation, so to estimate the spectral contribution of the radical cation we had to use a multi-component fitting, but the accuracy of this was not satisfactory (for example, it indicated confidently that the absorption of pure [*E*]- $\text{AO}^{\cdot+}$  at 500 nm (somewhat approximated by the broken teal line, Fig S13a) was <2/3 of the absorption of neutral *E*-AO at its ~360 nm  $\pi \rightarrow \pi^*$  band maximum, but could give only a low-confidence fit for the actual fraction (rough fit: 1/2)). We also performed the oxidation of isoelectronic DMO after isomerising it from all-*E* to nearly-all-*Z*, and this gave almost quantitative conversion to the desired radical cation before over-oxidation began. This allows us a confident estimate of the radical cation spectral shape (red line, Fig S13b) as well as its strength (absorption of  $\text{DMO}^{\cdot+}$  at 500 nm is (0.128/0.33) times that of its *E*-isomer's ~360 nm  $\pi \rightarrow \pi^*$  band maximum, i.e.  $\text{AO}^{\cdot+}$  should have  $\epsilon \sim 10,000 \text{ M}^{-1}\text{cm}^{-1}$  at 500 nm, which also will be used in quantitation).

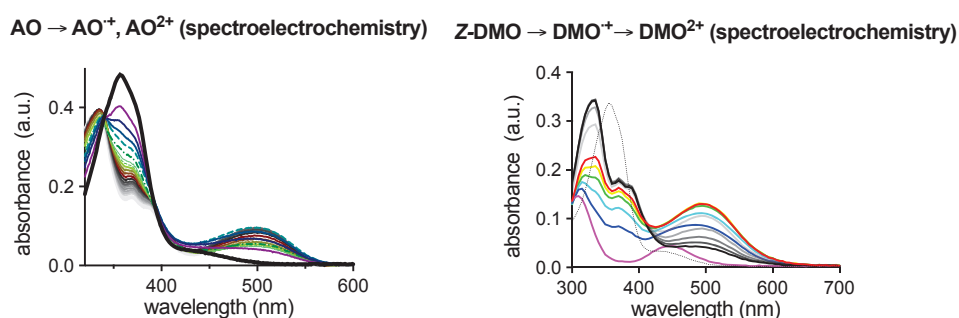


**Figure S13: (left panel)** Spectroelectrochemistry in 100% MeCN showing the spectral shift and intensity ratio for nearly-100%-*E*-AO [thick black line] →  $\text{AO}^{\cdot+}$  [360 nm peak drops, from purple to broken teal] →  $\text{AO}^{2+}$  [340 nm peak strengthens and moves to 330 nm, from broken teal to deep red to light grey] which is complicated to interpret since the double oxidation apparently begins before the first oxidation is complete. The broken teal line corresponds to the state with near-maximal observed concentration of  $\text{AO}^{\cdot+}$  (in presence of both neutral and dication species). **(right panel)** Absorbance and spectroelectrochemistry in 100% MeCN showing the spectral shift and intensity ratio for the isoelectronic 4,4'-dimethoxyazobenzene (DMO). The light dotted line shows the absorbance in the nearly-all-*E*-DMO state before the initial photoisomerisation to ca. 96% *Z* using 365 nm light (pink solid line). Then 96% *Z*-DMO →  $\text{DMO}^{\cdot+}$  →  $\text{DMO}^{2+}$  bulk electrooxidations are performed. In this experiment, an isosbestic point at 300 nm is maintained during the initial part (blue → red lines) until a state with nearly-pure- $\text{DMO}^{\cdot+}$  (red line) is observed; as oxidation continues (light grey → black lines), nearly-pure- $\text{DMO}^{\cdot+}$  is oxidised to nearly-pure- $\text{DMO}^{2+}$  (note the new isosbestic point at ca. 420 nm for solid red/grey/black traces).

## 7.2 TAS Methods

The femtosecond-TA data were acquired on a custom-built setup. Briefly, a regenerative Ti:sapphire amplifier (Astrella, Coherent, USA) is used as the pump laser, delivering pulses of 5 mJ pulse energy at 1 kHz pulse repetition rate. The output of the laser is then divided by a beam splitter. The first part is focused into a rotating CaF<sub>2</sub> plate to generate a broadband white light supercontinuum beam covering the spectral range 300 to 700 nm. This broadband pulse is subsequently split into two parts, which are used as reference and probe pulse. A second fraction of the Ti:sapphire output is used to pump an optical parametric amplifier (TOPAS prime, Light conversion, Lithuania) for generating pulses of about 100 fs pulse duration. The output of the amplifier is tunable across the UV-Vis-NIR spectral range. The repetition rate of the **pump pulses** is then reduced to **500 Hz** by a mechanical chopper. A Berek compensator and a polarizer are used to adjust the polarization difference of pump and the white light probe pulse to the magic angle of 54.7°. The probe pulse is focused into a quartz cuvette (pump/probe optical path length 10 mm, width 10 mm) by a concave mirror of 500 mm focal length. The spectra of probe and reference pulses are acquired by a 150 mm focal length Czerny-Turner spectrograph (SP2150, Princeton Instruments) equipped with two CCD arrays (Pascher Instruments AB, Sweden). Since strong contributions of coherent artifact signals<sup>64</sup> are observed during pump-probe pulse overlap, the transient absorption data recorded at delay times in the range  $-150 \text{ fs} < \Delta t < 150 \text{ fs}$  are removed from data analysis, because the multiexponential fitting algorithms cannot be applied. The TA data analysis of the remaining data includes a spectral preprocessing to correct for the chirp of the broadband pulse. Solutions were prepared with an OD between 0.1 and 0.2 (**NB-COOH** and **NB-AK** and **NB-AO** at 630 nm) in 1:1 acetonitrile: water.

**The goal of these TAS measurements was** to see if intermediates consistent with the photoisomerisation path of interest (photoredox-based  $Z \rightarrow E$ ) could be observed. *For researchers who wish to critically evaluate or reproduce such experiments, the following aspects are also of interest:* To excite the **NB** chromophore, **pump pulses of 630 nm** and pulse energy of **1.8 μJ** were used. The spatial profile of the pump pulse was slightly elliptical with a 700 μm long axis and a 558 μm short axis (beampath volume = 12 mm<sup>3</sup>, compare to bulk sample liquid volume = ca. 1500 mm<sup>3</sup>). However, pumping at 630 nm drives  $Z \rightarrow$ all- $E$  isomerisation; and probing with 300-700 nm can also drive isomerisation to majority- $E$ ; so the TAS measurement risks depleting the desired  $Z$ -isomer *in the measurement beampath* during the course of an acquisition, or entirely suppressing it. Aiming to maintain a significant and steady-state fraction of  $Z$ -dyad in this beampath, we continuously irradiated the test solutions with a **365 nm LED while stirring** during measurement (LED ca. 50 mW optical output, with lens, giving ca.  $\pm 75^\circ$  emission profile oriented at  $90^\circ$  to the pump/probe axis [from the side], with chip ca. 1.5 cm from pump/probe axis, i.e. on the order of 100 μW/mm<sup>2</sup> throughout the bulk sample). We confirmed by UV-Vis absorbance measurements before and immediately after TAS that this setup maintains e.g. "mostly- $Z$ -**NB-AO**" in the bulk sample, and that the chromophores did not degrade during measurement (steady-state reached). However, the pump/probe beampath experiences pump energy at 630 nm of  $(1.5 \mu\text{J}/\text{mm}^2 \times 500 \text{ s}^{-1}) = 750 \mu\text{W}/\text{mm}^2$ , which drives down the  $Z:E$  ratio from that which the UV LED would establish (the spectrally integrated intensity of the probe pulse over the range 300-700 nm is at least an order of magnitude lower than that the pump pulse, and is relatively evenly distributed in this wavelength range, so we ignore it as a potential influence on the  $Z:E$  distribution); counteracting this is the sample stirring which exchanges molecules between the beampath and the bulk so driving the beampath  $Z:E$  ratio back towards that for the UV LED illuminated bulk sample. We did not try to determine or estimate the **steady-state beampath  $Z:E$  ratio** during measurement, nor did we seek to optimise it by altering the illumination/stirring setup, since the results we obtained were mechanistically clear enough: we simply note that the beampath  $Z:E$  ratio is lower than that of the bulk sample, but we believe it is enough above

zero to allow interpretation. *NB*: We assume that **NB-AK** in the exciplex pathway evolves so rapidly that the concentration of exciplex intermediates is below the threshold for detection.

### 7.3 TAS Results

**Visible TAS Features:** TAS data are returned as  $\Delta\text{Abs}(t,\lambda)$  datasets (time-delay-series of absorption spectra differences between the ground state and post-pumped sample). These can be spectrally plotted for selected representative delay times (**Fig S14a-c**); or intercept traces at fixed wavelengths (typically, wavelengths at which strong spectral changes can be observed, that can also be maxima or minima) can be taken to temporally plot the molecular spectral evolution (e.g. 520 nm intercepts in **Fig S14d-e**, which plot the same raw data but with different normalisation processes, see below). These plots already show that **NB-AK** returns to the NB ground state without distinguishable differences of rate or form as compared to **NB-COOH** (**Fig S14e**), but there is significant faster return to ground state for **NB-AO** than for **NB-COOH** (**Fig S14d-e**). As per the discussion below, we will interpret this as reflecting a significant photoredox component in **NB-AO** and no photoredox component in **NB-AK**.

**TAS Data Processing:** We first normalise the  $\Delta\text{Abs}(t,\lambda)$  datasets of **NB-AO**, **NB-AK** and **NB-COOH** by multiplying all points by a constant, such that  $\Delta^*\text{Abs}(t_{\text{norm}}, 520 \text{ nm})$  is one. 520 nm is chosen since it is close to the differential absorption maximum for both the **NB<sup>\*(S1)</sup>** and **NB<sup>-</sup>** moieties (relative to **NB**). The normalisation time  $t_{\text{norm}}$  can be chosen freely, typically "late" ( $t_{\text{norm}} \sim 500 \text{ ps}$ ) or "early" (e.g.  $t_{\text{norm}} \sim 2 \text{ ps}$ ) to visually highlight different features (**Fig S14d-e**).

Normalisation at an "early" delay time (**Fig S14d**) is useful for tracking processes accessible to each molecule, but it is unsuited to direct quantitative analysis of differences between molecules (i.e. comparing **NB-AO** (photoredox allowed) with **NB/NB-AK** (no photoredox)) since this normalisation time is too close to the pump, so (i) the molecules are still rapidly evolving and at slightly different rates according to their structures, and (ii) photoredox also occurs during this timescale.

Normalisation at a "late" delay time (**Fig S14e**) is useful for quantitative analysis of pathway differences between molecules, since by this time **NB**, **NB-AO**, and **NB-AK** only access the same two pathways (nonradiative, or radiative, decays from **S1**) because electron back-transfer in the intermediate **NB<sup>-</sup>-AO<sup>+</sup>** to yield ground state **NB-AO** is already complete within ca. 350 ps; and under the data-supported assumption that the **NB<sup>\*(S1)</sup>**-moiety decay rates are similar across all three molecules (see below), late normalisation therefore highlights time periods where any *additional* competing pathways are taken by a conjugate.

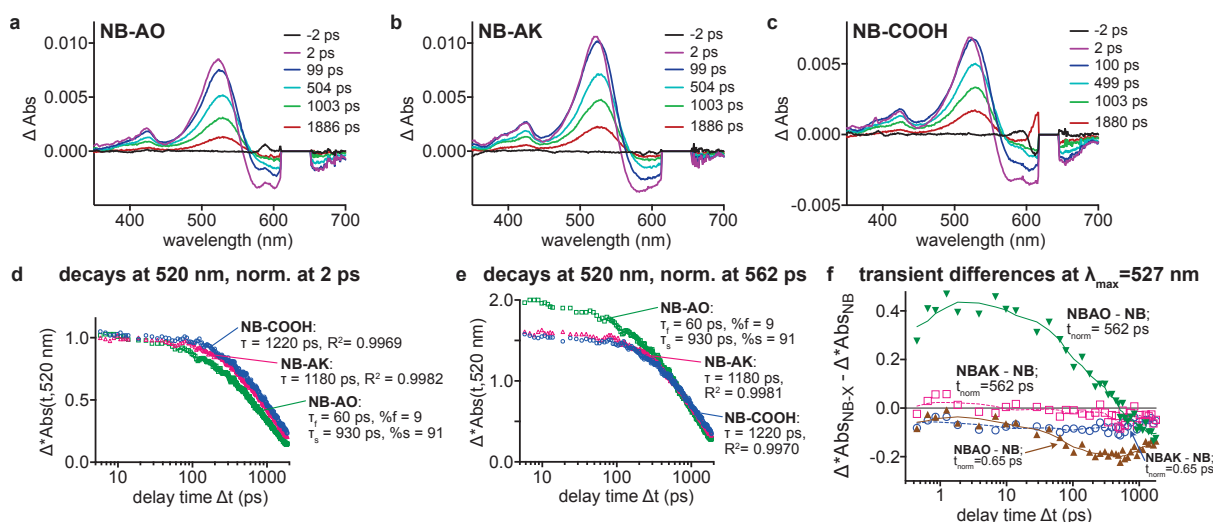


**Figure S14:** (a-c) Spectra extracted from TAS at selected time points before and after excitation for **NB-AO**, **NB-AK** and **NB-COOH**. (d-e)  $\Delta^*\text{Abs}(t, 520 \text{ nm})$  for **NB-COOH**, **NB-AO**, and **NB-AK**, at (d) early (2 ps) or (e) late (562 ps) normalisation, with unbiased mono- or biexponential fits for times  $t > 10 \text{ ps}$ . For biexponential fits,  $\tau_{f/s}$  and  $\%f/s$  indicate time constant and weighting of the faster/slower components. (f)  $\Delta(\Delta^*\text{Abs}(t,\lambda))$  for (**NB-AO** minus **NB**) and for (**NB-AK** minus **NB**), at early (0.65 ps) and late (562 ps) normalisation.

Then, we can subtract the non-photoredox decays of **NB** ( $\Delta^*Abs(t,\lambda)_{NB}$ ) from the sample (e.g.  $\Delta^*Abs(t,\lambda)_{NB-AO}$ ), and plot the remaining decay component(s) either at a fixed wavelength (e.g. at 527 nm: **Fig 2f** uses data normalised "late" at 562 ps, as reproduced in **Fig S14f** which additionally uses data normalised "early" at 0.65 ps), or as time series of difference spectra (**Fig 2d**, also normalised at 562 ps, which is reproduced in **Fig S15a**). This series of difference spectra is crucial to show the speciation in **NB-AO**, because the **NB<sup>•(S1)</sup>** moiety gives almost the same  $\Delta Abs$  "band" maximum (ca. 525 nm) as the **NB<sup>•-</sup>** (ca. 520 nm), and they have similar strength, so the simple  $\Delta Abs(t,\lambda)$  (**Fig S14a**) can confuse them.

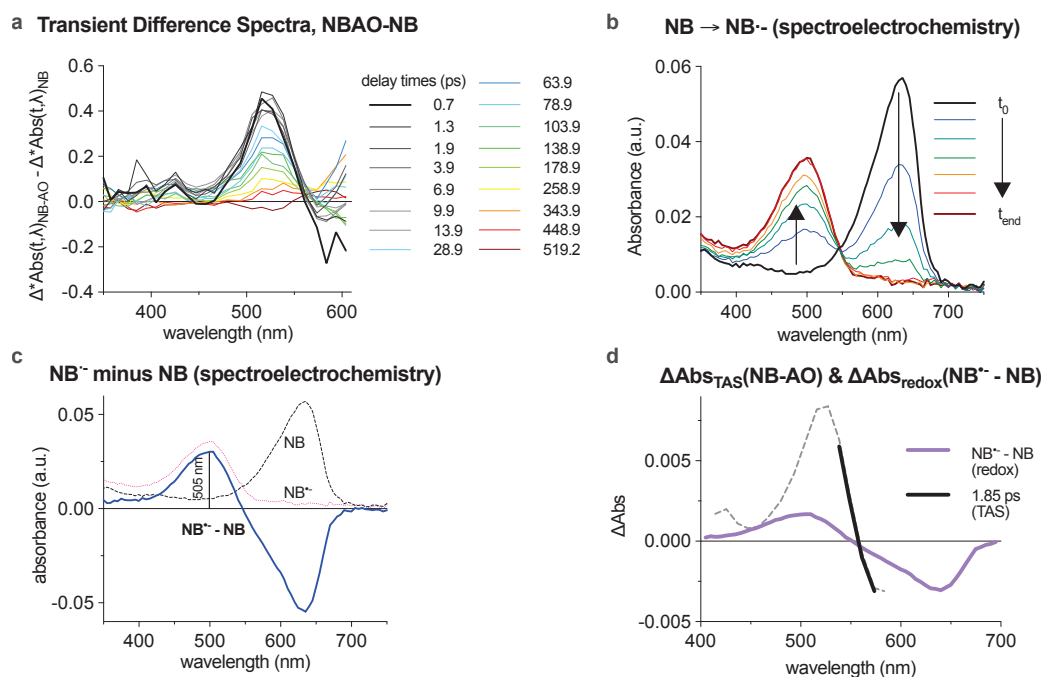


**Figure S15:** (a) The TAS time series of difference spectra  $\Delta(\Delta^*Abs(t < 520 \text{ ps}, \lambda))$  for **NB-AO** minus **NB**, normalised late (562 ps), in 50:50 MeCN:H<sub>2</sub>O. Note that data at  $t = 0.5\text{-}10$  ps have band maximum at ca. 520 nm and zero crossing point ca. 555 nm. (b) Spectroelectrochemistry in 100% MeCN showing the spectral shift and intensity ratio for  $\sim 100\%$  **NB** $\rightarrow$ **NB<sup>-</sup>** reduction (as **NB-COOH**). (c) Difference spectrum from spectroelectrochemistry for the **NB** $\rightarrow$ **NB<sup>-</sup>** reduction. The difference band maximum in 100% MeCN is at 505 nm ( $\Delta Abs = 0.030$ ), the difference band minimum is at 635 nm ( $\Delta Abs = -0.054$ ), the zero-crossing point is at 547 nm. (d) After scaling the  $\Delta Abs_{redox}$  spectrum from panel (c) to give the portion of  $\Delta\Delta Abs(510 \text{ nm})$  assigned to **NB<sup>-</sup>** at  $t = 1\text{-}10$  ps in panel (a), comparing the gradients in the region below the ground state bleach (550-580 nm) for the redox component (mauve) vs the overall bleach (black) suggests that **NB<sup>-</sup>** is a minor fate of the overall **NB-AO** ground state bleach (e.g. 15-30%).

#### TAS Interpretation (for brief summary plus further points, see **Supporting Note 4**)

Before proceeding, we note that (A) the absorption strength of **AO<sup>•+</sup>** at 520 nm is  $< 1/4$  of that of **NB<sup>•-</sup>** (see **section 7.1**); since we claim at best  $\pm 25\%$  accuracy for our quantifications, we will treat the difference spectra changes at 520 nm (**Fig S15a**) as arising solely from **NB<sup>•-</sup>**. (B) In TAS, we are not sure what E/Z proportion is being pumped; but it should be kept in mind that there are e.g. **four** relevant species for **NB-AO** during the first 350 ps, and the decay of **NB<sup>•-</sup>-AO** will include contributions from all of them (**E-NB<sup>•-</sup>-AO**, **Z-NB<sup>•-</sup>-AO**, **E-NB<sup>-</sup>-AO<sup>•+</sup>**, and **Z-NB<sup>-</sup>-AO<sup>•+</sup>**). Therefore, while a simple biexponential does fit the single-wavelength projection with acceptable  $R^2$  values (e.g. **Fig 2e**: "9% at 60 ps, 91% at 930 ps"), such a fit is not strictly appropriate for the multi-parameter mechanism we propose, and those fit parameters need not match the rates and percentages we suggest. We do not perform higher-order fitting even by expanding to fit more spectral data, since we feel this would risk over-fitting. It should also be noted that the absorption strengths of these species differ, so they will have different weighting in decays: which is not captured by the percentages of a simple fit.



(1) Some **NB<sup>-</sup>-AO<sup>+</sup>** forms rapidly and decays within 350 ps: For **NB-AO** vs **NB-COOH**, there are major differences in the  $\Delta(\Delta^*Abs(t, 527 \text{ nm}))$  subtraction projection (**Fig S14f**). The subtraction spectral series  $\Delta(\Delta^*Abs(t < 520 \text{ ps}, \lambda))$  (**Fig S15a**) shows this is due to a band centred around 520 nm which is very rapidly formed ( $t_{1/2} < 1 \text{ ps}$ ). This persists until ca. 10 ps elapsed, then drops to the baseline with half-life of ca. 70 ps (near-complete by around 350 ps elapsed). We assign this band to the **NB<sup>-</sup>** moiety in the **NB<sup>-</sup>-AO<sup>+</sup>** conjugate, since **NB<sup>-</sup>** in 100% MeCN solution spectroelectrochemistry has difference band maximum around 505 nm (**Fig 2b**, reproduced in **Fig S15b-c**) and we expected it to be solvatochromic so seeing it at ~520 nm in 50/50 MeCN/H<sub>2</sub>O in TAS did not raise concern, and since we ignore the 4-fold less intense contribution from **AO<sup>+</sup>** at this wavelength.

(2) The non-redox fraction of **NB-AO**, and [nearly] all **NB-AK**, evolve as NB-centred species with decay similar to **NB-COOH**: For **NB-AO**, although the redox fraction evolves at shorter delay times (**Fig S15a**), the late-normalised subtraction spectral series  $\Delta(\Delta^*Abs(t > 600 \text{ ps}, \lambda))$  shows no significant features (**Fig S16**, left panel), i.e. the non-redox fraction evolves identically to how **NB-COOH** would. For **NB-AK**, there are no major differences between its  $\Delta^*Abs(t, 527 \text{ nm})$  traces and those of **NB** at any time, which can be seen in that the late-normalised subtraction projection (**Fig S14f**, pink line) is essentially zero everywhere, their unsubtracted decay kinetics overlap (**Fig S14e**), and the subtraction spectral series (**Fig S16**, centre and right panels) are zero outside the region obscured by the pump: i.e. **NB-AK** evolves nearly identically to **NB-COOH**, supporting our picture that there is no *significant* photoredox in **NB-AK** (mismatched potentials).



**Figure S16:** late-normalised TAS subtraction spectral series at  $\Delta(\Delta^*Abs(t > 600 \text{ ps}, \lambda))$  for (**left**) **NB-AK** and (**middle**) **NB-AO** indicate no significant differences from each other or from **NB-COOH** [all are noise along the zero line]. By comparison, the differences between (**right**)  $\Delta(\Delta^*Abs(t < 500 \text{ ps}, \lambda))$  for **NB-AK** [also, noise along the zero line], vs **Fig S15a** (same period, **NB-AO**, gradual disappearance of a strong new band), are clear.

(3) We suggest that ca. 25% of **NB<sup>\*(S1)</sup>-AO** undergoes photoredox to **NB<sup>-</sup>-AO<sup>+</sup>** within 1-2 ps (with nonradiative electron back-transfer, optionally after *Z*→*E* isomerisation, then giving the electronic ground state of *E/Z-NB-AO* within the next ~350 ps; while the other 75% of molecules pass from **NB<sup>\*(S1)</sup>-AO** to ground state **NB-AO** by radiative and nonradiative decay with half-life ca. 0.96 ns (results of unbiased monoexponential fits to TAS decays at various wavelengths are: 0.9 ns [426 nm], 0.94 ns [520 nm], 1.06 ns [660 nm]; though we note that the unbiased fitting of the TAS data for decay at 520 nm ( $t > 10 \text{ ps}$ ) suggests a biexponential fit with the second time constant as 68 ps, which could be assigned as electron back-transfer)).

Two independent, rough approaches to estimate  $\Phi_{PR}$  may be useful:

(a) the fluorescence quantum yield for **NB-AO** (8% & 9% for mostly-*E* & mostly-*Z* respectively) is half of that for **NB** (16%; **Table S8**, **Fig S17**), while that for **NB-AK** is unaffected. This argues that >8% but <50% of **NB-AO** is quenched by photoredox.

(b) In TAS, at 516 nm: **NB-AO** reaches  $\Delta Abs \sim 0.0084$  at delay time 5 ps (redox plus singlet), and  $\Delta Abs \sim 0.0043$  at 524 ps (singlet only). By contrast, **NB** reaches  $\Delta Abs \sim 0.0067$  at 5 ps (singlet) and 0.0045 at 524 ps (singlet) (note, **NB-AK** has ratios within 5-10% of **NB**'s). Calculating backwards from the  $\Delta Abs$  value at 562 ps thus suggests that the **NB-AO**  $\Delta Abs \sim$



0.0084 at 5 ps corresponds to **0.0067 units from NB<sup>\*(S1)</sup>** plus **0.0015 from NB<sup>-</sup>-AO<sup>+</sup>**. This ~4:1 absorption ratio should not yet (see below) be interpreted as a molar ratio since the absorption strength of NB<sup>\*(S1)</sup> relative to NB<sup>-</sup> (or any other benchmark) is unknown (e.g. since the NB ground state bleach band is blocked by the pump region, which prevents benchmarking NB<sup>\*(S1)</sup> against NB using the NB-COOH spectrum). However, noting that the zero-crossing points are almost the same for the overall NB-AO and for the redox component (ca. 557 nm), it seems likely that their molar gradients in the region just below the ground state bleach (550-580 nm) will be similar as these regions are both dominated by NB bleach, with little contribution from either NB<sup>\*(S1)</sup> or NB<sup>-</sup> products. Gradient fitting in this region is error-prone, but typical fits suggest a redox component at 15-30% and a singlet at 85-70%: hence the rough value we suggest, that ca. 25% of total NB excitation funnels into photoredox. (Note too: this *does* now suggest that NB<sup>-</sup> and NB<sup>\*(S1)</sup> have similar molar extinction coefficients).

## 8 Fluorescence Quantum Yields

### 8.1 Mostly-E fluorescence quantum yields (integrating sphere measurements)

We first determined absolute quantum yields for fluorophore-azobenzene *conjugates* NB-AK and NB-AO (in **mostly-E** isomer state) compared to *parent fluorophores* NB-COOH, and to *physical mixtures* of the parents and mostly-E-azobenzenes (as a control against intermolecular inner filter effects reducing the detected fluorescence), by fluorimetry employing an integrating sphere (stocks made dark, sensible but not total precautions to block ambient light, thus "measured under mostly-E conditions").

The solutions had an absorbance of 0.1 at 600 nm for NB species, all in 1:1 acetonitrile:water, in spectroscopy-grade solvents without degassing and under air atmosphere. The steady state absorbance was measured on a Specord S600 (Analytik Jena) in 1 cm cuvettes. The emission spectra for quantum yield were measured on an Edinburgh FLS980 emission spectrofluorometer equipped with an integrating sphere in a 1 cm cuvette at 90° angle. Conjugate measurements were done twice, using slightly different emission ranges, as a control. Absorbance profiles did not change significantly during measurements (i.e. negligible direct photoisomerisation). We estimate an error ca. ±3% in the  $\Phi_{fl}$  measurements (**Table S8**).

**Table S8:** Fluorescence quantum yields (two separate measurements; integrating sphere setup).

compound	$\lambda_{ex}$ [nm]	emission range 1 [nm]	$\Phi_{fl}$ 1 [%]	emission range 2 [nm]	$\Phi_{fl}$ 2 [%]
<b>NB-COOH</b>	600	620-800	14	625-850	16
<b>E-NB-AO</b>	600	620-800	8	625-850	8
physical mixture <b>NB + E-AO</b>	600	620-850	15	<i>not repeated</i>	
<b>E-NB-AK</b>	600	620-800	16	625-850	17
physical mixture <b>NB + E-AK</b>	600	620-850	17	<i>not repeated</i>	

Note that there is fluorescence suppression only in conjugate **NB-AO**: which is consistent with an interpretation that its **E-AO** moiety performs fast photoelectron transfer to its excited NB<sup>\*</sup> to reduce it, whereas the **E-AK** moiety in **NB-AK** cannot (as electrochemistry had suggested).

Note also, at this concentration there is essentially no intermolecular photoelectron transfer quenching in the physical mixture with **AO**, and that there is no Lambert-Beer optical shielding of the NB moiety's fluorescence emission by either *E*-azobenzene (c.f. **chapter 8.2**).

## 8.2 Fluorescence of conjugates depends on their *E/Z* isomer state

Cuvette/PMT measurements have been performed as previously described.<sup>46</sup> We performed repeated photoisomerisations between PSS values, and measured their PSS fluorescence emission intensity values (**Fig S17**, middle panels). We used dilute solutions (**Fig S17**, left panels) to avoid potential for significant absorption of fluorescence emission before exiting the cuvette (although the significant and *E/Z*-dependent absorption from the azobenzenes is at wavelengths far shorter than the emission, so unlikely to be significant, see **chapter 8.1**).

The *E/Z*-dependent differences of fluorescence intensity are striking. (1) For the photoredox conjugate **NB-AO** the *Z*-isomer is more fluorescent than the *E*-isomer, while for the non-photoredox conjugate **NB-AK** the *Z*-isomer is less fluorescent than the *E*-isomer (see PSS at 365 nm, vs PSSs at long wavelength or mostly-*E*/mostly-dark states). (2) By using the %*E* composition of the PSSs known from HPLC measurements, we perform two-component analysis with the PSS-365 and the dark/PSS-long-wavelength fluorescence values, and extract *E* and *Z* isomer fluorescence intensities (in a.u.) (**Fig S17**, right panels).

The ratios of the *E*-conjugate's fluorescence intensity over that of the *Z*-conjugate are:

**NB-AO**: 0.9; and **NB-AK**: 1.2 (**Fig S17**, right panels).

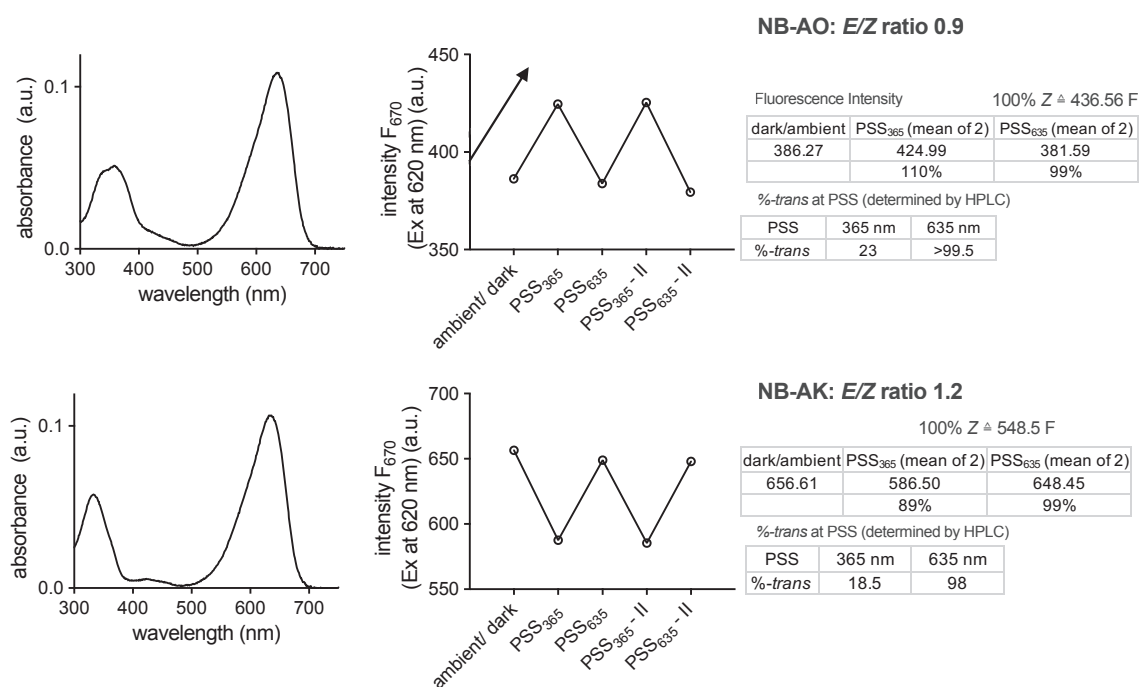


**Figure S17: Fluorescence dependency on *E/Z* ratio.** UV-Vis spectra are for dark state (nearly all-*E*) conjugates; other PSS absorption spectra are given in **Fig 1** and **Fig S5**, but *E/Z* absorption differences are not large and are localised in the near-UV/violet. %*E*(PSS) values from HPLC were used to analyse the FL(PSS) intensities and extract relative ratios between the pure-*E* and pure-*Z* conjugates' fluorescence intensities. Note that these are not determined at the same excitation wavelengths as used in integrating sphere quantum yield measurement.

## 9 Cell culture transfection and electrophysiology

HEK293T cells were cultured in Dulbecco's Modified Eagle Medium (DMEM; Corning) supplemented with 10% fetal bovine serum (FBS) and maintained at 37 °C and 5% CO<sub>2</sub> in a humidified incubator. For experiments, cells were plated at low density on poly-L-lysine coated 18 mm coverslips and transfected the following day with Lipofectamine 2000 (Thermo Fisher Scientific). SNAP-mGluR2<sup>65</sup>, GIRK1-F137S<sup>66</sup> and tdTomato as a transfection marker were co-transfected in a 1:1:0.2 ratio.

Whole-cell patch clamp recordings were performed 24 h after transfection as previously described<sup>25</sup> using an Axopatch 200B amplifier and a Digidata 1550B interface controlled by pClampex software (Molecular Devices). Voltage clamp recordings at -60 mV were performed in a high potassium solution (120 mM) to enable large inward currents upon receptor activation. Bath solution contained (in mM): 120 KCl, 25 NaCl, 10 HEPES, 2 CaCl<sub>2</sub>, 1 MgCl<sub>2</sub>. Pipettes of 3-5 MΩ resistance were filled with intracellular solution (in mM: 140 KCl, 10 HEPES, 5 EGTA, 3 MgCl<sub>2</sub>, 3 Na<sub>2</sub>ATP, 0.2 Na<sub>2</sub>GTP).

For labelling, cells were incubated with 1 μM **BAG** or **BANG** for 60 min at 37°C and used as described for similar compounds **BGAG**<sub>12,400</sub>, **BGAG**<sub>12,400</sub>-**Cy5-v1**, or **BGAG**<sub>12,400</sub>-**Cy5-v2**.<sup>25</sup> For photoswitching, a computer controlled CoolLED pE-4000 was used as illumination source and light was applied through a 40X objective. Light intensities at the focal plane were approximately (in mW/mm<sup>2</sup>): 9.6 for 385 nm, 4.9 for 525 nm, 5.1 for 660 nm, 1.7 for 740 nm and 2.8 for 770 nm. The photostimulation protocol was: (a) 2 s of 385 nm allowing receptor activation and evoked GIRK current to reach the steady state; then (b) maintenance in the dark to reach steady state current; then (c) 10 s of 525 nm, 660 nm, or 740 nm "photo-switch-off" was applied; then immediately (d) 525 nm was applied to finish the switch-off. 5-15 measurement cycles per cell were used to generate one datapoint in **Fig 4**; and 6-10 cells per wavelength per compound were used to make the dataset.

Data was analyzed using Clampfit (Molecular Devices) and Prism 9 (GraphPad). To quantify the photo-switch-off, the reduction of the maximum steady-state 385 nm-evoked GIRK current at the end of the 10 s period (typically this is at or near a plateau in the timecourse) was measured, normalized to the baseline, and expressed in percentages relative to extended 525 nm switch-off.

These results show that quantitative red/NIR singlet photoredox switching is applicable to biology. In biology, we believe it will bring several advantages: e.g. the free choice of *Z*→*E* wavelength, and the chance to improve the bioactivity switching index for compounds and targets where residual *Z*-isomer activity is problematic (for example, in 1:1 stoichiometry tethered ligand-enzyme complexes that we have been pursuing).

## 10 Chemical Synthesis

### 10.1 General

All **chemicals**, which were obtained from Sigma-Aldrich, TCI, Alfa Aesar, Acros, abcr or Carbolution were used as received and without further purification. Tetrahydrofuran (THF), dichloromethane (DCM) and dimethylformamide (DMF) were provided by Acros and were stored under argon atmosphere and dried over molecular sieves. TLC control, extractions and column chromatography were conducted using distilled, technical grade solvents. "Hexane" indicates a mixture of isomeric hexanes (e.g. 2-methylpentane, 3-methylpentane, 2,2-dimethylbutane, 2,3-dimethylbutane).

Unless stated otherwise, all **reactions** were performed without precautions in regard of potential air- and moisture-sensitivity and were stirred with Teflon-coated magnetic stir bars. Flash column **chromatography** was conducted under positive nitrogen pressure using Ceduran® Si60 silica gel from Merck GmbH. Reactions were **monitored** by thin layer chromatography (TLC) on Si60 F254 aluminium-backed sheets (Merck GmbH) and visualised by UV irradiation and/or KMnO<sub>4</sub> (3.0 g KMnO<sub>4</sub>, 20 g K<sub>2</sub>CO<sub>3</sub>, 0.30 g KOH, 0.30 L H<sub>2</sub>O).

**Analytical high performance liquid chromatography** coupled to mass spectrometry (HPLC-MS) was conducted using (1) an Agilent 1100 system, through a Hypersil Gold HPLC column from ThermoFisher Scientific GmbH, with a DAD detector and a unit resolution Agilent LC/MSD IQ mass spectrometer (ESI mode), with solvent A H<sub>2</sub>O with 0.1% formic acid and solvent B: MeCN with 0.1% formic acid (typical gradient: 10% to 100% MeCN within 5 min at a flow rate of 0.4 ml/min) or (2) an LCMS-2020 system (Shimadzu) equipped with an SPD-20AV UV-Vis photodiode array detector for product visualization on a C18 1.9 μm, 2.1 x 50 mm column (Supelco), with solvent A: H<sub>2</sub>O with 0.1% formic acid and solvent B: MeCN with 0.1% formic acid (typical gradient: 10% to 90% B within 6 min at a flow rate of 1 ml/min).

**Compound purity and isomer ratios** were determined by analytical HPLC with an Agilent 1100 system equipped with a DAD detector, using an Agilent Zorbax Eclipse Plus C18 column (4.6 mm x 250 mm, particle size 10 μm). Mixtures of water (analytical grade, 0.1% formic acid) and MeCN (analytical grade, 0.1% formic acid) were used as eluent systems. Typical gradient used was from 10% to 100% MeCN over 27 min.

**Preparative HPLC** purification was performed with (1) an Agilent 1260 equipped with a DAD detector, using an Agilent Zorbax Eclipse Plus C18 column (21.4 mm x 250 mm, particle size 10 μm with solvent A: H<sub>2</sub>O with 0.1% formic acid and solvent B: MeCN with 0.1% formic acid as eluent (typical gradient: 10% to 100% B within 27 min) or (2) an UltiMate 3000 system (Thermo Fisher Scientific) on a C18 5 μm, 21.2 x 250 mm column (Supelco, flow rate 8 ml/min) with solvent A: H<sub>2</sub>O with 0.1% TFA and solvent B: MeCN as eluent (typical gradient: 10% to 90% B within 60 min).

**Abbreviations:** DCM (dichloromethane), DMF (dimethylformamide), MeOH (methanol), MeCN (acetonitrile), HBTU((2-(1*H*-benzotriazol-1-yl)-1,1,3,3-tetramethyluronium hexafluorophosphate), DIPEA (diisopropylethylamine), TEA (triethylamine), EA (ethyl acetate), TFA(trifluoroacetic acid), AcOH (acetic acid), Boc (*tert*-butyloxycarbonyl), TSTU (*N,N,N',N'*-tetramethyl-*O*-(*N*-succinimidyl)uronium tetrafluoroborate), HATU (dimethylamino)-*N,N*-dimethyl(3*H*-[1,2,3]triazolo[4,5-*b*]pyridin-3-yloxy)methaniminium hexafluorophosphate), DBU (1,8-diazabicyclo[5.4.0]undec-7-ene).

### 10.2 NMR spectroscopy

Nuclear magnetic resonance (**NMR**) spectroscopy was performed using *Bruker Avance III HD Biospin* (<sup>1</sup>H: 400 MHz/<sup>13</sup>C: 100 MHz, with BBFO cryoprobe; or <sup>1</sup>H: 500 MHz/<sup>13</sup>C: 126 MHz) or *Bruker Avance III* (<sup>1</sup>H: 800 MHz /<sup>13</sup>C: 201 MHz, with TCI cryoprobe) spectrometers. NMR spectra were measured at 298 K, unless stated otherwise, and were analysed with MestreNova 12. H-NMR spectra chemical shifts (δ) in parts per million (ppm) relative to tetramethylsilane (δ = 0 ppm) are reported using the residual protic solvent (CHCl<sub>3</sub> in CDCl<sub>3</sub>: δ = 7.26 ppm, DMSO-*d*<sub>5</sub> in DMSO-*d*<sub>6</sub>: δ = 2.50 ppm, CHD<sub>2</sub>OD in CD<sub>3</sub>OD: δ = 3.31 ppm, CHDCl<sub>2</sub>

in CD<sub>2</sub>Cl<sub>2</sub>:  $\delta$  = 5.32 ppm, and CHD<sub>2</sub>CN in CD<sub>3</sub>CN:  $\delta$  = 1.94 ppm) as an internal reference. For <sup>13</sup>C-NMR spectra, chemical shifts in ppm relative to tetramethylsilane ( $\delta$  = 0 ppm) are reported using the central resonance of the solvent signal (CDCl<sub>3</sub>:  $\delta$  = 77.2 ppm, DMSO-d<sub>6</sub>:  $\delta$  = 39.5 ppm, CD<sub>3</sub>OD:  $\delta$  = 49.0 ppm, CD<sub>2</sub>Cl<sub>2</sub>:  $\delta$  = 54.0 ppm, CD<sub>3</sub>CN:  $\delta$  = 118.3 ppm) as an internal reference. For <sup>1</sup>H-NMR spectra in addition to the chemical shift the following data is reported in parentheses: multiplicity, coupling constant(s) and number of hydrogen atoms. The abbreviations for multiplicities and related descriptors are s = singlet, d = doublet, t = triplet, q = quartet, or combinations thereof, m = multiplet and br = broad. Where known products matched literature analysis data, reference for literature is given.

### 10.3 High-resolution mass spectrometry (HRMS)

HRMS was conducted either using a *Thermo Finnigan LTQ FT Ultra FourierTransform* ion cyclotron resonance spectrometer from *ThermoFisher Scientific GmbH*, Dreieich (Germany) applying electron spray ionisation (ESI) with a spray capillary voltage of 4 kV at temperature 250 °C with a method dependent range from 50 to 2000 u or on a *maXis II™ ETD* mass spectrometer (Bruker) coupled with a Shimadzu Nexera system controlled via *o-TOF-Control 4.1* and *Hystar 4.1 SR2 (4.1.31.1)* software (Bruker) of the Mass Spectrometry Core Facility of the Max-Planck Institute for Medical Research Heidelberg under the direction of Dr. S. Fabritz. All reported *m/z* values refer to positive ionization mode, unless stated otherwise.

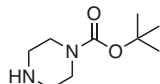


## 10.4 Synthesis

To request materials or analytical data, please reference the reaction number (e.g. **BW063**).

### 10.4.1 Azobenzene building blocks

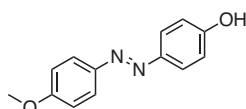
*tert*-butyl piperazine-1-carboxylate (**S1**, **BW063**; known compound)



**S1** was synthesized according to literature.<sup>67</sup>

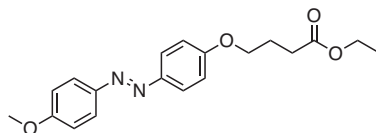
A solution of di-*tert*-butyl dicarbonate (6.43 g, 29.5 mmol, 1 eq.) in DCM (20 mL) was added to a solution of piperazine (5.06 g, 58.8 mmol, 2 eq.) in DCM (50 mL) at 0 °C. The reaction mixture was allowed to warm to room temperature and stirred at room temperature for 16 h. The suspension was filtered, and the filtrate was concentrated under reduced pressure. The resulting white solid was suspended in ice-cold water (100 mL), filtered, and the filtrate was basified to pH 12 with a saturated solution of potassium carbonate. The aqueous phase was extracted with methyl *tert*-butyl ether (3 x 100 mL). The combined organics were washed with brine (100 mL), dried (MgSO<sub>4</sub>) and concentrated under reduced pressure to yield **S1** (2.07 g, 11.1 mmol, 19%) as a colorless solid. Analytical data (H-NMR) match literature.<sup>67</sup>

4-((4-methoxyphenyl)diazenyl)phenol (**S2**, **BW192**; known compound)



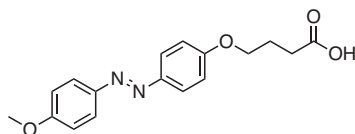
Sodium nitrite (2M aqueous solution, 3.65 mL, 7.3 mmol) were added to a solution of 4-methoxyaniline (824 mg, 6.69 mmol, 1 eq.) in MeOH (20 mL) and hydrochloric acid (2M aqueous solution, 20 mL) at 0 °C and stirred at 0 °C for 30 min. The reaction mixture was added slowly to a solution of phenol (678 mg, 7.30 mmol, 1.1 eq.) in MeOH (20 mL) and dipotassium hydrogen phosphate (0.5M aqueous solution, 20 mL) at 0 °C and stirred at 0 °C for 1 h. During the addition pH was adjusted to 10 with potassium hydroxide (1M aqueous solution). The reaction mixture was allowed to warm to room temperature, pH was adjusted to 7 with hydrochloric acid (2M aqueous solution) and extracted with EA (3 x 100 ml). The combined organics were dried (MgSO<sub>4</sub>), concentrated under reduced pressure and purified by silica gel column chromatography (5-25% ethyl acetate in hexane) to yield **S2** (1.10 g, 4.82 mmol, 72 %) as an orange solid. Analytical data (H-NMR) match literature.<sup>68</sup>

ethyl 4-(4-((4-methoxyphenyl)diazenyl)phenoxy)butanoate (**S3**, **BW257**; known compound)



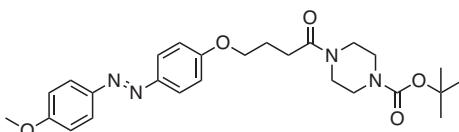
Ethyl 4-bromobutyrate (0.62 mL, 848 mg, 4.34 mmol, 2 eq.) were added to a solution of **S2** (496 mg, 2.17 mmol, 1 eq.) and potassium carbonate (902 mg, 6.52 mmol, 3 eq.) in acetone (20 mL) and refluxed for 16 h. The reaction mixture was quenched with water (50 mL) and extracted with EA (3 x 50 mL). The combined organics were dried (MgSO<sub>4</sub>), concentrated under reduced pressure and purified by silica gel column chromatography (0-10% EA in hexane) to yield **S3** (400 mg, 1.17 mmol, 54%) as an orange solid. Analytical data (H-NMR) match literature<sup>69</sup>.

4-(4-((4-methoxyphenyl)diazenyl)phenoxy)butanoic acid (**S4**, **AO-COOH**, **BW265**; *known*)



Potassium hydroxide (328 mg, 5.84 mmol, 5 eq.) was added to a solution of **S3** (400 mg, 1.17 mmol, 1 eq.) in MeOH (20 mL) and stirred at 50 °C for 16 h. The reaction mixture was concentrated under reduced pressure. The solid residue was suspended in hydrochloric acid (2M aqueous solution, 50 mL) and extracted with DCM (5 x 50 mL). The combined organics were dried (MgSO<sub>4</sub>) and concentrated under reduced pressure to yield **AO-COOH** (345 mg, 1.10 mmol, 94%) as an orange solid. Analytical data (H-NMR) match literature.<sup>69</sup>

*tert*-butyl-4-(4-(4-((4-methoxyphenyl)diazenyl)phenoxy)butanoyl)piperazine-1-carboxylate (**S5**, **BW270**, **BEW338**; *novel*)



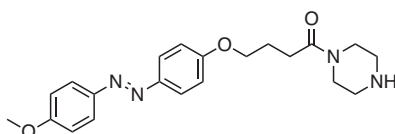
**AO-COOH** (100 mg, 0.32 mmol, 1 eq.), **S1** (88.9 mg, 0.48 mmol, 1.5 eq.), HBTU (145 mg, 0.38 mmol, 1.2 eq.) and TEA (134  $\mu$ L, 96.6 mg, 0.95 mmol, 3 eq.) were dissolved in DMF (3 mL) and stirred at room temperature for 16 h. The reaction mixture was concentrated under reduced pressure. The resulting solid was dissolved in EA (50 mL) and washed with a saturated aqueous solution of sodium hydrogen carbonate (5 x 50 mL). The organic phase was dried (MgSO<sub>4</sub>), concentrated under reduced pressure and purified by silica gel column chromatography (20-80% EA in hexane) to yield **S5** (132 mg, 0.27 mmol, 86%) as an orange solid.

**<sup>1</sup>H-NMR** (400 MHz; CDCl<sub>3</sub>):  $\delta$  = 7.91 – 7.83 (m, 4H), 7.04 – 6.96 (m, 4H), 4.12 (t,  $J$  = 5.8 Hz, 2H), 3.89 (s, 3H), 3.63 – 3.57 (m, 2H), 3.49 – 3.38 (m, 6H), 2.57 (t,  $J$  = 7.2 Hz, 2H), 2.18 (p,  $J$  = 6.7 Hz, 2H), 1.47 (s, 9H).

**<sup>13</sup>C-NMR** (101 MHz; CDCl<sub>3</sub>):  $\delta$  = 174.5, 171.0, 161.0, 156.0, 147.2, 140.5, 124.6, 124.5, 114.8, 114.3, 80.5, 67.4, 59.4, 55.7, 45.4, 29.6, 28.5, 24.9.

**HR-MS** (ESI)  $m/z$ : calculated for C<sub>26</sub>H<sub>35</sub>N<sub>4</sub>O<sub>5</sub><sup>+</sup>: 483.2620; found: 483.26028, (M + H)<sup>+</sup>.

4-(4-((4-methoxyphenyl)diazenyl)phenoxy)-1-(piperazin-1-yl)butan-1-one (**S6**, **AOpip**, **BW274**, **BEW337**; *novel*)



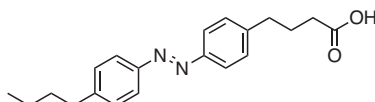
TFA (2 mL) was added dropwise to a solution of **S5** (130 mg, 0.27 mmol, 1 eq.) in DCM (2 mL) at 0 °C and stirred at 0 °C for 2 h. The reaction mixture was allowed to warm to room temperature and quenched with a saturated aqueous solution of sodium hydrogen carbonate (50 mL). The reaction mixture was extracted with DCM (3 x 50 mL). The combined organics were dried (MgSO<sub>4</sub>) and concentrated under reduced pressure to yield **AOpip** (100 mg, 0.26 mmol, 97%) as an orange solid.

**<sup>1</sup>H-NMR** (400 MHz; CDCl<sub>3</sub>):  $\delta$  = 7.91 – 7.83 (m, 4H), 7.04 – 6.96 (m, 4H), 4.12 (t,  $J$  = 5.9 Hz, 2H), 3.89 (s, 3H), 3.66 (s, 2H), 3.55 – 3.50 (m, 2H), 2.92 – 2.83 (m, 4H), 2.56 (t,  $J$  = 7.2 Hz, 2H), 2.18 (p,  $J$  = 6.5 Hz, 2H).

**<sup>13</sup>C-NMR** (101 MHz; CDCl<sub>3</sub>):  $\delta$  = 170.9, 161.7, 161.0, 147.2, 146.7, 124.5, 124.5, 114.8, 114.3, 67.4, 55.7, 46.0, 45.6, 42.1, 25.0.

**HR-MS** (ESI)  $m/z$ : calculated for C<sub>21</sub>H<sub>26</sub>N<sub>4</sub>O<sub>3</sub>: 382.20777; found: 383.20799, M<sup>+</sup>.

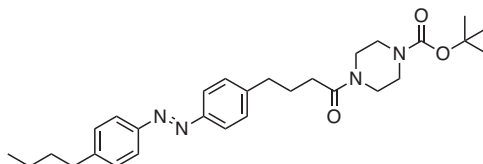
4-(4-((4-butylphenyl)diazenyl)phenyl)butanoic acid (**S7**, **AK-COOH**, **BW029**; **known**)



Known compound **AK-COOH** was synthesized according to literature.<sup>20</sup>

A solution of Oxone<sup>®</sup> (18.4 g, 59.8 mmol, 9 eq.) in water (150 mL) was added to a solution of 4-butylaniline (1.60 mL, 1.52 g, 10.1 mmol, 1.5 eq.) in DCM (150 mL) and stirred at room temperature for 16 h. The phases were separated, and the aqueous phase was extracted with DCM (2 x 50 mL). The combined organics were washed with hydrochloric acid (1M aqueous solution, 50 mL), a saturated aqueous solution of sodium hydrogen carbonate (50 mL) and water (50 mL). 4-(4-aminophenyl)butanoic acid (1.20 g, 6.70 mmol, 1 eq.) and AcOH (100 mL) were added to the organic phase, DCM was evaporated under reduced pressure and the resulting mixture was stirred at room temperature for 16 h. The reaction mixture was concentrated under reduced pressure, azeotroped with toluene (3 x 5 mL) and purified by silica gel column chromatography (3% MeOH in DCM + 0.5% AcOH) to yield **AK-COOH** (1.46 g, 4.50 mmol, 67%) as a red/orange solid. Analytical data (H-NMR) match literature.<sup>20</sup>

*tert*-butyl 4-(4-(4-((4-butylphenyl)diazenyl)phenyl)butanoyl)piperazine-1-carboxylate (**S8**, **BW281**, **BEW336**; **novel**)



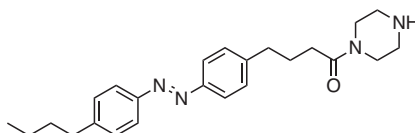
**AO-COOH** (100 mg, 0.31 mmol, 1 eq.), **S1** (86.1 mg, 0.46 mmol, 1.5 eq.), HBTU (140 mg, 0.37 mmol, 1.2 eq.) and TEA (130  $\mu$ L, 93.6 mg, 0.95 mmol, 3 eq.) were dissolved in DMF (3 mL) and stirred at room temperature for 16 h. Water (30 mL) was added, and the reaction mixture was extracted with DCM (5 x 50 mL). The combined organics were dried (MgSO<sub>4</sub>), concentrated under reduced pressure and purified by silica gel column chromatography (20-50% EA in hexane) to yield **S8** (119 mg, 0.24 mmol, 78%) as an orange solid.

<sup>1</sup>H-NMR (400 MHz; CDCl<sub>3</sub>):  $\delta$  = 7.83 (dd, *J* = 8.4, 2.6 Hz, 4H), 7.32 (dd, *J* = 8.4, 3.6 Hz, 4H), 3.59 (s, 2H), 3.46 – 3.32 (m, 6H), 2.77 (t, *J* = 7.4 Hz, 2H), 2.69 (t, *J* = 7.8 Hz, 2H), 2.35 (t, *J* = 7.4 Hz, 2H), 2.03 (p, *J* = 7.5 Hz, 2H), 1.69 – 1.61 (m, 2H), 1.46 (s, 9H), 1.38 (dq, *J* = 14.7, 7.3 Hz, 2H), 0.94 (t, *J* = 7.3 Hz, 3H).

<sup>13</sup>C-NMR (101 MHz; CDCl<sub>3</sub>):  $\delta$  = 171.4, 154.7, 151.4, 151.1, 146.5, 144.9, 129.3, 129.2, 123.0, 122.9, 80.5, 45.4, 41.5, 35.7, 35.3, 33.6, 32.4, 28.5, 26.5, 22.5, 14.1.

HR-MS (ESI) *m/z*: calculated for C<sub>29</sub>H<sub>41</sub>N<sub>4</sub>O<sub>3</sub><sup>+</sup>: 493.31732; found: 493.31742, (M + H)<sup>+</sup>.

4-(4-((4-butylphenyl)diazenyl)phenyl)-1-(piperazin-1-yl)butan-1-one (**S9**, **AKpip**, **BW283**, **BEW339**; **novel**)



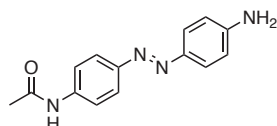
TFA (5 mL) was added dropwise to a solution of **S8** (110 mg, 0.22 mmol, 1 eq.) in DCM (5 mL) at 0 °C and stirred at 0 °C for 2 h. The reaction mixture was allowed to warm to room temperature, saturated aqueous solution of sodium hydrogen carbonate (50 mL) was added, and the mixture was extracted with DCM (3 x 50 mL). The combined organics were dried (MgSO<sub>4</sub>) and concentrated under reduced pressure to yield **AKpip** (84 mg, 0.21 mmol, 96%) as an orange solid.

**<sup>1</sup>H-NMR** (400 MHz; CDCl<sub>3</sub>):  $\delta$  = 7.83 (dd,  $J$  = 8.4, 2.8 Hz, 4H), 7.32 (dd,  $J$  = 8.4, 4.1 Hz, 4H), 3.66 (t,  $J$  = 5.1 Hz, 2H), 3.44 (t,  $J$  = 5.1 Hz, 2H), 3.16 (bs, 1H), 2.89 (q,  $J$  = 4.6 Hz, 4H), 2.76 (t,  $J$  = 7.4 Hz, 2H), 2.69 (t,  $J$  = 7.7 Hz, 2H), 2.33 (t,  $J$  = 7.5 Hz, 2H), 2.03 (p,  $J$  = 7.5 Hz, 2H), 1.73 – 1.58 (m, 2H), 1.38 (h,  $J$  = 7.3 Hz, 2H), 0.94 (t,  $J$  = 7.3 Hz, 3H).

**<sup>13</sup>C-NMR** (101 MHz; CDCl<sub>3</sub>):  $\delta$  = 171.2, 151.4, 151.1, 146.5, 144.9, 129.3, 129.2, 123.0, 122.9, 45.5, 41.8, 35.7, 35.3, 33.6, 32.2, 26.5, 22.5, 14.1.

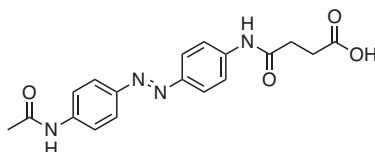
**HR-MS** (ESI)  $m/z$ : calculated for C<sub>24</sub>H<sub>33</sub>N<sub>4</sub>O<sup>+</sup>: 393.26489; found: 393.26516, (M + H)<sup>+</sup>.

*N*-(4-((4-aminophenyl)diazenyl)phenyl)acetamide (**S10**, **BW050**; known)



Sodium nitrite (2M aqueous solution, 5.50 mL, 11 mmol) was added to a solution of 4-aminoacetanilide (1.50 g, 10.0 mmol, 1 eq.) in MeOH (90 ml) and hydrochloric acid (2M aqueous solution, 30 mL) at 0 °C and stirred at 0 °C for 30 min. Sulfamic acid (131 mg, 1.35 mmol, 0.14 eq.) was added to the reaction mixture and stirred at 0 °C for 3 min. Subsequently, AcOH (30 mL) and aniline (1.20 mL, 1.22 g, 13.1 mmol, 1.3 eq.) were added before sodium acetate (13.7 g, 101 mmol, 10 eq.) was added portion wise and stirred at 0 °C for another 30 min. The reaction mixture was allowed to warm to room temperature, pH was adjusted to 7 with hydrochloric acid (2M aqueous solution) and extracted with EA (3 x 150 mL). The combined organics were dried (MgSO<sub>4</sub>), concentrated under reduced pressure and purified by silica gel column chromatography (10-50% EA in hexane) to yield **S10** (265 mg, 1.04 mmol, 10%) as an orange solid. Analytical data (H-NMR) match literature.<sup>5</sup>

4-((4-((4-acetamidophenyl)diazenyl)phenyl)amino)-4-oxobutanoic acid (**S11**, **AN-COOH**, **BW351**, **BEW442**; novel)



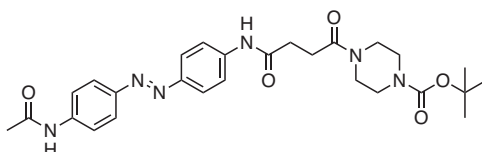
**S10** (80 mg, 0.315 mmol, 1 eq.), succinic anhydride (49.5 mg, 0.495 mmol, 1.6 eq.) and pyridine (40.5  $\mu$ L, 29.9 mg, 0.38 mmol, 1.2 eq.) were dissolved in anhydrous acetone (5 mL) under nitrogen atmosphere and heated to 60 °C for 16 h. The red precipitate was filtered and washed with cold acetone and diethyl ether to yield **AN-COOH** (59 mg, 0.17 mmol, 53%) as a red solid.

**<sup>1</sup>H-NMR** (400 MHz; D<sub>3</sub>COD):  $\delta$  = 7.86 (dd,  $J$  = 8.9, 1.2 Hz, 4H), 7.74 (dd,  $J$  = 9.0, 2.3 Hz, 4H), 2.74 – 2.63 (m, 4H), 2.17 (s, 3H).

**<sup>13</sup>C-NMR** (101 MHz; D<sub>3</sub>COD):  $\delta$  = 173.3, 171.8, 163.6, 157.3, 150.2, 148.9, 142.8, 124.5, 124.5, 121.0, 121.0, 32.9, 30.6, 24.0.

**HR-MS** (ESI)  $m/z$ : calculated for C<sub>18</sub>H<sub>19</sub>N<sub>4</sub>O<sub>4</sub><sup>+</sup>: 355.14008; found: 355.14007, (M + H)<sup>+</sup>.

*tert*-butyl 4-((4-((4-((4-acetamidophenyl)diazenyl)phenyl)amino)-4-oxobutanoyl) piperazine-1-carboxylate (**S12**, **BW358**)

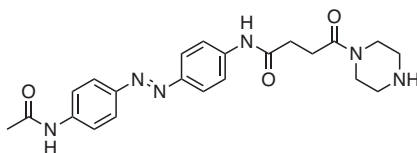


**AN-COOH** (55 mg, 0.16 mmol, 1 eq.), **S1** (57.8 mg, 0.31 mmol, 2. eq.), HBTU (70.6 mg, 0.19 mmol, 1.2 eq.) and TEA (87.3  $\mu$ L, 62.8 mg, 0.62 mmol, 4 eq.) were dissolved in DMF (3 mL) and stirred at room temperature for 16 h. The reaction mixture was concentrated under

reduced pressure and purified by silica gel column chromatography (10% MeOH in DCM) to yield **S12** (75.0 mg, 0.14 mmol, 93 %) as an orange solid that was immediately passed on without NMR characterisation.

**HR-MS** (ESI)  $m/z$ : calculated for  $C_{27}H_{35}N_6O_5^+$ : 523.26634; found: 523.26634, (M + H)<sup>+</sup>.

*N*-(4-((4-acetamidophenyl)diazenyl)phenyl)-4-oxo-4-(piperazin-1-yl)butanamide (**S13**, **ANpip**, **BW366**, **BEW444**; *novel*)



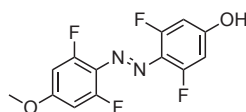
TFA (2 mL) was added dropwise to a solution of **S12** (70.0 mg, 0.13 mmol, 1 eq.) in DCM (2 mL) at 0 °C and stirred at 0 °C for 2 h. The reaction mixture was allowed to warm to room temperature, saturated aqueous solution of sodium hydrogen carbonate (50 mL) was added, and the mixture was extracted with a 3:1 mixture of DCM and propanol (3 x 50 mL). The combined organics were dried (MgSO<sub>4</sub>) and concentrated under reduced pressure to yield **ANpip** (55 mg, 0.13 mmol, 97%) as an orange solid.

**<sup>1</sup>H-NMR** (400 MHz; CD<sub>3</sub>OD):  $\delta$  = 7.86 (dd,  $J$  = 9.0, 1.5 Hz, 4H), 7.74 (dd,  $J$  = 8.9, 3.8 Hz, 4H), 3.64 – 3.55 (m, 4H), 2.98 – 2.87 (m, 2H), 2.82 (t,  $J$  = 5.1 Hz, 2H), 2.81 – 2.70 (m, 4H), 2.17 (s, 3H).

**<sup>13</sup>C-NMR** (101 MHz; CD<sub>3</sub>OD):  $\delta$  = 173.4, 172.6, 171.8, 150.2, 150.1, 142.8, 142.6, 124.5, 124.5, 121.0, 120.9, 46.1, 43.3, 32.7, 28.8, 24.0.

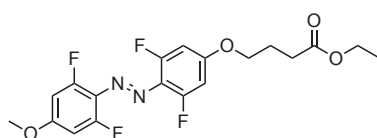
**HR-MS** (ESI)  $m/z$ : calculated for  $C_{22}H_{27}N_6O_3^+$ : 423.21392; found: 423.21385, (M + H)<sup>+</sup>.

4-((2,6-difluoro-4-methoxyphenyl)diazenyl)-3,5-difluorophenol (**S15**, **BW525**)



A solution of nitrosonium tetrafluoroborate (184 mg, 1.57 mmol, 1 eq.) in MeCN (3 mL) was added dropwise to a solution of 2,6-difluoro-4-methoxyaniline (250 mg, 1.57 mmol, 1 eq.) in MeCN (7 mL) at 0 °C and stirred at 0 °C for 5 min. The reaction mixture was added slowly to a solution of 3,5-difluorophenol (204 mg, 1.57 mmol, 1 eq.) in aqueous NaHCO<sub>3</sub>/Na<sub>2</sub>CO<sub>3</sub> buffer at pH = 10 (20 mL) at 0 °C and stirred at 0 °C for 1 h. During the addition the pH was adjusted to 10 with NaOH (2 M aqueous solution). The organic volatiles were removed under reduced pressure and the aqueous phase was extracted with EA (3 x 50 mL). The combined organics were dried (MgSO<sub>4</sub>), concentrated under reduced pressure and used without purification for the next step.

ethyl 4-(4-((2,6-difluoro-4-methoxyphenyl)diazenyl)-3,5-difluorophenoxy)butanoate (**S16**, **BW525**, **BEW543**; *novel*)



ethyl 4-bromobutyrate (28.5  $\mu$ L, 38.8 mg, 0.20 mmol, 2 eq.) was added to a solution of **S15** (29.8 mg, 0.10 mmol, 1 eq.) and potassium carbonate 41.2 mg (0.30 mmol, 3 eq.) in acetone (5 mL) and heated to 60 °C for 16 h. The reaction mixture was concentrated under reduced pressure. The crude material was suspended in saturated aqueous NH<sub>4</sub>Cl (30 mL) and extracted with DCM (3 x 30 mL). The combined organics were dried (MgSO<sub>4</sub>), concentrated under reduced pressure and purified by silica gel column chromatography (0-30% EA in hexane) to yield **S16** (30.0 mg (72.4  $\mu$ mol, 73%)) as an orange solid.

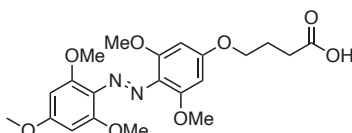


**<sup>1</sup>H-NMR** (500 MHz; (CD<sub>3</sub>)<sub>2</sub>SO):  $\delta$  = 6.96 (dd,  $J$  = 11.6, 7.3 Hz, 4H), 4.13 (t,  $J$  = 6.4 Hz, 2H), 4.08 (q,  $J$  = 7.2 Hz, 2H), 3.88 (s, 3H), 2.46 (t,  $J$  = 7.3 Hz, 2H), 1.99 (p,  $J$  = 7.0 Hz, 2H), 1.19 (t,  $J$  = 7.1 Hz, 3H).

**<sup>13</sup>C-NMR** (126 MHz; (CD<sub>3</sub>)<sub>2</sub>SO):  $\delta$  = 172.4, 162.1 (t,  $J$  = 14.7 Hz), 161.3 (t,  $J$  = 14.4 Hz), 157.4 (d,  $J$  = 7.5 Hz), 155.3 (d,  $J$  = 7.5 Hz), 148.7, 125.0 (t,  $J$  = 9.4 Hz), 106.4, 99.6 (ddd,  $J$  = 42.5, 24.1, 2.8 Hz), 68.1, 59.9, 56.7, 29.9, 23.8, 14.1.

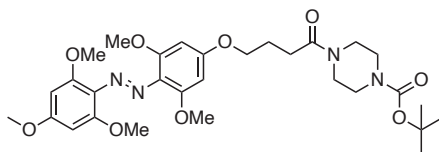
**HR-MS** (ESI)  $m/z$ : calculated for C<sub>19</sub>H<sub>19</sub>F<sub>4</sub>N<sub>2</sub>O<sub>4</sub><sup>+</sup>: 415.12755; found: 415.12722 (M + H)<sup>+</sup>.

4-(3,5-dimethoxy-4-((2,4,6-trimethoxyphenyl)diazenyl)phenoxy)butanoic acid (**S17**, **BW542**)



KOH (196 mg, 85%, 2.96 mmol, 59 eq.) was added to a solution of **S16** (21 mg, 0.05 mmol, 1 eq) in MeOH (10 mL) and heated to reflux until full conversion was indicated by LC/MS (usually 16 h). The reaction mixture was concentrated under reduce pressure. The resulting solid residue was suspended in hydrochloric acid (2 M aqueous solution, 50 mL) and extracted with 3:1 DCM: *n*-propanol (3 x 50 mL). The combined organics were dried (MgSO<sub>4</sub>) and concentrated under reduced pressure. The crude material was used for the next step without further purification.

*tert*-butyl-4-(4-(3,5-dimethoxy-4-((2,4,6-trimethoxyphenyl)diazenyl)phenoxy)butanoyl) piperazine-1-carboxylate (**S18**, BW542, BEW544, **AO(OMe)<sub>4</sub>pipBoc**; **novel**)



**S8** (18.9 mg, 0.101 mmol, 2 eq.), HBTU (23.1 mg, 0.06 mmol, 1.2 eq) and TEA (36  $\mu$ L, 25.6, 0.25 mmol, 5 eq.) were added to a solution of crude **S17** in DMF (2 mL) and stirred at room temperature for 16 h. The reaction mixture was concentrated under reduced pressure and purified by silica gel column chromatography (10-100% ethyl acetate in hexane) to yield **S18** (20.5 mg, 34.0  $\mu$ mol, 67%) as an orange solid.

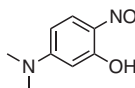
**<sup>1</sup>H-NMR** (500 MHz; ; (CD<sub>3</sub>)<sub>2</sub>SO):  $\delta$  = 6.33 (d,  $J$  = 3.9 Hz, 4H), 4.08 (t,  $J$  = 6.5 Hz, 2H), 3.83 (s, 3H), 3.71 (d,  $J$  = 1.6 Hz, 12H), 3.45 (t,  $J$  = 5.5 Hz, 4H), 3.37 – 3.32 (m, 2H), 3.31 – 3.27 (m, 2H), 2.54 – 2.50 (m, 2H), 1.98 (p,  $J$  = 6.5 Hz, 2H), 1.41 (s, 9H).

**<sup>13</sup>C-NMR** (126 MHz; (CD<sub>3</sub>)<sub>2</sub>SO):  $\delta$  = 170.3, 160.5, 159.8, 153.8, 153.1, 153.1, 128.1, 128.1, 92.1, 91.7, 79.1, 67.2, 56.1, 55.5, 44.6, 40.8, 28.6, 28.0, 24.3.

**HR-MS** (ESI)  $m/z$ : calculated for C<sub>30</sub>H<sub>43</sub>N<sub>4</sub>O<sub>9</sub><sup>+</sup>: 603.30246; found: 603.30323 (M + H)<sup>+</sup>.

## 10.4.2 Fluorophore building blocks

5-(dimethylamino)-2-nitrosophenol (**S19**, **BW260**; **known**)

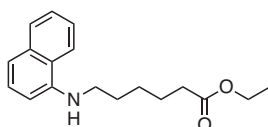


**S19** was synthesized according to literature.<sup>70</sup>

A solution of sodium nitrite (251 mg, 3.64 mmol; 1 eq.) in water (3 mL) was added to a solution of 3-(dimethylamino) phenol (500 mg, 3.64 mmol; 1 eq.) in hydrochloric acid (12M aqueous solution, 3 mL) and water (1 mL) at 0 °C and stirred at 0 °C for 1 h. The resulting red precipitate was filtered, washed with a saturated, aqueous solution of sodium acetate and

recrystallized from acetone to yield **S19** (342 mg, 2.06 mmol; 57%) as a red solid. Analytical data (H-NMR) match literature.<sup>70</sup>

ethyl 6-(naphthalen-1-ylamino)hexanoate (**S20**, **BW297**, **BEW326**; *novel*)



**S20** was synthesized according an adapted procedure from literature.<sup>71</sup>

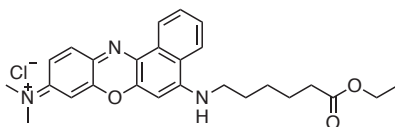
1-naphthalenamine (732 mg, 5.11 mmol, 1 eq.), ethyl 6-bromohexanoate (1.00 mL, 1.25 g, 5.26 mmol, 1.1 eq.) and potassium carbonate (2.12 g, 15.3 mmol, 3 eq.) were dissolved in MeCN (30 mL) and heated to reflux for 16 h. The reaction mixture was filtered and concentrated under reduced pressure. The crude material was purified by silica gel column chromatography (10% EA in hexane) to yield **S20** (320 mg, 1.12 mmol, 22 %) as a colorless oil.

**<sup>1</sup>H-NMR** (400 MHz; CDCl<sub>3</sub>):  $\delta$  = 7.96 – 7.62 (m, 2H), 7.47 – 7.41 (m, 2H), 7.35 (t,  $J$  = 7.9 Hz, 1H), 7.23 (d,  $J$  = 8.2 Hz, 1H), 6.62 (d,  $J$  = 7.6 Hz, 1H), 4.14 (q,  $J$  = 7.1 Hz, 2H), 3.30 (t,  $J$  = 7.1 Hz, 2H), 2.35 (t,  $J$  = 7.4 Hz, 2H), 1.81 (p,  $J$  = 14.7, 7.3 Hz, 2H), 1.72 (p,  $J$  = 7.6 Hz, 2H), 1.26 (t,  $J$  = 7.1 Hz, 3H).

**<sup>13</sup>C-NMR** (101 MHz; CDCl<sub>3</sub>):  $\delta$  = 173.8, 134.5, 128.8, 126.8, 126.6, 125.8, 124.8, 123.5, 119.9, 118.6, 117.4, 60.4, 55.2, 34.4, 29.2, 27.0, 24.9, 14.4.

**HR-MS** (ESI)  $m/z$ : calculated for C<sub>18</sub>H<sub>24</sub>NO<sub>2</sub><sup>+</sup>: 286.18016; found: 286.18030, (M + H)<sup>+</sup>.

*N*-(5-((6-ethoxy-6-oxohexyl)amino)-9*H*-benzo[*a*]phenoxazin-9-ylidene)-*N*-methylmethanaminium chloride (**S21**, **BW301**, **BEW332**; *novel*)



**S21** was synthesized according an adapted procedure from literature.<sup>72</sup>

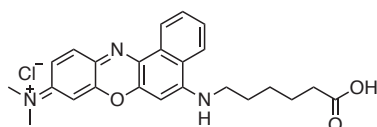
Hydrochloric acid (12M aqueous solution, 1.17 mL, 1.39 g, 14.2 mmol, 15 eq.) and **S19** (157 mg, 0.95 mmol, 1 eq.) were added to a solution of **S20** (270 mg, 0.95 mmol, 1 eq.) in ethanol (40 mL) at 0 °C. The reaction mixture was stirred at 0 °C for 10 min, allowed to warm to room temperature and heated to reflux for 16 h. The solvent was removed under reduced pressure and the crude material was purified by dry column chromatography (side products were eluted with EA and the desired product with 5% MeOH in DCM) to yield **S21** (74.3 mg, 0.16 mmol, 17 %) as a blue solid.

**<sup>1</sup>H-NMR** (500 MHz; CD<sub>3</sub>OD):  $\delta$  = 8.90 (d,  $J$  = 8.2 Hz, 1H), 8.35 (d,  $J$  = 8.5 Hz, 1H), 7.93 (ddt,  $J$  = 8.1, 7.1, 1.0 Hz, 1H), 7.88 – 7.81 (m, 2H), 7.28 – 7.24 (m, 1H), 6.99 (s, 1H), 6.91 – 6.86 (m, 1H), 4.10 (q,  $J$  = 7.2 Hz, 2H), 3.75 (t,  $J$  = 7.3 Hz, 2H), 3.32 (s, 6H), 2.39 (t,  $J$  = 7.3 Hz, 2H), 1.90 (p,  $J$  = 7.5 Hz, 2H), 1.74 (p,  $J$  = 7.4 Hz, 2H), 1.62 – 1.49 (m, 2H), 1.22 (t,  $J$  = 7.1 Hz, 3H).

**<sup>13</sup>C-NMR** (126 MHz; CD<sub>3</sub>OD):  $\delta$  = 175.3, 159.7, 157.4, 153.5, 149.4, 135.5, 133.8, 133.1, 132.7, 131.5, 131.1, 125.8, 124.9, 123.9, 116.5, 97.1, 94.6, 61.5, 45.7, 41.1, 34.8, 29.4, 27.5, 25.7, 14.5.

**HR-MS** (ESI)  $m/z$ : calculated for C<sub>26</sub>H<sub>30</sub>N<sub>3</sub>O<sub>3</sub><sup>+</sup>: 432.22799; found: 432.22817, M<sup>+</sup>.

*N*-(5-((5-carboxypentyl)amino)-9*H*-benzo[*a*]phenoxazin-9-ylidene)-*N*-methylmethanaminium chloride (**S22**, **NB-COOH**, **BW303**, **BEW333**; novel)



**NB-COOH** was synthesized according an adapted procedure from literature.<sup>73</sup>

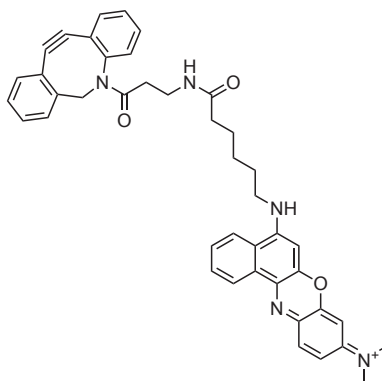
**S21** (71.0 mg, 0.15 mmol, 1 eq.) was dissolved in hydrochloric acid (1M aqueous solution, 15 mL) and heated to reflux for 2 h. The reaction mixture was concentrated under reduced pressure to yield **NB-COOH** (65.0 mg, 0.15 mmol, 97 %) as a blue solid.

<sup>1</sup>H-NMR (500 MHz; CD<sub>3</sub>OD):  $\delta$  = 8.95 – 8.88 (m, 1H), 8.55 – 8.12 (m, 1H), 7.97 – 7.90 (m, 1H), 7.91 – 7.80 (m, 2H), 7.30 – 7.23 (m, 1H), 7.03 – 6.98 (m, 1H), 6.93 – 6.87 (m, 1H), 3.76 (t, *J* = 7.6 Hz, 2H), 3.32 (d, *J* = 1.4 Hz, 6H), 2.40 (t, *J* = 7.3 Hz, 2H), 1.90 (p, *J* = 7.6 Hz, 2H), 1.74 (p, *J* = 7.4 Hz, 2H), 1.61 – 1.49 (m, 2H).

<sup>13</sup>C-NMR (126 MHz; CD<sub>3</sub>OD):  $\delta$  = 175.8, 159.8, 157.4, 153.6, 149.4, 135.6, 133.8, 133.1, 132.7, 131.5, 131.1, 125.8, 124.9, 123.9, 116.5, 97.2, 94.6, 45.7, 41.1, 34.5, 29.4, 27.5, 25.6.

**HR-MS** (ESI) *m/z*: calculated for C<sub>24</sub>H<sub>25</sub>N<sub>3</sub>O<sub>3</sub><sup>+</sup>: 404.19687; found: 404.19677, M<sup>+</sup>.

*N*-(5-((6-((3-(dibenzo[*b,f*]cyclooctyne)-3-oxopropyl)amino)-6-oxohexyl)amino)-9*H*-benzo[*a*]phenoxazin-9-ylidene)-*N*-methylmethanaminium (**S23**, **NB-DBCO**, **BW550**, **BEW548**; novel)



**NB-COOH** (5.7 mg, 0.01 mmol, 1 eq.), DBCO-amine (4.0 mg, 0.01 mmol, 1.1 eq., CAS: 1255942-06-3), HBTU (7.3 mg, 0.02 mmol, 1.5 eq.) and TEA (10  $\mu$ L, 7.2 mg, 0.07 mmol, 5.5 eq.) were dissolved in DMF (0.5 mL) and stirred at room temperature for 16 h. The reaction mixture was diluted with water (100  $\mu$ L) and hydrochloric acid (50  $\mu$ L, 2 M aqueous solution) and purified by reversed phase preparative HPLC to yield **NB-DBCO** (4.0 mg, 6.03  $\mu$ mol, 47%) as a blue solid.

<sup>1</sup>H-NMR (500 MHz; CD<sub>3</sub>OD):  $\delta$  = 8.98 – 8.92 (m, 1H), 8.38 – 8.34 (m, 2H), 7.98 – 7.88 (m, 2H), 7.84 (t, *J* = 7.7 Hz, 1H), 7.63 (d, *J* = 7.6 Hz, 1H), 7.48 – 7.24 (m, 6H), 7.16 (d, *J* = 7.5 Hz, 1H), 7.01 – 6.94 (m, 1H), 6.89 – 6.84 (m, 1H), 5.11 (d, *J* = 14.0 Hz, 1H), 3.73 (p, *J* = 7.0 Hz, 2H), 3.66 (d, *J* = 14.0 Hz, 1H), 3.32 (s, 6H), 3.32 (m, 1H), 3.26 (t, *J* = 6.5 Hz, 1H), 3.16 – 3.09 (m, 1H), 2.55 – 2.41 (m, 1H), 2.14 – 2.02 (m, 2H), 1.85 (p, *J* = 7.3 Hz, 2H), 1.65 – 1.57 (m, 2H), 1.44 (dt, *J* = 10.3, 6.6 Hz, 2H). (**NB**: the NMe<sub>2</sub> singlet with 6H, and multiplet with 1H, are overlapped by the CHD<sub>2</sub>OD signal, as confirmed by HSQC.)

<sup>13</sup>C-NMR (126 MHz; CD<sub>3</sub>OD):  $\delta$  = 175.8, 173.2, 167.7, 159.8, 157.4, 153.6, 152.6, 149.5, 149.4, 135.6, 133.8, 133.4, 133.2, 132.8, 131.6, 131.2, 130.4, 130.0, 129.7, 129.2, 128.9, 128.1, 126.4, 125.8, 125.0, 124.3, 123.9, 123.6, 116.5, 115.6, 97.2, 94.7, 56.6, 45.7, 41.1, 36.7, 36.4, 35.6, 29.2, 27.4, 26.1.

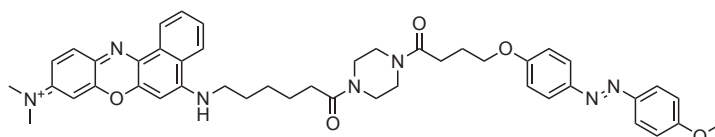
**HR-MS** (ESI) *m/z*: calculated for C<sub>42</sub>H<sub>40</sub>N<sub>5</sub>O<sub>3</sub><sup>+</sup>: 662.31257; found: 662.31313, M<sup>+</sup>.

### 10.4.3 NB-Azobenzene conjugates for in cuvette studies

#### General procedure A for conjugate coupling

1 eq. carboxylic acid, 1 eq. amine, 1.2 eq. HBTU and 5 eq. TEA were dissolved in DMF (10 mg/mL) and stirred at room temperature for 16 h. The reaction mixture was diluted with 12.5 vol-% water and 5 vol-% acetic acid and purified by reversed phase preparative HPLC. Typical gradient used for preparative HPLC: 9:1 water (0.1% formic acid) / MeCN (0.1% formic acid) to MeCN (0.1 % formic acid) over 27 min.

*N*-(5-((6-(4-(4-(4-((4-methoxyphenyl)diazenyl)phenoxy)butanoyl)piperazin-1-yl)-6-oxohexyl)amino)-9*H*-benzo[*a*]phenoxazin-9-ylidene)-*N*-methylmethanaminium methanoate (**S24**, **NB-AO**, **BW278**; *novel*)



**NB-AO** was synthesized according to *General procedure A*.

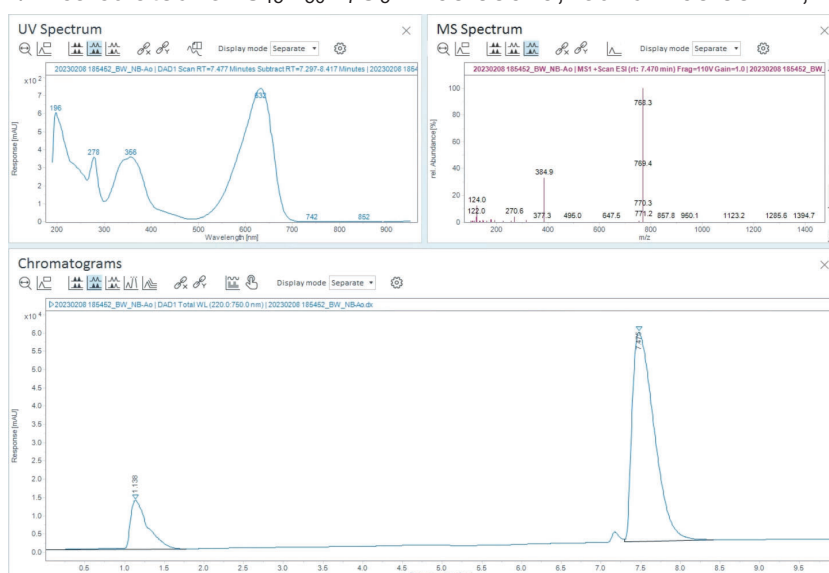
Carboxylic acid: **NB-COOH** (13.2 mg, 29.9  $\mu$ mol) Amine: **AOpip** (11.4 mg, 29.9  $\mu$ mol)

Yield: 9.6 mg (11.9  $\mu$ mol, 40%) as a blue solid.

**<sup>1</sup>H-NMR** (400 MHz; CD<sub>3</sub>OD):  $\delta$  = 8.89 (d, *J* = 8.1 Hz, 1H), 8.51 (s, 1H), 8.33 (d, *J* = 8.2 Hz, 1H), 7.93 (t, *J* = 7.6 Hz, 1H), 7.84 (t, *J* = 8.7 Hz, 2H), 7.82 – 7.73 (m, 4H), 7.24 (d, *J* = 9.5 Hz, 1H), 7.04 – 6.90 (m, 5H), 6.84 (d, *J* = 2.7 Hz, 1H), 4.09 (q, *J* = 5.8 Hz, 2H), 3.82 (d, *J* = 9.6 Hz, 3H), 3.71 (dt, *J* = 14.8, 7.2 Hz, 2H), 3.64 – 3.49 (m, 8H), 3.29 (s, 6H), 2.60 (q, *J* = 6.7 Hz, 2H), 2.46 (dt, *J* = 15.8, 7.0 Hz, 2H), 2.10 (p, *J* = 6.6 Hz, 2H), 1.86 (p, *J* = 15.2, 8.1, 7.7 Hz, 1H), 1.71 (p, *J* = 14.2, 7.0 Hz, 2H), 1.53 (h, *J* = 6.8 Hz, 2H).

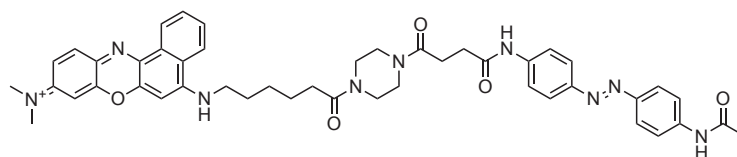
**<sup>13</sup>C-NMR** (101 MHz; CD<sub>3</sub>OD):  $\delta$  = 174.1, 173.6, 163.3, 162.4, 159.6, 157.3, 153.4, 149.3, 148.1, 135.5, 133.8, 133.1, 132.7, 132.4, 131.5, 131.1, 125.8, 125.3, 125.3, 124.9, 123.9, 116.5, 115.8, 115.2, 97.1, 94.6, 68.4, 56.1, 46.3, 45.6, 42.4, 41.1, 40.2, 33.5, 30.2, 29.4, 27.6, 25.8.

**HR-MS** (ESI) *m/z*: calculated for C<sub>45</sub>H<sub>50</sub>N<sub>7</sub>O<sub>5</sub><sup>+</sup>: 768.38679; found: 768.38721, M<sup>+</sup>.



LC/MS

*N*-(5-((6-(4-(4-((4-(4-acetamidophenyl)diazenyl)phenyl)amino)-4-oxobutanoyl)piperazin-1-yl)-6-oxohexyl)amino)-9*H*-benzo[*a*]phenoxazin-9-ylidene)-*N*-methylmethanaminium chloride (**S25**, **NB-AN**, **BW404**, **BEW445**; *novel*)



**NB-AN** was synthesized according to *General procedure A*.

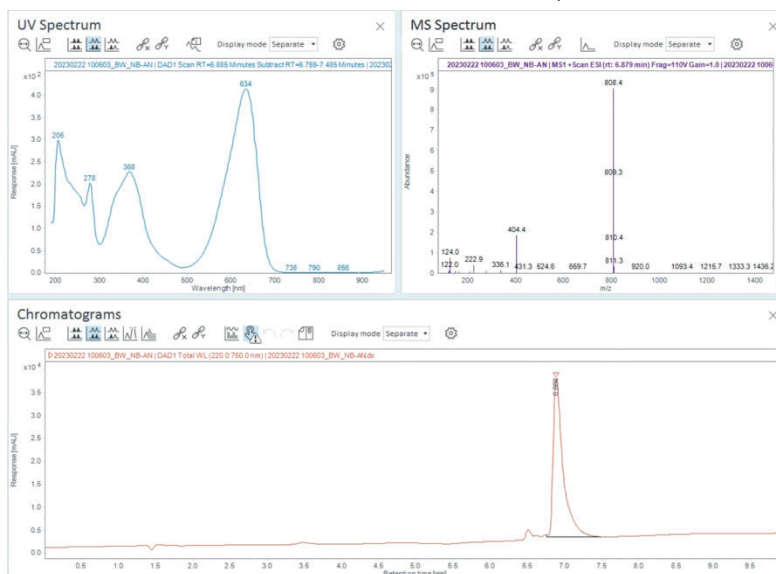
Carboxylic acid: **NB-COOH** (8 mg, 18.2 μmol) Amine: **ANpip** (7.7 mg, 18.2 μmol)

Yield: 2.9 mg (3.43 μmol, 19%) as a blue solid.

<sup>1</sup>**H-NMR** (400 MHz; CD<sub>3</sub>OD): δ = 8.95 – 8.87 (m, 1H), 8.55 (s, 1H), 8.34 (t, *J* = 8.5 Hz, 1H), 7.91 (t, *J* = 7.7 Hz, 1H), 7.81 – 7.74 (m, 4H), 7.74 – 7.64 (m, 4H), 7.26 – 7.17 (m, 1H), 6.96 (s, 1H), 6.90 – 6.81 (m, 1H), 3.75 (t, *J* = 7.2 Hz, 2H), 3.71 – 3.53 (m, 8H), 3.28 (s, 6H), 2.79 – 2.72 (m, 4H), 2.53 – 2.45 (m, 2H), 1.95 – 1.85 (m, 2H), 1.78 – 1.70 (m, 2H), 1.60 – 1.52 (m, 2H).

<sup>13</sup>**C-NMR** (101 MHz; CD<sub>3</sub>OD): δ = 174.4, 172.8, 171.9, 170.4, 148.5, 141.2, 136.7, 132.2, 131.4, 131.0, 129.7, 128.5, 124.3, 123.1, 123.1, 122.6, 119.5, 119.4, 95.8, 67.7, 56.2, 56.1, 55.9, 53.4, 41.2, 41.2, 39.6, 38.8, 30.2, 28.7, 28.1, 27.3, 26.2, 24.5, 24.5, 23.6, 22.6, 22.6, 13.0.

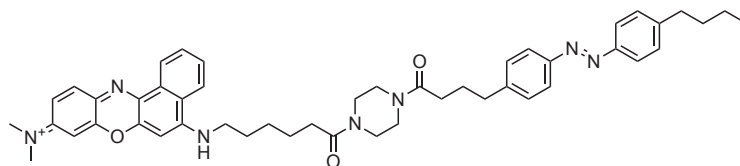
**HR-MS** (ESI) *m/z*: calculated for C<sub>46</sub>H<sub>50</sub>N<sub>9</sub>O<sub>5</sub><sup>+</sup>: 808.39294; found: 808.39284, M<sup>+</sup>.



LC/MS



*N*-(5-((6-(4-(4-(4-((4-butylphenyl)diazenyl)phenyl)butanoyl)piperazin-1-yl)-6-oxohexyl)amino)-9*H*-benzo[*a*]phenoxazin-9-ylidene)-*N*-methylmethanaminium chloride (**S26**, **NB-AK**, **BW284**, **BEW342**; *novel*)



**NB-AK** was synthesized according to *General procedure A*.

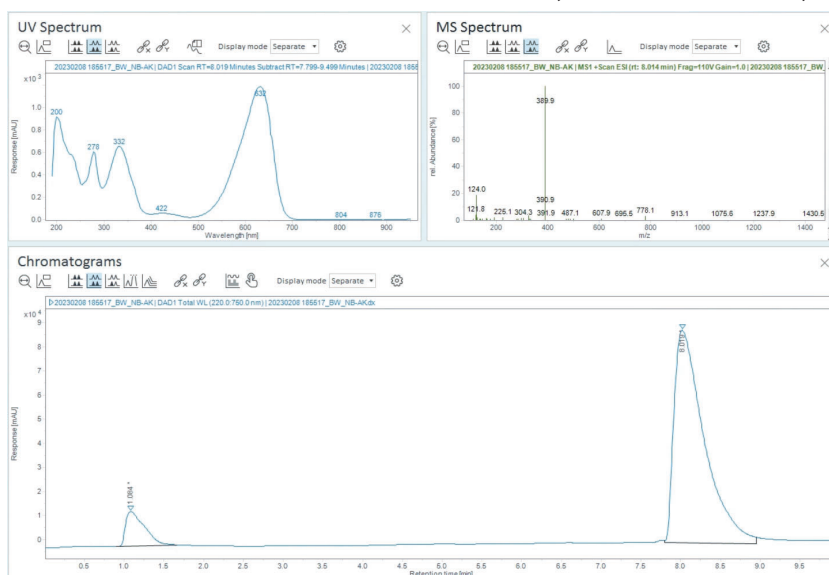
Carboxylic acid: **NB-COOH** (10 mg, 22.7  $\mu$ mol) Amine: **AKpip** (8.9 mg, 22.7  $\mu$ mol)

Yield: 8.2 mg (10.2  $\mu$ mol, 44%) as a blue solid.

**<sup>1</sup>H-NMR** (400 MHz; (CD<sub>3</sub>)<sub>2</sub>SO):  $\delta$  = 10.07 (s, 1H), 8.80 (d, *J* = 8.1 Hz, 1H), 8.52 (d, *J* = 8.2 Hz, 1H), 7.95 (d, *J* = 7.9 Hz, 1H), 7.87 (t, *J* = 7.9 Hz, 2H), 7.79 (t, *J* = 7.2 Hz, 4H), 7.47 – 7.34 (m, 4H), 7.25 (s, 1H), 7.07 (s, 1H), 6.88 (s, 1H), 3.73 (t, *J* = 7.1 Hz, 2H), 3.51 – 3.36 (m, 8H), 3.27 (s, 6H), 2.68 (q, *J* = 7.4 Hz, 4H), 2.34 (q, *J* = 6.1, 5.4 Hz, 4H), 1.85 (p, *J* = 7.6 Hz, 2H), 1.77 (p, *J* = 7.4 Hz, 2H), 1.66 – 1.54 (m, 4H), 1.45 (p, *J* = 7.5 Hz, 2H), 1.33 (h, *J* = 7.3 Hz, 2H), 0.91 (t, *J* = 7.3 Hz, 3H).

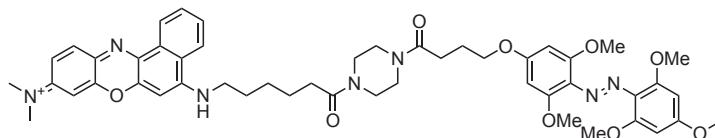
**<sup>13</sup>C-NMR** (201 MHz; (D<sub>3</sub>CO)<sub>2</sub>):  $\delta$  = 176.0, 169.3, 159.8, 157.4, 153.6, 152.2, 149.5, 147.9, 146.6, 133.8, 133.1, 132.8, 132.4, 131.5, 131.1, 130.4, 130.2, 129.9, 125.8, 125.5, 123.9, 123.8, 116.4, 114.7, 97.2, 94.7, 46.6, 45.7, 42.8, 41.1, 36.5, 34.9, 34.8, 33.1, 30.2, 27.8, 27.6, 27.5, 25.9, 23.4, 14.3.

**HR-MS** (ESI) *m/z*: calculated for C<sub>48</sub>H<sub>56</sub>N<sub>7</sub>O<sub>3</sub><sup>+</sup>: 778.44392; found: 778.44385, M<sup>+</sup>.



LC/MS

*N*-(5-((6-(4-(4-(3,5-dimethoxy-4-((2,4,6-trimethoxyphenyl)diazenyl)phenoxy)butanoyl) piperazin-1-yl)-6-oxohexyl)amino)-9*H*-benzo[*a*]phenoxazin-9-ylidene)-*N*-methylmethanaminium (**S27**, **NB-AO(OMe)<sub>4</sub>**, **BW543**; *novel*)



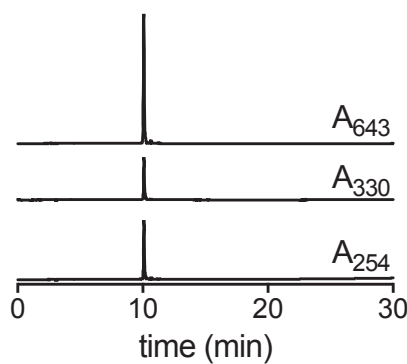
TFA (1 mL) was added to a solution of **AO(OMe)<sub>4</sub>** (6.9 mg, 11.4  $\mu$ mol) in DCM (1 mL) and stirred at room temperature for 1 h. All volatiles were removed under a stream of nitrogen and the crude material was azeotroped with toluene (3 x 2 mL). Deprotected **AO(OMe)<sub>4</sub>** was used without further purification.

**NB-AO(OMe)<sub>4</sub>** was synthesized according to *General procedure A*.

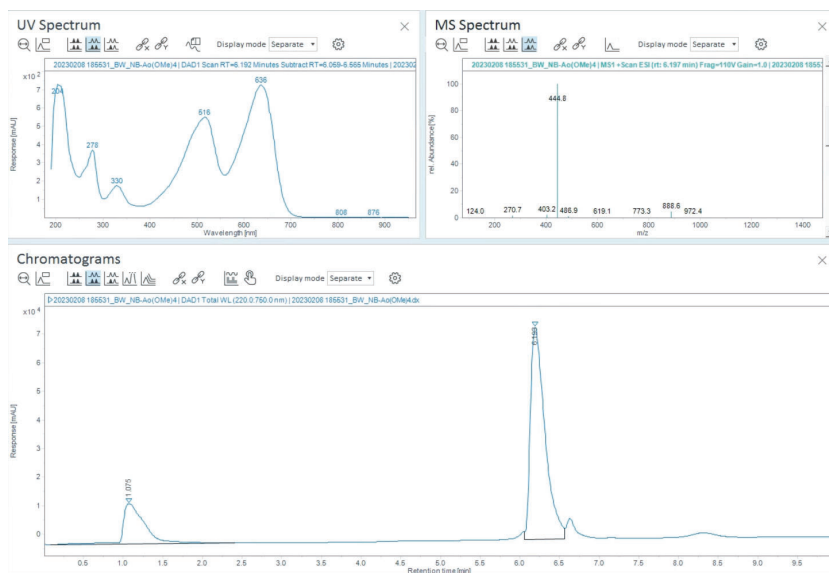
Carboxylic acid: **NB-COOH** (5 mg, 11.4  $\mu$ mol) Amine: deprotected **AO(OMe)<sub>4</sub>**

Yield: 0.4 mg (0.45  $\mu$ mol, 4%) as a blue solid.

**HR-MS** (ESI) *m/z*: calculated for  $C_{49}H_{58}N_7O_9^+$ : 888.42905; found: 888.42855,  $M^+$ .



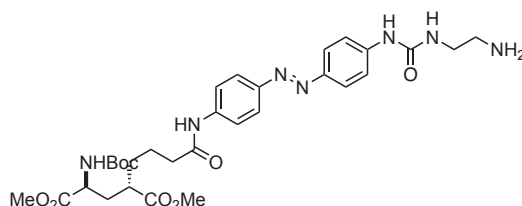
### HPLC-DAD trace



### LC/MS

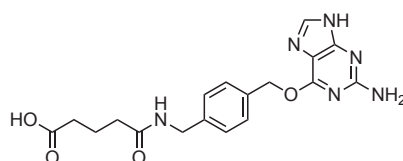
#### 10.4.4 Bioactive Photoswitches BAG and BANG

dimethyl (2*S*,4*S*)-2-(4-(((4-((4-(3-(2-aminoethyl)ureido)phenyl)diazenyl)phenyl)amino)-4-oxobutyl)-4-((*tert*-butoxycarbonyl)amino)pentanedioate (**S28**; known)



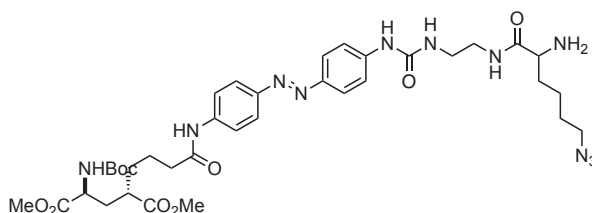
**S28** was synthesized as described in literature.<sup>25</sup>

5-(((4-(((2-amino-9*H*-purin-6-yl)oxy)methyl)benzyl)amino)-5-oxopentanoic acid (**S29**, **BG-COOH**; known)



**BG-COOH** was synthesized as described in literature.<sup>74</sup>

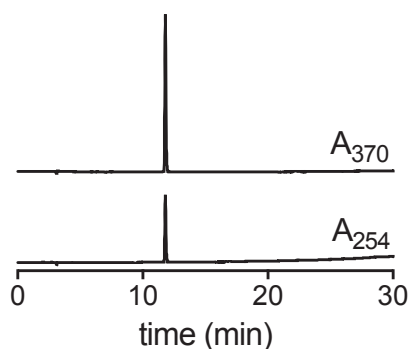
dimethyl(2*S*,4*S*)-2-(4-(((4-((4-(3-(2-(2-amino-6-azidohexanamido)ethyl)ureido)phenyl)diazenyl)phenyl)amino)-4-oxobutyl)-4-((*tert*-butoxycarbonyl)amino)pentanedioate (**S30**, **AW87**; novel)



**S30** was synthesized following an adapted procedure from literature.<sup>25</sup>

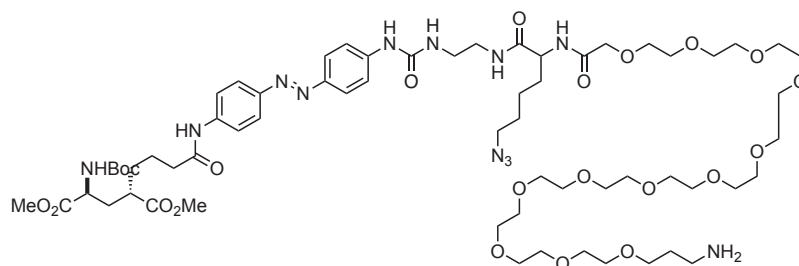
**S28** (8.0 mg, 12.5  $\mu\text{mol}$ , 1 eq.), Fmoc-L-Lys(N<sub>3</sub>)OH (5.9 mg, 15.0  $\mu\text{mol}$ , 1.2 eq., CAS: 159610-89-6), HBTU (6.0 mg, 15.8  $\mu\text{mol}$ , 1.3 eq.) and DIPEA (8.7  $\mu\text{L}$ , 6.5 mg, 49.9  $\mu\text{mol}$ , 4 eq.) were dissolved in DMSO (800  $\mu\text{L}$ ) and stirred at room temperature for 16 h. DBU (40  $\mu\text{L}$ ) was added and the reaction mixture was allowed to stir at room temperature for 10 min. AcOH (80  $\mu\text{L}$ ) was added and the crude material was purified by reversed phase preparative HPLC to yield **S30** (8.7 mg, 10.9  $\mu\text{mol}$ , 87%) as an orange solid.

**HR-MS** (ESI) *m/z*: calculated for C<sub>37</sub>H<sub>54</sub>N<sub>11</sub>O<sub>9</sub><sup>+</sup>: 796.41005; found: 796.40990, M<sup>+</sup>.



**HPLC-DAD trace**

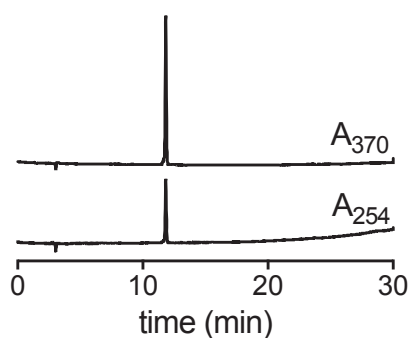
Dimethyl(2*S*,4*S*)-2-(4-((4-((4-(3-(45-amino-5-(4-azidobutyl)-4,7-dioxo9,12,15,18,21,24,27,30,33,36,39,42-dodecaoxa-3,6-diazapentatetracontyl)ureido)phenyl) diazenyl)phenyl)amino)-4-oxobutyl)-4-((*tert*-butoxycarbonyl)amino)pentanedioate (**S31**, **AW89**; *novel*)



**S31** was synthesized following an adapted procedure from literature.<sup>25</sup>

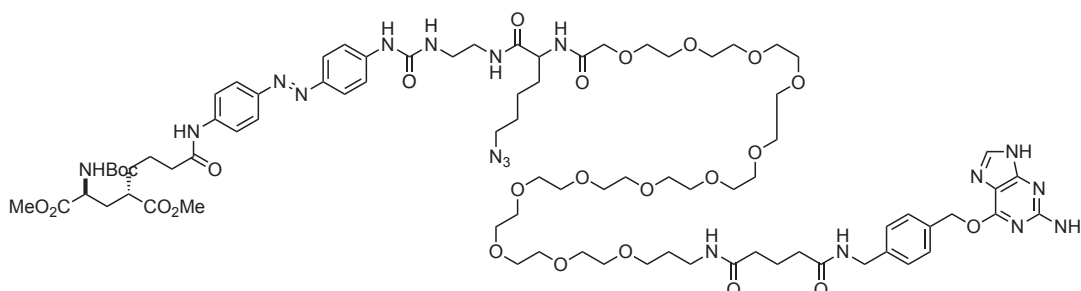
**S30** (10.6 mg, 13.3  $\mu\text{mol}$ , 1 eq.), Fmoc-N-amido-PEG12-acid (13.4 mg, 16.0  $\mu\text{mol}$ , 1.2 eq., CAS: 1952360-91-6), HBTU (6.4 mg, 16.9  $\mu\text{mol}$ , 1.3 eq.) and DIPEA (9.3  $\mu\text{L}$ , 6.9 mg, 53.5  $\mu\text{mol}$ , 4 eq.) were dissolved in DMSO (1 mL) and stirred at room temperature for 3 h. DBU (50  $\mu\text{L}$ ) was added, and the reaction mixture was allowed to stir at room temperature for 10 min. AcOH (100  $\mu\text{L}$ ) was added and the crude material was purified by reversed phase preparative HPLC to yield **S31** (11.2 mg, 8.03  $\mu\text{mol}$ , 60%) as an orange solid.

**HR-MS** (ESI)  $m/z$ : calculated for  $\text{C}_{49}\text{H}_{58}\text{N}_7\text{O}_9^+$ : 1395.76174; found: 1395.76314,  $\text{M}^+$ .



HPLC-DAD trace

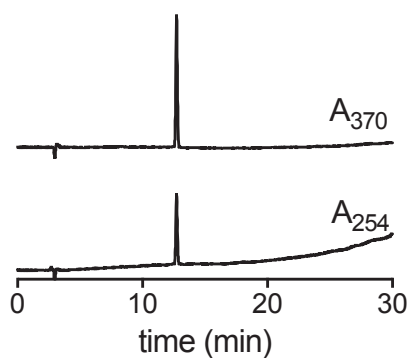
dimethyl (2*S*,4*S*)-2-(4-(((4-(3-(1-(4-(((2-amino-9*H*-purin-6-yl)oxy)methyl)phenyl)-49-(4-azidobutyl)-3,7,47,50-tetraoxo-12,15,18,21,24,27,30,33,36,39,42,45-dodecaoxa-2,8,48,51-tetraazatripentacontan-53-yl)ureido)phenyl)diazenyl)phenyl)amino)-4-oxobutyl)-4-((*tert*-butoxycarbonyl)amino)pentanedioate (**S32**, **AW92**; *novel*)



**S32** was synthesized following an adapted procedure from literature.<sup>25</sup>

**S31** (11.2 mg, 8.03  $\mu$ mol, 1 eq.), **BG-COOH** (3.2 mg, 8.32  $\mu$ mol, 1 eq.), HBTU (3.7 mg, 9.63  $\mu$ mol, 1.2 eq.) and DIPEA (6.0  $\mu$ L, 4.3 mg, 33.4  $\mu$ mol, 4.2 eq.) were dissolved in DMSO (1.1 mL) and stirred at room temperature for 5 h. Water (100  $\mu$ L) and AcOH (2  $\mu$ L) were added and the crude material was purified by reversed phase preparative HPLC to yield **S32** (8.7 mg, 4.94  $\mu$ mol, 62%) as an orange solid.

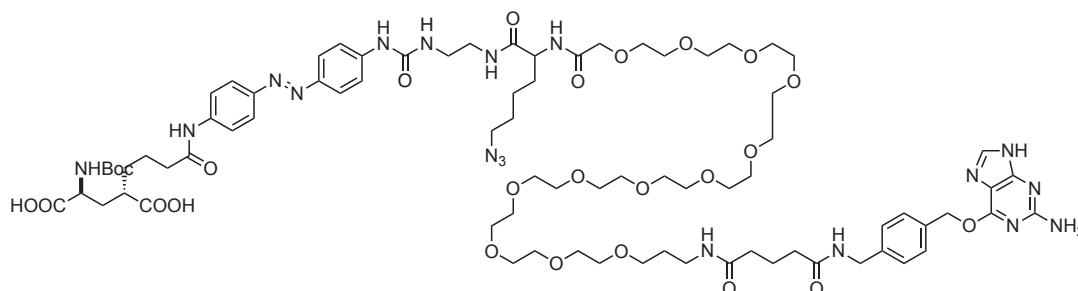
**HR-MS** (ESI) *m/z*: calculated for  $C_{82}H_{125}N_{18}O_{25}Na^{2+}$ : 892.44750; found: 892.44667, ( $M + H + Na$ )<sup>2+</sup>.



**HPLC-DAD trace**



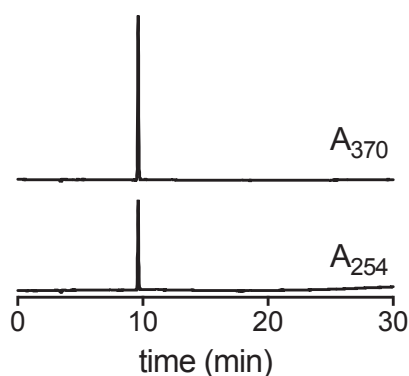
(2*S*,4*S*)-2-(4-((4-((3-(1-(4-(((2-amino-9*H*-purin-6-yl)oxy)methyl)phenyl)-49-(4-azidobutyl)-3,7,47,50-tetraoxo-12,15,18,21,24,27,30,33,36,39,42,45-dodecaoxa-2,8,48,51-tetraazatripentacontan-53-yl)ureido)phenyl)diazenyl)phenyl)amino)-4-oxobutyl)-4-((*tert*-butoxycarbonyl)amino)pentanedioic acid (**S33**, **AW96**; *novel*)



**S33** was synthesized following an adapted procedure from literature.<sup>25</sup>

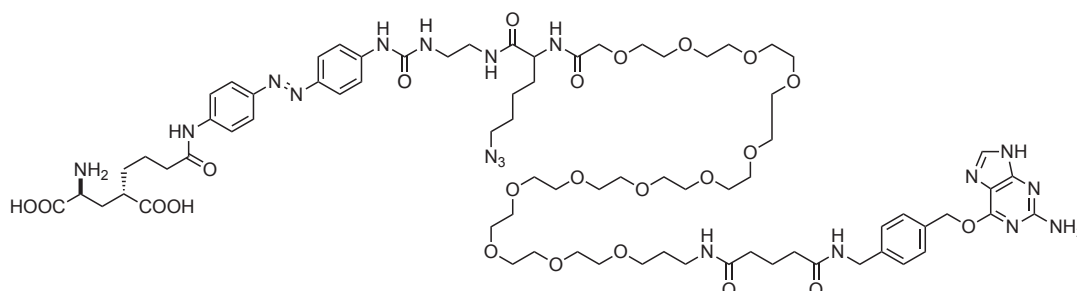
**S32** (8.7 mg, 4.94  $\mu\text{mol}$ , 1 eq.) were suspended in MeOH (400  $\mu\text{L}$ ) and LiOH (400  $\mu\text{L}$ , 1M aqueous solution) and stirred at room temperature for 45 min. AcOH (80  $\mu\text{L}$ ) was added and the crude material was purified by reversed phase preparative HPLC to yield **S33** (4.6 mg, 2.65  $\mu\text{mol}$ , 54%) as an orange solid.

**HR-MS** (ESI)  $m/z$ : calculated for  $\text{C}_{80}\text{H}_{121}\text{N}_{18}\text{O}_{25}\text{Na}^{2+}$ : 878.43185; found: 878.43113,  $(M + H + \text{Na})^{2+}$ .



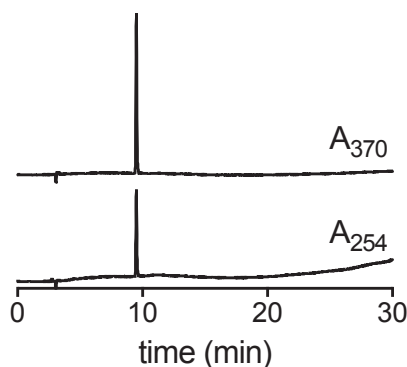
HPLC-DAD trace

(2S,4S)-2-amino-4-(4-((4-(3-(1-(4-(((2-amino-9H-purin-6-yl)oxy)methyl)phenyl)-49-(4-azidobutyl)-3,7,47,50-tetraoxo-12,15,18,21,24,27,30,33,36,39,42,45-dodecaoxa-2,8,48,51-tetraazatripentacontan-53-yl)ureido)phenyl)diazenyl)phenyl)amino)-4-oxobutyl)pentanedioic acid (**S34**, **BGAG**<sub>12,400</sub>-N<sub>3</sub> = "**BAG**", **BW547**; *novel*)

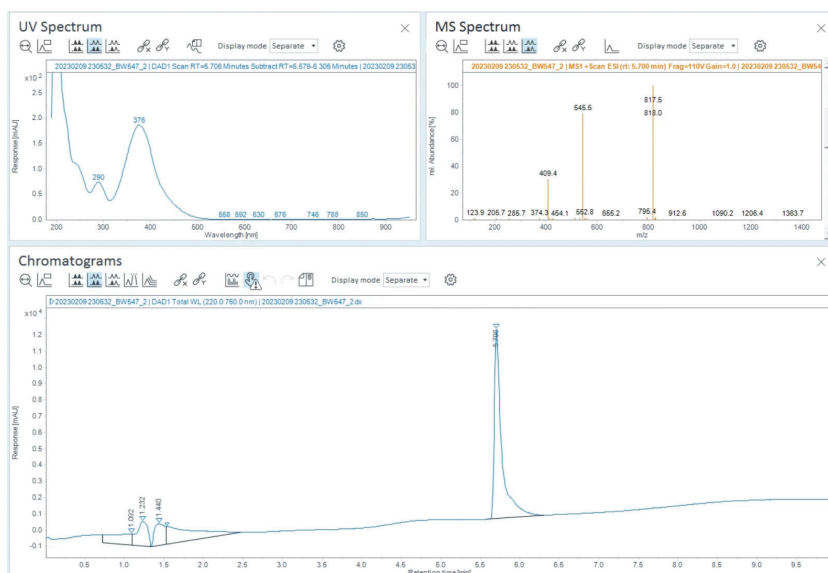


Ice-cold TFA (200  $\mu$ L) was added to **S23** (4.6 mg, 2.65  $\mu$ mol, 1 eq.) at 0  $^{\circ}$ C. The reaction mixture was vortexed and incubated for 15 min at 0  $^{\circ}$ C. All volatiles were removed under a stream of nitrogen. The resulting solid was dissolved in DMF (450  $\mu$ L) and water (50  $\mu$ L) and purified by reversed phase preparative HPLC to yield **BAG** (3.3 mg, 2.02  $\mu$ mol, 76%) as an orange solid.

**HR-MS** (ESI) m/z: C<sub>75</sub>H<sub>114</sub>N<sub>18</sub>O<sub>23</sub><sup>2+</sup>: 817.41466; found: 817.41485, (M + 2H)<sup>2+</sup>.

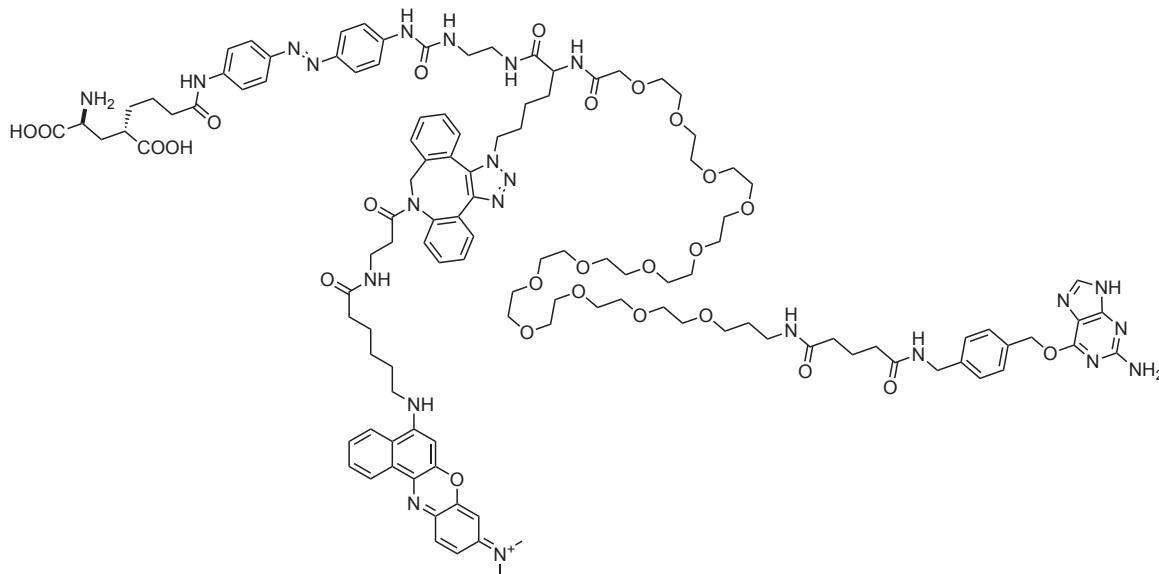


### HPLC-DAD trace



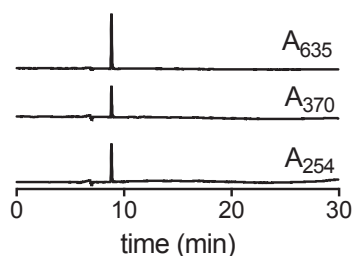
### LC/MS

*N*-5-((6-((3-(1-(49-((2-(3-(4-((4-((5*S*,7*S*)-7-amino-5,7-dicarboxyheptanamido)phenyl) diazenyl)phenyl)ureido)ethyl)carbamoyl)-1-(4-(((2-amino-9*H*-purin-6-yl)oxy)methyl)phenyl)-3,7,47-trioxo-12,15,18,21,24,27,30,33,36,39,42,45-dodecaoxa-2,8,48-triazatripentacontan-53-yl)-1,9-dihydro-8*H*-dibenzo[*b*,*f*][1,2,3]triazolo[4,5-*d*]azocin-8-yl)-3-oxopropyl)amino)-6-oxohexyl)amino)-9*H*-benzo[*a*]phenoxazin-9-ylidene)-*N*-methylmethanaminium  
**(S35, BGAG<sub>12,400</sub>-NB = "BANG"; *novel*)**

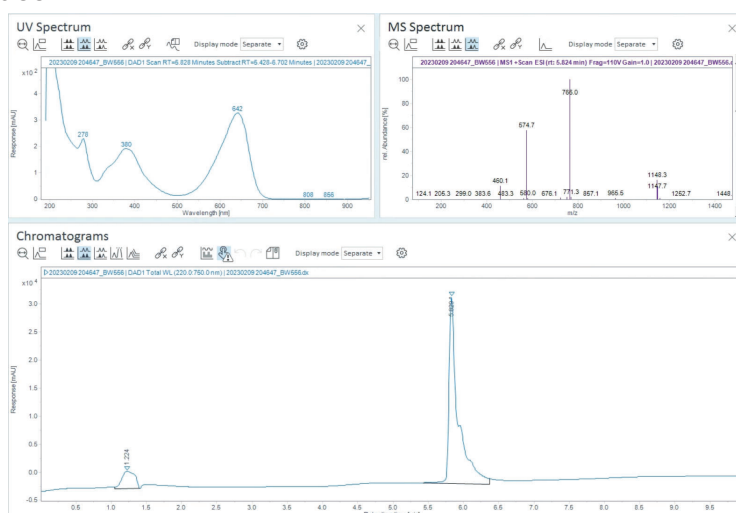


**NB-DBCO** (1.5 mg, 2.26  $\mu\text{mol}$ , 3.7 eq.) and **BGAG<sub>12,400</sub>-N<sub>3</sub>** (1 mg, 0.61  $\mu\text{mol}$ , 1 eq.) were dissolved in DMSO (250  $\mu\text{L}$ ) and stirred at room temperature for 6 h. The reaction mixture was diluted with water (200  $\mu\text{L}$ ) and purified by reversed phase preparative HPLC to yield **BANG** (1 mg, 0.44  $\mu\text{mol}$ , 71%) as a blue solid.

**HR-MS** (ESI) *m/z*: C<sub>117</sub>H<sub>153</sub>N<sub>23</sub>O<sub>26</sub><sup>2+</sup>: 1148.56898; found: 1148.57079, (M + H)<sup>2+</sup>.



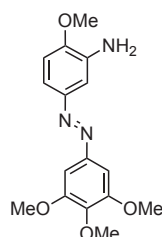
### HPLC-DAD trace



### LC/MS

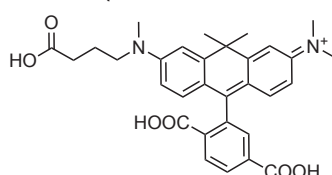
#### 10.4.5 CPY-PEGn-Azobenzene conjugates

2-methoxy-5-((3,4,5-trimethoxyphenyl)diazenyl)aniline (**S36**, **PST2**; **known**)



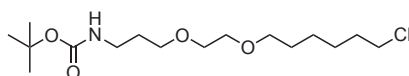
**PST2** was synthesized as described in literature.<sup>11</sup>

*N*-(7-((3-carboxypropyl)(methyl)amino)-10-(2,5-dicarboxyphenyl)-9,9-dimethylanthracen-2(9*H*)-ylidene)-*N*-methylmethanaminium (**S37**, **CPYC3COOH**; **known**)



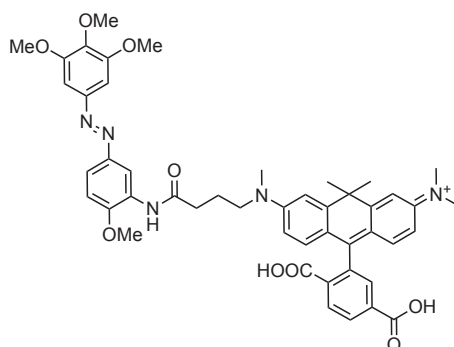
**CPYC3COOH** was custom synthesized by ATT Bioquest.

*tert*-butyl (3-(2-((6-chlorohexyl)oxy)ethoxy)propyl)carbamate (**S38**, **Boc-protected HaloTag chloroalkane ligand**; **known**)



**Boc-protected HaloTag chloroalkane ligand** was synthesized as described in literature.<sup>75</sup>

*N*-(10-(2,5-dicarboxyphenyl)-7-((4-((2-methoxy-5-((3,4,5-trimethoxyphenyl)diazenyl)phenyl)amino)-9,9-dimethylanthracen-2(9*H*)-ylidene)-*N*-methylmethanaminium (**S39**, **PST2-PEG(0)-CPY**; **novel**)



In a 4 mL dram vial, Boc-protected **PST2** (11.8 mg, 28.3  $\mu\text{mol}$ , 1 eq) was dissolved in DCM (150  $\mu\text{L}$ ). TFA (97  $\mu\text{L}$ ) was added, and the mixture was stirred for 2 h, after which solvents were removed under a stream of argon. Residual TFA was removed by repeated (3x) co-evaporation with toluene. The deprotected product was used without further purification.

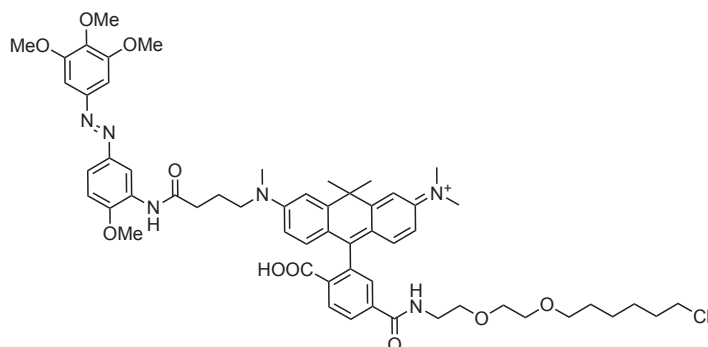
In a 20 mL dram vial, **CPYC3COOH** (15.0 mg, 28.3  $\mu\text{mol}$ , 1 eq.) was dissolved in DMF (1 mL) and DIPEA (25.0  $\mu\text{L}$ , 18.0 mg, 142  $\mu\text{mol}$ , 5 eq.) was added, after which solution turned from blue to colorless. HATU (9.7 mg, 25.5  $\mu\text{mol}$ , 0.9 eq.) was added, and the mixture was stirred at room temperature for 15 minutes. Deprotected **PST2** was added as a solution in DMF (500  $\mu\text{L}$ ). The reaction was stirred at room temperature for 20 h, at which point it was neutralized by addition of AcOH. Volatiles were removed under reduced pressure on a Biotage

V10 evaporation system, then the crude was redissolved and purified by reversed phase preparative HPLC to yield **PST2-PEG(0)-CPY** (15 mg, 18.1  $\mu\text{mol}$ , 64%).

**$^1\text{H}$  NMR** (400 MHz,  $\text{CD}_3\text{OD}$ )  $\delta$  = 8.72 (d,  $J$  = 2.4 Hz, 1H), 8.30 (d,  $J$  = 1.4 Hz, 2H), 7.87 (s, 1H), 7.74 (dd,  $J$  = 8.7, 2.4 Hz, 1H), 7.45 (s, 1H), 7.24 (s, 2H), 7.17 (d,  $J$  = 8.8 Hz, 1H), 7.01 (d,  $J$  = 2.5 Hz, 1H), 6.95 (dd,  $J$  = 9.5, 1.3 Hz, 2H), 6.82 (dd,  $J$  = 9.5, 2.4 Hz, 1H), 6.74 (dd,  $J$  = 9.4, 2.5 Hz, 1H), 3.97 (s, 3H), 3.87 (s, 6H), 3.85 (s, 3H), 3.79 (t,  $J$  = 8.3 Hz, 2H), 3.30 (s, 3H), 3.17 (s, 6H), 2.63 (t,  $J$  = 6.4 Hz, 2H), 2.13 (s, 2H), 1.89 (s, 3H), 1.74 (s, 3H).

**HR-MS** (ESI)  $m/z$ : calculated for  $\text{C}_{47}\text{H}_{50}\text{N}_5\text{O}_9^+$  828.3600; found 828.3603,  $\text{M}^+$ .

*N*-(10-(2-carboxy-5-((2-(2-((6-chlorohexyl)oxy)ethoxy)ethyl)carbamoyl)phenyl)-7-((4-((2-methoxy-5-((3,4,5-trimethoxyphenyl)diazenyl)phenyl)amino)-4-oxobutyl)(methyl)amino)-9,9-dimethylanthracen-2(9*H*)-ylidene)-*N*-methylmethanaminium (**S40**, **Halo-PST2-PEG(0)-CPY**; **novel**)



In a 4 ml dram vial, **Boc-protected HaloTag chloroalkane ligand** (5.3 mg, 16.5  $\mu\text{mol}$ , 1 eq.) was dissolved in 1:1 DCM:TFA (1 mL). After stirring for 15 minutes, solvents were removed under a stream of argon. Residual TFA was removed by repeated (3x) co-evaporation with toluene. The deprotected product was used without further purification.

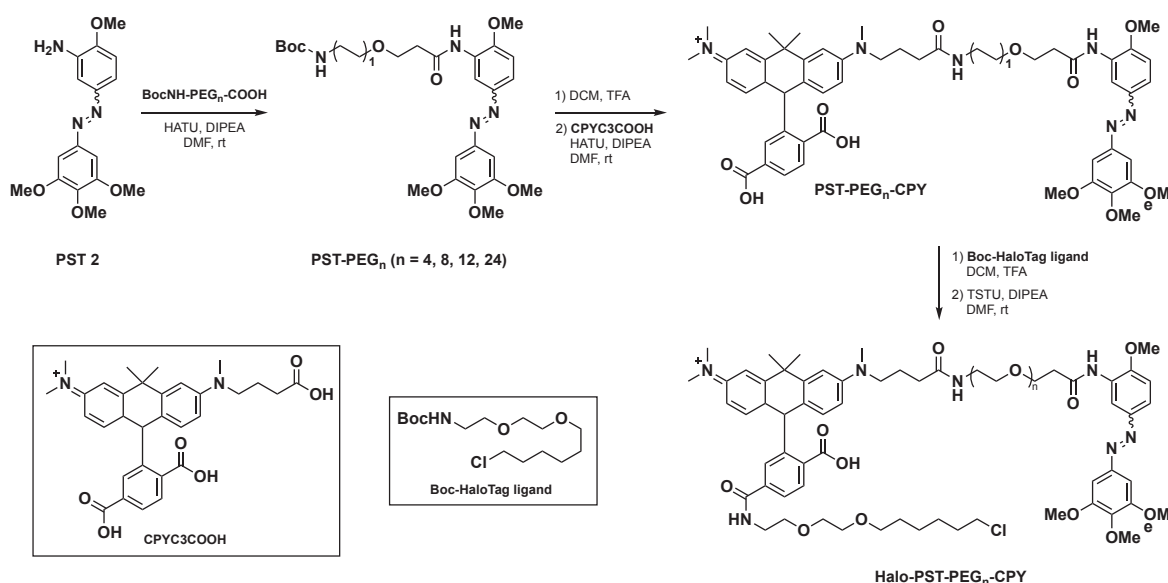
In a 20 mL dram vial, **PST2-PEG(0)-CPY** (15 mg, 18.1  $\mu\text{mol}$ , 1 eq.) was dissolved in DMF (1 mL) and DIPEA (22.0  $\mu\text{L}$ , 15.8 mg 126  $\mu\text{mol}$ , 5 eq.) and HATU (8.63 mg, 22.7  $\mu\text{mol}$ , 0.9 eq.) were added. The mixture was stirred for 15 minutes. Then the deprotected Halo Ligand was added as a solution in DMF. After reaching completion the reaction was neutralized by addition of AcOH. Volatiles were removed under reduced pressure on a Biotage V10 evaporation system, then the crude was redissolved and purified by HPLC to yield **Halo-PST2-PEG(0)-CPY** (6.9 mg, 6.70  $\mu\text{mol}$ , 37%).

**$^1\text{H}$  NMR** (400 MHz,  $(\text{CD}_3)_2\text{SO}$ )  $\delta$  = 9.37 (s, 1H), 8.79 (t,  $J$  = 5.6 Hz, 1H), 8.64 (s, 1H), 8.15 (s, 2H), 7.72 (dd,  $J$  = 8.7, 2.5 Hz, 1H), 7.67 (s, 1H), 7.24 (d,  $J$  = 8.9 Hz, 1H), 7.21 (s, 2H), 7.06 (s, 1H), 6.74 (s, 3H), 3.93 (s, 3H), 3.86 (s, 6H), 3.75 (s, 3H), 3.57 (t,  $J$  = 6.6 Hz, 2H), 3.53 – 3.45 (m, 4H), 3.45 – 3.35 (m, 4H), 3.29 (t,  $J$  = 6.5 Hz, 2H), 3.23 – 3.01 (m, 9H), 2.59 – 2.52 (m, 2H), 1.94 – 1.88 (m, 2H), 1.86 (s, 3H), 1.71 (s, 3H), 1.64 (dt,  $J$  = 14.5, 6.7 Hz, 2H), 1.39 (q,  $J$  = 6.9 Hz, 2H), 1.35 – 1.27 (m, 2H), 1.23 (qd,  $J$  = 7.6, 6.6, 3.9 Hz, 4H).

**HR-MS** (ESI)  $m/z$ : calculated for  $\text{C}_{57}\text{H}_{70}\text{N}_6\text{O}_{10}\text{Cl}^+$ : 1033.4836; found 1033.4835,  $\text{M}^+$ .



## Syntheses of Halo-PST-PEG<sub>n</sub>-CPY (S41- S44; *novel*)



**Halo-PST-PEG<sub>n</sub>-CPY** conjugates were prepared in a series of amide couplings. In a 20 mL dram vial, HATU (1.1 eq.), *t*Boc-amido-dPEG<sub>n</sub>-acid (1.1 eq.; n = 4, 8, 12, 24), and DIPEA (6 eq.) were dissolved in 1 mL DMF and stirred for ten minutes at room temperature. **PST 2** (1 eq.) was added and the reaction stirred at room temperature until complete conversion was observed by LCMS, at which point the reaction was neutralized with AcOH. Volatiles were removed under reduced pressure on a Biotage V-10 Evaporator, redissolved in DMF/H<sub>2</sub>O and the products purified by semi-preparative HPLC to yield boc-protected intermediates (**PST-PEG<sub>n</sub>**). Product identity and purity were assessed by LC-ESI-MS. Boc-protected intermediates were deprotected by treatment with 1:1 TFA:DCM at room temperature for 5 minutes, after which volatiles were removed under a stream of nitrogen and residual TFA removed by toluene azeotrope. Deprotected PST-PEG conjugates were coupled to **CPY-C3-COOH** as described above to yield **PST-PEG<sub>n</sub>-CPY**. Final coupling of the free 6-carboxy group to deprotected HaloTag chloroalkane ligand using TSTU (1.1 eq.) as coupling reagent yielded the final **Halo-PST-PEG<sub>n</sub>-CPY** series as waxy blue solids. Indicated yields are for the final coupling to the HaloTag ligand.

### **Halo-CPY-PEG<sub>4</sub>-PST (S41)**, 61% yield

<sup>1</sup>H NMR (400 MHz, (CD<sub>3</sub>)<sub>2</sub>SO): δ = 9.35 (s, 1H), 8.81 (t, *J* = 5.6 Hz, 1H), 8.66 (d, *J* = 2.4 Hz, 1H), 8.27 – 8.15 (m, 2H), 7.95 (t, *J* = 5.5 Hz, 1H), 7.75 (s, 1H), 7.71 (dd, *J* = 8.7, 2.4 Hz, 1H), 7.24 (d, *J* = 8.9 Hz, 1H), 7.22 (s, 2H), 6.84 – 6.77 (m, 3H), 3.95 (s, 3H), 3.89 (s, 6H), 3.75 (s, 3H), 3.71 (t, *J* = 6.1 Hz, 2H), 3.62 – 3.41 (m, 28H), 3.31 (t, *J* = 6.5 Hz, 2H), 3.26 – 3.17 (m, 9H), 2.69 (t, *J* = 6.1 Hz, 2H), 2.18 (t, *J* = 6.8 Hz, 2H), 1.87 (s, 3H), 1.85 – 1.78 (m, 2H), 1.72 (s, 3H), 1.69 – 1.61 (m, 2H), 1.45 – 1.38 (m, 2H), 1.38 – 1.29 (m, 2H), 1.29 – 1.21 (m, 2H).

**HR-MS** (ESI) *m/z*: calculated for C<sub>68</sub>H<sub>92</sub>N<sub>7</sub>O<sub>15</sub>Cl<sup>2+</sup>: 640.8164; found 640.8160, (M + H)<sup>2+</sup>.

### **Halo-CPY-PEG<sub>8</sub>-PST (S42)**, 63% yield

<sup>1</sup>H NMR (X, PEG8) (400 MHz, (CD<sub>3</sub>)<sub>2</sub>SO): δ = 9.35 (s, 1H), 8.79 (t, *J* = 5.5 Hz, 1H), 8.66 (d, *J* = 2.4 Hz, 1H), 8.17 (s, 2H), 7.95 (d, *J* = 5.6 Hz, 1H), 7.70 (dd, *J* = 8.7, 2.5 Hz, 1H), 7.24 (d, *J* = 8.8 Hz, 1H), 7.21 (s, 2H), 6.76 (s, 4H), 3.95 (s, 3H), 3.89 (s, 6H), 3.75 (s, 3H), 3.71 (t, *J* = 6.1 Hz, 2H), 3.64 – 3.38 (m, 44H), 3.31 (t, *J* = 6.5 Hz, 2H), 3.26 – 3.14 (m, 9H), 2.68 (t, *J* = 6.1 Hz, 2H), 2.54 (s, 3H), 2.24 – 2.13 (m, 2H), 1.86 (s, 3H), 1.83 – 1.77 (m, 2H), 1.71 (s, 3H), 1.69 – 1.62 (m, 2H), 1.45 – 1.37 (m, 2H), 1.35 – 1.29 (m, 2H), 1.28 – 1.22 (m, 2H).

**HR-MS** (ESI) *m/z*: calculated for C<sub>76</sub>H<sub>107</sub>N<sub>7</sub>O<sub>19</sub>Cl<sup>2+</sup>: 728.8689, found 728.8682, (M + H)<sup>2+</sup>.

**Halo-CPY-PEG<sub>12</sub>-PST (S43)**, 53% yield

<sup>1</sup>H NMR (400 MHz, (CD<sub>3</sub>)<sub>2</sub>SO):  $\delta$  = 9.35 (s, 1H), 8.79 (t,  $J$  = 5.6 Hz, 1H), 8.67 (d,  $J$  = 2.4 Hz, 1H), 8.21 – 8.03 (m, 2H), 7.93 (s, 1H), 7.71 (dd,  $J$  = 8.7, 2.5 Hz, 1H), 7.25 (d,  $J$  = 8.9 Hz, 1H), 7.22 (s, 2H), 6.70 (s, 4H), 3.96 (s, 3H), 3.90 (s, 6H), 3.76 (s, 3H), 3.72 (t,  $J$  = 6.1 Hz, 2H), 3.65 – 3.36 (m, 60H), 3.31 (t,  $J$  = 6.5 Hz, 2H), 3.27 – 3.20 (m, 2H), 3.17 (s, 9H), 2.69 (t,  $J$  = 6.2 Hz, 2H), 2.16 (d,  $J$  = 7.1 Hz, 2H), 1.87 (s, 3H), 1.82 – 1.76 (m, 2H), 1.72 (s, 3H), 1.69 – 1.63 (m, 2H), 1.41 (q,  $J$  = 6.9 Hz, 2H), 1.37 – 1.29 (m, 2H), 1.29 – 1.20 (m, 2H).

**HR-MS** (ESI)  $m/z$ : calculated for C<sub>84</sub>H<sub>123</sub>N<sub>7</sub>O<sub>23</sub>Cl<sup>2+</sup>: 816.9213; found 816.9212, (M + H)<sup>2+</sup>.

**Halo-CPY-PEG<sub>24</sub>-PST (S44)**, 65% yield

<sup>1</sup>H NMR (400 MHz, (CD<sub>3</sub>)<sub>2</sub>SO):  $\delta$  = 9.35 (s, 1H), 8.78 (t,  $J$  = 5.6 Hz, 1H), 8.66 (d,  $J$  = 2.5 Hz, 1H), 8.21 – 8.08 (m, 2H), 7.92 (s, 1H), 7.71 (dd,  $J$  = 8.7, 2.4 Hz, 1H), 7.25 (d,  $J$  = 8.9 Hz, 1H), 7.22 (s, 2H), 6.84 – 6.54 (m, 4H), 3.96 (s, 3H), 3.89 (s, 6H), 3.75 (s, 3H), 3.71 (t,  $J$  = 6.1 Hz, 2H), 3.60 (dd,  $J$  = 8.0, 6.2 Hz, 4H), 3.53 – 3.46 (m, 104H), 3.30 (t,  $J$  = 6.5 Hz, 2H), 3.23 (t,  $J$  = 5.7 Hz, 2H), 3.08 – 2.91 (m, 9H), 2.69 (t,  $J$  = 6.4 Hz, 2H), 2.17 (d,  $J$  = 9.0 Hz, 2H), 1.86 (s, 3H), 1.81 – 1.74 (m, 2H), 1.72 (s, 3H), 1.69 – 1.60 (m, 2H), 1.43 – 1.38 (m, 2H), 1.34 – 1.28 (m, 2H), 1.27 – 1.22 (m, 2H).

**HR-MS** (ESI)  $m/z$ : calculated for C<sub>108</sub>H<sub>173</sub>N<sub>7</sub>O<sub>35</sub>Cl<sup>3+</sup>: 721.0548; found 721.0541 (M + 2 H)<sup>3+</sup>.

## 11 References

- (1) Hüll, K.; Morstein, J.; Trauner, D. In Vivo Photopharmacology. *Chem. Rev.* **2018**, *118* (21), 10710–10747. <https://doi.org/10.1021/acs.chemrev.8b00037>.
- (2) Velema, W. A.; Szymanski, W.; Feringa, B. L. Photopharmacology: Beyond Proof of Principle. *J. Am. Chem. Soc.* **2014**, *136* (6), 2178–2191. <https://doi.org/10.1021/ja413063e>.
- (3) Fuchter, M. J. On the Promise of Photopharmacology Using Photoswitches: A Medicinal Chemist's Perspective. *J. Med. Chem.* **2020**, *63* (20), 11436–11447. <https://doi.org/10.1021/acs.jmedchem.0c00629>.
- (4) Dong, M.; Babalhavaeji, A.; Samanta, S.; Beharry, A. A.; Woolley, G. A. Red-Shifting Azobenzene Photoswitches for in Vivo Use. *Acc. Chem. Res.* **2015**, *48* (10), 2662–2670. <https://doi.org/10.1021/acs.accounts.5b00270>.
- (5) Banghart, M.; Mourot, A.; Fortin, D.; Yao, J.; Kramer, R.; Trauner, D. Photochromic Blockers of Voltage-Gated Potassium Channels. *Angew. Chem. Int. Ed.* **2009**, *48* (48), 9097–9101. <https://doi.org/10.1002/anie.200904504>.
- (6) Broichhagen, J.; Jurastow, I.; Iwan, K.; Kummer, W.; Trauner, D. Optical Control of Acetylcholinesterase with a Tacrine Switch. *Angew. Chem. Int. Ed.* **2014**, *53* (29), 7657–7660. <https://doi.org/10.1002/anie.201403666>.
- (7) Cheng, B.; Shchepakina, D.; Kavanaugh, M. P.; Trauner, D. Photoswitchable Inhibitor of a Glutamate Transporter. *ACS Chem. Neurosci.* **2017**, *8* (8), 1668–1672. <https://doi.org/10.1021/acschemneuro.7b00072>.
- (8) Volgraf, M.; Gorostiza, P.; Szobota, S.; Helix, M. R.; Isacoff, E. Y.; Trauner, D. Reversibly Caged Glutamate: A Photochromic Agonist of Ionotropic Glutamate Receptors. *J. Am. Chem. Soc.* **2007**, *129* (2), 260–261. <https://doi.org/10.1021/ja067269o>.
- (9) Fortin, D. L.; Banghart, M. R.; Dunn, T. W.; Borges, K.; Wagenaar, D. A.; Gaudry, Q.; Karakossian, M. H.; Otis, T. S.; Kristan, W. B.; Trauner, D.; Kramer, R. H. Photochemical Control of Endogenous Ion Channels and Cellular Excitability. *Nat. Methods* **2008**, *5* (4), 331–338. <https://doi.org/10.1038/nmeth.1187>.
- (10) Polosukhina, A.; Litt, J.; Tochitsky, I.; Nemargut, J.; Sychev, Y.; De Kouchkovsky, I.; Huang, T.; Borges, K.; Trauner, D.; Van Gelder, R. N.; Kramer, R. H. Photochemical Restoration of Visual Responses in Blind Mice. *Neuron* **2012**, *75* (2), 271–282. <https://doi.org/10.1016/j.neuron.2012.05.022>.
- (11) Borowiak, M.; Nahaboo, W.; Reynders, M.; Nekolla, K.; Jalinot, P.; Hasserodt, J.; Rehberg, M.; Delattre, M.; Zahler, S.; Vollmar, A.; Trauner, D.; Thorn-Seshold, O. Photoswitchable Inhibitors of Microtubule Dynamics Optically Control Mitosis and Cell Death. *Cell* **2015**, *162* (2), 403–411. <https://doi.org/10.1016/j.cell.2015.06.049>.
- (12) Borowiak, M.; Küllmer, F.; Gegenfurtner, F.; Peil, S.; Nasufović, V.; Zahler, S.; Thorn-Seshold, O.; Trauner, D.; Arndt, H.-D. Optical Manipulation of F-Actin with Photoswitchable Small Molecules. *J. Am. Chem. Soc.* **2020**, *142* (20), 9240–9249. <https://doi.org/10.1021/jacs.9b12898>.
- (13) Müller-Deku, A.; Meiring, J. C. M.; Loy, K.; Kraus, Y.; Heise, C.; Bingham, R.; Jansen, K. I.; Qu, X.; Bartolini, F.; Kapitein, L. C.; Akhmanova, A.; Ahlfeld, J.; Trauner, D.; Thorn-Seshold, O. Photoswitchable Paclitaxel-Based Microtubule Stabilisers Allow Optical Control over the Microtubule Cytoskeleton. *Nat Commun* **2020**, *11* (1), 4640. <https://doi.org/10.1038/s41467-020-18389-6>.
- (14) Küllmer, F.; Vepřek, N. A.; Borowiak, M.; Nasufović, V.; Barutzki, S.; Thorn-Seshold, O.; Arndt, H.-D.; Trauner, D. Next Generation Opto-Jasplakinolides Enable Local Remodeling of Actin Networks\*\*. *Angew. Chem. Int. Ed.* **2022**, *61* (48), e202210220. <https://doi.org/10.1002/anie.202210220>.
- (15) Reynders, M.; Matsuura, B. S.; Bérouti, M.; Simoneschi, D.; Marzio, A.; Pagano, M.; Trauner, D. PHOTACs Enable Optical Control of Protein Degradation. *Sci. Adv.* **6** (8), eaay5064. <https://doi.org/10.1126/sciadv.aay5064>.
- (16) Pfaff, P.; Samarasinghe, K. T. G.; Crews, C. M.; Carreira, E. M. Reversible Spatiotemporal Control of Induced Protein Degradation by Bistable PhotoPROTACs. *ACS Cent. Sci.* **2019**, *5* (10), 1682–1690. <https://doi.org/10.1021/acscentsci.9b00713>.
- (17) Wegener, M.; Hansen, M. J.; Driessen, A. J. M.; Szymanski, W.; Feringa, B. L. Photocontrol of Antibacterial Activity: Shifting from UV to Red Light Activation. *J. Am. Chem. Soc.* **2017**, *139* (49), 17979–17986. <https://doi.org/10.1021/jacs.7b09281>.
- (18) Tsai, Y.-H.; Essig, S.; James, J. R.; Lang, K.; Chin, J. W. Selective, Rapid and Optically Switchable Regulation of Protein Function in Live Mammalian Cells. *Nat. Chem.* **2015**, *7* (7), 554–561. <https://doi.org/10.1038/nchem.2253>.
- (19) Müller, M.; Niemeyer, K.; Urban, N.; Ojha, N. K.; Zufall, F.; Leinders-Zufall, T.; Schaefer, M.; Thorn-Seshold, O. BTDAzo: A Photoswitchable TRPC5 Channel Activator\*\*. *Angew. Chem. Int. Ed.* **2022**, *61* (36), e202201565. <https://doi.org/10.1002/anie.202201565>.
- (20) Frank, J. A.; Moroni, M.; Moshourab, R.; Sumser, M.; Lewin, G. R.; Trauner, D. Photoswitchable Fatty Acids Enable Optical Control of TRPV1. *Nat Commun* **2015**, *6* (1), 7118. <https://doi.org/10.1038/ncomms8118>.
- (21) Konrad, D. B.; Frank, J. A.; Trauner, D. Synthesis of Redshifted Azobenzene Photoswitches by Late-Stage Functionalization. *Chem. Eur. J.* **2016**, *22* (13), 4364–4368. <https://doi.org/10.1002/chem.201505061>.
- (22) Acosta-Ruiz, A.; Broichhagen, J.; Levitz, J. Optical Regulation of Class C GPCRs by Photoswitchable Orthogonal Remotely Tethered Ligands. *Methods Mol Biol* **2019**, *1947*, 103–136. [https://doi.org/10.1007/978-1-4939-9121-1\\_6](https://doi.org/10.1007/978-1-4939-9121-1_6).
- (23) Donthamsetti, P. C.; Broichhagen, J.; Vyklicky, V.; Stanley, C.; Fu, Z.; Visel, M.; Levitz, J. L.; Javitch, J. A.; Trauner, D.; Isacoff, E. Y. Genetically Targeted Optical Control of an Endogenous G Protein-Coupled Receptor. *J. Am. Chem. Soc.* **2019**, *141* (29), 11522–11530. <https://doi.org/10.1021/jacs.9b02895>.

- (24) Westphal, M. V.; Schafroth, M. A.; Sarott, R. C.; Imhof, M. A.; Bold, C. P.; Leippe, P.; Dhopeswarkar, A.; Grandner, J. M.; Katritch, V.; Mackie, K.; Trauner, D.; Carreira, E. M.; Frank, J. A. Synthesis of Photoswitchable  $\Delta^9$ -Tetrahydrocannabinol Derivatives Enables Optical Control of Cannabinoid Receptor 1 Signaling. *J. Am. Chem. Soc.* **2017**, *139* (50), 18206–18212. <https://doi.org/10.1021/jacs.7b06456>.
- (25) Gutzeit, V. A.; Acosta-Ruiz, A.; Munguba, H.; Häfner, S.; Landra-Willm, A.; Mathes, B.; Mony, J.; Yarotski, D.; Börjesson, K.; Liston, C.; Sandoz, G.; Levitz, J.; Broichhagen, J. A Fine-Tuned Azobenzene for Enhanced Photopharmacology in Vivo. *Cell Chem. Biol.* **2021**, *28* (11), 1648–1663. <https://doi.org/10.1016/j.chembiol.2021.02.020>.
- (26) Acosta-Ruiz, A.; Gutzeit, V. A.; Skelly, M. J.; Meadows, S.; Lee, J.; Parekh, P.; Orr, A. G.; Liston, C.; Pleil, K. E.; Broichhagen, J.; Levitz, J. Branched Photoswitchable Tethered Ligands Enable Ultra-Efficient Optical Control and Detection of G Protein-Coupled Receptors In Vivo. *Neuron* **2020**, *105* (3), 446–463.e13. <https://doi.org/10.1016/j.neuron.2019.10.036>.
- (27) Broichhagen, J.; Damijonaitis, A.; Levitz, J.; Sokol, K. R.; Leippe, P.; Konrad, D.; Isacoff, E. Y.; Trauner, D. Orthogonal Optical Control of a G Protein-Coupled Receptor with a SNAP-Tethered Photochromic Ligand. *ACS Cent Sci* **2015**, *1* (7), 383–393. <https://doi.org/10.1021/acscentsci.5b00260>.
- (28) Broichhagen, J.; Levitz, J. Advances in Tethered Photopharmacology for Precise Optical Control of Signaling Proteins. *Current Opinion in Pharmacology* **2022**, *63*, 102196. <https://doi.org/10.1016/j.coph.2022.102196>.
- (29) Rickhoff, J.; Arndt, N. B.; Böckmann, M.; Doltsinis, N. L.; Ravoo, B. J.; Kortekaas, L. Reversible, Red-Shifted Photoisomerization in Protonated Azobenzenes. *J. Org. Chem.* **2022**, *87* (16), 10605–10612. <https://doi.org/10.1021/acs.joc.2c00661>.
- (30) Dong, M.; Babalhavaeji, A.; Collins, C. V.; Jarrah, K.; Sadvovski, O.; Dai, Q.; Woolley, G. A. Near-Infrared Photoswitching of Azobenzenes under Physiological Conditions. *J. Am. Chem. Soc.* **2017**, *139* (38), 13483–13486. <https://doi.org/10.1021/jacs.7b06471>.
- (31) Yang, Y.; Hughes, R. P.; Aprahamian, I. Visible Light Switching of a BF<sub>2</sub>-Coordinated Azo Compound. *J. Am. Chem. Soc.* **2012**, *134* (37), 15221–15224. <https://doi.org/10.1021/ja306030d>.
- (32) Samanta, S.; Beharry, A. A.; Sadvovski, O.; McCormick, T. M.; Babalhavaeji, A.; Tropepe, V.; Woolley, G. A. Photoswitching Azo Compounds in Vivo with Red Light. *J. Am. Chem. Soc.* **2013**, *135* (26), 9777–9784. <https://doi.org/10.1021/ja402220t>.
- (33) Bléger, D.; Schwarz, J.; Brouwer, A. M.; Hecht, S. O -Fluoroazobenzenes as Readily Synthesized Photoswitches Offering Nearly Quantitative Two-Way Isomerization with Visible Light. *J. Am. Chem. Soc.* **2012**, *134* (51), 20597–20600. <https://doi.org/10.1021/ja310323y>.
- (34) Hansen, M. J.; Lerch, M. M.; Szymanski, W.; Feringa, B. L. Direct and Versatile Synthesis of Red-Shifted Azobenzenes. *Angew. Chem. Int. Ed.* **2016**, *55* (43), 13514–13518. <https://doi.org/10.1002/anie.201607529>.
- (35) Konrad, D. B.; Savasci, G.; Allmendinger, L.; Trauner, D.; Ochsenfeld, C.; Ali, A. M. Computational Design and Synthesis of a Deeply Red-Shifted and Bistable Azobenzene. *J. Am. Chem. Soc.* **2020**, *142* (14), 6538–6547. <https://doi.org/10.1021/jacs.9b10430>.
- (36) Müller-Deku, A.; Thorn-Seshold, O. Exhaustive Catalytic Ortho-Alkoxylation of Azobenzenes: Flexible Access to Functionally Diverse Yellow-Light-Responsive Photoswitches. *J. Org. Chem.* **2022**, *87* (24), 16526–16531. <https://doi.org/10.1021/acs.joc.2c02214>.
- (37) Siewertsen, R.; Neumann, H.; Buchheim-Stehn, B.; Herges, R.; Näther, C.; Renth, F.; Temps, F. Highly Efficient Reversible Z–E Photoisomerization of a Bridged Azobenzene with Visible Light through Resolved S<sub>1</sub>(Nπ\*) Absorption Bands. *J. Am. Chem. Soc.* **2009**, *131* (43), 15594–15595. <https://doi.org/10.1021/ja906547d>.
- (38) Lentès, P.; Stadler, E.; Röhricht, F.; Brahms, A.; Gröbner, J.; Sönnichsen, F. D.; Gescheidt, G.; Herges, R. Nitrogen Bridged Diazocines: Photochromes Switching within the Near-Infrared Region with High Quantum Yields in Organic Solvents and in Water. *J. Am. Chem. Soc.* **2019**, *141* (34), 13592–13600. <https://doi.org/10.1021/jacs.9b06104>.
- (39) Maier, M. S.; Hüll, K.; Reynders, M.; Matsuura, B. S.; Leippe, P.; Ko, T.; Schäffer, L.; Trauner, D. Oxidative Approach Enables Efficient Access to Cyclic Azobenzenes. *J. Am. Chem. Soc.* **2019**, *141* (43), 17295–17304. <https://doi.org/10.1021/jacs.9b08794>.
- (40) Frank, J. A.; Antonini, M.-J.; Chiang, P.-H.; Canales, A.; Konrad, D. B.; Garwood, I. C.; Rajic, G.; Koehler, F.; Fink, Y.; Anikeeva, P. In Vivo Photopharmacology Enabled by Multifunctional Fibers. *ACS Chem. Neurosci.* **2020**, *11* (22), 3802–3813. <https://doi.org/10.1021/acschemneuro.0c00577>.
- (41) Arnaud, R.; Lemaire, J. Isomérisation *cis*–*trans* de l'azobenzène catalysée par l'iode. III. *Can. J. Chem.* **1974**, *52* (10), 1868–1871. <https://doi.org/10.1139/v74-266>.
- (42) Ronayette, J.; Arnaud, R.; Lemaire, J. Isomérisation photosensibilisée par des colorants et photoréduction de l'azobenzène en solution. II. *Can. J. Chem.* **1974**, *52* (10), 1858–1867. <https://doi.org/10.1139/v74-265>.
- (43) Shimomura, M.; Kunitake, T. Fluorescence and Photoisomerization of Azobenzene-Containing Bilayer Membranes. *J. Am. Chem. Soc.* **1987**, *109* (17), 5175–5183. <https://doi.org/10.1021/ja00251a022>.
- (44) Isokuortti, J.; Kuntze, K.; Virkki, M.; Ahmed, Z.; Vuorimaa-Laukkanen, E.; Filatov, M. A.; Turshatov, A.; Laaksonen, T.; Priimagi, A.; Durandin, N. A. Expanding Excitation Wavelengths for Azobenzene Photoswitching into the Near-Infrared Range via Endothermic Triplet Energy Transfer. *Chem. Sci.* **2021**, *12* (21), 7504–7509. <https://doi.org/10.1039/D1SC01717A>.
- (45) Goulet-Hanssens, A.; Rietze, C.; Titov, E.; Abdullahu, L.; Grubert, L.; Saalfrank, P.; Hecht, S. Hole Catalysis as a General Mechanism for Efficient and Wavelength-Independent Z → E Azobenzene Isomerization. *Chem* **2018**, *4* (7), 1740–1755. <https://doi.org/10.1016/j.chempr.2018.06.002>.



- (46) Baumgartner, B.; Glembockyte, V.; Gonzalez-Hernandez, A. J.; Valavalkar, A.; Mayer, R.; Fillbrook, L.; Müller-Deku, A.; Steiner, F.; Gross, C.; Reynders, M.; Munguba, H.; Arefin, I.; Ofial, A.; Beves, J.; Dietzek-Ivanšić, B.; Broichhagen, J.; Tinnefeld, P.; Levitz, J.; Thorn-Seshold, O. A General Method for Near-Infrared Photoswitching in Biology, Demonstrated by the >700 Nm Photocontrol of Glutamate Receptors in Brain Slices. *in preparation* **2023**.
- (47) Goulet-Hanssens, A.; Utecht, M.; Mutruc, D.; Titov, E.; Schwarz, J.; Grubert, L.; Bléger, D.; Saalfrank, P.; Hecht, S. Electrocatalytic Z → E Isomerization of Azobenzenes. *J. Am. Chem. Soc.* **2017**, *139* (1), 335–341. <https://doi.org/10.1021/jacs.6b10822>.
- (48) Moreno, J.; Grubert, L.; Schwarz, J.; Bléger, D.; Hecht, S. Efficient Sensitized Z→E Photoisomerization of an Iridium(III)-Azobenzene Complex over a Wide Concentration Range. *Chem. Eur. J.* **2017**, *23* (56), 14090–14095. <https://doi.org/10.1002/chem.201703376>.
- (49) Greenfield, J. L.; Gerkman, M. A.; Gibson, R. S. L.; Han, G. G. D.; Fuchter, M. J. Efficient Electrocatalytic Switching of Azoheteroarenes in the Condensed Phases. *J. Am. Chem. Soc.* **2021**, *143* (37), 15250–15257. <https://doi.org/10.1021/jacs.1c06359>.
- (50) Laviron, E.; Mugnier, Y. A Study of the Isomerization of Cis-Azobenzene Anion Radical in Dimethylformamide. *J. Electroanal. Chem.* **1978**, *93*, 69–73.
- (51) Thorn-Seshold, O. Photoswitchable Cytotoxins. In *Molecular Photoswitches*; 2022; pp 873–919. <https://doi.org/10.1002/9783527827626.ch36>.
- (52) Thorn-Seshold, O.; Meiring, J. C. M. Photocontrolling Microtubule Dynamics with Photoswitchable Chemical Reagents. In *Microtubules: Methods and Protocols*; Inaba, H., Ed.; Springer US: New York, NY, 2022; pp 403–430. [https://doi.org/10.1007/978-1-0716-1983-4\\_26](https://doi.org/10.1007/978-1-0716-1983-4_26).
- (53) Edelstein, A. D.; Tsuchida, M. A.; Amodaj, N.; Pinkard, H.; Vale, R. D.; Stuurman, N. Advanced Methods of Microscope Control Using MManager Software. *J Biol Methods* **2014**, *1* (2), e10. <https://doi.org/10.14440/jbm.2014.36>.
- (54) Romero, N. A.; Nicewicz, D. A. Organic Photoredox Catalysis. *Chem. Rev.* **2016**, *116* (17), 10075–10166. <https://doi.org/10.1021/acs.chemrev.6b00057>.
- (55) Gak, V. Yu.; Nadochenko, V. A.; Kiwi, J. Triplet-Excited Dye Molecules (Eosine and Methylene Blue) Quenching by H<sub>2</sub>O<sub>2</sub> in Aqueous Solutions. *Journal of Photochemistry and Photobiology A: Chemistry* **1998**, *116* (1), 57–62. [https://doi.org/10.1016/S1010-6030\(98\)00230-5](https://doi.org/10.1016/S1010-6030(98)00230-5).
- (56) Jose, J.; Burgess, K. Benzophenoxazine-Based Fluorescent Dyes for Labeling Biomolecules. *Tetrahedron* **2006**, *62* (48), 11021–11037. <https://doi.org/10.1016/j.tet.2006.08.056>.
- (57) Jones, W. E.; Fox, M. A. Determination of Excited-State Redox Potentials by Phase-Modulated Voltammetry. *J. Phys. Chem.* **1994**, *98* (19), 5095–5099. <https://doi.org/10.1021/j100070a025>.
- (58) Rehm, D.; Weller, A. Kinetics of Fluorescence Quenching by Electron and H-Atom Transfer. *Isr. J. Chem.* **1970**, *8* (2), 259–271. <https://doi.org/10.1002/ijch.197000029>.
- (59) Narayanan, M.; Kodali, G.; Singh, V. R.; Velvadapu, V.; Stanley, R. J. Oxidation and Reduction Potentials of 8-Vinyladenosine Measured by Cyclic Voltammetry: Implications for Photoinduced Electron Transfer Quenching of a Fluorescent Adenine Analog. *J. Photochem. Photobiol. A* **2012**, *249*, 9–14. <https://doi.org/10.1016/j.jphotochem.2012.08.018>.
- (60) Connelly, N. G.; Geiger, W. E. Chemical Redox Agents for Organometallic Chemistry. *Chem. Rev.* **1996**, *96* (2), 877–910. <https://doi.org/10.1021/cr940053x>.
- (61) Aranzaes, J. R.; Daniel, M.-C.; Astruc, D. Metallocenes as References for the Determination of Redox Potentials by Cyclic Voltammetry - Permethylated Iron and Cobalt Sandwich Complexes, Inhibition by Polyamine Dendrimers, and the Role of Hydroxy-Containing Ferrocenes. *Can. J. Chem.* **2006**, *84* (2), 288–299. <https://doi.org/10.1139/v05-262>.
- (62) Hansch, Corwin.; Leo, A.; Taft, R. W. A Survey of Hammett Substituent Constants and Resonance and Field Parameters. *Chem. Rev.* **1991**, *91* (2), 165–195. <https://doi.org/10.1021/cr00002a004>.
- (63) Stadler, E.; Tassoti, S.; Lentès, P.; Herges, R.; Glasnov, T.; Zangger, K.; Gescheidt, G. In Situ Observation of Photoswitching by NMR Spectroscopy: A Photochemical Analogue to the Exchange Spectroscopy Experiment. *Anal. Chem.* **2019**, *91* (17), 11367–11373. <https://doi.org/10.1021/acs.analchem.9b02613>.
- (64) Dobryakov, A. L.; Kovalenko, S. A.; Ernsting, N. P. Coherent and Sequential Contributions to Femtosecond Transient Absorption Spectra of a Rhodamine Dye in Solution. *J. Chem. Phys.* **2005**, *123* (4), 044502. <https://doi.org/10.1063/1.1948383>.
- (65) Doumazane, E.; Scholler, P.; Zwier, J. M.; Trinquet, E.; Rondard, P.; Pin, J.-P. A New Approach to Analyze Cell Surface Protein Complexes Reveals Specific Heterodimeric Metabotropic Glutamate Receptors. *The FASEB Journal* **2011**, *25* (1), 66–77. <https://doi.org/10.1096/fj.10-163147>.
- (66) Vivaudou, M.; Chan, K. W.; Sui, J.-L.; Jan, L. Y.; Reuveny, E.; Logothetis, D. E. Probing the G-Protein Regulation of GIRK1 and GIRK4, the Two Subunits of the KACH Channel, Using Functional Homomeric Mutants. *J Biol Chem* **1997**, *272* (50), 31553–31560. <https://doi.org/10.1074/jbc.272.50.31553>.
- (67) Bartole, E.; Littmann, T.; Tanaka, M.; Ozawa, T.; Buschauer, A.; Bernhardt, G. [3H]UR-DEBa176: A 2,4-Diaminopyrimidine-Type Radioligand Enabling Binding Studies at the Human, Mouse, and Rat Histamine H<sub>4</sub> Receptors. *J. Med. Chem.* **2019**, *62* (17), 8338–8356. <https://doi.org/10.1021/acs.jmedchem.9b01342>.
- (68) Ishiba, K.; Morikawa, M.; Chikara, C.; Yamada, T.; Iwase, K.; Kawakita, M.; Kimizuka, N. Photoliquefiable Ionic Crystals: A Phase Crossover Approach for Photon Energy Storage Materials with Functional Multiplicity. *Angew. Chem. Int. Ed.* **2015**, *54* (5), 1532–1536. <https://doi.org/10.1002/anie.201410184>.

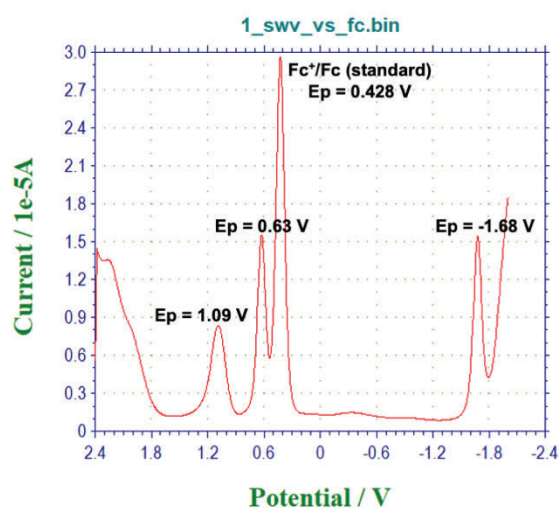
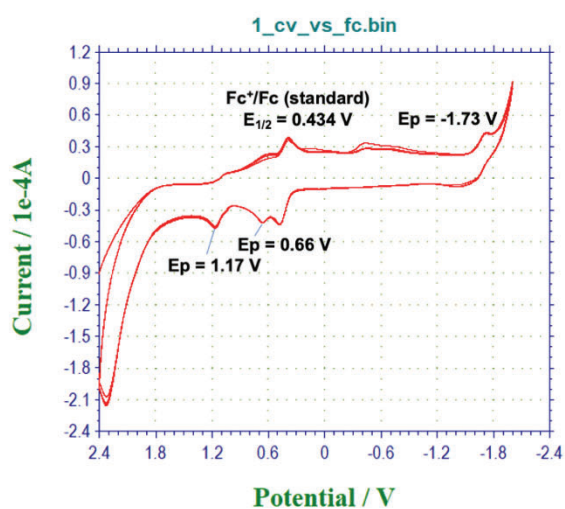


- (69) Cui, K.; Lu, X.; Cui, W.; Wu, J.; Chen, X.; Lu, Q. Fluorescent Nanoparticles Assembled from a Poly(Ionic Liquid) for Selective Sensing of Copper Ions. *Chem. Commun.* **2010**, 47 (3), 920–922. <https://doi.org/10.1039/C0CC03900D>.
- (70) Hu, M.; Fan, J.; Li, H.; Song, K.; Wang, S.; Cheng, G.; Peng, X. Fluorescent Chemodosimeter for Cys/Hcy with a Large Absorption Shift and Imaging in Living Cells. *Org. Biomol. Chem.* **2011**, 9 (4), 980–983. <https://doi.org/10.1039/C0OB00957A>.
- (71) Fei, M.; Wai-Yee, L.; Ching-Ying, C. Fluorescent Pyrene Compounds. US 2011/0097735A I.
- (72) Scilimati, A.; Ferorelli, S.; Iaselli, M. C.; Miciaccia, M.; Pati, M. L.; Fortuna, C. G.; Aleem, A. M.; Marnett, L. J.; Perrone, M. G. Targeting COX-1 by Mofezolac-Based Fluorescent Probes for Ovarian Cancer Detection. *Eur. J. Med. Chem.* **2019**, 179, 16–25. <https://doi.org/10.1016/j.ejmech.2019.06.039>.
- (73) Yan, X.; Yuan, P. M. Sulfonated [8,9]Benzophenoxazine Dyes and the Use of Their Labelled Conjugates. WO 01/83621 A2.
- (74) Levitz, J.; Broichhagen, J.; Leippe, P.; Konrad, D.; Trauner, D.; Isacoff, E. Y. Dual Optical Control and Mechanistic Insights into Photoswitchable Group II and III Metabotropic Glutamate Receptors. *Proc. Natl. Acad. Sci. U.S.A.* **2017**, 114 (17), E3546–E3554. <https://doi.org/10.1073/pnas.1619652114>.
- (75) Zhang, Y.; So, M.; Loening, A. M.; Yao, H.; Gambhir, S. S.; Rao, J. HaloTag Protein-Mediated Site-Specific Conjugation of Bioluminescent Proteins to Quantum Dots. *Angew. Chem. Int. Ed.* **2006**, 45 (30), 4936–4940. <https://doi.org/10.1002/anie.200601197>.

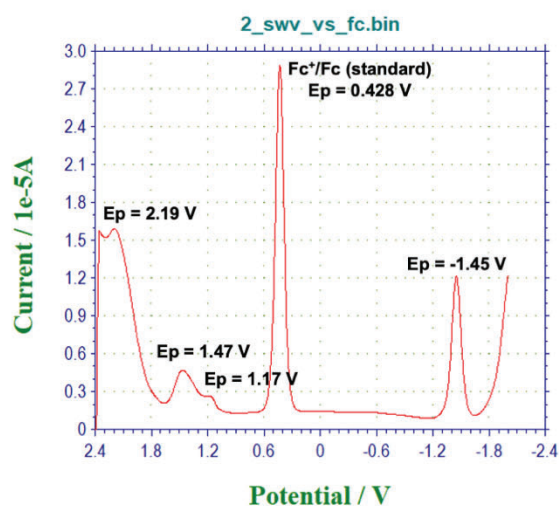
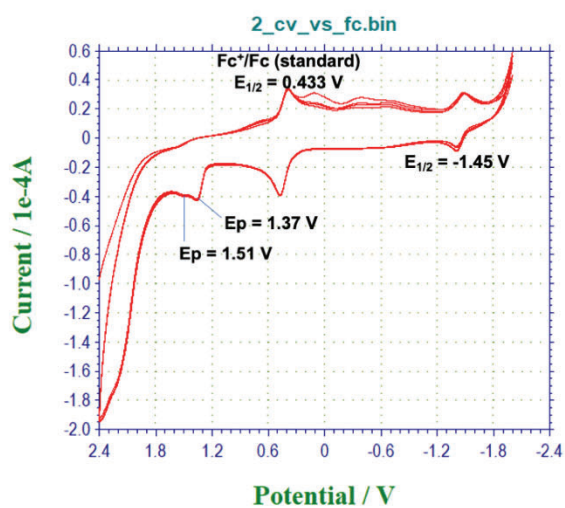
## 12 Appendices

### 12.1 Cyclic voltammetry and square wave voltammetry spectra: azobenzenes

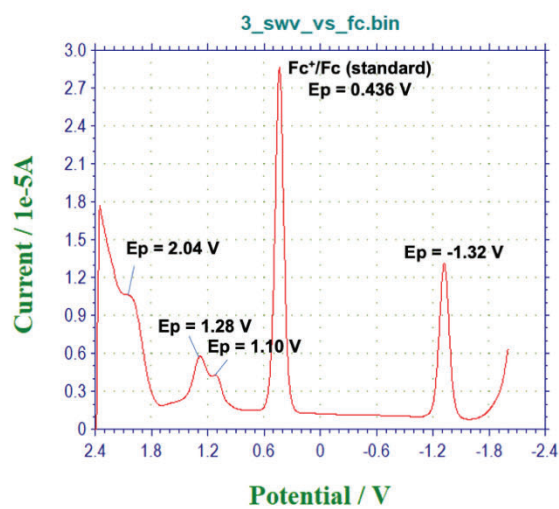
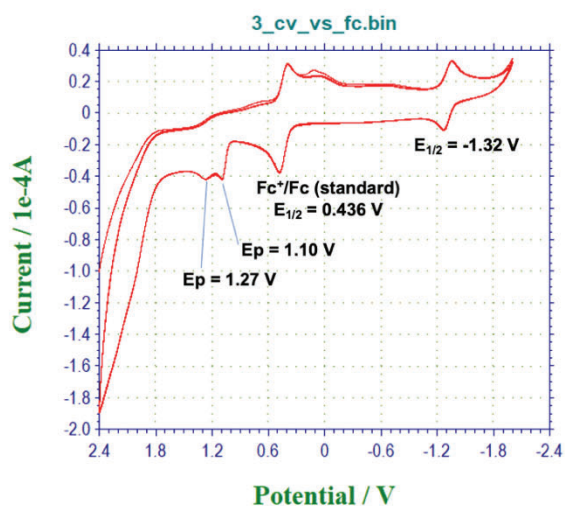
#### CV-1



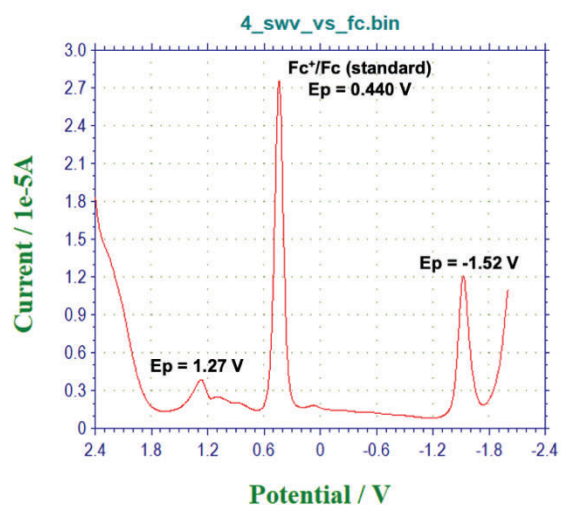
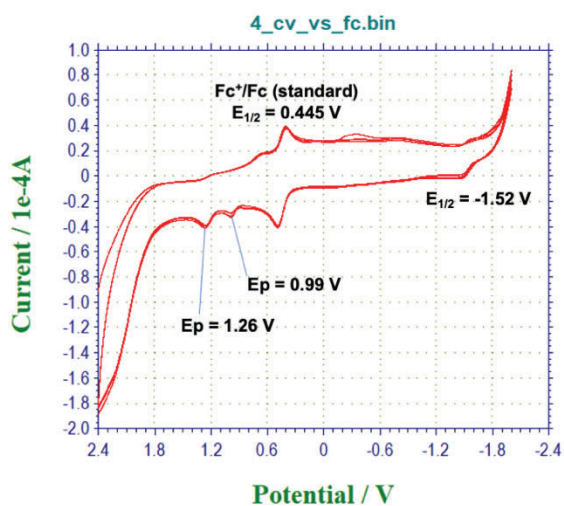
#### CV-2



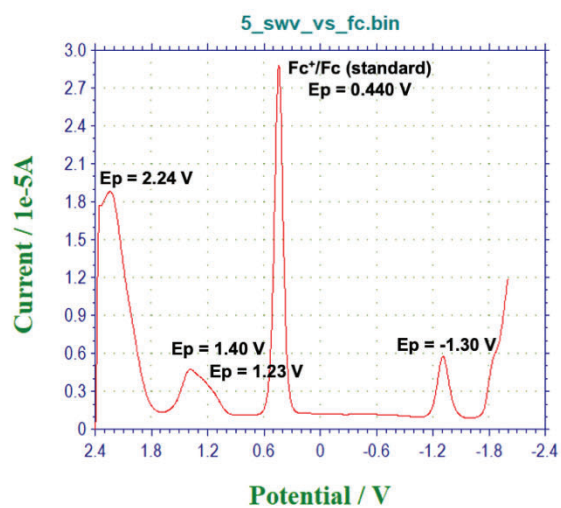
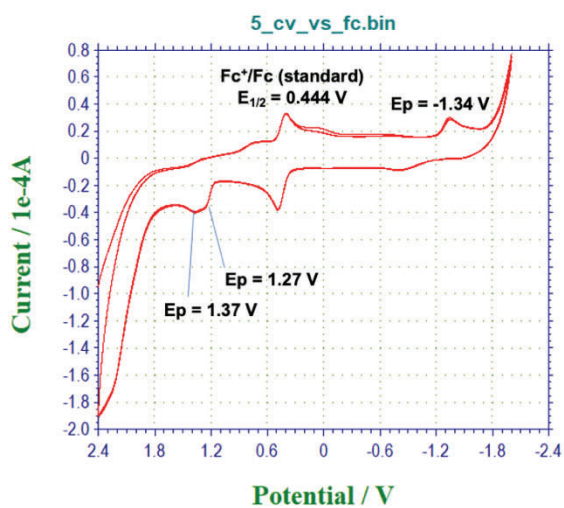
#### CV-3



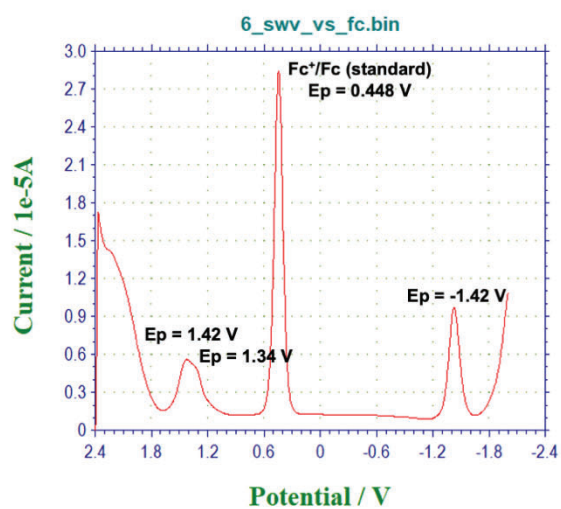
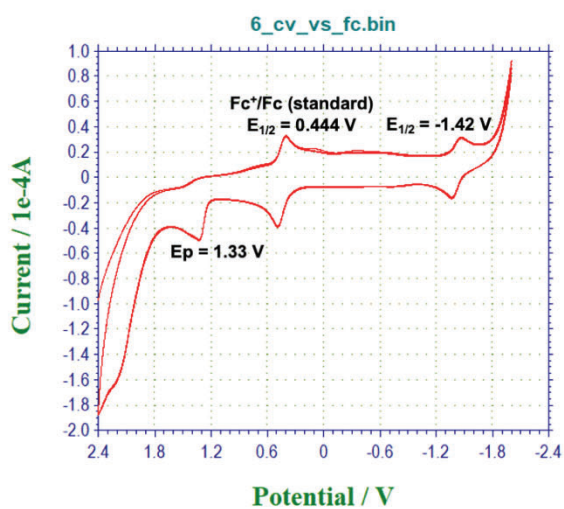
CV-4



CV-5

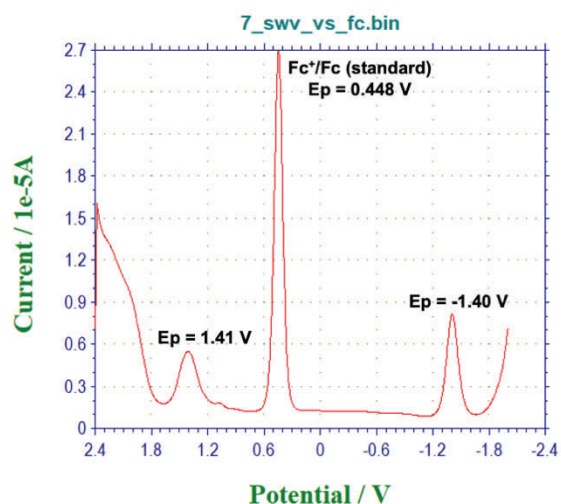
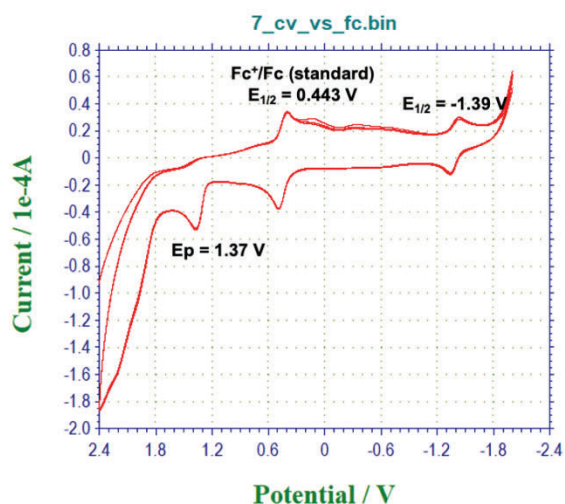


CV-6

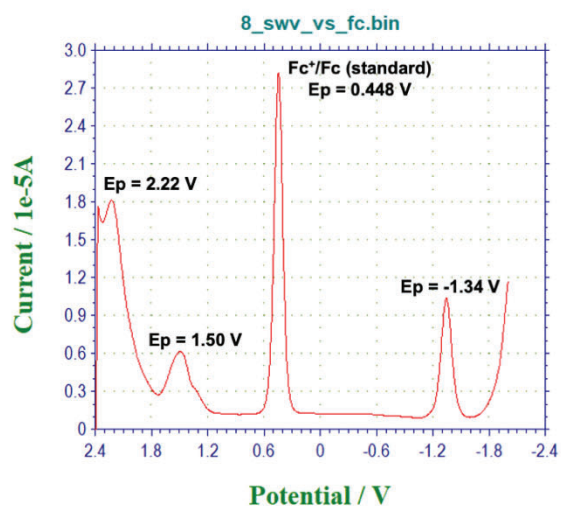
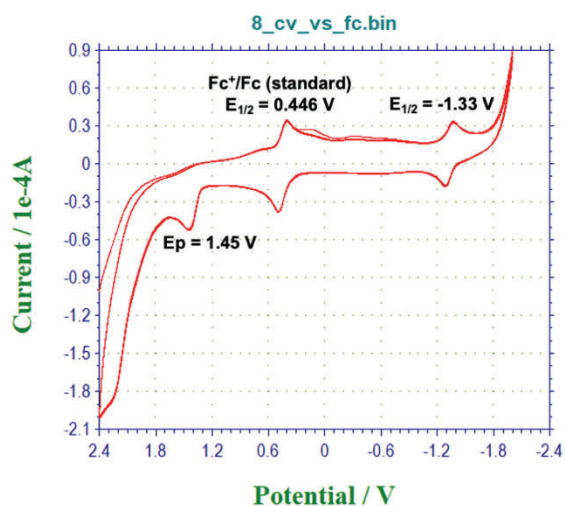




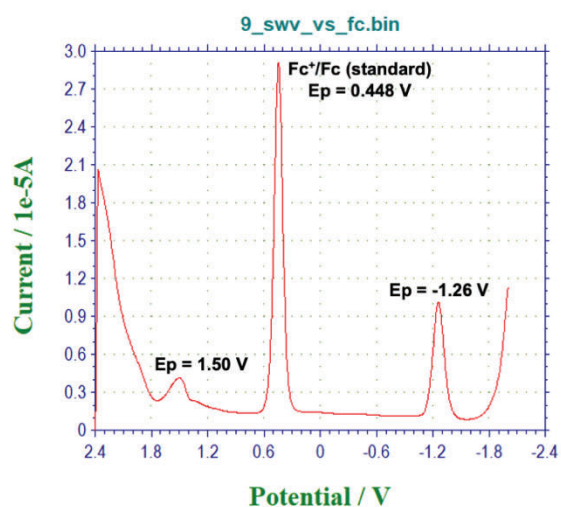
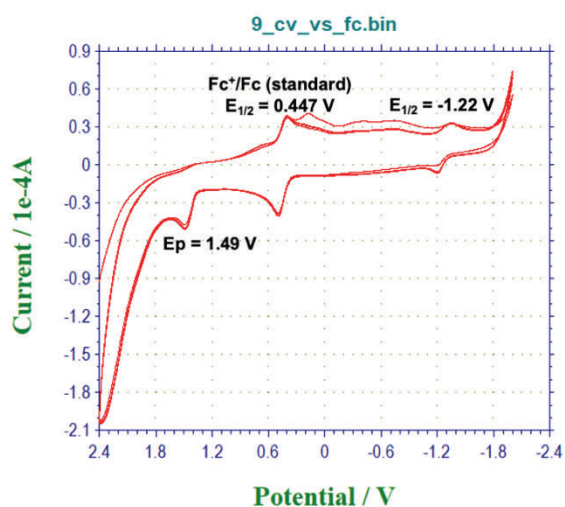
CV-7



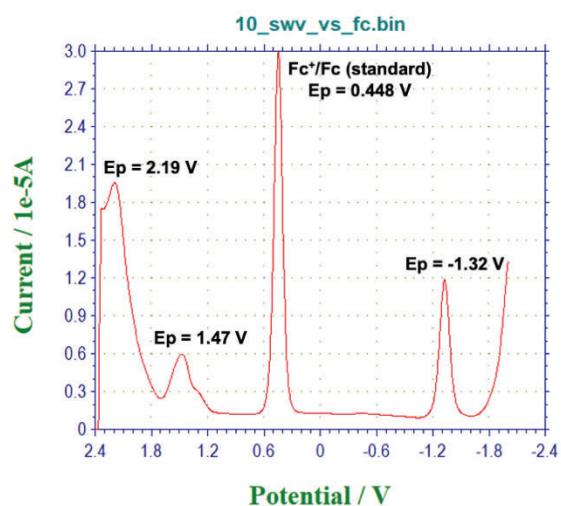
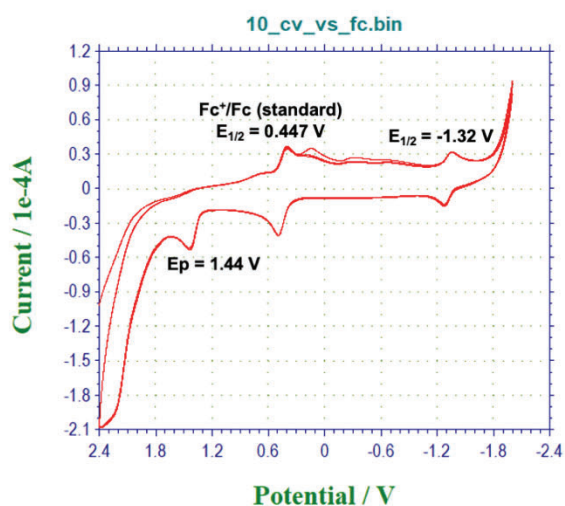
CV-8



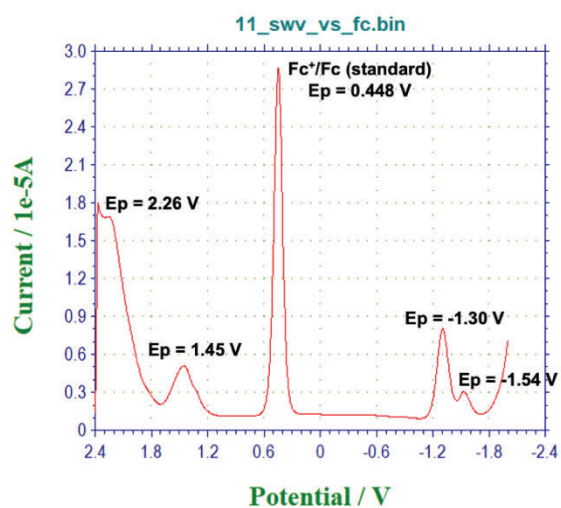
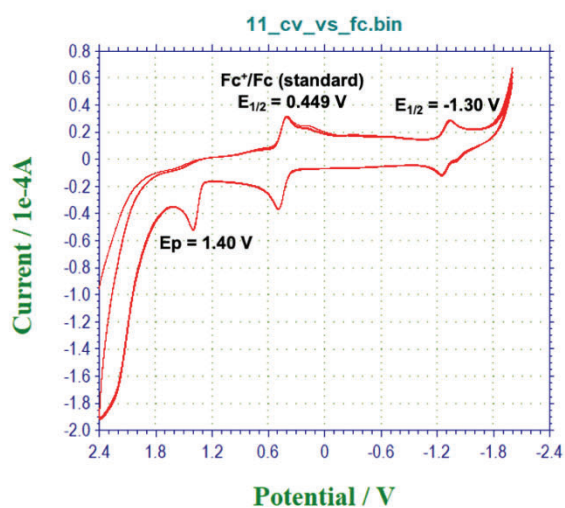
CV-9



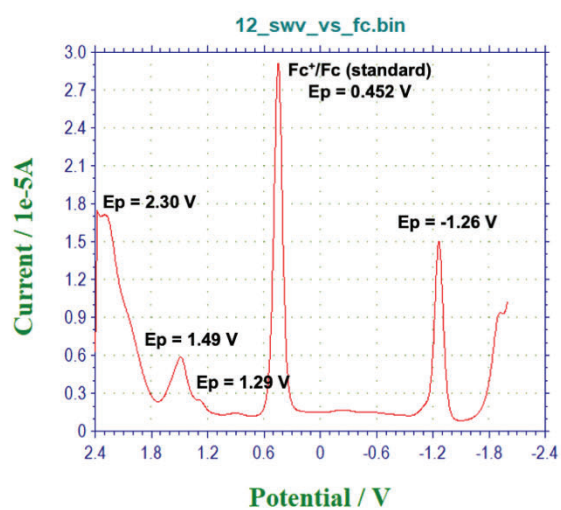
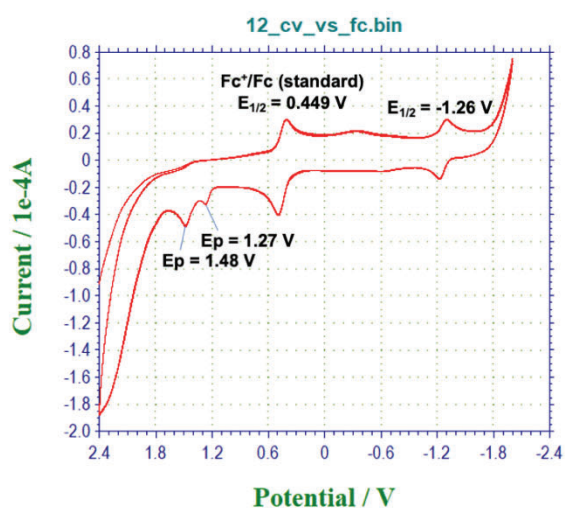
CV-10



CV-11

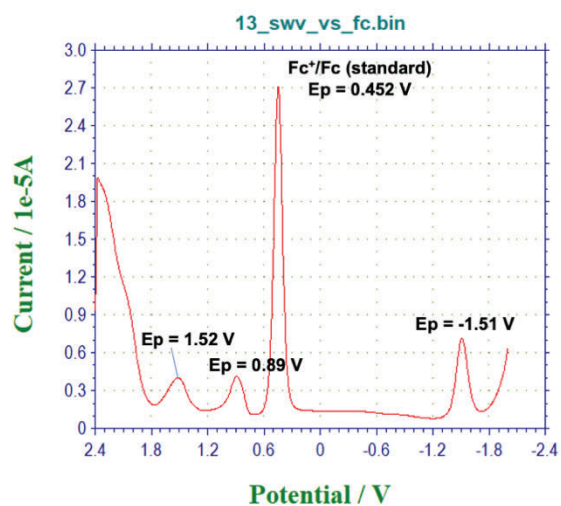
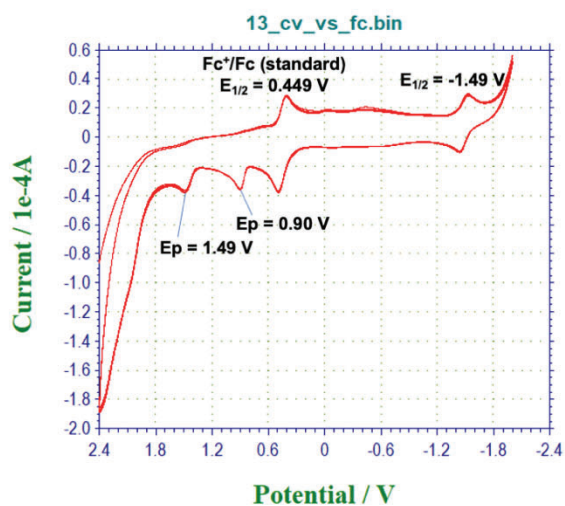


CV-12

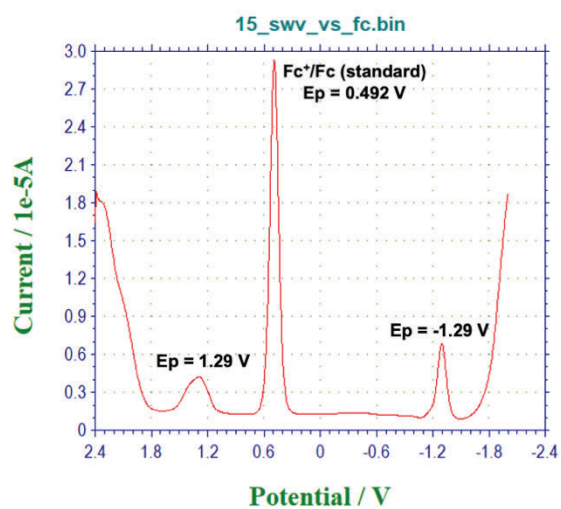
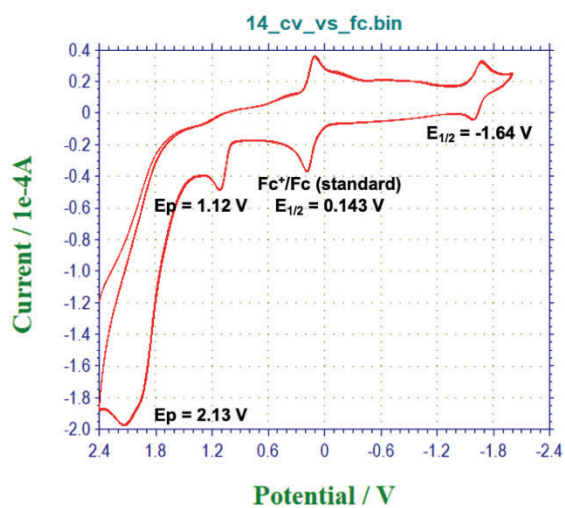




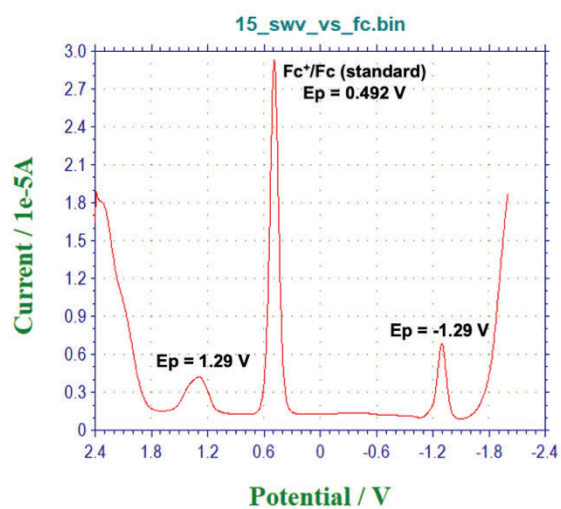
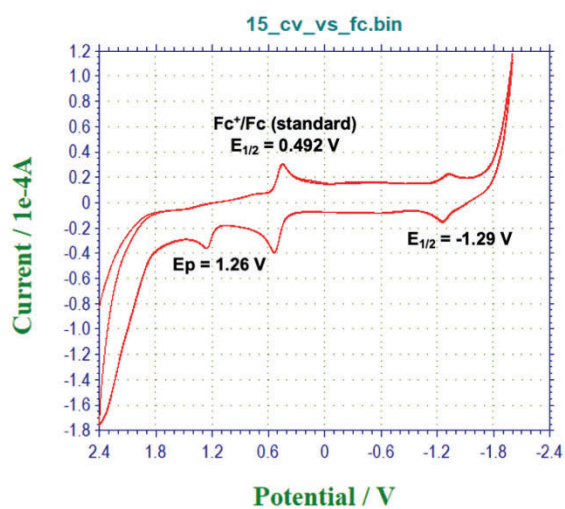
CV-13



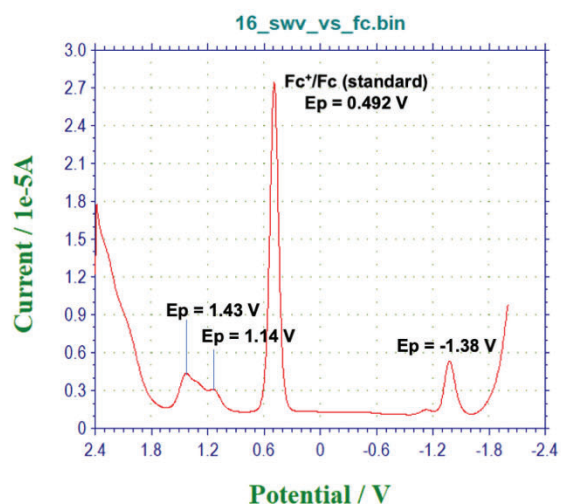
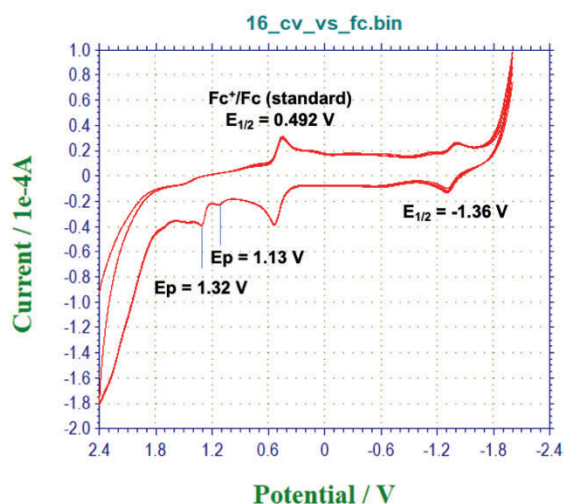
CV-14



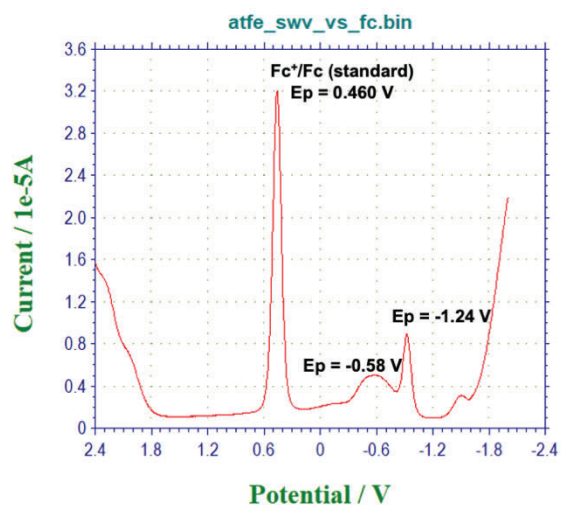
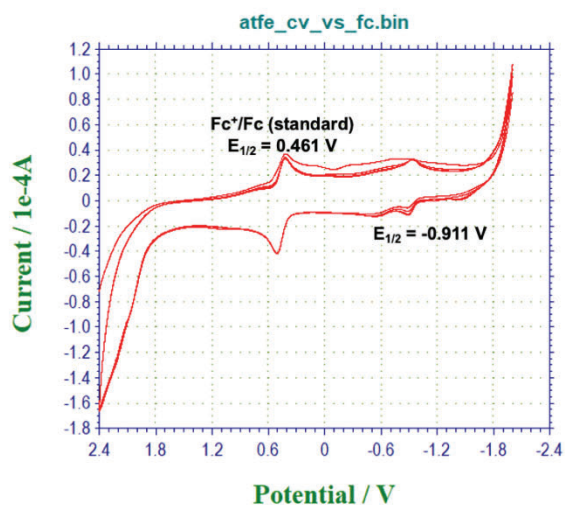
CV-15



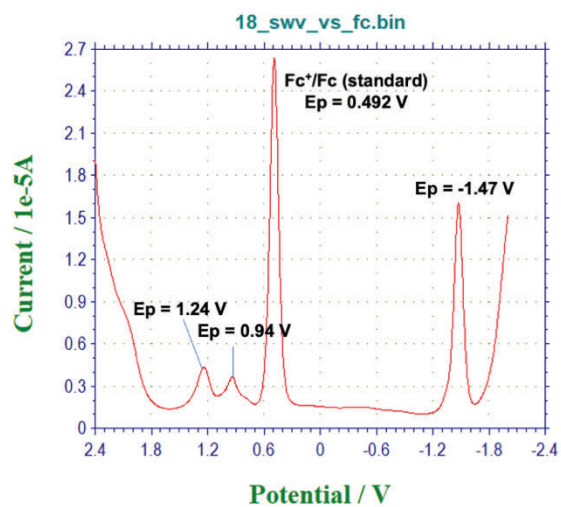
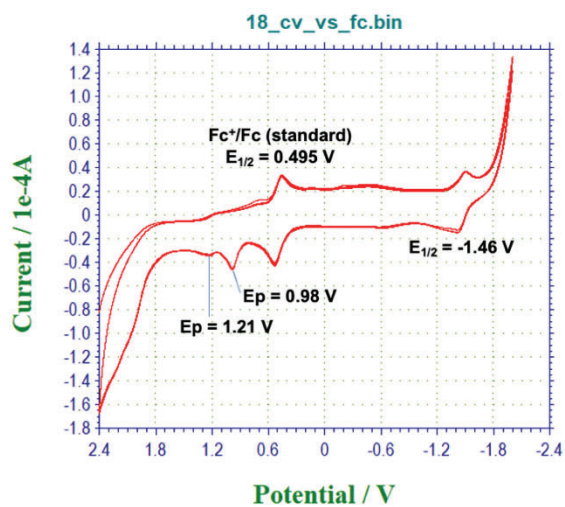
CV-16



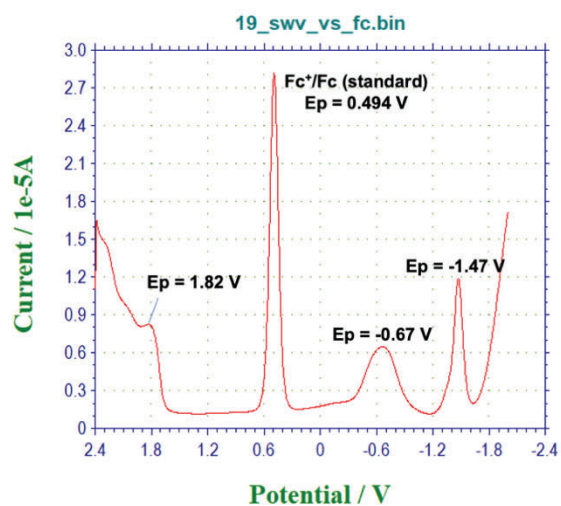
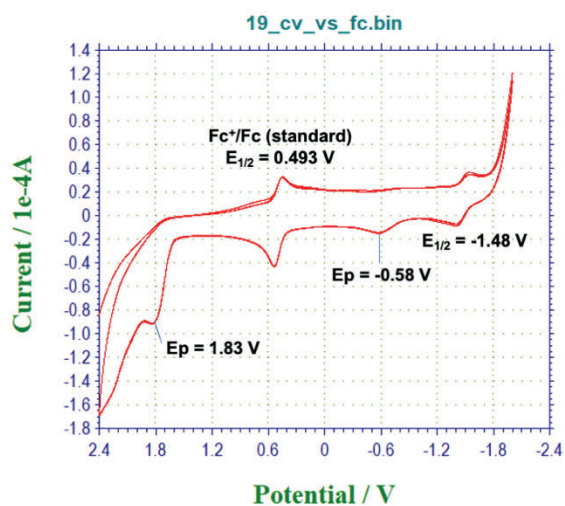
CV-17



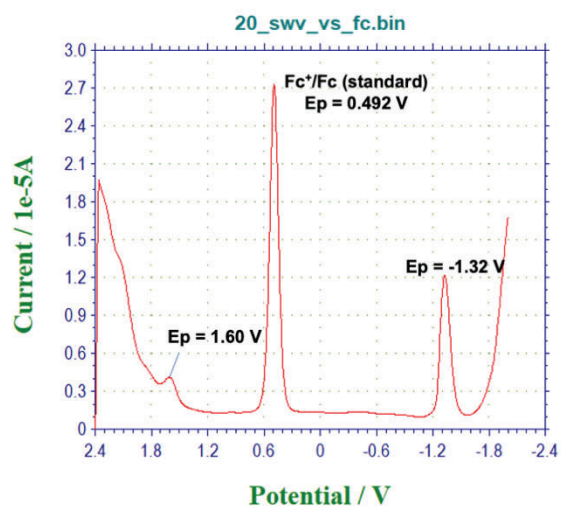
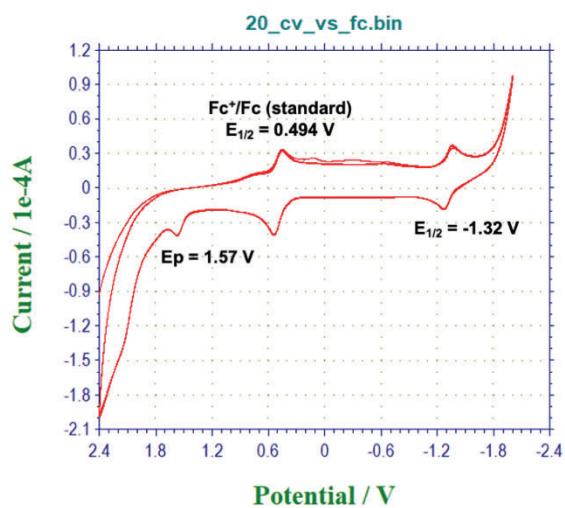
CV-18



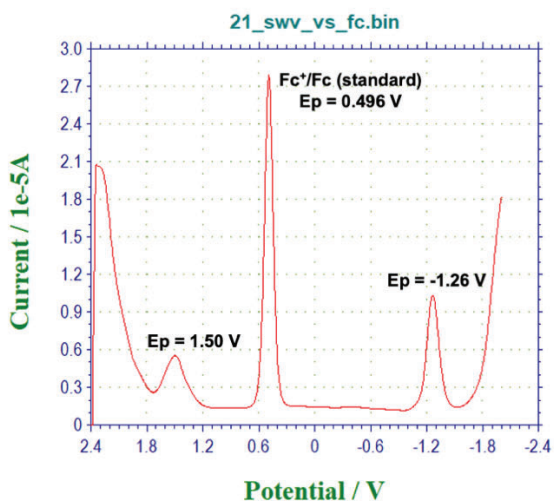
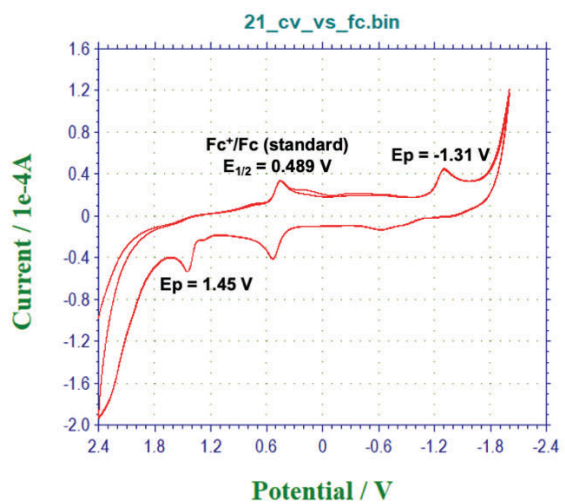
CV-19



CV-20

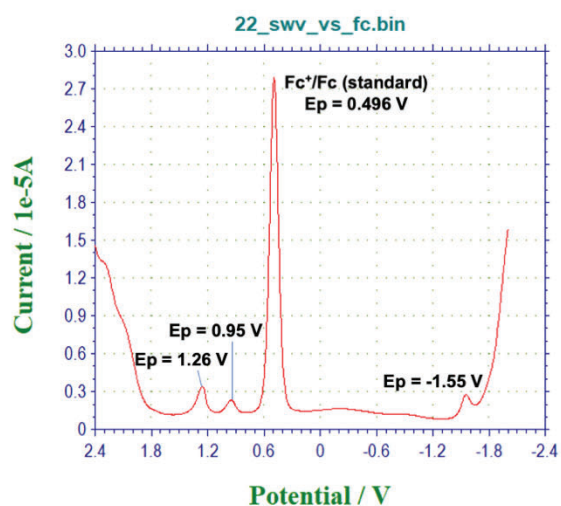
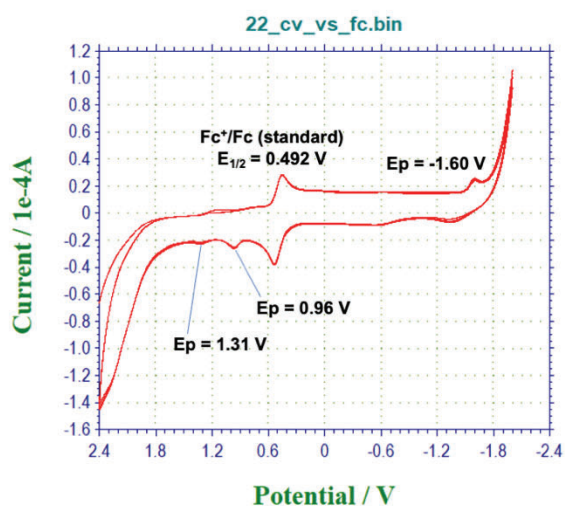


CV-21

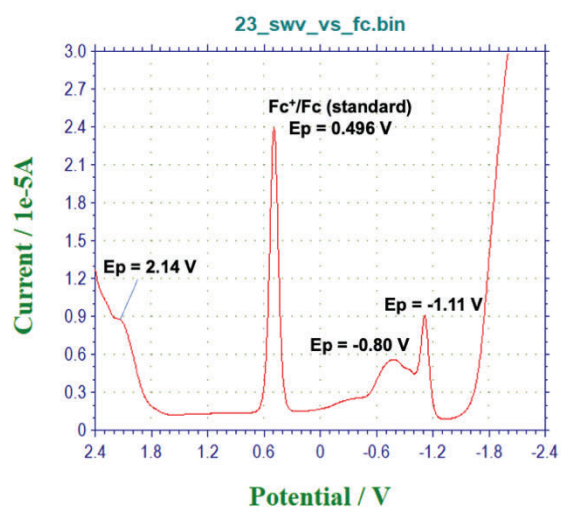
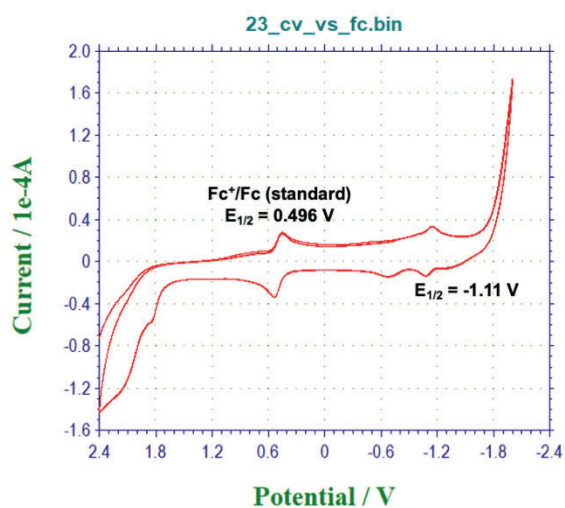




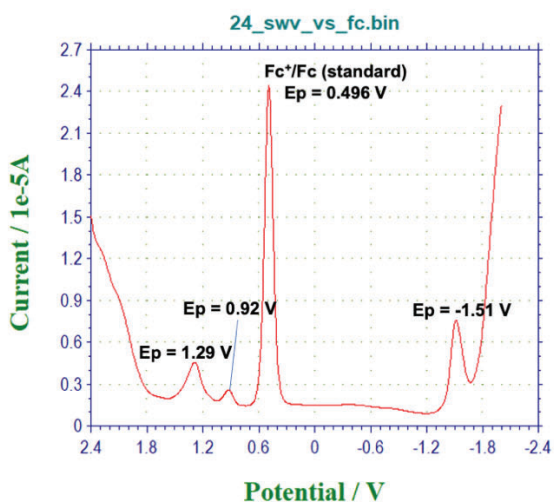
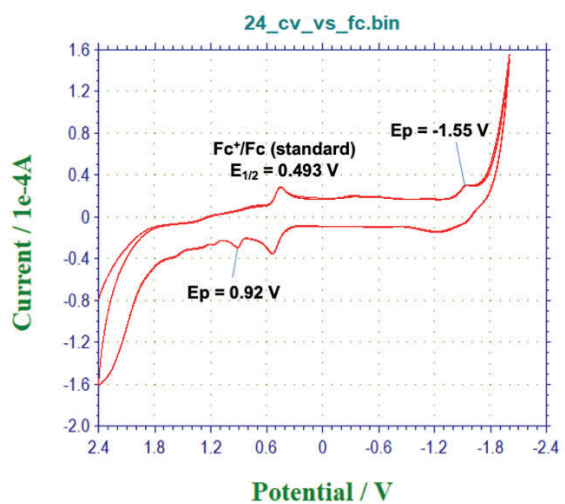
CV-22



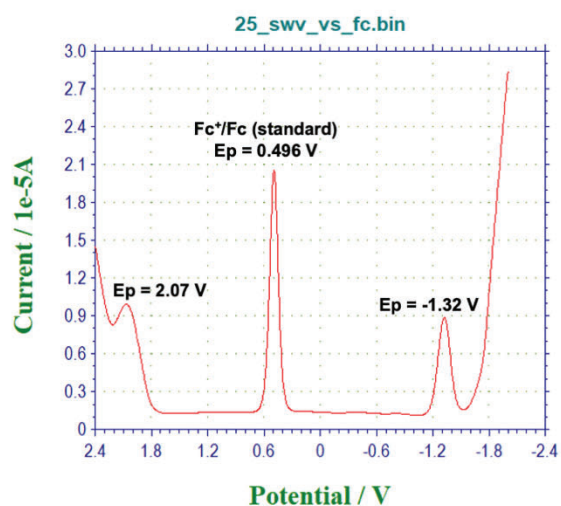
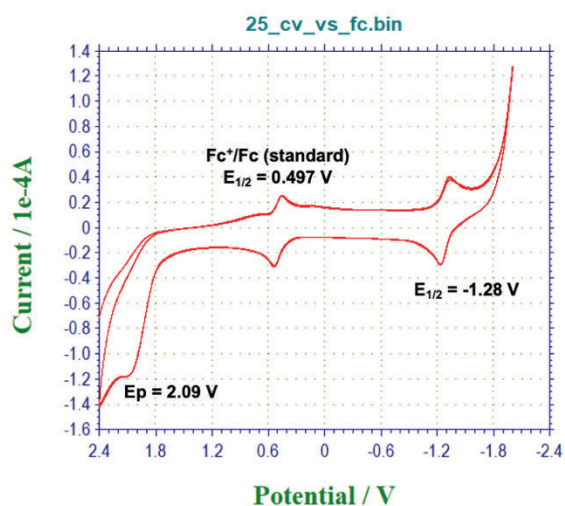
CV-23



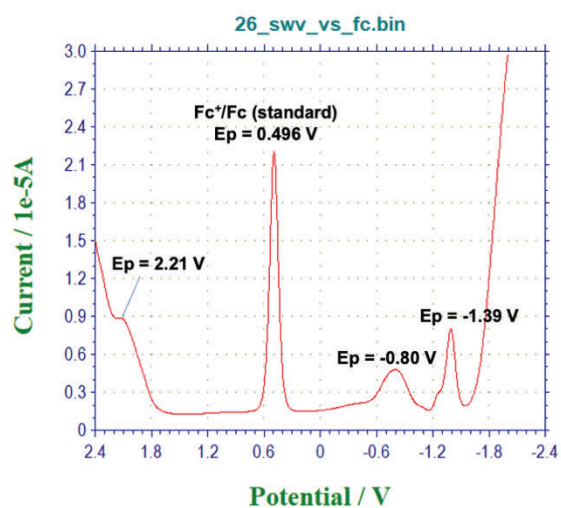
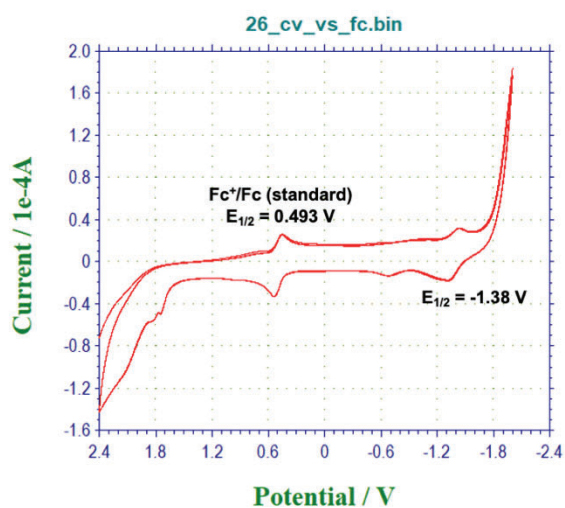
CV-24



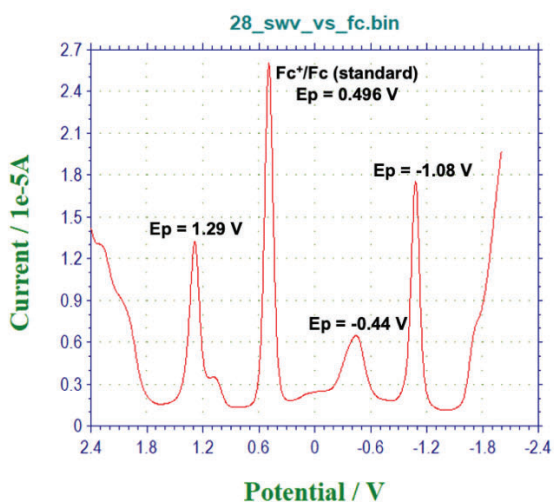
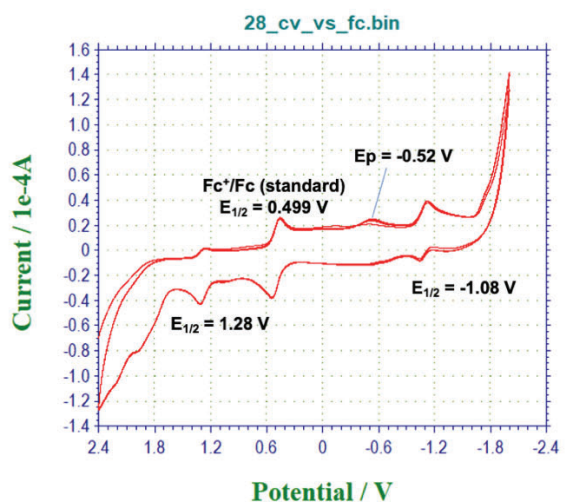
CV-25



CV-26

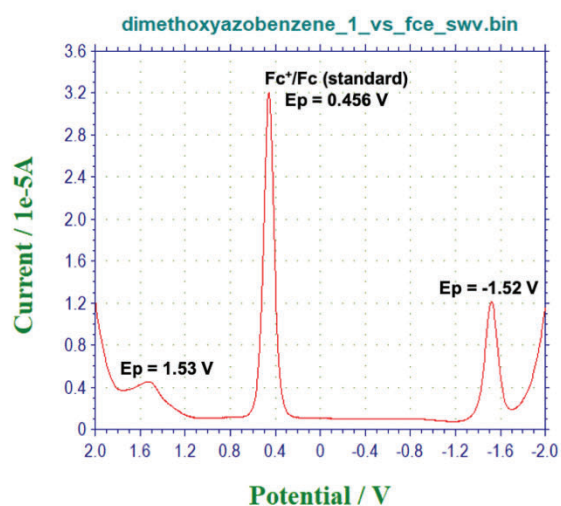
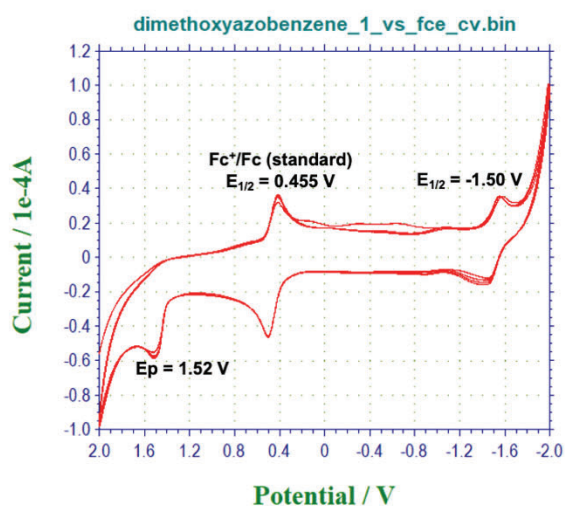


CV-27

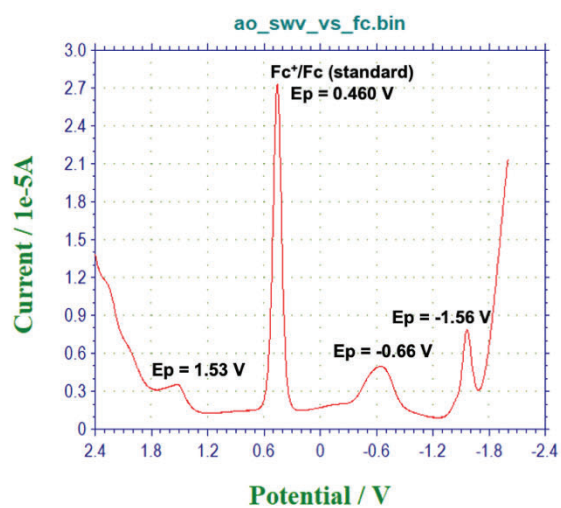
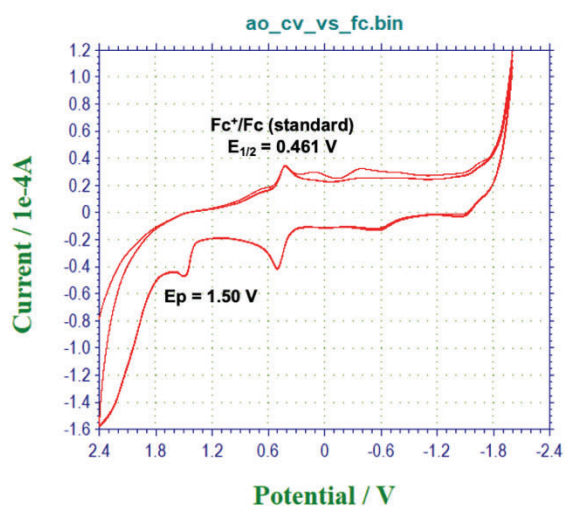




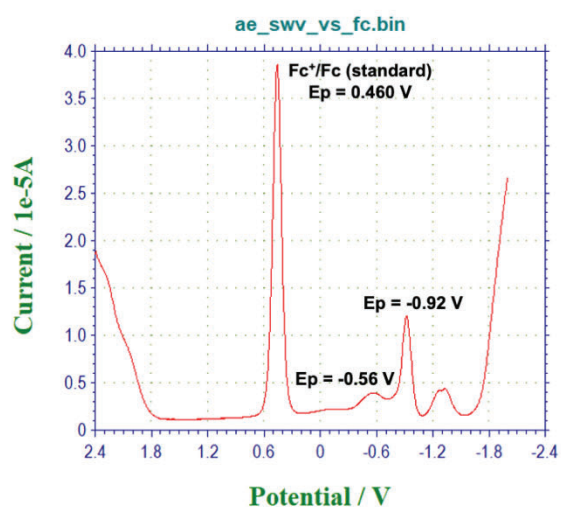
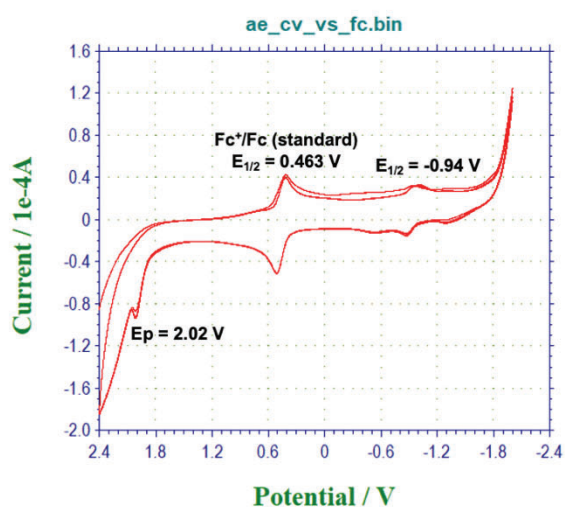
## CV-28



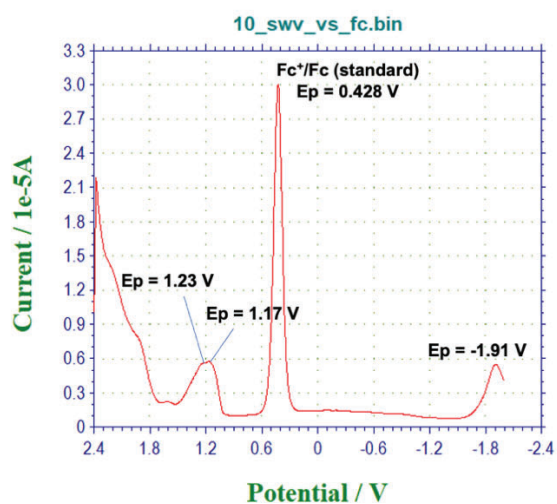
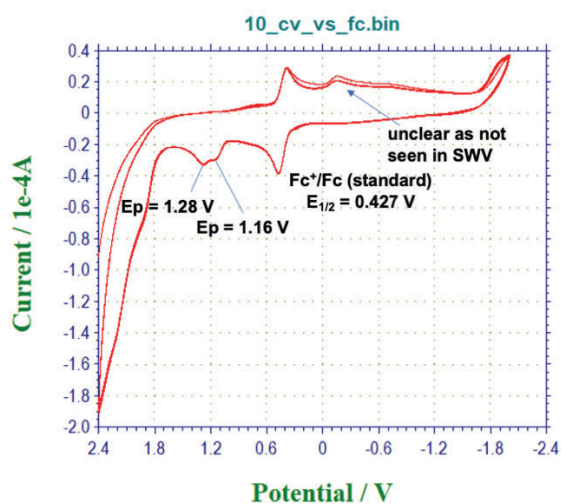
## CV-29



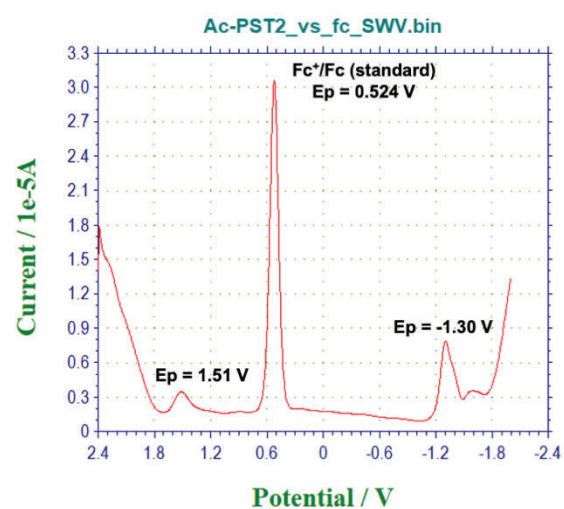
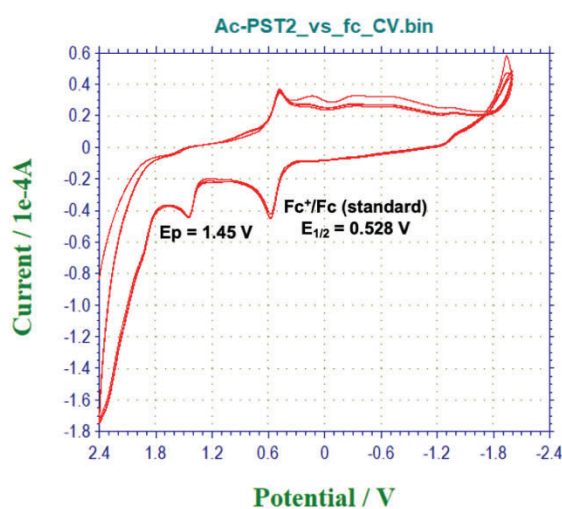
## CV-30



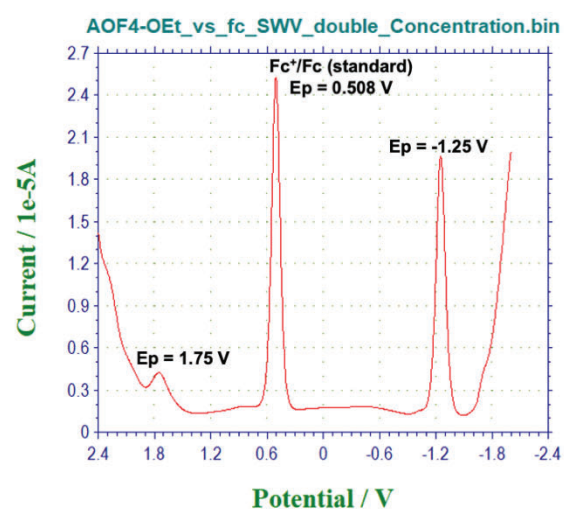
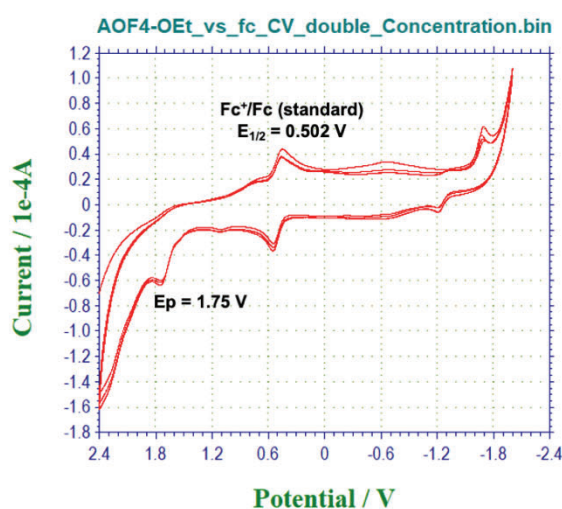
CV-31



CV-32

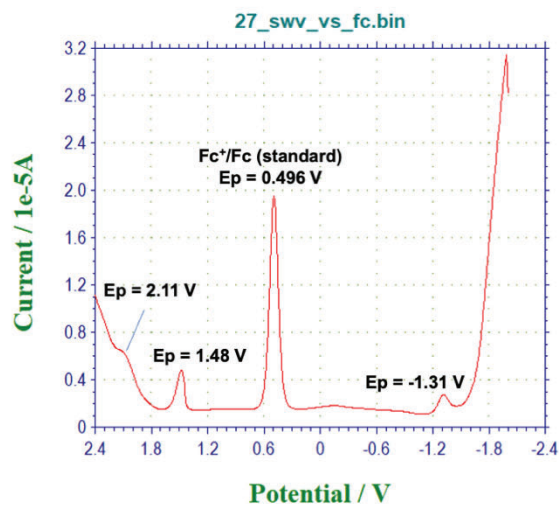
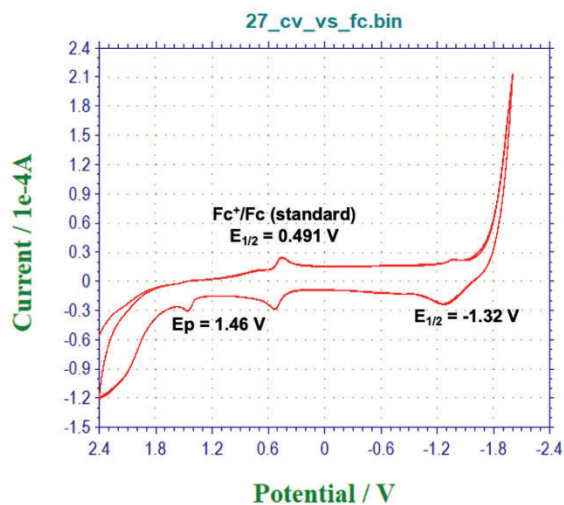


CV-33

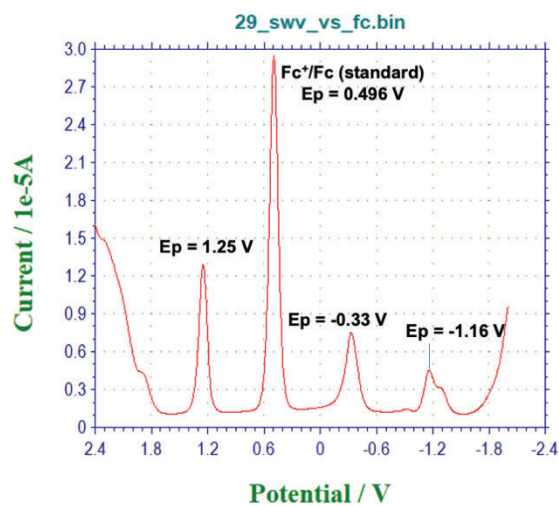
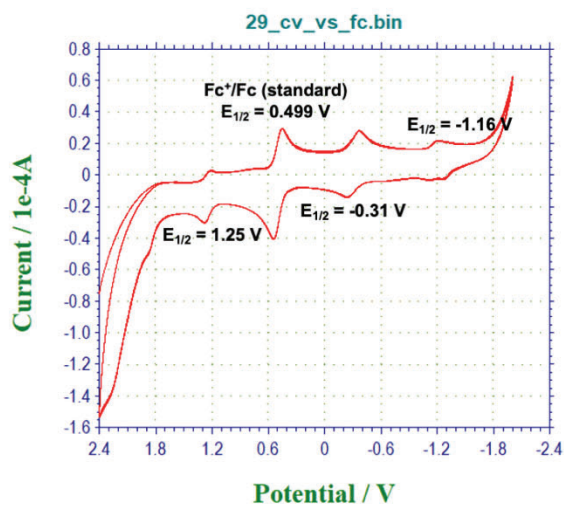


## 12.2 Cyclic voltammetry and square wave voltammetry spectra: fluorophores

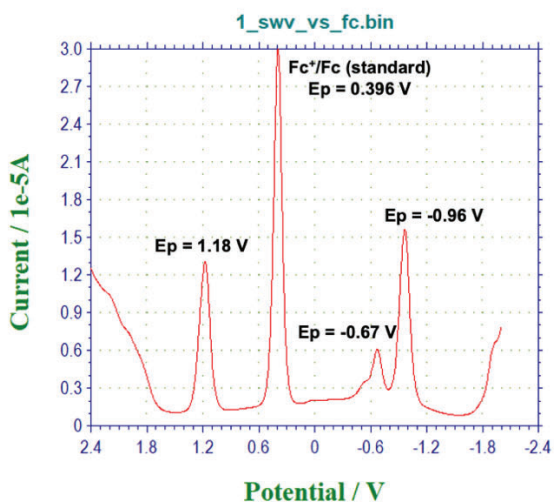
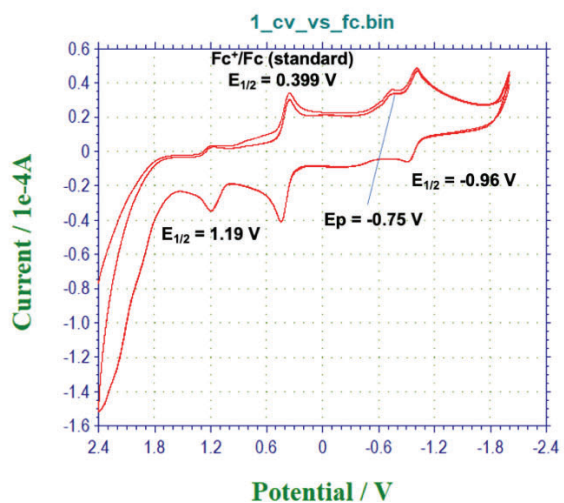
### Rhodamine B



### Oxazine 170

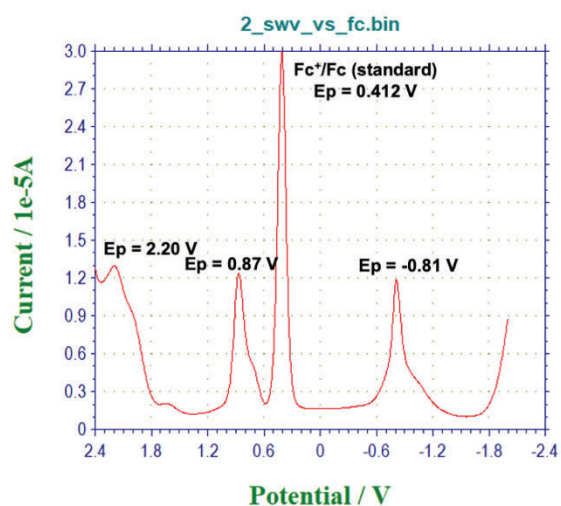
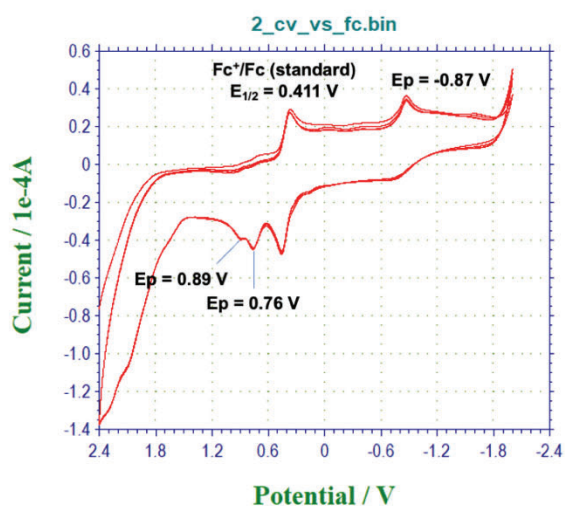


### Sulforhodamine B

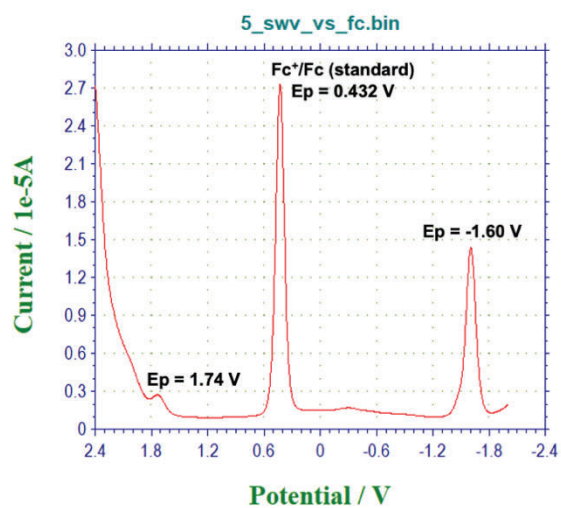
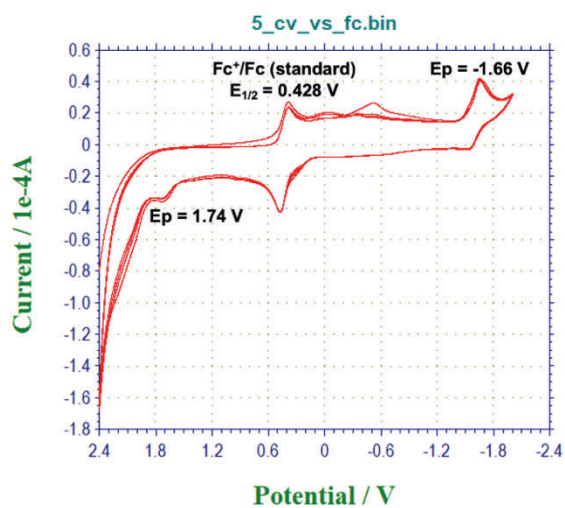




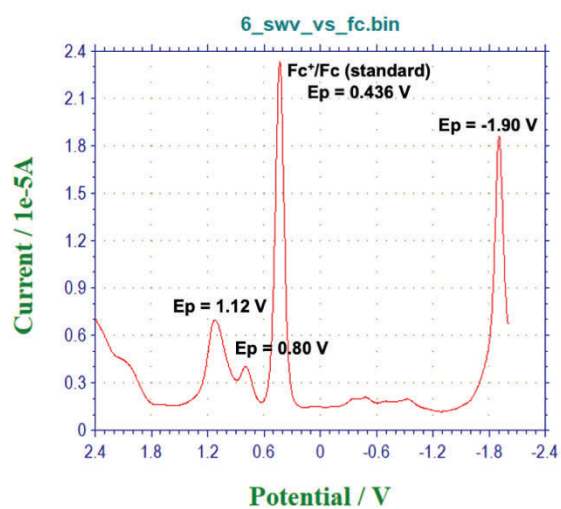
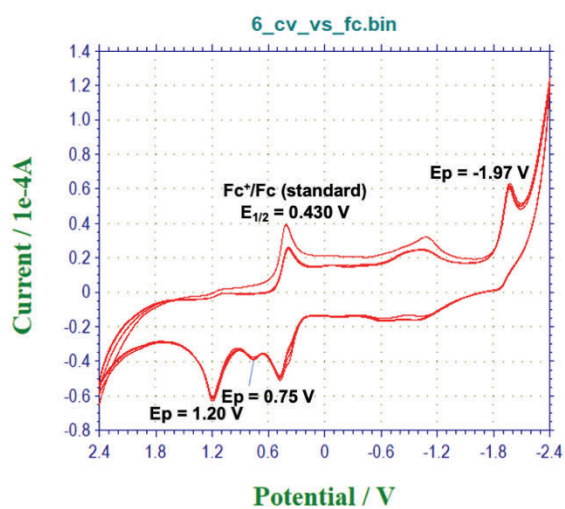
## Cy5



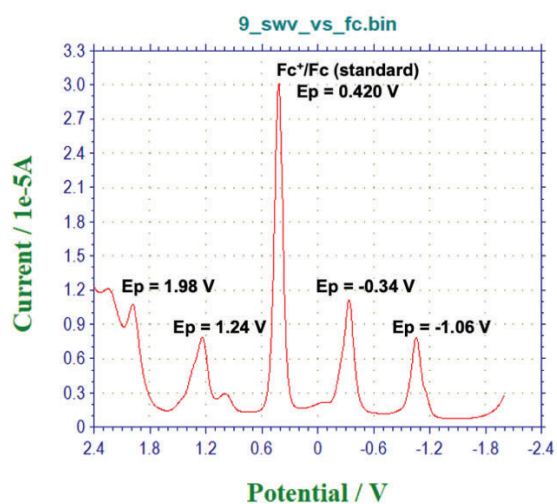
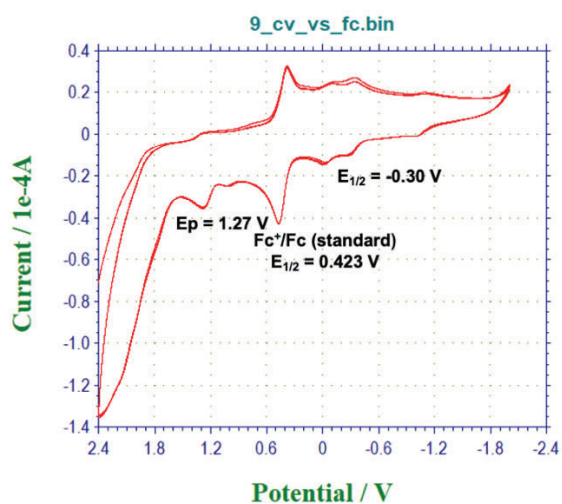
## Acridine



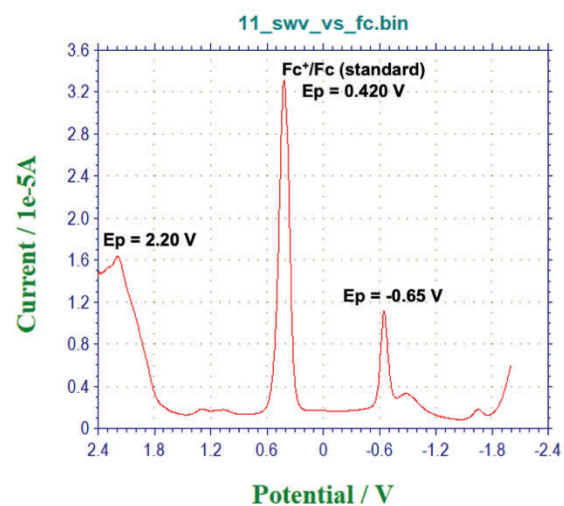
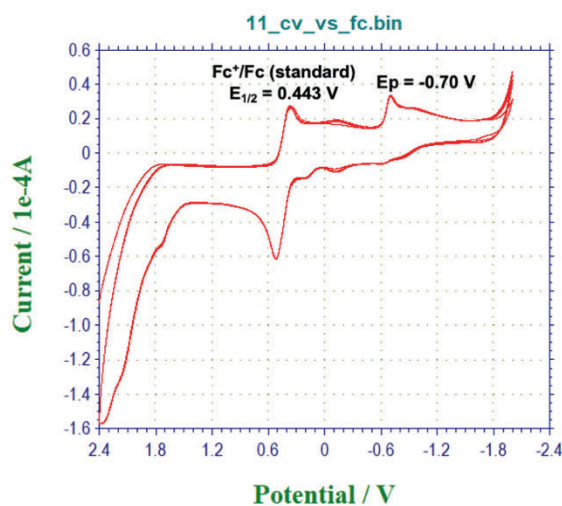
## Acridine Orange



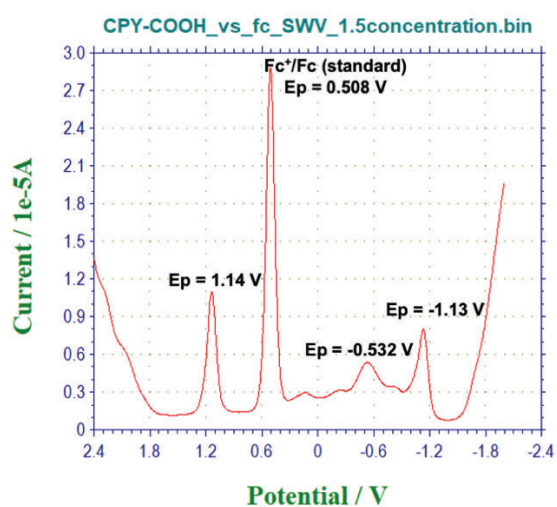
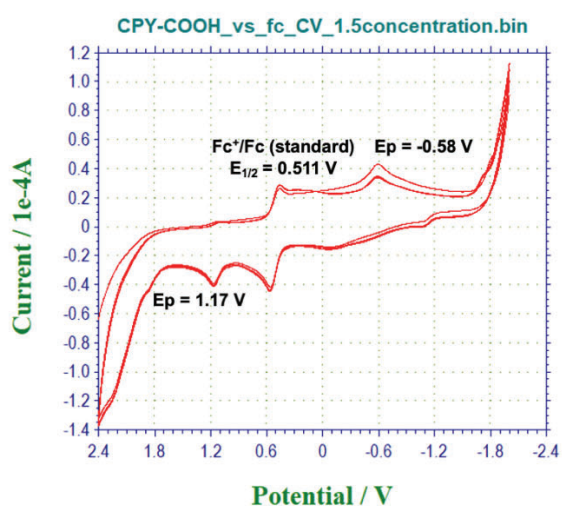
## Methylene Blue



## Cy7

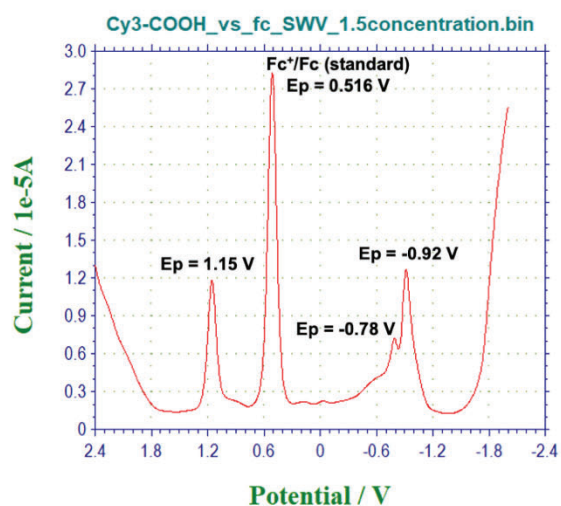
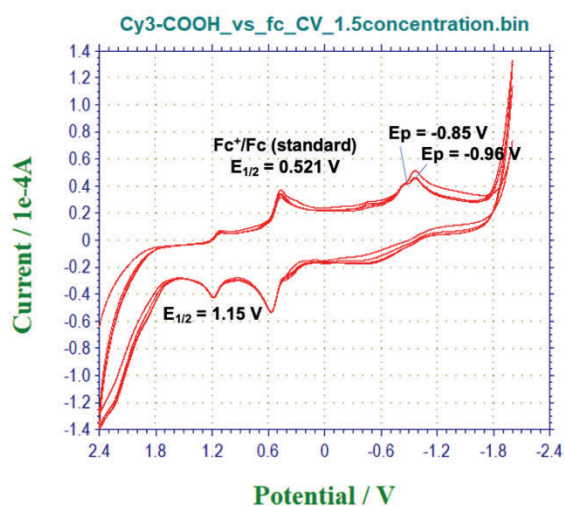


## CPY-COOH

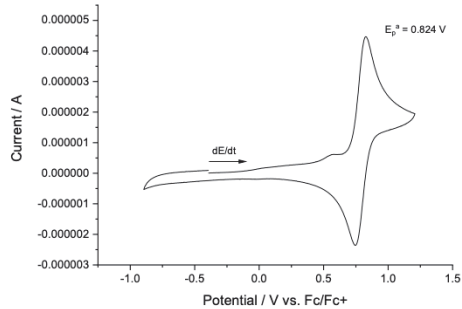




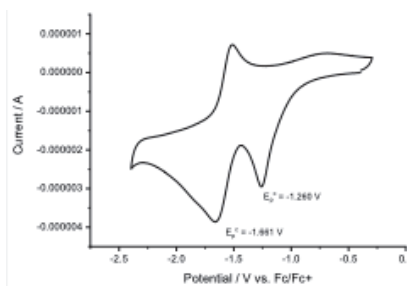
Cy3



Rhodamine B, PF<sub>6</sub><sup>-</sup> salt\*

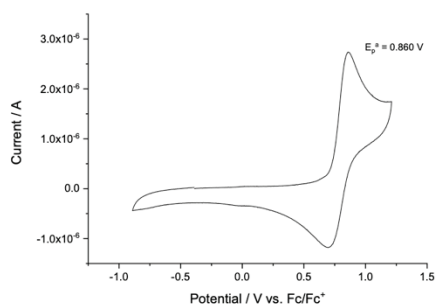


oxidation

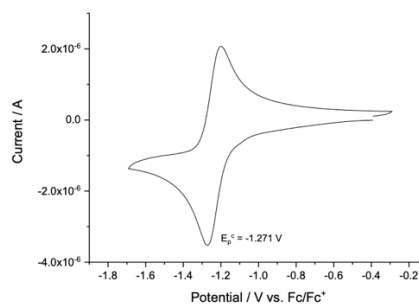


reduction

Rhodamine B methyl ester, PF<sub>6</sub><sup>-</sup> salt\*

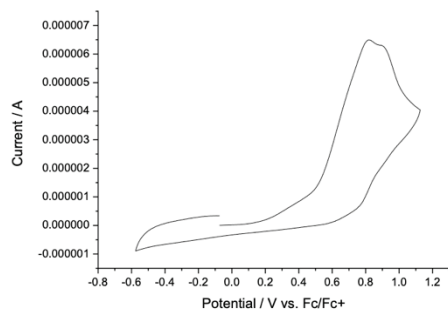


oxidation

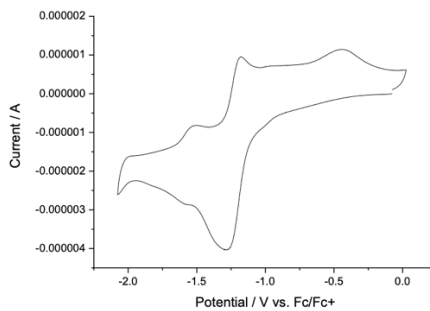


reduction

**Rhodamine B piperazine amide, Cl<sup>-</sup> salt\***

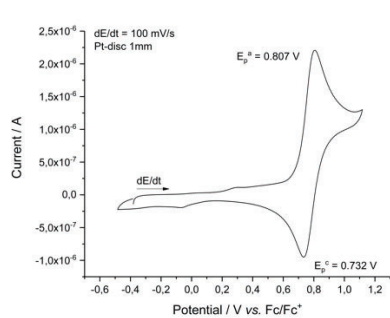


oxidation ( $E_p^a = 0.81$ )

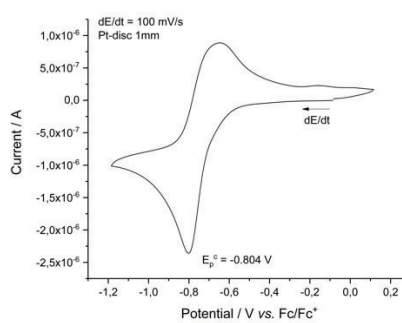


reduction ( $E_{1/2} = -1.25$ )

**Nile Blue, PF<sub>6</sub><sup>-</sup> salt\***

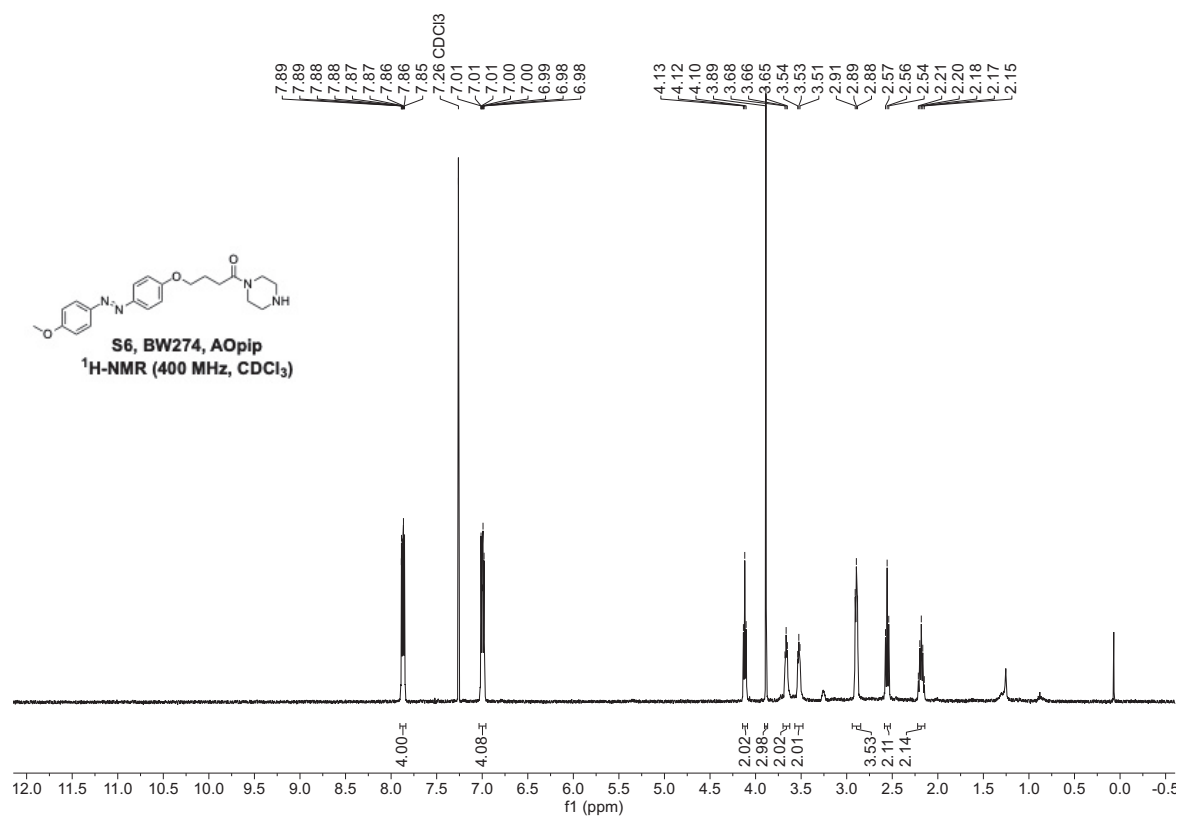
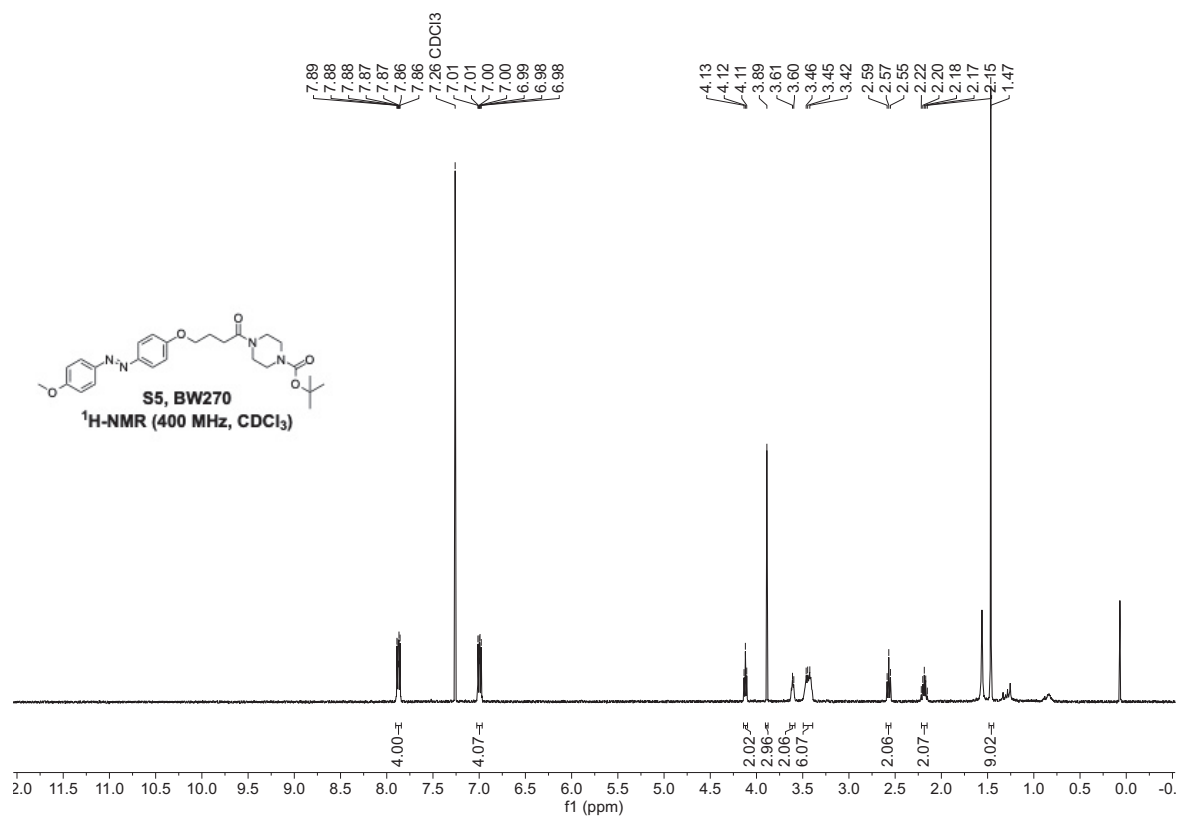


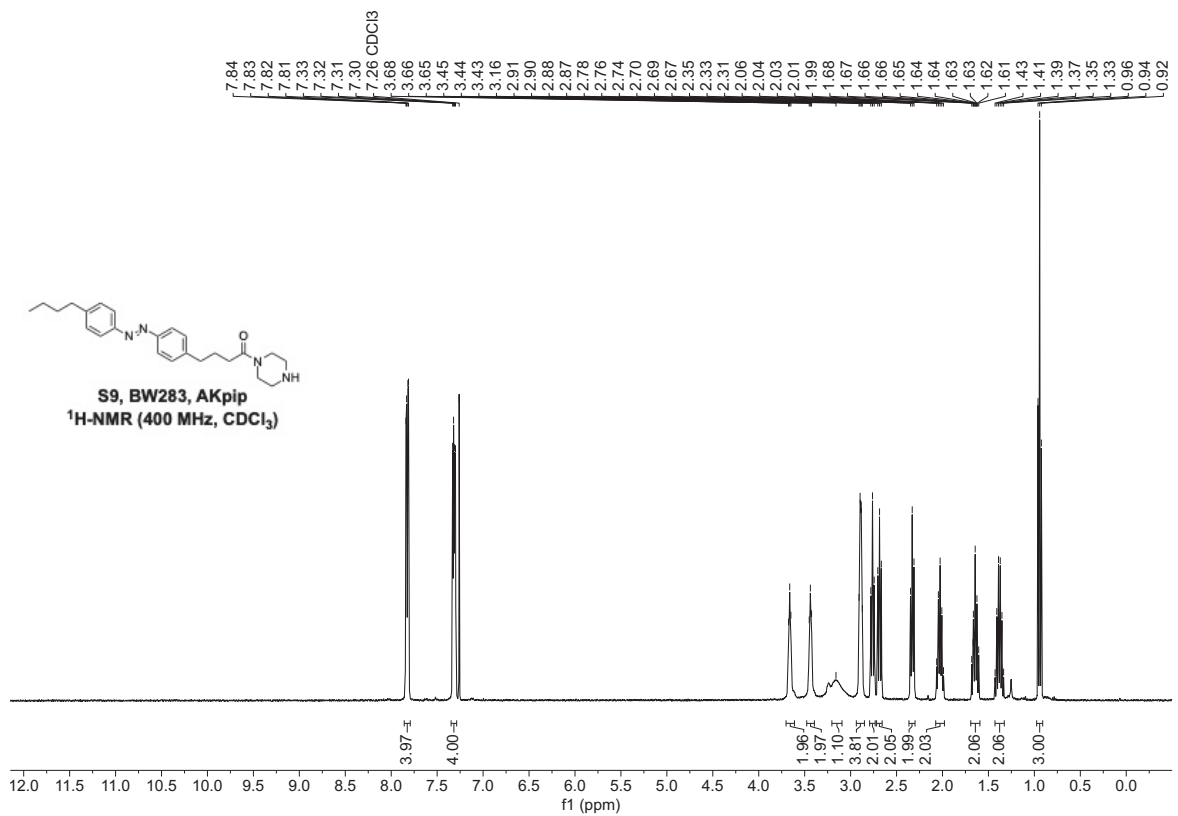
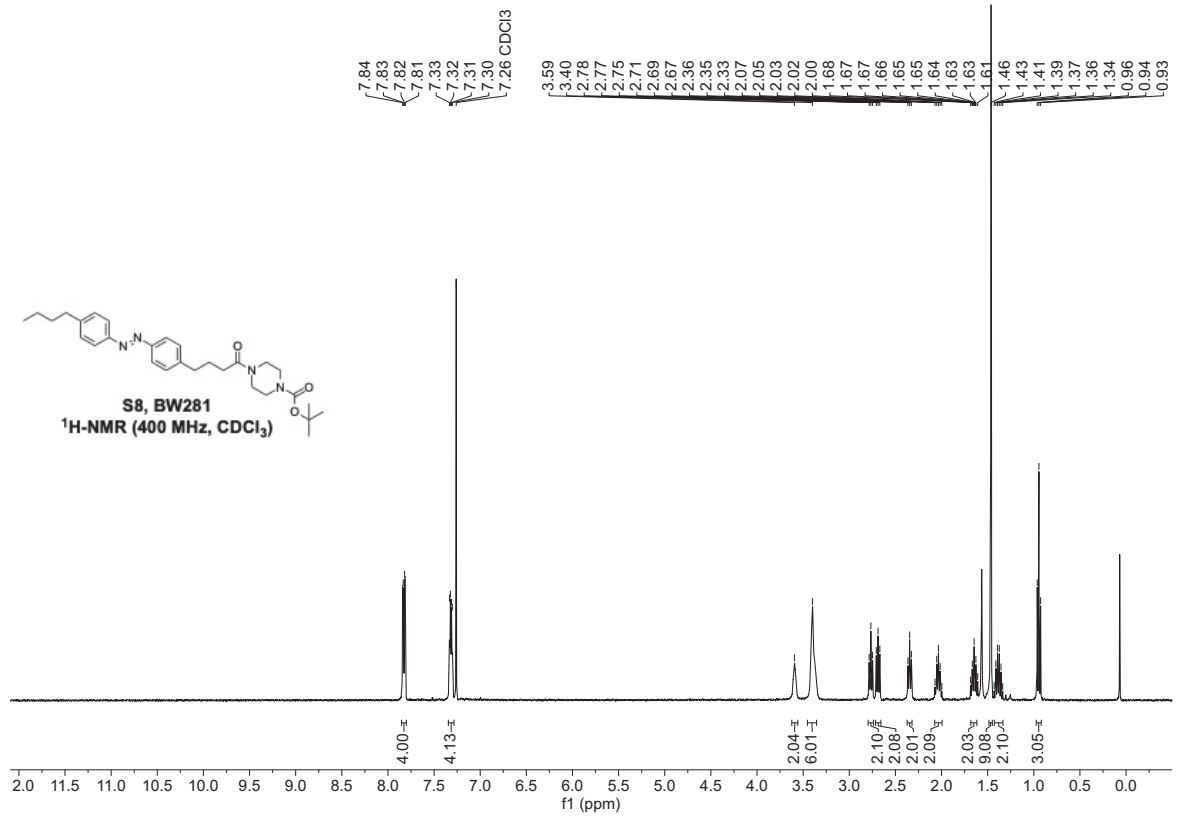
oxidation

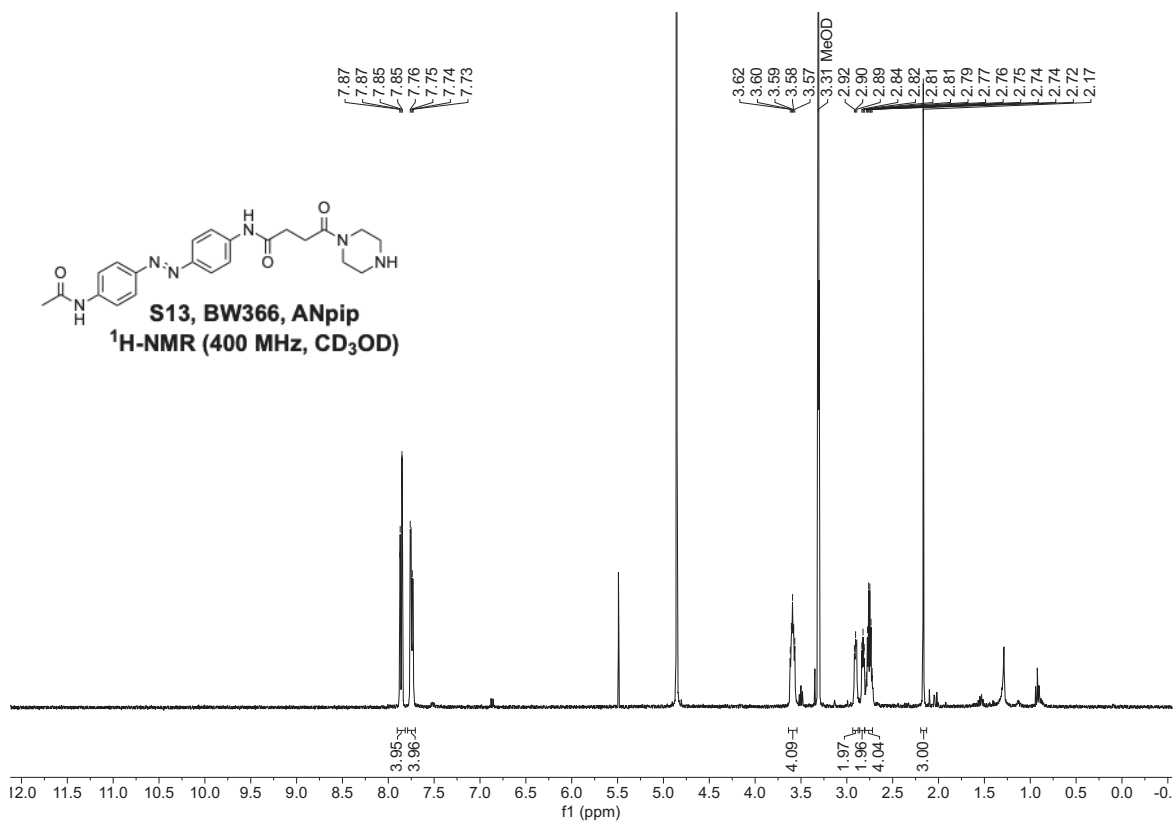
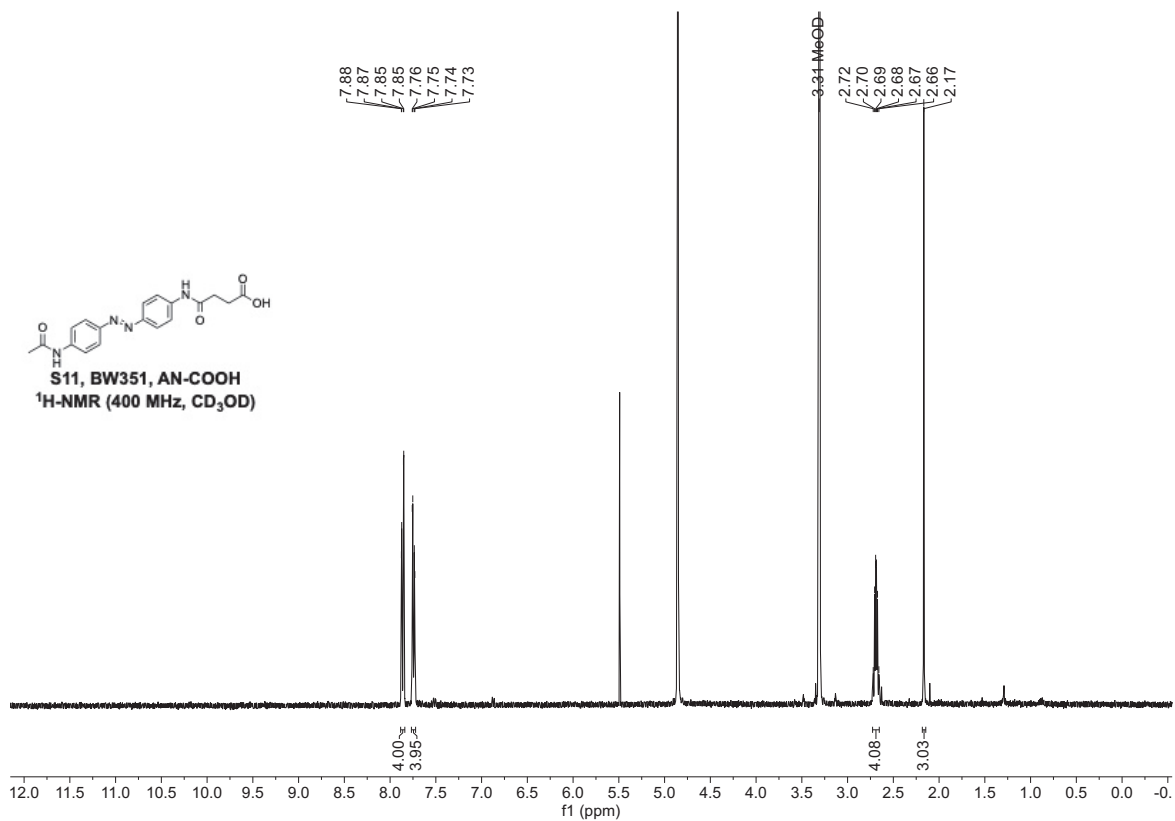


reduction

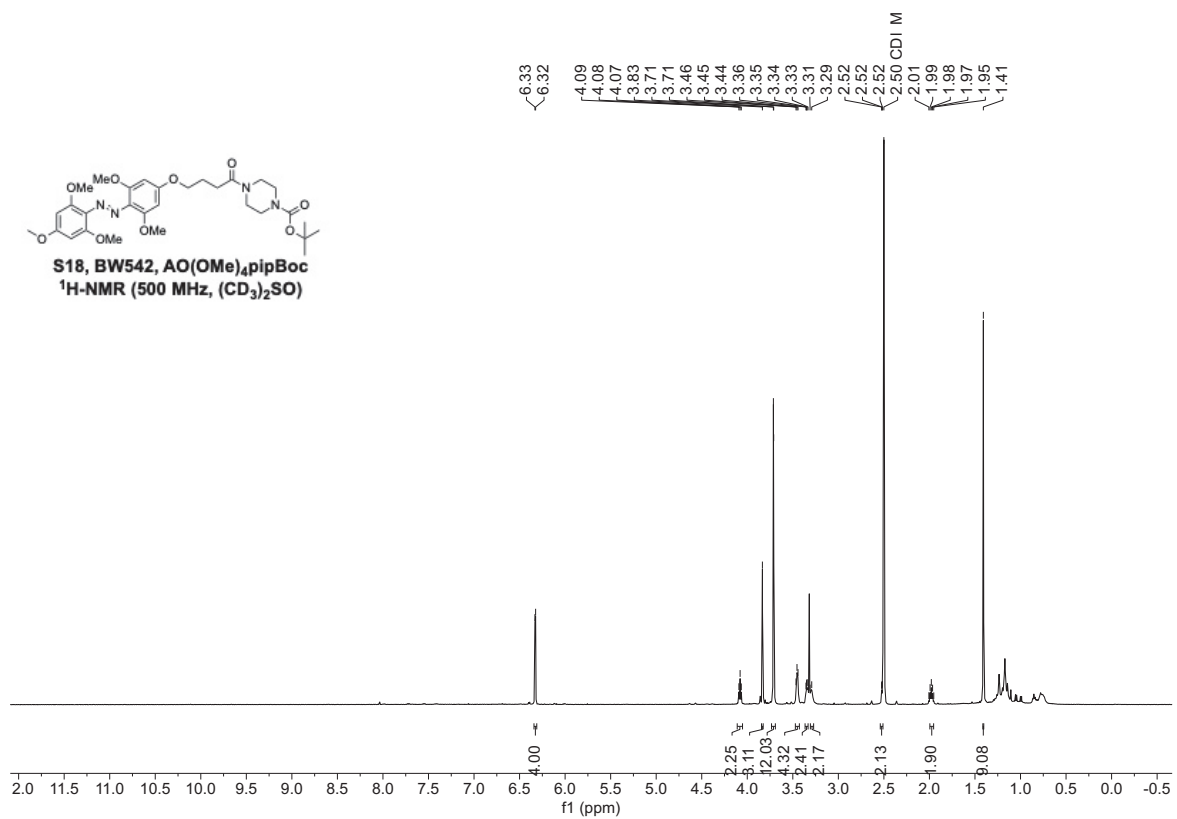
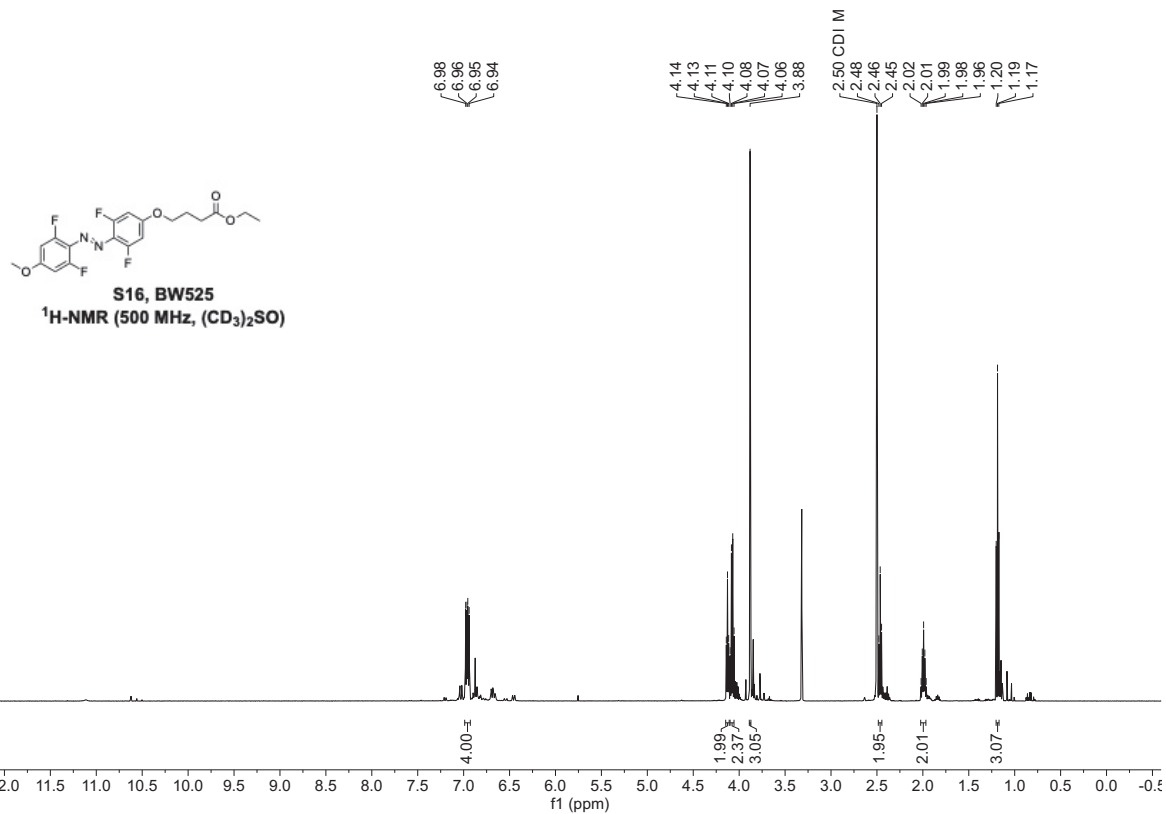
## 12.3 H-NMR spectra

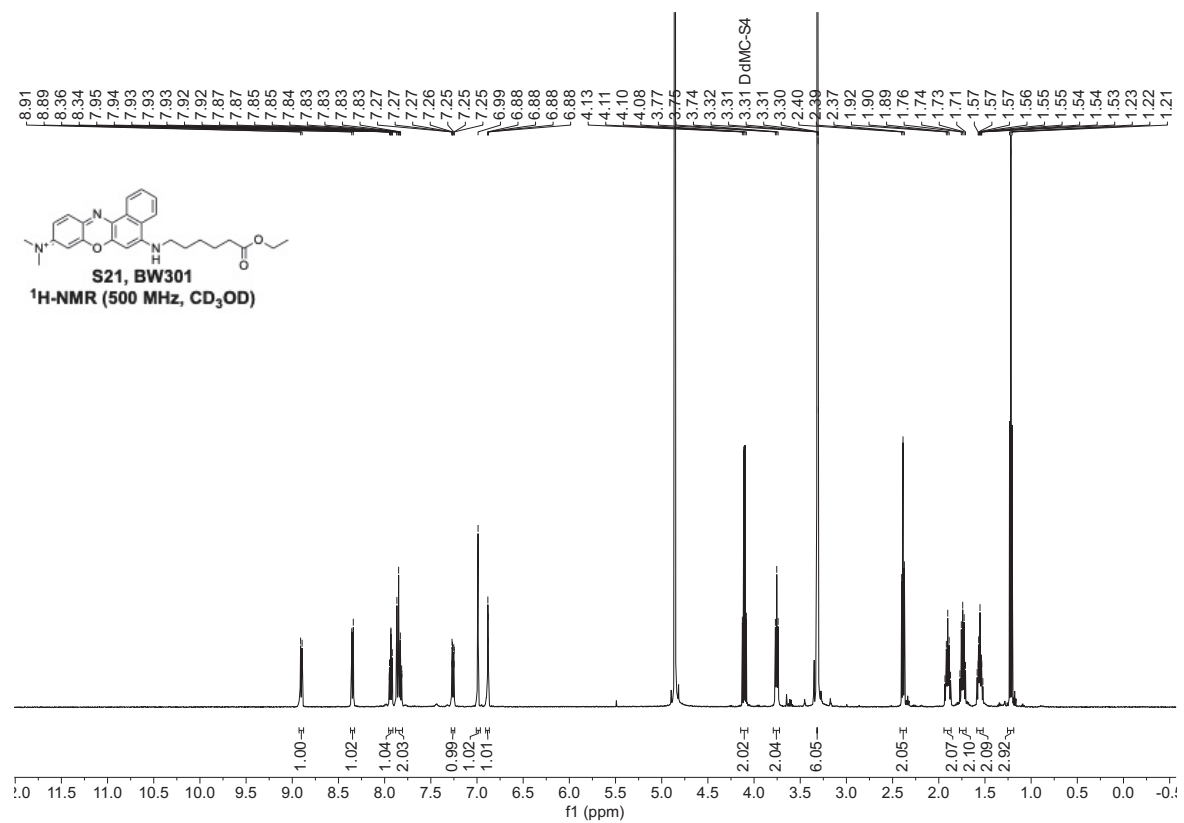
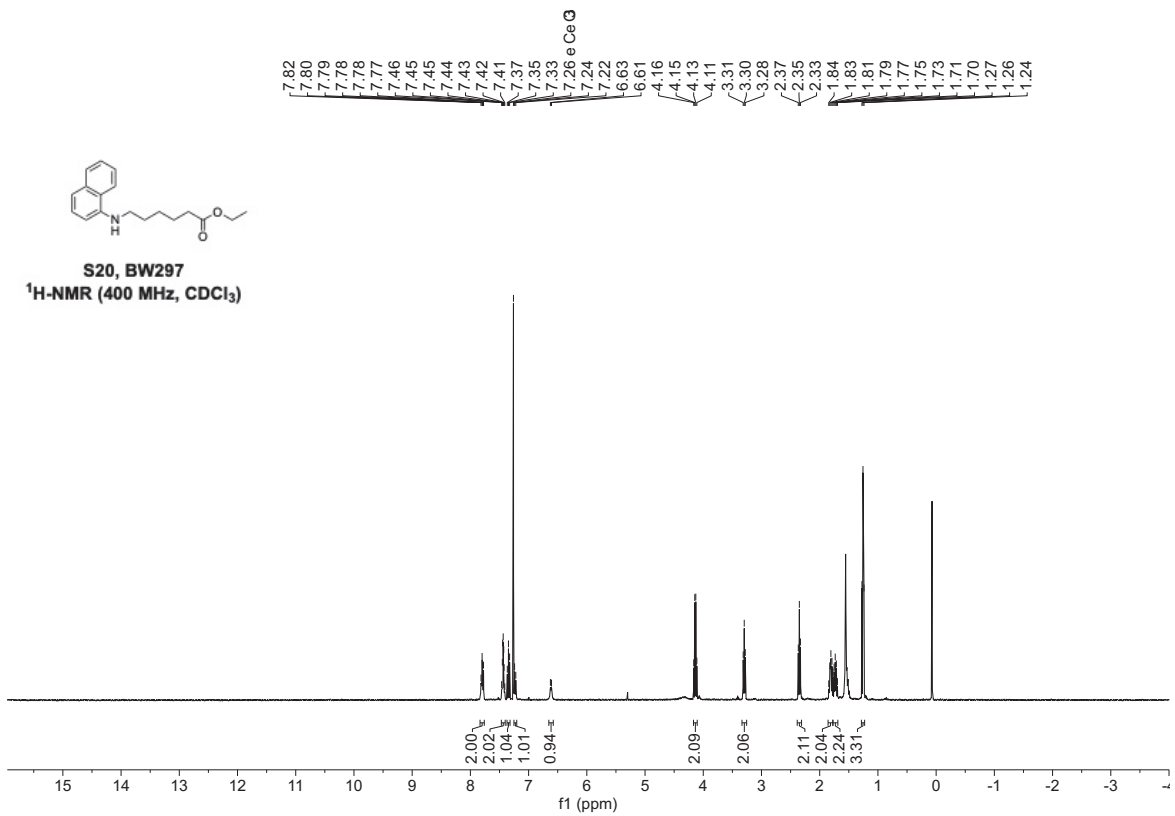


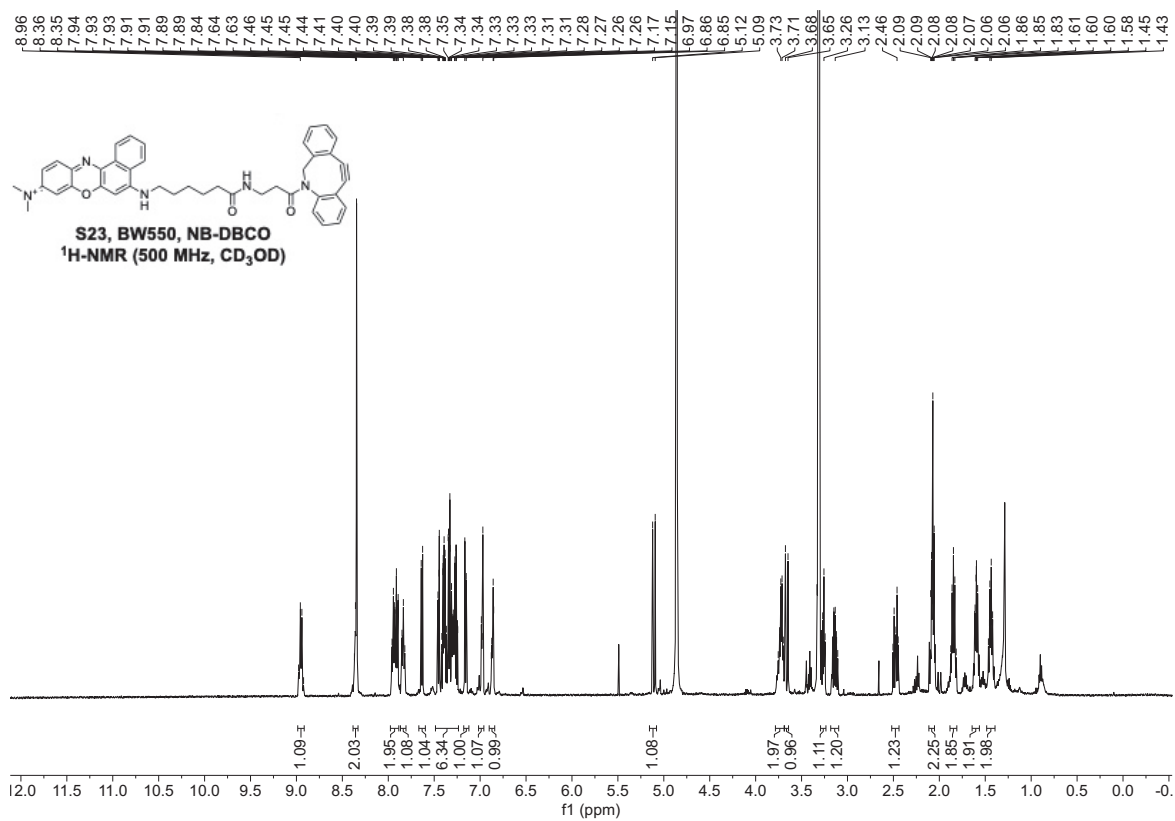
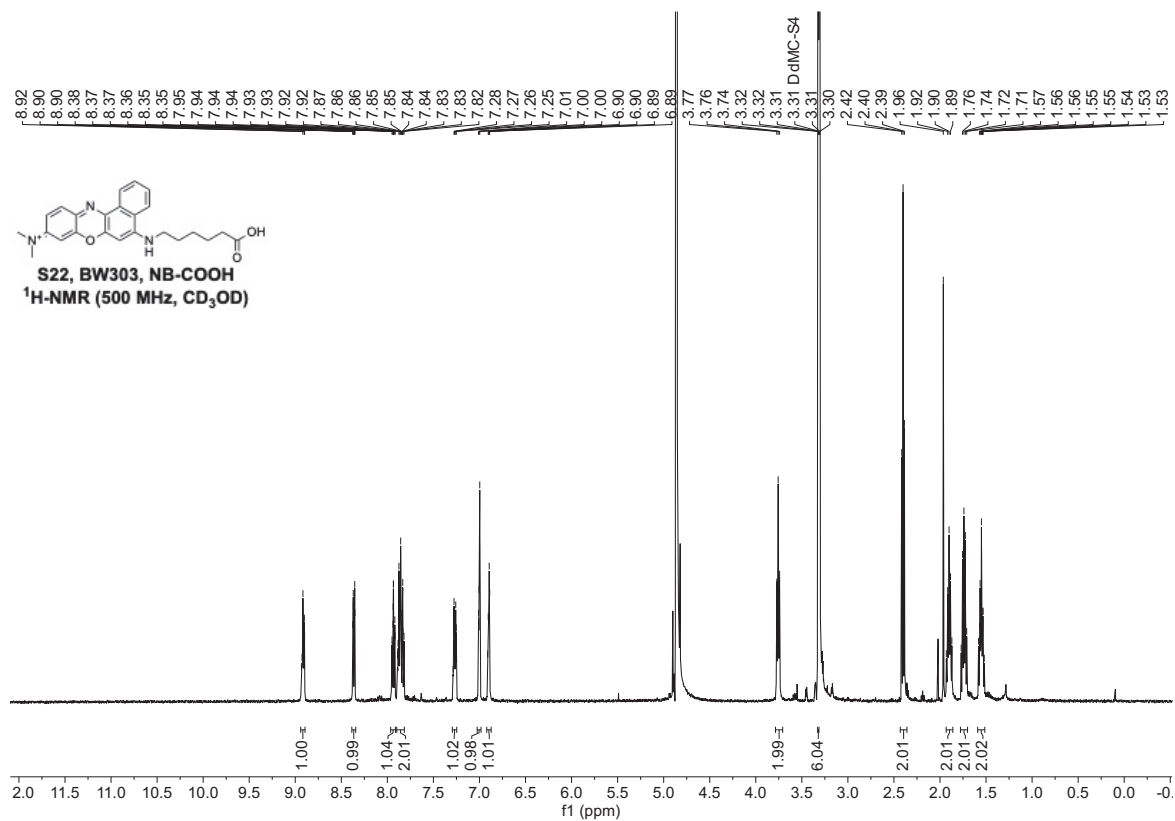


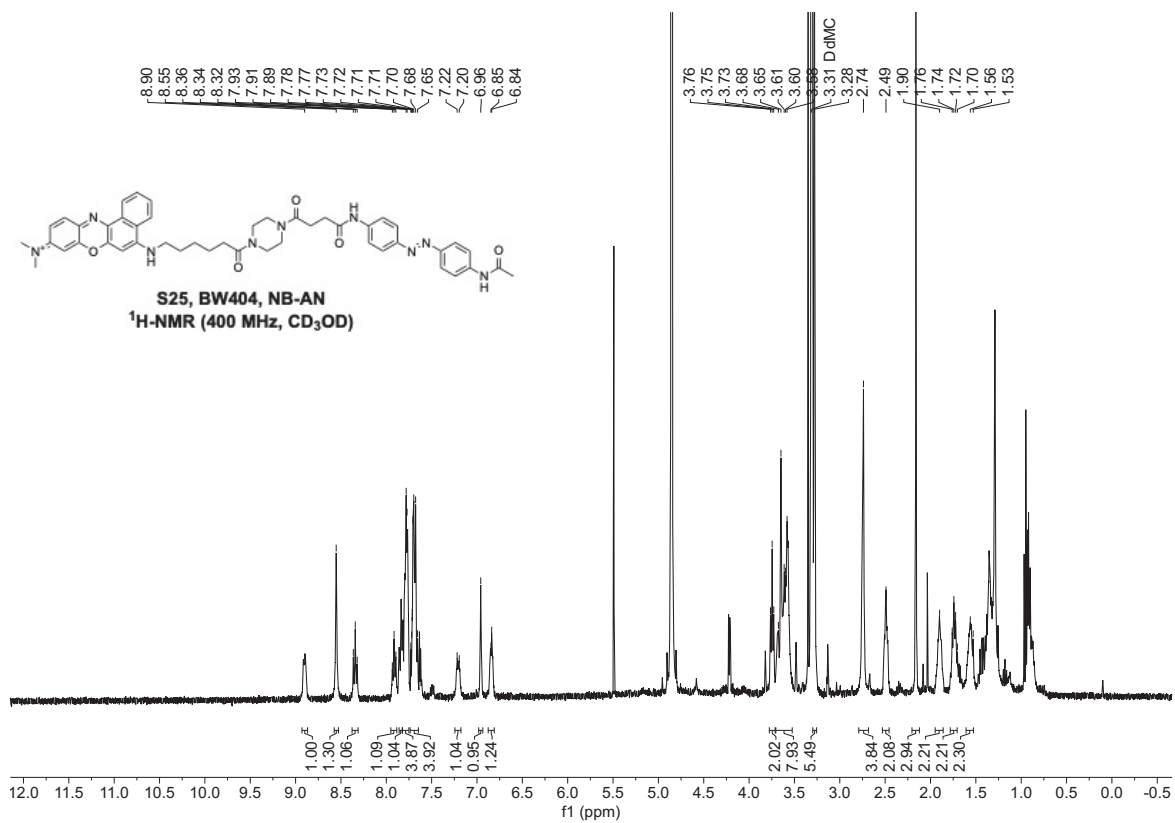
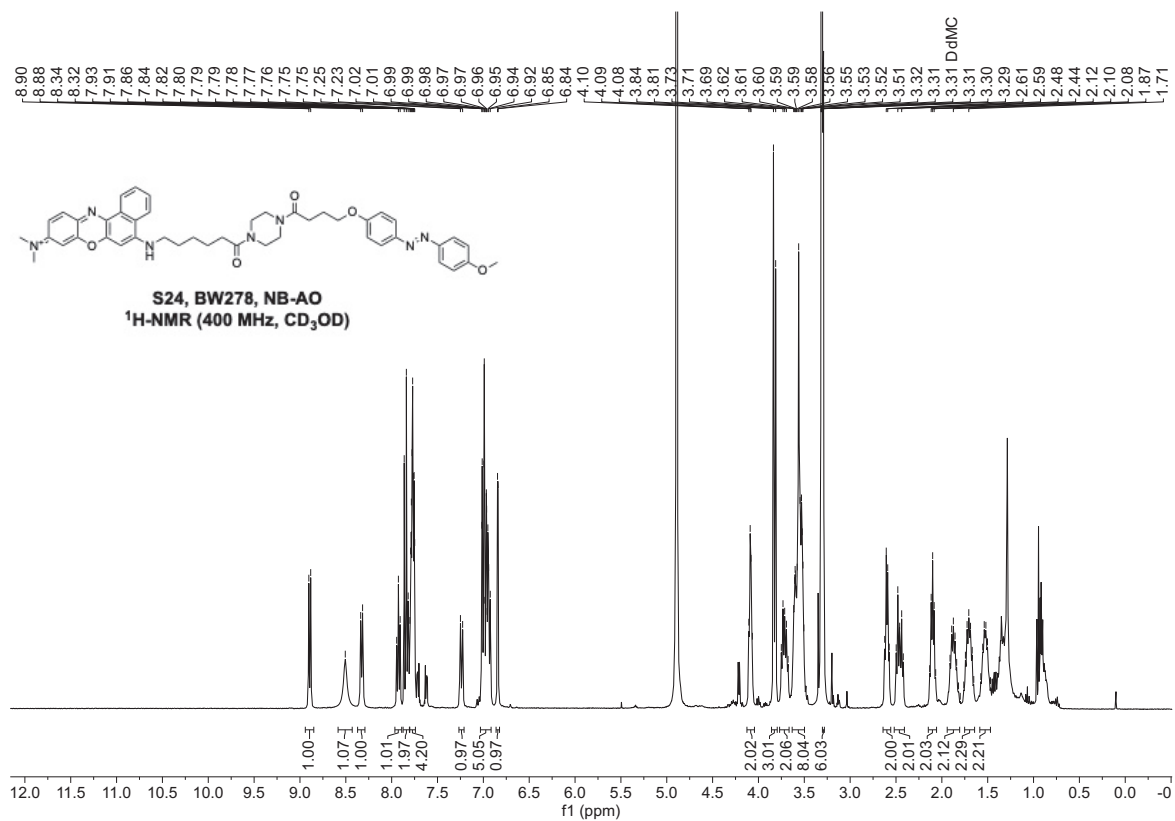


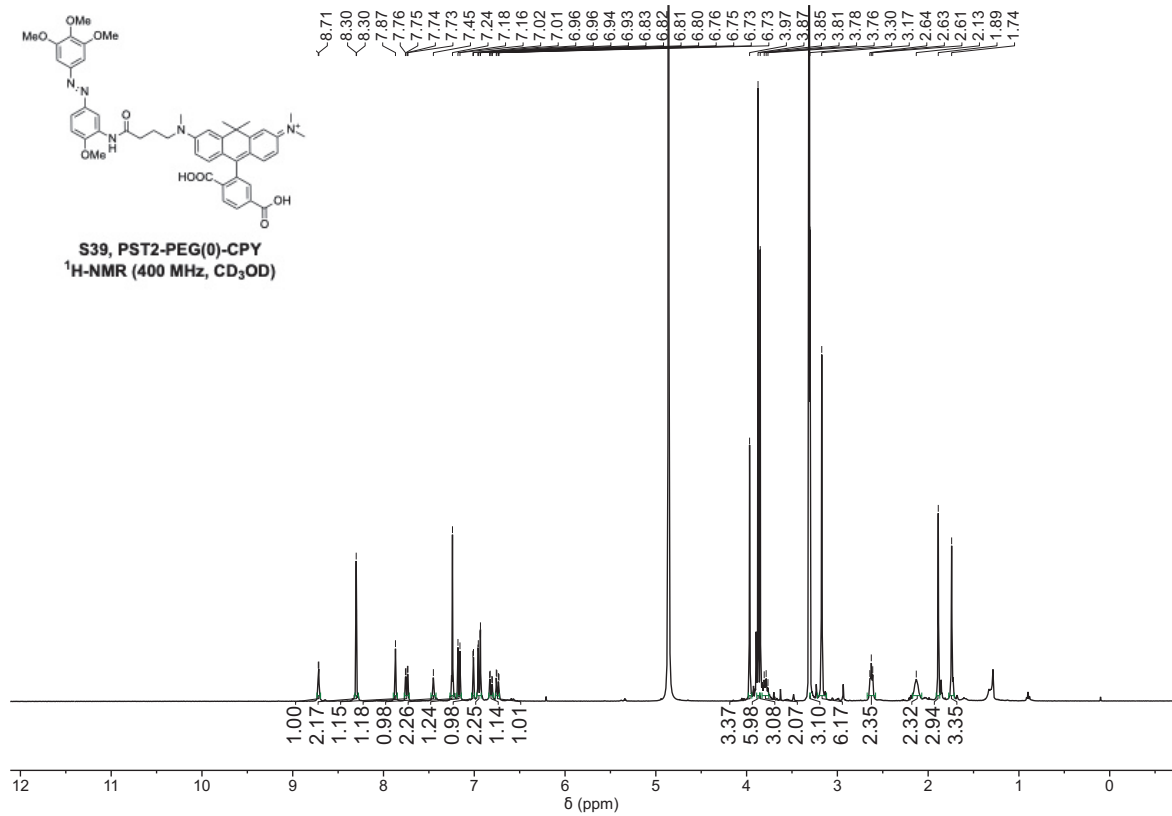
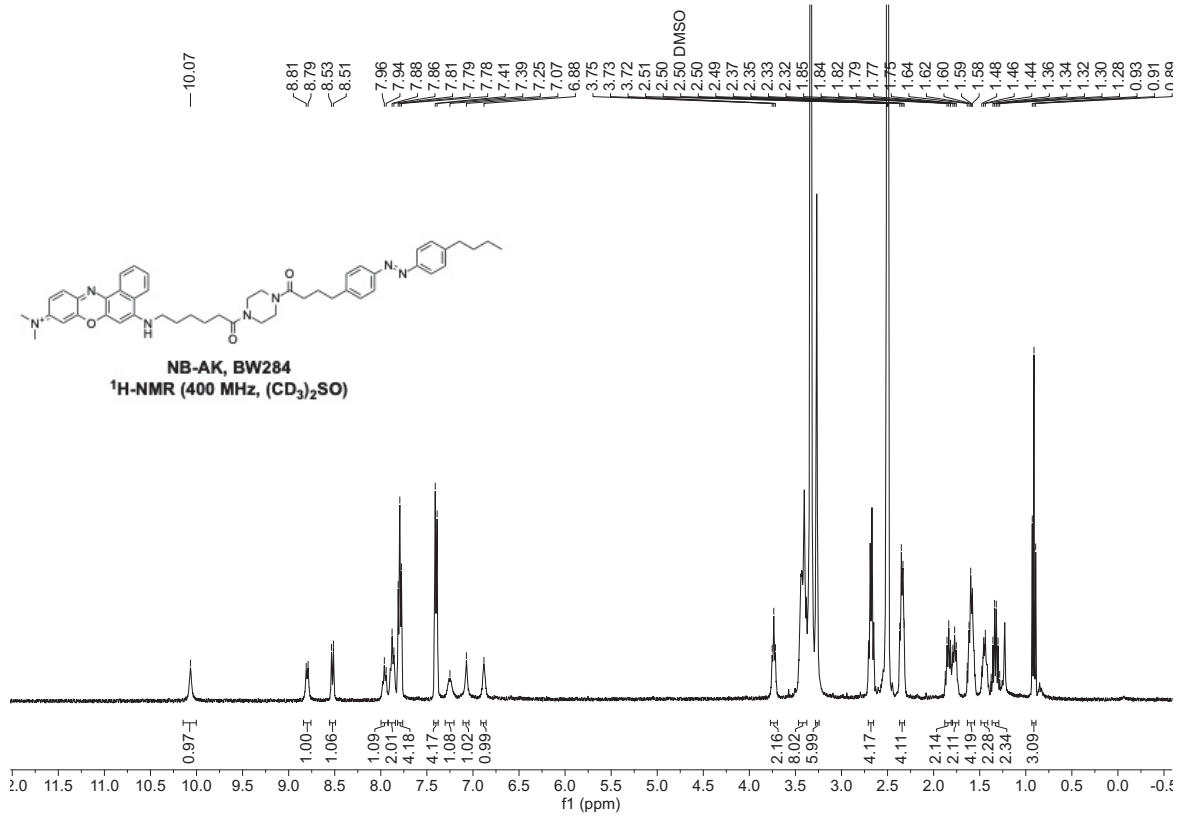




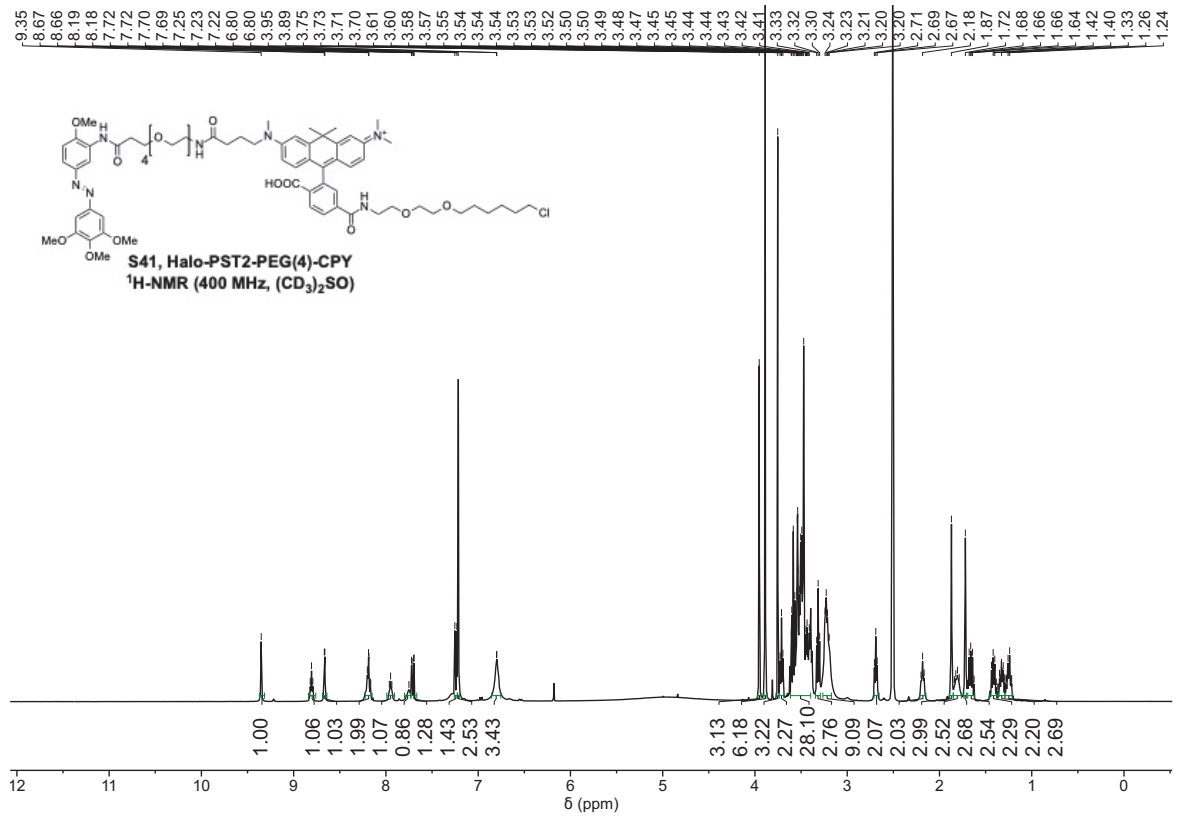
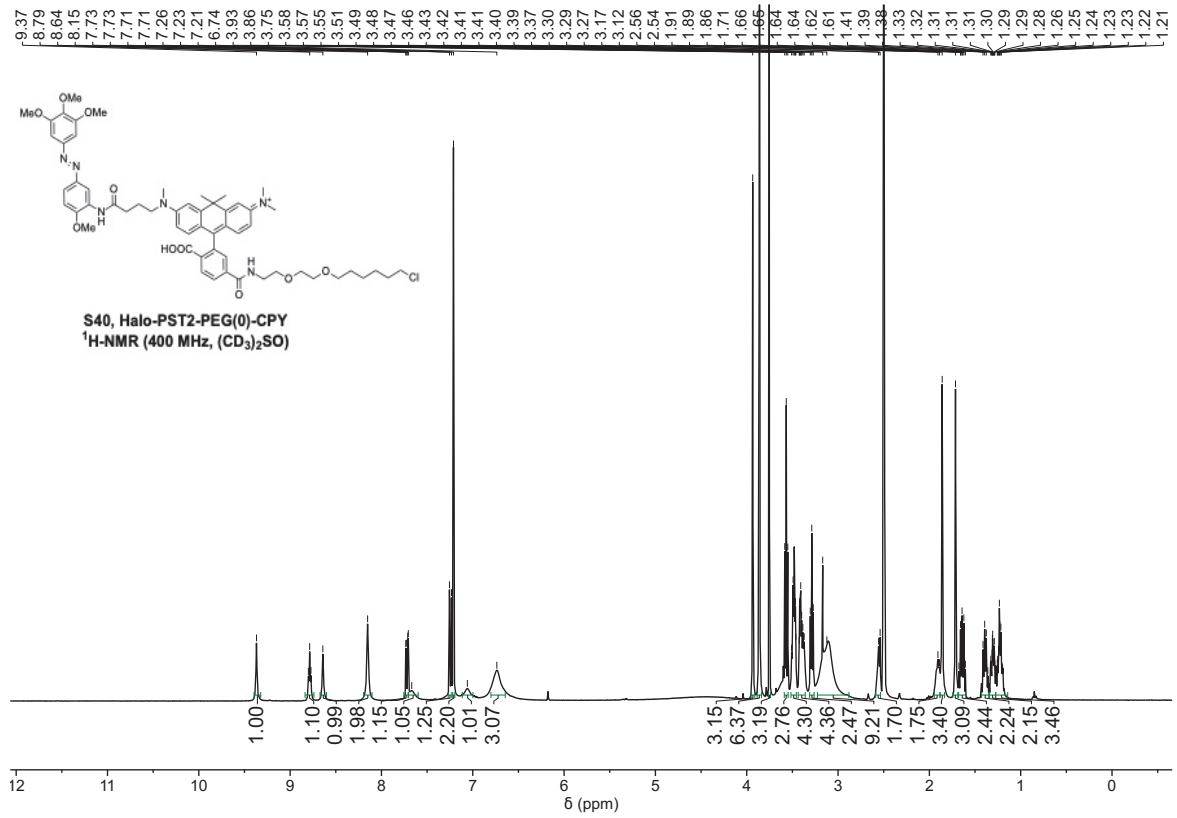


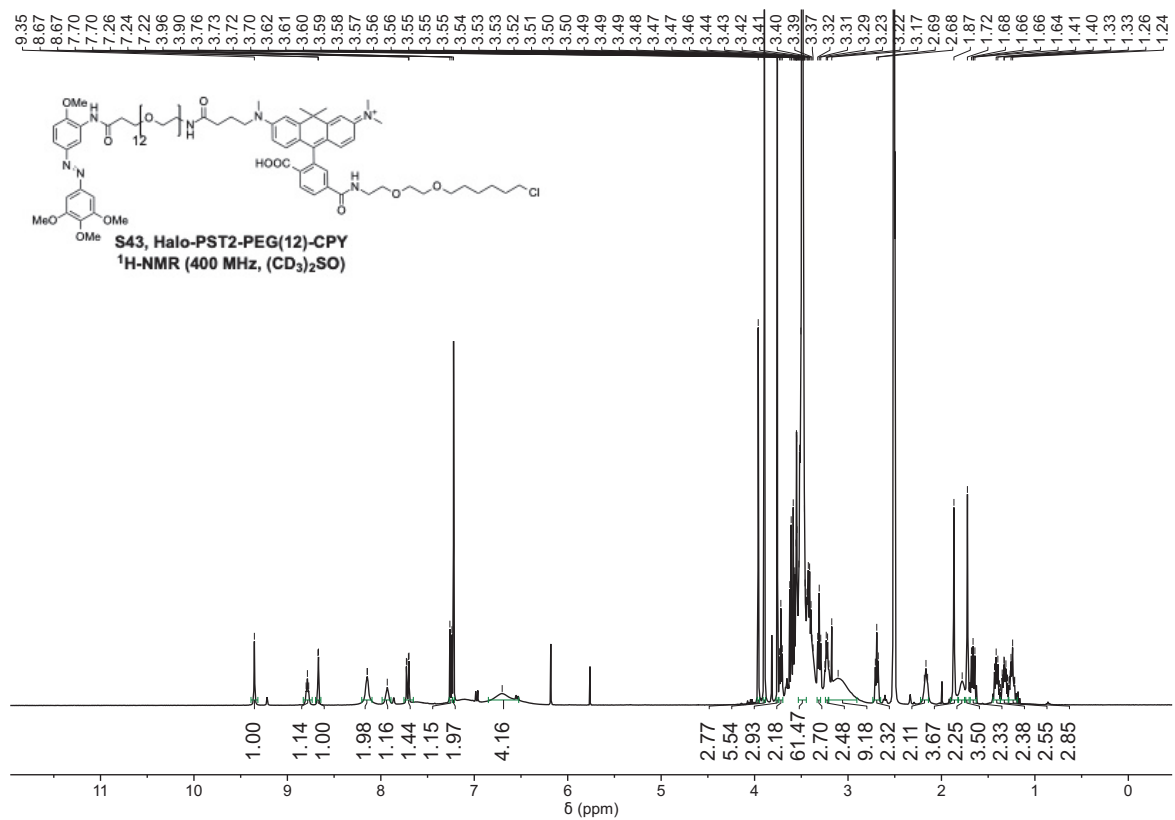
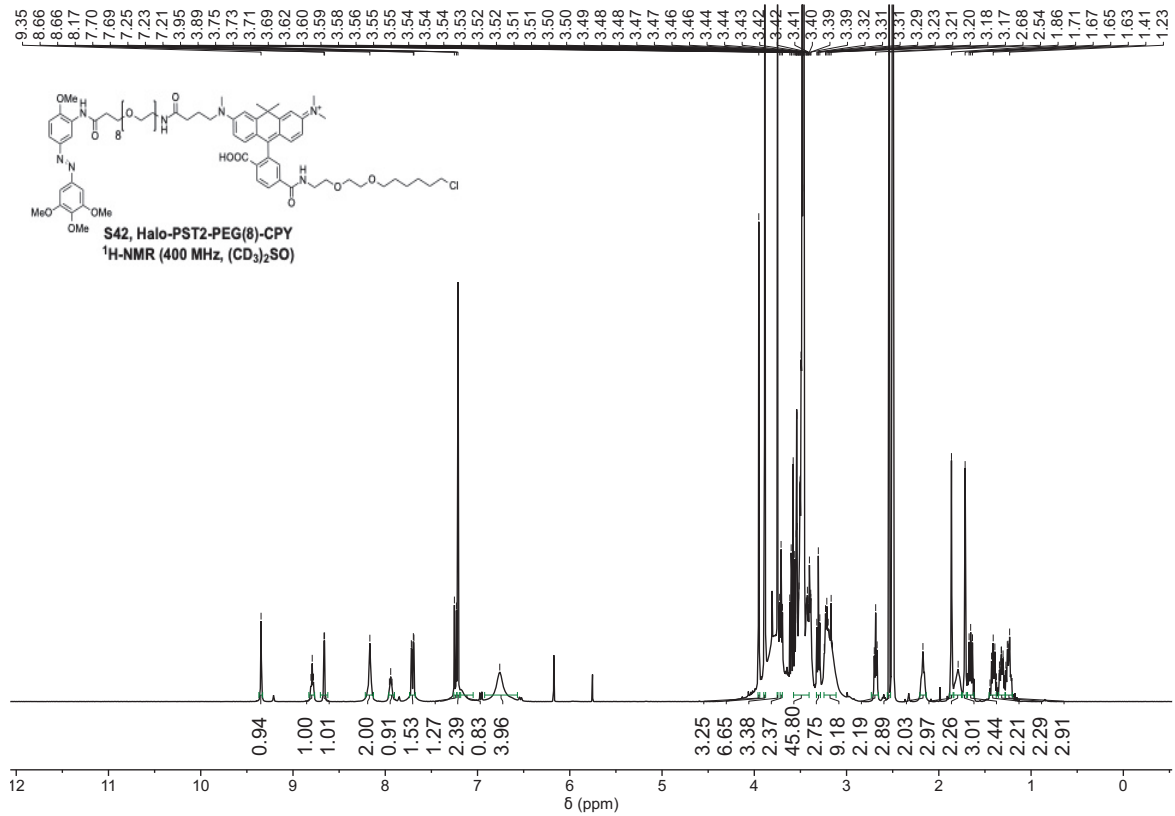


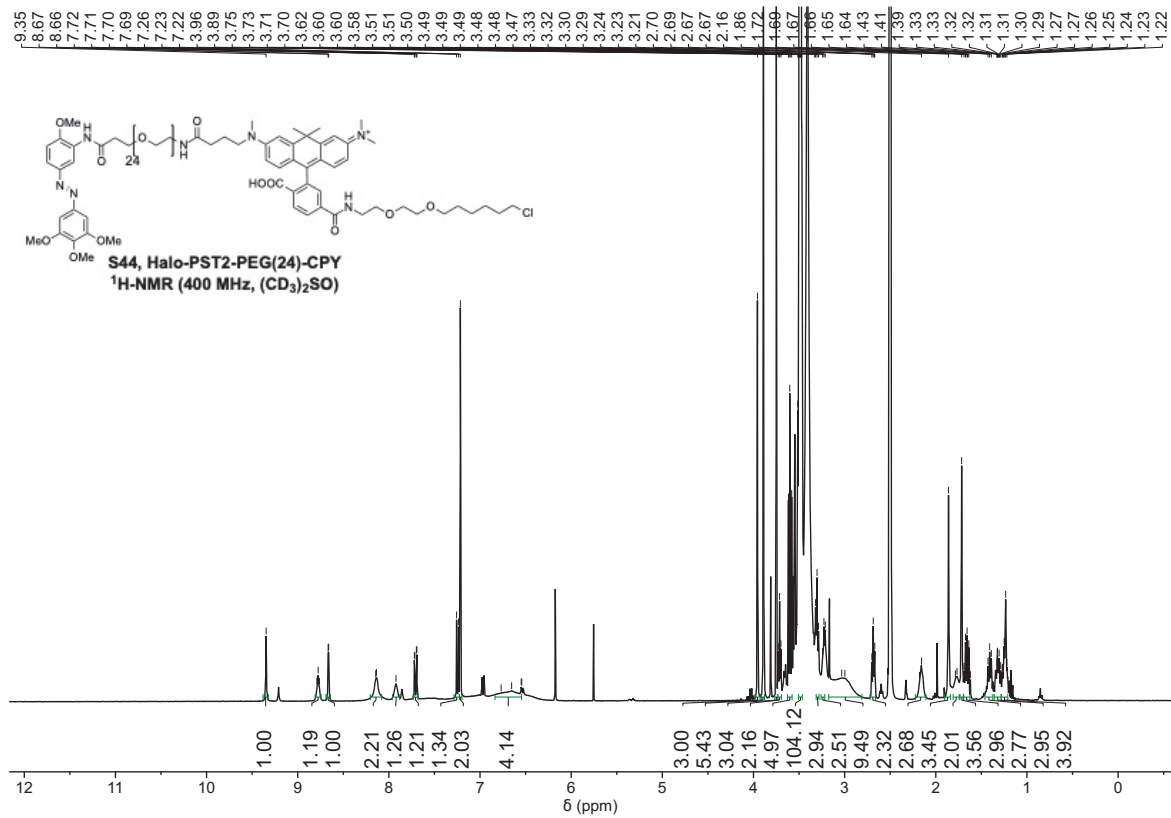












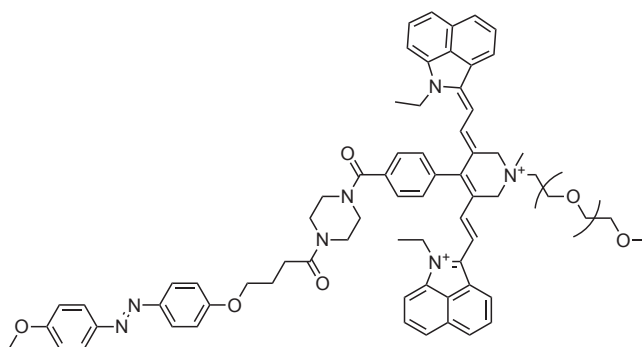
### 7.3 Supporting Information to chapter 4.1

General synthetic and analytical techniques see chapter 7.4.

**NorCy7** was synthesized by the Schnermann Lab, unpublished results.

**AO** was synthesized according to chapter 3.1.

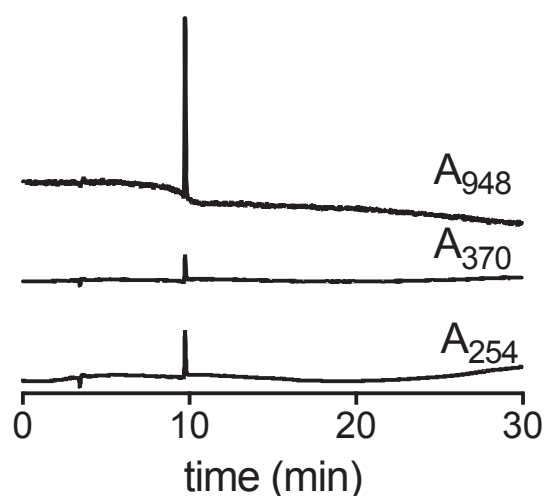
1-ethyl-2-((*E*)-2-((*Z*)-5-((*Z*)-2-(1-ethylbenzo[*cd*]indol-2(*H*)-ylidene)ethylidene)-4-(4-(4-(4-(4-((*E*)-(4-methoxyphenyl)diazenyl)phenoxy)butanoyl)piperazine-1-carbonyl)phenyl)-1-methyl-1-(2,5,8,11,14,17,20,23,26,29,32,35,38,41,44,47,50,53,56,59,62,65,68,71-tetracosaoxatriheptacontan-73-yl)-1,2,5,6-tetrahydropyridin-1-ium-3-yl)vinyl)benzo[*cd*]indol-1-ium (**NorCy7-AO**)



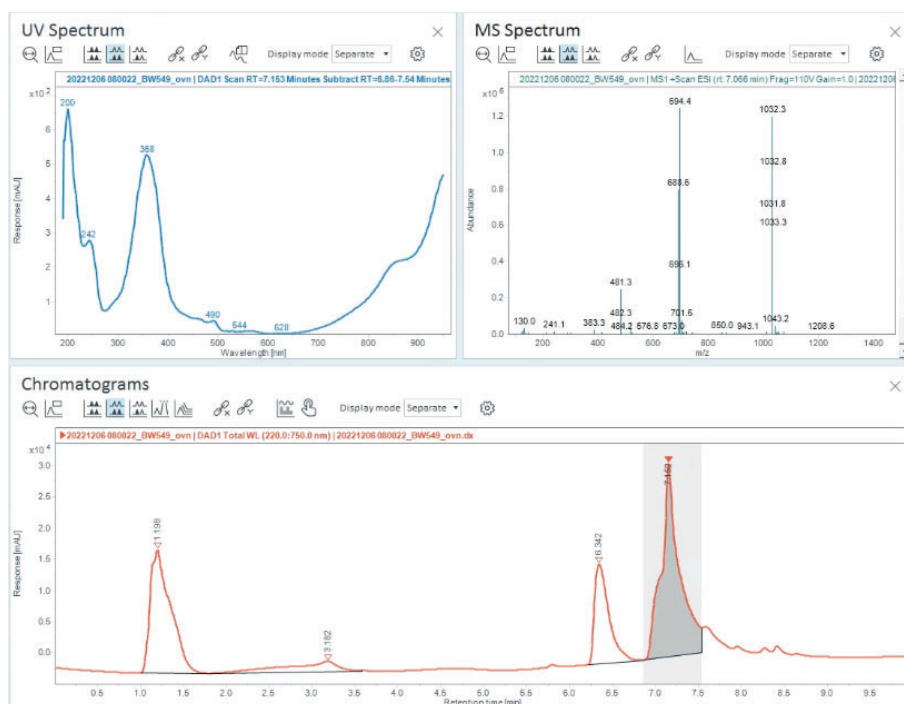
**NorCy7-COOH** (1 mg, 0.59  $\mu\text{mol}$ , 1 eq.), **AO** (0.4 mg, 1.2  $\mu\text{mol}$ , 2 eq.), HBTU (0.3 mg, 0.88  $\mu\text{mol}$ , 1.5 eq.) and DIPEA (0.5  $\mu\text{L}$ , 0.4 mg, 2.9  $\mu\text{mol}$ , 5 eq.) were dissolved in DMF (0.1 mL) and stirred at room temperature for 16 h. The reaction mixture was diluted with water (50  $\mu\text{L}$ ) and 0.1% formic acid in acetonitrile (100  $\mu\text{L}$ ) and purified via reversed phase preparative HPLC (9:1 water (0.1% formic acid) / MeCN (0.1% formic acid) to MeCN (0.1% formic acid) over 27 min) to yield **NorCy7-AO** (1 mg, 0.48  $\mu\text{mol}$ , 82%).

**HR-MS** (ESI)  $m/z$ : calculated for  $\text{C}_{113}\text{H}_{161}\text{N}_7\text{O}_{28}\text{Na}^{3+}$ : 696.04348; found: 696.04336 ( $\text{M} + \text{Na}$ ) $^{3+}$ .

#### HPLC-DAD



**LC-MS** (crude);  $m/z$ : = 1032  $\text{M}^{2+}$  at  $t_{\text{ret}}$  = 7.1 min



## UV/Vis spectroscopy

A custom-made cuvette adapter (**Figure 34**) for illumination was manufactured by Harald Ober (LMU CUP, Feinmechanik). The adapter has a sled where 1 inch optical filters from ThorLabs can be incorporated in the illumination pathway. For  $> 1000$  nm photoswitching we used a 1050 nm LED (M1050L4, ThorLabs) and a 1000 nm long pass filter (FELH1000, ThorLabs). The LED was focused via a polycarbonate lens.  $E \rightarrow Z$  photoswitching was performed by 365 nm illumination (50 mW/mm<sup>2</sup>, pE4000, CoolLED).

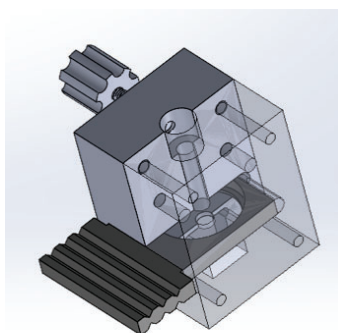


**Figure 34:** Custom-made cuvette illumination adapter with a sled that allows optical filter within the illumination pathway.



## 7.4 Supporting Information to chapter 4.2

**Chemicals** were obtained from Sigma-Aldrich, AttoTec, Abberior GmbH, TCI, Alfa Aesar, Acros, ABCR, or Carbolution, and were used as received without further purification unless stated otherwise.

**Solvents / eluents:** TLC control, extractions and column chromatography were conducted using distilled, technical grade solvents. "Hexane" indicates a mixture of isomeric hexanes (e.g. 2-methylpentane, 3-methylpentane, 2,2-dimethylbutane, 2,3-dimethylbutane).

**Reactions:** Unless stated otherwise, all reactions were performed without precautions in regard of potential air- and moisture-sensitivity and were stirred with Teflon-coated magnetic stir bars.

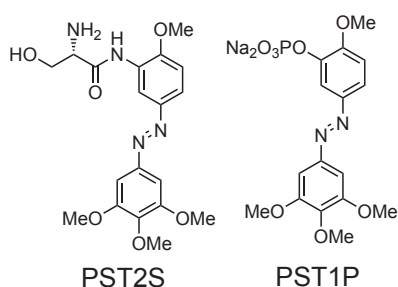
**Flash column chromatography** was conducted under positive nitrogen pressure using Ceduran® Si60 silica gel from Merck GmbH. Reactions were monitored by thin layer chromatography (TLC) on Si60 F254 aluminium-backed sheets (Merck GmbH) and visualised by UV irradiation and/or  $\text{KMnO}_4$  (3.0 g  $\text{KMnO}_4$ , 20 g  $\text{K}_2\text{CO}_3$ , 0.30 g KOH, 0.30 L  $\text{H}_2\text{O}$ ).

**Analytical high performance liquid chromatography (HPLC)** analysis was conducted using an Agilent 1100 system, through a Hypersil Gold HPLC column from ThermoFisher Scientific GmbH, with a DAD detector and a unit resolution Agilent LC/MSD IQ mass spectrometer (ESI mode). Mixtures of water (analytical grade, 0.1% formic acid) and MeCN (analytical grade, 0.1% formic acid) were used as eluent systems.

**Nuclear magnetic resonance (NMR) spectroscopy** was performed using Bruker Avance III HD Biospin spectrometers ( $^1\text{H}$ : 400 MHz /  $^{13}\text{C}$ : 101 MHz, with BBFO cryoprobe™; or  $^1\text{H}$ : 500 MHz /  $^{13}\text{C}$ : 126 MHz). NMR spectra were measured at 298 K, unless stated otherwise, and were analysed with MestreNova 12.  $^1\text{H}$ -NMR spectra chemical shifts ( $\delta$ ) in parts per million (ppm) relative to tetramethylsilane ( $\delta = 0$  ppm) are reported using the residual protic solvent ( $\text{CHCl}_3$  in  $\text{CDCl}_3$ :  $\delta = 7.26$  ppm;  $\text{CD}_3\text{SOCD}_2$  in  $(\text{CD}_3)_2\text{SO}$ :  $\delta = 2.50$  ppm;  $\text{CHD}_2\text{OD}$  in  $\text{CD}_3\text{OD}$ :  $\delta = 3.31$  ppm;  $\text{CHDCl}_2$  in  $\text{CD}_2\text{Cl}_2$ :  $\delta = 5.32$  ppm;  $\text{CHD}_2\text{CN}$  in  $\text{CD}_3\text{CN}$ :  $\delta = 1.94$  ppm;  $\text{CD}_3\text{COCD}_2$  in  $(\text{CD}_3)_2\text{CO}$ :  $\delta = 2.05$  ppm) as an internal reference. For  $^{13}\text{C}$ -NMR spectra, chemical shifts in ppm relative to tetramethylsilane ( $\delta = 0$  ppm) are reported using the central resonance of the solvent signal ( $\text{CDCl}_3$ :  $\delta = 77.2$  ppm,  $(\text{CD}_3)_2\text{SO}$ :  $\delta = 39.5$  ppm,  $\text{CD}_3\text{OD}$ :  $\delta = 49.0$  ppm,  $\text{CD}_2\text{Cl}_2$ :  $\delta = 54.0$  ppm,  $\text{CD}_3\text{CN}$ :  $\delta = 118.3$  ppm,  $(\text{CD}_3)_2\text{CO}$ :  $\delta = 29.8$  ppm) as an internal reference. For  $^1\text{H}$ -NMR spectra in addition to the chemical shift the following data is reported in parenthesis: multiplicity, coupling constant(s)  $J$  (in Hz), and number of hydrogen atoms. The abbreviations for multiplicities and related descriptors are s = singlet, d = doublet, t = triplet, q = quartet, or combinations thereof, m = multiplet and br = broad. Where known products matched literature analysis data, reference for literature is given.

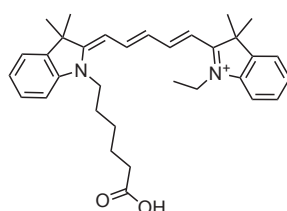
**High-resolution mass spectrometry (HRMS)** was conducted using a Thermo Finnigan LTQ FT Ultra FourierTransform ion cyclotron resonance spectrometer, applying electron spray ionisation (ESI) with a spray capillary voltage of 4 kV at temperature 250 °C with a method dependent range from 50 to 2000 u. All reported  $m/z$  values refer to positive ionization mode, unless stated otherwise.

## Synthesis



Known compounds **PST2S** and **PST1P** were synthesized according to Borowiak, Thorn-Seshold, *Cell*, **2015**.<sup>14</sup>

6-((*E*)-2-((2*E*,4*E*)-5-(1-ethyl-3,3-dimethyl-3*H*-indol-1-ium-2-yl)penta-2,4-dien-1-ylidene)-3,3-dimethylindolin-1-yl)hexanoate (**Cy5-COOH**)

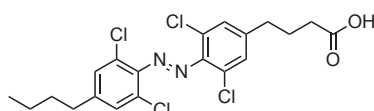


Known compound **Cy5-COOH** was synthesized according to Campo, *JOC*, **2014**.<sup>178</sup>

**Azo 1** was purchased from Glen Research.

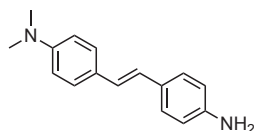
**Cy3B-NHS**, **Atto542-NHS**, **AlexaFluor647-NHS** and **AbberiorStar635P-NHS** were purchased from Sigma-Aldrich, AttoTec or Abberior GmbH.

4-(4-((4-butyl-2,6-dichlorophenyl)diazenyl)-3,5-dichlorophenyl)butanoic acid (**azo 2**)



Known compound **Azo 2** was synthesized according to Konrad, Trauner, *Chem. Eur. J.*, **2016**.<sup>43</sup>

4-(4-aminostyryl)-*N,N*-dimethylaniline (**S4.2-1**)

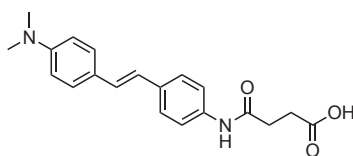


Was synthesized in 2 steps according to literature.

Step 1: Zhang, S., *Chinese Journal of Chemistry*, **2010**.<sup>179</sup>

Step 2: Masahiro S., *Bulletin of the Chemical Society of Japan*, **2016**.<sup>180</sup>

4-((4-(4-(dimethylamino)styryl)phenyl)amino)-4-oxobutanoic acid (**stilbene 1**)

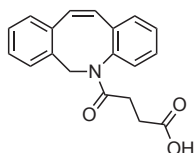


A pressure tube was charged with a solution of **S4.2-1** (100 mg, 0.42 mmol, 1.0 equiv.) and succinic anhydride (252 mg, 2.52 mmol, 6 equiv.) in acetone (2 mL). Pyridine (0.27 mL, 3.36 mmol, 8 eq.) was added to the solution, the pressure tube was sealed and the reaction mixture was stirred for 24 h at 70 °C. The precipitate was filtered, washed with ice cold acetone (5 mL) and diethyl ether (2 x 5 mL) to yield **stilbene 1** (56.9 mg, 0.17 mmol, 40%) as an off-white solid.

**<sup>1</sup>H-NMR** (400 MHz; (CD<sub>3</sub>)<sub>2</sub>SO):  $\delta$  = 9.98 (s, 1H), 7.60 – 7.41 (m, 4H), 7.39 (d, J = 8.9 Hz, 2H), 7.05 – 6.86 (m, 2H), 6.71 (d, J = 8.9 Hz, 2H), 2.92 (s, 6H), 2.57 – 2.52 (m, 4H).

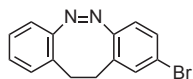
**HR-MS** (ESI) m/z: calculated for C<sub>20</sub>H<sub>23</sub>O<sub>3</sub>N<sub>2</sub><sup>+</sup>: 339.1703; found: 339.1705 (M + H)<sup>+</sup>.

(Z)-4-(dibenzo[*b,f*]azocin-5(6*H*)-yl)-4-oxobutanoic acid (**stilbene 2**)



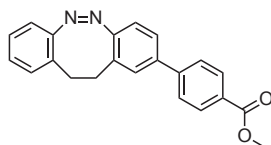
A pressure tube was charged with a solution of (Z)-5,6-dihydrodibenzo[*b,f*]azocine (100 mg, 0.48 mmol, 1 eq.) and succinic anhydride (215 mg, 2.15 mmol, 4.5 eq.) in acetone (5 mL, 0.10 M). Pyridine (0.23 mL, 2.87 mmol, 6 eq.) was added to the solution, the pressure tube was sealed and the reaction mixture was stirred for 24 h at 70 °C. After reaching r.t., the mixture was diluted with water (200 mL), acidified with an aqueous hydrogen chloride solution (2.0 M, 20 mL) and extracted with DCM (200 mL). The combined organic phases were dried over Na<sub>2</sub>SO<sub>4</sub> and the solvent was removed under reduced pressure to yield **stilbene 2** as a pale orange oil. Analytical data (H-NMR) match literature.<sup>181</sup>

2-bromo-11,12-dihydrodibenzo[*c,g*][1,2]diazocine (**S4.2-2**)



Known compound **S4.2-2** was synthesized according to Maier, Trauner, *JACS*, **2019**.<sup>48</sup>

methyl (Z)-4-(11,12-dihydrodibenzo[*c,g*][1,2]diazocin-2-yl)benzoate (**S4.2-3**)

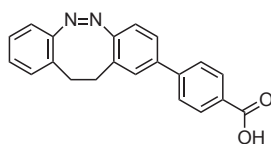


S4.2-2 (51.6 mg, 0.18 mmol, 1 eq.), 4-methoxycarbonylphenylboronic acid (86 mg, 0.48 mmol, 2.7 eq.), tetrakis(triphenylphosphine)palladium(0) (12.6 mg, 0.01 mmol, 0.06 eq.) and potassium phosphate (120 mg, 0.55 mmol, 3 eq.) were dissolved in dioxane (5 mL) under nitrogen atmosphere. Water (5 drops) was added and the mixture was heated to reflux for 16 h. The reaction mixture was diluted with water (20 mL) and extracted with DCM (3 x 20 mL). The combined organic phases were dried (MgSO<sub>4</sub>), concentrated under reduced pressure and purified *via* silica gel column chromatography (5-10% EtOAc in hexanes) to yield **S4.2-3** (57 mg, 0.17 mmol, 92%) as a yellow solid.

**<sup>1</sup>H-NMR** (500 MHz; CDCl<sub>3</sub>):  $\delta$  = 8.05 (d,  $J$  = 8.3 Hz, 2H), 7.55 (d,  $J$  = 8.2 Hz, 2H), 7.40 (dd,  $J$  = 8.1, 1.9 Hz, 1H), 7.24 (d,  $J$  = 1.9 Hz, 1H), 7.16 (ddd,  $J$  = 7.6, 7.0, 1.7 Hz, 1H), 7.07 – 6.99 (m, 2H), 6.94 (d,  $J$  = 8.2 Hz, 1H), 6.88 (dd,  $J$  = 7.7, 1.2 Hz, 1H), 3.92 (s, 3H), 3.05 – 2.83 (m, 4H).

**<sup>13</sup>C-NMR** (126 MHz; CDCl<sub>3</sub>):  $\delta$  = 167.04, 155.65, 155.39, 144.57, 144.09, 138.77, 130.21, 129.84, 129.18, 128.94, 128.65, 127.98, 127.39, 126.98, 125.75, 119.85, 118.98, 52.30, 32.22, 31.70.

4-(11,12-dihydrodibenzo[*c,g*][1,2]diazocin-2-yl)benzoic acid (**azo 4**)



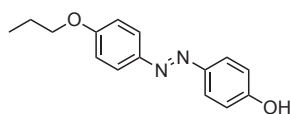
**S4.2-3** (48 mg, 0.14 mmol, 1 eq.) and potassium hydroxide (104 mg, 1.8 mmol, 13 eq.) were dissolved in methanol (10 mL) and stirred at 60°C for 16 h. The reaction mixture was concentrated under reduced pressure. The residue was redissolved in aqueous hydrochloric acid (2M, 15 mL) and extracted with EtOAc (3 x 15 mL). The combined organic phases were dried (MgSO<sub>4</sub>) and concentrated under reduced pressure to yield **azo 4** (35 mg, 0.11 mmol, 71%) as a yellow solid.

**<sup>1</sup>H-NMR** (500 MHz; (CD<sub>3</sub>)<sub>2</sub>SO):  $\delta$  = 7.96 (d,  $J$  = 8.4 Hz, 2H), 7.73 (d,  $J$  = 8.4 Hz, 2H), 7.56 (dd,  $J$  = 8.2, 2.0 Hz, 1H), 7.51 (d,  $J$  = 2.0 Hz, 1H), 7.24 – 7.16 (m, 1H), 7.15 – 7.05 (m, 2H), 7.02 – 6.95 (m, 1H), 6.89 (dd,  $J$  = 7.9, 1.3 Hz, 1H), 2.97 – 2.83 (m, 4H).

**<sup>13</sup>C-NMR** (126 MHz; (CD<sub>3</sub>)<sub>2</sub>SO):  $\delta$  = 167.05, 155.17, 155.00, 142.99, 137.47, 129.89, 129.70, 128.89, 128.30, 127.81, 127.28, 126.87, 126.60, 125.72, 125.31, 119.40, 118.46, 31.06, 30.81.

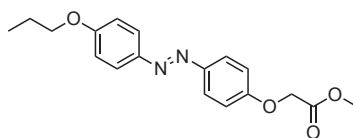
**HR-MS** (ESI)  $m/z$ : calculated for C<sub>21</sub>H<sub>15</sub>N<sub>2</sub>O<sub>2</sub><sup>-</sup>: 327.11390; found: 327.11366, (M - H)<sup>-</sup>.

4-((4-propoxyphenyl)diazenyl)phenol (**S4.2-4**)



Known compound **S4.2-4** was synthesized according to Jiang, *Polymer*, **2015**.<sup>182</sup>

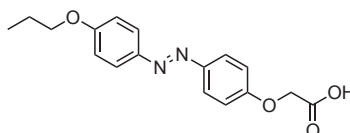
methyl -2-(4-((4-propoxyphenyl)diazenyl)phenoxy)acetate (**S4.2-5**)



**S4.2-4** (300 mg, 1.2 mmol, 1 eq.), methyl bromoacetate (0.24 mL, 386 mg, 2.53 mmol, 2.1 eq) and potassium carbonate (809 mg, 5.9 mmol, 5 eq.) were dissolved in acetone (10 mL) and stirred at 50 °C for 16 h. The reaction mixture was diluted with water (30 mL) and extracted with EtOAc (3 x 30 mL). The combined organic phases were dried (MgSO<sub>4</sub>) and concentrated under reduced pressure and purified via silica gel column chromatography (40% EtOAc in hexane) to yield **S4.2-5** (354 mg, 1.1 mmol, 91%) as a yellow solid.

<sup>1</sup>H-NMR (400 MHz; (CD<sub>3</sub>)<sub>2</sub>SO):  $\delta$  = 7.83 (dd,  $J$  = 9.0, 2.4 Hz, 4H), 7.11 (dd,  $J$  = 9.0, 3.8 Hz, 4H), 4.92 (s, 2H), 4.03 (t,  $J$  = 6.5 Hz, 2H), 3.72 (s, 3H), 1.77 (q,  $J$  = 7.0 Hz, 2H), 1.00 (t,  $J$  = 7.4 Hz, 3H).

2-(4-((4-propoxyphenyl)diazenyl)phenoxy)acetic acid (**azo 3**)



**S4.2-5** (300 mg, 0.92 mmol, 1 eq.) and potassium hydroxide (304 mg, 4.6 mmol, 5 eq.) were dissolved in methanol (10 mL) and stirred at 60°C for 16 h. The reaction mixture was concentrated under reduced pressure. The residue was redissolved in aqueous hydrochloric acid (2M, 30 mL) and extracted with EtOAc (3 x 30 mL). The combined organic phases were dried (MgSO<sub>4</sub>) and concentrated under reduced pressure to yield **azo 3** (284 mg, 0.9 mmol, 98%) as a yellow solid.

<sup>1</sup>H-NMR (400 MHz; (CD<sub>3</sub>)<sub>2</sub>SO):  $\delta$  = 7.83 (dd,  $J$  = 9.0, 2.1 Hz, 4H), 7.10 (dd,  $J$  = 9.0, 5.3 Hz, 4H), 4.80 (s, 2H), 4.03 (t,  $J$  = 6.5 Hz, 2H), 1.77 (q,  $J$  = 7.0 Hz, 2H), 1.00 (t,  $J$  = 7.4 Hz, 3H).

### Synthesis of fluorophore-azobenzene-DBCO conjugates

#### **General protocol A (GP-A): Amide couplings with fluorophore NHS ester**

A fluorophore NHS ester (1 eq.) was dissolved in DMF (5 mg/ml) and charged with a solution of a DBCO-azobenzene-piperazine (1.1 eq., in DMF 0.03 M) and DIPEA (3 eq.). The reaction mixture was vortexed and incubated at room temperature until full conversion of the starting material was confirmed by LC/MS. All volatile solvents were removed under a gentle stream of nitrogen and the crude material was used for coupling to DNA oligos without further purification.

#### **General protocol B (GP-B): Amide couplings with fluorophore carboxylic acid**

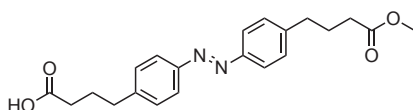
A fluorophore carboxylic acid (1 eq.) was dissolved in DMF (5 mg/ml) and charged with TSTU (1.1 eq.) and DIPEA (5 eq., 10% in DMF). The reaction mixture was vortexed and incubated at room temperature for 1 h. A DBCO-azobenzene-piperazine (0.8 eq., in DMF 0.03 M) was



added and the reaction mixture was vortexed and incubated at room temperature until full conversion of the starting material was confirmed by LC/MS. All volatile solvents were removed under a gentle stream of nitrogen and the crude material was used for coupling to DNA oligos without further purification.

### DBCO-AK-Piperazine Conjugate Synthesis

4-(4-((4-(4-methoxy-4-oxobutyl)phenyl)diazenyl) phenyl)butanoic acid (**S4.2-6**)



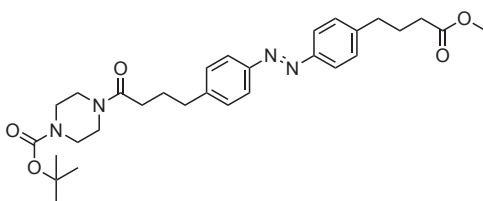
A solution of Oxone® (5.73 g, 18.6 mmol, 9 eq.) in water (30 mL) was added to a solution of known compound methyl 4-(4-aminophenyl)butanoate<sup>183</sup> (0.50 g, 2.6 mmol, 1.25 eq.) in DCM (30 mL, 0.09 M), and the biphasic reaction mixture was vigorously stirred at room temperature for 20 h. The phases were separated, the aqueous phase was extracted with DCM (3 x 60 mL) and the combined organic phases were washed with water (60 mL). 4-(4-aminophenyl)butanoic acid (0.37 g, 2.1 mmol, 1 eq.) and AcOH (100%, 30 mL) were added and stirred at room temperature for 15 min. The reaction mixture was then concentrated under reduced pressure, co-evaporated with toluene (2 x 20 mL) and purified by silica gel flash column chromatography (DCM/AcOH: 100/0 to 99/1) to yield **S4.2-6** (0.64 g, 1.75 mmol, 84%) as an orange solid.

**HRMS** (ESI):  $m/z$  C<sub>21</sub>H<sub>23</sub>N<sub>2</sub>O<sub>4</sub><sup>-</sup> [M-H]<sup>-</sup>: calc.: 367.16633, found: 367.16662.

**<sup>1</sup>H-NMR** (400 MHz, methylene chloride-*d*<sub>2</sub>)  $\delta$  (ppm): 7.84 (dd,  $J$  = 8.4, 1.2, 4H), 7.40–7.31 (m, 4H), 3.65 (s, 3H), 2.75 (dt,  $J$  = 10.4, 7.6, 4H), 2.38 (dt,  $J$  = 23.3, 7.4, 4H), 2.06–1.92 (m, 4H).

**<sup>13</sup>C-NMR** (101 MHz, methylene chloride-*d*<sub>2</sub>)  $\delta$  (ppm): 179.1, 174.0, 151.6, 151.6, 145.5, 145.3, 129.6, 123.2, 123.2, 51.8, 35.3, 35.2, 33.7, 33.5, 26.8, 26.5.

*tert*-butyl 4-(4-(4-((4-(4-methoxy-4-oxobutyl)phenyl)diazenyl) phenyl)butanoyl)piperazine-1-carboxylate (**S4.2-7**)



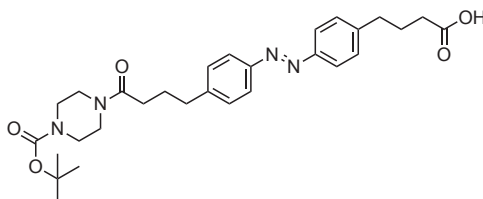
*N*-Boc-piperazine (303 mg, 1.63 mmol, 2.0 eq.), HBTU (371 mg, 0.97 mmol, 1.2 eq.) and TEA (0.79 mL, 5.7 mmol, 7 eq.) were added to a solution of **S4.2-6** (300 mg, 0.81 mmol, 1 eq.) in DMF (25 mL, 0.03 M). The reaction mixture was stirred at room temperature for 16 h, concentrated under reduced pressure, and purified by silica gel flash column chromatography (hexanes/EtOAc: 90/10 to 70/30) to yield **2** as an orange oil (173 mg, 0.39 mmol, 49%).

**HRMS** (ESI):  $m/z$  C<sub>25</sub>H<sub>33</sub>N<sub>4</sub>O<sub>3</sub><sup>+</sup> [M-Boc+2H]<sup>+</sup>: calc.: 437.25472, found: 437.25462.

**<sup>1</sup>H-NMR** (500 MHz, chloroform-*d*<sub>1</sub>)  $\delta$  (ppm): 7.85–7.81 (m, 4H), 7.32 (dd, *J* = 8.3, 3.3, 4H), 3.68 (s, 3H), 3.62–3.34 (m, 8H), 2.75 (dt, *J* = 17.0, 7.5, 4H), 2.39–2.28 (m, 4H), 2.08–1.96 (m, 4H), 1.46 (s, 9H).

**<sup>13</sup>C-NMR** (126 MHz, chloroform-*d*<sub>1</sub>)  $\delta$  (ppm): 174.0, 171.5, 154.7, 151.4, 151.4, 145.0, 144.9, 129.3, 129.3, 123.0, 80.5, 51.7, 45.5, 41.6, 35.3, 35.1, 33.5, 32.3, 28.5, 26.5, 26.4.

4-(4-((4-(4-(*tert*-butoxycarbonyl)piperazin-1-yl)-4-oxobutyl)phenyl)diazenyl)phenyl)butanoic acid (**S4.2-8**)



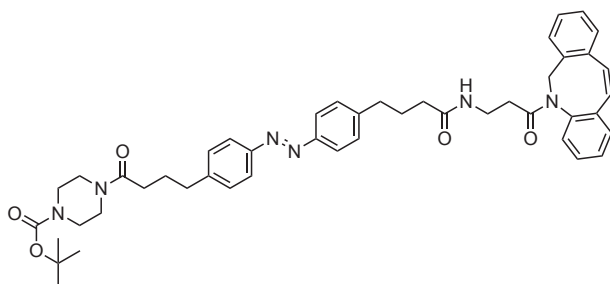
An aqueous solution of lithium hydroxide (15.0 mL, 2 M) was added to a solution of **S4.2-7** (150 mg, 0.28 mmol, 1 eq.) in MeOH (15 mL, 0.02 M). The reaction mixture was stirred at 50 °C for 2 h, adjusted to pH 6 using AcOH and extracted with EtOAc (3 x 150 mL). The combined organic phases were dried (Na<sub>2</sub>SO<sub>4</sub>), concentrated under reduced pressure and purified by silica gel flash column chromatography (EtOAc) to yield **S4.2-8** (40 mg, 0.08 mmol, 27%) as an orange oil.

**HRMS** (ESI): *m/z* C<sub>29</sub>H<sub>37</sub>N<sub>4</sub>O<sub>5</sub><sup>-</sup> [M-H]<sup>-</sup>: calc.: 521.27694, found: 521.27692.

**<sup>1</sup>H-NMR** (400 MHz, acetone-*d*<sub>6</sub>)  $\delta$  (ppm): 7.90–7.81 (m, 4H), 7.48–7.40 (m, 4H), 3.55–3.47 (m, 4H), 3.45–3.34 (m, 4H), 2.81–2.74 (m, 4H), 2.45 (t, *J* = 7.3, 2H), 2.37 (t, *J* = 7.3, 2H), 2.02–1.91 (m, 4H), 1.44 (s, 9H).

**<sup>13</sup>C-NMR** (101 MHz, acetone-*d*<sub>6</sub>)  $\delta$  (ppm): 174.4, 171.5, 155.0, 152.0, 151.9, 146.8, 146.5, 130.2, 123.6, 123.6, 80.0, 45.9, 41.9, 35.8, 35.5, 33.5, 32.7, 28.5, 27.5, 27.3.

*tert*-butyl 4-(4-(4-((4-(4-(3-(11,12-didehydrodibenzo[*b,f*]azocin-5(6*H*)-yl)-3-oxopropyl)amino)-4-oxobutyl)phenyl)diazenyl)phenyl)butanoyl)piperazine-1-carboxylate (**S4.2-9**)



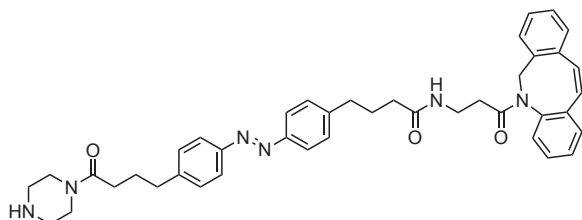
Commercial DBCO-amine (15.0 mg, 0.05 mmol, 1 eq.), HBTU (30.9 mg, 0.08 mmol, 1.5 eq.) and TEA (45.5  $\mu$ L, 0.30 mmol, 6 eq.) were added to a solution of **S4.2-8** (34.0 mg, 0.07 mmol, 1.2 eq.) in DMF (2.5 mL, 0.03 M). The reaction mixture was stirred at room temperature for 16 h, concentrated under reduced pressure, and purified by silica gel flash column chromatography (DCM/MeOH: 100/0 to 97/3) to yield **S4.2-9** (40 mg, 0.05 mmol, 95%) as a yellow oil.

**HRMS** (ESI):  $m/z$   $C_{47}H_{52}N_6NaO_5^+$   $[M+Na]^+$ : calc.: 803.38969, found: 803.38985.

**$^1H$ -NMR** (400 MHz, methylene chloride- $d_2$ )  $\delta$  (ppm): 7.87 – 7.77 (m, 4H), 7.69 – 7.57 (m, 2H), 7.46 – 7.21 (m, 9H), 7.19 (dd,  $J = 7.3, 1.6$  Hz, 1H), 6.18 (t,  $J = 5.8$  Hz, 1H), 5.10 (d,  $J = 14.0$  Hz, 1H), 3.67 (d,  $J = 13.9$  Hz, 1H), 3.53 (t,  $J = 5.4$  Hz, 2H), 3.41 – 3.32 (m, 6H), 3.34 – 3.07 (m, 2H), 2.73 (t,  $J = 7.6$  Hz, 2H), 2.60 (t,  $J = 7.6$  Hz, 2H), 2.34 (t,  $J = 7.5$  Hz, 2H), 2.06 – 1.88 (m, 6H), 1.86 – 1.74 (m, 2H), 1.43 (s, 9H).

**$^{13}C$ -NMR** (101 MHz, methylene chloride- $d_2$ )  $\delta$  (ppm): 173.2, 172.3, 171.8, 154.8, 151.5, 148.7, 145.6, 142.0, 132.5, 129.6, 129.5, 129.1, 128.8, 128.7, 128.4, 128.1, 127.5, 127.2, 125.9, 123.4, 123.2, 122.8, 118.3, 114.9, 110.8, 108.2, 80.3, 55.9, 54.4, 54.1, 53.8, 53.6, 53.3, 45.7, 41.8, 36.1, 35.8, 35.5, 35.4, 34.9, 32.7, 28.4, 27.3, 26.9.

*N*-(3-(11,12-didehydrodibenzo[*b,f*]azocin-5(6*H*)-yl)-3-oxopropyl)-4-(4-((4-(4-oxo-4-(piperazin-1-yl)butyl)phenyl)diazenyl)phenyl) butanamide (**DBCO-AK-Piperazine**)

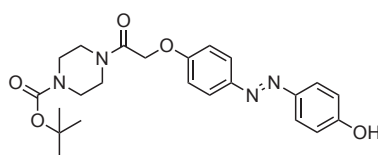


TFA (400  $\mu$ L) was added to a solution of **S4.2-10** (18.5 mg, 0.02 mmol, 1 eq.) in DCM (600  $\mu$ L, 0.04 M) and stirred at room temperature for 20 min. All volatile solvents were removed under a gentle stream of nitrogen to yield solid and **DBCO-AK-Piperazine** was used for subsequent experiments without further purification.

**HRMS** (ESI):  $m/z$   $C_{42}H_{45}N_6O_3^+$   $[M+H]^+$ : calc.: 681.35476, found: 681.35480.

### DBCO-AO-Piperazine Conjugate Synthesis

*tert*-Butyl 4-(2-(4-((4-hydroxyphenyl)diazenyl)phenoxy)acetyl)piperazine-1-carboxylate (**S4.2-10**)



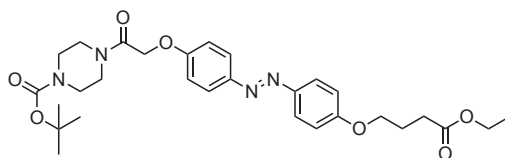
*N*-Boc-piperazine (273 mg, 1.47 mmol, 2 eq.), HBTU (334 mg, 0.88 mmol, 1.2 eq.) and TEA (0.79 mL, 5.7 mmol, 7 eq.) were added to a solution of known compound 2-(4-((4-hydroxyphenyl)diazenyl)phenoxy)acetic acid<sup>184</sup> (200 mg, 0.74 mmol, 1 eq.) in DMF (15 mL, 0.05 M) and stirred at room temperature for 2 h. The mixture was concentrated under reduced pressure and purified by silica gel flash column chromatography (hexanes/EtOAc: 90/10 to 50/50) to yield **6** (269 mg, 0.61 mmol, 83%) as an orange/red oil.

**HRMS** (ESI):  $m/z$   $C_{23}H_{28}N_4NaO_5^+$   $[M+Na]^+$ : calc.: 463.19574, found: 463.19516.

**$^1H$ -NMR** (400 MHz, acetone- $d_6$ )  $\delta$  (ppm): 7.88–7.76 (m, 4H), 7.17–7.09 (m, 2H), 7.03–6.95 (m, 2H), 4.98 (s, 2H), 3.63–3.39 (m, 8H), 1.45 (s, 9H).

<sup>13</sup>C-NMR (101 MHz, acetone-*d*<sub>6</sub>) δ (ppm): 166.8, 161.2, 160.9, 155.0, 148.2, 147.1, 125.4, 124.8, 116.5, 116.0, 80.1, 67.7, 45.7, 42.3, 28.5.

*tert*-butyl 4-(2-(4-((4-(4-ethoxy-4-oxobutoxy)phenyl)diazenyl) phenoxy)acetyl)piperazine-1-carboxylate (**S4.2-11**)



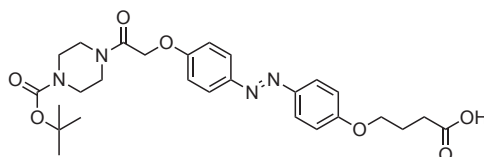
Ethyl 4-bromobutyrate (0.29 mL, 2.04 mmol, 4.5 eq.) was added to a mixture of **S4.2-10** (200 mg, 0.45 mmol, 1 eq.) and K<sub>2</sub>CO<sub>3</sub> (126 mg, 0.91 mmol, 2 eq.) in acetone (15 mL, 0.03 M). The mixture was stirred at 60 °C for 16 h, concentrated under reduced pressure and purified by silica gel flash column chromatography (DCM/MeOH: 100/0 to 99/1) to yield **S4.2-11** (50 mg, 0.09 mmol, 20%) as an orange solid.

**HRMS** (ESI): *m/z* C<sub>29</sub>H<sub>39</sub>N<sub>4</sub>O<sub>7</sub><sup>+</sup> [M+H]<sup>+</sup>: calc.: 555.28133, found: 555.28130.

<sup>1</sup>H-NMR (400 MHz, methylene chloride-*d*<sub>2</sub>) δ (ppm): 7.91–7.82 (m, 4H), 7.08–6.98 (m, 4H), 4.78 (s, 2H), 4.20–4.06 (m, 4H), 3.60–3.40 (m, 8H), 2.52 (t, *J* = 7.3, 2H), 2.18–2.07 (m, 2H), 1.45 (s, 9H), 1.32–1.19 (m, 3H).

<sup>13</sup>C-NMR (101 MHz, methylene chloride-*d*<sub>2</sub>) δ (ppm): 173.3, 166.3, 161.6, 160.2, 154.7, 148.0, 147.3, 124.8, 124.7, 115.3, 115.1, 80.3, 68.0, 67.6, 60.8, 45.5, 42.2, 31.1, 28.4, 25.0, 14.4.

4-(4-((4-(2-(4-(*tert*-butoxycarbonyl)piperazin-1-yl)-2-oxoethoxy)phenyl)diazenyl) phenoxy)butanoic acid (**S4.2-12**)

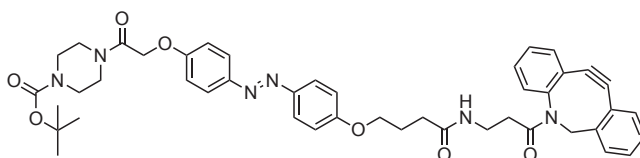


An aqueous solution of lithium hydroxide (1.0 M, 0.51 mL, 0.51 mmol, 10 eq.) was added to a solution of **S4.2-11** (28 mg, 0.05 mmol, 1 eq.) in THF (1 mL, 0.05 M). The reaction mixture was stirred at room temperature for 1 h, adjusted to pH 7 with an aqueous NH<sub>4</sub>Cl solution (2 M), and extracted with a DCM:*i*PrOH mixture (3:1, 3 × 20 mL). The combined organic phases were dried (Na<sub>2</sub>SO<sub>4</sub>) and concentrated under reduced pressure to yield **S4.2-12** (21 mg, 0.04 mmol, 77%) as a yellow/orange oil.

**HRMS** (ESI): *m/z* C<sub>27</sub>H<sub>35</sub>N<sub>4</sub>O<sub>7</sub><sup>+</sup> [M+H]<sup>+</sup>: calc.: 527.25003, found: 527.24991.

<sup>1</sup>H-NMR (400 MHz, acetone-*d*<sub>6</sub>) δ (ppm): 7.97–7.75 (m, 4H), 7.15–7.08 (m, 4H), 4.97 (s, 2H), 4.17 (t, *J* = 6.3, 2H), 3.66–3.29 (m, 8H), 2.53 (t, *J* = 7.3, 2H), 2.15–2.07 (m, 2H), 1.45 (s, 9H).

*tert*-Butyl 4-(2-(4-((4-(4-((3-(11,12-didehydrodibenzo[*b,f*]azocin-5(6*H*)-yl)-3-oxopropyl)amino)-4-oxobutoxy)phenyl)diazenyl)phenoxy)acetyl)piperazine-1-carboxylate (**S4.2-13**)



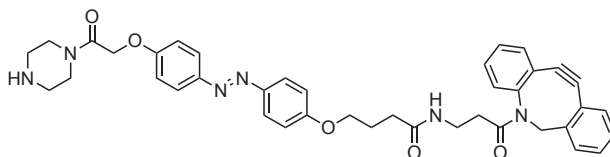
DBCO-amine (11.5 mg, 0.04 mmol, 1.05 eq.), HBTU (22.5 mg, 0.06 mmol, 1.5 eq.) and TEA (38.5  $\mu$ L, 0.27 mmol, 7 eq.) were added to a solution of **S4.2-12** (21 mg, 0.04 mmol, 1 eq.) in DMF (4 mL, 0.01 M), and stirred at room temperature for 1 h. The reaction mixture was concentrated under reduced pressure and purified *via* silica gel flash column chromatography (DCM/MeOH: 100/0 to 98/2) to yield **S4.2-13** (19 mg, 0.02 mmol, 44%) as a yellow/orange oil.

**HRMS** (ESI):  $m/z$   $C_{45}H_{49}N_6O_7^+$   $[M+H]^+$ : calc.: 785.36572, found: 785.36518.

**$^1H$ -NMR** (400 MHz, chloroform- $d_7$ )  $\delta$  (ppm): 7.91 – 7.84 (m, 4H), 7.81 – 7.73 (m, 2H), 7.66 (d,  $J$  = 7.5 Hz, 1H), 7.43 – 7.33 (m, 5H), 7.04 (d,  $J$  = 9.0 Hz, 2H), 6.98 (d,  $J$  = 9.0 Hz, 2H), 6.18 (t,  $J$  = 6.0 Hz, 1H), 5.11 (d,  $J$  = 14.0 Hz, 1H), 4.78 (s, 2H), 4.00 (t,  $J$  = 6.0 Hz, 2H), 3.69 (d,  $J$  = 13.9 Hz, 1H), 3.63 – 3.53 (m, 4H), 3.50 – 3.35 (m, 8H), 2.23 (t,  $J$  = 7.4 Hz, 2H), 2.02 (dt,  $J$  = 14.5, 7.0 Hz, 2H), 1.46 (s, 9H).

**$^{13}C$ -NMR** (101 MHz, chloroform- $d_7$ )  $\delta$  (ppm): 172.5, 166.6, 161.2, 159.5, 154.6, 151.1, 148.1, 147.1, 140.1, 132.2, 129.1, 128.8, 128.7, 128.5, 128.0, 127.4, 126.7, 125.8, 124.6, 123.0, 122.6, 116.9, 115.0, 114.9, 111.6, 107.9, 80.7, 68.1, 67.4, 55.7, 45.5, 42.2, 35.5, 34.9, 32.9, 28.5, 25.2.

*N*-(3-(11,12-didehydridibenzo[*b,f*]azocin-5(6*H*)-yl)-3-oxopropyl)-4-(4-((4-(2-oxo-2-(piperazin-1-yl)ethoxy)phenyl)diazenyl)phenoxy)butanamide (**DBCO-AO-Piperazine**)



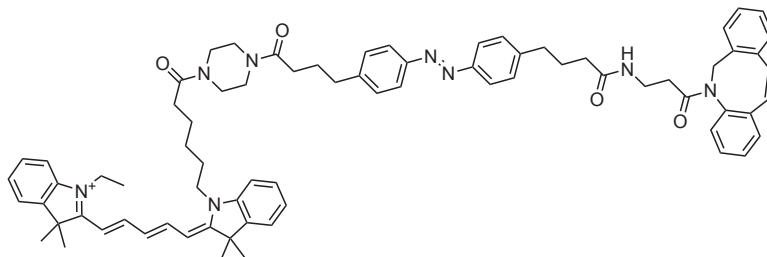
TFA (100%, 80  $\mu$ L, 1.27 mmol, 80 eq.) was added to a solution of **S4.2-13** (10.0 mg, 12.7  $\mu$ mol, 1 eq.) in DCM (120  $\mu$ L, 0.11 M) and stirred at room temperature for 15 min. All volatiles were removed under a gentle stream of nitrogen. **DBCO-AO-Piperazine** was obtained as an orange/red oil that was used for the next step without further purification.

**HRMS** (ESI):  $m/z$   $C_{40}H_{41}N_6O_5^+$   $[M+H]^+$ : calc.: 685.31329, found: 685.31282.



## DBCO-Azo-Piperazine-Dye Conjugate Synthesis

2-((1*E*,3*E*)-5-((*Z*)-1-(6-(4-(4-(4-((4-(4-((3-(11,12-didehydrodibenzo[*b*,*f*]azocin-5(6*H*)-yl)-3-oxopropyl)amino)-4-oxobutyl)phenyl)diazenyl) phenyl)butanoyl)piperazin-1-yl)-6-oxohexyl)-3,3-dimethylindolin-2-ylidene)penta-1,3-dien-1-yl)-1-ethyl-3,3-dimethyl-3*H*-indol-1-ium (Cy5-AK-DBCO)

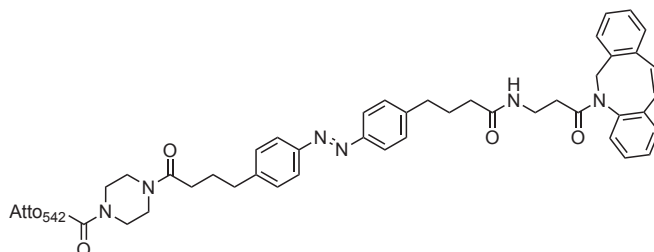


**Cy5-AK-DBCO** was synthesized according to **GP-B**, using:

as fluorophore acid: "Cy5 acid",<sup>178</sup> CAS number: 756457-35-9 (1.5 mg, 3.02  $\mu\text{mol}$ , 1 eq.); and as DBCO-azobenzene-piperazine: **DBCO-AK-Piperazine** (82  $\mu\text{L}$ , 0.03 M in DMF, 2.42  $\mu\text{mol}$ , 0.8 eq.).

**HRMS** (ESI):  $m/z$   $\text{C}_{75}\text{H}_{83}\text{N}_8\text{O}_4^+$   $[\text{M}]^+$ : calc.: 1159.65318, found: 1159.65425.

*N*-(3-(11,12-didehydrodibenzo[*b*,*f*]azocin-5(6*H*)-yl)-3-oxopropyl)-4-(4-((4-(4-(4-Atto<sub>542</sub>-piperazin-1-yl)-4-oxobutyl)phenyl) diazenyl)phenyl)butanamide (**Atto542-AK-DBCO**)



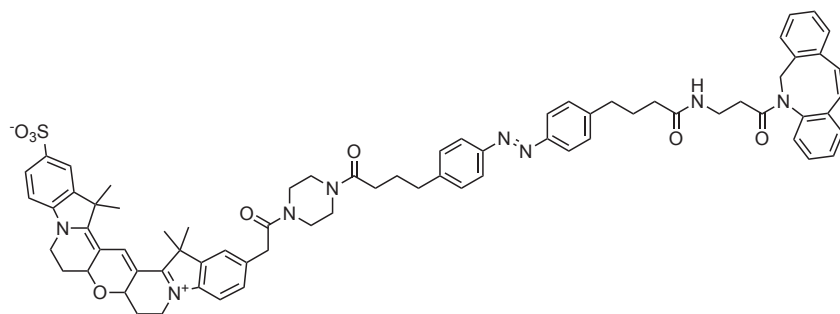
**Atto542-AK-DBCO** was synthesized according to **GP-A**, using:

as fluorophore NHS ester: commercial "Atto542 NHS ester" (1.0 mg, 0.89  $\mu\text{mol}$ , 1 eq.)

as DBCO-azobenzene-piperazine: **DBCO-AK-Piperazine** (34  $\mu\text{L}$ , 0.03 M in DMF, 0.98  $\mu\text{mol}$ , 1.1 eq.)

**HRMS** (ESI): Atto542 molecular formula is not reported, but using the quoted mass after coupling, expected  $m/z$   $[\text{M}]^+$  is 1576; found: 1576.4974.

*N*-(3-(11,12-didehydrodibenzo[*b,f*]azocin-5(6*H*)-yl)-3-oxopropyl)-4-(4-((4-(4-(4-Cy3B-piperazin-1-yl)-4-oxobutyl)phenyl)diazenyl)phenyl)butanamide (**Cy3B-AK-DBCO**)



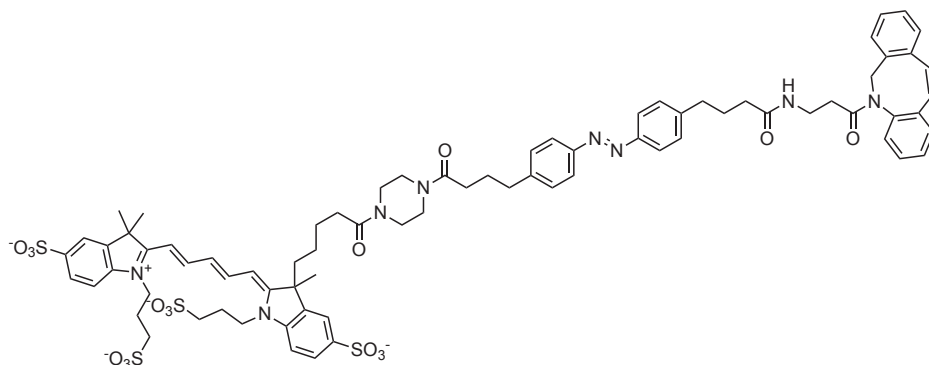
**Cy3B-AK-DBCO** was synthesized according to **GP-A**, using:

as fluorophore NHS ester: commercial "Cy3B NHS ester" CAS number 228272-52-4 (1.0 mg, 1.52  $\mu\text{mol}$ , 1 eq.),

as DBCO-azobenzene-piperazine: **DBCO-AK-Piperazine** (57  $\mu\text{L}$ , 0.03 M in DMF, 1.67  $\mu\text{mol}$ , 1.1 eq.).

**HRMS** (ESI):  $m/z$   $\text{C}_{73}\text{H}_{76}\text{N}_8\text{O}_8\text{S}^{2+}$   $[\text{M}+2\text{H}]^{2+}$ : calc.: 612.27479, found: 612.2762.

2-((1*E*,3*E*)-5-((*Z*)-3-(5-(4-(4-(4-((4-(4-((3-(11,12-didehydrodibenzo[*b,f*]azocin-5(6*H*)-yl)-3-oxopropyl)amino)-4-oxobutyl)phenyl) diazenyl)phenyl)butanoyl)piperazin-1-yl)-5-oxopentyl)-3-methyl-5-sulfonato-1-(3-sulfonatopropyl)indolin-2-ylidene)penta-1,3-dien-1-yl)-3,3-dimethyl-1-(3-sulfonatopropyl)-3*H*-indol-1-ium-5-sulfonate (**AF647-AK-DBCO**)



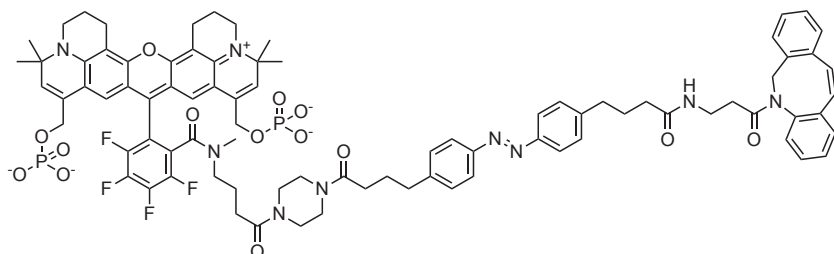
**AF647-AK-DBCO** was synthesized according to **GP-A**, using:

as fluorophore NHS ester: commercial "AlexaFluor647 NHS ester", CAS number 1620475-28-6 (1.0 mg, 0.95  $\mu\text{mol}$ , 1 eq.)

as DBCO-azobenzene-piperazine: **DBCO-AK-Piperazine** (30  $\mu\text{L}$ , 0.03 M in DMF, 0.88  $\mu\text{mol}$ , 0.9 eq.)

**HRMS** (ESI):  $m/z$   $\text{C}_{77}\text{H}_{83}\text{N}_8\text{O}_{16}\text{S}_4^{3-}$   $[\text{M}]^{3-}$ : calc.: 501.16088, found: 501.16091.

*N*-(3-(11,12-didehydrodibenzo[*b,f*]azocin-5(6*H*)-yl)-3-oxopropyl)-4-(4-((4-(4-AbberiorStar635P-piperazin-1-yl)-4-oxobutyl)phenyl)diazenyl)phenyl)butanamide (**AbberiorStar635P-AK-DBCO**)



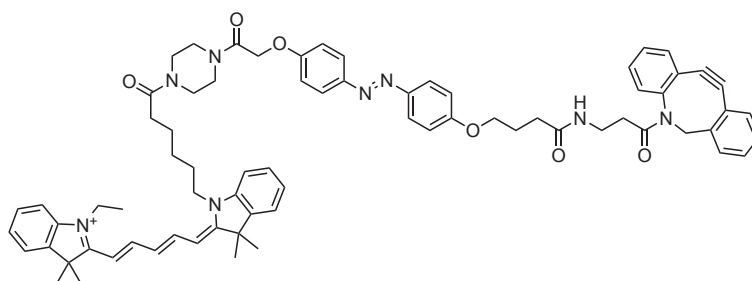
**AbberiorStar635P-AK-DBCO** was synthesized according to **GP-A**, using:

as *fluorophore NHS ester*: commercial "AbberiorStar635P NHS ester" (1.0 mg, 0.97  $\mu\text{mol}$ , 1 eq.), and

as *DBCO-azobenzene-piperazine*: **DBCO-AK-Piperazine** (50  $\mu\text{L}$ , 0.03 M in DMF, 1.5  $\mu\text{mol}$ , 1.5 eq.)

**HRMS** (ESI):  $m/z$   $\text{C}_{85}\text{H}_{88}\text{F}_4\text{N}_9\text{O}_{14}\text{P}_2^+$   $[\text{M}+4\text{H}]^+$ : calc.: 1596.5857, found: 1596.5883.

2-((1*E*,3*E*)-5-((*Z*)-1-(6-(4-(2-(4-((4-(4-((3-(11,12-didehydrodibenzo[*b,f*]azocin-5(6*H*)-yl)-3-oxopropyl)amino)-4-oxobutoxy)phenyl) diazenyl)phenoxy)acetyl)piperazin-1-yl)-6-oxohexyl)-3,3-dimethylindolin-2-ylidene)penta-1,3-dien-1-yl)-1-ethyl-3,3-dimethyl-3*H*-indol-1-ium (**Cy5-AO-DBCO**)



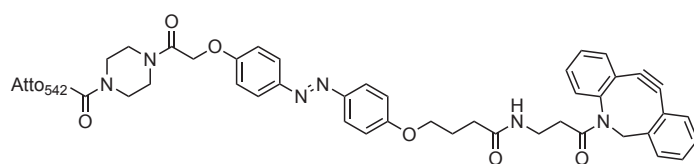
**Cy5-AO-DBCO** synthesized according to **GP-B**, using:

as *fluorophore acid*: Cy5 acid (1.5 mg, 3.02  $\mu\text{mol}$ , 1 eq.), and

as *DBCO-azobenzene-piperazine*: **DBCO-AO-Piperazine** (83  $\mu\text{L}$ , 0.03 M in DMF, 2.4  $\mu\text{mol}$ , 0.8 eq.)

**HRMS** (ESI):  $m/z$   $\text{C}_{73}\text{H}_{79}\text{N}_8\text{O}_6^+$   $[\text{M}]^+$ : calc.: 1163.61171, found: 1163.61310.

## Atto542-AO-DBCO



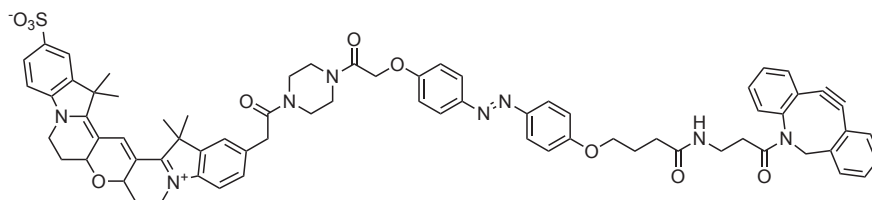
**Atto542-AO-DBCO** was synthesized according to **GP-A**, using:

as fluorophore NHS ester: Atto542 NHS ester (1.0 mg, 0.89  $\mu\text{mol}$ , 1 eq.), and

as DBCO-azobenzene-piperazine: **DBCO-AO-Piperazine** (34  $\mu\text{L}$ , 0.03 M in DMF, 0.98  $\mu\text{mol}$ , 1.1 eq.).

**HRMS** (ESI): using the quoted Atto542 mass after coupling, expected  $m/z$   $[M]^-$  is calc.: ~1578, found: 1578.4958.

*N*-(3-(11,12-didehydrodibenzo[*b,f*]azocin-5(6*H*)-yl)-3-oxopropyl)-4-(4-((4-(2-(4-Cy3B-piperazin-1-yl)-2-oxoethoxy)phenyl)diazenyl)phenoxy)butanamide (**Cy3B-AO-DBCO**)



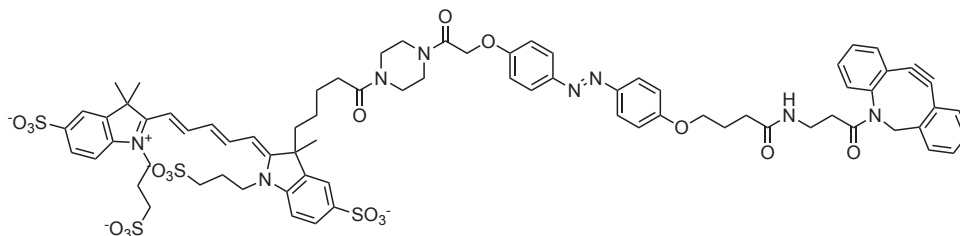
**Cy3B-AO-DBCO** was synthesized according to **GP-A**, using:

as fluorophore NHS ester: Cy3B NHS ester (1.0 mg, 1.5  $\mu\text{mol}$ , 1 eq.), and

as DBCO-azobenzene-piperazine: **DBCO-AO-Piperazine** (85  $\mu\text{L}$ , 0.03 M in DMF, 1.7  $\mu\text{mol}$ , 1.1 eq.).

**HRMS** (ESI):  $m/z$   $\text{C}_{71}\text{H}_{72}\text{N}_8\text{O}_{10}\text{S}^{2+}$   $[M+2H]^{2+}$ : calc.: 614.25406, found: 614.2547.

2-((1*E*,3*E*)-5-((*Z*)-3-(5-(4-(2-(4-((3-(11,12-didehydrodibenzo[*b,f*]azocin-5(6*H*)-yl)-3-oxopropyl)amino)-4-oxobutoxy)phenyl) diazenyl)phenoxy)acetyl)piperazin-1-yl)-5-oxopentyl)-3-methyl-5-sulfonato-1-(3-sulfonatopropyl)indolin-2-ylidene)penta-1,3-dien-1-yl)-3,3-dimethyl-1-(3-sulfonatopropyl)-3*H*-indol-1-ium-5-sulfonate (**AF647-AO-DBCO**)



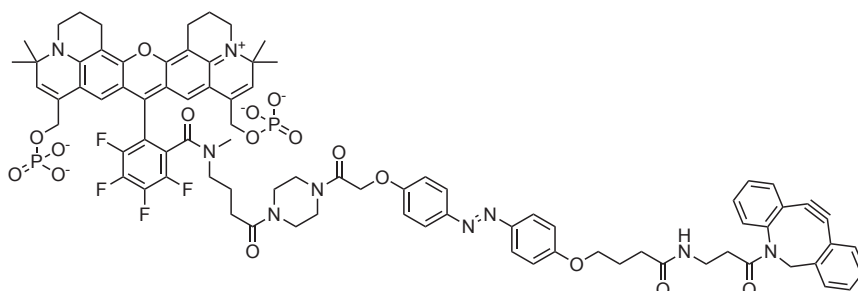
**AF647-AO-DBCO** was synthesized according to **GP-A**, using:

as fluorophore NHS ester: AlexaFluor647 NHS ester (1.0 mg, 0.95  $\mu\text{mol}$ , 1 eq.), and

as DBCO-azobenzene-piperazine: **DBCO-AO-Piperazine** (36  $\mu\text{L}$ , 0.03 M in DMF, 1.0  $\mu\text{mol}$ , 1.1 eq.).

**HRMS** (ESI):  $m/z$   $\text{C}_{75}\text{H}_{79}\text{N}_8\text{O}_{18}\text{S}_4^{3-}$   $[M]^{3-}$ : calc.: 502.48039, found: 502.48034.

*N*-(3-(11,12-didehydrodibenzo[*b,f*]azocin-5(6*H*)-yl)-3-oxopropyl)-4-(4-((4-(2-(4-AbberiorStar635P-piperazin-1-yl)-2-oxoethoxy)phenyl)diazenyl)phenoxy)butanamide (**AbberiorStar635P-AO-DBCO**)



**AbberiorStar635P-AO-DBCO** synthesized according to **GP-A**, using:

as fluorophore NHS ester: AbberiorStar635P NHS ester (1.0 mg, 0.97  $\mu\text{mol}$ , 1 eq.), and

as DBCO-azobenzene-piperazine: **DBCO-AO-Piperazine** (37  $\mu\text{L}$ , 0.03 M in DMF, 1.1  $\mu\text{mol}$ , 1.1 eq.).

**HRMS** (ESI):  $m/z$   $\text{C}_{83}\text{H}_{84}\text{F}_4\text{N}_9\text{O}_{16}\text{P}_2^+$   $[\text{M}+4\text{H}]^+$ : calc.: 1600.5442, found: 1600.5796.

#### Fluorophore- labeled DNA sequences:

3'-amine or 3'-azide DNA oligos were synthesised with three sequences: a **21-nt** "permanent sequence" (5'-TATGAGAAGTTAGGAATGTTA-3'), a **8-nt** "DNA-PAINT sequence" (5'-GGAATGTT-3') and a **17-nt** "permanent sequence" (5'-ATGATGTAGGTGGTAGA-3'). The 21-nt amine oligos were coupled to commercial fluorophore NHS esters to give reference ("comparator") fluorescent DNA oligos and 17-nt amine oligos were azobenzenes and stilbenes by DCC mediated amide coupling to yield photostabilizer-oligos for proximity studies; the azide oligos were coupled to the synthesised fluorophore-azobenzene-DBCO conjugates by copper-free click chemistry. Oligo synthesis, coupling, purification, quality control and analysis were performed by commercial service provider according to standard procedures (Ella Biotech GmbH (82256 Fürstfeldbruck, Germany)).

Example analytical data for comparator oligo: **AbberiorStar635P-21nt**: MW: 7835; ESI-MS (found):  $m/z$  = 869.8 ( $\text{M}^9$ ); ESI-MS (deconvoluted): 7838.1 Da.

Analytical data for 21-nt oligos bearing compounds of the invention:

**Cy5-AK-21nt**: MW: 8192; ESI-MS (found):  $m/z$  = 743.7 ( $\text{M}^{11-}$ ); ESI-MS (deconvoluted): 8191.3 Da. **Atto542-AK-21nt**: MW: 8608; ESI-MS (found):  $m/z$  = 781.6 ( $\text{M}^{11-}$ ); ESI-MS (deconvoluted): 8608.6 Da. **Cy3B-AK-21nt**: MW: 8255; ESI-MS (found):  $m/z$  = 824.6 ( $\text{M}^{10-}$ ); ESI-MS (deconvoluted): 8255.6 Da. **AlexaFluor647-AK-21nt**: MW: 8540; ESI-MS (found):  $m/z$  = 609.0 ( $\text{M}^{14-}$ ); ESI-MS (deconvoluted): 8539.8 Da. **AbberiorStar635P-AK-21nt**: MW: 8625; ESI-MS (found):  $m/z$  = 861.8 ( $\text{M}^{10-}$ ); ESI-MS (deconvoluted): 8628.1 Da. **Cy5-AO-21nt**: MW: 8196; ESI-MS (found):  $m/z$  = 818.5 ( $\text{M}^{10-}$ ); ESI-MS (deconvoluted): 8195.0 Da. **Atto542-AO-21nt**: MW: 8612; ESI-MS (found):  $m/z$  = 781.9 ( $\text{M}^{11-}$ ); ESI-MS (deconvoluted): 8612.4 Da. **Cy3B-AO-21nt**: MW: 8259; ESI-MS (found):  $m/z$  = 825.0 ( $\text{M}^{10-}$ ); ESI-MS (deconvoluted): 8258.9 Da. **AlexaFluor647-AO-21nt**: MW: 8544; ESI-MS (found):  $m/z$  = 710.9 ( $\text{M}^{12-}$ ); ESI-MS (deconvoluted): 8543.0 Da. **AbberiorStar635P-AO-21nt**: MW: 8629; ESI-MS (found):  $m/z$  = 862.2 ( $\text{M}^{10-}$ ); ESI-MS (deconvoluted): 8632.1 Da.



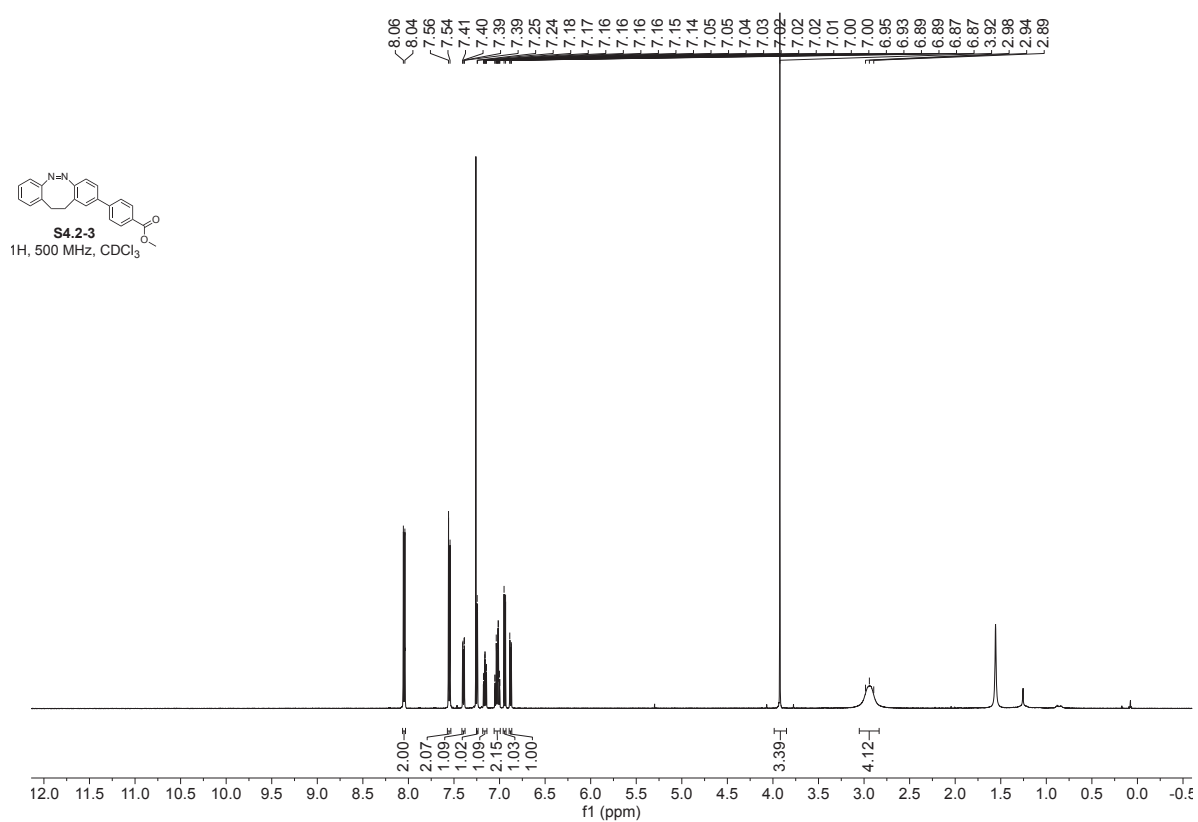
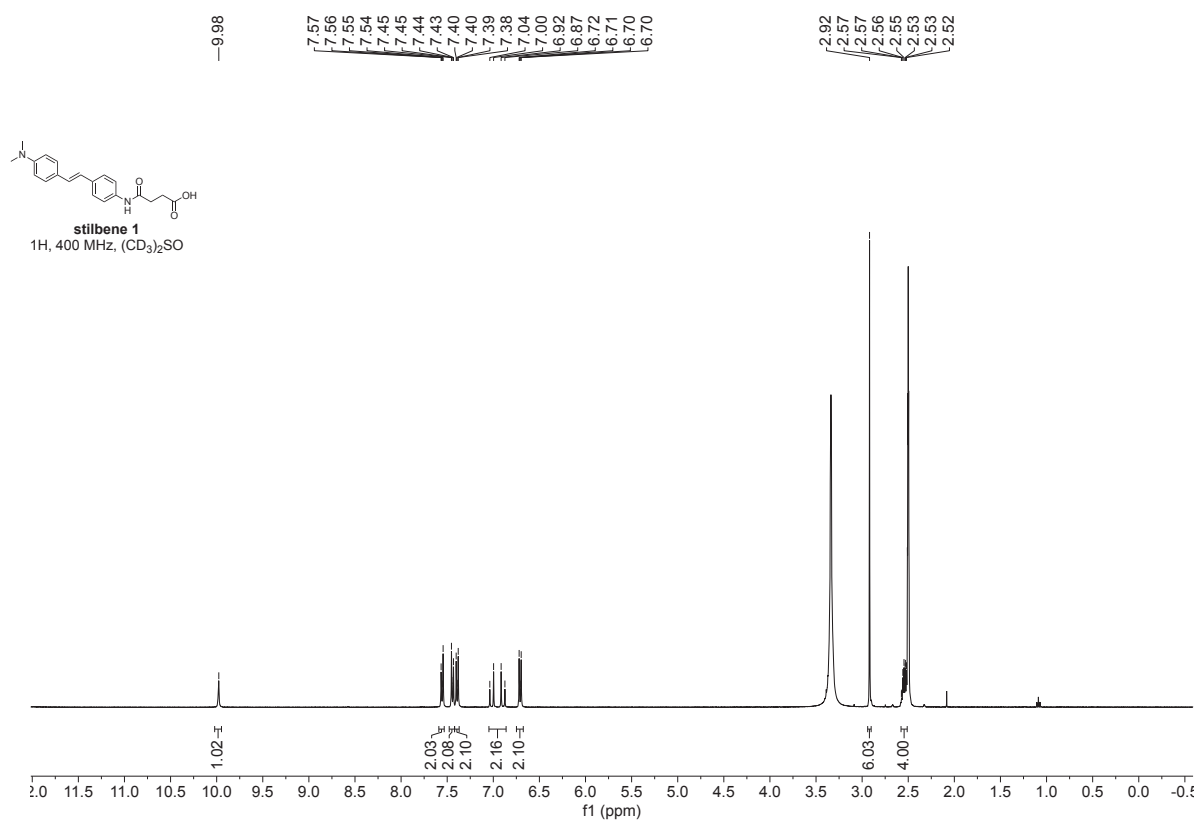
Analytical data for 8-nt oligos bearing compounds of the invention:

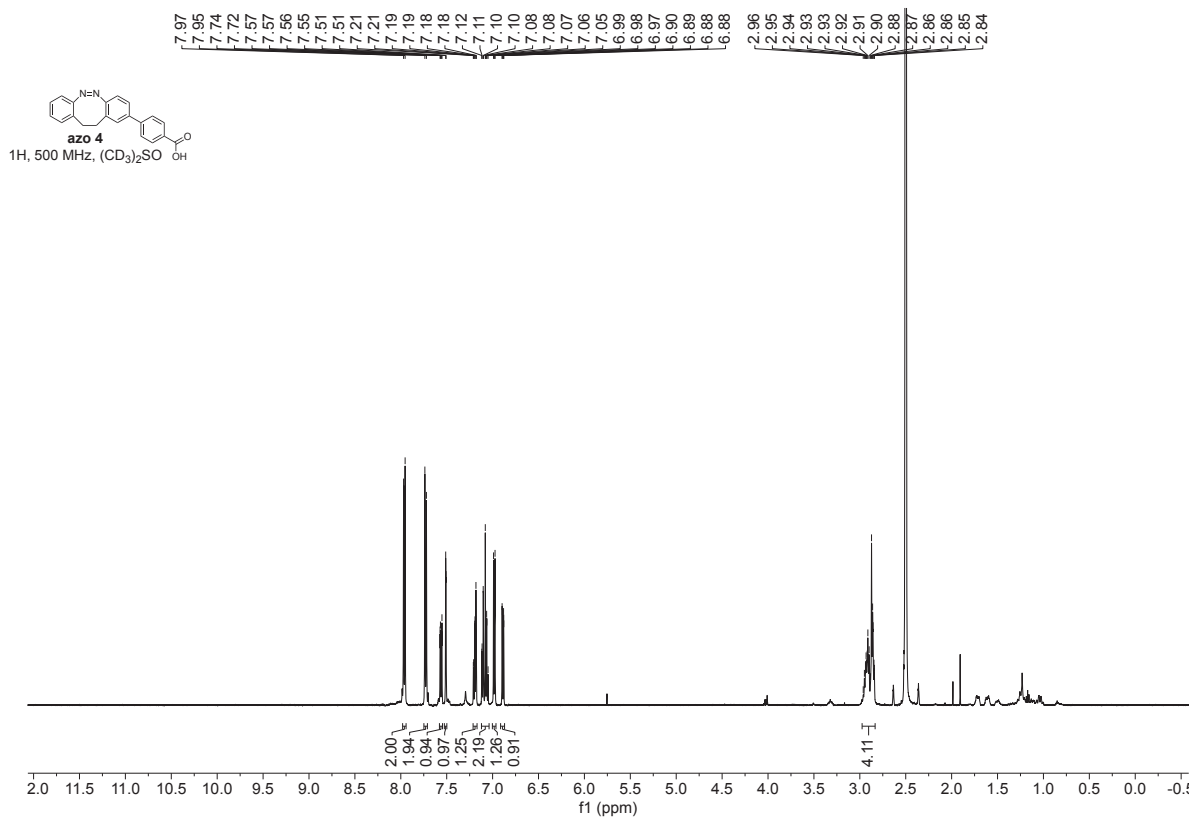
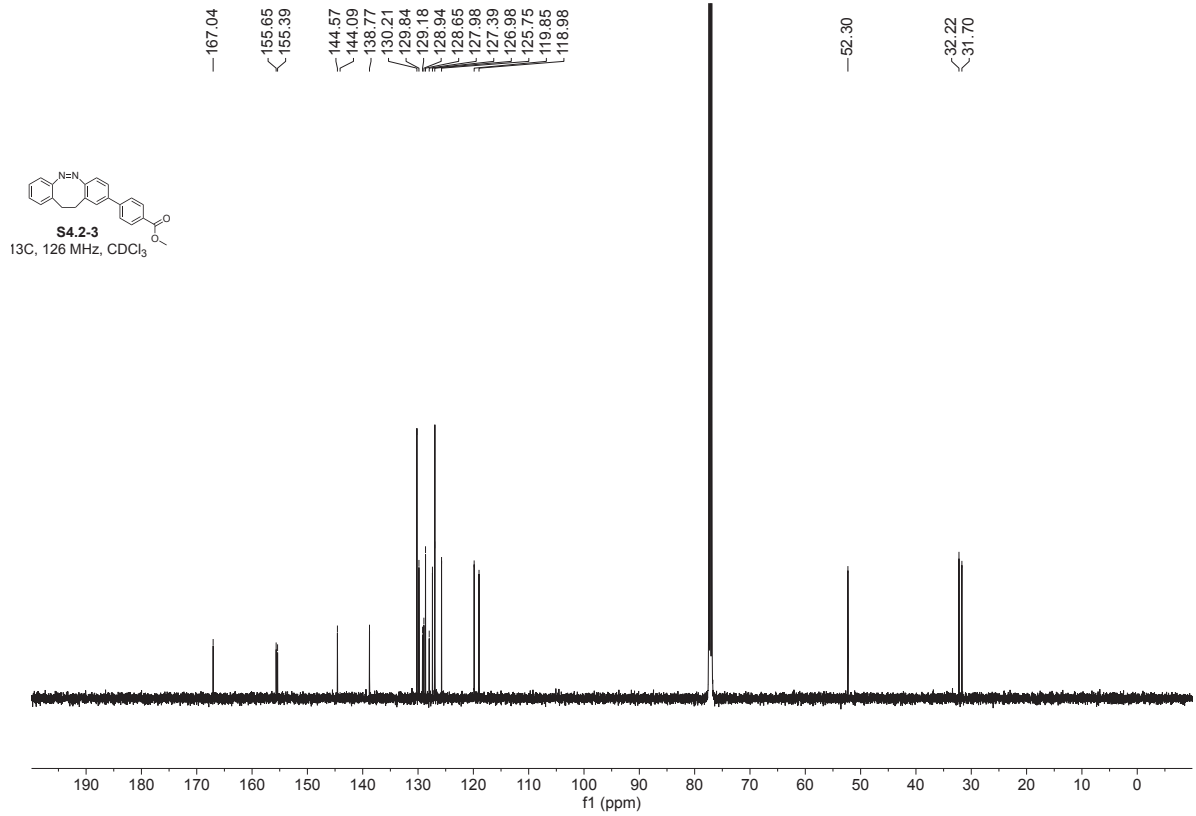
**Cy5-AK-8nt:** MW: 4109; ESI-MS (found):  $m/z = 820.4$  ( $M^5$ ); ESI-MS (deconvoluted): 4107.1 Da. **Atto542-AK-8nt:** MW: 4525; ESI-MS (found):  $m/z = 753.1$  ( $M^6$ ); ESI-MS (deconvoluted): 4524.4 Da. **Cy3B-AK-8nt:** MW: 4172; ESI-MS (found):  $m/z = 833.3$  ( $M^5$ ); ESI-MS (deconvoluted): 4171.4 Da. **AlexaFluor647-AK-8nt:** MW: 4454; ESI-MS (found):  $m/z = 741.6$  ( $M^6$ ); ESI-MS (deconvoluted): 4454.4 Da. **AbberiorStar635P-AK-8nt:** MW: 4542; ESI-MS (found):  $m/z = 907.9$  ( $M^5$ ); ESI-MS (deconvoluted): 4544.4 Da. **Cy5-AO-8nt:** MW: 4113; ESI-MS (found):  $m/z = 821.3$  ( $M^5$ ); ESI-MS (deconvoluted): 4111.4 Da. **Atto542-AO-8nt:** MW: 4529; ESI-MS (found):  $m/z = 646.0$  ( $M^7$ ); ESI-MS (deconvoluted): 4528.8 Da. **Cy3B-AO-8nt:** MW: 4176; ESI-MS (found):  $m/z = 834.1$  ( $M^5$ ); ESI-MS (deconvoluted): 4175.3 Da. **AlexaFluor647-AO-8nt:** MW: 4458; ESI-MS (found):  $m/z = 636.1$  ( $M^7$ ); ESI-MS (deconvoluted): 4459.8 Da. **AbberiorStar635P-AO-8nt:** MW: 4546; ESI-MS (found):  $m/z = 908.7$  ( $M^5$ ); ESI-MS (deconvoluted): 4548.5 Da.

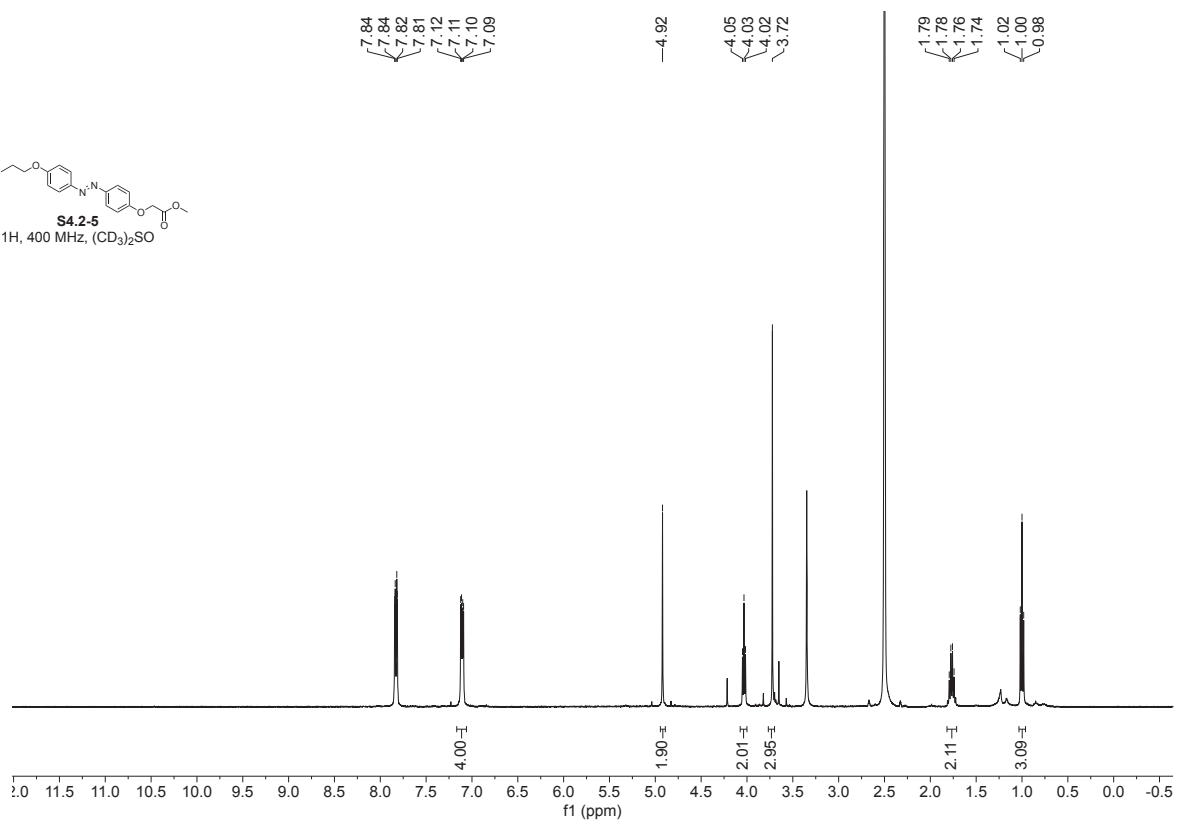
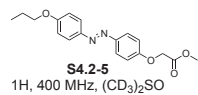
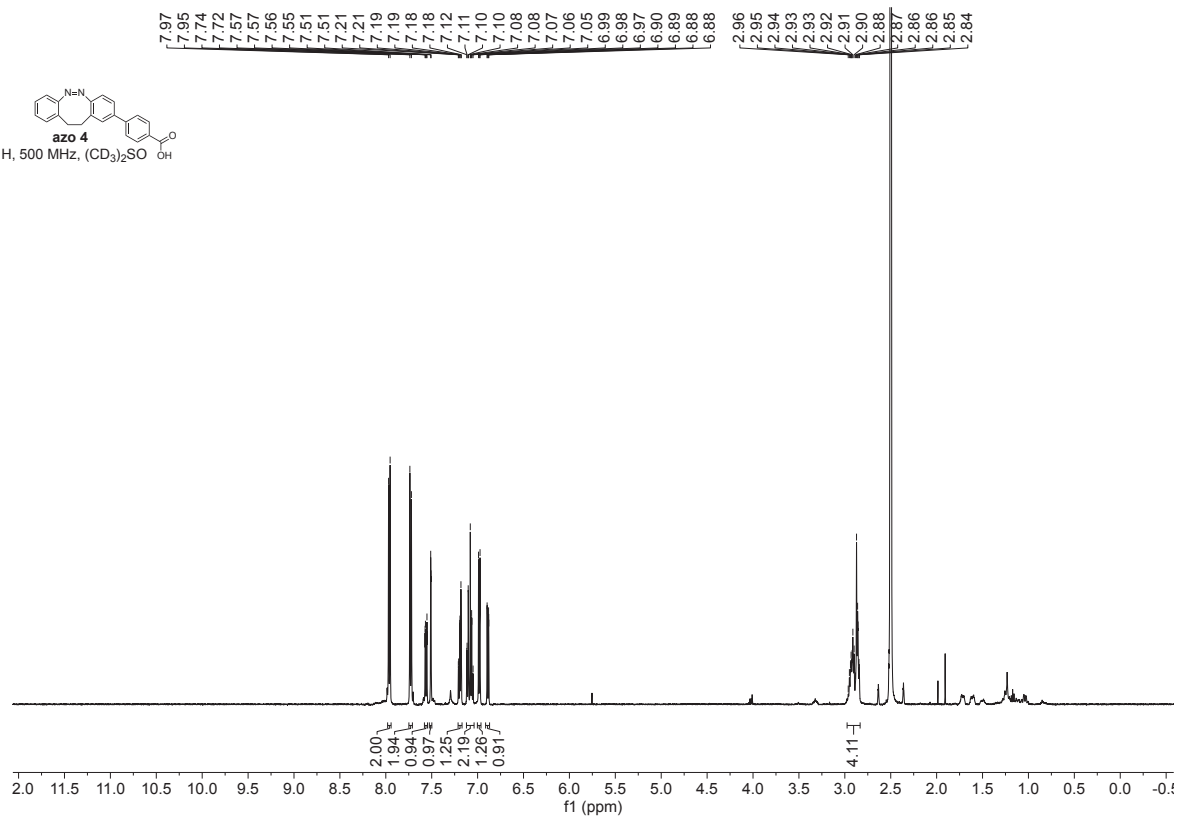
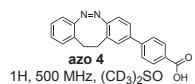
### Single-molecule localisation microscopy of fluorophore-azobenzene conjugates

To enable single-molecule studies and characterization the fluorophore-azobenzene conjugates as well as parent fluorophores were coupled to the 3'-end of a 21-nt long DNA strand, which was subsequently hybridized to a biotin labelled complementary strand. The ds-DNA conjugates were immobilized on the BSA-biotin coated glass coverslips via biotin-Neutravidin interaction and imaged on a commercial Nanoimager S (ONI Ltd., UK) as described by Scheckenbach et al.<sup>185</sup> Oxygen was removed using an enzymatic oxygen scavenging system consisting of glucose-oxidase-catalase (1% (wt/v) D-(+)-glucose (Sigma Aldrich, USA), 165 units/mL glucose oxidase (G2133, Sigma Aldrich, USA), 2170 units/mL catalase (C3155, Sigma Aldrich, USA)) in 2 x PBS and 10 mM MgCl<sub>2</sub> buffer. The single molecules were excited at 532 nm (for ATTO542 conjugates) and 639 nm (for AlexaFluor647, Cy5, AberriorStar635P conjugates) using 9 mW laser power and photobleaching movies were recorded at 50 ms/frame time resolution. The obtained data was analysed using Image J 1.53 to subtract the background and extract single-molecule fluorescence vs. time trajectories. The picked trajectories were analyzed with a custom Python code utilizing a Hidden Markov Model to identify the blinking and bleaching events. The photon budget until photobleaching, average count rate (brightness) and survival time was extracted for every single molecule. The mean values for these parameters (**Figure 30**) were obtained by compiling the ensemble histogram of all analyzed single molecules and fitting it to an exponential decay function. The single-molecule trajectories at the higher time resolution (10 ms) were acquired on the confocal microscope while exciting molecules with 639 nm laser at 2  $\mu$ W excitation power as described before.<sup>186</sup>

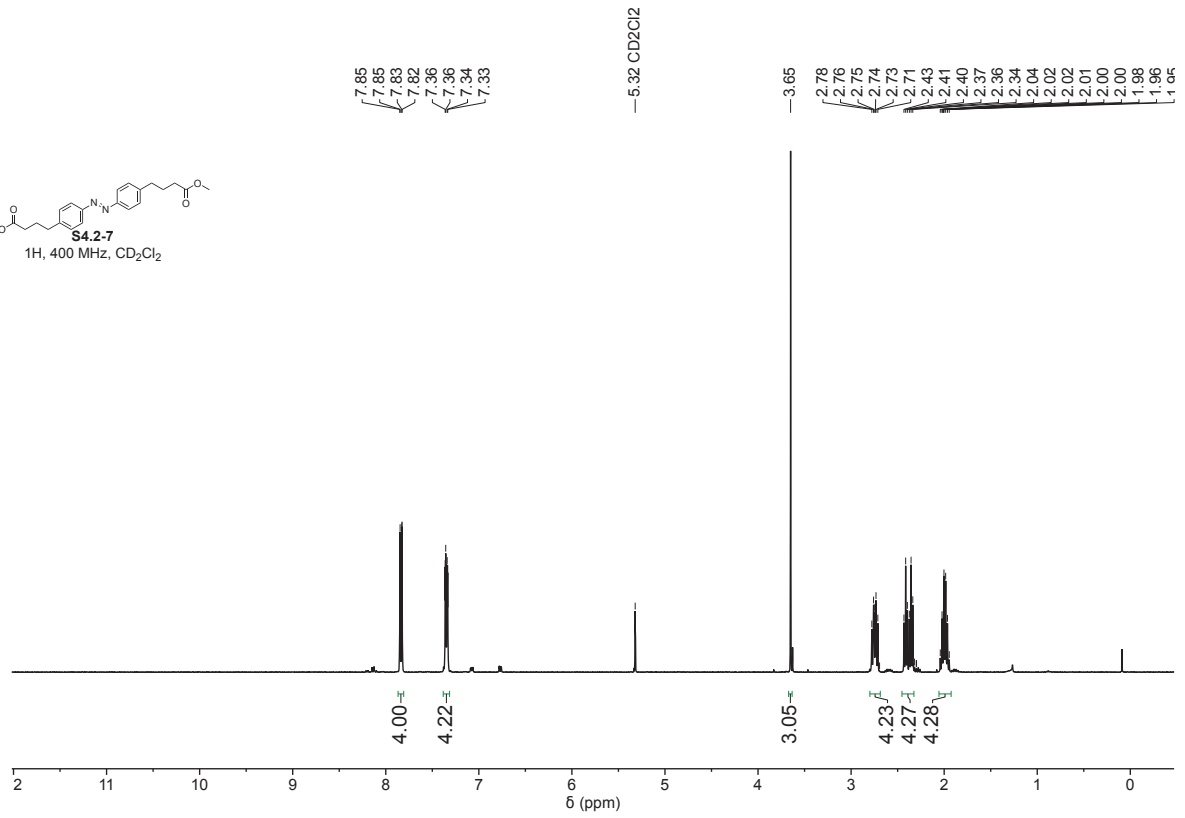
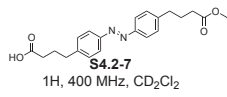
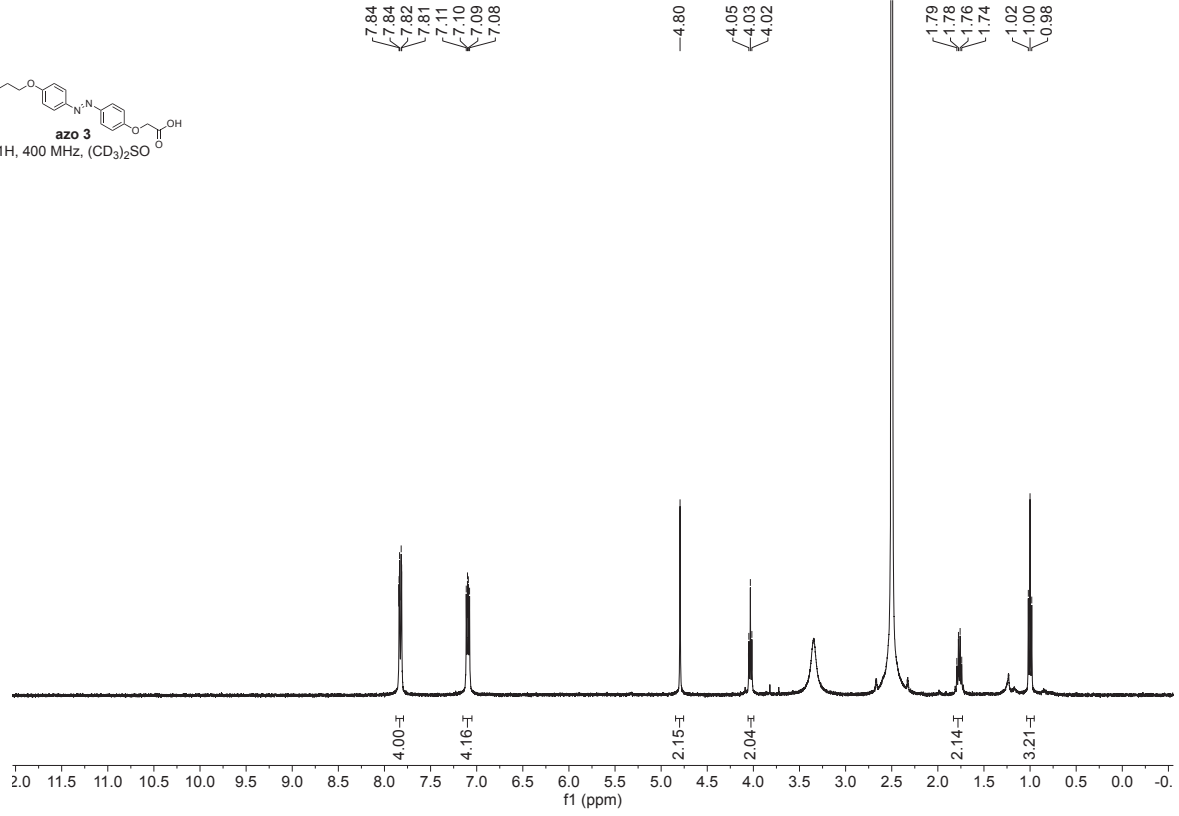
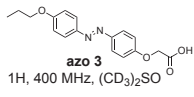
# NMR spectra

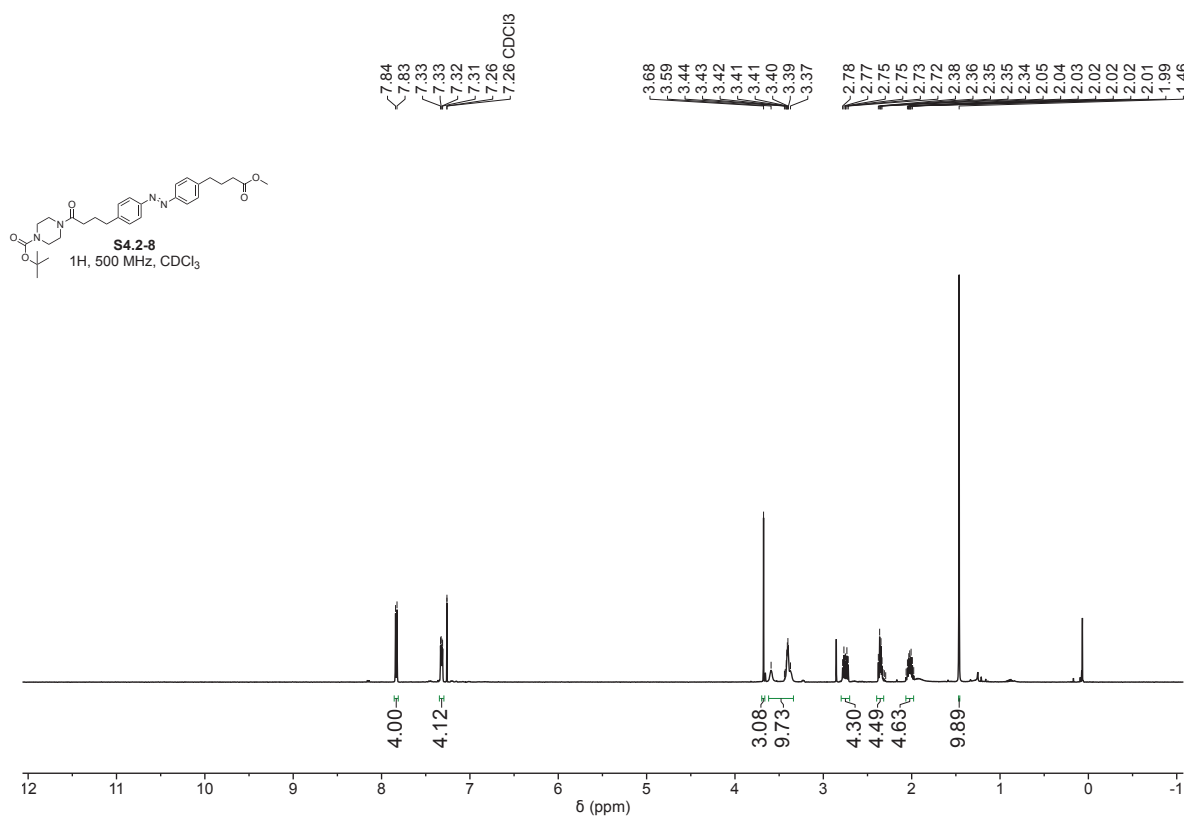
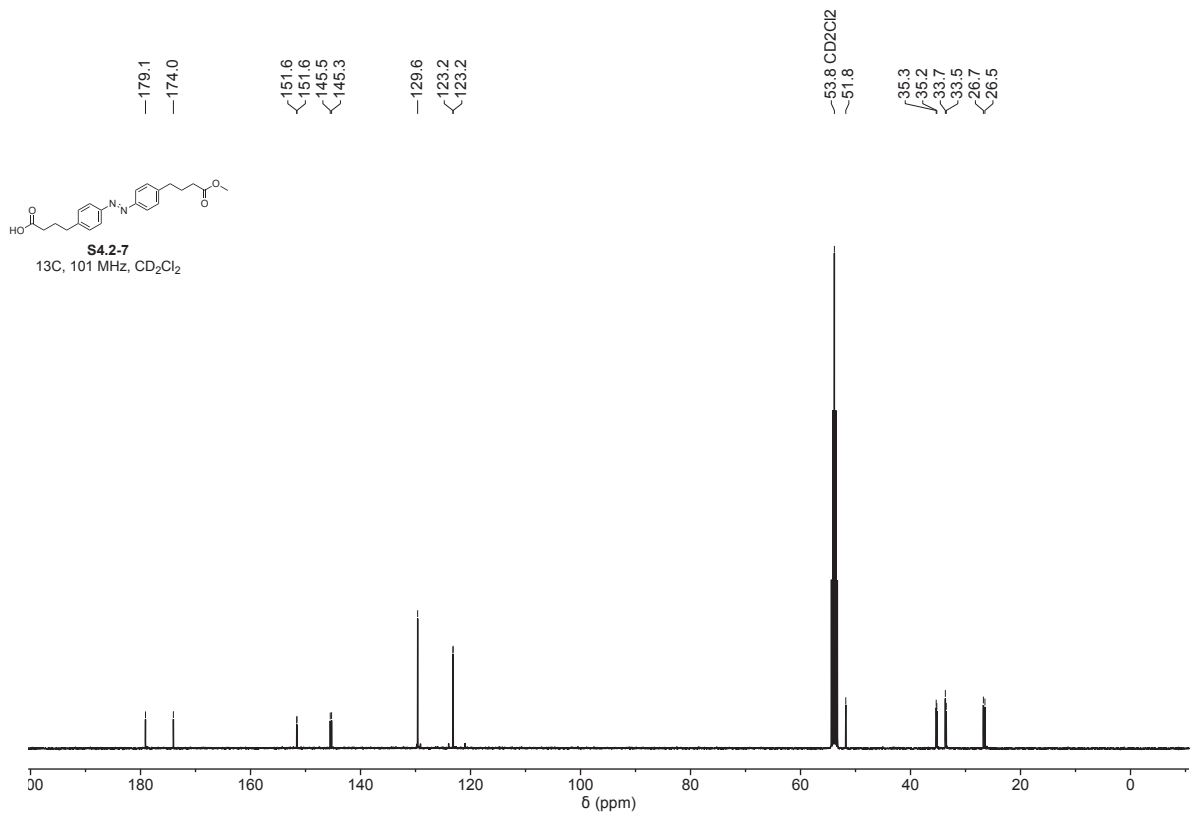


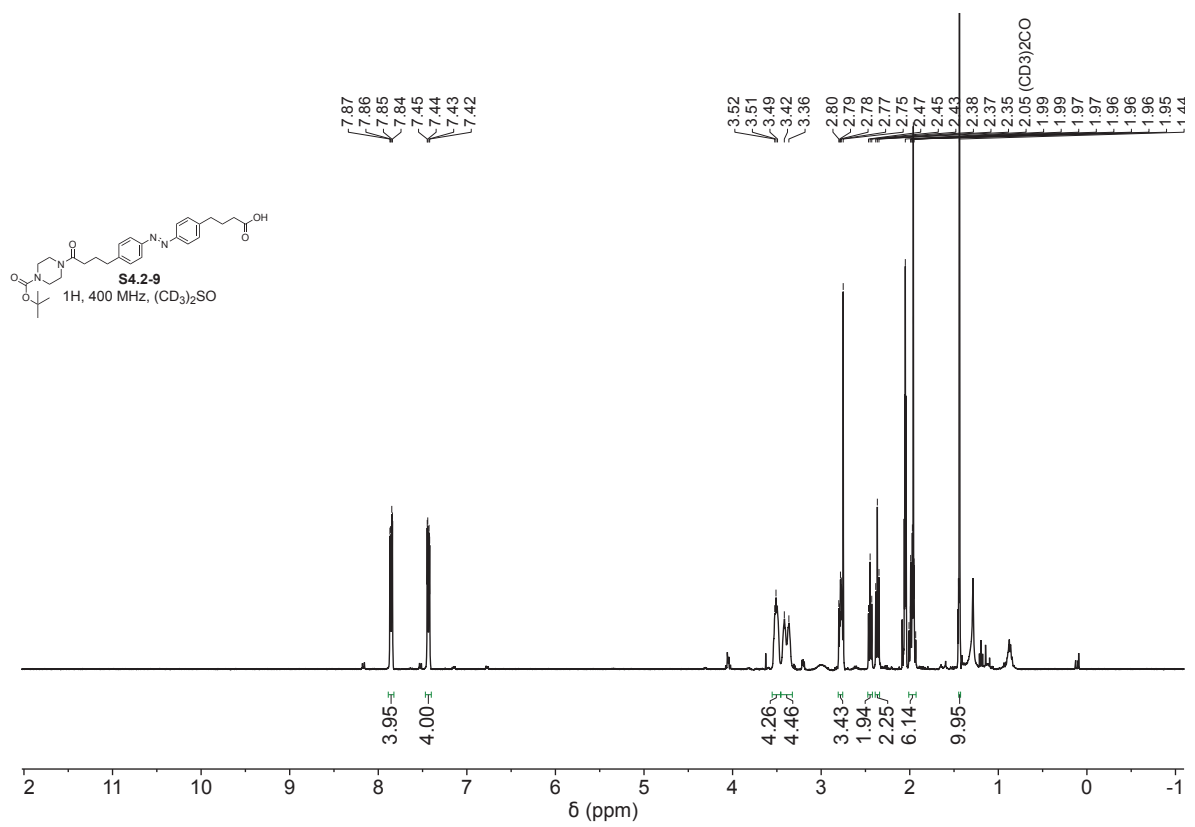
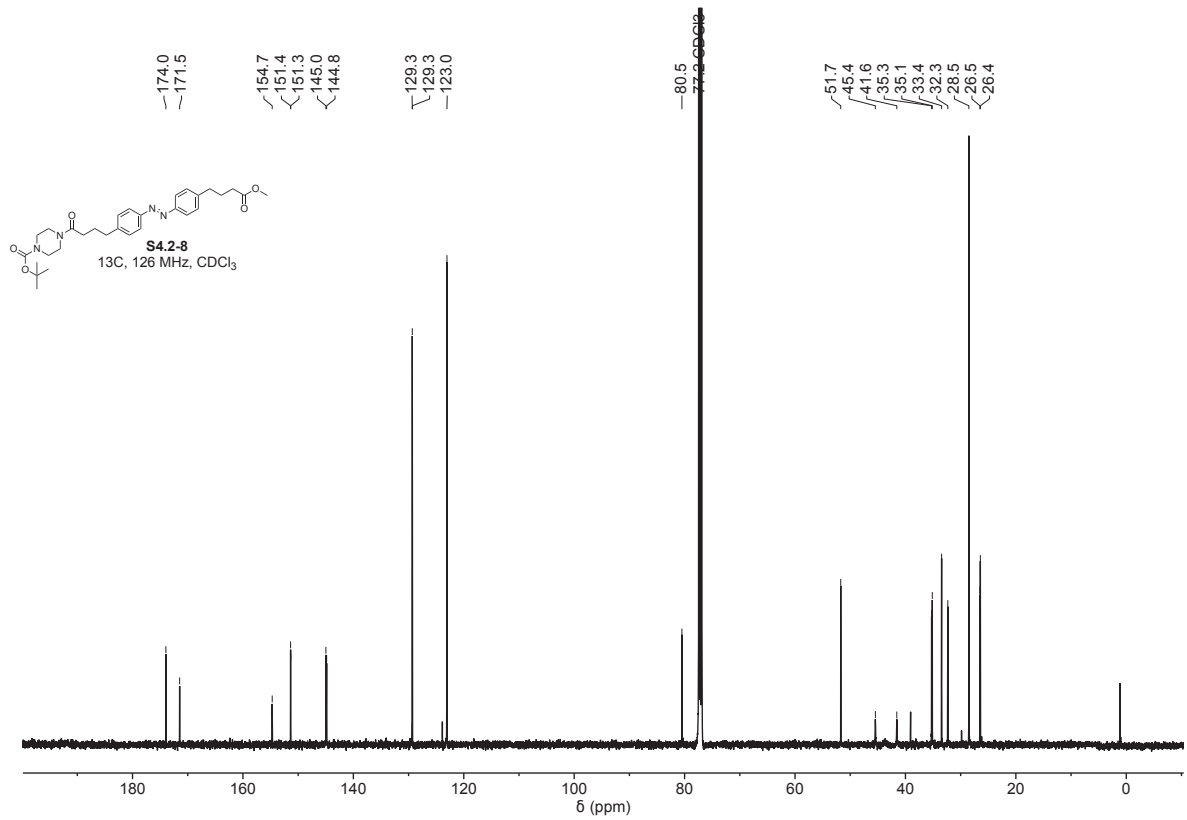


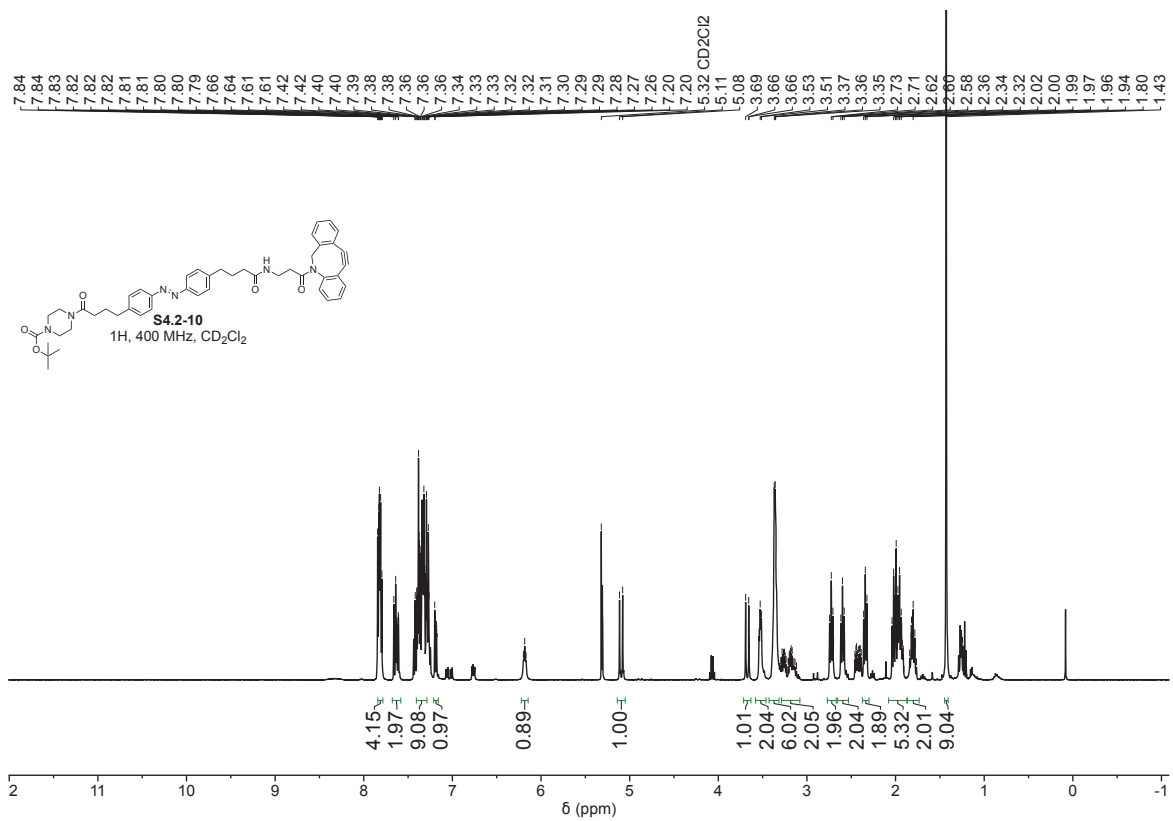
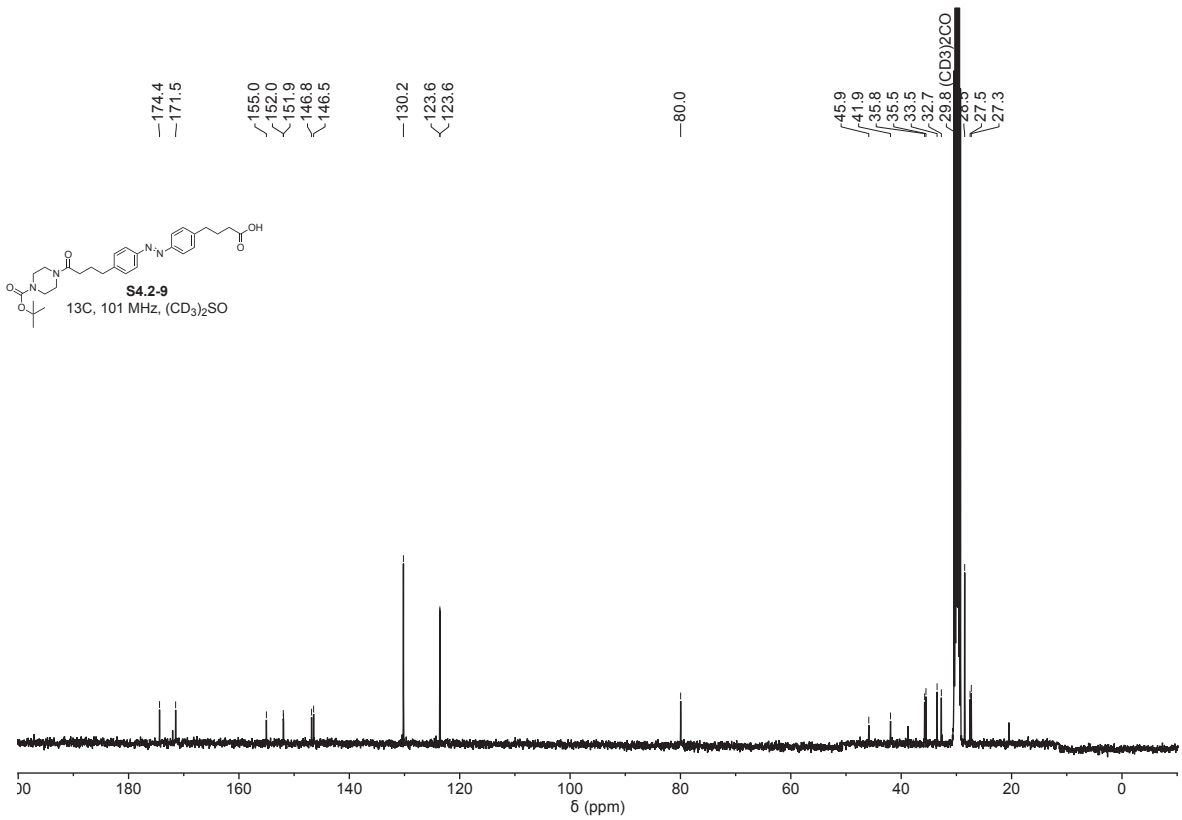


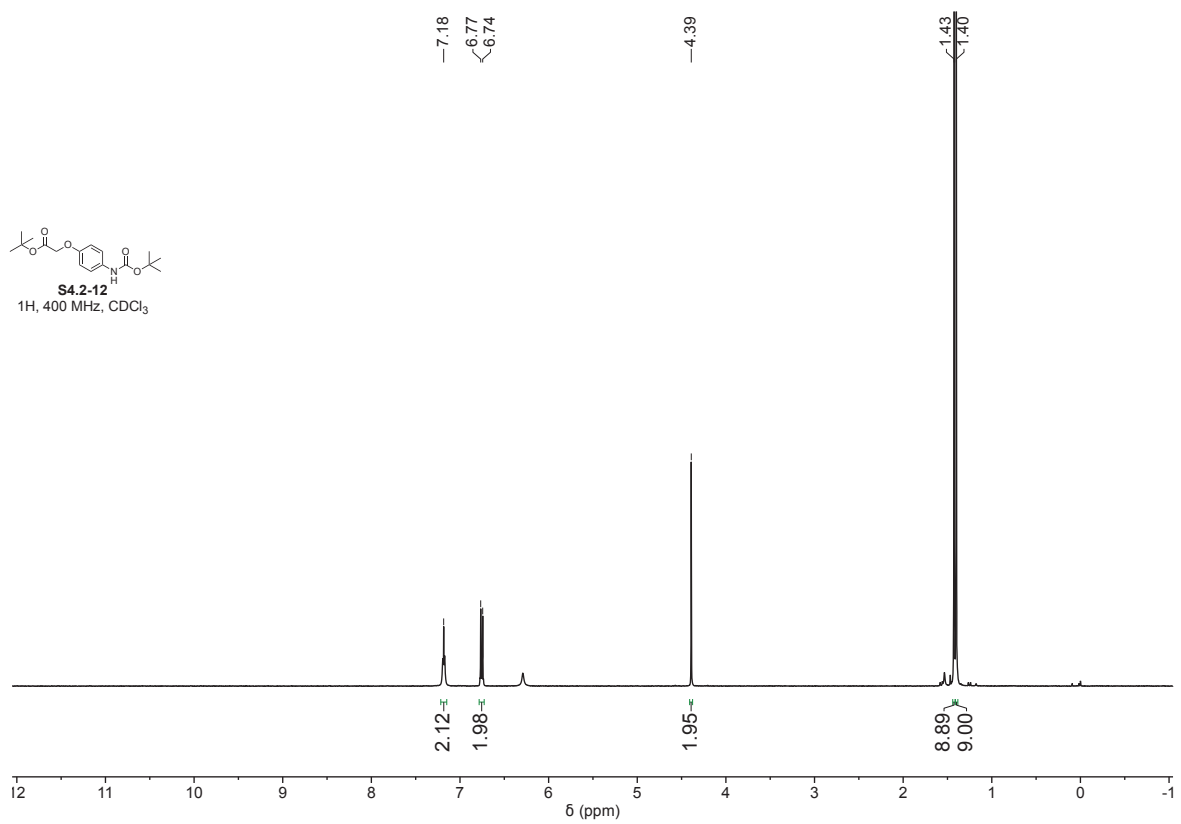
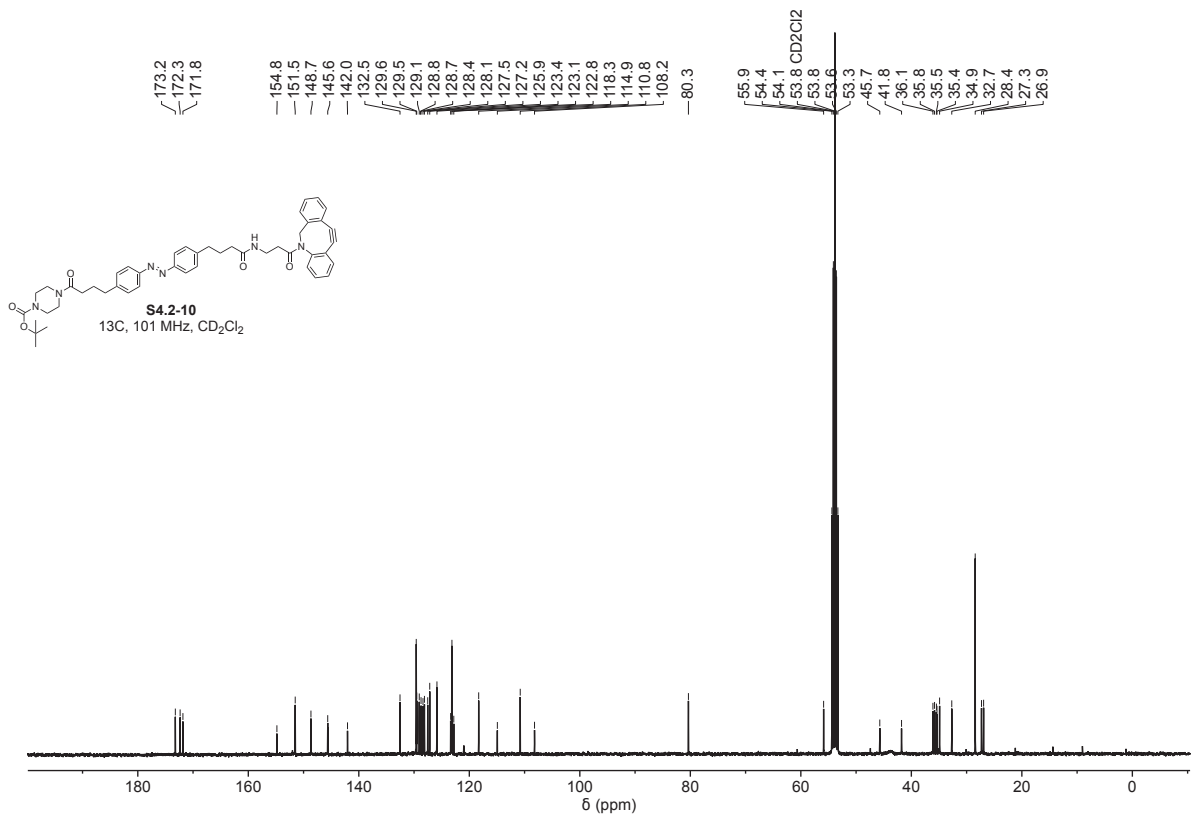




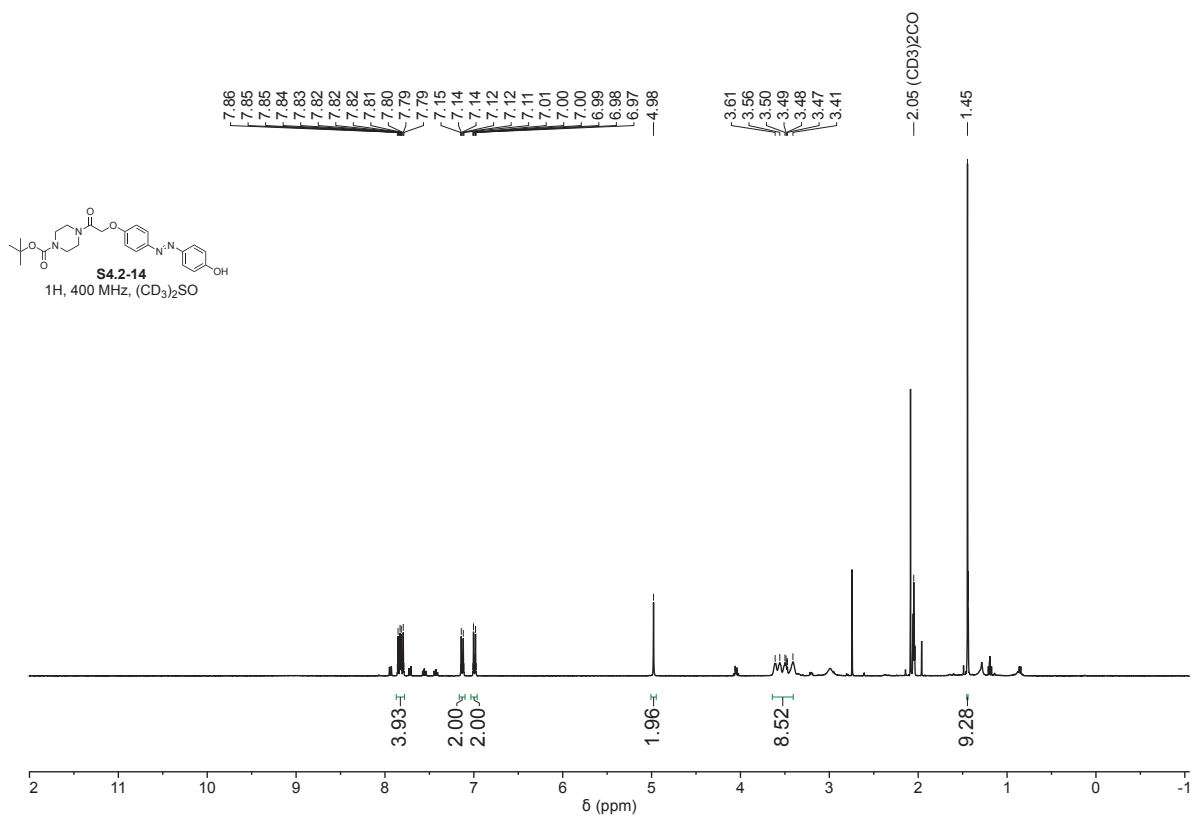
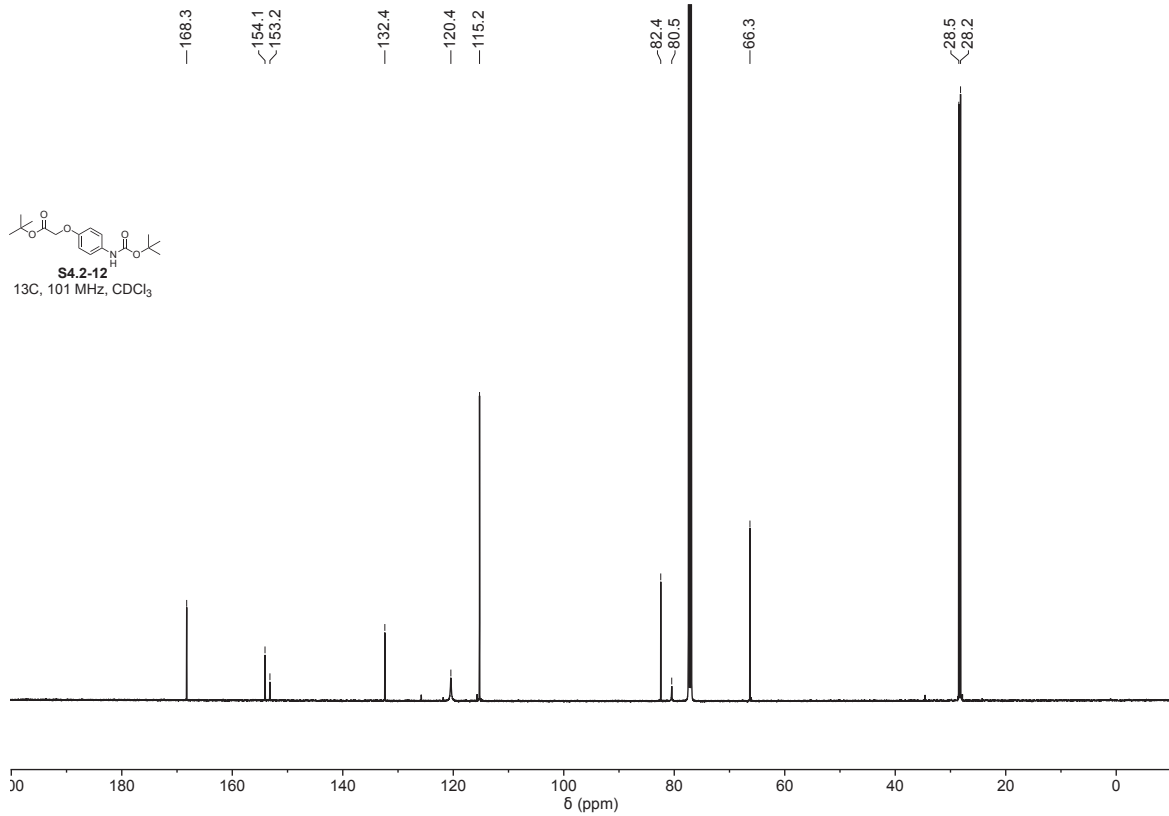


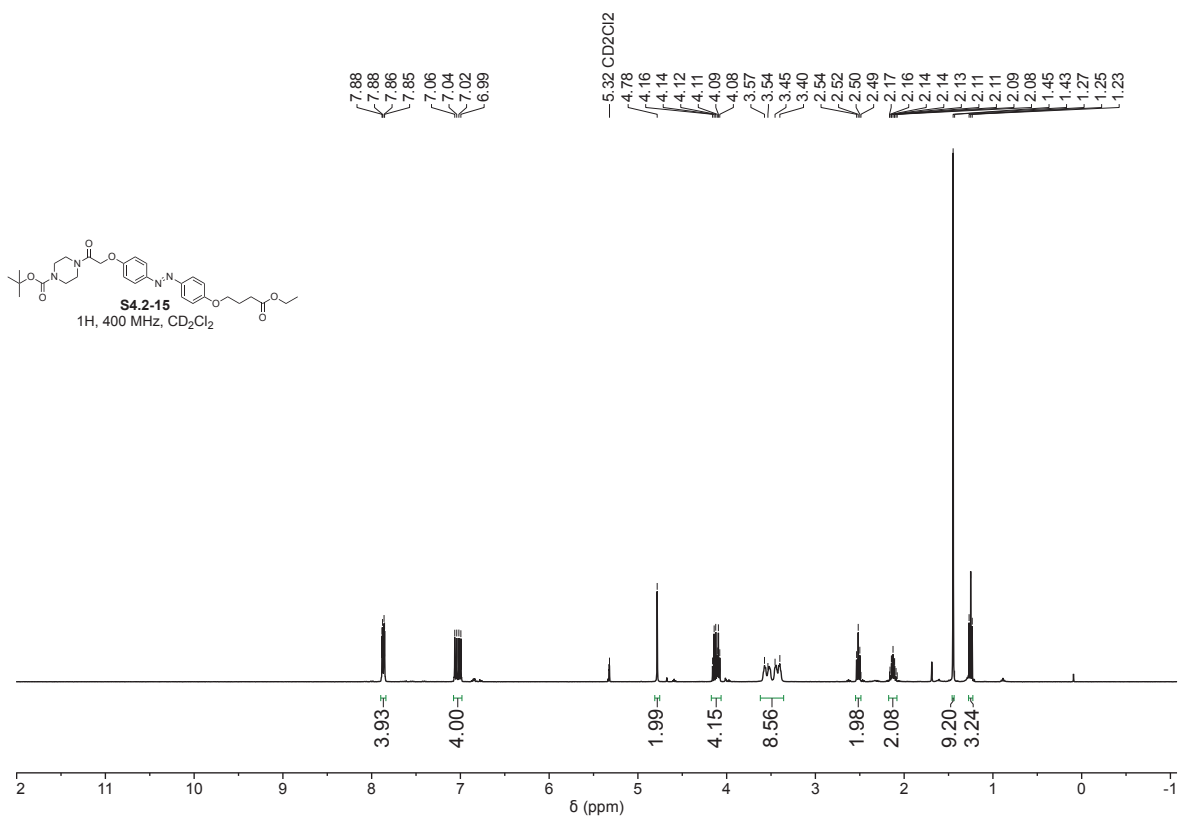
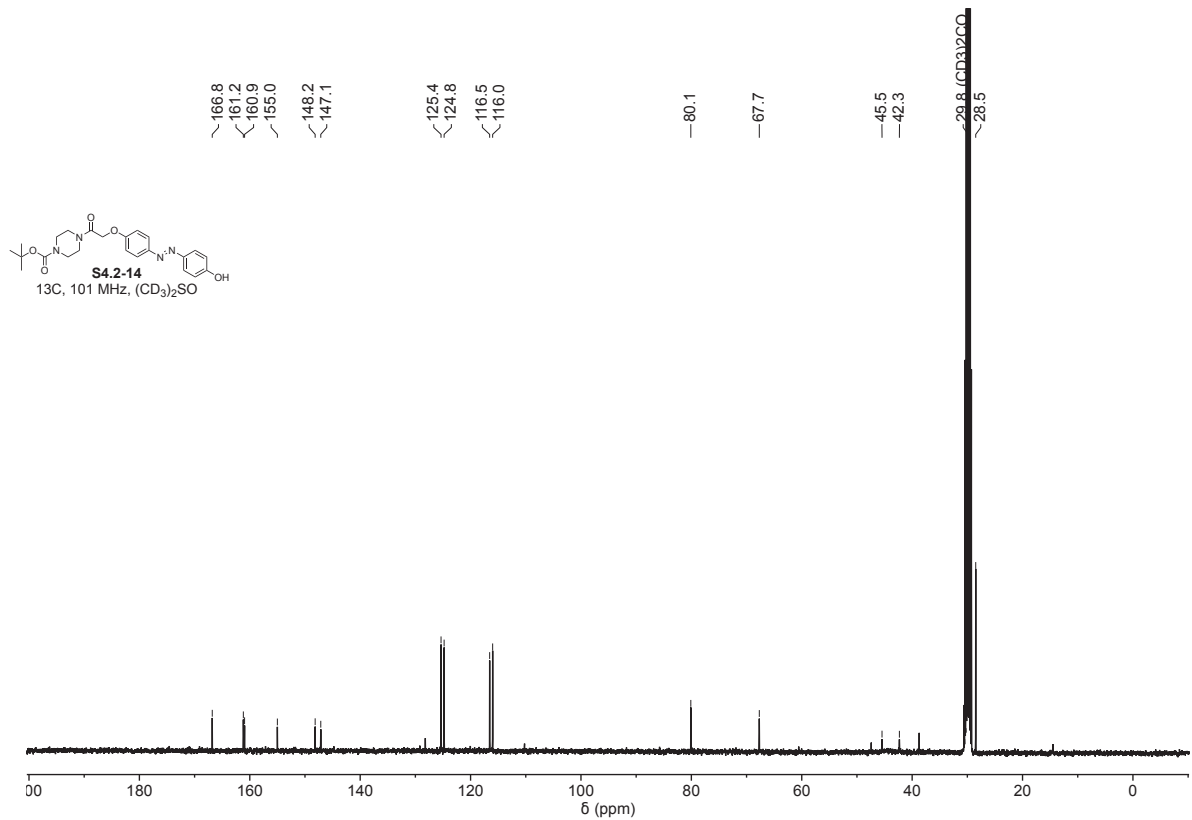


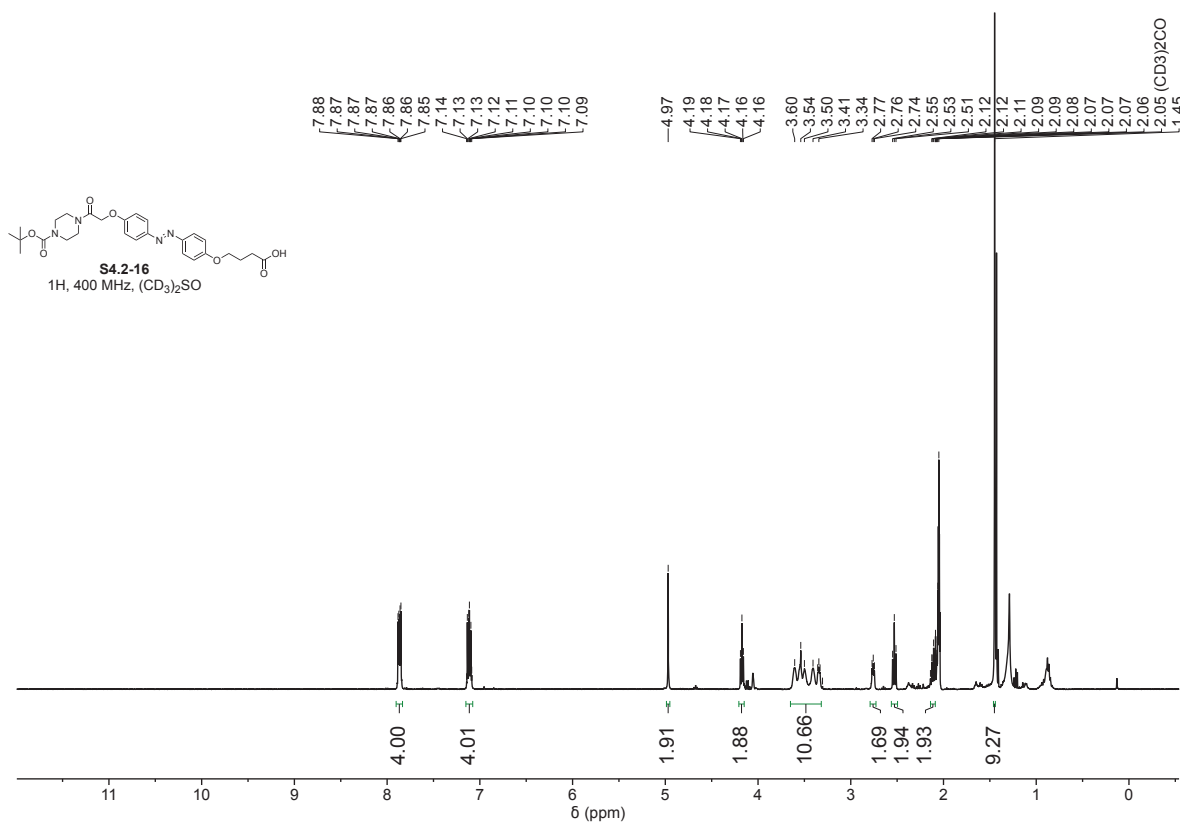
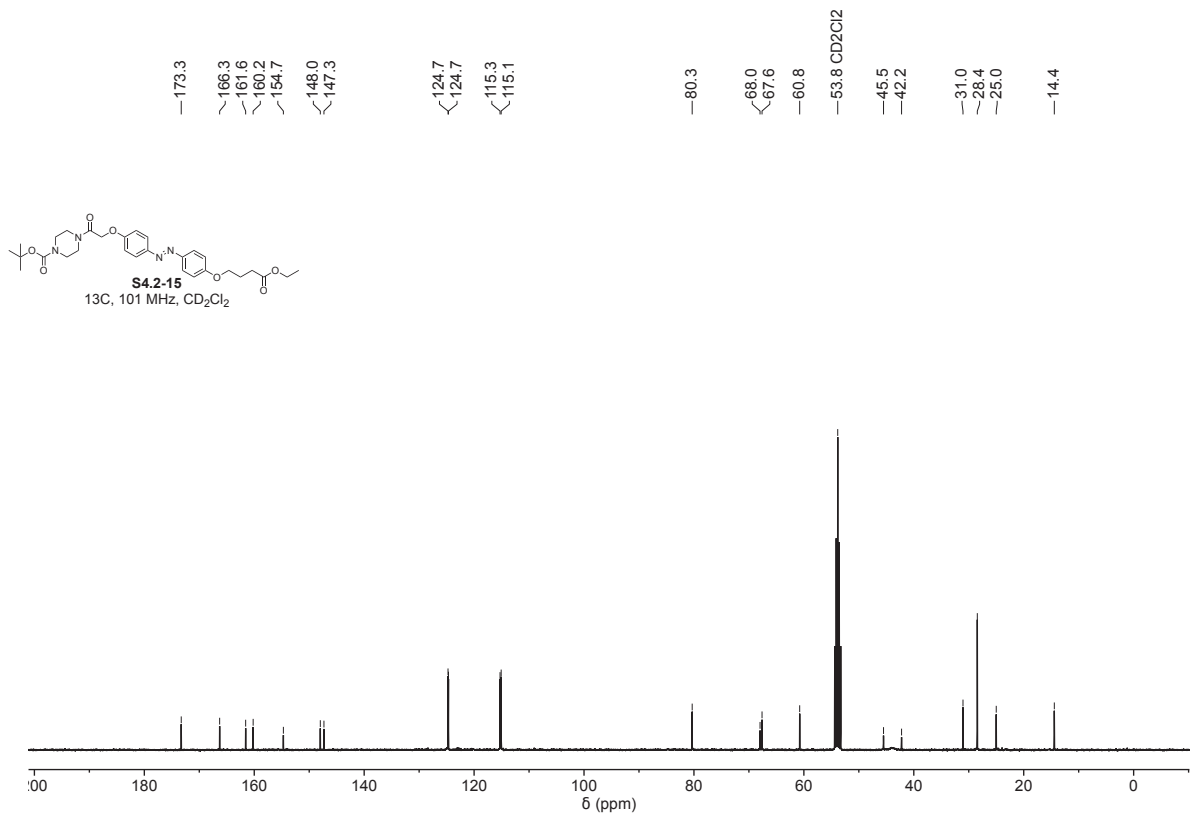


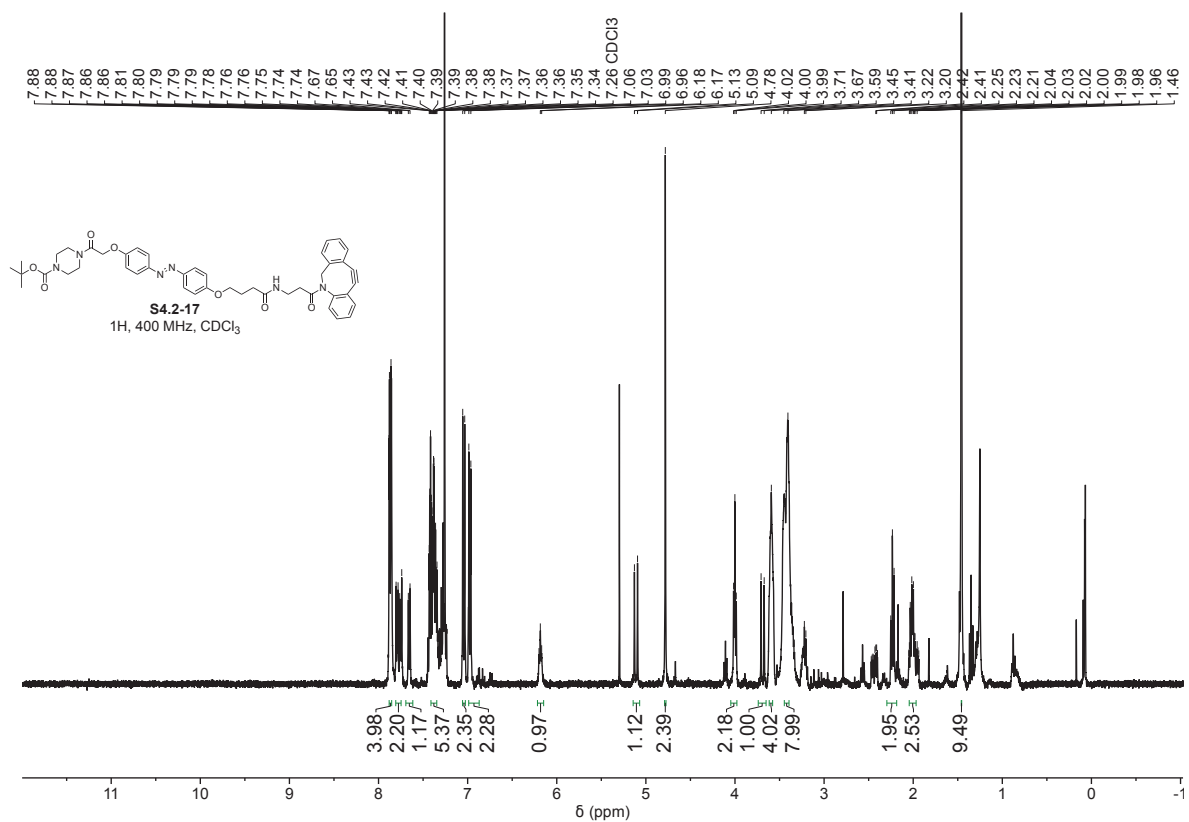
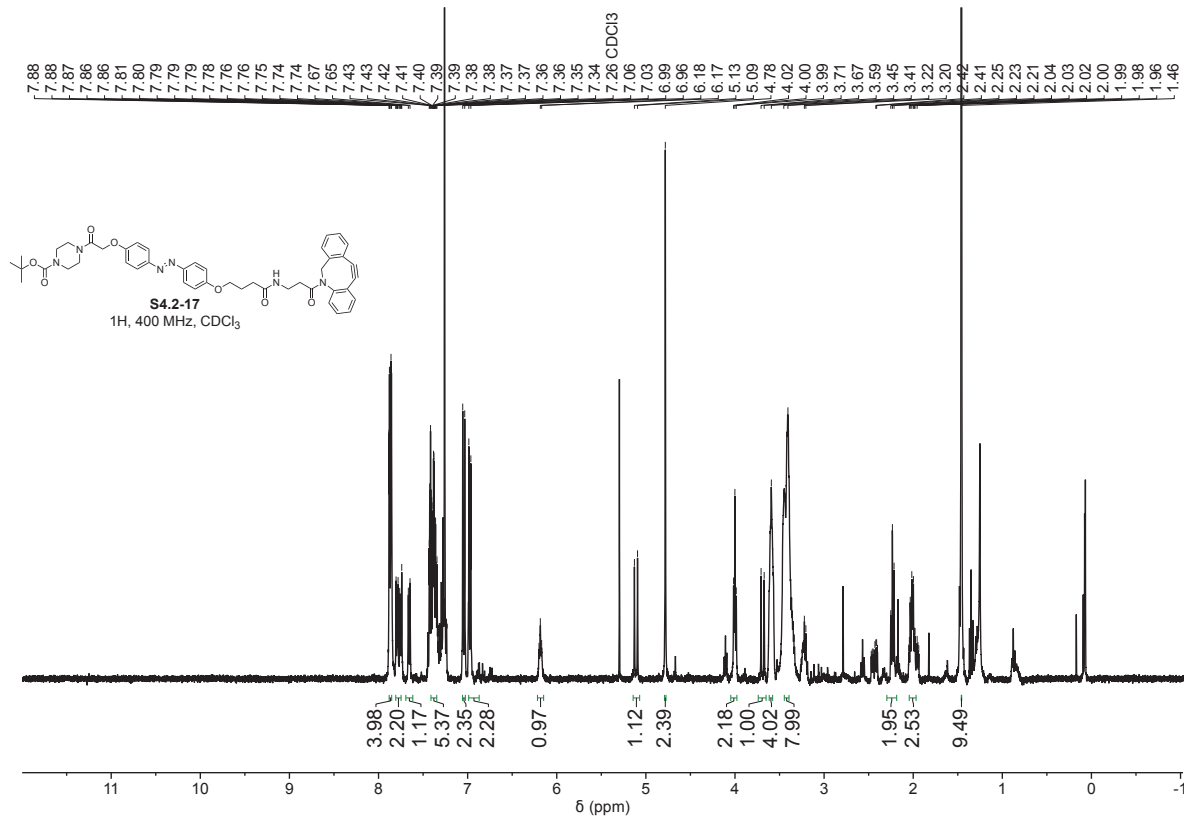










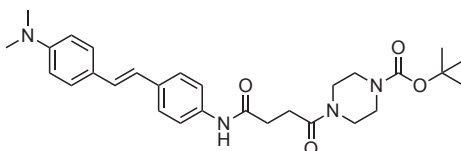


## 7.5 Supporting Information to chapter 5.2

General synthetic and analytical techniques see chapter 7.4.

### Synthesis

*tert*-butyl 4-(4-((4-(4-(dimethylamino)styryl)phenyl)amino)-4-oxobutanoyl)piperazine-1-carboxylate (**S5.2-1**)



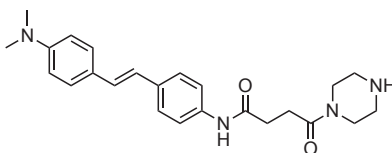
**Stilbene 1** (40 mg, 118  $\mu\text{mol}$ , 1 eq.), *N*-Boc-piperazine (44 mg, 23  $\mu\text{mol}$ , 2 eq.), HBTU (53.8 mg, 142  $\mu\text{mol}$ , 1.2 eq.) and TEA (81.9  $\mu\text{L}$ , 59.8 mg, 591  $\mu\text{mol}$ , 5 eq.) were dissolved in DMF (2 mL) and stirred at room temperature for 16 h. The solvent was removed under reduced pressure and purified via silica gel column chromatography (75% EtOAc in hexane) to yield **S5.2-1** (52.1 mg, 103  $\mu\text{mol}$ , 87%) as a brown solid.

**$^1\text{H-NMR}$**  (500 MHz;  $(\text{CD}_3)_2\text{SO}$ ):  $\delta$  = 9.98 (s, 1H), 7.51 (dd,  $J$  = 60.0, 8.5 Hz, 4H), 7.40 (d,  $J$  = 8.7 Hz, 2H), 7.04 – 6.87 (m, 2H), 6.72 (d,  $J$  = 8.9 Hz, 2H), 3.50 – 3.41 (m, 4H), 3.30 – 3.27 (m, 4H), 2.93 (s, 6H), 2.61 (dt,  $J$  = 37.7, 7.0 Hz, 4H), 1.42 (s, 9H).

**$^{13}\text{C-NMR}$**  (126 MHz;  $(\text{CD}_3)_2\text{SO}$ ):  $\delta$  = 170.9, 170.5, 162.8, 154.3, 150.3, 138.6, 133.0, 127.7, 126.6, 125.7, 123.8, 119.4, 112.78, 79.6, 44.9, 41.4, 38.7, 36.3, 31.8, 31.3, 28.5, 28.0.

**HR-MS** (ESI)  $m/z$ : calculated for  $\text{C}_{29}\text{H}_{39}\text{N}_4\text{O}_4^+$ : 507.29658; found: 507.2966 ( $\text{M} + \text{H}$ ) $^+$ .

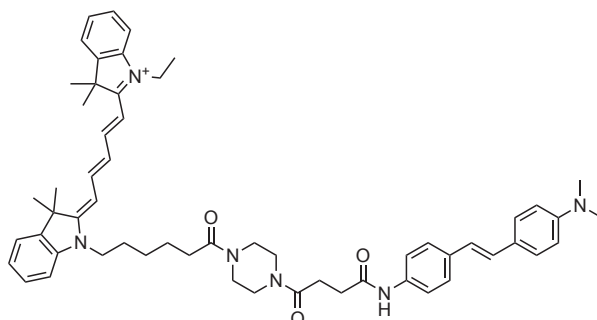
*N*-(4-(4-(dimethylamino)styryl)phenyl)-4-oxo-4-(piperazin-1-yl)butanamide (**DMS**)



TFA (1.5 mL) was added to a solution of **S5.2-1** (20 mg, 39.5  $\mu\text{mol}$ , 1 eq.) in DCM (1.5 mL) at 0  $^\circ\text{C}$  and stirred at 0  $^\circ\text{C}$  for 2 h. The reaction mixture was quenched with aqueous  $\text{NaHCO}_3$  (sat., 60 mL) and extracted with DCM (3 x 70 mL). The combined organic phases were dried ( $\text{MgSO}_4$ ) and concentrated under reduced pressure to yield **DMS** (12.7 mg, 31.2  $\mu\text{mol}$ , 79%) as a yellow solid. **DMS** was used for the next step without further purification.



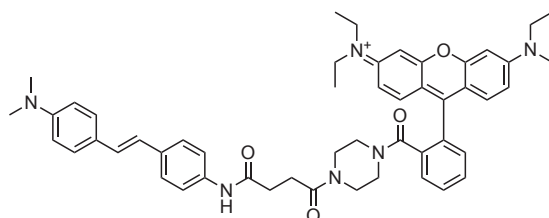
2-((1*E*,3*E*)-5-((*E*)-1-(6-(4-(4-((4-(4-(dimethylamino)styryl)phenyl)amino)-4-oxobutanoyl)piperazin-1-yl)-6-oxohexyl)-3,3-dimethylindolin-2-ylidene)penta-1,3-dien-1-yl)-1-ethyl-3,3-dimethyl-3*H*-indol-1-ium (**Cy5-DMS**)



**DMS** (4 mg, 9.84  $\mu\text{mol}$ , 1 eq.), **Cy5-COOH** (4.9 mg, 9.84  $\mu\text{mol}$ , 1 eq.), HBTU (4.5 mg, 11.8  $\mu\text{mol}$ , 1.2 eq.) and TEA (7  $\mu\text{L}$ , 5 mg, 49.2  $\mu\text{mol}$ , 5 eq.) were dissolved in DMF (1.0 mL) and stirred at room temperature for 16 h. The reaction mixture was diluted with 0.1% FA in 1:1 water:MeCN (300  $\mu\text{L}$ ) purified *via* reversed phase preparative HPLC (9:1 water (0.1% formic acid) / MeCN (0.1% formic acid) to MeCN (0.1% formic acid) over 27 min) to yield **Cy5-DMS** (1.9 mg, 2.1  $\mu\text{mol}$ , 22%) as a blue solid.

**HR-MS** (ESI)  $m/z$ : calculated for  $\text{C}_{57}\text{H}_{69}\text{N}_6\text{O}_3^+$ : 885.54257; found: 885.5427 ( $\text{M} + \text{H}$ )<sup>+</sup>.

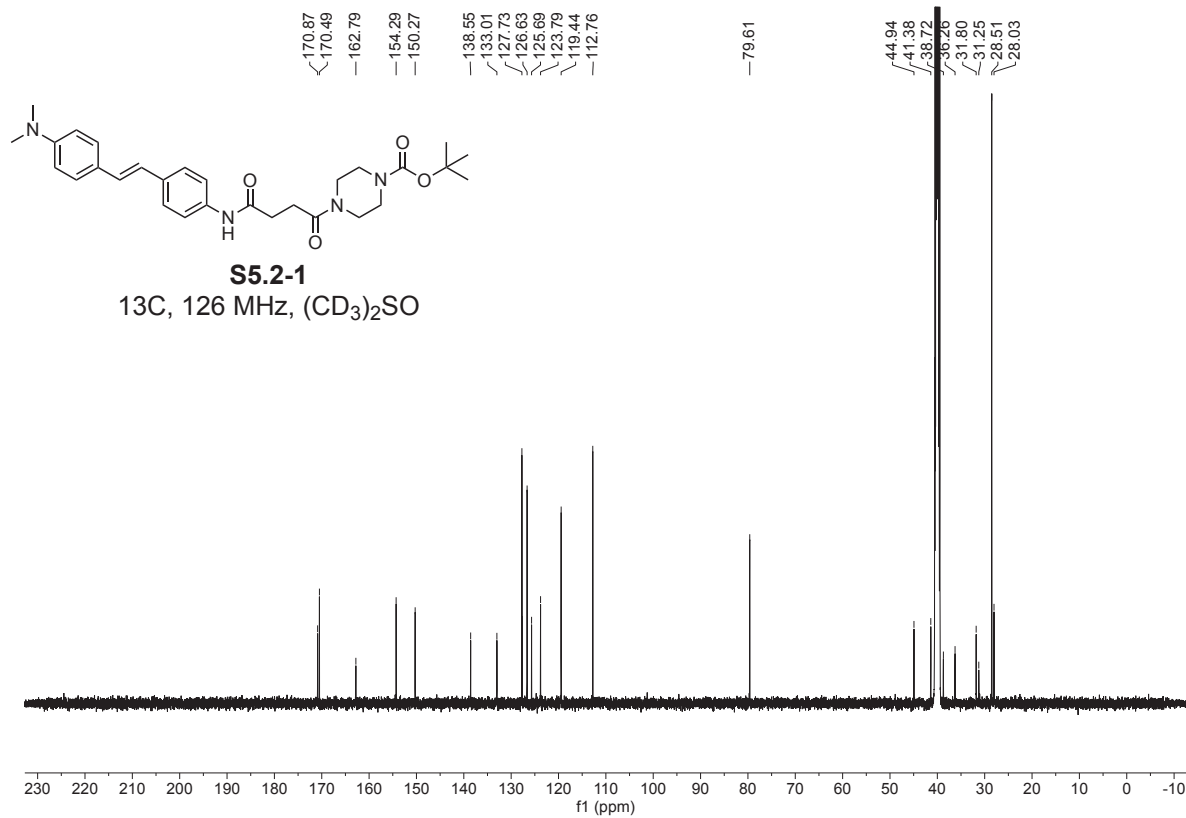
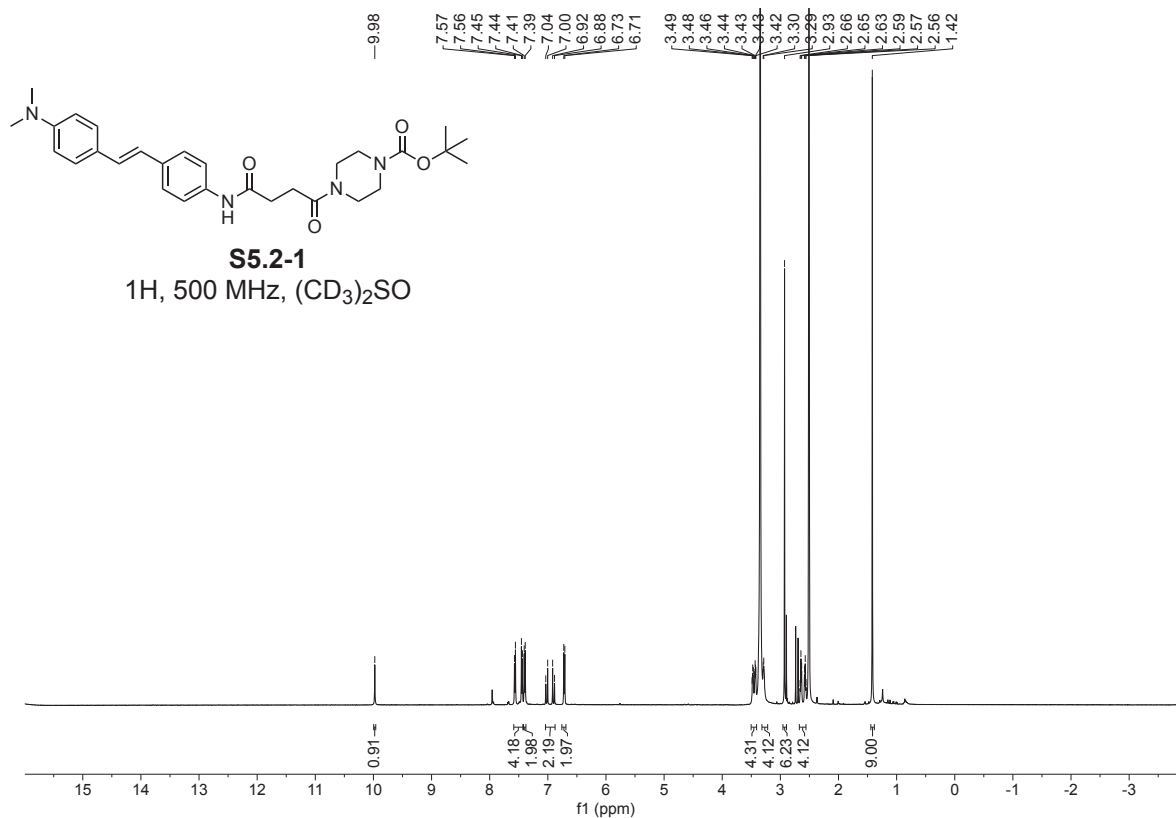
*N*-(6-(diethylamino)-9-(2-(4-(4-((4-(4-(dimethylamino)styryl)phenyl)amino)-4-oxobutanoyl)piperazine-1-carbonyl)phenyl)-3*H*-xanthen-3-ylidene)-*N*-ethylethanaminium (**RhB-DMS**)



**DMS** (4 mg, 9.84  $\mu\text{mol}$ , 1 eq.), **Rhodamine B** (4.7 mg, 9.84  $\mu\text{mol}$ , 1 eq.), HBTU (4.5 mg, 11.8  $\mu\text{mol}$ , 1.2 eq.) and TEA (7  $\mu\text{L}$ , 5 mg, 49.2  $\mu\text{mol}$ , 5 eq.) were dissolved in DMF (1.0 mL) and stirred at room temperature for 16 h. The reaction mixture was diluted with 0.1% FA in 1:1 water:MeCN (300  $\mu\text{L}$ ) purified *via* reversed phase preparative HPLC (9:1 water (0.1% formic acid) / MeCN (0.1% formic acid) to MeCN (0.1% formic acid) over 27 min) to yield **RhB-DMS** (3.5 mg, 4.2  $\mu\text{mol}$ , 43%) as a pink solid

**HR-MS** (ESI)  $m/z$ : calculated for  $\text{C}_{52}\text{H}_{59}\text{N}_6\text{O}_4^+$ : 831.45923; found: 831.4590 ( $\text{M} + \text{H}$ )<sup>+</sup>.

NMR spectra:



## 8 Abbreviations

AcOH (acetic acid)	fs TAS (femtosecond transient absorption spectroscopy)
AK (4-(4-((4-butylphenyl)diazenyl)phenyl)-1-(piperazin-1-yl)butan-1-one)	GFP (green fluorescent protein)
AN ( <i>N</i> -(4-((4-acetamidophenyl)diazenyl)phenyl)-4-oxo-4-(piperazin-1-yl)butanamide)	GPCR (g-protein coupled receptor)
AO (4-(4-((4-methoxyphenyl)diazenyl)phenoxy)-1-(piperazin-1-yl)butan-1-one)	HBTU ((2-(1 <i>H</i> -benzotriazol-1-yl)-1,1,3,3-tetramethyluronium hexafluorophosphate)
AO(OMe) <sub>4</sub> (4-(4-(3,5-dimethoxy-4-((2,4,6-trimethoxyphenyl)diazenyl)phenoxy)butanoyl) piperazine)	(HPLC) high performance liquid chromatography
ATP (adenosine triphosphate)	(HRMS) High-resolution mass spectrometry
BAG (benzyl guanine azobenzene glutamate)	<i>i</i> PrOH (propan-2-ol)
BANG (benzyl guanine azobenzene Nile blue glutamate)	LOV (light-oxygen voltage sensors)
BBQ (black berry quencher)	MB (methylene blue)
BGAG (benzyl guanine azobenzene glutamate)	MeCN (acetonitrile)
BHQ (black hole quencher)	MeOH (methanol)
Boc ( <i>tert</i> -butyloxycarbonyl)	mGluR2 (metabotropic glutamate receptor)
CAN (ceric ammonium nitrate)	NA (numerical aperture)
COT (cyclooctatetraene)	NB (nile blue)
CV (cyclic voltammetry)	NHS ( <i>N</i> -hydroxysuccinimide)
DABCYL	NIR (near-infrared)
DAD (diode array detector)	NMR (nuclear magnetic resonance)
DBCO (dibenzocyclooctyne)	ONB ( <i>ortho</i> nitrobenzyl)
DCA (diacyl-cyclooctatetraene)	PALM (photoactivatable localization microscopy)
DCM (dichloromethane)	PAL (photoaffinity label)
DIPEA (diisopropylethylamine)	PCL (photochromic ligand)
DMF (dimethylformamide)	PEG (polyethylene glycol)
DNA PAINT	PET (photoinduced electron transfer)
ESI (electron spray ionization)	PHOTAC (Photochemically Targeting Chimeras)
EtOAc (ethyl acetate)	POI (protein of interest)
EYpip (Eosin Y- piperazineamide);	PORTL (photoswitchable orthogonal remotely tethered ligands)
Fc (Ferrocene)	FCS (fluorescence correlation spectroscopy)
Flpip (fluorescein - piperazineamide).	PSS (photostationary state)
FRET (Förster resonance energy transfer)	PST2 (2-methoxy-5-((3,4,5-trimethoxyphenyl)diazenyl)aniline)
	PTL (photoswitchable tethered ligand)

RhBpip (Rhodamine B - piperazineamide);  
ROXS (reducing and oxidizing system)  
SCE (standard calomel electrode)  
SMLM (single molecule localization microscopy)  
SP-MC (spyropropan-merocyanine)  
SRhBpip  
(Sulforrhodamine B - piperazineamide);  
STED (stimulated emission depletion)  
STORM (Stochastic optical reconstruction microscopy)  
SWV (square wave voltammetry)

TEA (triethylamine)  
TET triplet energy transfer  
TFA (trifluoroacetic acid)  
THF (tetrahydrofuran)  
TLC (thin layer chromatography)  
TSQ (triplet state quencher)  
TSTU (*N,N,N',N'*-tetramethyl-*O*-(*N*-succinimidyl)uronium tetrafluoroborate)  
 $\tau_{fl}$  (fluorescence lifetime)  
 $\phi_{fl}$  (fluorescence quantum yield)  
 $\phi_{ISC}$  (Inter system crossing quantum yield)

## 9 Acknowledgements

First, I thank my supervisor **Dr. Oliver Thorn-Seshold** for accepting me as a PhD student in his group and pushing me to the limit (and over it) of what I knew and could. My project turned out to be different, much broader, more interdisciplinary, and more successful to what I (and you) expected, and I am confident that it will fly high in the end. It has been a challenging time, but I grew as a scientist and a person.

Furthermore, I want to thank **Prof. Dr. Don Lamb** for accepting to be second assessor and chair in my PhD thesis committee, and the other members of my thesis committee: **Prof. Dr. Philip Tinnefeld**, **Prof. Dr. Achim Hartschuh**, **Prof. Dr. Ralph Jungmann** and **Prof. Dr. Stefan Hecht**.

I thank my fantastic collaboration partners, without whom my PhD project could not have been that successful. Special thanks are going to **Dr. Viktorija Glembockyte**, who introduced me to the field of photophysics. It was a very great collaboration; I hope it will also pay off also for you.

I want to thank all current and former members of the TS group for making the last 4.5 years a special time that I do not want to miss. Huge thanks are going to **Lukas**, for not only sharing my fascination about science gossip but also for sharing his flat during the first months of my PhD. I hope it was only the start of a great friendship. I also want to acknowledge **Li**, who was and still is the glue who keeps the group together; I am very proud that you have been my Senpai!

I am very grateful to the **Boehringer Ingelheim Fonds** who supported me throughout my PhD financially and personal. The network you built is awesome; I am very proud to be part of it.

I don't want to miss the opportunity to thank all those people who accompanied me on my way before starting my PhD; no matter whether my time in Munich, Heidelberg or Zurich, especially I want to thank **Robert** and **Xiao**; both of you made huge contributions to my scientific and personal development.

Weiterhin möchte ich meiner Familie, Freunden und all denen Danken, die einen Anteil an meinem bisherigen Werdegang (fachlich oder persönlich) hatten.

Ein sehr großes Dankeschön gilt meinen Eltern **Ottilie** und **Paul**. Vielen Dank für eure andauernde Unterstützung in allen Belangen und euer uneingeschränktes Vertrauen in mich und all meine Entscheidungen, auch wenn Ihr sie teilweise für Größenwahnsinnig gehalten habt (und sie das auch waren). Ihr habt den Weg bereitet für alles, was ich erreichen konnte. Ohne euch wäre ich heute nicht an diesem Punkt.

Weiterhin möchte ich meinen Schwiegereltern **Angelika** und **Luis** danken. Dafür wie herzlich Ihr mich bei euch aufgenommen habt, mir den Rücken im Alltag freigehalten habt und natürlich die herausragenden Lunchpakete für die Mittagspause.

Ganz besonderer Dank gilt meiner Frau **Maria**. Vielen Dank für deine Unterstützung in den letzten sechs Jahren, dein Verständnis für lange Labortage, Wochenendarbeit und schlechte Laune (wenn die Wissenschaft nicht so wollte wie ich), das Durchhalten/Aufmuntern und Ablenken in den stressigen Monaten des Zusammenschreibens und das du dir meinen Wissenschaftsbullshit ohne Murren angehört hast. Vielen Dank, dass du **Josephine** und **Charlotte** in mein Leben gebracht hast. Ihr habt mir gezeigt was wirklich wichtig ist. Ich kann gar nicht in Worte fassen, was Ihr mir bedeutet: Ich liebe euch!

Ich freue mich auf die nächsten gemeinsamen Jahre zu viert (und mehr), die neuen Aufgaben, Kapitel und Momente, im Job, beim Hofbauer und im Familienleben.

Ich kann es kaum erwarten!